



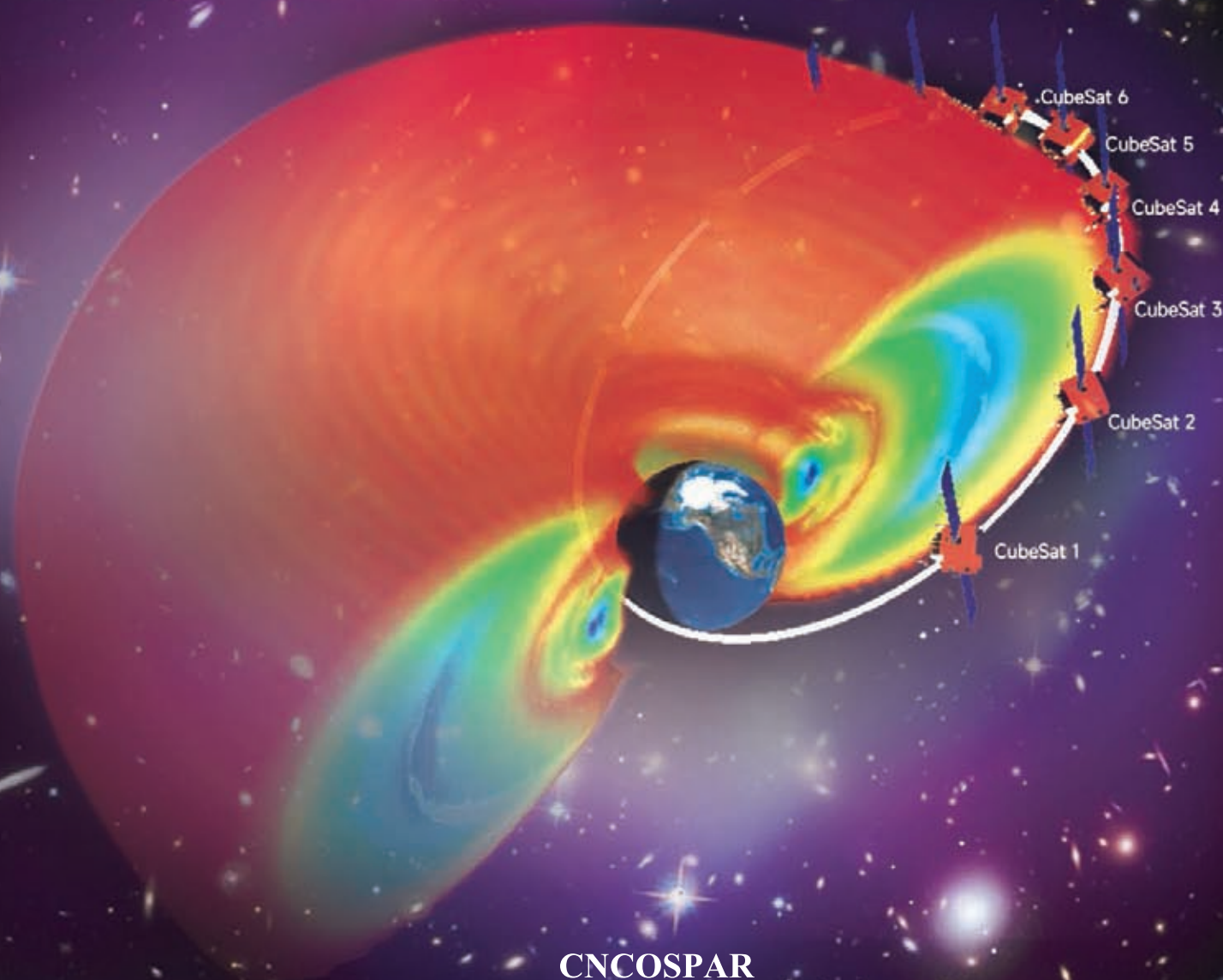
SPACE SCIENCE ACTIVITIES IN CHINA

National Report 2020—2022

Chief Editor: GUO Huadong

Deputy Chief Editor: WU Ji, LI Lei

Editorial Staffs: SUN Weiyong, SONG Yana



CNCOSPAR
JULY 2022

Members of the Chinese National Committee for COSPAR (CNCOSPAR)

President

GUO Huadong, Academician, Chinese Academy of Sciences (CAS)

Vice Presidents

HUANG Weidong Researcher
LI Ming Researcher, China Academy of Space Technology (CAST)
WANG Qi'an Researcher, National Remote Sensing Center, Ministry of Science and Technology (MOST)
YU Qi Deputy Director General, Department of System Engineering, China National Space Administration (CNSA)

Members

AI Guoxiang Academician, National Astronomical Observatories, CAS
HU Wenrui Academician, Institute of Mechanics, CAS
WANG Shui Academician, University of Science and Technology of China (USTC)
OUYANG Ziyuan Academician, National Astronomical Observatories, CAS
GONG Huixing Academician, Shanghai Institute of Technical Physics, CAS
TU Chuanyi Academician, Peking University
LÜ Daren Academician, Institute of Atmospheric Physics, CAS
LI Tipei Academician, Institute of High Energy Physics, CAS
GU Yidong Academician, Technology and Engineering Center for Space Utilization, CAS
WU Yirong Academician, Institute of Electronics, CAS
GUO Huadong Academician, Institute of Remote Sensing and Digital Earth, CAS
WANG Weihua Academician, Institute of Physics, CAS
ZHOU Zhixin Academician
WANG Jianyu Academician, Chinese Academy of Sciences Shanghai Branch
DOU Xiankang Academician, Wuhan University
CHANG Jin Academician, Purple Mountain Observatory, CAS
WANG Chi Academician, National Space Science Center, CAS
XU Ronglan Researcher, National Space Science Center, CAS
XIAO Zuo Professor, Peking University
CAI Zhenbo Researcher, China Academy of Space Technology (CAST)
LI Yinghui Researcher, Beijing Institute of Space Medico-Engineering
GAN Weiqun Researcher, Purple Mountain Observatory, CAS
YAN Yihua Researcher, National Astronomical Observatories, CAS
ZHANG Xingwang Researcher, Institute of Semiconductors, CAS

WANG Jingsong	Researcher, China Meteorological Administration
CAO Jinbin	Professor, Beihang University
FANG Guangyou	Researcher, Institute of Electronics, CAS
WANG Shijie	Researcher, Institute of Geochemistry, CAS
FENG Xueshang	Researcher, National Space Science Center, CAS
DONG Xiaolong	Researcher, National Space Science Center, CAS
LU Feng	Researcher, Institute of Geographical Sciences and Natural Resources Research, CAS
JIANG Luhua	Researcher, Institute of High Energy Physics, CAS
GAO Ming	Researcher, Technology and Engineering Center for Space Utilization, CAS
LONG Mian	Researcher, Institute of Mechanics, CAS
CHEN Hongbin	Researcher, Institute of Atmospheric Physics, CAS
LU Jinying	Senior Engineer, China Academy of Space Technology (CAST)
SUN Yeqing	Professor, Institute of Environmental System Biology, Dalian Maritime University
PAN Mingxiang	Researcher, Institute of Physics, CAS
WEI Jianyan	Researcher, National Astronomical Observatories, CAS
ZHANG Tao	Researcher, Shanghai Institute of Technical Physics, CAS
DING Mingde	Professor, Department of Astronomy, Nanjing University
LI Chunlai	Researcher, National Astronomical Observatories, CAS
HUANG Maohai	Researcher, National Astronomical Observatories, CAS
XUE Hongwei	Shanghai Institute for Biological Sciences, CAS
LIU Lin	Professor, Department of Astronomy, Nanjing University
XU Minqiang	Professor, Harbin Institute of Technology
DENG Yulin	Professor, Beijing Institute of Technology
LIU Siqing	Researcher, National Space Science Center, CAS
SUN Yueqiang	Researcher, National Space Science Center, CAS

Secretary General

WU Ji, Researcher, National Space Science Center, CAS

Deputy Secretary General

LI Lei, Researcher, National Space Science Center, CAS

ZHUANG Yan, Division Director, Bureau of International Cooperation, CAS

YAN Jingye, Researcher, National Space Science Center, CAS

Secretariat Contact

LI Xiaoyu, XU Yongjian

CN-COSPAR Secretariat

c/o NSSC, No.1 Nanertiao, Zhongguancun, 100190, Beijing, China

Tel: 86 10 6258 6404

Fax: 86 10 6263 2257

E-mail: xuyongjian@nssc.ac.cn

Preface

The past two years has witnessed the smooth implementation of dedicated Chinese space science missions, the deep space exploration program, and the manned spaceflight program. Despite the impact of Covid-19, several missions in the framework of the second phase of the Strategic Priority Program on Space Science (SPP II) have been launched including the Gravitational wave high-energy Electromagnetic Counterpart All-sky Monitor (GECAM), the Taiji-1 (the first technology demonstration mission of Taiji Program) and the Scientific Satellite for Sustainable Development Goals-1 (SDGSAT-1), while other mission are progressing well, e.g. the Advanced space-based Solar Observatory (ASO-S), the Einstein Probe (EP), and Solar wind Magnetosphere Ionosphere Link Explorer (SMILE), an ESA-China joint mission.



In the field of deep space exploration, the Chang'e 5 mission has successfully brought back 1731 gram lunar samples to Earth in 2020 which is supposed to be the youngest samples returned to Earth: just 1.2 billion years old. The Tianwen-1 Mars exploration mission has been successfully implemented with orbiting, landing and roving all in one mission. The Zhurong rover named after the Chinese Fire God has also produced substantial scientific data and roved more than 1000 meter on the red planet. In the field of manned spaceflight, the construction of the Chinese Space Station (CSS), kicked off by the launch of the core module in 2021, is underway, and Chinese Astronauts extended their continuous stay in space up to 6 months. The construction of CSS will be finished this year with two experiment modules attached to it soon.

With the support of the Chinese Academy of Sciences, the dedicated space science program in China is taking shape. Solid achievements have been achieved by the first phase of the Strategic Priority Program on Space Science (SPP I) which includes 4 space science missions, e.g. the Dark Matter Particle Explorer (DAMPE), ShiJian-10 (SJ-10), Quantum Experiments at Space Scale (QUESS) and Hard X-ray Modulation Telescope (HXMT). In May 2018, the second phase of the Strategic Priority Program on Space Science (SPP II) was officially approved by the Chinese Academy of Sciences which focuses on two major themes: How the universe and life originate and evolve, and what is the relationship between the solar system and human beings. Currently, the mission selection for the third phase of the Strategic Priority Program on Space Science (SPP III) is underway to identify and foster the future scientific missions.

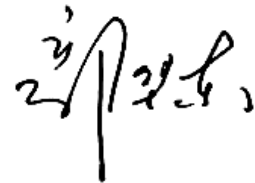
As stated in the *White Paper on China's Space Program: A 2021 Perspective*, in the next five years, China will continue with the research and development of programs such as the satellite for space gravitational wave detection, EP, ASO-S, SMILE, and the high precision magnetic field measurement satellite, focusing on the subjects of the extreme universe, ripples in time and space, the panoramic view of the sun and the Earth, and the search for habitable planets. China will continue to explore frontier areas and research into space astronomy, heliophysics, lunar and pla-

netary science, space earth sciences, and fundamental physics and life sciences in space, to generate more original scientific findings.

In this report, the PIs of scientific missions and the leading experts in various fields of space science in China will present the major programs, the highlights of mission achievements, the progress of the missions to be launched, the future mission planning, and the recent progress of individual disciplines.

It is noteworthy that the Chinese space science community attaches great importance to international cooperation and the Chinese Academy of Sciences is devoted to promoting international cooperation from the payload level all the way to the mission level, as demonstrated in the SMILE mission. We are willing to strengthen cooperation with interested international partners to continuously expand the frontiers of human knowledge.

I wish you can get a general picture of the recent progress in space research in China and also invite you to use the published data of the Chinese missions.



Prof. GUO Huadong
Academician, Chinese Academy of Sciences
President, Chinese National Committee for COSPAR

Photos

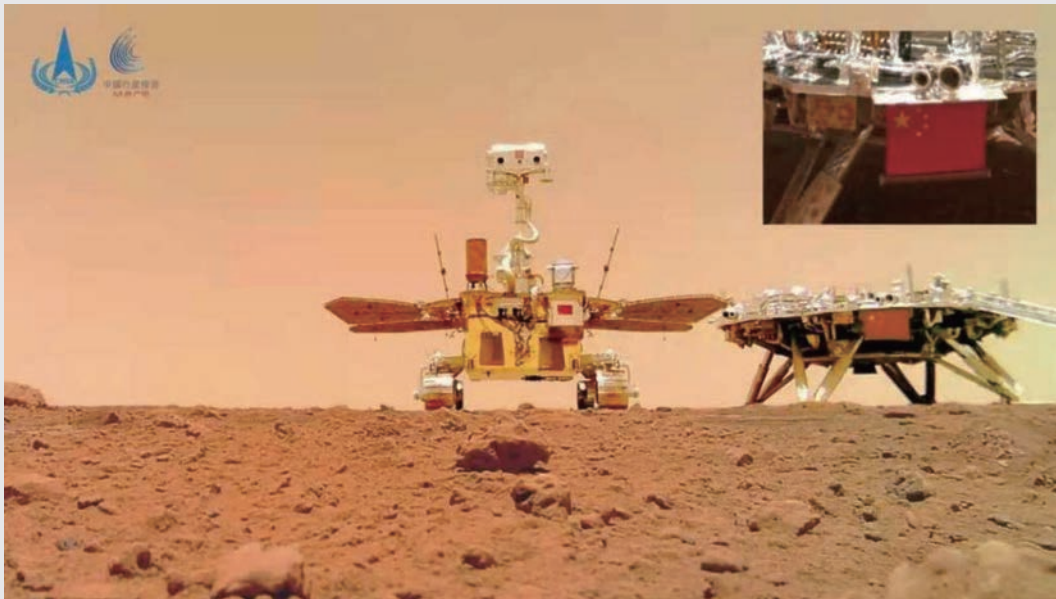


Launch of the Tianhe core module of China Space Station on 29 April 2021

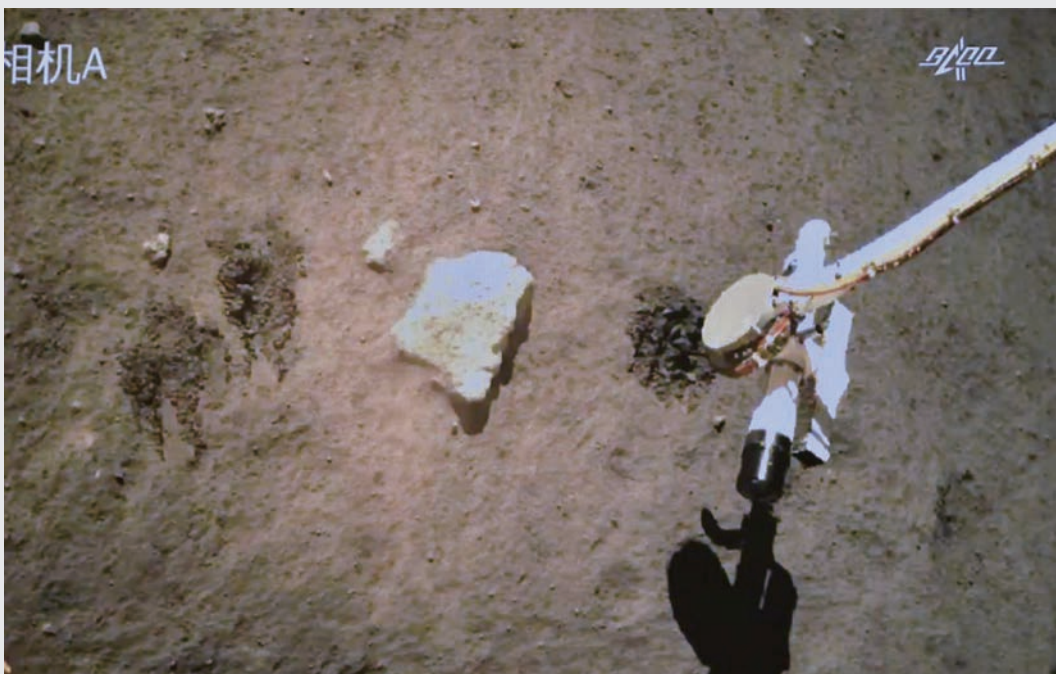


Tianhe core module of China Space Station

Photos

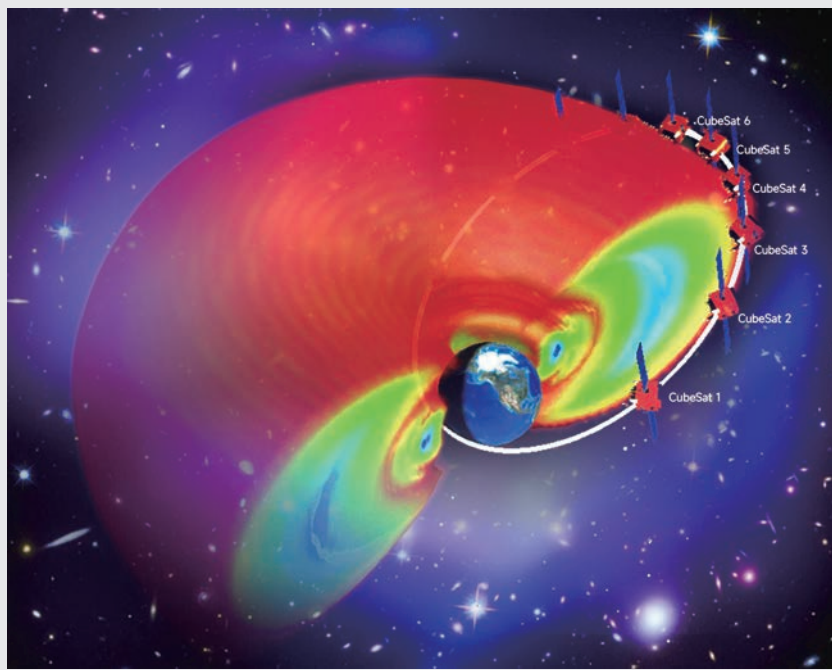


Lander and Rover (Zhurong) of Tianwen-1 mission, the first Chinese Mars Exploration Mission (Credit: CNSA)



Lunar sample collection by the CE-5 mission (Credit: CNSA)

Photos

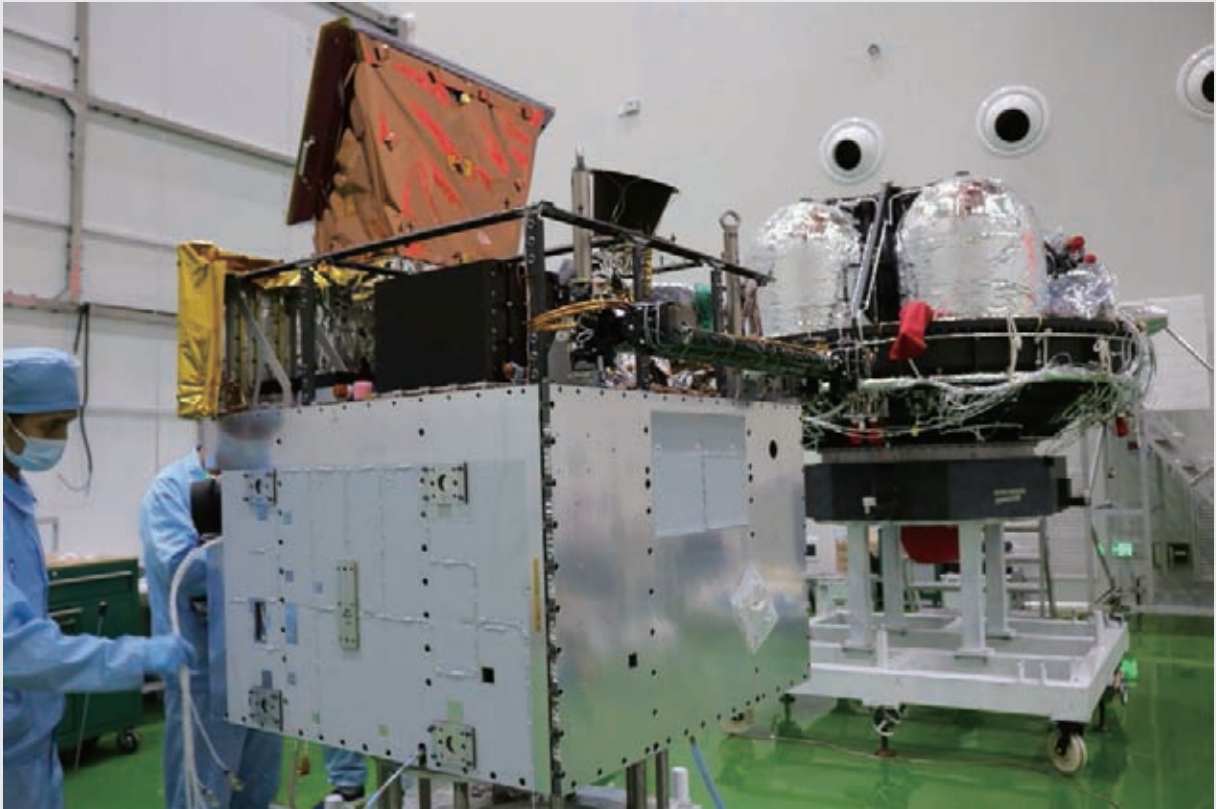


The CORBES, a proposed mission by NSSC, coordinated by COSPAR/TGCSS, using a constellation of CubeSats to probe the energetic particles of radiation belts

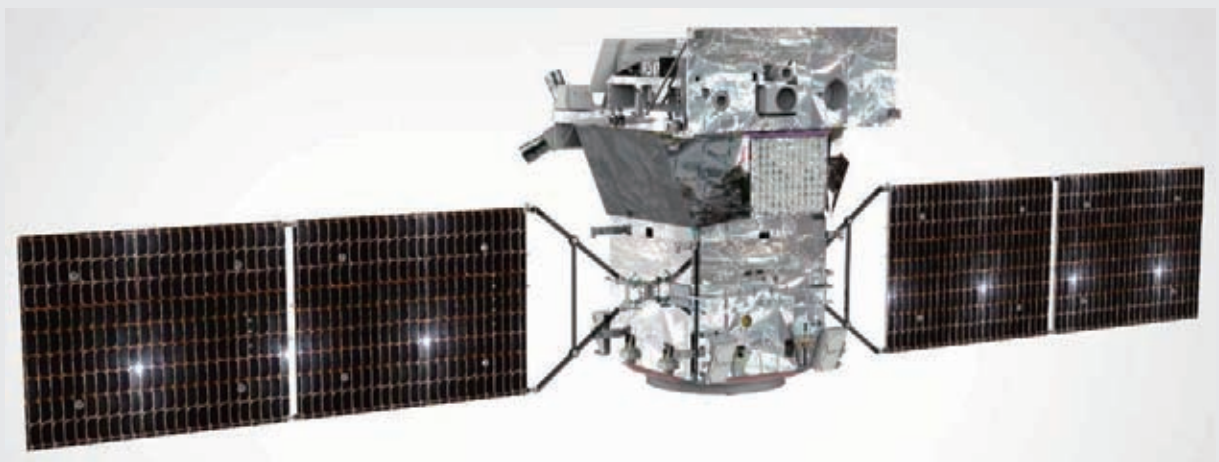


Daocheng Solar Radio Telescope (DSRT) of the Meridian Project (II) is under construction

Photos



SMILE qualification module integration in Shanghai (Credit: IAMC, CAS)



ASO-S satellite

Article Index

Part I: Major Space Programs

- Recent Progress in Space Science and Applications of China's Space Station in 2020-2022
..... *GAO Ming, ZHAO Guangheng, GU Yidong* (1)
- A Brief Introduction to the International Lunar Research Station Program and the Interstellar Express Mission
..... *XU Lin, LI Hui, PEI Zhaoyu, ZOU Yongliao, WANG Chi* (10)
- China's Space Science Program (2025–2030): Strategic Priority Program on Space Science (III).....
..... *WANG Chi, SONG Tingting, SHI Peng, LI Ming, FAN Quanlin* (13)

Part II: Achievement Highlights

- Overview of the Latest Scientific Achievements of Chang'E-4 Mission of China's Lunar Exploration Project
..... *CHEN Yuesong, TANG Yuhua, FAN Yu, YAN Jun, WANG Chi, ZOU Yongliao* (18)
- The GECAM Mission and Preliminary Results *XIONG Shaolin* (37)
- Recent Status of Taiji Program in China *LUO Ziren, ZHANG Min, WU Yueliang* (41)
- Progress of SDGSAT-1 Mission *GUO Huadong, DOU Changyong, CHEN Hongyu, FU Bihong* (44)
- Construction Progress of Chinese Meridian Project Phase II.....
..... *WANG Chi, XU Jiyao, LÜ Daren, YUE Xinan, XUE Xianghui,*
CHEN Gang, YAN Jingye, YAN Yihua, LAN Ailan, WANG Jiangyan, WANG Xin, TIAN Yufang (49)
- Introduction to the Chinese Ha Solar Explorer Mission *FANG Cheng, LI Chuan* (56)
- Current Status and Main Scientific Outcomes of the CSES Mission.....
..... *ZEREN Zhima, HUANG Jianping, LIU Dapeng, YANG Yanyan, YAN Rui, ZHAO Shufan,*
ZHANG Zhenxia, LIN Jian, CUI Jing, CHU Wei, WANG Qiao, LU Hengxin,
XU Song, GUO Feng, YANG Dehe, ZHOU Na, LIU Qinqin, HUANG He,
WANG Jie, TAN Qiao, LI Wenjing, LÜ Fangxian, ZHU Keying, SHEN Xuhui (60)

Part III: Mission Progress

- Status Update of the Einstein Probe Mission *YUAN Weimin, BAO Congying* (74)
- Progress Report on ASO-S..... *GAN Weiqun* (81)
- Recent Advance in the Solar Wind Magnetosphere Ionosphere Link Explorer (SMILE) Mission
..... *WANG Chi, BRANDUARDI-RAYMONT Graziella, ESCOUBET C P* (84)
- Research Advances of the Chinese Meridian Project in 2020–2021.....
..... *WANG Chi, WANG Jiangyan, XU Jiyao* (90)
- Progress of International Meridian Circle Program
..... *LIU William, MICHEL Blanc, WANG Chi, XU Jiyao, LI Hui,*
REN Liwen, LIU Zhengkuan, ZHU Yajun, LI Guozhu, LI Lei, ZEREN Zhima, YANG Fang (100)

Part IV: Research Progress of Space Science Disciplines

- Space Astronomy *ZHANG Shuangnan, YI Shuxu* (104)
- Space Solar Physics in China: 2020–2022 *GAN Weiqun, FAN Quanlin* (124)

A Brief Review of Interplanetary Physics Research Progress in Mainland China during 2020–2022	
.....	<i>ZHAO Xinhua, HE Jiansen, SHEN Chenglong,</i>
.....	<i>FENG Shiwei, JIANG Chaowei, LI Huichao, QIN Gang, LUO Xi</i> (128)
Magnetospheric Physics in China: 2020–2021	<i>CAO Jinbin, YANG Junying</i> (143)
Ionospheric Investigations Conducted by Chinese Mainland Scientists in 2020–2021	
.....	<i>LIU Libo, LEI Jiuhou, LIU Jing</i> (167)
Advances in the Researches of the Middle and Upper Atmosphere in China in 2020–2022	
.....	<i>CHEN Zeyu, XU Ji Yao, CHEN Hongbin, CHEN Wen,</i>
.....	<i>REN Rongcai, HU Xiong, ZHU Yajun, XUE Xianghui, LU Gaopeng, ZHANG Shaodong,</i>
.....	<i>HUANG Kaiming, TIAN Wenshou, ZHANG Jiankai, HU Dingzhu, RAO Jian, HU Yongyun, XIA Yan</i> (198)
Recent Progress of Earth Science Satellite Missions in China	
.....	<i>SHI Jiancheng, LÜ Daren, WANG Yu, DU Yan, PANG Yong,</i>
.....	<i>YANG Dongxu, WANG Xin, DONG Xiaolong, YANG Xiaofeng</i> (225)
Progress of Fengyun Meteorological Satellites Since 2020	
.....	<i>ZHANG Peng, XU Zhe, GUAN Min, XIE Lizi, XIAN Di, LIU Chang</i> (236)
Current Status and Main Application Achievements of Ocean Satellites	
.....	<i>LIN Mingsen, ZHANG Youguang</i> (245)
Space Environment Measurements and Applications on the Tianhe Core Module of China Space Station	
.....	<i>LIU Siqing, SUN Yueqiang, ZHONG Qiuzhen, WEI Fei,</i>
.....	<i>LI Yongping, ZHANG Xianguo, LIN Ruilin, LI Zhitao, REN Tingling,</i>
.....	<i>LUO Bingxian, CHANG Zhen, WANG Chunqin, PENG Songwu, AI Jiangzhao</i> (258)
Progress of Planetary Science in China	
.....	<i>HUI Hejiu, RONG Zhaojin, ZHANG Jinhai, HU Sen, LIN Honglei, WEI Yong, LIN Yangting</i> (268)
Recent Progress of Microgravity Science Research in China	
.....	<i>ZHAO Jianfu, DU Wangfang, KANG Qi, LAN Ding, LI Kai,</i>
.....	<i>LI Weibin, LIU Youcheng, LUO Xinghong, MIAO Jianyin, WANG Qinggong,</i>
.....	<i>WANG Shuangfeng, ZHANG Tao, ZHANG Xingwang, ZHANG Yonghai, ZHENG Huiqiong</i> (285)
Space Life Science in China	
.....	<i>MA Hong, ZHANG Chen, LI Yujuan, LÜ Xuefei,</i>
.....	<i>LI Xiaoqiong, ZHANG Ying, YANG Chunhua, LIU Huayan, FAN Yunlong, DENG Yulin</i> (298)
Progress on Space Materials Science in China: I Debris Shielding Fibrous Materials and High Specific Energy Lithium Sulfur Batteries	
.....	<i>WU Nan, LIU Shuangke, ZHANG Xiaoshan, SUN Weiwei, ZHENG Chunman, WANG Yingde</i> (305)
Progress of Materials Science in Space Technology in China (2020–2022)	
.....	<i>WEI Qiang, DONG Shaoming</i> (314)
Progress of China's Space Debris Research	
.....	<i>LIU Jing, YANG Xu, CHENG Haowen, JIANG Hai, ZHANG Yao, WANG Yueer</i> (326)
Progress of Planetary Defense Research in China	<i>LI Mingtao</i> (332)
Progress of Radiation Belt Exploration by a Constellation of Small Satellites TGCSS/SGRB, COSPAR	
.....	<i>WU Ji, YANG Xiaochao, DAI Lei</i> (338)

Prof. Wing-Huen Ip received the CAS/COSPAR Jeoujang JAW Award in 2020

Part I: Major Space Programs

Recent Progress in Space Science and Applications of China's Space Station in 2020–2022

GAO Ming, ZHAO Guangheng, GU Yidong

Technology and Engineering Center for Space Utilization, Chinese Academy of Sciences, Beijing 100094

Abstract

China scheduled to complete the assembly of the T-shaped Tiangong Space Station in 2022, and will enter a new stage of utilization. There are more than 20 experiment racks inside the modules, and more than 50 external on-board payloads mounting spaces, which will support large-scale science and technology experiments during the operation. The development of internal experiment racks and external research accommodations approved during the construction has been completed, of which 4 racks in Tianhe core module, including High Microgravity Level research Rack (HMLR) and Container-less Materials Processing Rack (CMPR), have finished on-orbit tests; while other racks in Wentian and Mengtian experiment modules are under comprehensive ground tests. The Chinese Space Survey Telescope (CSST) has advanced much in the last two years with 24 pre-launch research projects funded and 4 joint science center built in preparation for CSST's future scientific observations and operations. The systematic research planning for China's Space Station (CSS) during 2022–2032 is updated with the researches classified into four important areas: space life sciences and human research, microgravity physical sciences, space astronomy and Earth science, and new space technologies and applications. According to the planning, more than 1000 experiments are expected to perform in CSS during the operating period. Overall, the CSS utilization missions are proceeding as planned, which will contribute to the major scientific or application output and have a positive impact on the quality of life on Earth.

Key words

China's Space Station (CSS), Space utilization, Experiment racks, Chinese Space Survey Telescope (CSST), Research planning

1 Recent Progress of the CSS

China launched the CSS's core module Tianhe on 29 April 2021 at Wenchang Satellite Launch Center, kicking off the construction of CSS. It is expected to complete the three-module space station with six related missions in 2022, totaling eleven missions for the assembly of CSS. Two new space station modules, named Wentian and Mengtian, are prepared to be launched in

the coming months, docking with the Tianhe core module and formally completing the T-shaped space station by the end of the year.

One major objective of the space station is to build a national space laboratory at an internationally advanced level, carrying out large-scale multi-disciplinary scientific experiments or key technological tests, serving educational purposes and obtaining research results of great scientific value or promising application. In addition,

the CSS will contribute to the peaceful development and utilization of space resources for mankind through international or regional cooperation^[1–3]. At present, 21 internal experimental racks and more than 50 external payloads mounting spaces are provided by the CSS^[1], which will meet the requirements of large-scale multidisciplinary space experiments, and have unique advantages such as astronaut’s participation in the experiments, operation, maintenance and upgrading of experimental equipment; returnable experiment samples; and information transmission between the CSS and Earth. The space station is expected to operate in orbit for more than 10 years, with sufficient experimental resources, which provides a historic opportunity for multi-disciplinary and serialized long-term space research.

2 Space Science and Application Missions of the CSS

The scientific experiments and application research will use the internal experiment racks, external experiment platforms or the accompanying CSST. The experiment racks consisting of numerous technical hardware are installed in the pressurized module and play a key role in supporting scientific experiments of various disciplines. The extravehicular experiment platforms are deployed on the exterior of the CSS, to which payload adapters or large payload hanging sites are installed to

provide standard mechanical, thermal, electrical, and data interfaces for exposed payloads. Until now, three external facilities for sciences and applications were approved and developed. The CSST is a major science project of China Manned Space Program (CMSP), which will fly independently in the same orbit as the CSS while keeping a large distance apart.

2.1 Brief Introduction of Internal Racks and External Facilities

The internal experiment racks can be categorized into disciplinary racks or supporting racks in accordance with their uses. The disciplinary racks provide special research conditions for disciplines such as life sciences and biotechnology, and microgravity physics, while the supporting racks support the routine operations such as sample storage, high microgravity experiments, variable gravity experiment comparison, payload adjustment and detection^[4]. 21 experiment racks including 12 disciplinary racks, 4 supporting racks and 5 general purpose payload installation racks have been deployed inside the Tiangong space station modules. A brief introduction of the main components and prime functions of the racks are shown in Table 1^[1].

Three external facilities are arranged outside of the modules occupying three payload adapters to support the exposure research of biological samples, materials and components. The prime functions of external facilities are shown in Table 2^[1].

Table 1 Overview of experiment racks’ chief components and prime functions

No.	Classification	Name	Main components	Prime functions
1	disciplinary racks	Human System research Rack	Medical sample microscopic observation and recording apparatus Medical sample preparation unit Weightlessness physiological effect research unit Cardiovascular research unit Space Raman spectrometer Basic cognitive ability measuring unit Motion characteristic measuring unit	Supporting research on human physiological effects and human abilities in long-term space environment and experiments aiming at developing new protection technologies
2		Medical Sample Analysis Rack	Space centrifuge Space medical sample refrigerator	Support samples centrifuged and refrigerated (4 °C)
3		Life and Ecology research Rack (LER)	Common creature cultivation unit Small centrifuge experiment unit Microbe detection unit Small controlled life ecological experiment unit Small common creature cultivation unit	Gravity biology and radiation biology research using biological individuals (plants, insects, small mammals, aquatic organisms, microorganisms, <i>etc.</i>), cells, tissues, microbes, <i>etc.</i> ; Research on the foundation and application of biological regeneration life support system
4		Biotechnology experiment Rack (BTR)	Cell and tissue experiment unit Cell and tissue detection and regulation unit Crystallization and analysis of protein	Microgravity cell and tissue cultivation, protein crystallization, biomolecule construction, biomechanical research and biotechnology transformation research

Continued 1

No.	Classification	Name	Main components	Prime functions
5		Fluid Physics research Rack (FPR)	Fluid dynamics unit Complex fluid unit	Hydrodynamics research, experiments of various transparent systems (model alloy, protein crystallization, solution crystal growth, supercritical fluid); particle experiment, colloid and other complex fluid (soft matter) research
6		Two-Phase System research Rack (TPSR)	Optical observation platform Gas management unit Small-flow liquid supply unit Large-flow liquid supply unit	Evaporation and condensation phase changes with interface, phase changes enhanced by heat transfer, two-phase heat transfer and fluid management, two-phase loop system dynamics
7		Combustion Science research Rack (CSR)	Exhaust purification and collection subsystem Oxidant and diluent subsystem Combustion chamber and experimental plug-in	Research on microgravity combustion process and dynamics of solid, liquid and gas, experiment of aerospace propulsion combustion, fire prevention experiment of manned mission materials
8		High-Temperature Materials research Rack (HTMR)	Batch sample management unit High-temperature furnace unit X-ray real-time observation unit	Scientific experiments on crystal growth, solution growth and solidification of metal alloy, semiconductor, inorganic multifunctional materials encapsulated by ampoule structure
9		Container-less Materials Processing Rack (CMPR)	Container-free experimental platform Vacuum and pressure unit	Solidification mechanism of metallic and nonmetallic material, deep supercooling research, accurate measurement of thermophysical property of high-temperature melt, preparation of new materials, <i>etc.</i>
10		Cold Atom Physics research Rack (CAPR)	Physical subsystem Rubidium potassium laser Optical trap laser Complementary magneto-optical plug laser Optical lattice laser Polarized molecular laser	Quantum properties of the critical point at ultra-low temperature for large scale and long-life-time Bose and Fermi quantum degenerate gas
11		High-Precision Time-Frequency System (HPTFS)	Optical atomic clock Active hydrogen maser Cold atomic microwave clock Precision orbit determination unit	Fundamental physics and applied research with the frequency stability and uncertainty of a few parts in 10^{-17}
12		Aerospace Basic Test Rack	Payload installation unit	Carry out experiments aiming at verifying the basic and key technologies of space in microgravity and other space environments
13	supporting racks	Glovebox and Cold Storage Rack (GCSR)	Scientific glove box Cryogenic storage apparatus	The scientific glove box provides the enclosed and clean environment for the operation of life science and other scientific experiments, <i>e.g.</i> samples preparation The cryogenic storage device provides preservation of biological or other samples at -80°C , -20°C and 4°C
14		Variable Gravity research Rack (VGR)	Centrifuge	Normal gravity, low gravity and supergravity experiments in the range of 0.01–2g for the experiments of fluid, life and materials sciences
15		High Microgravity Level research Rack (HMLR)	Suspension test bench	Support fundamental physical experiments and other scientific experiments that need high microgravity level
16		on-orbit Maintenance and Manipulation Workbench (MMW)	Mobile maintenance platform Diagnostic unit	Preparation, cleaning, welding, lubrication, assembly, testing, fault diagnosis and maintenance of payload module or unit; on-orbit experiment of independent payloads
17		Universal Payload Installation Rack	Payload integrated management unit Thermal control unit	Provides information and power supply interfaces, heat dissipation environments and nitrogen, vacuum, and exhaust gas interfaces for individual payload

Table 2 Prime functions of external facilities

No.	Name	Prime functions
1	Space Biology Exposure Experiment Device	Research on the animal model (nematodes), plants and plant seeds, microbes, and biological tissues, <i>etc.</i> in the extravehicular cosmic radiation environment
2	Extravehicular Materials Exposure Experiment Device	Space damage and service performance study of applied materials (lubrication, thermal control, film coating, shape memory, functional coating, polymer, composite material, <i>etc.</i>); Study of tribology
3	Universal Extravehicular Device for Components	Support on-orbit tests of components and subassembly, <i>e.g.</i> obtaining on-orbit operation parameters and reliability test data

In the construction of Tiangong space station, the chief aim is to complete the assembly and conduct on-orbit test of the scientific experiment racks, create favorable experimental conditions for the subsequent large-scale and systematic scientific research, and explore effective space experimental methods and approaches in the space station. More than 100 experimental projects have been approved using the various onboard scientific experiment racks and are expected to make progress in the frontier of scientific research such as the multi-level influence study of comprehensive environment (*e.g.* microgravity) on living bodies, the breakthrough of space high-strength/high-efficiency heat exchange technology of spacecraft power system, the space preparation mechanism of important strategic or new high-performance materials, the test of equivalent principle and the measurement of gravitational redshift.

2.2 Advancement of the CSST

The 2m-aperture CSST is a major science project of China Manned Space (CMS)^[5–6]. It is expected to start science operations in 2024 and has a nominal mission lifetime of 10 years or more.

During normal observations, the CSST will fly independently in the same orbit as China's Tiangong space station but keep a large distance apart. It can dock with the space station for refueling and servicing as scheduled or as needed. With a cook-type three-mirror anastigmat design, the CSST can achieve superior image quality within a large Field of View (FoV), which gives it an advantage for survey observations. Being an off-axis telescope without obstruction, its Point Spread Function (PSF) does not have diffraction spikes from mirror support structures and is thus helpful for precision photometry, position, and shape measurements when properly sampled. The radius encircling 80% energy of the PSF within the CSST's central 1.1 square degrees of FoV is specified to be no more than 0.15", including all wavefront errors in the optics and instruments and dynamical effects such as the telescope's attitude control and vibration.

The CSST will be launched with 5 first-generation instruments including a Survey Camera, a Terahertz Receiver, a Multichannel Imager, an Integral Field Spectrograph, and a Cool Planet Imaging Coronagraph. The Survey Camera is equipped with 30 detectors of 9000 pixel×9000 pixel for science observations, each with a filter or two grating elements mounted above, a

defocused 9000 pixel×9000 pixel detector for flux calibration in r band, eight 640×512 near-infrared detectors, two Fine Guide Sensors, and four wavefront sensors. The primary task of the CSST is to carry out a high-resolution large-area multiband imaging and slitless spectroscopy survey covering the wavelength range of 255 nm to 1000 nm. Precision cosmology is the main science driver of the survey, and, therefore, the main area of sky selected for observation is at the median-to-high galactic latitude and median-to-high ecliptic latitude. It will take the Survey Camera roughly 7 years of operation accumulated over 10 years of orbital time to image roughly 17500 square degrees of the sky in NUV, u, g, r, i, z, and y bands and take slitless spectroscopy of the same sky in 3 bands. The point-source 5σ limiting magnitudes in g and r bands can reach 26th magnitude (AB mag) or higher. The spectral resolution ($R=\lambda/\Delta\lambda$) of the slitless spectrograph is specified to be on average no less than 200, and the wide-band-equivalent limiting magnitudes in GV (400–620 nm) and GI (620–1000 nm) bands will reach the 23rd magnitude or higher. In addition, a number of deep fields will be selected for more observations to reach at least one magnitude deeper than the wide-area survey. The Multichannel Imager plans to observe five ultra-deep fields of 300 square minutes in total to 30th magnitude in the visible.

To fully explore the CSST's potential and to prepare for its science and operations, CMS funded 24 pre-launch research projects that were selected by the CSST Science Committee. These projects cover a wide range of research fields, including Cosmology, galaxies and active galactic nuclei, Milky Way science, stellar science, astrometry, transients, exoplanets, and the solar system. In addition, there is a project aiming to optimize the survey plan and observation strategy for the overall science return. The projects are managed by the CSST joint science center (hosted at National Astronomical Observatories, NAOC) and are coordinated at Peking University Science Center, NAOC Science Center, Yangtze River Delta Region Science Center (hosted at Shanghai Astronomical Observatory), and Guangdong-Hong Kong-Macao Greater Bay Area Science Center (hosted at Sun Yat-Sen University). In total, about 400 researchers from more than 30 institutes are involved.

The research projects are classified into two categories: (i) research areas that are expected to be competi-

tive or necessary and that require large, coordinated efforts to prepare in advance (12 projects); (ii) Exploratory studies, feasibility studies, and planning of research programs (12 projects).

Several category 1 projects also serve as much needed extensions to the scientific data reduction (sub) system and will deliver high-level science data pipelines and/or simulations for the broader CSST community. Such projects include Error analysis and optimization of photometry measurements, Redshift survey with slitless spectroscopy, Numerical simulation methods and emulators for cosmology, High-level tool pack for galaxy image analyses, High-level tool pack for galaxy spectrum analyses, and Fundamentals and methods of astrometry.

Although the CSST main survey will miss much of the galactic plane and the ecliptic plane, its data will still be invaluable for studies of the Milky Way and its neighbors, stellar science, and high-inclination solar system objects. Patchy observations in the galactic plane, in or near the budge, and in the ecliptic plane are under consideration to enhance CSST science. Because the main survey takes only two or four exposures per filter (grating) at each pointing direction, it is not well suited for regular time-domain studies. Nevertheless, a huge number of transients will be caught by the CSST Survey Camera. Methods to identify (and even classify) them need to be developed. Small dedicated programs can also be implemented or combined with deep fields to achieve better time resolution.

Unlike the Survey Camera, the other four instruments all have a small FoV. They enable unique capabilities for detailed studies of individual objects or small fields. The Terahertz Receiver will be used to carry out spectral line surveys or mapping of star-forming regions of the Milky Way, nearby galaxies, late-type stars, and solar system objects. The Multichannel Imager can observe the same field in three bands simultaneously, capable of obtaining instantaneous color of fast varying objects such as fast transients, comets, and spinning asteroids. The Integral Field Spectrograph splits its $6'' \times 6''$ FoV into 32×32 units and obtains 1024 spectra of these units. It can provide both two-dimensional spatial information and spectral information of the target, particularly helpful for investigations of the co-evolution of supermassive black holes and galaxies and star formation in the nearby universe. The Cool-Planet Imaging

Coronagraph aims to realize 10^{-8} high-contrast direct imaging of exoplanets in the visible. It plans to follow up exoplanets discovered by radial velocity observations, study planet formation and evolution, and probe proto-planet disks.

The combined advantage of its aperture, angular resolution, wavelength coverage, and versatile instruments makes the CSST highly competitive, and, at the same time, its observations will also be highly complementary with other large projects of its time, such as the Vera Rubin Observatory, the James Webb Space Telescope, the Euclid mission, and the Roman Space Telescope. The 24 pre-launch research projects comprise a crucial step in the preparation of both Chinese astronomers and the CSST science program for exciting opportunities of studies from the solar system to cosmology and beyond in the near future.

2.3 Progress of On-orbit Test of Scientific Experiment Racks

On-orbit testing has been implemented on the experiment racks that were already installed in the Tianhe core module, which was launched in 2021, and these racks will be used for container-free material science and high microgravity experiments. With regard to other experiment racks in Wentian and Mengtian experiment modules, the development work has been finished and the ground testing has begun, as it is shown in Fig. 1. On-orbit testing progress for HMLR and CMPR is shown as follows.

(1) HMLR

The HMLR adopts the internationally advanced technology “magnetic levitation & jet suspension” as double-layer vibration isolation scheme. Specifically, the magnetic levitation vibration isolation is realized by wireless energy transmission and wireless communication technology without umbilical cord in the inner layer, and the jet suspension vibration isolation is realized by binocular vision measurement and jet propulsion technology without umbilical cord in the outer layer, which meets the requirements of different microgravity environments. At present, the HMLR has completed the on-orbit function test and fine adjustment of parameters, and carried out the verification work of jet suspension, magnetic levitation control test, and double-layer suspension test. The test results in Fig. 2 showed that the microgravity level has been achieved in the order of



Fig.1 Part of science experiment racks in Wentian and Mengtian are being tested on the ground

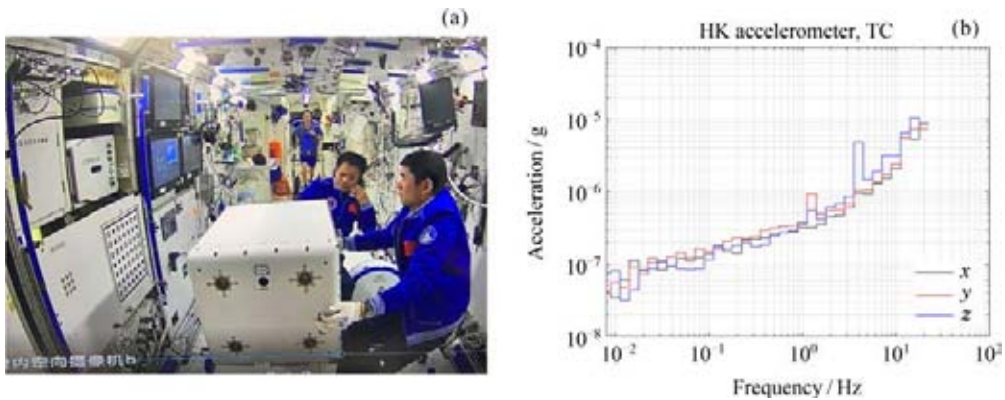


Fig.2 (a) Astronauts are conducting the test, (b) microgravity level of the suspension test

10^{-6} – 10^{-7} g at $f \leq 0.1$ Hz, and the best microgravity level at some frequency points is better than 10^{-7} g . Further optimization of the control system and longer time of high microgravity verification will be conducted lately.

(2) CMPR

The CMPR is an electrostatic levitation facility developed to study the solidification mechanism and thermophysical property under ultra-high temperature for metal, ceramics and glass using container-less process in microgravity environment. The main performances of the container-less experimental device included: (i) a coupling laser heating system with semiconductor laser with an output power of 300 W and carbon dioxide laser, which can heat melt metals and non-metals up to 3000°C; (ii) a molecular pump vacuum system and argon pressurization unit are installed in the rack to adjust

experiment environment of the container-less process from 10^{-4} Pa to 3 atm; (iii) a series of optical devices are mounted on a polyhedron chamber with 38 faces for position controlling of the sample with an accuracy of ± 0.1 mm, for the thermophysical property measurement of density, viscosity, surface tension, specific heat and spectral emissivity, and also providing a triggering nucleation function to realize phase selective solidification under different supercooling degrees.

The on-orbit functional verification of the rack and electrostatic levitation facility has been completed. A 2-mm diameter spherical sample of Zr was melted and some thermophysical property was measured in microgravity as shown in Fig. 3. In the future, the container-less scientific experiments will be conducted on superalloys and functional materials.

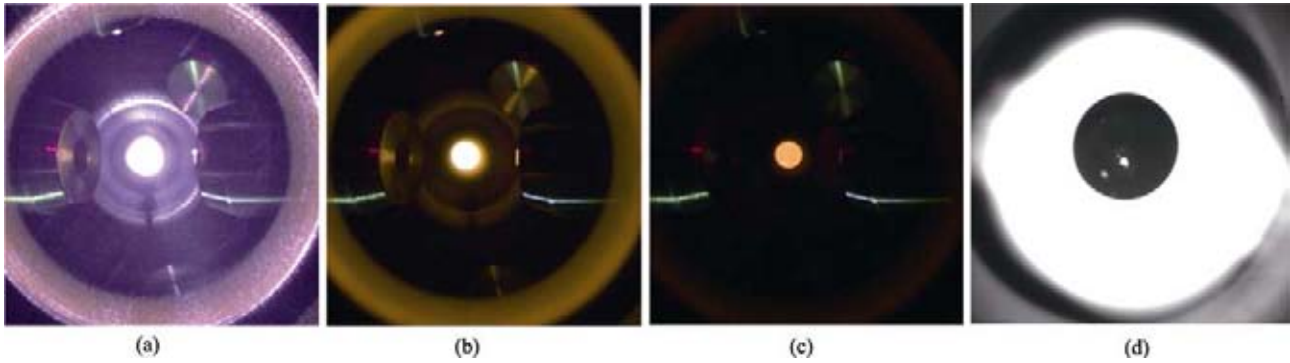


Fig.3 (a) Laser heating, (b) sample melting (1990 oC), (c) under cooling state, (d) density measurement

2.4 Progress of the International Cooperation Projects

CSS attaches great importance to the organization and development of international cooperation projects. Through the joint project solicitation released with the United Nations Office for Outer Space Affairs, a total of 9 projects from 17 countries and 23 entities were selected^[7], which will be conducted in the LER, CSR, TPSR and extravehicular payload adapter. Through a joint call between Chinese Manned Space Agency (CMSA) and European Space Agency (ESA), 10 China-Europe cooperation projects were selected, mainly using onboard experiment racks such as BTR, LER, TPSR, FPR, HTMR and CFPR. To date, all international cooperation projects are advancing as planned, and it is expected that most of them will be implemented on-orbit between 2023 and 2025.

CSS will continue to expand cooperation with European countries and countries of the “the belt and road initiative”, further strengthening the cooperation with relevant international organizations and countries in the field of space science and application; actively participating in international science projects; continually improving the comprehensive application benefits of CSS and the influence of national science and technology. During the operation, the CSS will solicit and select international cooperation projects on a regular basis.

3 CSS Utilization Planning for 2022–2032

CSS completed a long-term and systematic planning for space utilization in 2021. The planning could be categorized into four main areas^[8–10]: space life sciences and

human research, microgravity physical sciences, space astronomy and Earth science, and new space technologies and applications. Within these four areas, new devices will be developed and more than 1000 experiments will be performed during the operation period of 2022–2032. The primary research of these areas is described as follows.

The space life sciences and human research is dedicated to solving the scientific problems faced by human long-term space survival, through constantly improving the experiment supporting the ability of related facilities, and systematically carrying out fundamental and exploratory space experiments. In terms of research on the influence and mechanism of various factors of space environment on life from molecules to tissues and organs, the laws of space growth and breeding of cognitive living bodies will be explored, and the main health issues faced by long-term survival of human beings in space will be studied. In terms of research on the closed-loop ecosystem, the system development and evolution law of multi-generation replacement of organisms will be revealed. With respect to research on the origin of life, the formation mechanism, the occurrence and evolution conditions of primitive cells in special space environment will be explored. In addition, to promote the national economic development and people's medical and health services, the special space environment will be used to develop high-tech products *e.g.* stem cells, regenerative medicine, targeted drugs and synthetic bio-manufacturing.

The main goal of microgravity physics is to investigate the law of matter movement and its influence on the law of movement when the effect of gravity almost disappears, including fluid physics and thermo-physics, combustion science, materials science as well as the

fundamental physics. Fluid physics and thermo-physics are to study new phenomena and new laws of fluid motion and thermal (mass) transportation, to obtain a systematic understanding of turbulent flow transfer processes, multiphase flow thermal mass transport, soft matter self-organization phenomenon far from equilibrium state, *etc.*, and serving space applications in aerospace thermal and propellant management. The study of combustion science is to decouple the effect of gravity field on flame, reveal the essence and law of traditional and new fuel combustion, develop spacecraft fire prevention and fire extinguishing technology, and promote technological progress in the energy technology. The study of materials science is to reveal the processing and preparation laws of various types of materials in space environments, grow new materials that have important application backgrounds, study the laws of service performance of space application materials in the outer space environment, and provide a scientific basis for the research and development of advanced materials for aerospace. The study of fundamental physics includes experiments of ultra-cold atomic physics under extreme conditions, low-temperature quantum phase transition, general relativity testing, developing and using advanced high-precision time-frequency technology, and developing microgravity complex plasma research, to promote the understanding of fundamental physics.

The space astronomy and Earth science is a comprehensive interdisciplinary subject that uses spacecraft to observe and study cosmic objects and all spheres of the Earth system (the atmosphere, hydrosphere, lithosphere and biosphere, extending to the Earth ionosphere, magnetosphere and solar-terrestrial space). Space astronomy plays an important role in the scientific research of the space station: through the CSST, large-scale multi-color photometry and spectral survey for more than 10 years is expected to make major breakthroughs in the fundamental problems of cosmology, the formation and evolution of active galactic nuclei and supermassive black holes, the formation and evolution of galaxies and stars, temporary source/source change and sudden astronomical events, *etc.* Furthermore, a cosmic High-Energy Radiation Detection facility (HERD) is scheduled to explore the extreme physics of the universe^[11]. In addition, some other gamma-ray and soft X-ray polarization detection, milky way thermal baryon measurement, and ultraviolet astronomy facilities are also planned to ensure accurate measurement of multiple astrophysical

quantities. Geoscience focuses on space environment monitoring, studying the coupling relationship between ionosphere and magnetosphere, and building a more refined space weather and space environment prediction model. In addition, new Earth observation technologies applied in the fields of global climate change, natural resources survey and natural disaster early warnings are encouraged.

The new space technologies and applications area keep keen eyes on the frontier of new space application technology, and makes systematic layout for future manned lunar exploration and deep space exploration. The on-orbit manufacturing and construction technology verification is planned, including the test verification of on-orbit assembly and construction of large components and space payloads, high-precision on-orbit additive manufacturing, *etc.* Space robots and intelligent control technologies are planned to reduce astronauts' on-orbit work. Other technologies such as new technologies for autonomous navigation of spacecraft in Earth-Moon space, new space energy and propulsion technology, environmental control and life support system technology and other basic technologies are also planned to serve space exploration and discovery purposes and support the sustainable development of space utilization.

4 Conclusions

China aims to have the CSS fully assembled by the end of 2022, and large-scale space science and application tasks will be conducted thereafter, providing a historic opportunity for the leap-forward development of space science and applications. With the CSS starting its regular operation, in the follow-up, the solicitation of experimental projects will be carried out regularly to ensure sufficient project reserves. In addition, the new generation of payloads will be approved and launched to meet the requirements of on-orbit experiments and to continuously improve the on-orbit scientific experiment supporting and sample analysis abilities.

The CSS is completely open to the world, and provides opportunities for countries around the world to use the space station to carry out scientific experiments, which is a concrete embodiment of China's concept of building a community with a shared future for mankind and building a new type of international cooperation in the "new region" of outer space. Regular international projects solicitation will be released, and scientists from

all over the world can submit project requirements through China Manned Space Agency, the United Nations Office for Outer Space Affairs, or national space agencies under bilateral cooperation agreements. Chinese scientists are actively encouraged to initiate extensive cross-regional or transnational cooperation to improve the human science and technologies.

References

- [1] China Manned Space Agency. Scientific Experiment Resource Manual of China's Space Station [R], 2019
- [2] GAO M, ZHAO G, GU Y. Space Science and Application Mission in China's Space Station (in Chinese). *Bull Chin Acad Sci*, 2015, 30(6): 721-732
- [3] GU Y, GAO M, ZHAO G. Space Research Plan of China's Space Station[J]. *Chinese Journal of Space Science*, 2016, 36(5)
- [4] United Nations Office for Outer Space Affairs, China Manned Space Agency. Handbook-China Space Station and its Resources for International Cooperation[R], 2018
- [5] ZHAN H. Consideration for a large-scale multi-color imaging and slitless spectroscopy survey on the Chinese space station and its application in dark energy research (in Chinese)[J]. *Sci Sin Phys. Mech. Astron.*, 2011, 41: 1441-1447
- [6] ZHAN H. The wide-field multiband imaging and slitless spectroscopy survey to be carried out by the Survey Space Telescope of China manned space program (in Chinese)[J]. *Chinese Science Bulletin*, 2021, 66:1290-1298
- [7] China Manned Space Agency. List of Selected Space Science Experiment Projects for the 1st Cycle Concerning UN/China Cooperation on the Utilization of China Space Station [EB/OL]. [2020-03-11]. http://www.cmse.gov.cn/art/2019/6/12/art_22_33158.html
- [8] GU Y. The China Space Station: a new opportunity for space science[J]. *National Science Review*, 2022, 9(1): nwab219
- [9] ZHAO B. Scientific aspirations of the Chinese Space Station program: an interview with Ming Gao[J]. *National Science Review*, 2021, 8(11): nwab161
- [10] GU Y, GAO M, ZHAO G. Science Research and Utilization Planning of China's Space Station in Operation Period 2022-2032[J]. *Chinese Journal of Space Science*, 2020, 40(5): 609-614
- [11] HUANG X, LAMPERSTORFER A S, TSAI Y L S, *et al.* Perspective of monochromatic gamma-ray line detection with the High Energy cosmic-Radiation Detection (HERD) facility onboard China's space station[J]. *Astroparticle Physics*, 2016, 78: 35-42

A Brief Introduction to the International Lunar Research Station Program and the Interstellar Express Mission

XU Lin¹, LI Hui¹, PEI Zhaoyu², ZOU Yongliao¹, WANG Chi¹

1. State Key Laboratory of Space Weather/National Space Science Center, Chinese Academy of Sciences, Beijing 100190
2. Lunar Exploration and Space Engineer Center, China National Space Administration, Beijing 100190

Abstract

China has planned and implemented a series of lunar and deep space exploration programs since the first lunar exploration satellite Chang'E-1 launched in 2007. In the future, China has initiated the international lunar research station program, which aims to build a shared platform on the Moon jointly with many other countries for long-term and continuous lunar exploration, lunar-based observations and experiments, as well as in-situ resource utilization. In addition, China has also proposed an interstellar express mission to unveil the mysteries of the outer heliosphere, nearby interstellar space, and their interactions. This paper gives a brief introduction to the International Lunar Research Station program and the Interstellar Express mission.

Key words

Lunar exploration, Deep space exploration, International lunar research station, Outer Heliospheric exploring, International cooperation

1 International Lunar Research Station Program (ILRS)

Since the beginning of the 21st century, the Moon has once again become a hot spot of exploration, accompanying the trend change from launch of individual missions to establishing a research station via multiple missions, and both scientific research and applications of the Moon are equally concerned. ESA promoted the concept of Moon Village; Russia announced a series of lunar missions; NASA has granted the Artemis program, aiming to build a lunar base; Five missions of China's Lunar Exploration Program (CLEP) have been carried

out, with the first probe Chang'E-1 launched in 2007 and Chang'E-4 landed for the first time on the far side of the Moon in 2019. Chang'E-5 has collected and returned the youngest lunar samples dated 2.0 Ga, marking the completion of all three phases of CLEP: orbiting, landing, and returning. The fourth phase of the CLEP, consisting of three missions Chang'E-6, 7 and 8, have been scheduled to explore the lunar south pole region for multiple goals, including lunar exploration, Moon-based experiments and observations, in-situ resource utilization, and returning samples from the far side of the Moon. According to the overall plan of lunar exploration program, the fourth phase of the CLEP is the first phase of the International Lunar Research Sta-

* Supported by National Key Research and Development Program of China (2020YFE0202100)

Received June 29, 2022

tion (ILRS) program.

1.1 Cooperation in Science

ILRS refers to a comprehensive scientific experiment facility constructed jointly on the lunar surface and/or in lunar orbit by attracting potential international partners. The facility is designed for multi-discipline and multi-purpose scientific research activities, including exploration and utilization of the Moon, moon-based observation, basic scientific experiments, and technology verification, with the capability of long-term unmanned operation with the prospect of subsequent human presence. The research areas of ILRS are: (i) the geological survey of the Moon, (ii) lunar-based astronomy observations, (iii) space environment observation of the Sun-Earth-Moon system, (iv) lunar-based fundamental science experiment, (v) lunar in-situ resource utilization.

1.2 Mission Planning

The construction of ILRS is divided into three phases: reconnaissance, construction, and utilization.

Phase I (before 2026): “reconnaissance”, mainly to explore the Moon with the approved missions, while selecting landing sites for subsequent missions and conducting related technical verification tests. China’s missions include Chang’E-6 and Chang’E-7.

(1) Chang’E-6 will explore the far side of the Moon and return lunar samples to Earth.

(2) Chang’E-7 will explore the lunar south pole region of the Moon, including the morphology, composition and tectonics, deep interior structure and magnetic field, water ice and volatile matter, and the lunar surface environment. Furthermore, the Earth’s magnetotail and plasmasphere will be observed from the Moon, and the Moon-Earth VLBI measurement and observation experiment system with a baseline of 400000 km will be constructed for the first time.

Phase II (before 2035): “construction”. This phase may consist of two stages.

(1) Before 2030: China’s mission includes Chang’E-8, which will detect the lunar multi-physical fields and regional geological features, make long-term and large-scale observations of the Earth’s macroscopic phenomena, and carry out lunar terrestrial small ecosystem experiments and in-situ extraction experiments of rare gases.

(2) From 2031 to 2035: Five missions are scheduled to carry out detailed regional geological surveys, space physical observations of the Sun-Earth-Moon system,

lunar-based astronomical observation, lunar in-situ utilization resources experiments, lunar-based life science experiments, fundamental physics experiments, and to collect the lunar samples and return to Earth. Through this stage of construction, the lunar research station will be completed.

Phase III (after 2036): “Utilization”. This phase will use this scientific research station to carry out continuous scientific exploration and technical verification. It will support manned lunar missions, and expand and maintain the modules for each system as needed.

2 Exploration for Deep Space and Outer Heliosphere

2.1 Deep Space Exploration Mission

Mars is the closest and most similar to Earth among the eight planets in our solar system. As a result, it logically becomes a top priority for space exploration. So far, missions for Mars exploration have been established by the United States, Russia, Europe, Japan, and India. China’s first Mars program, Tianwen-1, which has completed orbiting, landing, and wandering in a single mission, was successfully launched in July 2020. On 10 February 2021, Tianwen-1 arrived at Mars with the goal of investigating Martian surface geology and interior structure, searching for evidence of present and historic water presence, and characterizing Mars’ space environment and atmosphere.

The Tianwen-1 mission is only the start of China’s planetary exploration, and many new endeavors are in the pipeline. For instance, the next Tianwen-2 mission will orbit the main belt comet, 133P, and discover the near-Earth asteroid, 2016HO3. It will also collect surface samples and return them to Earth. The project design is now complete, and the prototype development process has moved on to the next phase. The Tianwen-3 mission, designed to retrieve samples from Mars, is also in the works. It will land on Mars, collect surface samples, meanwhile gather ambient geological field data through in-situ measurements, and then fly back to Earth. In addition to Mars, Tianwen-4 will also explore Jupiter and its moon system, as well as undertake interplanetary exploration beyond Jupiter.

2.2 Heliospheric Boundary Exploration Mission

In addition to planetary exploration, China has also proposed an interstellar exploration mission to explore

the outer heliosphere and its boundary, and the typical celestial bodies in the outer solar system during its journey. The heliosphere is a great bubble due to the interaction between the solar wind and the interstellar wind, which prevents solar system planets from being hit by cosmic rays with very high energy. However, there exists an extreme imbalance between inner heliospheric exploration and outer heliospheric exploration. A specially designed mission with well-chosen modern instruments is needed to unveil the mysteries of the outer heliosphere, nearby interstellar space, and their interactions.

The concept of the first Chinese outer heliospheric exploration mission focusing on the heliospheric boundary region, namely Interstellar Express, was proposed in 2015. The China National Space Administration (CNSA) kicked off the pre-study to investigate the scientific objectives, technical readiness, and economic affordability, etc. in 2021. With the aim of perceiving the deep space environment of our Earth's homeland and exploring typical celestial bodies in the outer solar system, this mission designs four scientific tasks.

- (1) Directly measuring the unexplored heliosphere.
- (2) Heliosphere panoramic imaging.
- (3) The detection of the giant planet system during a fly-by.
- (4) Archaeological study of the solar system.

The mission consists of two spacecraft traveling in opposite directions, one heading for the heliospheric nose region and the other for the tail region. The preliminary mission profile of payload configuration, tra-

jectory design, and related engineering issues are being discussed as well.

3 Summary

The International Lunar Research Station program is an international cooperation plan first initiated by China, which will jointly establish a new science and application platform on the Moon with many other countries based on the approved and planned missions. Using this platform, it will be possible to carry out long-term, continuous exploration and observation on the Moon, leading to innovational achievements in lunar science. The platform will support fundamental experiments in life science and physics, and will also develop key techniques for in-situ lunar resource utilization to support sustainable activities on the Moon.

Complementary to the ILRS program, China has also designed a preliminary roadmap for deep space and outer heliosphere explorations. Following Tianwen-1, China also plans to return samples from asteroids and Mars, and explore Jupiter system, through these missions from Tianwen-2 to Tianwen-4 missions. In addition, China has also conducted a conceptual study of deep space and outer heliosphere exploration, the Interstellar Express mission, which plans to launch two satellites toward the nose and tail directions of the heliosphere, respectively, in order to reveal the properties of the heliosphere and its interactions with the interstellar medium.

China's Space Science Program (2025–2030): Strategic Priority Program on Space Science (III)*

WANG Chi, SONG Tingting, SHI Peng, LI Ming, FAN Quanlin

National Space Science Center, Chinese Academy of Sciences, Beijing 100190

Abstract

The Strategic Priority Program (SPP) on Space Science, which is under the leadership of the Chinese Academy of Sciences (CAS), has established China's space science satellite series from scratch. A number of major scientific achievements have been made by the first phase of the Program (SPP I), while SPP II has been currently being implemented. The future development of space science needs urgent top-level planning and advanced layout to clarify the overall goal and investment portfolio from 2025 to 2030. We will briefly introduce the initiative and possible space science missions of SPP III, including the preparatory work which already started in July 2021. Following the effective administrative tradition since SPP I, National Space Science Center (NSSC, CAS) is responsible for the whole procedure, including soliciting, assessment, and implementation of SPP III. Brief information on the 13 candidate missions will be described, including missions in the fields of astronomy & astrophysics, exoplanets, heliophysics & planetary & Earth science, respectively.

Key words

Space science, Strategic Priority Program (SPP), Space science missions, Space exploration

1 Introduction

One ultimate goal of China's space activities is to explore the geospace, solar system, and vast universe, revealing the secrets of the nature. Space science, space technology and space application are three main themes of China's space activities. Since 2011, The Strategic Priority Program (SPP) on space science, which is under the leadership of the Chinese Academy of Sciences (CAS), has been successfully implemented, the scientific achievements of Dark Matter Particle Explorer (DAMPE), Quantum Experiment at Space Scale (QUESS), ShiJian-10 (SJ-10) and Hard X-ray Modulation Tele-

scope (HXMT), *etc.* are significantly important and have attracted much attention around the globe.

In order to promote space science in China, CAS launches the selection and deployment of the New Horizon Program (*i.e.* SPP III) in July 2021, a space science program for the 15th Five-year Plan period. SPP III will carry out cutting-edge explorations and researches on four major themes: the extreme universe, ripples in time and space, the panoramic view of the sun and Earth, and the search for habitable planets, with a vision of achieving major discovery and acquiring new knowledge through original scientific achievements.

The selection of SPP III candidate missions follows

* Supported by SPP II (XDA15060102)

Received May 27, 2022

“Three Principles” and “Five Persistences”. The former means we must adhere to the principles of giving priority to scientific goals, balanced development of disciplines, and technological and economic feasibility. While the latter emphasizes that we should bind to scientific objectives, selection on a competitive and comprehensive basis, scientific output, principle investigator leadership, and openness at home and abroad.

SPP III solicits new mission concepts from research institutes, universities and industries across the country. There are totally 17 proposals submitted before 31 December 2021.

NSSC has conducted the first round evaluation of SPP III mission candidates during 11–13 February 2022. The science mission advising panel was setup and members of the National Space Science Committee and other domestic experts in various fields were invited for the assessment. 13 projects have passed this round of selection. NSSC will carry out a series of specific assessments within the first half of 2022, including overseas assessment of scientific significances, as well as mission profiles on Concurrent Design Facility (CDF), and engineering technology readiness assessment and budget request rationality evaluation. After the above comprehensive procedures, a ranking recommendation of these candidate missions will be given, which will provide solid inputs for the approval of SPP III program by CAS administrations.

2 Brief Description on Candidate Mission Proposals of SPP III

The 13 space science candidate flight missions are categorized into four fields, *i.e.* space astronomy and astrophysics, exoplanets, heliophysics and planetary and Earth Science, where the exoplanets are actually a newly cut-crossing discipline emerging from traditional science disciplines. Among them, two candidates are large missions, while others belong to medium and small sized missions. The main ideas of the candidates in each field are introduced briefly as followings.

2.1 Space Astronomy and Astrophysics

Space astronomy and astrophysics aim to discover the origin and evolution of the universe and of life itself. SPP III will address the scientific issues in some specific astrophysics science themes, for example, the matter inside Neutron Stars (NSs), the space-time in the

vicinity of the Black Hole horizon, and the extremely magnetized vacuum close to magnetars and accreting pulsars. Besides, possible characteristic features of gamma rays and electrons/positrons from dark matter annihilation or decay, the early history of the Universe, *etc.* are of high interests.

There are 3 space science missions proposed in this field, aiming to address some above mentioned fundamental scientific questions.

(1) Enhanced X-ray Timing and Polarimetry (eXTP) Mission

eXTP will address key unsolved problems of fundamental science: the equation of state of cold ultra-dense matter, the effects of strong-field gravity, and the physics of the strongest magnetic fields in nature. eXTP, which is a powerful X-ray observatory orbiting the Earth at 550 km, can continuously monitor the X-ray sky and enable multi-messenger studies for gravitational waves and neutrino sources. This large mission is led by China with major contributions from some European countries, aiming for liftoff not early than 2027^[1].

(2) Dark Matter Particle Explorer-2 (DAMPE-2)

While DAMPE has impressed the scientific community with its precise measurements of the energy spectrums of cosmic ray electrons, protons and the Galactic Cosmic-Ray (GCR) helium. Its successor DAMPE-2 will hold significant improvements, dedicating to detecting possible characteristic features of gamma rays and electrons/positrons from dark matter annihilation or decay, new spectral structures of GCR beyond 100 TeV, as well as transients associated with events of gravitational waves, tidal disruptions, and high energy neutrinos.

(3) Discovering the Sky at the Longest Wavelength (DSL) Mission

This mission consists of a linear array of micro-satellites placed on a lunar orbit, which will open up a new window of astronomical radio observation at frequencies below 30 MHz, with great potentials for new and unexpected discoveries, and provide new insights into the various astrophysical processes in the planets and stars, the Milky Way, galaxies and supermassive black holes. It will also make high precision measurements of the global spectrum with minimum systematic error, to probe the history of the early Universe, by observing the redshifted radio signal of neutral hydrogen from the cosmic dark ages after the Big Bang, and the cosmic dawn when the first stars and galaxies formed^[2].

2.2 Exoplanets

Exoplanet exploration might be one of the hottest mission types since it encourages us to dwell on the fundamental question “Are we alone?” with some confidence. SPP III will address some scientific issues in this field, including but not limited to: the formation of diverse nearby planetary systems and the emergence of other worlds for solar-type stars. How common are habitable Earth-like planets orbiting around solar-type stars? How do Earth-like planets form and evolve?

In order to answer these scientific questions, there are currently 2 missions proposed for application, both are destined for a halo orbit around the L2 point of the Earth-Sun system.

(1) Closeby Habitable Exoplanet Survey (CHES) Mission

CHES is devoted to discover Earth-like planets of the nearby solar-type stars via ultra-high-precision relative astrometry with 1 μs precision at 500–900 nm. The major scientific goals are two-folds: to search for the terrestrial planets in habitable zones orbiting 100 FGK stars within 10 pc; further to conduct a comprehensive survey and census on the nearby planetary systems^[3].

(2) Earth 2.0 (ET) Mission

ET is a wide-field and ultra-high-precision photometric survey mission, mainly composed of six transit telescopes and one microlensing telescope. ET is designed to measure, for the first time, the occurrence rate and the orbital distributions of Earth-sized planets, including the elusive habitable Earth-like planets orbiting stars just like a sun.

2.3 Heliophysics

Heliophysics paves the way to understand the Sun and its interactions with the Earth, the solar system and the interstellar medium, including space weather. SPP III will answer some aspirational questions persisted in the field of heliophysics, such as the origin of the solar cycles and solar dynamo. What are the characteristics and dynamics of the solar interior? The outward propagation of the solar eruptions and their impacts on the Earth space environment. How does the global magnetic field distribute and evolve? What is the composition of interstellar gas in our galactic neighborhood and how does it influence the heliosphere and its evolution?

There are currently 4 missions proposed for flight, aiming to advance our understanding the solar activities

and their influence on Earth and the solar system.

(1) Solar Ring (SOR) Mission

SOR is proposed to monitor and investigate the Sun and inner heliosphere from a full 360° perspective in the ecliptic plane. This large mission will deploy three 120°-separated spacecraft on the 1 AU orbit. Solar Ring mission aims to address the origin of solar cycle, the origin of solar eruptions and the origin of severe space weather with necessary in-situ instruments and imagers^[4].

(2) Solar Polar-orbit Observatory (SPO)

SPO will directly image the solar poles in an unprecedented way with a spacecraft traveling in a large inclination ($\geq 80^\circ$) off the ecliptic plane and a small ellipticity. SPO will unveil the origin of the solar magnetic activity cycle that shapes the living environment of human beings, to determine the generation mechanism of the high-speed solar wind that connects the Sun and celestial bodies in the solar system, and to construct data-driven global heliospheric numerical models which serves as the foundation for space weather prediction.

(3) Earth-occulted Solar Eclipse Observatory (ESEO)

It is proposed to place a solar telescope near the second Lagrange point (L2) of the Earth-Sun system exploiting the Earth's occultation to explore the inner corona. As a small mission, ESEO might be very beneficial to reveal the early stage of the solar eruptions in the inner corona and subsequently how the Earth's far magnetotail will respond if being “plowed”.

(4) Chinese Heliospheric Interstellar Medium Explorer (CHIME)

This candidate spacecraft, being placed at distances up to 3 AU away from the Sun, might provide the first in situ measurements of pristine interstellar gas and dust in their high-density regions at 2–3 AU from the Sun, as well as global energetic neutral atom images of heliospheric outer boundaries. CHIME will be launched into an elliptical, heliocentric orbit with perihelion at about 1 AU and aphelion at about 3 AU.

2.4 Planetary and Earth Science

The mysteries of our planet Earth and other celestial bodies across the solar system are awaiting unlocking. This understanding serves the fundamental need to improve our lives on Earth, advancing the frontier for all humanity stepping out of Earth. SPP III will address some key issues in the field of planetary and Earth sci-

ence as follows: how do Greenhouse Gases (GHGs) impact and respond to climate change? what are the spatial and temporal variations of multiscale ocean dynamics? how can we trace the 1st 10 Million Years Evolution of the Dichotomic Solar System? the geological and thermal history of Venus, the mechanisms of super-greenhouse effect, past and current habitable environments, and the possible existence of life on Venus.

There are currently 4 candidate missions dedicated to address the above questions.

(1) E-type Asteroid Sample Return (ASR) Mission

ASR is aimed to explore the E-type 1989 ML asteroid and return samples collected from up to three sites. Careful investigation of the returned samples will reveal the 1st 10 Ma evolution of the nebula under extremely reducing conditions in the inner solar system. It is highly hoped to shed light on the formation of the dichotomy of the solar system through comparison with those acquired from the C-type asteroids Ryugu and Bennu, both formed in the outer solar system. The entire mission will take approximately 4 years to accomplish.

(2) Venus Volcano Imaging and Climate Explorer (VOICE) Mission

VOICE is an orbiting mission of a polar-circular orbit of about 350 km to investigate Venusian geological evolution, atmospheric thermal-chemical processes, surface-atmosphere interactions, and habitable environment and life in the clouds.

(3) Climate and Atmospheric Components Exploring Satellites (CACES)

This small mission consists of two Low-Earth-Orbit (LEO-LEO) satellites in sun-synchronous orbits. It focuses on benchmark climate variables and atmospheric composition observations. CACES promises to provide a deeper understanding of the major challenge in the Earth system science that how GHGs impact and respond to climate change and weather disasters and support the carbon emission calculation in 2028, as well as China's targets of achieving a carbon peak by 2030 and carbon neutrality by 2060^[5].

(4) Ocean Surface Current multiscale Observation Mission (OSCOM)

OSCOM is dedicated to the frontier of ocean multiscale dynamics and energetics based on satellite Doppler oceanography. It will contribute to the study of ocean sub-mesoscale non-equilibrium dynamics, multiscale processes, mass/energy exchanges between ocean and atmosphere, biogeochemical cycles, and climate change,

all of which are implemented through simultaneous observation of Ocean Surface Currents (OSC), Ocean Surface Vector Winds (OSVW), and Ocean Surface Wave Spectrum (OSWS) by a Doppler Scatterometer (DOPS)^[6].

3 Pre-Phase A Studies of Future Science Missions under SPP III

SPP III will continue to adopt the program management model of SPP I and II. Besides the flight missions, SPP III will also carry out preliminary and advanced research projects on the science mission concepts to be deployed in the next five years or beyond, that is, through the concept study as well as concept and technology development of the future space science missions, thus to form a complete research and exploration portfolio.

At present, the first Call of SPP III concept and technology development of the future science mission candidates has been completed, and more than 20 proposals have been submitted, including Very Large Area Gamma-ray Space Telescope (VLAST), Space Weather exploration program, Ceres Exploration program, Gravity Experimental Satellite, *etc.*

These proposals cover all fields of space science, *i.e.* space astronomy & astrophysics, exoplanets, heliophysics, planetary science, Earth science, space biology and fundamental physics, establishing a sound basis for space science and exploration missions in the next decade. They present the researchers' aspirational attempts to achieve scientific objectives, such as "indirect detection of dark matter space", "physical properties and eruption laws of corona and stellar corona", "origin of Ceres and its underground ocean and volcanic geological activities", and "the origin and nature of material inertia", *etc.*

In the second half of 2022, NSSC will organize a panel of experts to review these pre-phase A candidates and make project priority recommendations, which will serve as the effective inputs for SPP III final portfolio.

4 Management of SPP III

The comprehensive evaluation of SPP III science mission candidates will be completed by the middle of 2022, and a list of recommended missions will be provided as a decision-making reference for CAS headquarters. By the middle of 2023, the necessary prepara-

tory work of SPP III such as the demonstration of its implementation roadmap and the evaluation of the total budget will be completed, striving to get the program adopted during the late “14th Five-Year Plan” period, *i.e.* around 2024.

Thanks to the advanced experiences learned from SPP I & II, a complete mission planning and management chain has been established, covering the strategic planning, mission proposal, mission concept study, concept and technology development, design & fabrication, launch and in-orbit operation of flight missions, data analysis and research, as well as scientific outcome evaluation. The “Principal Investigator + Mission Commander + Chief Engineer” system has been set up for the mission management. Nevertheless, SPPs have attracted the major space science communities and related institutions across China and abroad to participate in the research and mission implementation^[7].

5 Summary

SPP III is an effective approach to promote China's space activities, and make great contributions to international space science and exploration.

In order to produce original achievements with science excellence continuously, SPP III will be targeted at the frontiers of space science, taking scientific significance and originality of scientific achievements as the most important factor. It is expected that SPP III will select 5–7 space science missions depending on the available budget, technique readiness, and reasonable manufacture schedule.

During the implementation of the mission, NSSC/CAS

will continue to uphold the open policy, welcoming international cooperation at every level such as mission level, payload level, or just data sharing. China's space science program will continuously produce new knowledge, new theories, and new ideas through scientific exploration. It will eventually benefit life on the Earth and make great contributions to humanity.

References

- [1] ZHANG S N, SANTANGELO A, FEROCI M, *et al.* The enhanced X-ray timing and polarimetry mission—eXTP[J]. *Science China Physics, Mechanics & Astronomy*, 2019, **62**(2): 29502
- [2] CHEN X L, YAN J Y, DENG L, *et al.* Discovering the sky at the longest wavelengths with a lunar orbit array[J]. *Philosophical Transactions of the Royal Society A: Mathematical, Physical and Engineering Sciences*, 2021, **379**(2188): 20190566. DOI: 10.1098/rsta.2019.0566
- [3] JI J H, WANG S. China's future missions for deep space exploration and exoplanet space survey by 2030[J]. *Chinese Journal of Space Science*, 2020, **40**(5): 729-731. DOI: 10.11728/cjss2020.05.729
- [4] WANG Y M, JI H S, WANG Y M, *et al.* Concept of the solar ring mission: an overview[J]. *Science China Technological Sciences*, 2020, **63**(9): 1699-1713
- [5] LIU C L, KIRCHENGAST G, SUN Y Q, *et al.* Exploring greenhouse gases water and climate changes: scientific opportunities for the climate and atmospheric composition exploring satellites mission[J]. *Chinese Journal of Space Science*, 2020, **40**(2): 151-168. DOI: 10.11728/cjss2020.02.151
- [6] DU Y, DONG X L, JIANG X W, *et al.* Ocean surface current multiscale observation mission (OSCOM): Simultaneous measurement of ocean surface current, vector wind, and temperature[J]. *Progress in Oceanography*, 2021, **193**: 102531
- [7] WANG C, SUN L L, FAN Q L, *et al.* Progress and prospects of the strategic priority program on space science[J]. *Chinese Journal of Space Science*, 2020, **40**(5): 618-625. DOI: 10.11728/cjss2020.05.618

Part II: Achievement Highlights

Overview of the Latest Scientific Achievements of Chang'E-4 Mission of China's Lunar Exploration Project*

CHEN Yuesong¹, TANG Yuhua², FAN Yu¹, YAN Jun³,
WANG Chi^{1,4}, ZOU Yongliao^{1,4}

1. National Space Science Center, Chinese Academy of Sciences, Beijing 100190
2. Lunar Exploration and Space Engineering Center, Beijing 100190
3. National Astronomical Observatories, Chinese Academy of Sciences, Beijing 100101
4. State Key Laboratory of Space Weather, National Space Science Center, Chinese Academy of Sciences, Beijing 100190

Abstract

On 3 January 2019, the Chang'E-4 probe successfully landed in the Von Kármán crater in the South Pole-Aitken Basin on the far side of the Moon. On 4 January, the Yutu-2 rover was successfully separated from the lander and the scientific payloads were powered on to conduct scientific exploration. It was the first time that man-made probe achieved soft landing and roving on the far side of the Moon. Based on the data obtained by scientific payloads on the Chang'E-4, the research team obtained geological information such as landing area topography, structure and composition; demonstrated the existence of deep materials—mainly olivine and low-calcium pyroxene in the South Pole-Aitken basin; achieved high-precision imaging of the layered structure of lunar subsurface in the roving area; discovered carbonaceous spheroidal meteorite residues and impact glass; preliminarily revealed the geological evolutionary history of the South Pole-Aitken basin; for the first time, obtained information of the radiation dose of energetic particles at the lunar surface and the structure of the lunar neutral atomic energy spectrum; discovered the lunar mini-magnetosphere and contributed new knowledge of the radiation hazards at the lunar surface. This article summarizes the latest scientific achievement from the Chang'E-4 mission over the past three years.

Key words

Chang'E-4, Scientific objectives, Scientific payloads, Scientific achievement

1 Chang'E-4 Mission Overview

The Chang'E-4 mission consists of three parts: the lander, Yutu-2 rover and Queqiao relay satellite. On 3 January 2019, Chang'E-4 probe successfully landed in the Von Kármán crater in the South Pole-Aitken Basin on the far side of the Moon. The exact landing position

is 177.5991°E, 45.4446°S, and the elevation is about -5935 m (Liu *et al.*, 2019).

On 4 January, the Yutu-2 rover was successfully separated from the lander and rolled onto the lunar surface. The scientific payloads on board worked normally and the data were effectively transmitted down. Until May 2022, Chang'E-4 has worked on the lunar surface

* Supported by National Key Research and Development Program of China (2020YFE0202100)

Received July 5, 2022

for 42 months and the rover has walked 1180 m (Fig. 1). It became the longest working probe on the surface of the Moon.

1.1 Scientific Objectives of Chang'E-4 Mission

There were four scientific objectives for Chang'E-4 mission: (i) low-frequency radio astronomical study on the lunar surface; (ii) shallow structure investigation at the lunar far side of roving area; (iii) the topographic and the mineralogical composition investigation for the lunar far side of roving area; (iv) neutrons radiation dose and neutral atoms study on lunar environment (Jia *et al.*, 2019).

1.2 Scientific Payloads on Chang'E-4 Mission

To achieve the scientific objectives, there were nine scientific payloads equipped on the Chang'E-4, four of which were mounted on the lander.

(1) Landing Camera (LCAM). It turned on during the decent phase while landing on the moon and obtained the lunar feature map and topographic map of the landing area at each altitude from 2 km–4 m.

(2) Terrain Camera (TCAM). It was installed on the top of stand on the lander and obtained the optical im-

age of the landing site. The imaging distance was 5 m to infinity.

(3) Low Frequency Spectrometer (LFS). It detected solar low-frequency radio features at 0.1–80 MHz during the lunar day.

(4) Lunar Lander Neutron & Dosimetry (LND). It measured energetic particle radiation dose at the lunar surface, particles in the Earth's radiation belt, and secondary particles caused by galactic cosmic ray interactions with the lunar surface.

There were four scientific payloads mounted on the Yutu-2 rover.

(1) Panoramic Camera (PCAM). It was installed on the top of the mast above the rover and the imaging distance was 3 m- to infinity. As the rover moved and the mast rotated, it could acquire 3D optical images of the lunar surface in the survey area.

(2) Lunar Penetrating Radar (LPR). It had high-frequency channel and low-frequency channel. While the rover was moving, it could detect the deep surface structure and the internal structure and thickness of the lunar soil along the rover's roving route.

(3) Visible and Near-Infrared Imaging Spectrometer (VNIS). It could obtain the spectrum of detection target at 450–2400 nm full band and the hyperspectral image data at the band range of 450–950 nm.

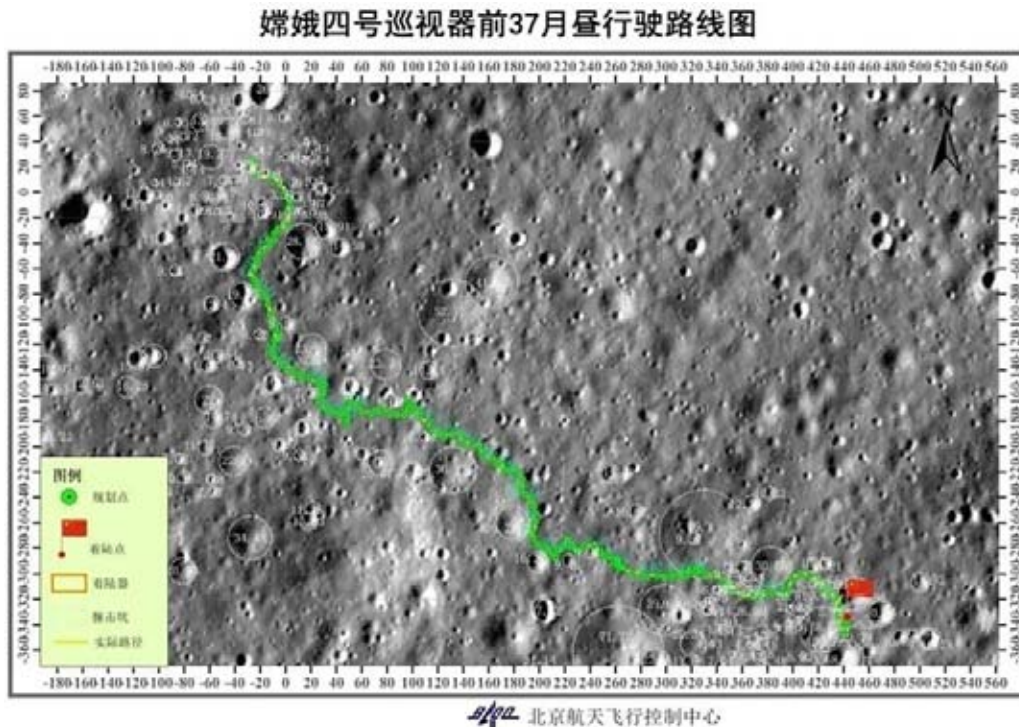


Fig. 1 Route map of the Yutu-2 rover (<https://mp.weixin.qq.com/s/utRYQ7WbGiQNq1engYJmQ>)

(4) Advanced Small Analyzer for Neutrals (ASAN). It could measure neutral atoms produced by the interaction of the solar wind with the lunar surface, including the lunar soil material sputtered by the solar wind and the solar wind material scattered by the lunar surface.

The Netherlands-China Low Frequency Explorer Instrument (NCLE) on the communication relay satellite. It could acquire the sky background radio survey images at low-frequency bands for monitoring studies of planetary radio emission changes.

1.3 Operation of Scientific Payloads

Landing Camera: it was turned on during the decent phase and took pictures of the landing site. It just turned on one time and lasted for 9 min. After a successful soft landing on the Moon, the landing camera completed its exploration mission.

Terrain Camera: it worked on the first lunar day after landing and turned on for 46 times. It completed imaging of low-frequency radio spectrometer antenna unlocking process, dynamic photographing movement at X-point and in-situ turning of the Rover, circling shooting with -60° to $+45^\circ$ pitch angle and taking pictures of the rover. While the lander entered the first lunar night, the terrain camera completed its exploration mission.

Panoramic Camera: it took pictures of the lander during the first lunar day and completed up-down circling shooting by color imaging during the second lunar day. It was turned on to take pictures when the rover drove to the detection point and it can be planned to take multiple sets of panchromatic or color images at fixed points when objects of interest occur.

LPR: it synchronously works while the rover is moving every lunar day.

VNIS: imaging or calibration can be taken when the solar altitude angle is high around the lunar noon or objects of interest occur. It detects the tarcting rut of the rover and lunar soil, rocks and impact crater along the way.

ASAN: it starts to work when the solar altitude angle is high around the lunar noon or objects of interest occur. Detection modes include high voltage mode and ion mode.

LFS: it started to work at lunar noon to detect low-frequency signals from space.

LND: it chooses the opportunity to start working when the probe awakes in the lunar day. It can work during the whole lunar day.

2 Scientific Achievement of Chang'E-4

2.1 Topography of the Landing and Roving Area

2.1.1 Topography and Impact Crater Features

The major impact craters in the Von Kármán region include the Von Kármán M impact crater, the Von Kármán impact crater, the Leibnitz impact crater, the Finsen impact crater, the Alder impact crater, and the Von Kármán L and L' impact craters. The Von Kármán impact crater is located within a magnesite ring unit in the northwestern South Pole-Aitken Basin, and was flooded by one or more lunar mare basalt, after which ejecta from numerous impact craters in the surrounding area was ejected into its interior. The crater floor was modified by geologic processes such as impact ejecta, volcanism, and tectonic movement. A 5-centimeter resolution DEM covering $380\text{ m} \times 390\text{ m}$ was produced by using panoramic stereoscopic images, revealing that the overall topography of the Von Kármán impact crater in the landing area is high in the northeast and low in the southwest, with wavy undulations in the southeast to northwest directions (Fig. 2). At the 100-meter baseline, the overall bottom of the Von Kármán impact crater is very flat, with a local slope of about 10° ; at the 10-meter baseline, the two-way slope near the landing site varies considerably, and the maximum slope in and around some impact craters can be greater than 20° ; at the meter and tens of meters baselines, the two-way slope of the landing area is similar to that of the lunar mare (2.0° – 3.4°) (Fu *et al.*, 2020; Guo *et al.*, 2021a; Qiao *et al.*, 2019).

The basalt plain is covered with a large number of secondary craters formed by younger impact craters. Among them, the secondary crater formed by the Finsen impact crater from the east side of the Von Kármán impact crater has the most prominent influence on the topography of the landing site and the Yutu-2 roving route, and it is an important part of controlling the regional geomorphology. The secondary crater of the Finsen impact crater is significantly degraded and appears as a discrete linear depression and bulge in the topographic landscape. Using LROC NAC orthophotography, panoramic camera images, and 1-centimeter resolution DEMs, 4333 impact craters of 100 m or larger were extracted within the entire landing area ($2.4^\circ \times 1^\circ$, $51\text{ km} \times 30\text{ km}$), 11787 impact craters were extracted in the area of

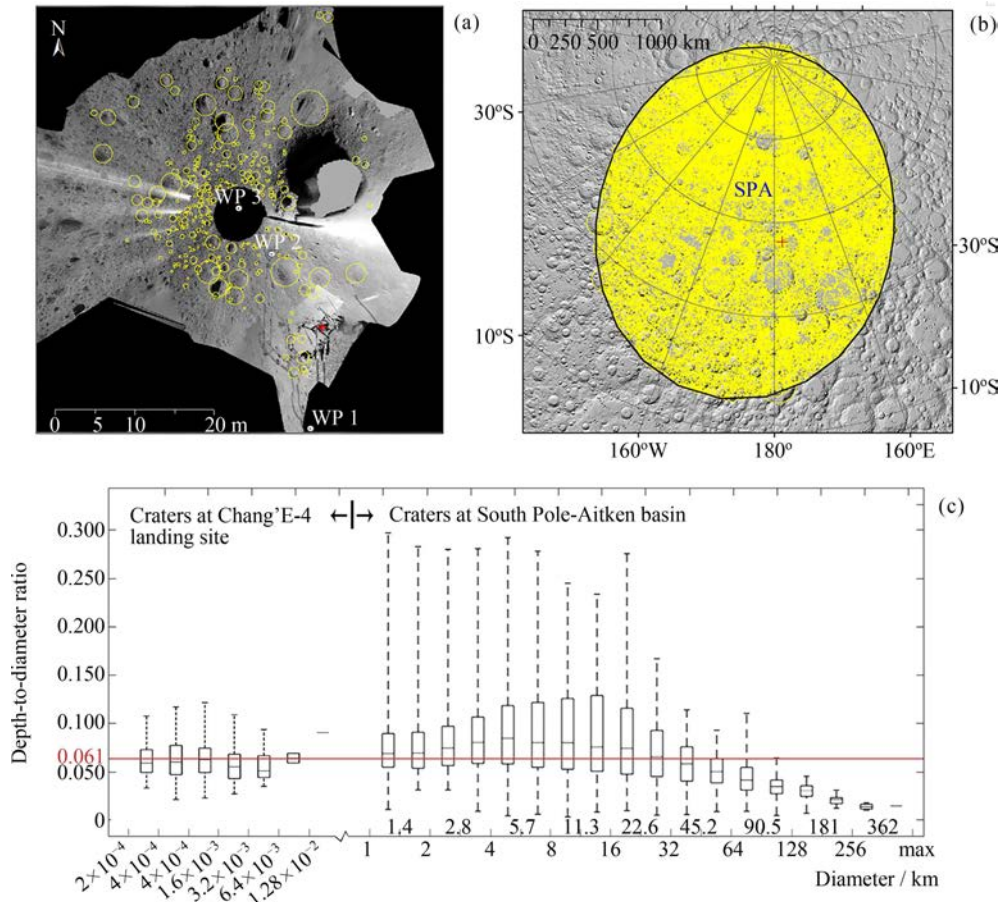


Fig. 2 Comparison of crater depth-to-diameter ratios between (a) small craters (>0.1 m) at Chang'E-4 landing site; and (b) large craters (>1 km) in the SPA basin; (c) Box-and-whisker plot of crater depth-to-diameter ratios (Wu *et al.*, 2021)

3.2 km \times 3.0 km from the landing site, 738 impact craters of meter to sub-meter scale were extracted within 60 m from the camera, and 1023 impact craters of diameter larger than 10 cm were identified along the Yutu-2 roving route. Within 60 m, 738 impact craters of meter to sub-meter scale were extracted, 1023 impact craters with diameters larger than 10 cm were identified within 50 m \times 50 m of the landing site, and some fresh impact craters with diameters ranging from < 1 m to 3 m were scattered along the Yutu-2 roving route. The relationship between depth and diameter of impact craters has a good consistency, but the distribution of depth-diameter ratios is scattered, and the depth-diameter ratios of small impact craters at 10cm scale are significantly smaller than those of kilometer-scale impact craters, indicating the inclusion of impact craters at different degradation stages and indicating the unique process of small impact crater formation in mature lunar soils (Jia *et al.*, 2021; Wu *et al.*, 2021; Gou *et al.*, 2020;

Guo *et al.*, 2021; Ding *et al.*, 2020a; Ding *et al.*, 2020).

2.1.2 Characteristics of the Impact Ejecta

The thickness of the ejecta covered by the landing area is about 60–70 m, with the uppermost NE-SW distributed linear ejecta from Finsen Crater superimposed on the SE-NW ejecta from Adler Crater, and the thickness of ejecta from Finsen and Adler Craters at the landing site is about 30 m and 35 m, respectively (Fig. 3). The cumulative thickness of ejecta is consistent with the difference in elevation between the landing site and the basalts at the base of the Von Kármán crater (Di *et al.*, 2019). The Finsen impact crater formed a large string of secondary craters on the lunar mare basalt at the base of both the Von Kármán and Leibniz impact craters, and the secondary craters are extremely well preserved on the lunar mare at the base of the Leibniz impact crater with well-defined crater rims, while the secondary craters of Finsen craters are highly degraded on the lunar mare at the base of the Von Kármán impact craters.

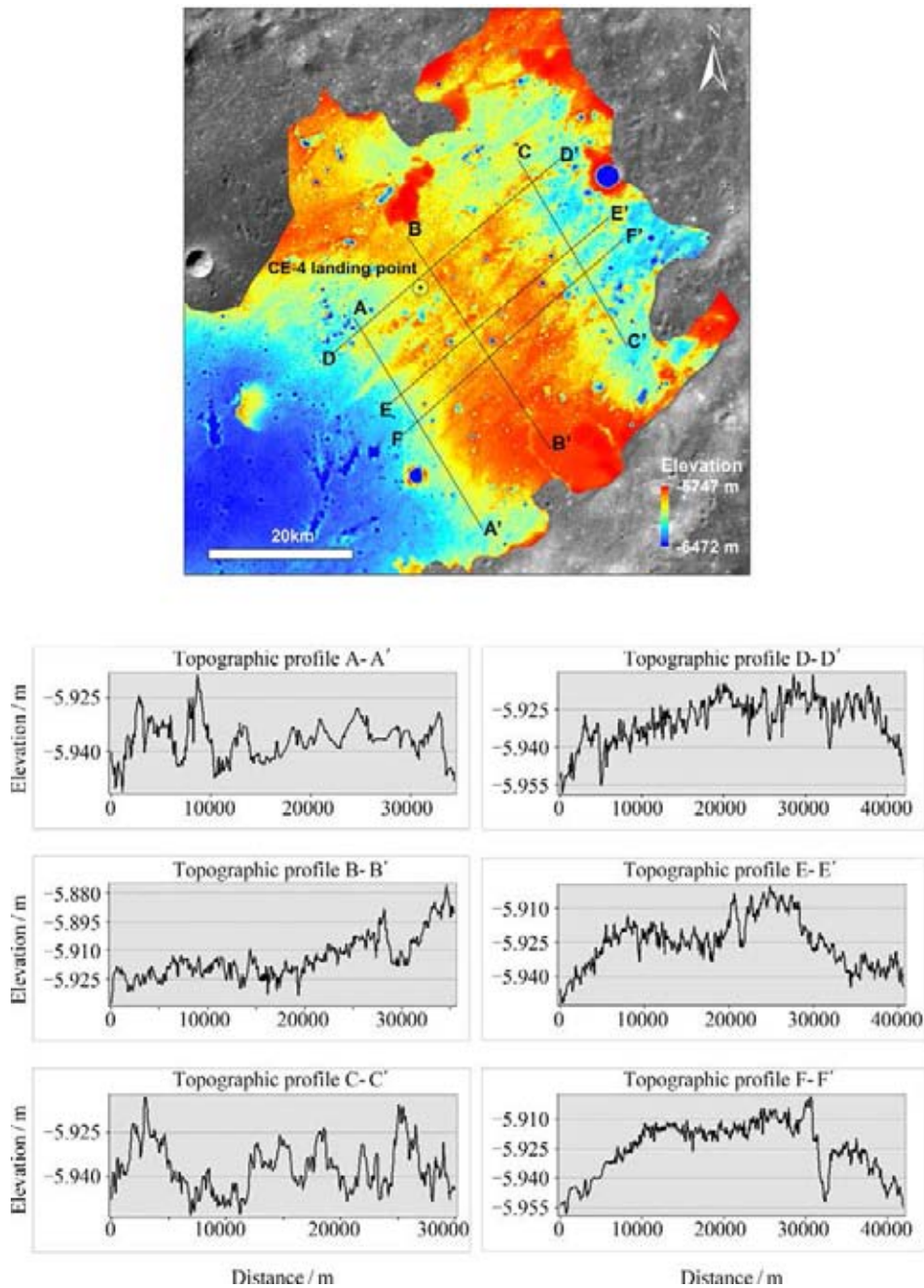


Fig. 3 SLDEM2015 and topographic profiles of the context of the Chang'E-4 landing site (Di *et al.*, 2019)

Two profiles of ejecta, detected by LPR, from a small fresh impact crater show that the ejecta is not the dense rocks excavated by the impact, but the loose lunar soil closed by instantaneous pore closure under the impact effect. The study suggests that the lunar mare basalts at the base of the Von Kármán impact crater may have been filled with large amounts of loose impact ejecta prior to the formation of the Finsen impact crater, resulting in a smaller initial topography and faster degradation rate in the subsequently superimposed Finsen

secondary crater here, indicative of a more ancient sub-surface source of material (Xiao *et al.*, 2021).

2.1.3 Characteristics of Lunar Soil and Gravel

Using the LPR high-frequency channel data and the three-dimensional velocity tracking method, the dielectric constant of the material in the depth below the lunar rover path down to 50 m was obtained and found to be similar to that of typical lunar soil material. The average value of the estimated dielectric constant from the lunar surface down to 4 cm is about 3.11 ± 0.085 , and there

are about 93 locations with dielectric constants larger than 4, indicating high-density non-lunar soil characteristics (Fig. 4). The estimated loss angle tangent of the high-frequency LPR within about 400 ns is about 0.005, indicating that the dielectric properties of the material in the surface layer larger than 40 m are similar to those of typical lunar soil material. The overall rock abundance in the Chang'E-4 landing area is very low, about 0.21%, which is typical characteristics of mature lunar soil. In the vertical profile, the thickness of lunar soil on the roving route is about 12 m. The average particle size of lunar soil material increases with depth, indicating that the lunar soil production rate at the landing site may be

much larger than the normal lunar soil production rate on the lunar surface. The high maturity of the lunar soil at the landing site revealed by the rover traces, reveals the relative influence of local topography and spatial weathering rate on the strength of the lunar soil. It is believed that the high dielectric constant region in the mature lunar soil is caused by surface exposure or buried rocks, and the distribution of lunar surface rock fragments provides new clues to decipher the formation and evolution of lunar soil (Ding *et al.*, 2021; Wu *et al.*, 2021; Lai *et al.*, 2019; Lai *et al.*, 2021b; Li *et al.*, 2020; Song *et al.*, 2020; Xiao *et al.*, 2021; Tang *et al.*, 2020).

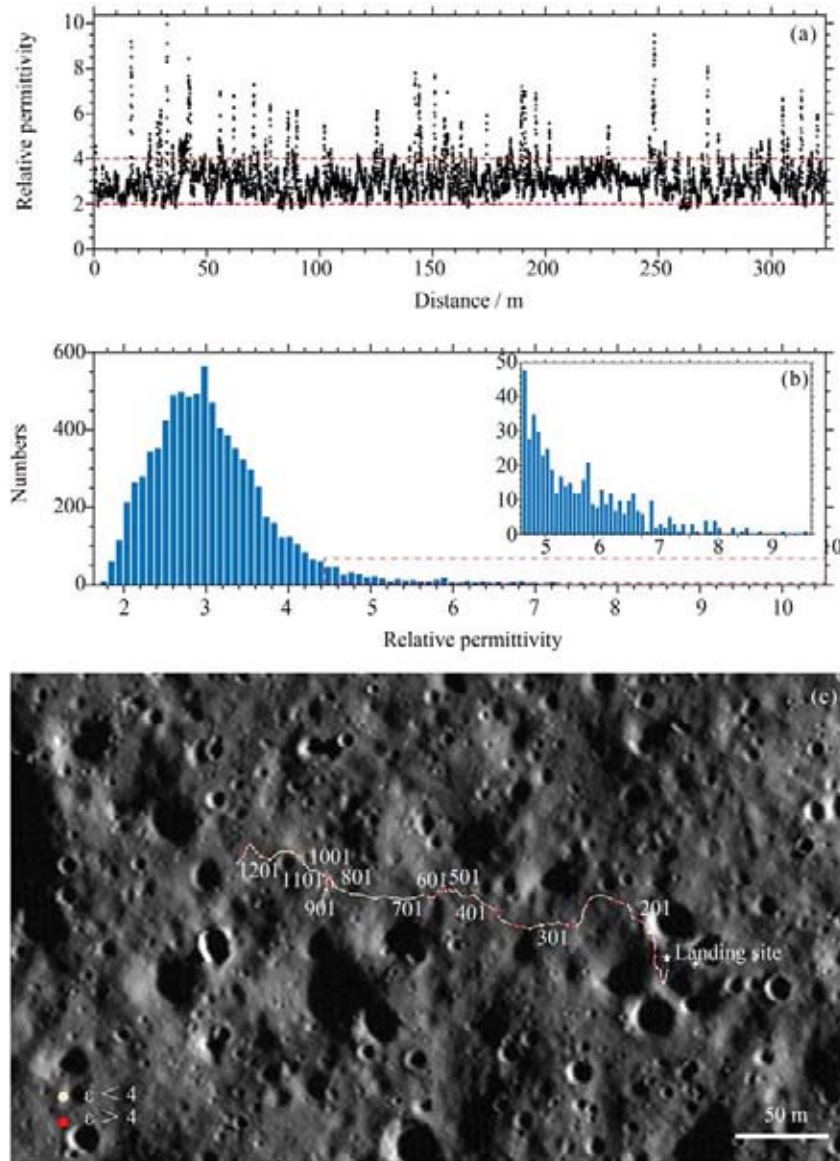


Fig. 4 Relative permittivity derived for the top-most (about 4 cm thick) regolith along the path of Yutu-2 in the first 12 lunar days (Ding *et al.*, 2021)

2.2 Deep Material and Material Composition of the Landing Region

2.2.1 Luminosity, Thermal Radiation Characteristics and Space Weathering of Lunar Soil in the Landing Region

An in-situ photometric experiment was conducted by using VNIS on the same region of the lunar surface during the tenth lunar day, and the spectra of the same target were successfully obtained under the conditions of different observational geometric angles of solar altitude and orientation. It was found that the quality of the spectral data gradually decreases as the solar altitude angle decreases, which affects the accuracy of the inversion of the composition of the materials (Fig.5) (Lin *et al.*, 2020a, Lin *et al.*, 2020b; Lin *et al.*, 2020c; Yang *et al.*, 2020).

VNIS measured a series of spectra from the same region of the lunar surface and at different moments of the

same lunar day to further confirm the lifting characteristics of the reflected spectra after $2\ \mu\text{m}$ under high temperature conditions at the lunar surface, and the results show that the thermal contribution in the reflected spectra significantly increases the pyroxene and/or glass abundance at the landing site surface temperature of $346 \pm 8\ \text{K}$ from 14:28 to 14:41 lunar local time (Fig. 6). The thermal contribution in the reflectance spectra significantly increases the estimation error of pyroxene and/or glass abundance, and the thermal radiative character is found to be significantly influenced by the microscale roughness in addition to the material composition (Lin *et al.*, 2021).

Based on the maximum similarity between the simulated spectra and the in-situ measured spectra of Yutu-2, it is estimated that the sub-microscopic Fe content of the lunar soil in the Chang'E-4 landing region is about $0.32 \pm 0.06\ \text{wt.}\%$ and the FeO content is about $12.6 \pm 0.6\ \text{wt.}\%$. The calculation shows that the maturity of the

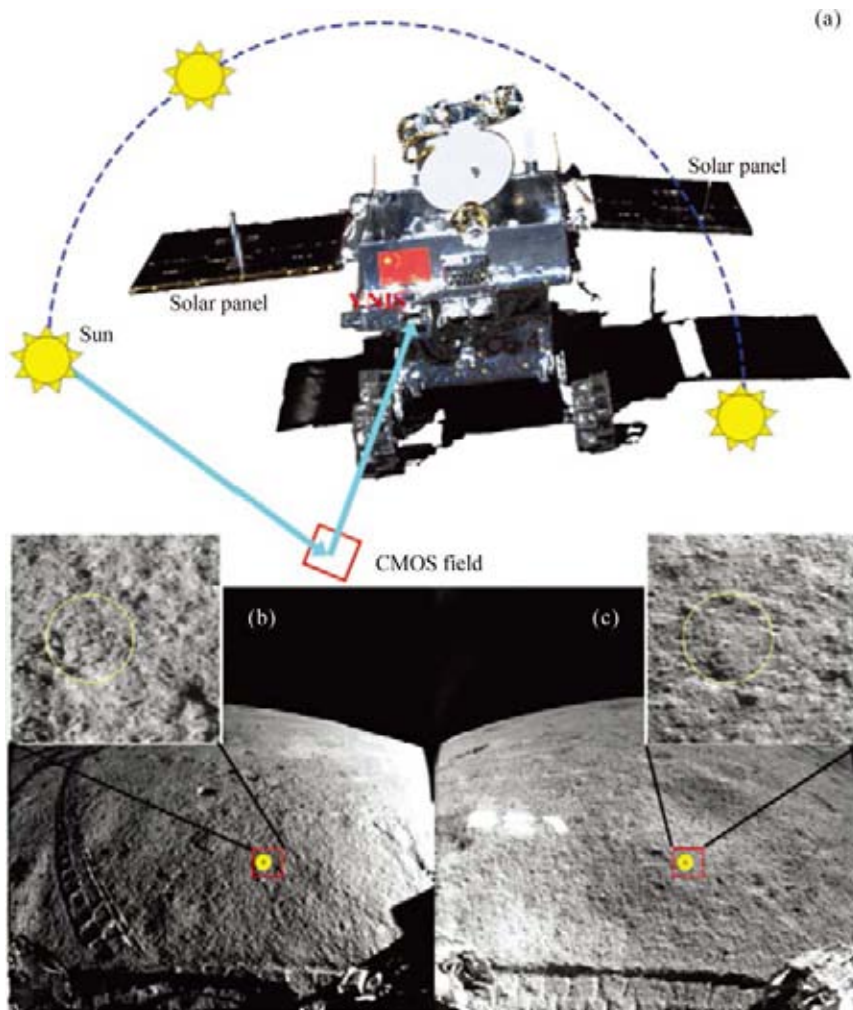


Fig. 5 Spectrophotometric measurements of lunar regolith by the Yutu-2 rover (Lin *et al.*, 2020)

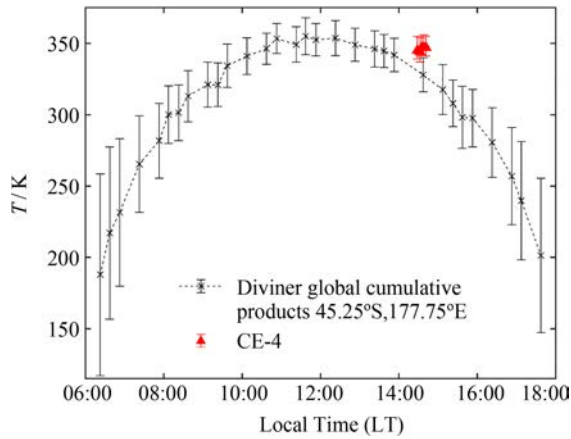


Fig. 6 Temperature at the Chang'E-4 landing site (Lin *et al.*, 2021)

lunar soil in the landing region is 82 ± 15 , which indicates that the lunar soil in the Chang'E-4 landing region, mainly originating from the Finsen impact crater ejecta, is highly likely to be mature lunar soil (Gou *et al.*, 2020a). It indicates that the rapid formation process of lunar soil in the Chang'E-4 landing region adequately mixed the most surficial of highly mature lunar soil, which is consistent with the geological background that the landing region has experienced more than 3 billion years of space weathering.

2.2.2 Characteristics of deep Material Composition and Distribution in the Landing Region

Von Kármán crater is predominantly flooded by low-Ti basalts (1.5–3 wt.% TiO_2), rich in clinopyroxene and low in olivine. The basalts are affected by ejecta from the Finsen crater, with obvious compositional heterogeneity and lower FeO (content compared to the lunar mare basaltic samples). Local basalts not affected by the Finsen crater ejecta were excavated by the Zhinyu crater lying in the west of the landing site. The composition of the basalt varies with depth, suggesting Von Kármán crater has experienced at least three lava flooding events, and thus has formed three basaltic layers. The relatively homogeneous Mg values, *i.e.* $\text{Mg}/(\text{Fe}+\text{Mg})$, of the olivine among the three basaltic layers suggest that the source of the three mare basalts may have similar compositions or may be from a magma chamber where the melt composition evolved over time. The non-mare materials from craters such as Finsen have a different composition, with the central peaks characterized by an Mg-rich, low-Ca pyroxene composition, and the crater walls and their ejecta by relatively Fe/Ca-rich pyroxene

compositions. These characteristics are consistent with the mineralogies of the pyroxene-bearing zone and compositional anomaly zone in the South Pole-Aitken Basin (Gou *et al.*, 2021a).

The analysis of infrared spectral data by spectral parameter analysis, spectral unmixing, and spectral matching indicates that the different exploration targets on the Yutu-2 rover roving route may have inhomogeneous material composition, and various rock types such as plagioclase, saprolite/gabbro have been identified, revealing the mixing degree of different source reservoirs from Von Kármán basalt, South Pole-Aitken impact melt, lunar mantle material, and crustal source ejecta material (Huang *et al.*, 2020).

The interpretation results of the spectra of the first two detection points of the first lunar day, by using the modified Gaussian model, show that the detection target has the highest olivine content, followed by low-calcite pyroxene and the least high-calcite pyroxene. The relative content ratios of olivine, low-calcite pyroxene and high-calcite pyroxene minerals of the two detection points are 48:42:10 and 55:38:7, respectively (Li *et al.*, 2019). The matching results of the spectral lookup table built based on the Hapke radiative transfer model found that the detection targets of the first two lunar days had a high content of plagioclase, about 60%, and a low content of magnesian-iron minerals (Hu *et al.*, 2019). Empirical model calculations based on Apollo samples found that the lunar soil targets of the first three lunar days generally contain close to 60% of clastic agglomerates and fewer magnesian and iron minerals such as olivine, which is consistent with the landing region having undergone a longer period of space weathering (Lin *et al.*, 2020c). The analysis based on the combination of spectral parameters such as absorption position and band area ratio reveals that the target spectra of the first three months of diurnal loam are dominated by olivine and pyroxene features, and the pyroxene minerals are dominated by monoclinic pyroxene with a composition between high and low calcium pyroxene, and this pyroxene composition is consistent with the rapid cooling crystallization of the magma (Chen *et al.*, 2020).

The Yutu-2 lunar rover carried out the first spectroscopic detection of the rock target on the third lunar day, and the fitting results of the modified Gaussian model indicated that the magnesium-rich olivine and magnesium-rich plagioclase minerals in the rock were essentially equivalent (Gou *et al.*, 2019; Gou *et al.*, 2020b;

Gou *et al.*, 2021b). Analysis based on the Hapke radiative transfer model finds that the clasts contain about 48% plagioclase, about 38% low-calcium pyroxene, and about 14% olivine, corresponding to olivine-bearing thalassic rocks (Lin *et al.*, 2020c). The clasts have a moderately fine-grained structure and are unlikely to be plutonic rocks, but are consistent with the rapid crystallization conditions of magma lakes formed by the South Pole-Aitken Basin impact (Lin *et al.*, 2020c). The match results between the stone spectra and the spectra of lunar rocks and lunar meteorites in the NASA RELAB database indicate that the stone is enriched in plagioclase minerals (60%–80%), probably from the ejecta of the Zhinyu impact crater (Ma *et al.*, 2020).

The combination of Hapke model and sparse unmixing algorithm was used to obtain the mineral content and chemical composition information of detection targets in the first 21 lunar days. The mineral composition is dominated by plagioclase, followed by pyroxene and little olivine, which corresponds to the mineralogical characteristics of norite/gabbro, and the content of low-calcium pyroxene exceeds that of high-calcium pyroxene in most of the detection targets. In terms of

chemical composition, FeO content varies widely (7.42–18.82 wt.%), TiO₂ content is generally low (1.48–2.1 wt.%), while Mg values are low-medium (Mg[#] about 55) (Zeng *et al.*, 2021; Ling *et al.*, 2019).

Synthesizing the results of existing in situ spectra of the Chang'E-4 landing and roving region, most studies suggest that the main mineral in the area is plagioclase, followed by pyroxene (more low-calcium pyroxene than high-calcium pyroxene), and less olivine. The material composition and rock structure characteristics suggest that the South Pole-Aitken Basin basement is likely not a single genesis of material such as primitive deep lunar material exposed by simple excavation or differentiated crystallization in impact melt lakes, but a mixture of multiple sources, indicating the complexity of the South Pole-Aitken Basin composition and geological processes.

2.2.3 Discovery of Impact Remnants and Impact Glass from Carbonaceous Chondrite

During the 8th and 9th lunar days of the mission's operation, the rover approached a small fresh impact crater and discovered some mysterious “glassy” materials around the center (Fig. 7). The spectral analysis of this

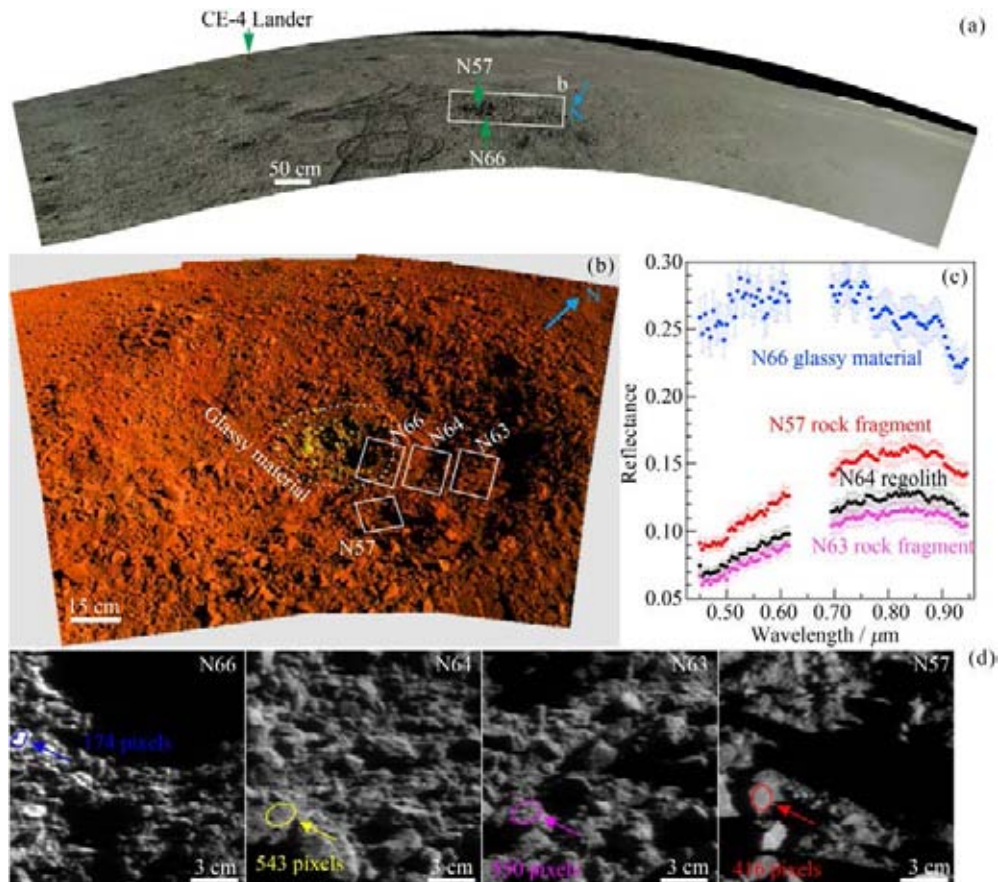


Fig. 7 Images and reflectance spectra of the targeted small crater (Yang *et al.*, 2021)

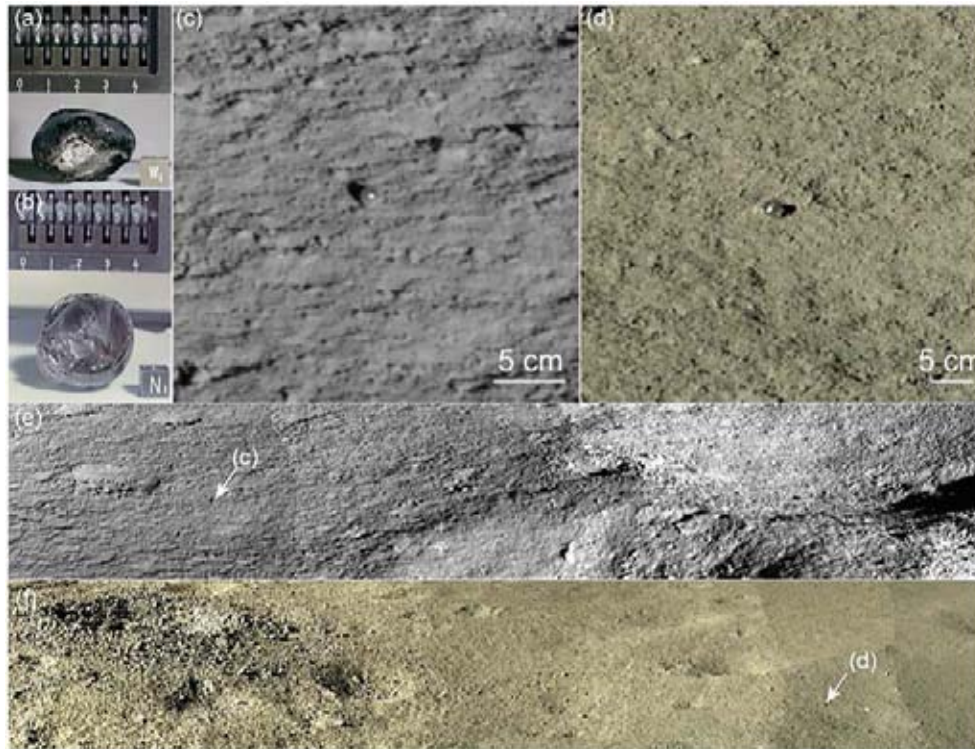


Fig. 8 Centimeter-sized glass globules collected by the Apollo 16 missions (a) (b) and those observed by the Chang'E-4 mission (c) (d). Note that the Apollo 16 mission was landed in the lunar highland, but the landing region was dominated by distal ejecta from the nearside. (e) (f) The two globules are accompanied by similar-sized fragments excavated by fresh impact craters nearby (Xiao *et al.*, 2021)

“glassy” material shows that it is similar to the Apollo impact melt breccias 70019 and 15546 (Gou *et al.*, 2020c). The detailed spectral analysis shows that the material contains a large amount of impact glass, which might be formed from another larger impact crater, suggesting that the lunar soil is evolving and maturing in the process of repeated impact smashing and welding into rock. This provides a new perspective to understand the formation mechanism of lunar soil (Lin *et al.*, 2020d). The comparison with the spectra of a large number of carbonaceous chondrites shows that the “glassy” material has a high spectral similarity with the carbonaceous meteorite. The quantitative unmixing analysis using the radiative transfer model shows that the carbonaceous chondrite component in the “glassy” material is over 40 wt.%. The formation age of this small impact crater estimated based on impact crater degradation models suggest that the crater should have formed within one million years ago. Similar carbonaceous chondrite remnants may be common on the lunar surface (Yang *et al.*, 2021).

Several centimeter-diameter translucent glass spheres were found on the moon. It is the first international dis-

covery of hand specimen-sized, translucent, lunar glass spheres. Analysis revealed that the glass spheres are not the direct landing products of lunar volcanic activity or foreign impactors, but impact glass of special composition (Fig.8), which may be a common material of lunar soil on the lunar highland. These findings have important implications for demonstrating that far impact glasses are inherent products of impact events on Earth-like objects, for inversion of the early impact history of the inner solar system, and for impact mechanics studies (Xiao *et al.*, 2021).

2.3 Subsurface Structure of Landing and Roving Region

The LPR high-frequency channel reveals structural information at depths larger than 40 m below the lunar surface of the roving route, divided into three main geological units (Fig.9). The first layer, about 0–12 m, is a layer of fine-grained lunar soil, with most of the material grain size less than 1 cm and fewer stones inside; the second layer, about 12–20 m, is a layer of ejecta mixed with fine-grained lunar soil and broken stones, in which a large number of stones are interspersed; the third layer,

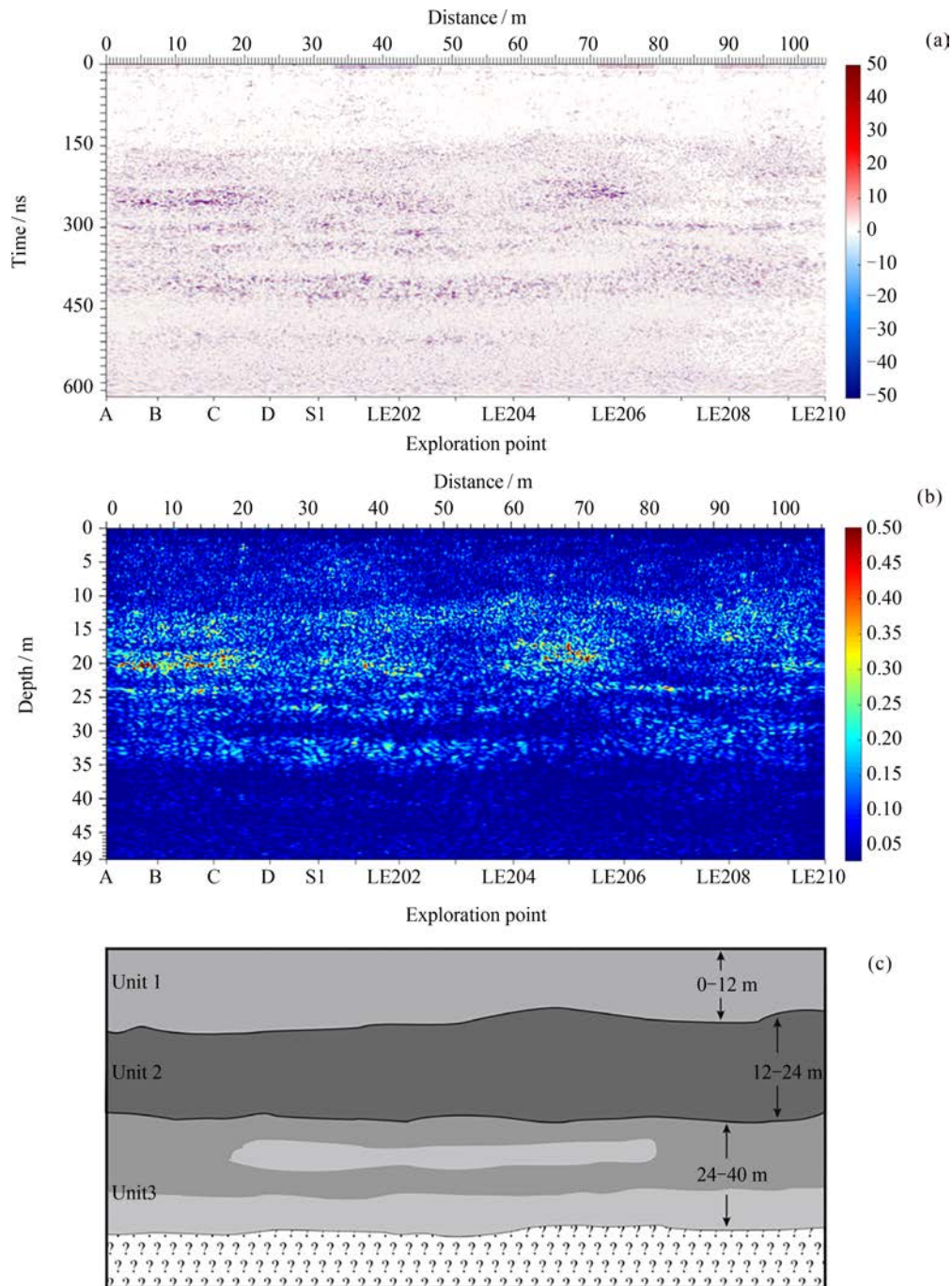


Fig. 9 LPR data at 500 MHz (Li *et al.*, 2020)

about 20–45 m, consists of discontinuous interlayer material with large differences in echo signals, showing alternating superposition of coarse-grained and fine-grained material. Studies by multiple teams have cross-checked these three subsurface structures, but there are large differences in the upper and lower boundaries of each material layer and their source interpretations, reflecting the complex geological history of the younger lunar geological units (Li *et al.*, 2020; Dong *et al.*,

2020a; Lai *et al.*, 2019; Lai *et al.*, 2020; Lai *et al.*, 2021a; Li *et al.*, 2020; Giannakis *et al.*, 2020; Xiao *et al.*, 2021; Xu *et al.*, 2021; Zhang J. *et al.*, 2021; Zhang L. *et al.*, 2020, 2021; Zhou *et al.*, 2021; Guo *et al.*, 2021a).

The LPR low-frequency channel penetrates to a depth more than 400 m below the lunar surface, and the radar echo signal reveals at least three layers of deep (> 40 m) subsurface structures (Fig.10). In terms of specific stratification and source interpretation, different interpretations

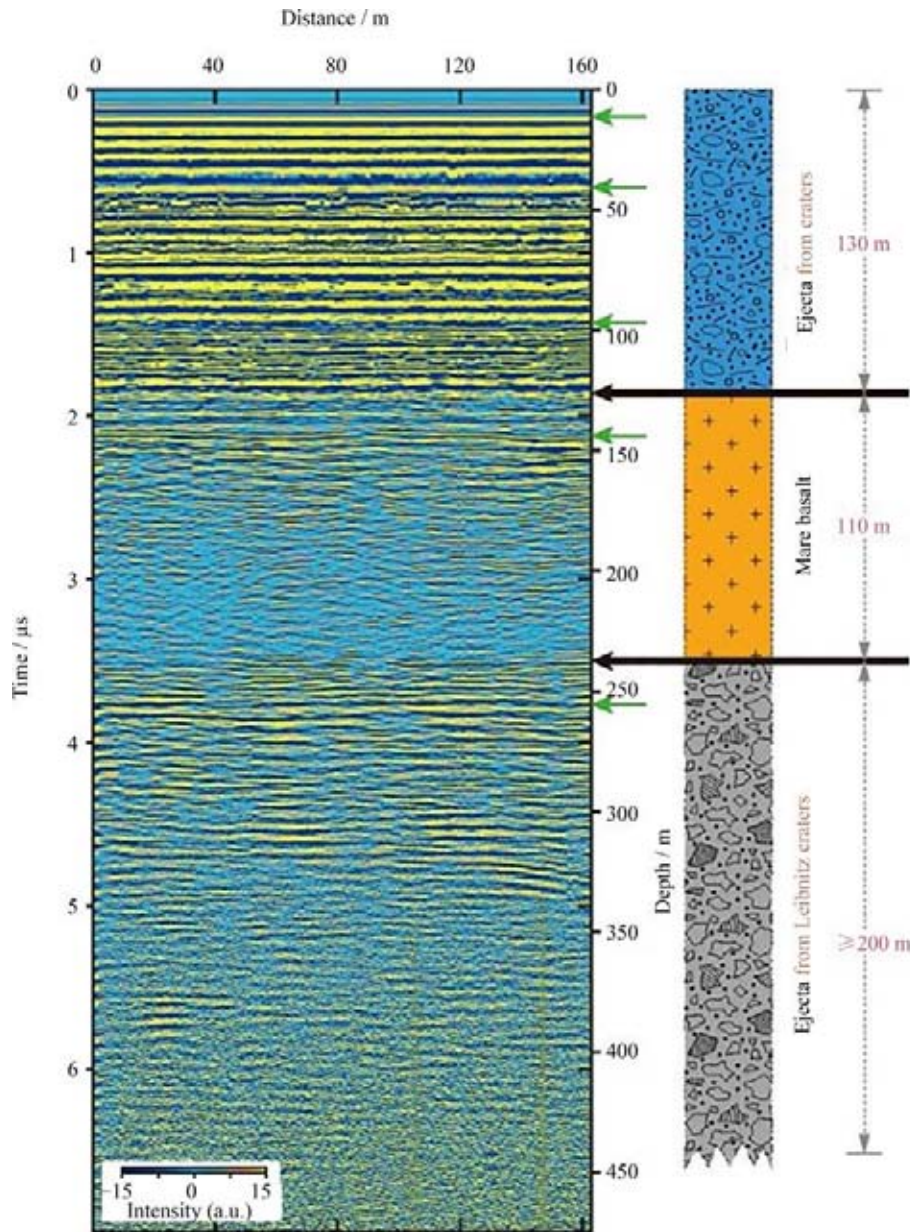


Fig. 10 Low-frequency LPR profile along the track of the Yutu-2 rover (Zhang *et al.* Nat. Astron., 2021)

have been obtained according to different data analysis methods and geological perspectives, and the main difference lies in the understanding of the source of the material within the surface layer to 100 m. Some views suggest that the material in this layer is mainly ejecta from different impact craters; other views suggest that the material at depth more than 40 m is mainly lunar mare basalt with some volcanic debris deposits interspersed by less late perturbations; some views also suggest that it is a spurious signal from LPR system itself (Lai *et al.*, 2020; Zhang L *et al.*, 2020; Zhang J *et al.*, 2021; Yuan Y *et al.*, 2021).

2.4 Geological Evolution of Von Kármán Impact Crater Region in the Far Side of the Moon

Based on the stratigraphic relationships of impact craters and the exposure of the central peak of the South Pole-Aitken Basin, the magnesian pyroxene unit lies beneath the calcium pyroxene unit. The materials of the magnesian ring represent the main material that formed in the excavation and melting of the South Pole-Aitken Basin impact event. No widespread distribution of olivine has been found in its interior, suggesting that the

main component of the upper lunar mantle may be pyroxene. The surface material of Chang'E-4 landing site and roving area is mainly from the Finsen impact crater, which is underlain by multi-period impact crater ejecta and multi-period basalts within the Von Kármán crater (Huang *et al.*, 2018).

VNIS observed multiple mineral assemblages at the surface, including anorthosite, sapolite/gabbro, impact melt breccia and other rock types, and these compositional characteristics may represent the deep lunar crust and possibly even the upper lunar mantle, with various degrees of mixing of impact melting from the South Pole-Aitken forming event and lunar mare basalt filling the Von Kármán crater. The surface lunar regolith has been subjected to long-term space weathering, and the lunar regolith in the landing and roving area is mature and contains some extralunar materials (Hu *et al.*, 2019; Lin *et al.*, 2019; Huang *et al.*, 2020; Yang *et al.*, 2021).

The low-frequency radar analysis shows that the shallow structure of the landing area consisted of three units, which are the strong-reflecting unit, a weak-reflecting unit and the medium-reflecting unit from top to bottom. Combining the constraints of regional geology and spatial distribution of large impact craters, the geological interpretation of the landing area is as follows (Lai *et al.*, 2020; Li *et al.*, 2020; Zhang *et al.*, 2021): The total thickness of the surface strong reflective unit is about 130 m, which is ejecta multiple impact craters and the basalt breccia layer at the bottom; the total thickness of the weak reflective unit is about 110 m, which is the basaltic layer of multiple eruptions; the thickness of the medium reflective unit is larger than 200 m, which is the ejecta of Leibniz impact crater in the northern part of the landing area. The high-frequency radar signal reveals a fine structure of the upper part of the strongly reflecting unit, characterized by a lunar regolith layer of about 12 m at the top, largely free of boulders, and a strip of ejecta of about 22 m below it. All of the ejecta are from the Finsen crater, with a total thickness of about 34 m.

Based on the results of remote sensing interpretation and Chang'E-4 in-situ exploration, the impact crater statistics estimate the model age of mare formation at the landing site to be about 3.2–3.7 billion years. The sequence of geological evolution of the landing and roving area from old to new is as follows: The Von Kármán impact crater formed in the Pre-Nectarian, after

which ejecta from the Leibniz impact crater covered part of the Von Kármán impact crater floor; between about 3.2 and 3.7 billion years, lunar mare basalt filled part of the interior of the Von Kármán impact crater. It is likely that ejecta from the Alder crater was mixed in during the time of the basalt infill; after the basalt emplacement, they were covered by distal ejecta from Mare Orientale basin. Subsequently, ejecta from the Finsen crater covered the most superficial layers of the landing and roving area; the materials in these layers underwent a long period of modification including meteorite contamination (Huang *et al.*, 2018; Gou *et al.*, 2021; Xiao *et al.*, 2021; Yang *et al.*, 2022).

2.5 Lunar Surface Environment after Chang'E-4

2.5.1 Particle Radiation Environment on the Moon Surface

The analysis of the observational data obtained by LND during two lunar days from January to February 2019 shows that the particle radiation dose rate at the lunar surface is $13.2 \mu\text{Gy}\cdot\text{h}^{-1}$ (Si), of which the radiation dose rate of neutral particles (neutrons and gamma rays) is $3.1 \mu\text{Gy}\cdot\text{h}^{-1}$ (Si), accounting for about 23% of the total, with a quality factor of 4.32 and a dose equivalent of about $60 \mu\text{Sv}\cdot\text{h}^{-1}$ (Fig. 11). There are significant differences between the cosmic ray energy spectra measured by LND, especially the proton energy spectrum, and the predictions given by the widely used CRÈME models: the mean values of the flux ratios between LND and the CRÈME96 and CRÈME2009 models reach 1.69 ± 0.17 and 2.25 ± 0.23 , respectively, which provide strong constraints on the improvement of the CRÈME models, and the cosmic ray energy spectrum also provides tests and constraints for other related theoretical models. Observations data of LND over the 2-year period from January 2019 to December 2020 show that the average total absorbed dose rate of lunar surface particle radiation in silicon is $12.66 \pm 0.45 \mu\text{Gy}\cdot\text{h}^{-1}$ and the absorbed dose rate of neutral particles is $2.67 \pm 0.16 \mu\text{Gy}\cdot\text{h}^{-1}$. The radiation dose rate shows a slow decrease with time over the 2-year period, while the change in the LET spectrum is small (Zhang S *et al.*, 2020; Wimmer Robert F *et al.*, 2020; Hou *et al.*, 2020; Zhang S *et al.*, 2021).

Observations by LND also confirm the morning and evening symmetry of the cosmic ray fluxes. Extraction

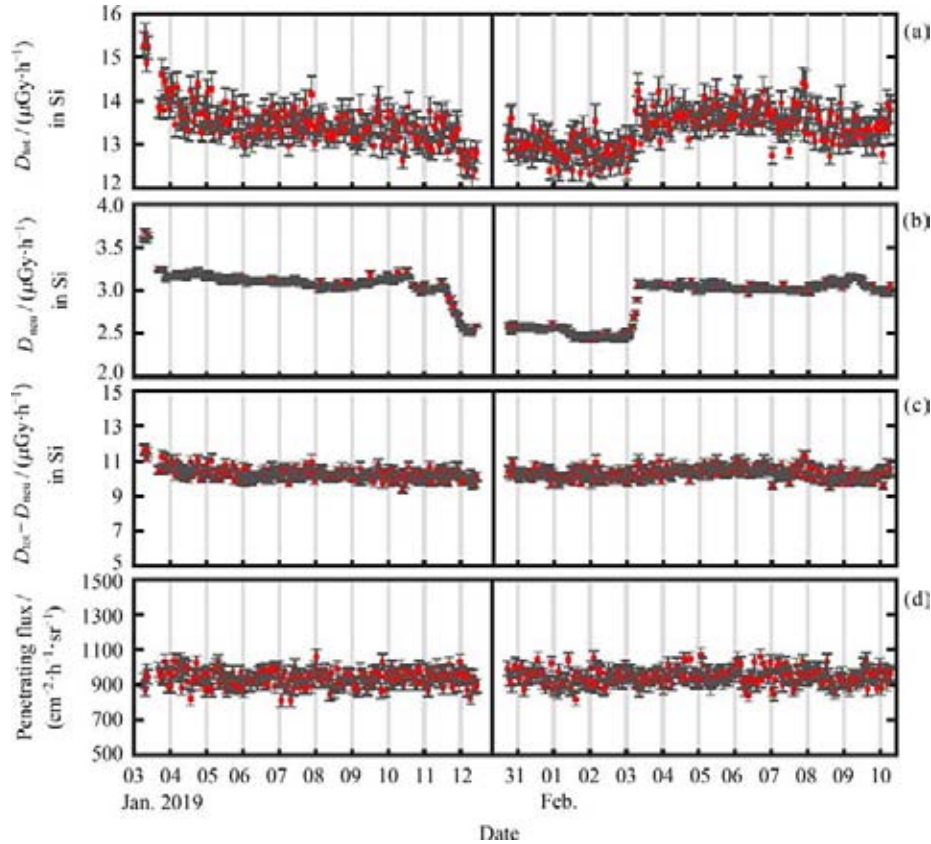


Fig. 11 Temporal evolution of the radiation environment on the Moon as measured by LND on Chang'E-4 during the first and second lunar days after Chang'E-4 landed (Zhang S. *et al.*, 2020)

of the $3\text{He}/4\text{He}$ flux ratio reveals a significant enhancement at about 12 MeV/nuclei and a very significant difference between the $3\text{He}/4\text{He}$ flux ratio values measured by LND and the predictions given by the GALPROP model, providing strong constraints on the GALPROP model as well as other related theoretical models (Luo *et al.*, 2022).

On 6 May 2019, LND detected the first SEP event on the far side of the Moon. This event with a very small peak flux and short duration, is a typical impulsive solar energetic particle event (impulsive SEPs). Both electrons and protons were found to exhibit a good velocity dispersion distribution, showing that the time of particle release from the acceleration region is one hour earlier for electrons than for protons (Fig.12). Further analysis reveals that the energy inflection point is about 2.5 MeV and originates from an M1.0 class flare (Xu *et al.*, 2020).

2.5.2 Interaction of the Solar Wind with the Moon

The observation results of ASAN show that the hydrogen ENA energy spectrum is in good agreement with the large-scale observations of Chandrayaan-1 and IBEX when the energy is higher than the solar wind ion

energy above $0.1 E_{\text{sw}}$, while the hydrogen ENA fluxes measured by ASAN are higher than the results of Chandrayaan-1 and IBEX when it is lower than $0.1 E_{\text{sw}}$ (Fig.13). The component above $0.1 E_{\text{sw}}$ is mainly hydrogen ENA generated by the backscattering of solar wind ions, and the component below this energy is mainly ENA from the sputtering of lunar surface material (Wieser *et al.*, 2020; Zhang A *et al.*, 2020).

Analysis of the ENA energy spectrum from January 2019 to October 2020 reveals that the ENA differential fluxes on the dawnside are higher than those on the duskside during most lunar days, and the ENA differential fluxes in different energy ranges on the dawnside and duskside are positively correlated with solar wind state parameters such as flux, density, and dynamic pressure. The cutoff energy and temperature of ENA on the duskside are lower than those on the dawnside under the same energy solar wind bombardment (Fig.14), suggesting that the solar wind on the duskside may be affected by the lunar micro-magnetosphere and slowed down by the electrostatic field above the magnetic anomaly, resulting in a narrower energy spectrum and lower temperature (Wang *et al.*, 2021).

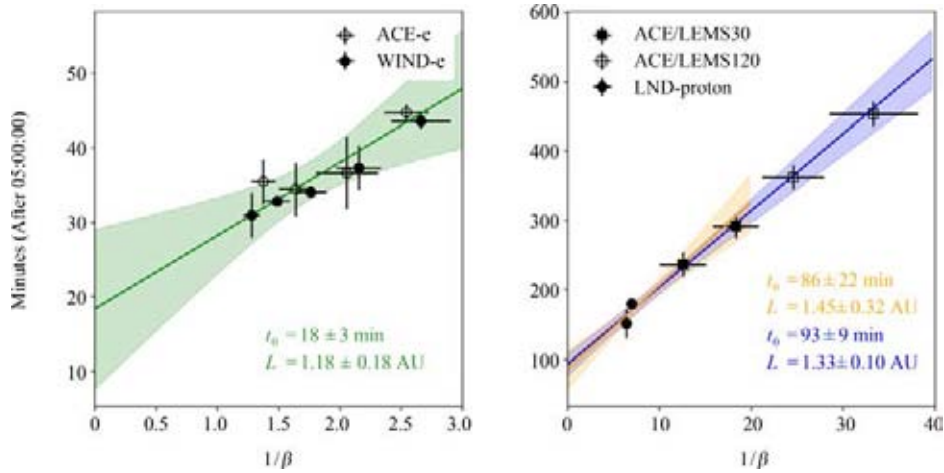


Fig. 12 Velocity dispersion analysis of the SEPs on 6 May 2019 (electrons shown in the left and protons shown in the right panel). Wind and ACE electron data are used to determine the electron release time (Xu *et al.*, 2020)

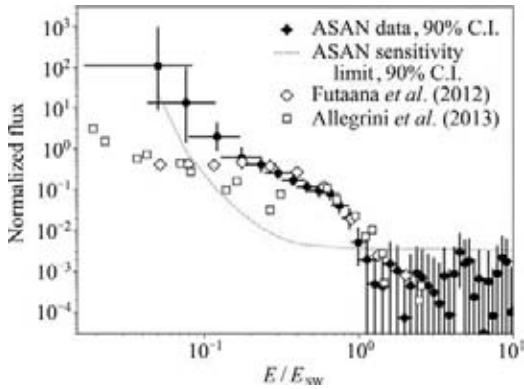


Fig. 13 Average hydrogen ENA energy spectrum observed by the ASAN on 1 May 2019 06:18–10:45 UTC, normalized to the solar wind energy E_{sw} (Zhang A *et al.*, 2020)

2.5.3 First Observation of the Lunar Mini-magnetosphere on the Lunar Surface

The landing site of Chang'E-4 is located at the eastern edge of the mare imbrium antipodal region, the largest magnetic anomaly of the Moon. When Chang'E-4 is downstream of the magnetic anomaly (duskside), the overall particle flux measured by the neutral atom detector is lower than that measured when it is upstream of the magnetic anomaly (dawnside) (Fig.15). Combined with global Hall MHD simulations, it is confirmed that the lunar mini-magnetosphere is responsible for the flux difference, and the effect of the micro-magnetosphere on the solar wind is mainly deflection and deceleration,

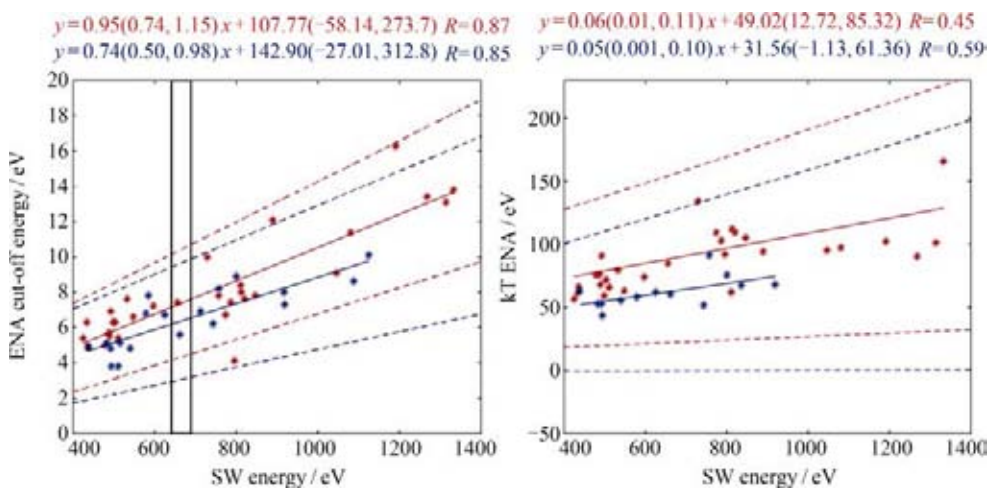


Fig. 14 Left: Relationships between solar wind energy and ENA cutoff energy on the dawnside (red line) and duskside (blue line). The dashed lines indicate 95% confidence intervals. The rectangle indicates two events in which the solar wind energy was similar (about 680 eV) on both the dawnside and duskside. Right: Relationships between solar wind energy and ENA absolute temperature on the dawnside (red line) and duskside (blue line). The dashed lines are 95% confidence intervals (Wang *et al.*, 2021)

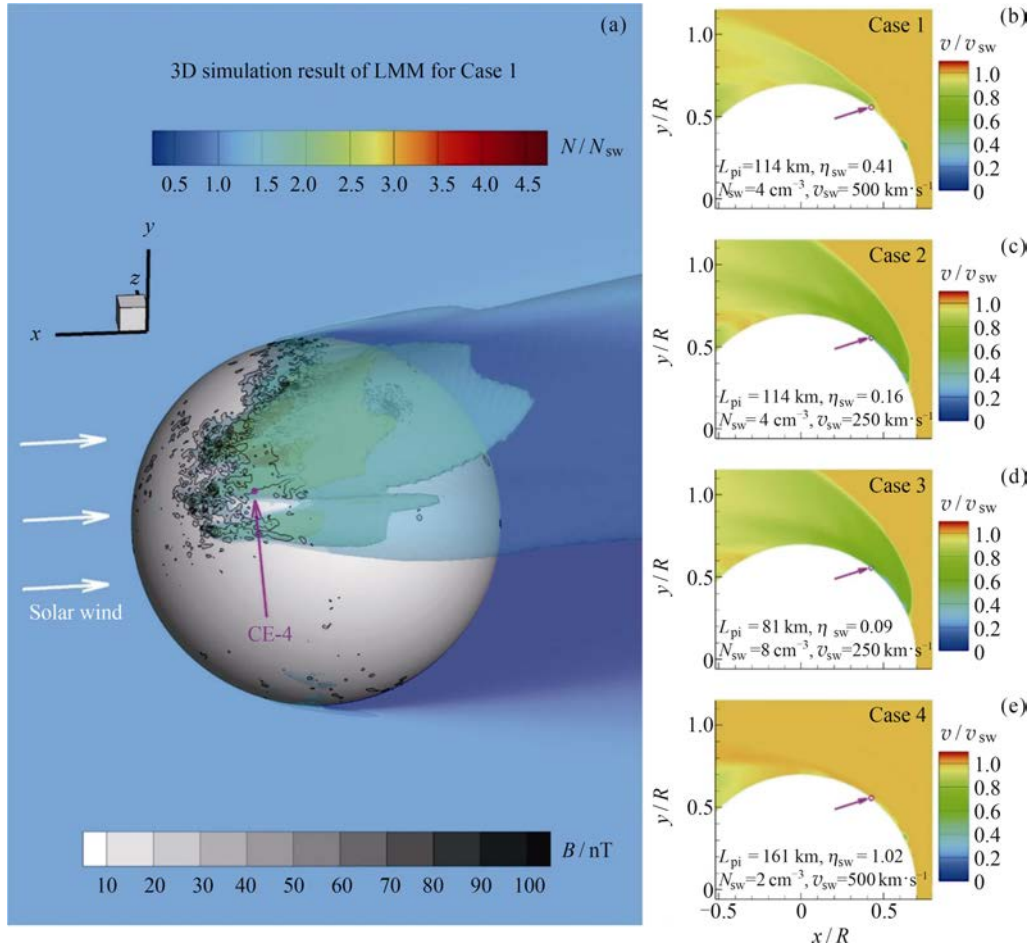


Fig. 15 3D view of the simulation result for Case 1, where the white arrows indicate the direction of the solar wind, the central ball represents the lunar body with gray contours to show the magnitudes of the crustal magnetic fields, the 3D colored contours show the number densities normalized by the solar wind number density (N_{sw}), and the magenta circle indicates the location of Chang'E-4 (Xie *et al.*, 2021)

rather than complete blockage of the solar wind, with an average blockage efficiency of about 50% (Xie *et al.*, 2021).

2.6 Lunar Low-frequency Radio Observations

The relay communication satellite and the lander of Chang'E-4 mission separately carry two science payloads, NCLE and LFS. Their objectives are exploring the electromagnetic wave radiation environment on the far side of the Moon and in lunar space, detecting solar HF-VHF band bursts during peak solar activity years.

Since the lander of Chang'E-4 is the backup model of the Chang'E-3 lander, the electromagnetic shielding design specifically for low-frequency radio observation cannot be carried out, and the noise from the probe platform brings serious impact on low-frequency radio observation (Fig.16). When designing the instrument, a short antenna was added and a pair-cancellation algo-

rithm was used to reduce the detector background noise, however this could not be completely eliminated (Zhang *et al.*, 2019). Therefore, a thematic assessment of the achievability of the scientific goal of low-frequency radio detection was conducted, and concluded that when the solar flux density is less than $10^{-21} \text{ W}\cdot\text{m}^{-2}\cdot\text{Hz}^{-1}$, the low-frequency radio spectrometer cannot detect the solar low-frequency radio radiation; When the flux density of the solar burst is greater than $10^{-18} \text{ W}\cdot\text{m}^{-2}\cdot\text{Hz}^{-1}$, the solar low-frequency radio radiation can be detected in 100 kHz to 8 MHz; When the peak flux density of the solar burst is greater than $10^{-16} \text{ W}\cdot\text{m}^{-2}\cdot\text{Hz}^{-1}$, the solar low-frequency radio radiation can be detected in the full frequency band from 100 kHz to 40 MHz.

LFS has worked 41 lunar days for scientific observations. Tests confirm the noise deduction effect is basically consistent with the ground test. A three-antenna spectrum is generated by using detection data, so it is

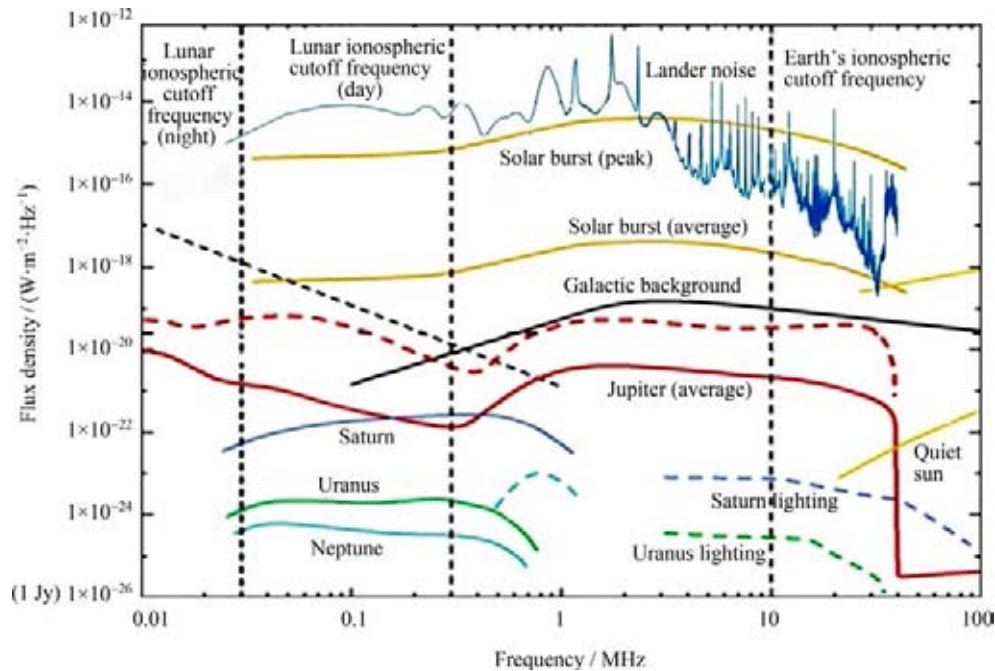


Fig. 16 Radio emission levels on surface of the Moon (Zhang *et al.*, 2019)

known that LFS can obtain radio phenomena similar to the solar burst, and data processing methods for cosmic background radiation and other stable spectral signal are also effective (Jiao *et al.*, 2021). Unfortunately, no significant scientific phenomena have been found so far.

3 Future Prospects

At present, the lander and rover of Chang'E-4 have been working normally on the far side of the Moon for more than 3 years. All systems are working normally. Yutu-2 lunar rover is walking to the northwest direction, and plans to detect the lunar mare basalt area with thin ejecta coverage. Currently, the rover has travelled about 1.1 km. The Chang'E-4 mission has demonstrated the high richness and complexity of lunar geological processes over a longer roving route. Although the current scientific understanding is still controversial for the interpretation of some phenomena, it is still expected to further reveal the evolution of the surface topography and geological structure of the landing region in three dimensions, providing a basis for comparison to correct and constrain the existing geological interpretation. 2021–2024 are solar maximum years, and the LFS/NCLE is expected to have the opportunity to obtain solar burst detection results.

In 2021, Phase IV of China's lunar exploration pro-

ject was kicked-off. Taking advantage of a long period of continuous solar illumination at the lunar south pole, different detection means such as orbiting and remote sensing, landing and in-situ detection, roving, leaping and sampling can be used on the following subjects: (i) detection of volatiles in the lunar south pole and distribution and storage of water in lunar soil in permanent shadow area; (ii) assessment of fugacity, content, distribution and origin of lunar water; (iii) in-situ utilization experiments of lunar rare gas and other resources; (iv) in-depth exploration of the lunar space environment, deep material, internal structure; (v) observation on earth and astronomical objects from the moon as a platform; (vi) experiments in the micro-enclosed terrestrial ecosystems under the lunar surface environment. Basic model of the lunar research station will be established to carry out large-scale, full-scale, long-period scientific observations and researches, to gain scientific understanding.

Acknowledgments

High tribute should be paid to the core scientific research team of the Chang'E-4 mission for providing information and assistance. Thanks to LIU Yang, GOU Sheng, LIN Honglei, XIAO Zhiyong, ZHANG Jinhai, HUANG Jun, LI Lei, CAO Jinbin for providing material and suggestions to the manuscript.

References

- [1] LIU Jianjun, REN Xin, YAN Wei, *et al.* Descent trajectory reconstruction and landing site positioning of Chang'E-4 on the lunar farside[J]. *Nature Communications*, 2019
- [2] JIA Yingzhuo, ZOU Yongliao, *et al.* The scientific objectives and payloads of Chang'E-4 mission, *Planetary and Space Science*, 2018, 162(SI), p. 207-215.
- [3] WU B, LI Y, LIU W, *et al.* Centimeter-resolution topographic modeling and fine-scale analysis of craters and rocks at the Chang'E-4 landing site[J]. *Earth and Planetary Science Letters*, 2021, 553: 116666
- [4] FU X H , QIAO L , ZHANG J , *et al.* The subsurface structure and stratigraphy of the Chang'E-4 landing site: orbital evidence from small craters on the Von Kármán crater floor[J]. *Research in Astronomy and Astrophysics*, 2020, 20(01): 59-70
- [5] GOU Sheng, YUE Zongyu, DI Kaichang, *et al.* Mare basalt flooding events surrounding Chang'E-4 landing site as revealed by Zhinyu crater ejecta[J]. *Icarus*, 2021, 360
- [6] QIAO L, LING Z, FU X, Li B. Geological characterization of the Chang'E-4 landing area on the lunar farside[J]. *Icarus*, 2019, 333: 37-51
- [7] JIA M, DI K, YUE Z, *et al.* Multi-scale morphologic investigation of craters in the Chang'E-4 landing area[J]. *Icarus*, 2021, 355: 114164
- [8] GOU S, YUE Z, DI K, *et al.* In situ spectral measurements of space weathering by Chang'E-4 rover[J]. *Earth and Planetary Science Letters*, 2020a, 535: 116117
- [9] DING C, XIAO Z, WU B, *et al.* Fragments delivered by secondary craters at the Chang'E 4 landing site[J]. *Geophysical Research Letters*, 2020, 47, e2020GL087361
- [10] DI K, ZHU M H, YUE Z, *et al.* Topographic evolution of Von Kármán crater revealed by the lunar rover Yutu - 2[J]. *Geophysical Research Letters*, 2019, 46
- [11] XIAO Z, DING C, XIE M, *et al.* Ejecta from the Orientale basin at the Chang'E-4 landing site[J]. *Geophysical Research Letters*, 2021, 48, e2020GL090935
- [12] DING C, XIAO Z, WA B, *et al.* Rock fragments in shallow lunar regolith: Constraints by the lunar penetrating radar onboard the Chang'E-4 mission[J]. *Journal of Geophysical Research: Planets*, 2021, 126, e2021JE006917
- [13] LAI J, XU Y, ZHANG X, *et al.* Comparison of dielectric properties and structure of lunar regolith at Chang' E - 3 and Chang' E - 4 landing sites revealed by ground - penetrating radar[J]. *Geophysical Research Letters*, 2019, 46: 12783-12793
- [14] LAI J, CUI F, XU Y, Liu C, Zhang L. Dielectric Properties of Lunar Materials at the Chang'E-4 Landing Site. *Remote Sensing*. 2021; 13(20): 4056.
- [15] Li C, *et al.* , 2020. The Moon's farside shallow subsurface structure unveiled by Chang'E-4 Lunar Penetrating Radar. *Science Advances*, 6: eaay6898.
- [16] SONG Hanjie, LI Chao, ZHANG Jinhai, *et al.* Rock location and property analysis of lunar regolith at Chang'E-4 landing site based on local correlation and semblance analysis[J]. *Remote Sensing*, 2020, 13(1)
- [17] TANG Z, LIU J, WANG X, *et al.* Physical and mechanical characteristics of lunar soil at the Chang' E - 4 landing site[J]. *Geophysical Research Letters*, 2020, 47, e2020GL089499.
- [18] LIN H, YANG Y, LIN Y, *et al.* Photometric properties of lunar regolith revealed by the Yutu-2 rover[J]. *Astronomy & Astrophysics*, 2020a, 638: A35
- [19] LIN H, XU R, YANG W, *et al.* In situ photometric experiment of lunar regolith with visible and near - infrared imaging spectrometer on board the Yutu - 2 lunar rover[J]. *Journal of Geophysical Research: Planets*, 2020b, 125(2), e2019JE006076
- [20] LIN H, LIN Y, YANG W, *et al.* New insight into lunar regolith - forming processes by the lunar rover Yutu - 2[J]. *Geophysical Research Letters*, 2020c, 47, e2020GL087949.
- [21] YANG Y, LIN H, LIU Y, *et al.* The effects of viewing geometry on the spectral analysis of lunar regolith as inferred by in situ spectrophotometric measurements of Chang'E - 4[J]. *Geophysical Research Letters*, 2020, 47(8): e2020GL087080
- [22] LIN H, LI S, LIN Y, *et al.* Thermal modeling of the lunar regolith at the Chang'E-4 landing site[J]. *Geophysical Research Letters*, 2021, 48(6), e2020GL091687
- [23] WU Y, KÜHRT E, GROTT M, *et al.* Chang'E-4 rover spectra revealing Micro-scale surface thermophysical properties of the Moon[J]. *Geophysical Research Letters*, 2021, 48(4): e2020GL089226.
- [24] HUANG J, XIAO Z, XIAO L, *et al.* Diverse rock types detected in the lunar South Pole-Aitken Basin by the Chang'E-4 lunar mission[J]. *Geology*, 2020, 48: 723-727
- [25] LI Chunlai, LIU Dawei, LIU Bin, *et al.* Chang'E-4 initial spectroscopic identification of lunar far-side mantle-derived materials[J]. *Nature*, 2019, 569(7756)
- [26] HU X, MA P, YANG Y, *et al.* Mineral abundances inferred from in situ reflectance measurements of Chang'E-4 landing site in South Pole-Aitken basin[J]. *Geophysical Research Letters*, 2019, 46: 9439-9447
- [27] LIN H, HE Z, YANG W, *et al.* Olivine-norite rock detected by the lunar rover Yutu-2 likely crystallized from the SPA impact melt pool[J]. *National Science Review*, 2020c, 7: 913-920
- [28] CHEN Jian, LING Zongcheng, QIAO Le, *et al.* Mineralogy of Chang'E-4 landing site: preliminary results of visible and near-infrared imaging spectrometer[J]. *Science China(Information Sciences)*, 2020, 63(04): 195-206
- [29] GOU S, DI K, YUE Z, *et al.* Lunar deep materials observed by Chang'E-4 rover[J]. *Earth and Planetary Science Letters*, 2019, 528: 115829
- [30] GOU S, DI K, YUE Z, *et al.* Forsteritic olivine and magnesium-rich orthopyroxene materials measured by Chang'E-4 rover[J]. *Icarus*, 2020b, 345: 113776
- [31] GOU S, YUE Z, DI K, *et al.* Absolute model age of lunar Finsen crater and geologic implications[J]. *Icarus*, 2021b, 354: 114046
- [32] MA P, SUN Y, ZHU M H, *et al.* A plagioclase-rich rock measured by Yutu-2 Rover in Von Kármán crater on the far side of the Moon[J]. *Icarus*, 2020, 350: 113901
- [33] ZENG Q, CHEN S, ZHANG Y, *et al.* Mineralogical and chemical properties inverted from 21-lunar-day VNIS observations taken during the Chang'E-4 mission[J]. *Sci. Rep.* , 2021, 11, 15435
- [34] LING Zongcheng, QIAO Le, LIU Changqing, *et al.* Composition, mineralogy and chronology of mare basalts and non-mare materials in Von Kármán crater: landing site of the Chang'E-4 mission[J]. *Planetary and Space Science*, 2019, 179

- [35] GOU S, YUE Z, DI K, *et al.* Impact melt breccia and surrounding regolith measured by Chang'E-4 rover[J]. *Earth and Planetary Science Letters*, 2020c, **544**: 116378
- [36] YANG Y, LI S, ZHU M H, *et al.* Impact remnants rich in carbonaceous chondrites detected on the Moon by the Chang'E-4 rover[J]. *Nat. Astron.*, 2021
- [37] Li C *et al.* The Moon's farside shallow subsurface structure unveiled by Chang'E-4 Lunar Penetrating Radar[J]. *Science Advances*, 2020, **6**: eaay6898
- [38] DONG Z, FANG G, ZHAO D, *et al.* Dielectric properties of lunar subsurface materials[J]. *Geophysical Research Letters*, 2020a, **47**, e2020GL089264
- [39] LAI J, XU Y, BUGIOLACCHI R, *et al.* First look by the Yutu-2 rover at the deep subsurface structure at the lunar farside[J]. *Nat. Commun.* 2020, 11: 3426
- [40] LAI J, XU Y, BUGIOLACCHI R, *et al.* A complex paleo-surface revealed by the Yutu-2 rover at the lunar farside[J]. *Geophysical Research Letters*, 2021a, **48**, e2021GL095133
- [41] HUANG J, XIAO Z, FLAHAUT J, *et al.* Geological characteristics of Von Kármán crater, northwestern south pole - Aitken Basin: Chang'E - 4 landing site region[J]. *Journal of Geophysical Research: Planets*, 2018, **123**(7): 1684-1700
- [42] GIANNAKIS I, ZHOU F, WARREN C, GIANNOPOULOS A. Inferring the shallow layered structure at the Chang'E-4 landing site: a novel interpretation approach using lunar penetrating radar[J]. *Geophysical Research Letters*, 2021, **48**, e2021GL092866
- [43] XIAO Z, YAN P, WU B, *et al.* Translucent glass globules on the Moon[J]. *Science Bulletin*, 2021,
- [44] XU L, ZHANG X, QIAO L, LAI J, *et al.* Evaluating the thickness and stratigraphy of ejecta materials at the Chang'E-4 landing site[J]. *Astronomical Journal*, 2021, **162**: 29
- [45] ZHANG J, ZHOU B, LIN Y, *et al.* Lunar regolith and substructure at Chang'E-4 landing site in South Pole-Aitken basin[J]. *Nat. Astron.*, 2021, **5**: 25-30
- [46] ZHANG L, LI J, ZENG Z, *et al.* Stratigraphy of the Von Kármán crater based on Chang'E - 4 Lunar penetrating radar data[J]. *Geophysical Research Letters*, 2020, **47**: e2020GL088680
- [47] ZHANG L, XU Y, BUGIOLACCHI R, *et al.* Rock abundance and evolution of the shallow stratum on Chang'E-4 landing site unveiled by lunar penetrating radar data[J]. *Earth and Planetary Science Letters*, 2021, **564**, 116912
- [48] ZHOU H, FENG X, DONG Z, *et al.* Application of denoising CNN for noise suppression and weak signal extraction of lunar penetrating radar data[J]. *Remote Sens.*, 2021, **13**: 779
- [49] GUO D, FA W, ZENG X, *et al.* Geochemistry of the Von Kármán crater floor and thickness of the non-mare ejecta over the Chang'E-4 landing area[J]. *Icarus*, 2021a, 359 114327
- [50] YUAN Y, ZHU P, XIAO L, *et al.* Intermittent volcanic activity detected in the Von Kármán crater on the farside of the Moon[J]. *Earth and Planetary Science Letters*, 2021, **569**: 117062
- [51] ZHANG S Y, *et al.* First measurements of the radiation dose on the lunar surface[J]. *Science advances*, 2020, **6**: 39
- [52] HOU D H, ZHANG S Y, *et al.* Removing the dose background from radioactive sources from active dose rate measurements in the Lunar Lander Neutron & Dosimetry (LND) experiment on the Chang'E 4[J]. *Journal of Instrument*, 2020, **15**: 1
- [53] WIMMER ROBERT F, *et al.* The Lunar Lander Neutron and Dosimetry (LND) Experiment on Chang'E4[J]. *Space Science Review*, 2020, **216**: 104
- [54] ZHANG Shenyi, HOU Donghui, WIMMER-SCHWEINGRUBER R F, *et al.* Radiation Dose of LND on the Lunar Surface in Two Years[J]. *Journal of Space Science*, 2021, **41**(3): 439-444
- [55] LUO Pengwei, ZHANG Xiaoping, FU Shuai, *et al.* First measurements of low-energy cosmic rays on the surface of the lunar farside from Chang'E-4 mission[J]. *Sci. Adv.*, 2022, **8** (2), eabk1760
- [56] XU Zigong, GUO Jingnan, ROBERT F, *et al.* First solar energetic particles measured on the lunar far-side[J]. *Astrophysical Journal Letters*, 2020, 902: L30
- [57] WIESER M, BARABASH S, WANG X D, *et al.* The Advanced Small Analyzer for Neutrals (ASAN) on the Chang'E-4 Rover Yutu-2[J]. *Space Science Reviews*, 2020, **216**: 73
- [58] ZHANG Aibing, *et al.* (2020), Emission of energetic neutral atoms measured on the lunar surface by Chang'E-4[J]. *Planetary and Space Science*, 189
- [59] WANG Huizi, XIAO Chao, SHI Quanqi, *et al.* Energetic neutral atoms distribution on the lunar surface and its relationship with solar wind conditions[J]. *Astrophysical Journal Letters*, 2021, 922: L41
- [60] XIE L, LI L, ZHANG A, *et al.* Inside a lunar mini-magnetosphere: First energetic neutral atom measurements on the lunar surface[J]. *Geophysical Research Letters*, 2021, **48**, e2021GL093943
- [61] ZHANG T, SU Y. Research of the Method for Reducing Background of Very Low Frequency Radio Spectrum on Chang'E-4[J]. *Astronomical Research & Technology*, 2019, **16**(03): 312-320
- [62] JIAO K, WANG M Y, ZHANG L J, *et al.* Analysis of the capability of Chang'E-4 low frequency radio Spectrometer 2C data in detecting the dark ages[J]. *Astronomical Research & Technology*, 2021, **18**(04): 472-476

GECAM Mission and Preliminary Results

XIONG Shaolin (On behalf of GECAM team)

Key Laboratory of Particle Astrophysics, Institute of High Energy Physics, Chinese Academy of Sciences, Beijing 100049

Abstract

Gravitational wave high-energy Electromagnetic Counterpart All-sky Monitor (GECAM) is a dedicated gamma-ray all-sky monitor composed of two microsattellites launched on 9 December 2020. Each GECAM satellite is equipped with 25 Gamma-Ray Detectors (GRD) and 8 Charged Particle Detectors (CPD), to measure the positional, temporal and spectral properties of high energy transients. Due to the anomalies in the satellite power supply, only one satellite (GECAM-B) can observe about 10 h per day since 14 January 2021. As the power supply recovered on 30 May 2022, GECAM-B can work in full duty. GECAM-B has detected many gamma-ray transients, including Gamma-Ray Bursts (GRBs), Soft Gamma-ray Repeaters (SGRs), bursts from X-Ray Binaries (XRBs), Solar Flares (SFLs) and Terrestrial Gamma-ray Flashes (TGFs). GECAM-B can also unveil the potential gamma-ray counterparts of Gravitational Waves (GWs) and Fast Radio Bursts (FRBs). With the novel application of Beidou Navigation Satellite System (BDS), GECAM-B became the first Chinese space telescope that can downlink data in near real-time (time latency <1 min), which is critically important for joint observations in multi-wavelength and multi-messenger astronomy era.

Key words

GECAM, Gravitational wave electromagnetic counterpart, High energy transients

1 Introduction

Since the first detection of gravitational wave from binary black hole merger (GW150914) by LIGO^[1], the pursuit of the Gravitational Wave Electromagnetic counterpart (GWEM) became important and urgent. However, the existing gamma-ray monitors were insufficient to capture the transient GWEM in gamma-rays which occurs randomly all over the sky, because either the Field of View (FOV) is constrained by the Earth or the sensitivity is inadequate.

In response to the GWEM science opportunity, GECAM was proposed in the March of 2016 to provide 100% all-sky monitoring in X-ray and soft gamma-ray bands based on the constellation design of two identical

microsattellites (denoted as GECAM-A and GECAM-B, see Fig. 1). Promoted by the first detection of GW EM (especially the GRB 170871A) of binary neutron star merger (GW170817)^[2-4], GECAM was selected and funded by the Chinese Academy of Sciences (CAS) in July 2018.

Two GECAM satellites were launched together to an orbit of 600 km height and 29° inclination angle on 9 December 2020. Due to the anomalies in the satellite power supply, GECAM-A has not been able to observe yet while GECAM-B can observe about 10 hours per day since 14 January 2021. As the power supply recovered on 30 May 2022, GECAM-B can work in full duty, with an effective observation time of about 20 hours (since the detector will be turned off during the South

Atlantic Anomaly, SAA). More information about GECAM can be found at the GECAM website*.

2 Scientific Objectives

GECAM is a dedicated all-sky monitor with a very large instantaneous field of view in the X-ray and soft gamma-ray band. The primary science objectives are: (i) monitor and characterize the high energy counterparts of Gravitational Waves (GWs), to reveal the underlying physics of neutron stars, black holes and binary mergers; (ii) monitor and characterize the high-energy counterparts of Fast Radio Burst (FRBs), to reveal the origin and emission mechanism; (iii) discover various types of gamma-Ray Bursts (GRBs) and Soft Gamma-Ray Repeaters (SGRs), to deepen our understanding of their burst physics.

3 Instruments

GECAM is composed of two microsatellites, each of which is equipped with 25 Gamma-Ray Detectors (GRD) and 8 Charged Particle Detectors (CPD) pointing to different directions to cover a very large field of view^[5]. Both GRD and CPD detectors are based on SiPM technology which allows the detector and satellite very compact and light-weighted but with good performance in detection^[6,7].

To meet requirements of low energy threshold, wide energy range, large collecting area, as well as high temporal and spectral resolution, GRD employs a 3-inch LaBr₃ crystal^[8] coupled with a customized 64-chip SiPM array^[9] to detect gamma-rays, rendering GECAM the first application of the novel LaBr₃+SiPM detector

technology in space.

4 In-flight Performance

Since GECAM-A has not been able to observe owing to the power supply shortage, we just list the characteristics of GECAM-B in Table 1.

We have developed a dedicated in-flight trigger and localization software for GECAM, which can monitor the count rates in different time scales and energy ranges of GECAM detectors and unveil various types of bursts in real-time^[10]. A series of testing and validation of this software with a dedicated GRB simulator was implemented before launch^[11]. As shown in Fig.2^[12], GECAM-B successfully triggered hundreds of various bursts since launch^[10].

With the novel application of the short message service of the Beidou navigation satellite System (BDS), GECAM-B can downlink the trigger data to the GECAM Scientific Application Center almost in real-time,

Table 1 Characteristics of GECAM-B

Parameters	Values	Notes
Orbit	600 km, 29°	–
Life time	3 years	Goal: 5 years
GRD energy range	15 keV–5 MeV	–
Field of view	60% all-sky	All-sky unocculted by Earth
Burst sensitivity	2×10^{-8} erg·cm ⁻² ·s ⁻¹	20 s, 10–1000 keV
Burst localization accuracy	2° (1 σ stat.)	Flux= 1×10^{-6} erg·cm ⁻² ·s ⁻¹ , 10 s
Absolute timing accuracy	< 3 μ s	–
Relative timing accuracy	0.1 μ s	Between detectors
Time latency of trigger data	60 s	For the first BDS message

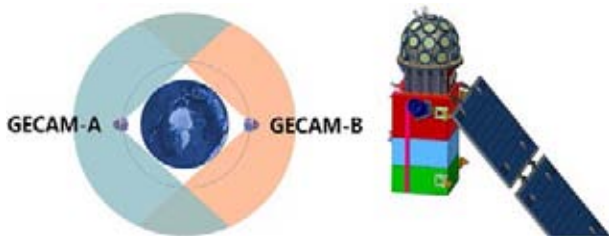


Fig. 1 Left: Design of GECAM mission which is composed of two microsatellites (GECAM-A and GECAM-B). Currently, only GECAM-B is working. Right: The layout of each GECAM satellite, which is equipped with 25 gamma-ray detectors and 8 charged particle detectors

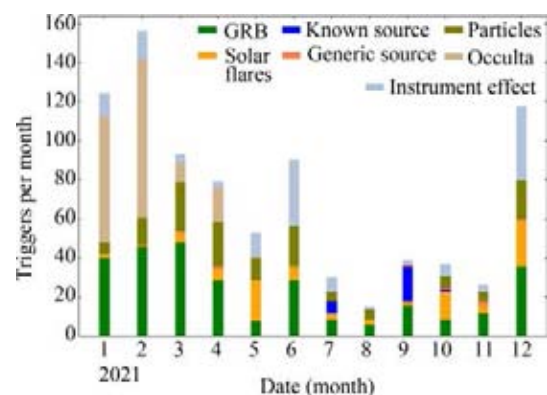


Fig. 2 GECAM-B triggers in each month of 2021

* <http://gecam.ihep.ac.cn>

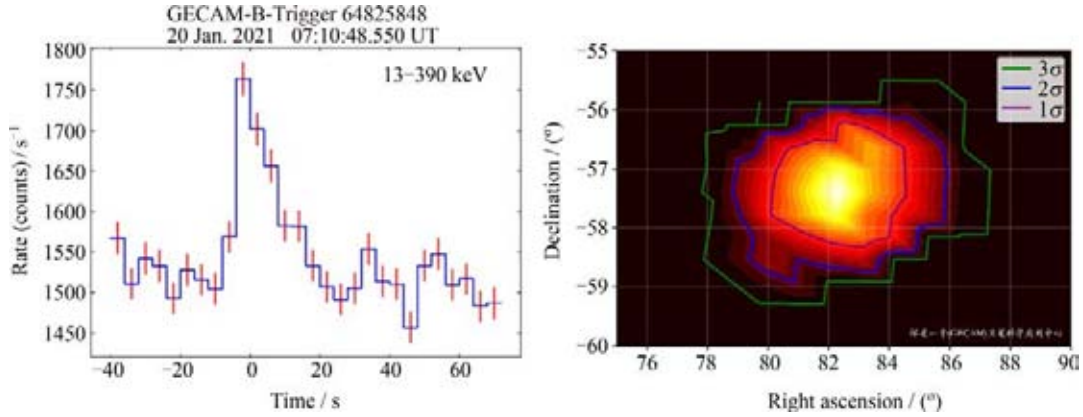


Fig. 3 Left: GECAM real-time light curve of gamma-ray burst downlinked through the Beidou navigation system. Right: Low-latency GECAM localization map of a gamma-ray burst (GRB 211105A)

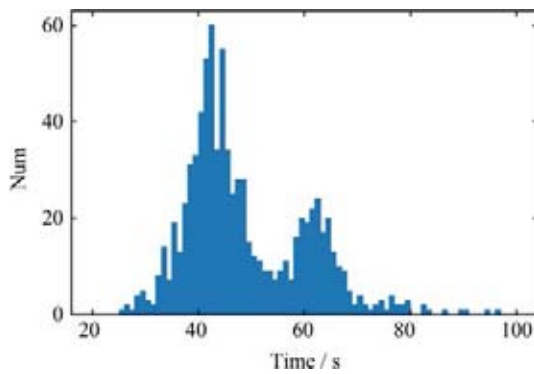


Fig. 4 Distribution of time delay of the first trigger message of GECAM-B^[12]. The horizontal axis is the time delay which is defined as the time difference between the trigger time and the receiving time of the first trigger message. The vertical axis is the number of triggers in each bin of time delay

including trigger time, light curves, localization and so on (see Fig.3). Usually, there are 31 BDS messages for each trigger. As shown in Fig. 4, the typical latency of the first trigger message is less than 60 s with respect to the burst time^[12]. Within 10 minutes after the burst time, all trigger messages will be received and then automatically processed for refined location and classification of the burst^[12]. Both the in-flight and on-ground trigger results will be distributed to the community to guide other space-borne or ground-based telescopes to do follow-up observations of interesting bursts^[13,14]. GECAM-B is the first Chinese space mission with the capability of sending prompt astronomical alerts to the world-wide community.

5 Preliminary Results

Since the launch in December 2020, GECAM-B has

detected hundreds of transients in hard X-ray and soft gamma-rays, including Gamma-Ray Bursts (GRBs), Soft Gamma-Ray Repeaters (SGRs), bursts from X-ray Binaries (XRB), Solar Flares (SLF) and Terrestrial Gamma-ray Flashes (TGFs).

GECAM-B has triggered >90 GRBs in-flight, while more GRB candidates were found in ground search, which needs further classification and verification. These GRBs are either detected by GECAM-B alone or jointly detected by GECAM-B and other GRB detectors, such as Fermi/GBM, Insight-HXMT, Swift/BAT, Konus-Wind and GRID^[16-18]. GECAM-B also detected about 200 bursts from magnetars including SGR J1935+2154, SGR 1830-0645 and the newly-discovered SGR J1555.2-5402. Together with GECAM-B and Fermi/GBM observations, we find that there is a likely period of 126.88 ± 2.05 days in the burst activity of SGR J1935+2154^[19], which has important implication for the magnetar physics. GECAM-B also detected many bursts from X-ray Binaries in the Milky Way. During a bright Type-I X-ray burst from 4U 0614+09, GECAM-B detected and confirmed a spin frequency of 413 Hz^[20].

GECAM-B also monitored for potential gamma-ray counterparts of many Fast Radio Burst (FRBs), including the FRB 20201124A detected by FAST^[21]. GECAM-B will seek for gamma-ray counterparts of Gravitational Waves (GWs) during the forthcoming O4 observation of LIGO/Virgo/KAGRA.

In addition, we have developed novel burst search^[22] and localization algorithms^[23] for GECAM to uncover more weak bursts and provide more accurate positions for bursts, respectively. Finally, a dedicated pipeline (denoted as ETJASMIN) to jointly analyze observation

data from multiple satellites has been built for GECAM^[24].

References

- [1] ABBOTT B P, *et al.* LIGO Scientific Collaboration and Virgo Collaboration[J]. *Phys. Rev.*, X 6, 041015
- [2] ABBOTT B P, *et al.* GW170817: observation of gravitational waves from a binary neutron star inspiral[J]. *Phys. Rev. Lett.*, 2017, **119**: 161101
- [3] ABBOTT B P, *et al.* *ApJL*, 2017, **848**: L13
- [4] LI T P, *et al.* *Sci. China-Phys. Mech. Astron.* 2018, **61**: 031011
- [5] LI X Q, WEN X Y, AN Z H, *et al.* The technology for detection of gamma-ray burst with GECAM satellite[J]. *Radiat Detect Technol Methods*, 2022, **6**: 12-25
- [6] LÜ P, *et al.* *JINST*, 2018, 13: P08014
- [7] ZHANG D, *et al.* *NIMA*, 2019, **921**: 8-13
- [8] AN Z H, SUN X L, ZHANG D L, *et al.* The design and performance of GRD onboard the GECAM satellite[J]. *Radiat Detect Technol. Methods*, 2022, **6**:43-52
- [9] ZHANG D L, *et al.* arXiv:2112.04770
- [10] ZHAO X Y, *et al.* arXiv:2112.05101
- [11] CHEN C, *et al.* *Exp. Astron.*, 2021, **52**: 45-58
- [12] HUANG Y, *et al.* submitted
- [13] <https://gcn.gsfc.nasa.gov/gcn3/31047.gcn3>
- [14] <https://gcn.gsfc.nasa.gov/gcn3/31048.gcn3>
- [15] XIAO S, *et al.* *MNRAS*, 2022, 511, 1: 964-971
- [16] WANG X, *et al.* *ApJ*, 2021, 922, 2: 237
- [17] SONG X Y, *et al.* *ApJ*, 2022, **931**: 112
- [18] SVINKIN D S, *et al.* *APJS*, 2022, **259**: 34
- [19] XIE S L, *et al.* arXiv:2205.08003
- [20] CHEN Y P, *et al.* arXiv:2112.04790
- [21] XU H, *et al.* arXiv:2111.11764
- [22] CAI C, *et al.* *MNRAS*, 2022, **508**: 3910-3920
- [23] XIAO S, *et al.* *ApJ*, 2021, 920: **43**
- [24] XIAO S, *et al.* *MNRAS*, 2022, **514**: 2397-2406

Recent Status of Taiji Program in China*

LUO Ziren^{1,2,3}, ZHANG Min^{1,2,4}, WU Yueliang^{1,2,4}

1. Taiji laboratory for Gravitational Universe, University of Chinese Academy of Science, Beijing 100049
2. Hangzhou Institute for Advanced Study, University of Chinese Academy of Sciences, Hangzhou 310024
3. Institute of Mechanics, Chinese Academy of Science, Beijing 100190
4. International Center for Theoretical Physics Asia-Pacific, UCAS, Beijing 100190

Abstract

The Taiji-1 satellite is a pilot satellite mission of Taiji program, which is used to verify Taiji's key technology and also to testify the feasibility of Taiji roadmap. Taiji-1 was launched on 31 August 2019 and its designed mission was successfully completed. The in-orbit scientific achievements of Taiji-1 satellite in the first stage have been published and now it has entered the extended task phase. Taiji-2 will prepare all the technology needed by Taiji-3, and remove all the technical obstacles faced by Taiji-3.

Key words

Gravitational wave, Taiji program, Global gravity field model

Taiji is a Chinese space-borne Gravitational Wave (GW) detection mission led by Chinese Academy of Science^[1-3]. Taiji will be launched in 2030 s^[2,3] in order to have at least 1-year overlap with LISA to form a LISA-Taiji network^[4]. To ensure the launching date, a three-step plan has been established. The first step has been accomplished by launching a pilot study satellite known as Taiji-1 in 2019^[5]. The second step is to launch the Taiji pathfinder (also called Taiji-2) no later than 2025. The final step is to launch Taiji (also called Taiji-3), which is similar to the LISA constellation, in 2030s.

During Taiji-1's operating time, the working principle of the optical metrology system and drag-free control system were verified properly (see Fig. 1^[5]). Since these two technologies were the most essential for Taiji-2, the success of Taiji-1 laid a solid foundation for Taiji-2.

On 20 July 2021, Taiji scientific collaboration team released the scientific achievements of Taiji-1 satellite

in the first stage. The results of the first-stage in-orbit test and data analysis show that the Taiji-1 has achieved the highest precision of space laser interferometry in China. The accuracy of displacement measurement of the laser interferometer on Taiji-1 reached $100 \text{ pm} \cdot \text{Hz}^{-1/2}$, $25 \text{ pm} \cdot \text{Hz}^{-1/2}$ in some frequency bands. The accuracy of the gravitational reference sensor on the satellite reached $10^{-10} \text{ ms}^{-2} \cdot \text{Hz}^{-1/2}$, and the sensing accuracy and range ratio reach the best level of $2 \times 10^{-6} \text{ Hz}^{-1/2}$ in China. For the first time in the world, the on-orbit verification of the micro-thruster Radio-Frequency (RF) and dual-mode Hall electric propulsion technology has been realized. The micro-propulsion system achieves $0.15 \mu\text{N} \cdot \text{Hz}^{-1/2}$ noise level, and the thrust measurement accuracy is better than $0.02 \mu\text{N} \cdot \text{Hz}^{-1/2}$. The first in-orbit experiment of drag-free control of satellite was carried out in China, and the residual acceleration is better than $10^{-8} \text{ ms}^{-2} \cdot \text{Hz}^{-1/2}$. The temperature control of the satellite platform reaches $\pm 2.6 \text{ mK}$. The above results of these

* Supported by Strategic Priority Research Program of the Chinese Academy of Science (XDA15021100)

Received May 27, 2022

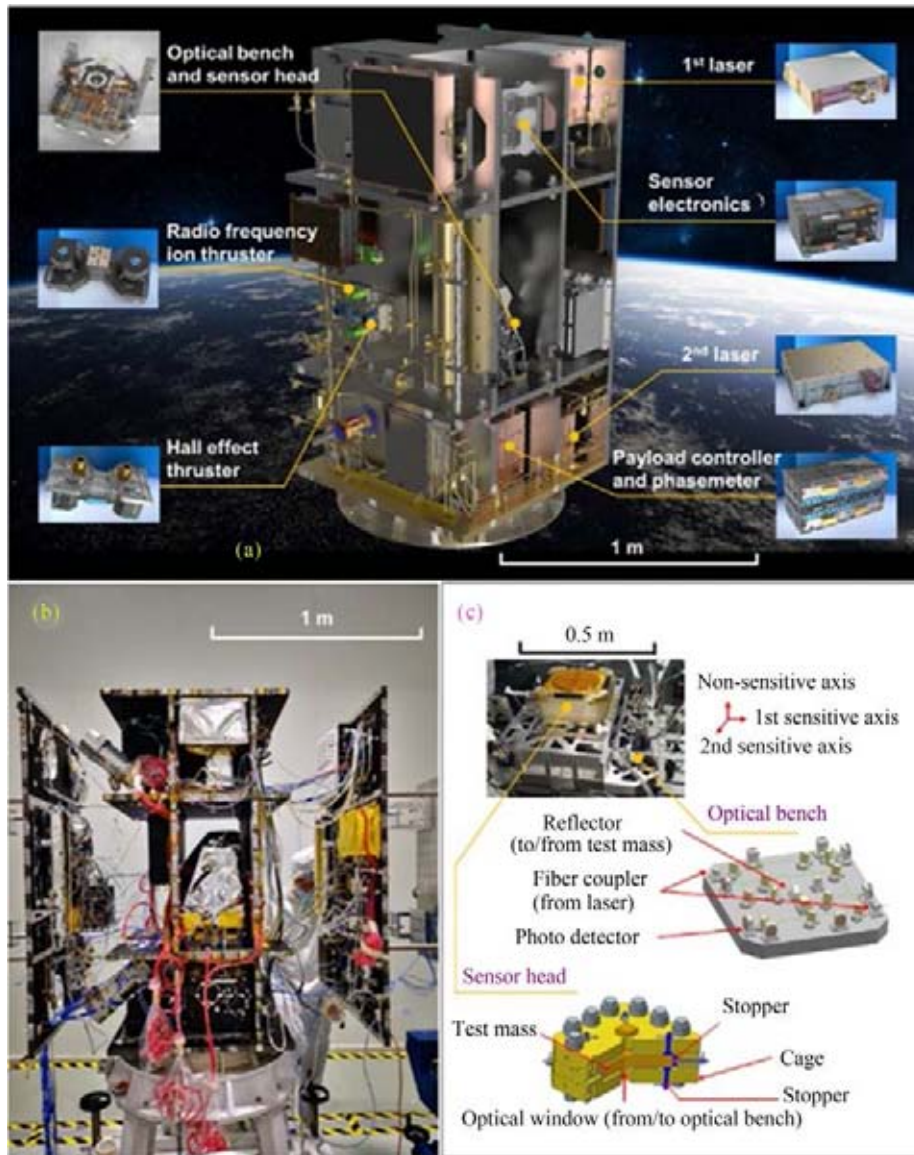


Fig. 1 Anatomy of Taiji-1 and its payloads. (a) The distribution of the payloads in Taiji-1. (b) Taiji-1 satellite before assembly. (c) The core measurement unit, which contains an optical bench and a sensor head

in-orbit tests have been published in *Communications Physics*^[5].

Meanwhile, *International Journal of Modern Physics A* of the World Scientific Press has published more detailed experimental results of Taiji-1 in the form of an album^[6], including 26 papers, from more than 180 researchers, and more than 30 cooperative institutions. This album covers the interferometer system, gravitational reference sensor, micro-thruster system, drag-free control, ultra-stable and ultra-static satellite technology, and introduces the data processing process of Taiji-1 in detail.

After finishing its planned tasks, Taiji-1 has entered the extended task phase since 2021. Taiji-1 continues

collecting the data of the precision orbit determinations, the satellite attitudes, and the non-conservative forces exerted on the S/C. Therefore, during its free-fall, Taiji-1 can be viewed as operating in the high-low satellite-to-satellite tracking mode of a gravity recovery mission. By using the data from both the Beidou navigation system and the inertial sensor, a China’s first domestically developed global gravity field model (monthly averaged)^[7] (see Fig. 2) and as the approved extended free-falling phase with minimal disruptions and disturbances, Taiji-1 will provide us the independent measurement of both the static and the monthly variable global gravity field.

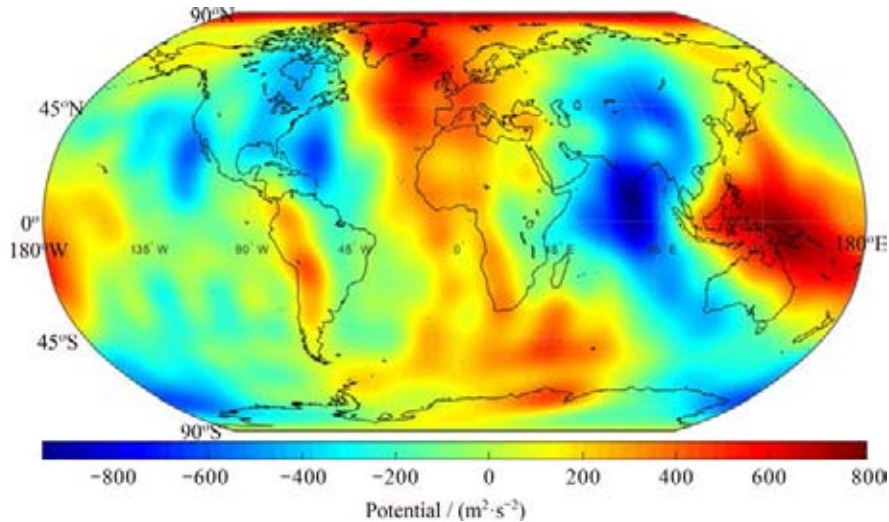


Fig. 2 Global gravity field model. Represented by spheroidal harmonics up to degree and order (d/o) 20

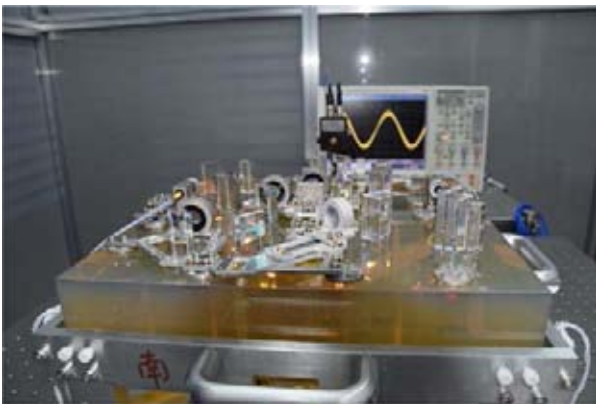


Fig. 3 Principle prototype of Taiji-2's laser metrology system

Since Taiji-1's launch, the research and development of Taiji-2's key technologies have been carried out in an orderly manner. According to interface and function, Taiji-2's key technologies are divided into five categories, such as laser metrology system, inter-satellite laser link maintaining system, gravitational reference sensor system, drag-free and micro-thruster system and hyper-stable and hyper-static satellite platform. The principle prototypes of Taiji-2's key technologies have been developed and the prototype of the laser metrology system is shown in Fig. 3. The ground verifications of Taiji-2's key technologies have been completed and all the test items and performances meet Taiji-2's requirements.

The other important issue for Taiji-2 is to verify the algorithm of time delay interferometry. In the other satellite of Taiji-2, an optical fiber interferometer is set up

to simulate a short arm of tens of kilometers. By using this optical fiber interferometer, together with the ranging data and clock synchronization data, the techniques of time delay interferometry can be applied. Despite of the path length noise of the fiber interferometer, the feasibility of the algorithm of time delay interferometry can be verified.

Once Taiji-2 is launched, the technologies could be verified by flight demonstration. It will remove all the technical obstacles faced by Taiji-3.

References

- [1] HU W R, WU Y L. The Taiji program in space for gravitational wave physics and the nature of gravity[J]. *National Science Review*, 2017, **4**(5): 685-686
- [2] LUO Z R, GUO Z K, JIN G, et al. A brief analysis to Taiji: science and technology[J]. *Results in Physics*, 2020, **16**: 102918
- [3] LUO Z R, WANG Y, WU Y L, et al. The Taiji program: a concise overview[J]. *Progress of Theoretical and Experimental Physics*, 2021, **2021**(5): 05A108. DOI: 10.1093/ptep/ptaa083
- [4] RUAN W H, LIU C, GUO Z K, et al. The LISA-Taiji network[J]. *Nature Astronomy*, 2020, **4**(2): 108-109
- [5] The Taiji Scientific Collaboration. China's first step towards probing the expanding universe and the nature of gravity using a space borne gravitational wave antenna[J]. *Communications Physics*, 2021, **4**(1): 34
- [6] WU L Y, HU W R. Special issue on Taiji program in space for gravitational universe with the first run key technologies test in Taiji-1[M]//. *International Journal of Modern Physics A: Particles and Fields; Gravitation; Cosmology*. Singapore: World Scientific, 2021
- [7] WU L M, XU P, ZHAO S H, et al. Independent global gravity field model from Taiji-1 observations[J]. *Microgravity Science and Technology*

Progress of SDGSAT-1 Mission*

GUO Huadong^{1,2}, DOU Changyong^{1,2}, CHEN Hongyu³, FU Bihong³

1. International Research Center for Big Data for Sustainable Development (CBAS), Beijing 100101
2. Aerospace Information Research Institute, Chinese Academy of Sciences, Beijing 100101
3. Innovation Academy for Microsatellites, Chinese Academy of Sciences, Shanghai 201204

Abstract

The Sustainable Development Science Satellite 1 (SDGSAT-1), formerly known as CASEarth (Guangmu) Earth science satellite, was developed by the Chinese Academy of Sciences (CAS) and supported by the Strategic Priority Research Program of the CAS “Big Earth Data Science Engineering (CASEarth)”. It is the world’s first science satellite dedicated to serving the United Nations 2030 Sustainable Development Agenda (2030 Agenda), and also is the CAS’s first Earth science satellite. SDGSAT-1 is the first SDG satellite operated by the International Research Center for Big Data for Sustainable Development (CBAS), which was successfully launched into its orbit on 5 November 2021, and its first set of data acquired by its three payload systems, *i.e.*, Thermal Infrared Spectrometer (TIS), Glimmer Imager (GI), and Multispectral Imager (MSI) were released on 20 December 2021. Now SDGSAT-1 is under in orbit testing.

Key words

Sustainable development science satellite, UN 2030 Agenda, Sustainable Development Goals (SDG)

1 Introduction

As the big data era is coming, in January 2018, the Chinese Academy of Sciences (CAS) launched a project entitled “Big Earth Data Science Engineering (CASEarth)” Strategic Priority Research Program of the CAS to carry out systematic research on big Earth data, aiming to provide a new impetus for interdisciplinary, cross-scale, macro-scientific discoveries using big Earth data^[1]. One of the major objectives of CASEarth project is designing and developing a science satellite to provide continuous Earth observing data for the research in support of new big data-driven, multidisciplinary, scientific discoveries in Earth system sciences, social economics sciences, and sustainable development associated disciplines.

The implementation of the UN 2030 Agenda for Sustainable Development (2030 Agenda) is faced with an urgent need for data and methods^[2]. The Sustainable

Development Science Satellite 1 (SDGSAT-1) is the world’s first science satellite dedicated to serving the 2030 Agenda. To meet the requirements of monitoring, evaluation and research on indicators of SDGs, SDGSAT-1 aims to depict traces of anthropic activities by synergetic observation of its three payloads, *i.e.*, Thermal Infrared Spectrometer (TIS), Glimmer Imager (GI) and Multispectral Imagers (MSI), in day and night observing modes, serving the realization of global SDGs, and providing support for the study of the SDG indicators related to human-nature interaction.

2 Scientific Objectives

By detecting the parameters representing the interaction between human activities and the Earth environment, and converting the integrated detection data to SDGs application information, the correlation and coupling

* Supported with funding from the Strategic Priority Research Program of the Chinese Academy of Sciences (XDA19010000)

Received May 27, 2022

between human activities and natural environment related indicators can be studied. Taking full advantage of SDGSAT-1 in macroscopic, dynamic, large-range, multi-load and day-night collaborative exploration of the Earth surface, the scientific objectives is to study the environmental changes and evolution rules mainly caused by human activities, such as urbanization level (SDG11), human settlement pattern (SDG2, SDG6), energy consumption (SDG13) and coastal ecology (SDG14, SDG15); as well as, to explore new methods and approaches for detecting surface environmental elements under low-light conditions such as night light or moonlight.

3 SDGSAT-1 Mission Configuration

After more than one and half years’ requirement analysis and project argumentation, the SDGSAT-1 mission was formally approved by CAS in January 2019. There are 6 major engineering systems, namely Satellite system, Launch Vehicle system, Launch site system, Tracking Telemetry and Command (TT&C) system, Ground Support system, and Scientific Application system^[3]. The engineering development process is supervised by “Space Science (Phase II)” Strategic Priority Research Program of the CAS.

Under the mission configuration framework, the engineering objectives of the SDGSAT-1 mission are: (i) to develop a 760 kg weight satellite equipped by three payload systems, with an operational lifetime no less than 3 years; (ii) to develop a CZ-6 carrier rocket system with the capability that can send the SDGSAT-1 into its 505 km orbit, and execute launch campaign; (iii) to complete the TT&C task both in active and in-orbit operation stage; (iv) to develop ground support and scientific application systems to ensure that the data receiving, data processing, data calibration (radiometric and geometric), and data products production, etc., all the links of data chain can work in normal operation.

4 Technical Specifications

SDGSAT-1 flies in a Sun-synchronous orbit with altitude of 505 km and inclination angle of 97.5°, resulting in an imaging spatial resolution of 30 m for TIS and 10 m for GI and MSI, respectively. The orbit allows SDGSAT-1 to revisit same spot on the Earth surface in 11 days^[4]. By working in “Thermal Infrared + Multispectral”, “Thermal Infrared + Glimmer”, and single

payload observing modes in orbit, SDGSAT-1 can collect multiple types of datasets by its synergetic observations in both day and night time.

To ensure data quality, SDGSAT-1 has various on-board calibration working modes, i.e., Moon calibration, blackbody calibration, LED lamp calibration, which guarantee the accurate quantitative detecting applications. Table 1 showed technical specifications of SDGSAT-1

Table 1 Technical specifications of SDGSAT-1

Type	Index	Specifications
Orbit	Type	Sun-synchronous orbit
	Altitude/km	505
	Inclination/(°)	97.5
Thermal infrared spectrometer	Swath width /km	300 km
	Bands/μm	8–10.5
		10.3–11.3
		11.5–12.5
Spatial resolution /m	30	
Glimmer/Multispectral imager	Swath width /km	300
	Bands of glimmer imager/nm	P: 450–900
		B: 430–520
		G: 520–615
		R: 615–900
	Spatial resolution of glimmer imager/m	P:10, RGB: 40
	Bands of multispectral imager/nm	B1: 380–420
B2: 420–460		
B3: 460–520		
B4: 520–600		
B5: 630–690		
Spatial resolution of multispectral imager /m	B6: 765–805	
	B7: 805–900	
	10	

5 Launch and First Set of Imagery

After almost 3 years of development, on 5 November 2021, SDGSAT-1 was successfully launched into the orbit from the Taiyuan Satellite Launch Center (TSLC). About one month later, on 20 December 2021, the first set of images, including the images of Yangtze River Delta, Shandong Peninsula, Namtso in Tibet, Aksu in Xinjiang, Beijing, Shanghai and Paris in France, acquired by instruments onboard SDGSAT-1 were officially released in Beijing. The images suggest that the payload systems of SDGSAT-1 are of good quality and expected to meet its scientific objectives (see Fig.1–3).



Description

The image shows details of the urban structure of Beijing, with landmarks such as the main urban ring road traffic and urban network, Tian'anmen Square and Capital Airport clearly visible.

Color low-light data clearly show that the main urban area of Beijing is dominated by warm yellow light (high pressure sodium light), while the sub-center of the city, Yizhuang Economic Development Zone, Daxing, Fangshan, Shijingshan and the eastern part of Changping are dominated by mid-tone green light (LED light). Water Cube (blue), National Center for the Performing Art and urban neon lights can be clearly identified, showing the colorful city night scene, and reflects the regional economic development and night activity level.

Fig. 1 Color and panchromatic Glimmer image of Beijing



Description

The Yellow River estuary colorful, distinct layers. The image shows that the water of Yellow River gradually mixed with seawater after entering the sea, and the sediment into the sea migrated with the mixed water and gradually dissipated.

Fig. 2 Multispectral image of the Yellow River estuary

Glimmer imager has the capability to reflect the level of social economic development and human settlement pattern by detecting the intensity and distribution of night light, to serve the investigation of the indicators of SDG 11. Multispectral image showing transparency and suspended matter in various turbidity water bodies can serve the monitoring and evaluation of water quality in SDG 6 and SDG 14. By detecting temperature dynamic changes of the Earth surface, the Thermal Infrared image can support the study of indicators/targets of SDG 2, SDG 7 and SDG 13.

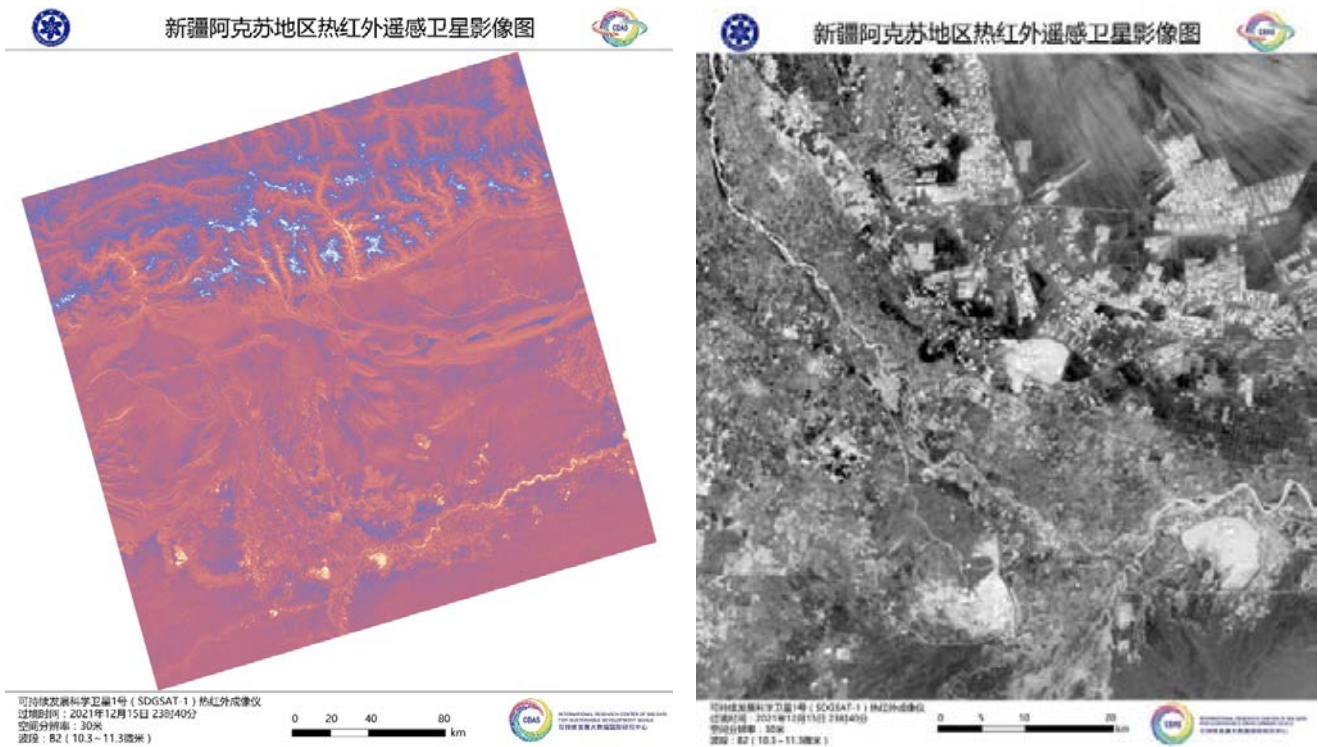
6 Conclusion

As the world’s first sustainable development science satellite, SDGSAT-1 demonstrate potential power in support

of monitoring, evaluation and study of SDGs representing the interaction between human activities and natural environment. Scientific and technological innovation is an important means to support the realization of SDGs, and Earth Observation can make an important contribution to the global implementation of the 2030 Agenda. CBAS is looking forward to collaborate with related stakeholders to fully use the advantage of Earth Observing systems to contribute to the realization of global SDGs.

Acknowledgements

The authors wish to thank the CASEarth Small Satellite research teams of CASEarth project and SDGSAT-1 Engineering Project Teams for their continuous efforts and contributions.



Description

Thermal infrared image of Aksu area at night. In the color figure, bright orange represents high temperature, while blue and purple represent low temperature. The upper part of the image is the northern mountainous area, with high valley temperature and low ridge temperature. The lower part is Tarim River, lakes and reservoirs, and the bright temperature at night is higher than surrounding features. Urban residential areas (Aksu city and Alar city) show higher temperature.

The degree of brightness and shade in the partial black and white picture represents the brightness temperature. In the middle is the farm of the Xinjiang Construction Corps. The visible bright bars are the frozen winter rest plots after watering, and the dark area is the dry sandy land.

Fig. 3 Thermal Infrared image of Aksu Region, Xinjiang

References

- [1] GUO H D. Big Earth data: a new frontier in Earth and information sciences[J]. *Big Earth Data*, 2017, 1(1/2): 4-20. DOI: 10.1080/20964471.2017.1403062
- [2] United Nations. The Sustainable Development Goals Report 2021[R]. New York: United Nations, 2021
- [3] Chinese Academy of Sciences. General Requirements for Guangmu Earth Science Satellite Engineering Development[R]. Beijing: Chinese Academy of Sciences, 2021
- [4] GUO H D, CHEN H Y, CHEN L F, *et al.* Progress on CASEarth satellite development[J]. *Journal of Space Science*, 2020, 40(5): 707-717. DOI: 10.11728/cjss2020.05.707

Construction Progress of Chinese Meridian Project Phase II*

WANG Chi¹, XU Jiyao¹, LÜ Daren², YUE Xinan³,
XUE Xianghui⁴, CHEN Gang⁵, YAN Jingye¹, YAN Yihua¹,
LAN Ailan¹, WANG Jiangyan¹, WANG Xin², TIAN Yufang²

1. State Key Laboratory of Space Weather, National Space Science Center, Chinese Academy of Sciences, Beijing 100190
2. LAGEO, Institute of Atmospheric Physics, Chinese Academy of Sciences, Beijing 100029
3. Key Laboratory of Earth and Planetary Physics, Institute of Geology and Geophysics, Chinese Academy of Sciences, Beijing 100191
4. School of Earth and Space Sciences, University Science and Technology of China, Hefei 230026
5. Department of Space Physics, School of Electronic Information, Wuhan University, Wuhan 430072

Abstract

The Chinese Meridian Project (CMP) is the Space Environment Ground Based Comprehensive Monitoring Network of China, a national major science and technology infrastructure project. The CMP consists of the Space Environment Monitoring System, Data Communication System, and Science Application System. Its construction has been divided into two steps: the Phase I was from 2008 to 2012; the Phase II started at the end of 2019, expected to be completed at the end of 2023. Beyond 2023, the CMP as a whole will be in operation to make observations. This report introduces the construction progress of CMP Phase II in the past two years, covering the construction progress of both the Data Communication System and the Science Application System. As for the Space Environment Monitoring System, this report mainly gives an introduction to the construction progress of large-scale advanced monitoring equipment, such as, the solar radio telescope, interplanetary scintillation telescope, incoherent scatter radar, high frequency radar, MST radar, and large-aperture Helium Lidar. In addition, this paper presents the construction plan for the next two years and the future outlook as well.

Key words

Chinese Meridian Project, Ground-based observation network, Space weather, Solar-terrestrial physics

1 Introduction to the Chinese Meridian Project

The Space Environment Ground Based Comprehensive Monitoring Network of China (hereinafter referred to as

the Chinese Meridian Project, CMP) is a national major science and technology infrastructure project. The CMP is composed of the Space Environment Monitoring System, Data Communication System, and Science Application System.

The constructions of the project are carried out in two

* Supported by the Chinese Meridian Project

Received May 27, 2022

steps: CMP Phase I and Phase II. The Phase I has built 15 conventional observation stations along longitude 120°E and latitude 30°N. The instruments include magnetometers, radio radar sets, optical observation equipment, and sounding rockets^[1]. The construction of Phase I started in 2008 and completed in 2012. Since 2012, the CMP Phase I has entered into operation.

The CMP Phase II started construction at the end of 2019, and is expected to be completed by the end of 2023. On the basis of CMP Phase I, it will add 16 stations. Finally, a whole-space environment monitoring network will be set up, composed of 31 stations and nearly 300 instruments along longitudes 100°E and 120°E, and latitudes 30°N and 40°N.

The CMP adopts geomagnetic, radio, optical and other means to build a networked monitoring capacity for the ionosphere, middle and upper atmosphere and geomagnetism in China (three networks). Internationally advanced large-scale monitoring equipment will be deployed in four key monitoring areas: high latitude in the polar region, middle latitude in the north of China, low latitude in Hainan and the Tibetan Plateau, carrying out comprehensive fine detection of the space environment (four focuses). A series of advanced solar interplanetary monitoring equipment is added to build the monitoring capability of the whole chain of solar terrestrial space (one chain). The framework of one chain, three networks and four focuses will realize the multi-element and comprehensive three-dimensional detection of the solar terrestrial space environment for the first time in the world.

The scientific goals of CMP are: (i) to explore the propagation and evolution of space weather events and the paths and characteristics affecting the space environment, through monitoring of the whole chain with nationwide coverage and high temporal and spatial resolution from the solar atmosphere to near Earth space; (ii) to reveal the characteristics of change and differences of space environment over different regions of

China, as well as the fine process of space environment change in special regions such as the Tibetan Plateau, the north and south of China; (iii) to study the coupling process of solid Earth, lower atmosphere and near-Earth space environment under special geological and geographical conditions in China.

For a detailed introduction to CMP Phase II, please refer to Ref.[2]. The timeline of the construction and operation of the whole CMP is shown in Fig. 1.

2 Main Construction Progress of Various Systems and Monitoring Equipment of CMP Phase II

The CMP is divided into three systems, that are, the Data Communication System, Scientific Application System, and Space Environment Monitoring System.

The Data Communication System is responsible for data transmission, collection, processing, distribution and sharing. The Scientific Application System is in charge of various advanced data products, application demonstration, model research and development, formulation and implementation of the joint scientific observation campaign plan, international cooperation, scientific research, *etc.* The Space Environment Monitoring System performs conventional and intensive observations, data acquisition and data inversion of various monitoring equipment. It is also responsible for the normal operation of monitoring equipment, equipment maintenance, transformation and upgrading of equipment, *etc.*

2.1 Construction of the Data Communication System and Scientific Application System

The Data Communication System and Scientific Application System will be installed in the integrated information and operation control center building. The building is located in Huairou campus of National Space

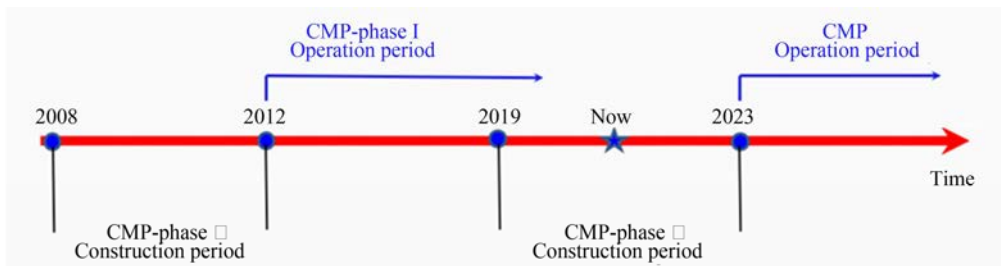


Fig. 1 Timeline of CMP's construction and operation

Science Center of Chinese Academy of Sciences. It will become an important control hub, data center and research platform of CMP. The main construction of this building has been completed, as shown in Fig. 2. It is estimated that the construction of the Data Communication System and Science Application System will be accomplished at the end of 2022. From then on, these two systems will be eligible to promote joint testing with the Space Environment Monitoring System.

2.2 Construction Status of the Space Environment Monitoring System

The Space Environment Monitoring System is composed of eight subsystems which belong to “one chain” (solar interplanetary monitoring chain subsystem), three networks (geomagnetic monitoring network subsystem, ionospheric monitoring network subsystem, and middle and upper atmospheric monitoring network subsystem), and four focuses (polar high latitude monitoring subsystem, north middle latitude monitoring subsystem, south low latitude monitoring subsystem, and Tibetan Plateau monitoring subsystem).

The three networks in the Space Environment Monitoring System in CMP are mainly made up of magnetometers, atmosphere electric field monitors, ionosondes, TEC and scintillation monitors, lidars, Meteor radar sets, airglow imagers, and other conventional observation equipment. The construction and installation of these equipment will be completed by the end of 2022 and then put into use.

In addition to these conventional monitoring instruments for three networks, the CMP will build a series of internationally advanced large-scale monitoring equipment for the observation of the four key areas—four focuses, and a series of advanced solar interplanetary monitoring equipment for monitoring the whole chain of solar terrestrial space—one chain. The internationally



Fig. 2 Building of the Integration Information and Operation Control Center

advanced large-scale monitoring equipment includes solar radio telescope, interplanetary scintillation telescope, incoherent scatter radar, high frequency radar, MST radar, large-aperture Helium Lidar, and so on. These advanced large-scale monitoring instruments will be developed, installed and put into use by the end of 2023. Here is a brief introduction to the development and construction progress of some of them.

2.2.1 Solar Radio Telescope

The Solar Radio Telescope is one of the key observatories in the solar interplanetary monitoring chain subsystem of CMP Phase II, which is an important tool to monitor and diagnose solar activities. Two solar radio telescopes will be built in the CMP. One is the Daocheng Solar Radio Telescope (DSRT), and another is the Mingantu Spectral Radiograph (MUSER).

DSRT is located at Daocheng, Sichuan province (100.246°E, 29.011°N), south-west of China, and is surrounded by mountains which provide an excellent radio environment. The interferometric array of DSRT is composed of 313 antennas of six meters in diameter. All antennas are uniformly distributed along a circle of 1000 meters in diameter. A calibration antenna is placed on the top of a tower at the center of the circle, from where an arbitrary calibration signal is transmitted to all antennas omni-directionally. Combining with dedicated internal calibration and traditional astronomical calibration sources, DSRT will enable accurate phase calibration over the 313 elements, therefore providing highly dynamic radio images of solar bursts (Fig. 3). The operational frequency band of DSRT is 150–450 MHz for tracing Coronal Mass Ejection (CME) in the high atmosphere region of the Sun.

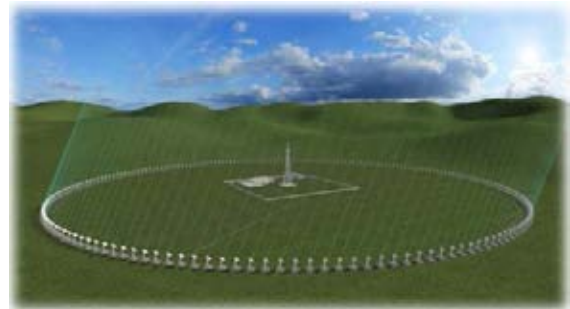


Fig. 3 Artistic concept of DSRT. 313 element antennas form a circular array of 1000 m in diameter. A 100 m tower locates right at the center and carries a transmitting antenna on the top for amplitude/phase calibration of the system

At the time of this report so far, a 16-element small system has been installed for observation and concept verification (see Fig. 4). The whole system with 313 element antennas will be installed by the end of 2022. DSRT will be tested and commissioned in 2023. At the end of 2023, it will be reviewed for acceptance and enter the observation stage.

The construction of Mingantu Spectral Radioheliograph (MUSER) was fulfilled during 2009–2016 and it covers the frequency range of 400 MHz–2 GHz. MUSER is located at Mingantu, Inner Mongolia (42.71°N, 115.25°E, 1365 m). In the CMP Phase II, MUSER’s frequency regime will be extended to 30–400 MHz with 224 Logarithm-Periodic Dipole Antennas (LPDAs)^[3]. The array configuration for extending MUSER to a lower frequency range of 30–400 MHz with 100 LPDAs has been optimized to achieve minimum RMS deviation of antenna distributions in the axial direction and minimum RMS deviation of antenna distributions with respect to a Gaussian distribution in the radial direction.

The basement construction of MUSER was finished in 2021 and the facilities will be constructed in 2022. The technical acceptance will be carried out at the end of 2023 before use.

2.2.2 Interplanetary Scintillation Telescope

The Interplanetary Scintillation (IPS) telescope is one of the key monitoring equipment in the solar interplanetary monitoring chain subsystem of CMP Phase II, which is

an important tool to monitor the propagation of solar eruptions in interplanetary space.

In the CMP Phase II, a three-station interplanetary scintillation telescope system will be built. The main station locates at Mingantu, Inner Mongolia (42.71°N, 115.25°E, with an altitude of 1365 m), where 3 cylinder antennas will place side by side, with 140 m long in the N-S direction and 40 m long in the E-W direction. Two 30 m dish antennas will be constructed at other two sub-stations respectively in Abaga County (44.73°N, 115.12°E, 1163 m) and Sunit Right County (43.50°N, 113.06°E, 1075 m) in Inner Mongolia^[4].

The IPS basement construction was finished in 2021 and the facilities will be constructed in 2022.

These radio facilities of solar radio telescopes and interplanetary scintillation telescopes will be key tools for monitoring solar disturbances from the Sun to the Earth’s environment and they will play a fundamental role in studying and monitoring space weather.

2.2.3 Sanya Incoherent Scatter Radar

The Incoherent Scatter Radar (ISR) is one of the most powerful ground-based instruments for detecting multiple plasma parameters of the ionosphere from 100 km to 1000 km. Sanya Incoherent Scatter Radar (SYISR) is a tristatic system located in Sanya, Hainan. It is one of the advanced large-scale monitoring equipment of CMP Phase II, which belongs to the south low latitude monitoring subsystem.

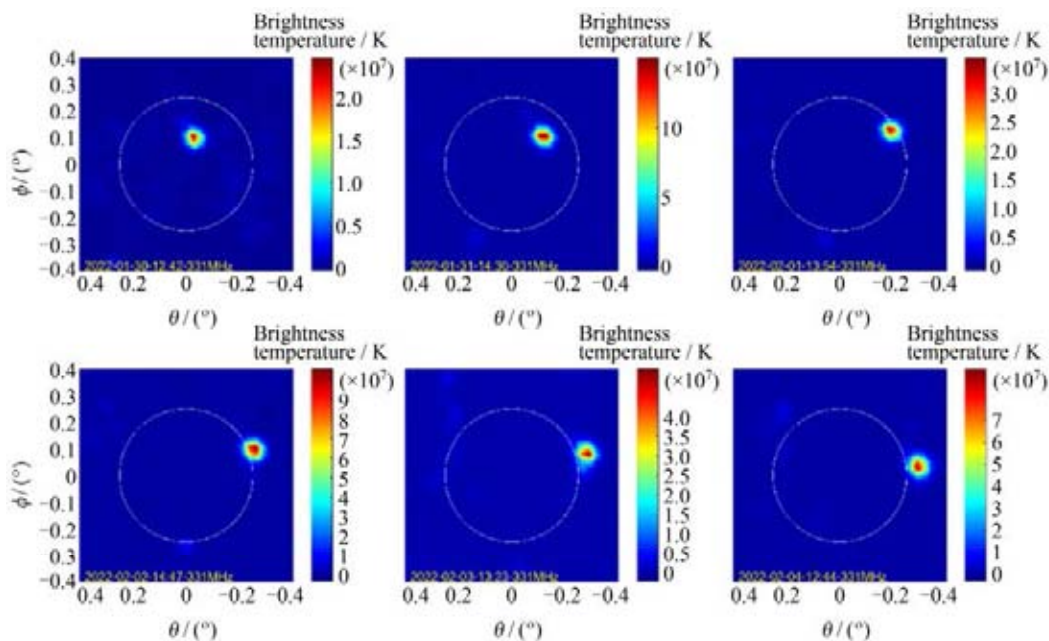


Fig. 4 Preliminary observation with 16-element only showing the high temperature spot rotating along with the rotation of the Sun in six days

Supported by the CMP Phase II, SYISR will extend the current Sanya transmitter/receiver from 4,096 channels (located at Sanya, 18.3°N, 109.6°E)^[5], which is supported by the Natural Science Foundation of China, to 8320 channels. Simultaneously, two new 4096-channel receivers in Wenchang (19.6°N, 110.8°E) and Fuke (19.5°N, 109.1°E) will be built^[6,7]. The sketch map is shown in Fig. 5. The signal transmitted by Sanya station will be collected by all three stations after being scattered by the ionospheric plasma, which could be used to derive the plasma density, temperature, and velocity. Through the combination of three independent observations of the same scatter volume by three receivers, we can derive the vector information of the 3D velocity of plasma, which will be greatly beneficial to the investigation of low latitude ionospheric dynamics.

The whole system will be completed at the end of 2022 and is now under construction in full swing.

2.2.4 Middle Latitude Agile High-frequency Radar Group

In the CMP Phase II, a Middle Latitude Agile High-frequency Radar Group (MiLARG) will be set up to continuously observe the distribution and movements of the ionospheric irregularities over the north of China. It is the core monitoring equipment in the north middle latitude monitoring subsystem. The MiLARG is composed of six (three pairs) High-Frequency (HF) radar sets deployed at Hejing (42.8°N, 83.7°E), Siziwang (41.8°N, 111.9°E) and Longjing (42.8°N, 129.4°E). The high-frequency radar sets are all digital phased array radar

sets which can operate over a wide range from 8 to 20 MHz with a Field of View (FOV) of about 78°. At every radar site, two radar sets are designed to form a large FOV of about 156°. Moreover, the radar sets at neighboring sites will have common coverage to obtain the velocity of echoes. Therefore, the coverage of MiLARG can be up to about 120° (see Fig. 6).

MiLARG is under construction. At present, the radar to the northwest at Siziwang station (SZW for short) has been completed and in trial operation. The first observation of ionosphere from SZW on 14 March 2022 is illustrated in Fig. 7. Ionosphere echoes within about 2,000 km were observed.

The construction of MiLARG is expected to be completed by the end of 2022. Joint commissioning and testing will be carried out in 2023.

2.2.5 MST Radar

The Mesosphere Stratosphere Troposphere radar (MST Radar) has proven to be a powerful tool for investigating various atmospheric dynamics in the lower and middle atmosphere and ionosphere. The MST radar works in the VHF band, observing the atmosphere under all weather conditions and at all times by detecting the echoes from the atmospheric refractive index variations induced by the fluctuations in humidity, temperature, electron density, *et al.* The MST radar can provide continuous high time-height resolutions and quasi-simultaneous observations of the horizontal wind and vertical velocities of different height range below 100 km except for about 25–60 km.

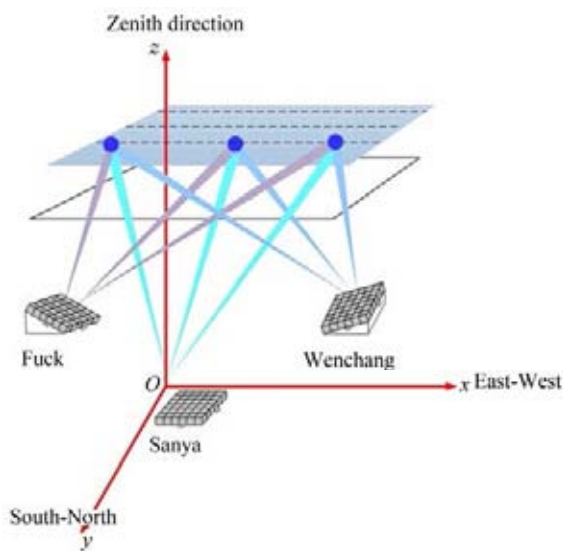


Fig. 5 Sketch map of Sanya Incoherent Scatter Radar (SYISR) Tristatic System

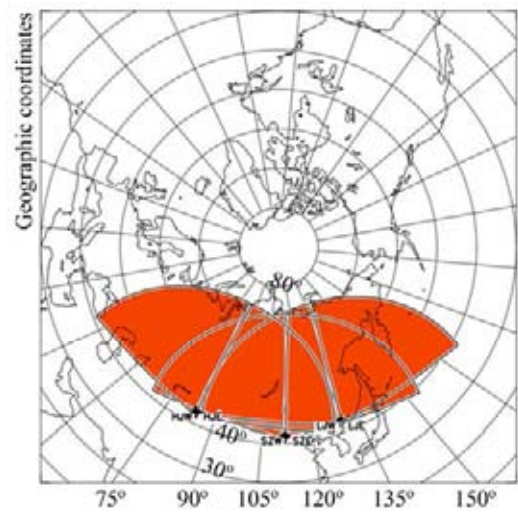


Fig. 6 Coverage of the Middle Latitude Agile Radar Group (MiLARG)

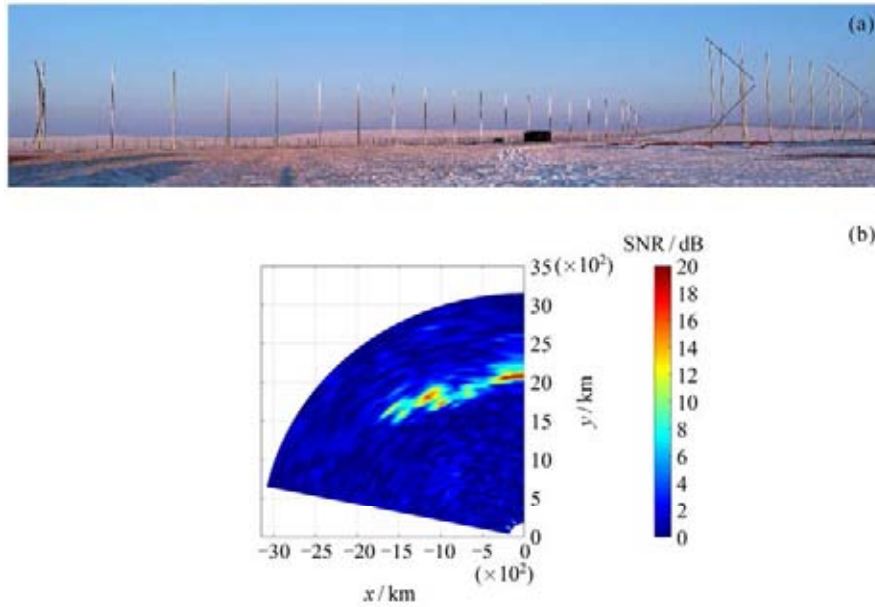


Fig. 7 SZW radar has been in trial operation. (a) Full view of SZW radar. (b) Echo from ionosphere

In the CMP Phase I, two MST radar sets have been built, that are Beijing MST Radar at Xianghe of Hebei province (39.78°N , 116.95°E) and Wuhan MST Radar at Chongyang of Hubei province (29.51°N , 114.13°E), respectively.

In the CMP Phase II, two new powerful MST radar sets will be established. One is Tibetan Plateau MST Radar at Yangbajing of Tibetan Plateau (30.08°N , 90.53°E ; 4300 m). Another is Qinzhou MST radar at Qinzhou City in Guangxi Province (22.132°N , 108.272°E).

With advanced technology and under scientific design, the MST radar will be the first full digital full polarized active phased array radar to lead the development of MST radar sets. They have a circular array of 153 m in diameter, consisting of 931 3-element crossed Yagi antennas. The peak power is close to 2 MW.

The two new MST radar sets are under construction, to be finished by the end of 2022. Then joint commissioning and testing will be carried out in 2023. After that, they will enter into the observation stage.

The four MST radar sets of CMP, which are the Beijing MST radar, Wuhan MST radar, Qinzhou MST radar, and Tibetan Plateau MST radar, will play a unique role in broadening our knowledge of the turbulence, gravity waves, planetary waves, tides, mean circulation, interaction between different scales of dynamical and electrodynamic processes, and vertical coupling between layers from the boundary layer to the ionosphere.

2.2.6 Large-Aperture Helium Lidar

The Large-Aperture Helium Lidar (LAHL) supported

by the CMP Phase II is designed to investigate the metastable Helium in the Earth's thermosphere, which has a significant population between 200–1000 km for the resonant remote sensing^[8]. The Lidar will be located at Fuke (19.5°N , 109.1°E) in Hainan province. It is one of the key equipment in the south low latitude monitoring subsystem.

The key scientific goal of the LAHL is to explore the interaction between the neutral and ions, wave-induced transport and its influence on the constituent, as well as the geomagnetic effect on the neutral atmosphere within the thermospheric region using the metastable helium as the tracer.

The state-of-the-art instruments of LAHL, *e.g.*, the telescope array, modern high-power pulse laser, as well as high-efficiency and low-noise detectors, enable observations of the neutral metastable helium at an altitude of 1000 km with a vertical resolution of 50 km and time resolution of 30 min to 1 hour.

The telescope array consists of an array of six one-meter diameter telescopes yielding a total collecting area of approximately 4.5 m^2 . The array is designed so that each telescope can be pointed to the same atmospheric region. The back-scattered metastable helium fluorescence photons collected by each telescope, are combined together through a 0.7 m diameter telescope which is mounted at the center of the 6-telescope array (Fig. 8). The primary mirrors of the telescopes are made of glass ceramics, and their RMS error of the surface accuracy is below $\lambda/40$ at 632.8 nm after multilayer dielectric coating.

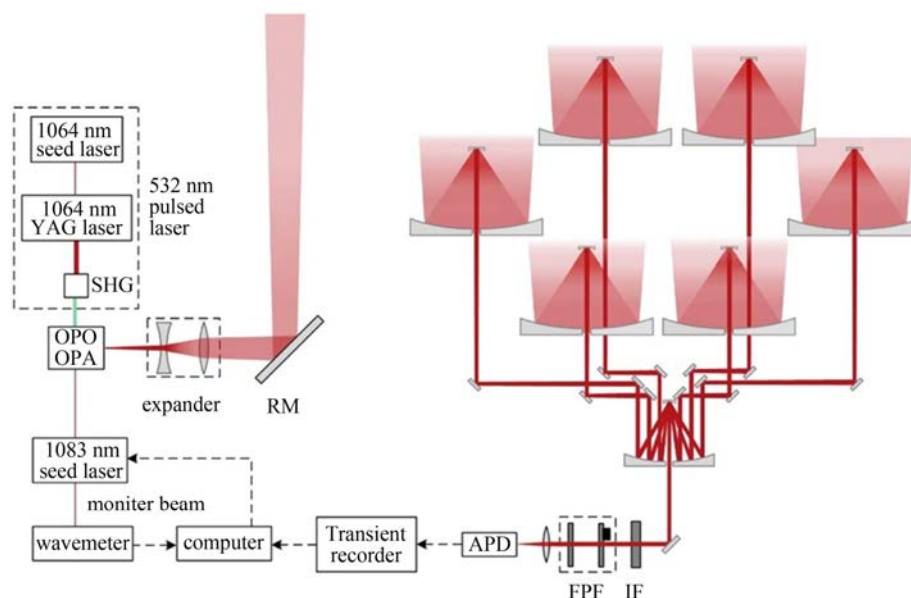


Fig.8 Sketch map of the Large-Aperture Helium Lidar (LAHL)

The modern high power pulse laser is generated by an OPO+OPA system, which is pumped by a high power 532 nm seeded Nd: YAG laser. The output 1083 nm laser is designed to have a linewidth of 200 MHz, a pulse power of 140 mJ, and a repetition rate of 50 Hz. Three such laser systems will finally be combined and achieve a total power of about 20W @1083 nm.

At present, we have developed a demonstration system which can output 80 mJ pulses at 1083 nm with a linewidth smaller than 200 MHz. The measured center frequency accuracy of the laser is smaller than 20 MHz within 30 min.

The equipment is planned to be tested, accepted and observed in 2023.

3 Prospect and Plan of Construction in the Next Two Years

At present, all the monitoring equipment of CMP Phase II are in the process of development and installation. By the middle of 2023, all equipment installation will be finished. Joint testing of the whole system will be started. The national acceptance of CMP Phase II is expected to be carried out by the end of 2023.

In addition, all monitoring equipment of CMP Phase I will be upgraded by the end of 2023 and incorporated into CMP Phase II to form a complete CMP monitoring system. In this regard, the CMP will complete all construction tasks.

After 2023, the CMP will enter the operation stage. We believe and expect that the CMP will produce outstanding scientific research results in the future.

References

- [1] WANG C. New chains of space weather monitoring stations in China[J]. *Space Weather*, 2010, **8**(8): S08001. DOI: 10.1029/2010SW000603
- [2] WANG C, CHEN Z Q, XU J Y. Introduction to Chinese meridian project - phase II[J]. *Chin J Space Sci*, 2020, **40**(5): 131-135. DOI: 10.11728/cjss2020.05.131
- [3] YAN Y H, CHEN Z J, WANG W, et al. Mingantu spectral radioheliograph for solar and space weather studies[J]. *Frontiers in Astronomy and Space Sciences*, 2021, **8**: 584043. DOI: 10.3389/fspas.2021.584043
- [4] YAN Y H, WANG W, CHEN L J, et al. New interplanetary scintillation array in China for space weather[J]. *Sun and Geosphere*, 2018, **13**(2): 153-155. DOI: 10.31401/SunGeo.2018.02.05
- [5] YUE X A, WAN W X, XIAO H, et al. Preliminary experimental results by the prototype of Sanya Incoherent Scatter Radar[J]. *Earth and Planetary Physics*, 2020, **4**(6): 579-587. DOI: 10.26464/epp2020063
- [6] LI M Y, YUE X A, ZHAO B Q, et al. Simulation of the signal-to-noise ratio of Sanya incoherent scatter Radar Tristatic System[J]. *IEEE Transactions on Geoscience and Remote Sensing*, 2021, **59**(4): 2982-2993. DOI: 10.1109/TGRS.2020.3008427
- [7] ZHANG N, LI M Y, ZHAO B Q, et al. A detection performance analysis of Sanya incoherent scatter Radar Tristatic System[J]. *Radio Science*, 2021, **56**(5): e2020RS007144. DOI: 10.1029/2020RS007144
- [8] GERRARD A J, KANE T J, MEISEL D D, et al. Investigation of a resonance Lidar for measurement of thermospheric metastable helium[J]. *Journal of Atmospheric and Solar-Terrestrial Physics*, 1997, **59**(16): 2023-2035

Introduction to the Chinese H α Solar Explorer Mission

FANG Cheng, LI Chuan

1. School of Astronomy and Space Science, Nanjing University, Nanjing 210023
2. Key Laboratory for Modern Astronomy and Astrophysics, Ministry of Education, Nanjing 210023

Abstract

The Chinese H α Solar Explorer (CHASE) mission, dubbed as “Xihe”— Goddess of the Sun, was launched on 14 October 2021 as the first solar space mission of China National Space Administration (CNSA). The CHASE mission aims to test an ultra-high precision and stability platform, and to acquire solar H α Spectroscopic observations with high temporal and spectral resolutions. Since its launch, the in-orbit performance of the scientific payload — H α Imaging Spectrograph (HIS) has been excellent. The first set of data has been calibrated and analyzed recently. The CHASE science data are expected to advance our understanding of the plasma dynamics in the solar lower atmosphere, and to investigate the Sun as a star for stellar physics.

Key words

Space-based telescope, Solar physics, Solar activities

1 Introduction

The Chinese H α Solar Explorer (CHASE) mission was approved by China National Space Administration (CNSA) in June 2019. It was dubbed as “Xihe” in Chinese — Goddess of the Sun. At 18:51 on 14 October 2021 (China Standard Time), the CHASE was launched into a Sun-synchronous orbit with an average altitude of 517 km. The CHASE satellite has a weight of 508 kg and a size of 1210 mm \times 1210 mm \times 1330 mm. The life time of the CHASE mission is designed to be 3 years. The CHASE mission aims to test a new satellite platform with ultra-high precision and stability, and to perform solar H α spectroscopic observations that are important for exploring the plasma dynamics in the solar lower atmosphere, namely the photosphere and chromosphere^[1]. A topical issue on the CHASE mission was

recently published to help users of CHASE data better understand its payload, technical parameters, observational modes, and data processing^[2–7].

Since the first applications of spectrographs and filters in the earlier 20th century, the solar H α observations have usually been obtained with ground-based telescopes^[8–11], which suffer from seeing and weather effects of the Earth’s atmosphere, and cannot provide all-day observations. The CHASE mission acquires, for the first time in space, solar H α spectroscopic observations with very high spectral and temporal resolutions. Along with the X-ray and Extreme Ultraviolet Imager (X-EUVI) onboard the FY-3E mission launched in July 2021^[12], and the Advanced Space-based Solar Observatory (ASO-S) to be launched in the last quarter of 2022^[13], the CHASE mission marks a milestone for Chinese solar observations to glide into the space age^[14].

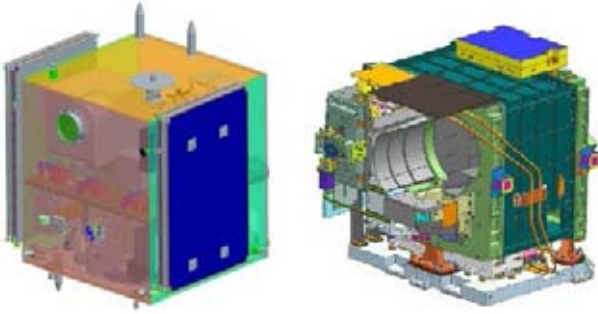


Fig. 1 Schematic view of the CHASE satellite (left panel) and the HIS instrument (right panel)

2 Science and Instrumentation

The primary goal of the CHASE mission is to investigate the plasma dynamics in the solar lower atmosphere, and to understand the physical mechanisms of solar eruptions. Specifically, the scientific objectives of the CHASE mission include: (i) Formation, dynamics, and chirality of solar filaments; (ii) Dynamics of solar activity in the photosphere and chromosphere; (iii) Comparative studies of the solar and stellar physics. For more details, one may refer to Li *et al.*^[3]

The scientific payload for the CHASE mission is the Ha Imaging Spectrograph (HIS), which has a weight of 54.9 kg and a size of 635 mm × 556 mm × 582 mm. It utilizes the ultra-high precision and stability platform to achieve solar Ha spectroscopic observations without requirement for a guide telescope or an imaging stabilization system. Fig.1 shows the schematic view of the CHASE satellite and the HIS instrument.

The CHASE/HIS has two observational modes: Raster Scanning Mode (RSM) and Continuum Imaging Mode (CIM). The RSM acquires solar spectroscopic observations in Ha (6559.7–6565.9 Å) and Fe I (6567.8–6570.6 Å) wavebands. The instrument spectral resolution or the spectral full width at half maximum (FWHM) is 0.072 Å, and the pixel spectral resolution is 0.024 Å. The RSM has three sub-modes: full-Sun scanning, region-of-interest scanning, and sit-stare spectroscopy. The first two have temporal resolutions of 30–60 s, and the last one has a temporal resolution less than 10 ms. The CIM acquires high-cadence (1 s) and full-Sun images at the continuum around 6689 Å with a FWHM of 13.4 Å. The CIM is designed to study the photospheric activities, and to test the stability of the satellite platform. More detailed instrument design and in-orbit performance are described by Liu *et al.*^[6]. Table 1 summarizes the key technical parameters of CHASE/HIS.

Table 1 Key parameters of CHASE/HIS

Primary aperture	180 mm
Effective focal length	1820 mm
Field of view	40' × 40'
RSM	
Passbands	6559.7–6565.9 Å 6567.8–6570.6 Å
Instrument FWHM	0.072 Å
Pixel spectral resolution	0.024 Å
Pixel spatial resolution	0.52"
Scanning time	30–60 s
Exposure time	<10 ms
Quantization (ADC)	12 bit
CIM	
Center wavelength	6689 Å
Passband FWHM	13.4 Å
Pixel spatial resolution	0.52"
Exposure time	<5 ms
Frame rate	1 s
Quantization (ADC)	10 bit

3 In-orbit Observations

After the successful launch of the CHASE mission on 14 October 2021, it obtained the first-light images on 24 October 2021. Up to date, the CHASE/HIS operates well in-orbit as expected. Routine observations have started recently. The raw data are transmitted to three ground stations (Miyun, Kashi and Sanya) located in China, and then transferred to the Solar Science Data Center of Nanjing University (SSDC-NJU) through a dedicated internet access. The Level 1 science data and higher-level products are produced and released to community by SSDC-NJU. Detailed calibration procedures of CHASE data are described by Qiu *et al.*^[4]

The calibration flow of RSM data involves several steps including the dark-field and flat-field correction, slit image curvature corrections, wavelength and intensity calibration, and coordinate transformation. Fig.2 shows an example of the raw RSM spectrum (upper panel) and the calibrated Level 1 spectrum (bottom panel). It can be found that the digital offsets, slit image curvature, bright and dark stripes due to irregularities of the slit, and non-uniform responses on the detector, *etc.*, are removed. The calibrated RSM Level 1 spectrum shows clearly three spectral lines, and the features of

solar limb darkening, scanning of an active region and a sunspot. The calibrated spectral profiles and its comparison with the BASS2000 ground-based spectra are shown in Fig.3. Both emission intensities are calibrated by using the continuum intensity at around 6500 Å given by Ref.[15].

For a full-Sun scanning, over 4600 steps are needed, which takes only about 46 s. One single step produces a spectrum as shown in Fig.2. Taking one specific wavelength along the slit from every step, we can splice an image at this wavelength. Fig.4 shows an example of the full-Sun image at H α center (6562.8 Å) produced by

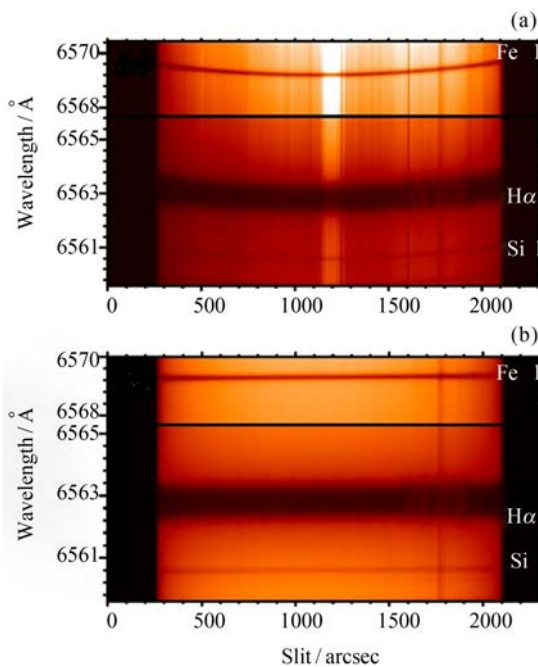


Fig. 2 Raw RSM spectrum observed at 06:01:27 UT on 22 December 2021, and the calibrated Level 1 RSM spectrum

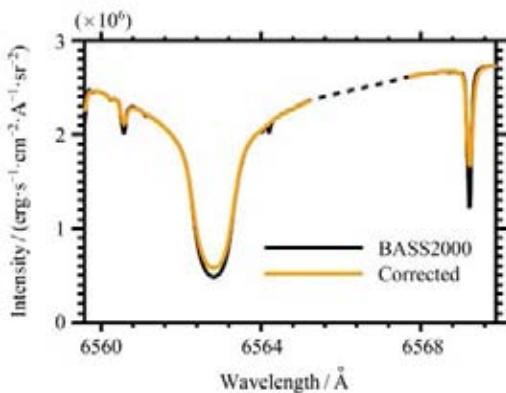


Fig. 3 Comparison between the calibrated spectral profiles and the ones from BASS2000

a scanning sequence at 06:01:05–06:01:52 UT on 22 December 2021. It has to be noticed that a scanning sequence produces 376 solar images at different wavelengths.

The RSM of CHASE obtains precise Fe I and H α spectral profiles for every pixel on the full solar disk or in the region of interest, that are able to derive simultaneously the photospheric and chromospheric Dopplergrams. Fig.5 shows an example of the chromospheric Dopplergram derived by using the full-Sun H α spectral profiles. The accuracy of velocity field is estimated to be better than 0.06 km·s⁻¹. The blue and red arrows indicate the y-axis of the detector and the solar north pole. The differential rotation from poles to the equator and the complex velocity distributions are clearly distinguished.

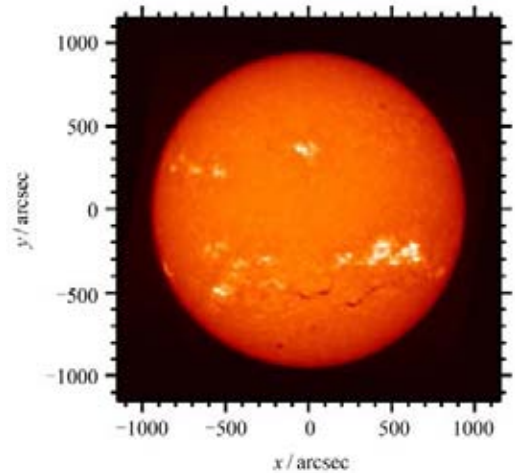


Fig. 4 Full-Sun spectroscopic image at the H α center of 6562.8 Å

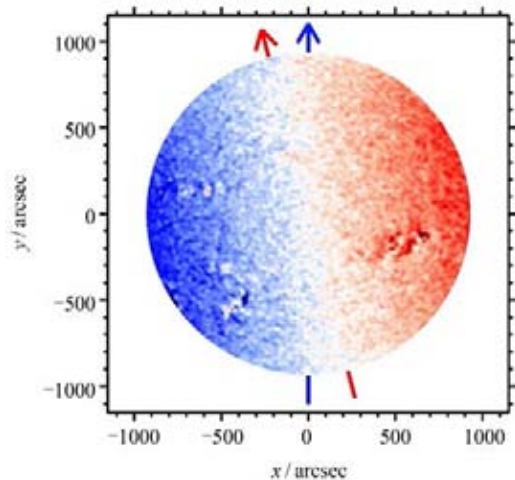


Fig. 5 Higher-level product: the full-Sun chromospheric Dopplergram

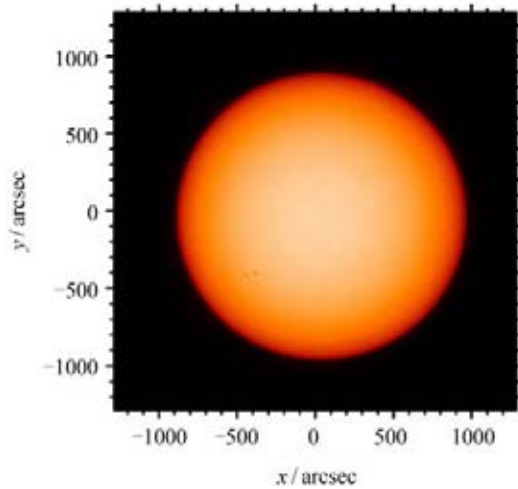


Fig. 6 Calibrated CIM photospheric image

The calibration procedures for CIM data include the dark-field and flat-field correction, and the transformation to the heliographic coordinates. Figure 6 displays the Level 1 CIM image observed at 02:02:40 UT on 25 November 2021.

4 Summary

Up to date, the in-orbit performance of the CHASE mission has been excellent. The first set of data has obtained and calibrated. The FITS formatted Level 1 science data are released to public through the website at SSDC-NJU (<https://ssdc.nju.edu.cn>). The CHASE data are expected to advance our understanding of the plasma dynamics in the solar atmosphere, and to investigate the Sun as a star for stellar physics.

Acknowledgements

The CHASE mission is supported by China National Space Administration (CNSA).

References

[1] LI C, FANG C, LI Z, et al. Chinese Ha solar explorer (CHASE)-a

complementary space mission to the ASO-S[J]. *Research in Astronomy and Astrophysics*, 2019, **19**(11): 165-170

- [2] FANG C, DING M D, LI C, et al. The Chinese Ha solar explorer – CHASE mission[J]. *Science China Physics, Mechanics & Astronomy*, 2022, **65**: 289601
- [3] LI C, FANG C, LI Z, et al. The Chinese Ha solar explorer (CHASE) mission: an overview[J]. *Science China Physics, Mechanics & Astronomy*, 2022, **65**: 289602
- [4] QIU Y, RAO S H, LI C, et al. Calibration procedures for the CHASE/HIS science data[J]. *Science China Physics, Mechanics & Astronomy*, 2022, **65**: 289603
- [5] ZHANG W, CHENG W Q, YOU W, et al. Levitated-body ultra-high pointing accuracy and stability satellite platform of the CHASE mission[J]. *Science China Physics, Mechanics & Astronomy*, 2022, **65**: 289604
- [6] LIU Q, TAO H J, CHEN C Z, et al. On the technologies of Ha Imaging Spectrograph for the CHASE mission[J]. *Science China Physics, Mechanics & Astronomy*, 2022, **65**: 289605
- [7] ZHANG W, YANG Y, YOU W, et al. Autonomous navigation method and technology implementation of high-precision solar spectral velocity measurement[J]. *Science China Physics, Mechanics & Astronomy*, 2022, **65**: 289606
- [8] FANG C, CHEN P F, LI Z, et al. A new multi-wavelength solar telescope: optical and near-infrared solar eruption tracer (ONSET)[J]. *Research in Astronomy and Astrophysics*, 2013, **13**(12): 1509-1517
- [9] LIU Z, XU J, GU B Z, et al. New vacuum solar telescope and observations with high resolution[J]. *Research in Astronomy and Astrophysics*, 2014, **14**(6): 705-718
- [10] PÖTZI W, VERONIG A M, TEMMER M, et al. 70 years of sunspot observations at the Kanzelhöhe observatory: systematic study of parameters affecting the derivation of the relative sunspot number[J]. *Solar Physics*, 2016, **291**(9): 3103-3122
- [11] FANG Cheng, GU Bozhong, YUAN Xiangyan, et al. 2.5 m wide-field and high-resolution telescope[J]. *Scientia Sinica Physica, Mechanica & Astronomica*, 2019, **49**(5): 059603 (方成, 顾伯忠, 袁祥岩, 等. 2.5 m大视场高分辨率望远镜[J]. *中国科学: 物理学力学 天文学*, 2019, **49**(5): 059603)
- [12] ZHANG P, HU X Q, LU Q F, et al. FY-3E: the first operational meteorological satellite mission in an early morning orbit[J]. *Advances in Atmospheric Sciences*, 2022, **39**(1): 1-8
- [13] GAN W Q, ZHU C, DENG Y Y, et al. Advanced space-based solar observatory (ASO-S): an overview[J]. *Research in Astronomy and Astrophysics*, 2019, **19**(11): 156
- [14] CHEN P F. Chinese solar physics gliding into the space age[J]. *Science China Physics, Mechanics & Astronomy*, 2018, **61**(10): 109631
- [15] COX A N. *Allen's Astrophysical Quantities*[M]. New York: Springer, 1999

ZEREN Zhima, HUANG Jianping, LIU Dapeng, YANG Yanyan, YAN Rui, ZHAO Shufan, ZHANG Zhenxia, Lin Jian, Cui Jing, CHU Wei, WANG Qiao, LU Hengxin, XU Song, GUO Feng, Yang Dehe, ZHOU Na, Liu Qinqin, HUANG He, WANG Jie, TAN Qiao, LI Wenjing, LÜ Fangxian, Zhu Keying, SHEN Xuhui. Current Status and Main Scientific Out-comes of the CSES Mission. *Chinese Journal of Space Science*, 2022, 42(4). DOI:10.11728/cjss2022.04.yg06

Current Status and Main Scientific Outcomes of the CSES Mission

ZEREN Zhima, HUANG Jianping, LIU Dapeng, YANG Yanyan, YAN Rui, ZHAO Shufan, ZHANG Zhenxia, LIN Jian, CUI Jing, CHU Wei, WANG Qiao, LU Hengxin, XU Song, GUO Feng, YANG Dehe, ZHOU Na, LIU Qinqin, HUANG He, WANG Jie, TAN Qiao, LI Wenjing, LÜ Fangxian, ZHU Keying, SHEN Xuhui

National Institute of Natural Hazards, Ministry of Emergency Management, Beijing 100085

Abstract

This report briefly introduces the current status of the CSES (China Seismo-Electromagnetic Satellite) mission which includes one probe CSES 01 in-orbit (launched in February 2018), and the second probe CSES 02 (will be launched in 2023) under development. The CSES 01 has been steadily operating in orbit for over four years, providing abundant global geophysical field data, including the background geomagnetic field, the electromagnetic field and wave, the plasma (in-situ and profile data), and the energetic particles in the ionosphere. The CSES 01 platform and the scientific instruments generally perform well. The data validation and calibration are vital for CSES 01, for it aims to monitor earthquakes by extracting the very weak seismic precursors from a relatively disturbing space electromagnetic environment. For this purpose, we are paying specific efforts to validate data quality comprehensively. From the CSES 01 observations, we have obtained many scientific results on the ionosphere electromagnetic environment, the seismo-ionospheric disturbance phenomena, the space weather process, and the Lithosphere-Atmosphere-Ionosphere coupling mechanism.

Key words

CSES mission, Satellite platform, Scientific payloads, Data validation, Electromagnetic environment, Seismic-ionospheric disturbance, Space weather process

1 Introduction

It is widely accepted that the global geophysical field observations from satellites have significant application in natural disaster prevention and scientific research. Strong earthquakes are one of the most destructive natural hazards, claiming countless deaths and economic losses in human history. Promoting earthquake disaster preven-

tion and reduction capability is a common issue faced by all countries worldwide. Driven by the objective of earthquake disaster prevention and mitigation, China proposed a stereoscopic earthquake monitoring system from ground to space early in 2003 by launching a series of Low Earth Orbit (LEO) electromagnetism and gravity satellites in the following decades^[1]. This CSES mission is called the Zhangheng mission, named after the ancient

Chinese scientist Zhangheng who invented the world's first seismo-scope in the second century CE^[2]. The electromagnetism satellite mission is called Zhangheng-01 (or ZH-1), and the gravity satellite mission is called Zhangheng-02 (or ZH-2). The electromagnetism satellite mission, also known as the China Seismo- Electromagnetic Satellite (CSES 01 or ZH-1), already has one probe being launched in orbit on 2 February 2018, and the second one being approved in September 2018 and under development at present, the third one is under planning as a constellation around 2030. The gravity satellite mission is still under scientific demonstration discussion.

The scientific objectives of the ZH-1 mission are to obtain global observation on the background geomagnetic field, the electromagnetic field and waves, the in-situ and profile ionospheric plasma parameters, and the energetic particles; to monitor and study the ionospheric perturbations which could be associated with the natural hazards (such as seismic activities, volcano eruptions, the intense geomagnetic storms) or human activities (*e.g.*, the electric power transmission system, or the artificial VLF radio wave transmitters). Besides that, the ZH-1 mission also supports the research on geophysics, space science, and radio science by providing a data-sharing service for international cooperation and the scientific community.

On 2 February 2018, the first probe of the ZH-1 mission, which is also abbreviated as the ZH-1(01) or CSES 01, was launched successfully in orbit. CSES 01 is the first space-based platform in China for earthquake observation and geophysical field measurement, which was approved in 2013 after ten years of scientific and engineering demonstration. The second probe CSES 02 is under construction and will be launched around February 2023. The following sections will introduce the current status of CSES 01 and CSES 02 and some selected main scientific outcomes.

2 Current Status of CSES Mission

2.1 CSES 01

On 2 February 2018, the CSES 01 was launched into a sun-synchronous circular orbit at an altitude of 507 km in the topside ionosphere, and it has been steadily operating in space for over four years up to now. Among its scientific objectives, short-term earthquake prediction is listed as the top scientific goal. To serve the need for emergence response to disastrous earthquakes, such as the 2008 Mw 7.9 Wenchuan earthquake, CSES 01 is

designed to provide real-time data over China's territory by direct downlinking data to the ground segment.

To meet the scientific goals, CSES is designed to carry nine scientific payloads, including the High Precision Magnetometer (HPM) for the total magnetic field observations^[3-5]; the three-axis Search-Coil Magnetometer (SCM), and the Electric Field Detector (EFD) for the electromagnetic field detection at a broad frequency range from DC to HF^[6,7]; a Langmuir Probe (LAP) and Plasma Analyzer Package (PAP) for in-situ plasma parameters measurements^[8,9]; the High Energetic Particle Package (HEPP) and Italian Energetic Particle Detector (IEPD) for high energy particles^[10,11]; the GNSS Occultation Receiver (GOR) and Tri-Band Beacon (TBB) to measure electron density profiles^[12,13].

Up to now, the scientific instruments generally perform well, except for the PAP, EFD, and TBB, which have certain defects in different aspects^[14]. PAP was contaminated after four months in orbit, leading to lower absolute values than expected; further evaluation suggests that the relative values of ion densities can be used in scientific applications. EFD is heavily interfered with by the satellite-internal communication over the equatorial region and has a high noise level in the HF band. The middle frequency band (400 MHz) of TBB (which needs the ground-based receivers to realize the coherent beacon system) malfunctioned after launch, so the data quality of TBB is still under evaluation. We suggest extra caution when using PAP, EFD, and TBB for scientific research.

The CSES 01 flies 15.2 orbits around the global Earth per day at the local time around 02:00 am (night-side) and 02:00 pm (dayside), respectively. It has a 5-day revisiting period for the same area. The scientific data are packed into HDF (Hierarchical Data Format) with the descending (orbit path from north polar to south polar) and ascending (from south to north) half orbits data files, respectively. There are five levels of data in total based on the working principles of each payload, which are described as follows.

Level 0: The data is reconstructed after a series of preprocessing, including frame synchronization, de-randomization, decoding, and de-formatting of the raw telemetry data.

Level 1: The data obtained after the general error elimination, physical units convert, format conversion, *etc.* based on the Level-0 data.

Level 2: The calibrated physical values correspond to Level 1 data with orbit information after coordination system transformation and necessary data inversion.

Level 2A: Only EFD in the ULF band and GOR deliver the Level 2A data. For EFD, Level 2A is generated after eliminating the $V_s \times B$ effect in the ULF band, where V_s is the velocity of satellite, B is the geomagnetic field; For GOR data, it is the TEC values obtained after conversion with precision orbit determination information on Level 2.

Level 3: Time sequential data along satellite orbits generated after resampling, necessary spectral analysis based on Level 2 data.

Level 4: The global interpolation maps of physical values from Level 2 data.

CSES 01 has been in orbit over 22868 circles until 16 March 2022, producing over 300 TB of scientific data. The Level 2 data products that can be directly used for scientific applications are accessible via the website to the international scientific community*.

Within the past two years, we have achieved much progress in data processing, data validation, and scientific application.

In the field of data processing, one progress is that a wave vector analysis tool for the electromagnetic waves of the CSES was developed by Hu *et al.*^[15], which can provide the waveform spectrum transform, Singular Value Decomposition (SVD), and Poynting flux methods. According to the specific electromagnetic wave events, we validated the algorithm code by comparison with DEMETER's observations. We applied the tool to analyze the propagation feature of the waves, confirming that the CSES 01 has a good performance on the electromagnetic field observations. Qing *et al.*^[16] evaluated the CSES Precise Orbit Determination (POD) based on GPS and BDS observations. Results show that the CSES orbit consistency can reach up to 3 cm in 3D RMS, which can satisfy the centimeter-level requirements of the scientific application. See details in Ref.[15,16].

The data validation and calibration are vital for CSES 01, for it aims to monitor earthquakes by extracting the very weak seismic precursors from a relatively disturbing space electromagnetic environment. For this purpose, we are paying specific efforts to validate data quality comprehensively. For the electromagnetic field detection payloads, we cross-calibrated the consistency of HPM, EFD, and SCM in their overlapped detection

frequency range and firstly evaluated the timing system and the sampling time differences between EFD and SCM^[17]. A sampling time synchronization method was put forward for EFD and SCM waveform data. The consistency between FGM and SCM in the Ultra-Low-Frequency (ULF) range is validated by using the Magnetic Torque (MT) signal source as a reference. Yang *et al.*^[18] validated the HPM data through comparison with the Swarm satellite constellation, and the result demonstrates a good data quality of the HPM. Based on the data validation work, the potential magnetic field disturbances are flagged in the second version of HPM data. To the ionospheric plasma parameters, Yan *et al.*^[19] firstly discovered a Sudden Drop (SD) in the plasma potential (V_p) and floating potential (V_f) data and a Spike (SP) in the dayside V_p and V_f data. According to the analysis of I - V curves both inside and outside the SD and SP structures, we exclude the possibility of probe contamination and confirm that the scientific data of CSES LAP are reliable. These two regular features depend on the solar illumination conditions and the corresponding adjustment of the satellite-current system equilibrium. For data validation, see details in Ref.[17–19].

For the scientific application, the most important achievement is the CSES Global Geomagnetic Field Model (CGGM 2020.0), which was built at the end of 2019. The model is derived by solving a series of mathematical Spherical Harmonic (SH) Gauss coefficients. CGGM 2020.0 can provide a prediction of Earth's static main field up to SH degree and order 15 and a linear secular variation up to degree and order 8 with an expansion in 2nd order B-splines. This model is validated by the International Association of Geomagnetism and Aeronomy (IAGA) and finally has been selected as one of 15 international candidate models for calculation of the 13th generation International Geomagnetic Reference Field (IGRF-13)**. We have published the CGGM 2020.0 coefficient (in IGRF type) on the CSES scientific data sharing website***, and a CGGM 2020.0 Calculator is also provided to calculate magnetic field predictions in the given time and position. The corresponding papers were published in 2021; see details in Ref.[20, 21].

* <https://www.leos.ac.cn>

** <https://www.ngdc.noaa.gov/IAGA/vmod/igrf.html>

*** <https://leos.ac.cn/#/article/info/236>

Based on the CSES 01 observations, we have also progressed scientific research on the electromagnetic field environment, seismo-ionospheric disturbance phenomena, space weather, and Lithosphere-Atmosphere-Ionosphere coupling. Up to now, the incomplete statistics show that around 146 scientific papers have been published*. Some of the new scientific results of CSES 01 achieved since 2020 are introduced in the following Section 3.

2.2 CSES 02

The CSES 02 project was proved in April 2018 and was officially initiated in September 2018. As a successor of CSES 01, the CSES 02 is the first operational satellite of the ZH-1 mission, which will directly serve for routine natural hazards monitoring.

CSES 02 also will provide the same physical field parameters as the CSES 01; its scientific payloads are mostly inherited from the ones from the CSES 01 but with specific optimizations based on CSES 01's in-orbit performance. The payloads of CSES 02 include the High Precision Magnetometer (HPM02), Search Coil Magnetometer (SCM02), Electric Field Detector (EFD02), Langmuir Probe (LAP02), Plasma Analyzer Package (PAP02), Energetic Electron Spectrometer (EES, and HEPD02), GNSS Occultation Receiver (GOR02), Tri-Band Beacon Transmitter (TBB02), and Ionospheric Photometer (IPM). The IPM is newly added to improve the ionosphere and atmosphere tomography capability, and the EES is a substitution for the CSES 01's HEPP.

The platform of CSES 02 is remodeled upon the CAST2000, which offers a standard multi-mission platform at a very attractive cost. Technically, the platform

architecture is generic, and adaptations are limited to relatively minor changes in several electrical interfaces and software modules. The platform includes eight units: Data Transmission subsystem (DTs), structure and Mechanism Subsystem (SMs), Thermal Control subsystem (TCs), Attitude and Orbital Control subsystem (AOCs), Power Supply subsystem (PSs), Telemetry and Telecommand subsystem (TTCs), Onboard Data Handling subsystem (OBDHs) and scientific payloads. Some performance improvements of CSES-02 are also made based on CSES 01; the working area enlarges from 65 degrees north-south latitude to the whole globe. CSES 02 files together with CSES 01 in the same orbit space, with an orbital altitude of about 507 km and a high orbital inclination of 97.4°, the ascending node and descending node-Local Time (LT) is 02:00 and 14:00, respectively as shown in Fig. 1.

More in-depth international cooperation has been carried out in the CSES 02 project, especially between China and Italy. The Sino-Italy cooperation team is called the CSES-Limadou team which was built during the CSES 01 project on the energetic particle payload and corresponding scientific applications. Italy's CSES-LIMADOU team is led by the ASI (Italy Space Agency), and is composed of scientists and engineers from the INFN, INAF-IAPS, University of Trento, University of Rome Tor Vergata. The successful cooperation led to a very good foundation for the in-depth cooperation on CSES 02, which got approved by the two countries' leaders. In March 2019, China's President Xi Jinping visited Rome and witnessed the signing of the cooperation agreement on CSES 02 between CNSA (China National Space Agency) and ASI. In the CSES 02 project,

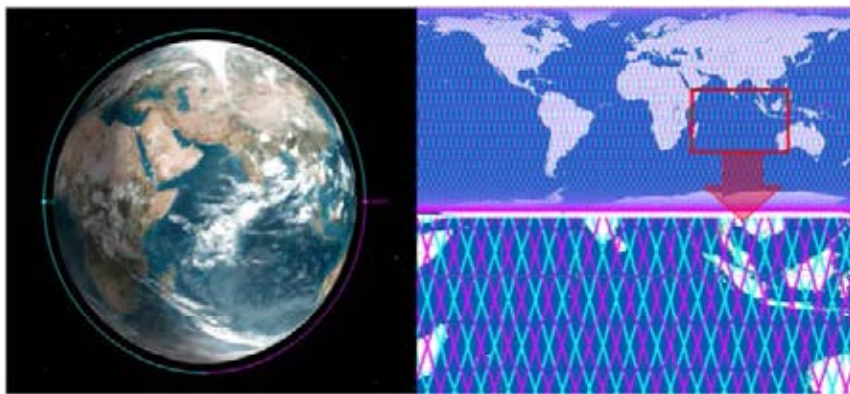


Fig. 1 Orbit design of CSES 01 and CSES 02, and their footprints on the ground

* <https://leos.ac.cn/#/scientificResearch/pathQBtbfcszmCmzTPdhipdnATjwMhJzcpb>

the Italy side is responsible for developing the Electric Field Detector (EFD02) and the High Energy Particle Detector (HEPD02). The outbreak of the COVID-19 pandemic caused a delay in the design and procurement of the Italy side. So the HEPD02 and EFD02 have been particularly affected by the worsening global shortage of semiconductors and raw materials. However, the Italy team is trying their best to minimize the impacts of this situation. The flight model of HEPD02 and EFD02 will be tested at acceptance levels, calibrated, and will be delivered to China by September 2022.

The developments of the satellite platform and Chinese scientific payloads are progressing smoothly. All of them are in the development stage of the flight model, which will be delivered by May 2022. Although the Italian side payloads EFD02 and HEPD02 are affected by the global COVID-19 pandemic, if they can be delivered by September 2022, it will not impact the scheduled launch time of CSES 02.

3 Selected Main Scientific Outcomes

3.1 Electromagnetic Environment Revealed by the CSES Mission

The ionosphere is a highly dynamic region because it is a coupling area between the Lithosphere, Atmosphere, the inner magnetosphere, and the solar wind. Especially in the high-latitude ionosphere, there are energetic particles precipitated from the radiation belts and a variety of intense electromagnetic emissions are excited. The most common and typical ELF/VLF whistler-mode waves in the high-latitude ionosphere include ionospheric hiss waves^[22,23], chorus waves (which occasionally appear)^[24,25], and quasiperiodic waves^[26,27]. Zhima *et al.*^[2] found the Quasiperiodic waves (QP) accompanied by simultaneous energetic electron precipitations in the high-latitude ionosphere from CSES 01 data, as shown in Fig. 2. The

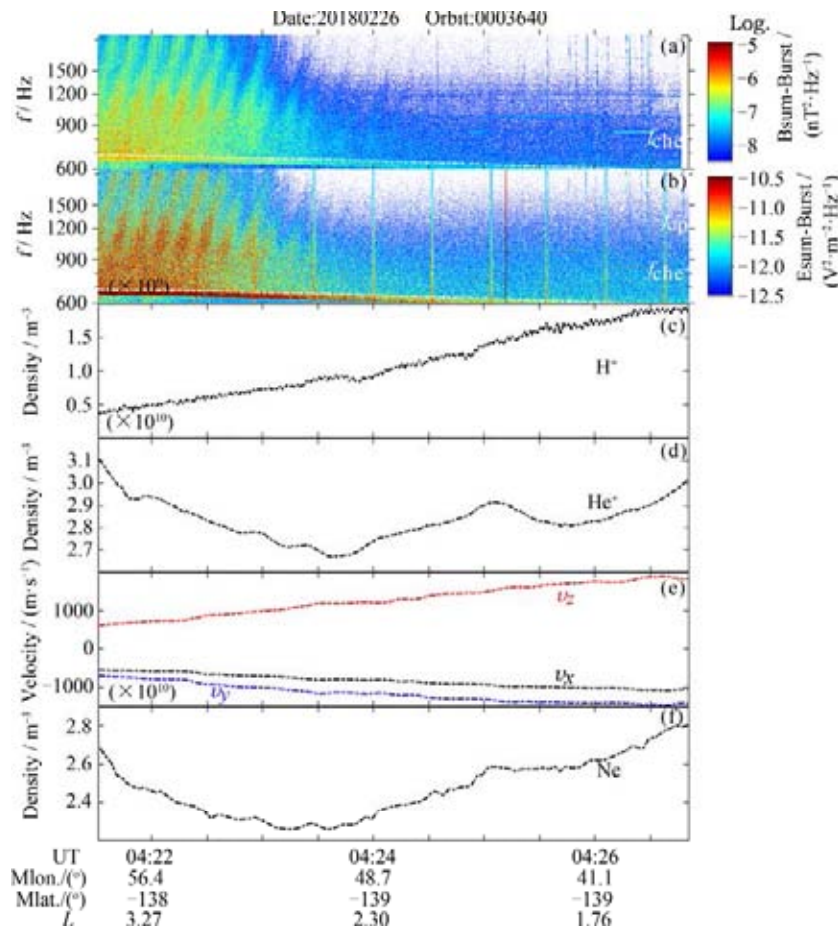


Fig. 2 ELF/VLF QP waves recorded by CSES satellite in the high-latitude upper ionosphere on 26 February 2018. (a)(b) Power spectral density values (PSD) of the magnetic field and the electric field. (c)(d) Density of H⁺ and He⁺. (e) Drifting velocity of ions. (f) the density of electron density. Data are displayed as a function of Universal Time (UT), geomagnetic longitude (mlon), geomagnetic latitude (mlat) and L shell, respectively

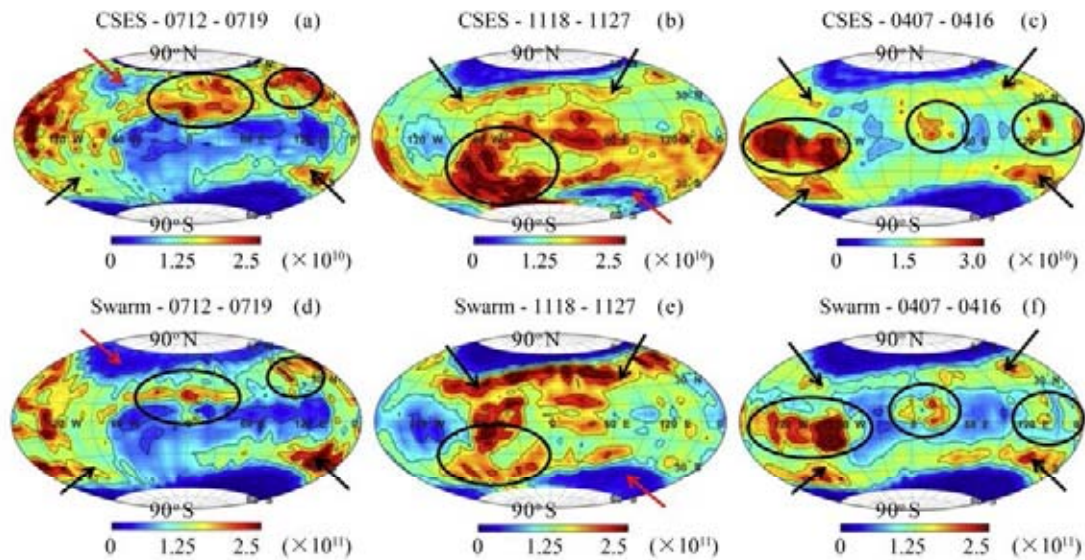


Fig. 3 Global distributions of N_e at 02:00 LT of CSES (up panels) and Swarm (bottom panels) under the quiet geomagnetic conditions. From left to right: N_e measurements during 12–19 July 2018, 18–27 November 2018, and 7–16 April 2019, corresponding to roughly at the summer solstice, winter solstice, and spring equinox, respectively. For CSES observations, N_e value range from 0 to 2.5×10^{10} or $3 \times 10^{10} \text{ m}^{-3}$, while for Swarm one, N_e is mainly from 0 to $2.5 \times 10^{11} \text{ m}^{-3}$

new features of QP waves observed by CSES 01 are the well-pronounced rising-tone structures and very short repetition periods that previous studies do not often report. The majority of QP waves appear at geomagnetic latitudes from 50° to 65° , and L shell from 3.5 to 4, mainly inside the plasmapause. The QP waves obliquely propagate towards decreasing L shell directions with right-handed polarization, with wave normal angles varying from 30° to 50° .

The global distribution of N_e/T_e derived from CSES was revealed by Yan *et al.*^[28]. Results show that the large-scale ionospheric structures, such as the Equatorial Ionization Anomaly (EIA), the longitudinal Wavenumber (WN3/4), the Weddell Sea Anomaly (WSA), the northern Midlatitude Summer Nighttime Anomaly (MSNA), and the midlatitude ionospheric trough, are well represented by the CSES measurements. For the global distribution of T_e at dayside, a clear ETA structure is found in the equatorial region, showing seasonal variations. A notable feature of T_e measured by CSES is the abnormal increases/decreases in the dayside/nightside T_e over the WSA region in winter, which is consistent with previous research. Fig. 3 shows the global distributions of N_e at 02:00 LT of CSES (up panels) and Swarm

(bottom panels) under the quiet geomagnetic conditions. We observed that the global distributions N_e with WSA and MSNA from CSES and Swarm are quite consistent during conjunction periods of the two satellite although the different absolute values of N_e .

More details about the electromagnetic field, the ionospheric plasma distribution can be found in Ref. [2,28].

3.2 Seismo-ionospheric Disturbances and LAIC Mechanism

Since the CSES launched on 2 February 2018, there are 38 strong shallow EQs (M 7⁺, depth shallower than 100 km) occurred worldwide* until December 2021, the epicenter distribution is shown in Fig. 4. The previous studies^[29–31] demonstrate that the seismo-ionospheric perturbation phenomena predominately appear during the shallow strong EQs, so we mainly focus on the strong EQs with a depth shallower than 30 km. The possible seismic ionospheric disturbances are listed in Table 1. Besides the single case studies, some statistical studies were also recently carried out using CSES data. For example, Zhu *et al.*^[32] statistically examined the about 2.5 years of N_e data from CSES during the M 4.8⁺

* <https://www.ceic.ac.cn/>

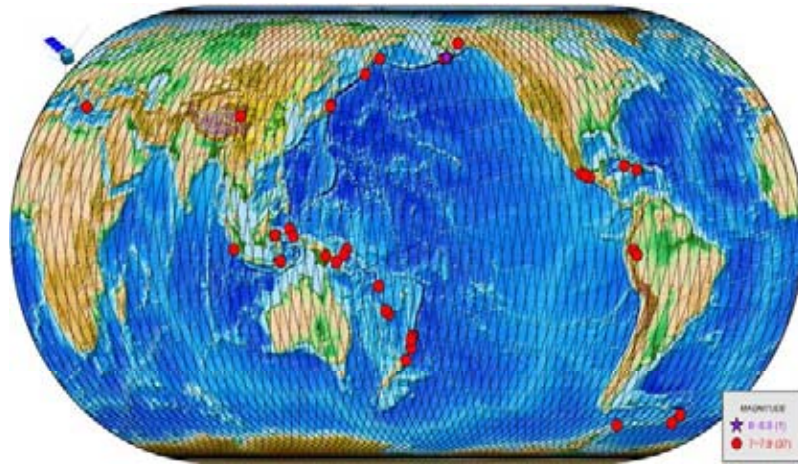


Fig. 4 Global earthquake activity occurred after the launch of CSES from February 2018 to 1 December 2021. The overlapped black lines are the orbit trajectories of the CSES

Table 1 Possible seismo-ionospheric disturbances recorded by the CSES during the shallow strong EQs

No.	Place	UTC	Latitude /($^{\circ}$)	Longitude /($^{\circ}$)	Magnitude /M	Depth /km	Possible seismo-ionospheric perturbation
1	Mexico	2018-02-16 23:39:38	16.6	-97.75	7.1	10	The abnormal emissions in frequency 155.5 Hz and 1.405 kHz The electron density and ion (O^+) density increased two days before the mainshock
2	Papua New Guinea	2018-02-25 17:44:42	-6.19	142.77	7.5	20	The magnetic field enhancement in the frequency 155 Hz nearest the epicenter 7 and 3 days before the mainshock. The electron/ion disturbed 7, 6, 5, and 2 days before mainshock
3	Loyalty Islands Region	2018-08-29 03:51:54	-21.95	170.1	7.1	20	The electron density increased; the PSD values of the electromagnetic field in ELF frequency increase; the energetic particle flux in the 0.1–3 MeV increased during the mainshock
4	Indonesia	2018-09-28 10:02:44	-0.25	119.9	7.4	10	The electron density significantly increased on 12 and 2 days before the mainshock.
5	Papua New Guinea	2018-10-10 20:48:18	-5.70	151.25	7.1	20	The abnormal emissions in ULF/ELF/VLF frequency 9 and 4 days before the mainshock The electron density, and energetic particle flux were disturbed 5, and 2 days before and on the mainshock day
6	Kmadek islands, New Zealand	2019-06-15 22:55:00	-30.80	-178.10	7.2	20	The in-situ and occultation electron density abnormally increased within one week before the mainshock
7	Southern waters of Cuba	2020-01-28 19:10:22	19.46	-78.79	7.7	10	The electron density increased over the conjugate area on January 27 and the epicenter area on January 28
8	Mexico	2020-06-23 15:29:04	16.14	-95.75	7.4	10	The electron density got disturbed 3 days before the mainshock.
9	Sumatra island, Indonesia	2020-08-18 22:29:21	-4.31	101.15	7.0	10	The electron density significantly increased 10 days before the mainshock
10	Maduo County, Qinghai, China	2021-05-21 18:04:11	34.59	98.34	7.4	17	The electron density, and the electromagnetic field in ULF/ELF band observed simultaneous increases 8 days before the mainshock. The energetic electron in the energy level 0.1 to 3 MeV increased 7 days and 6 days before the mainshock The electric field intensity in the VLF band increased one day before the mainshock
11	Near Alaska Peninsula	2021-07-29 06:15:46	55.40	-158.00	8.1	10	The abnormal ULF wave appeared on 10, 2 days before the mainshock The Infrared hyperspectral methane, OLR, aerosol, and other long-term observation data observed anomalies more than a month before the earthquake
12	South water of Alaska	2021-08-14 11:57:42	55.30	-157.75	7.0	10	The abnormal ULF emissions occurred on 12,4 days before and on the mainshock day
13	Haiti region	2021-08-14 12:29:07	18.35	-73.45	7.3	10	The electromagnetic field intensity in the ULF/ELF band increased on August 9, 8, 4 days, and one day before the mainshock. The energetic particle flux in 100 to 200 keV increased 4 and 3 days before the mainshock

EQs worldwide. The results show that the significant variations of ionospheric parameters related to earthquakes mainly occurred 1 to 7 days and 13 to 15 days before the earthquakes, respectively, and within 200 km from the epicenters.

The Lithosphere-Atmosphere-Ionosphere is a coupling system; the electromagnetic emissions, the chemistry gases emitted by the stressed rocks in the EQ preparation zones lead to the variation geophysical and geochemical field, thus directly impacting the ground-based instruments. The seismic signals also can couple into the atmosphere, breaking the chemical reaction balance there, leading to the formation of local electric currents, air ionization, atmospheric gas condensation, the plasma parameter irregularity^[33]. Therefore, besides CSES data, the CSES scientific application center also collects multi-source data. At present, the multi-source observations from infrared/hyperspectral remoting sensing satellites, the ground-based electromagnetic field instruments, the ionosondes, and the ground-based GNSS receivers can be collected at the first time to comparatively explore the seismic signals with the CSES data.

For example, Liu *et al.*^[34] applied a multi-parametric approach to climatological data before the Ms 8.0 2008 Wenchuan and Ms 7.0 2013 Lushan Earthquakes (EQs) to detect anomalous changes associated with the preparing phase of those large seismic events. The results show a chain of processes occurred within two months

before the EQs: AOD anomalous response is the earliest, followed by SKT, TCWV, and SLHF in the EQs. A close spatial relation between the seismogenic Long-Menshan Fault (LMSF) zone and the extent of the detected anomalies indicates that some changes occurred within the faults before the EQs, as shown in Fig. 5.

We also pay increasing effort to study the Lithosphere-Atmosphere-Ionosphere Coupling (LAIC) mechanisms. There are mainly three coupling mechanisms: electromagnetic wave, electric field, and geochemistry channel. Zhao *et al.*^[35] constructed a LAIC model for ELF Electromagnetic (EM) wave radiated from a current source in the Lithosphere. The simulated EM field at the altitude of the CSES is compared with the sensitivity of Electromagnetic (EM) sensors onboard the CSES. The results illustrate that an earthquake with a magnitude over 6.0 may be detected by the EM sensors of the CSES, as shown in Fig. 6. It is noted whether the anomaly can be detected depends on the focal depth, seismogenic environment, and ionospheric parameters.

The CSES magnetic data are helpful in the study of the lithospheric magnetic field signal caused by magnetized rocks in the crust and uppermost mantle. Wang *et al.*^[36] derived a lithospheric magnetic anomaly map over China and surrounding regions which is consistent with the lithospheric part of the CHAOS-7 model (Fig. 7). In particular, it reveals four major magnetic anomalies containing long-wavelength signals at the altitude of

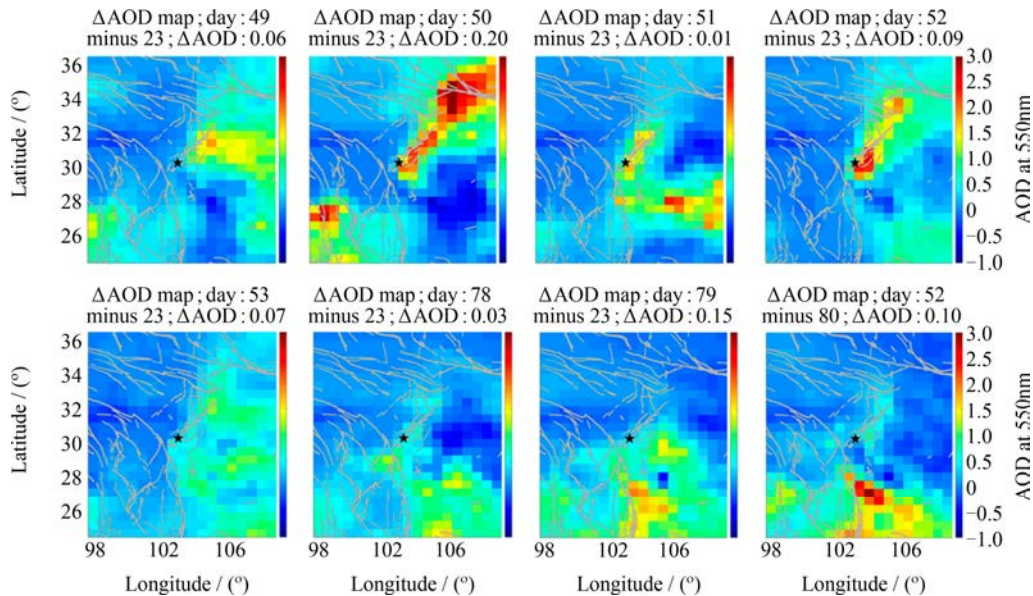


Fig. 5 MERRA-2 AOD at 18:00 UTC 2013 in the region of EQ epicenter (indicated by a star in the maps). Grey lines indicate main seismic faults in the research area; on the 49-53th, 78-80th days, respectively, with the value on 23th (20 February 2013) subtracted. Latitude (North) and longitude (East) are in degrees

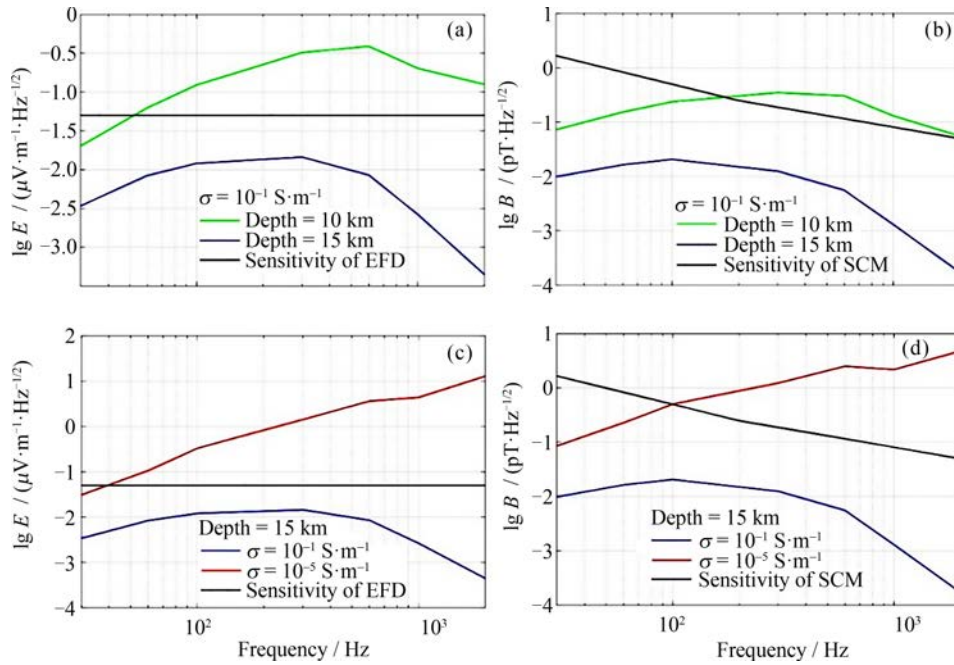


Fig. 6 (a)(b) is a comparison between a simulated EM field at CSES altitude from an M 6 earthquake with different source depths and sensitivity of CSES EM sensors (10 km, 15 km; lithospheric conductivity is 10^{-4} – $10^{-1} \text{ S}\cdot\text{m}^{-1}$); (c)(d) is comparison under different lithospheric conductivity and sensitivity of CSES EM sensors (source depth is 15 km; lithospheric conductivity is 10^{-4} – $10^{-5} \text{ S}\cdot\text{m}^{-1}$)

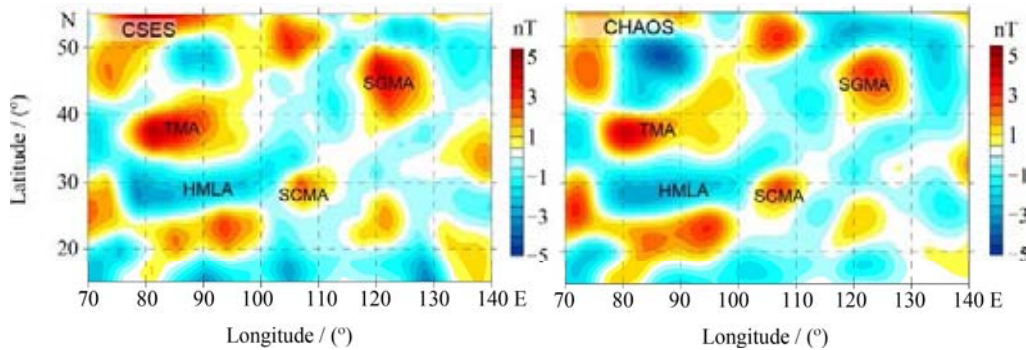


Fig. 7 Lithospheric magnetic anomaly map over China and surrounding regions at average 507 km altitude (a) derived from CSES data and (b) given by the CHAOS-7 model. Abbreviations: TMA, Tarim magnetic high anomaly; SCMA, Sichuan magnetic high anomaly; SGMA, Songliao-Greater Khingan magnetic high anomaly; HMLA, Himalayan-Tibetan magnetic low anomaly

Low-Earth-Orbiting satellites.

Based on previous studies and the CSES observations, we suggest that monitoring the short-term precursors from a stereoscopic system between the lithosphere-ionosphere is possible^[14]. However, it is admitted that it still has a long way to identify the seismo-ionospheric precursors from the electromagnetism satellites correctly. Due to the complexity of the EQ preparation mechanism and the limitation of observation technology and data analysis methods, there are many challenges, and we need a multidisciplinary perspective to explore this topic.

See more details about the seismic-ionospheric perturbations phenomenon and the LAIC mechanism revealed by CSES observations in Zhima *et al.*^[14], Zhu *et al.*^[32], Liu *et al.*^[34], Zhao *et al.*^[38,35], and Wang *et al.*^[36].

3.3 Space Weather Process

The high-quality measurements of the space environment by instruments onboard CSES provide us an opportunity to investigate the electromagnetic signal, ionospheric disturbance, and high energy particle acceleration and loss mechanisms during space weather events. In the four years of operation, certain numbers of geo-

magnetic storms occurred, and CSES's multi-type payloads show a very good response capability to the process of the space weather event.

Yang *et al.*^[39] investigated the multi-payload response to an intense storm event that started on 25 August 2018, with a minimum Dst of -176 nT. Fig. 8 presents dayside plasma and electric field observations from LAP, PAP, EFD, and GOR. The electron and oxygen density (temperature) are greatly enhanced (reduced) during the main and early recovery phases, indicating that this is a positive storm event. Further analysis reveals a simultaneous variation of electric field and plasma parameters, implying that electric field penetration quite probably is the cause of this positive storm. $N_m F_2$ is enhanced by a factor of about 2 during storm time, and the position of $h_m F_2$ moves upward by >100 km for the two selected events, which can again support the statement that electric field penetration should play an important role in this positive storm event.

Liu *et al.*^[40] detailedly reported the oxygen variation during this storm; the relative variation of the oxygen ion density (N_O^+) observed by the PAP appears consistent with the Dst index, showing a high negative correlation. The values of Dst index on August 24 and 25 are

higher than -30 nT, while the values of N_O^+ for orbit No. 3087_0 and 3102_0 orbits are low during this period. On August 26, as the Dst index rapidly drops to the lowest value, the N_O^+ for orbit No. 3117_0 orbit also increases to the maximum value. The Dst index gradually increases from 27 to 29 August, and the N_O^+ for the orbits No.3132_0, 3147_0, and 3163_0 orbits decrease accordingly. From August 30 to 31, the Dst index increased above -30 nT, and the N_O^+ for orbits No. 3178_0 and 3193_0 orbits continued to decrease. The above results indicate that the relative variation of N_O^+ well reflects the evolution processing of this positive geomagnetic storm event.

Zhang *et al.*^[41] found that, at extremely low L -shells ($L \approx 2$), a weak flux enhancement (increased by 2–3 times) of 100 s keV electrons and the corresponding formation of butterfly PADs appeared during the geomagnetic storm in August 2018. According to a numerical simulation of wave and particle interaction model, magnetosonic waves are thought to play an important role in electron acceleration and formation of butterfly PADs during this storm. During this storm, the chorus waves were proven to be able to play a significantly important role in diffusing and accelerating the

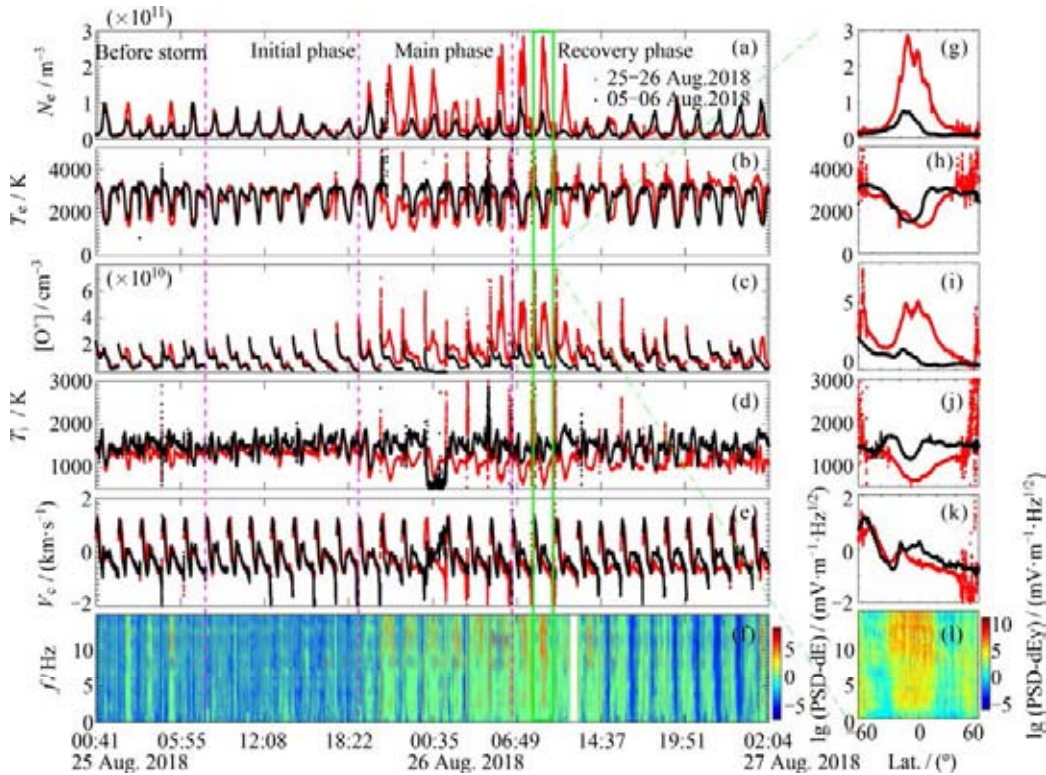


Fig. 8 Dayside plasma and electric field observations during 5–6 August (black curves) and 25–26 August (red curves)

1–3 MeV electrons even in extremely low L -shells ($L \approx 3$) during storms. The CSES's energetic particle data present that the loss mechanism of protons was energy dependence which is consistent with some previous studies. For protons at low energy 2–20 MeV, the fluxes were decreased during the storm's main phase and did not come back quickly during the recovery phase, which is likely to be caused by the Coulomb collision to neutral atmosphere density variation. At higher energy 30–100 MeV, it was confirmed that the magnetic field line curvature scattering plays a significant role in the proton loss phenomenon during this storm shown in (see Fig. 9). At the highest energies > 100 MeV, the fluxes of protons kept a stable level and did not exhibit a significant loss during this storm.

The temporal and spatial distributions of the ELF/

VLF wave activities and energetic particle precipitations in the ionosphere during the intense storm were reported by Zhima *et al.*^[42] based on the CSES's electromagnetic field observations. A good correlation of the ionospheric ELF/VLF wave activities with energetic particle precipitations during the various evolution phases of the geomagnetic storm is revealed by CSES (see Fig. 10). The ELF/VLF whistler-mode waves recorded by CSES mainly include structure-less VLF waves, structured VLF quasiperiodic emissions, structure-less ELF hiss waves, *etc.* Wave vector analysis shows that the ELF/VLF whistler-mode waves mostly likely from the radiation belt obliquely propagate Earthward during storm time. The results suggest that particles in high latitude ionosphere most likely precipitate from the outer radiation belt due to interactions with ELF/VLF waves which

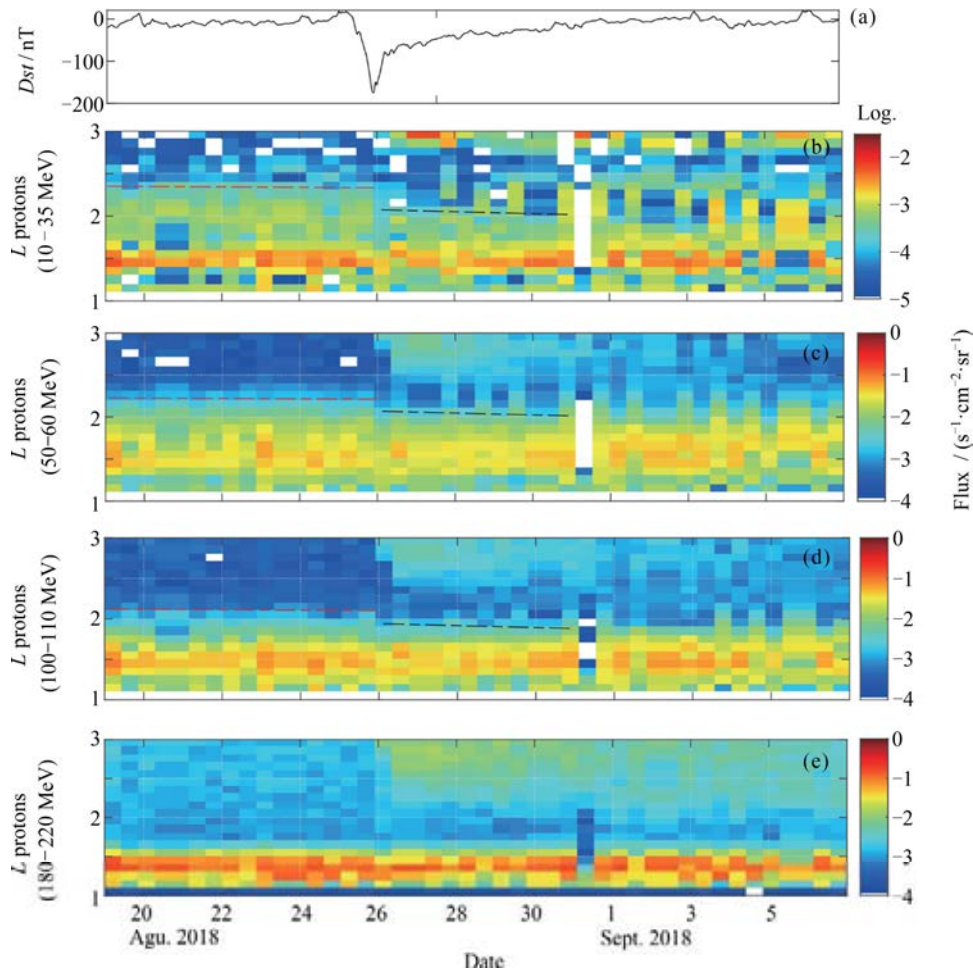


Fig. 9 Proton evolution during the large magnetic storm of August 2018 observed by HEPP-H onboard CSES satellite. The outer boundary of the inner radiation belt are denoted by red dotted lines before 26 August (quiet time) and black dotted lines after August 26 (storm time). The flux enhancement within the region of $L > 2.5$ appearing from August 26 could come from the high-energy electron contamination

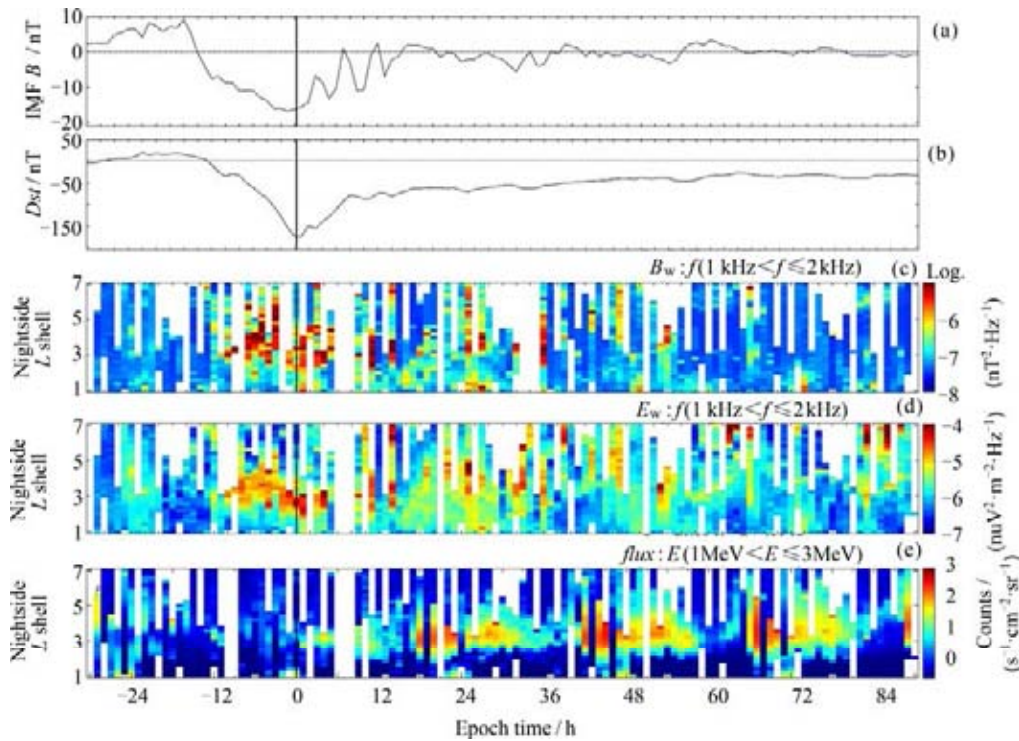


Fig. 10 Variation of ionospheric wave intensity and energetic flux during the geomagnetic storm occurred in 2018

are generated by strong temperature anisotropy after injection of energetic particle injections by the solar wind.

The CSES's good performance on the observation of the space weather event allows us to provide the estimates of the Dst index on the CSES orbit-by-orbit basis and define it as the CSES- Dst index. Fig. 11 presents a CSES (in red) and Swarm Alpha (in blue) based Dst index from 1–31 August 2018, together with the ground-based determined Dst -index (in black). It is seen that the CSES and Swarm-based Dst indexes well capture the main variations in the ground-based determined Dst index. It should be noted that the offset of 10 to 20 nT is expected since the ground-determined Dst index is relative to an unknown offset, while the satellite determined value has the correct offset. As described in Yang *et al.*^[18], using CSES CDSM and FGM data, we can also derive the storm time variation for ionosphere current systems, such as Sq, eastward Equatorial Electrojets (EEJs), Counter Equatorial Electrojet (CEJs), Field Aligned Currents (FACs).

More details about the CSES's performance on the space weather event observations can be found in the works of Yang *et al.*^[18,39], and Liu *et al.*^[40], Zhang *et al.*^[41], and Zhima *et al.*^[2,42].

4 Conclusions

Since the launch of CSES 01 in February 2018, the CSES 01 has been steadily operating in orbit for over four years, acquiring much global geophysical field data. Up to now, the CSES 01 platform and the scientific instruments generally perform well, except for certain payloads that have certain defects. CSES 01 has been in orbit over 22868 circles until 16 March 2022, producing over 300TB of scientific data. The Level 2 data products are accessible via the website to the international scientific community*. We are paying great efforts to produce high-quality data.

In the electromagnetic environment, the quasiperiodic waves accompanied by simultaneous energetic electron precipitations in the high-latitude ionosphere are recorded by CSES 01. The new features of QP waves observed by CSES are the well-pronounced rising-tone structures and very short repetition periods that previous studies do not often report. CSES well depicts the large-scale ionospheric structures, such as the Equatorial Ionization Anomaly (EIA), the longitudinal wavenumber (WN3/4), *etc.*

* <https://www.leos.ac.cn/>

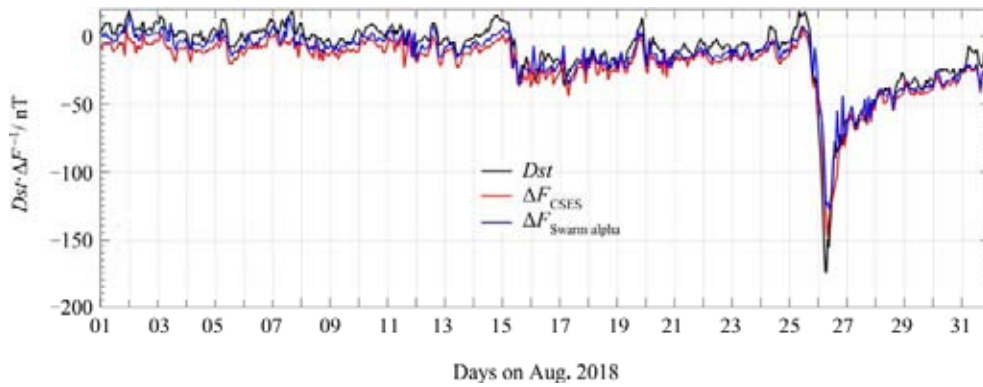


Fig. 11 *Dst* index determined by ground observatory data (black) and the satellite-derived equivalent from CSES (red) and Swarm Alpha (blue) magnetic data between 1 and 31 August 2018

There are 38 strong shallow EQs ($M 7^+$, depth shallower than 100 km) worldwide from CSES 01's launch to December 2021; pieces of evidence of the possible seismic ionospheric disturbances are accumulating. Besides CSES data, the CSES scientific application center also collects multi-source observations from infrared/hyperspectral remote sensing satellites, the ground-based electromagnetic field instruments, the ionosondes, and the ground-based GNSS receivers to comparatively explore the seismic signals with the CSES data. For the seismic-ionospheric disturbance mechanism, we constructed a LAIC model for ELF electromagnetic wave propagation from the Lithosphere, and the simulation shows that CSES can sense the electromagnetic waves radiated by an earthquake with a magnitude over 6.0.

In the four years of operation, CSES's multi-type payloads show a very good response capability to the process of the space weather event. The temporal and spatial distributions of the ELF/VLF wave activities and energetic particle precipitations in the ionosphere during the intense storm are well depicted by CSES 01. One important discovery is that CSES 01 captured a weak flux enhancement (increased by 2–3 times) of 100s keV electrons, and the corresponding formation of butterfly PADs appeared during the geomagnetic storm in August 2018.

Acknowledgments

We acknowledge the CSES scientific mission which was funded by China National Space Administration (CNSA) and China Earthquake Administration (CEA), the data in this study can be downloaded from the website <https://www.leos.ac.cn/>.

Reference

- [1] SHEN X H, ZHANG X M, YUAN S G, *et al.* The state-of-the-art of the China Seismo-Electromagnetic Satellite mission[J]. *Science China Technological Sciences*, 2018, **61**(5): 634-642
- [2] ZHIMA Z, HUANG J P, SHEN X H, *et al.* Simultaneous observations of ELF/VLF rising-tone quasiperiodic waves and energetic electron precipitations in the high-latitude upper ionosphere[J]. *Journal of Geophysical Research: Space Physics*, 2020, **125**(5): e2019JA027574
- [3] CHENG B J, ZHOU B, MAGNES W, *et al.* High precision magnetometer for geomagnetic exploration onboard of the China Seismo-Electromagnetic Satellite[J]. *Science China Technological Sciences*, 2018, **61**(5): 659-668
- [4] ZHOU B, YANG Y Y, ZHANG Y T, *et al.* Magnetic field data processing methods of the China Seismo-Electromagnetic Satellite[J]. *Earth and Planetary Physics*, 2018, **2**(6): 455-461
- [5] POLLINGER A, LAMMEGGER R, MAGNES W, *et al.* Coupled dark state magnetometer for the China Seismo-Electromagnetic Satellite[J]. *Measurement Science and Technology*, 2018, **29**(9): 095103
- [6] CAO J B, ZENG L, ZHAN F, *et al.* The electromagnetic wave experiment for CSES mission: search coil magnetometer[J]. *Science China Technological Sciences*, 2018, **61**(5): 653-658
- [7] HUANG J P, SHEN X H, ZHANG X M, *et al.* Application system and data description of the China Seismo-Electromagnetic Satellite[J]. *Earth and Planetary Physics*, 2018, **2**(6): 444-454
- [8] YAN R, GUAN Y B, SHEN X H, *et al.* The Langmuir Probe onboard CSES: data inversion analysis method and first results[J]. *Earth and Planetary Physics*, 2018, **2**(6): 479-488
- [9] LIU C, GUAN Y B, ZHENG X Z, *et al.* The technology of space plasma *in-situ* measurement on the China Seismo-Electromagnetic Satellite[J]. *Science China Technological Sciences*, 2019, **62**(5): 829-838
- [10] CHU W, HUANG J P, SHEN X H, *et al.* Preliminary results of the high energetic particle package on-board the China seismo-electromagnetic satellite[J]. *Earth and Planetary Physics*, 2018, **2**(6): 489-498
- [11] LI X Q, XU Y B, AN Z H, *et al.* The high-energy particle package onboard CSES[J]. *Radiation Detection Technology and Methods*,

- 2019, **3**(3): 22
- [12] LIN J, SHEN X H, HU L C, *et al.* CSES GNSS ionospheric inversion technique, validation and error analysis[J]. *Science China Technological Sciences*, 2018, **61**(5): 669-677
- [13] CHEN L, OU M, YUAN Y P, *et al.* Preliminary observation results of the Coherent Beacon System onboard the China Seismo-Electromagnetic Satellite-1[J]. *Earth and Planetary Physics*, 2018, **2**(6): 505-514
- [14] ZHIMA Z, YAN R, LIN J, *et al.* The possible seismo-ionospheric perturbations recorded by the China-seismo-electromagnetic satellite[J]. *Remote Sensing*, 2022, **14**(4): 905
- [15] HU Yunpeng, ZHIMA Zeren, HUANG Jianping, *et al.* Algorithms and implementation of wave vector analysis tool for the electromagnetic waves recorded by the CSES satellite[J]. *Chinese Journal of Geophysics*, 2020, **63**(5): 1751-1765
- [16] QING Y, LIN J, LIU Y, *et al.* Precise orbit determination of the China seismo-electromagnetic satellite (CSES) using onboard GPS and BDS observations[J]. *Remote Sensing*, 2020, **12**(19): 3234
- [17] ZHIMA Z, ZHOU B, ZHAO S F, *et al.* Cross-calibration on the electromagnetic field detection payloads of the China Seismo-Electromagnetic Satellite[J]. *Science China Technological Sciences*, 2022, **65**(6): 1415-1426
- [18] YANG Y Y, ZHOU B, HULOT G, *et al.* CSES high precision magnetometer data products and example study of an intense geomagnetic storm[J]. *Journal of Geophysical Research: Space Physics*, 2021, **126**(4): e2020JA028026
- [19] YAN R, GUAN Y B, MIAO Y Q, *et al.* The regular features recorded by the Langmuir probe onboard the low earth polar orbit satellite CSES[J]. *Journal of Geophysical Research: Space Physics*, 2022, **127**(1): e2021JA029289
- [20] YANG Y Y, HULOT G, VIGNERON P, *et al.* The CSES global geomagnetic field model (CGGM): an IGRF-type global geomagnetic field model based on data from the China Seismo-Electromagnetic Satellite[J]. *Earth, Planets and Space*, 2021, **73**(1): 45
- [21] ALKEN P, THÉBAULT E, BEGGAN C D, *et al.* International geomagnetic reference field: the thirteenth generation[J]. *Earth, Planets and Space*, 2021, **73**(1): 49
- [22] CHEN L J, SANTOLÍK O, HAJOŠ M, *et al.* Source of the low-altitude hiss in the ionosphere[J]. *Geophysical Research Letters*, 2017, **44**(5): 2060-2069
- [23] ZHIMA Z, CHEN L J, XIONG Y, *et al.* On the origin of ionospheric hiss: a conjugate observation[J]. *Journal of Geophysical Research: Space Physics*, 2017, **122**(11): 11784-11793
- [24] PARROT M, SANTOLÍK O, NĚMEC F. Chorus and chorus-like emissions seen by the ionospheric satellite DEMETER[J]. *Journal of Geophysical Research: Space Physics*, 2016, **121**(4): 3781-3792
- [25] ZHIMA Z, CAO J B, LIU W L, *et al.* DEMETER observations of high-latitude chorus waves penetrating the plasmasphere during a geomagnetic storm[J]. *Geophysical Research Letters*, 2013, **40**(22): 5827-5832
- [26] HAYOSH M, NĚMEC F, SANTOLÍK O, *et al.* Propagation properties of quasiperiodic VLF emissions observed by the DEMETER spacecraft[J]. *Geophysical Research Letters*, 2016, **43**(3): 1007-1014
- [27] NĚMEC F, BEZDĚKOVÁ B, MANNINEN J, *et al.* Conjugate observations of a remarkable quasiperiodic event by the low-altitude DEMETER spacecraft and ground-based instruments[J]. *Journal of Geophysical Research: Space Physics*, 2016, **121**(9): 8790-8803
- [28] YAN R, ZHIMA Z, XIONG C, *et al.* Comparison of electron density and temperature from the CSES satellite with other space-borne and ground-based observations[J]. *Journal of Geophysical Research: Space Physics*, 2020, **125**(10): e2019JA027747
- [29] NĚMEC F, SANTOLÍK O, PARROT M. Decrease of intensity of ELF/VLF waves observed in the upper ionosphere close to earthquakes: a statistical study[J]. *Journal of Geophysical Research: Space Physics*, 2009, **114**(A4): A04303
- [30] PARROT M, BERTHELIER J J, LEBRETON J P, *et al.* Examples of unusual ionospheric observations made by the DEMETER satellite over seismic regions[J]. *Physics and Chemistry of the Earth, Parts A/B/C*, 2006, **31**(4/5/6/7/8/9): 486-495
- [31] PULINETS S, OUZOUNOV D. Lithosphere-atmosphere-ionosphere coupling (LAIC) model – An unified concept for earthquake precursors validation[J]. *Journal of Asian Earth Sciences*, 2011, **41**(4/5): 371-382
- [32] ZHU K Y, ZHENG L, YAN R, *et al.* The variations of electron density and temperature related to seismic activities observed by CSES[J]. *Natural Hazards Research*, 2021, **1**(2): 88-94
- [33] PULINETS S, OUZOUNOV D. The Possibility of Earthquake Forecasting: Learning from Nature[M]. IOPscience, 2018. DOI:10.1088/978-0-7503-1248-6 Corpus ID: 133839066
- [34] LIU Q Q, DE SANTIS A, PISCINI A, *et al.* Multi-parametric climatological analysis reveals the involvement of fluids in the preparation phase of the 2008 Ms 8.0 Wenchuan and 2013 Ms 7.0 Lushan earthquakes[J]. *Remote Sensing*, 2020, **12**(10): 1663
- [35] ZHAO S F, SHEN X H, LIAO L, *et al.* A lithosphere-atmosphere-ionosphere coupling model for ELF electromagnetic waves radiated from seismic sources and its possibility observed by the CSES[J]. *Science China Technological Sciences*, 2021, **64**(11): 2551-2559
- [36] WANG J, SHEN X H, YANG Y Y, *et al.* Initial scalar lithospheric magnetic anomaly map of China and surrounding regions derived from CSES satellite data[J]. *Science China Technological Sciences*, 2021, **64**(5): 1118-1126
- [37] ZHAO S F, SHEN X H, ZHOU C, *et al.* The influence of the ionospheric disturbance on the ground based VLF transmitter signal recorded by LEO satellite—Insight from full wave simulation[J]. *Results in Physics*, 2020, **19**: 103391
- [38] YANG Y Y, ZHIMA Z R, SHEN X H, *et al.* The first intense geomagnetic storm event recorded by the China seismo-electromagnetic satellite[J]. *Space Weather*, 2020, **18**(1): e2019SW002243
- [39] LIU D P, ZEREN Z, SHEN X H, *et al.* Typical ionospheric disturbances revealed by the plasma analyzer package onboard the China Seismo-Electromagnetic Satellite[J]. *Advances in Space Research*, 2021, **68**(9): 3796-3805
- [40] ZHANG Z, CHEN L, LIU S, *et al.* Chorus acceleration of relativistic electrons in extremely low L-shell during geomagnetic storm of August 2018[J]. *Geophysical Research Letters*, 2020, **47**(4): e2019GL086226
- [41] ZHIMA Z, HU Y P, SHEN X H, *et al.* Storm-time features of the ionospheric ELF/VLF waves and energetic electron fluxes revealed by the China seismo-electromagnetic satellite[J]. *Applied Sciences*, 2021, **11**(6): 2617

Part III: Mission Progress

Status Update of the Einstein Probe Mission

YUAN Weimin, BAO Congying (On behalf of the Einstein Probe team)

National Astronomical Observatories, Chinese Academy of Sciences, Beijing 100012

Abstract

The Einstein Probe (EP) is a mission dedicated to time-domain astronomy to monitor the sky in the soft X-ray band, led by the Chinese Academy of Sciences with participation from ESA and MPE. Its wide-field imaging capability is achieved by using established technology of the micro-pore lobster-eye X-ray focusing optics. Complementary to this is deep X-ray follow-up capability enabled by a Wolter-I type X-ray telescope. EP is also capable of fast transient alerts triggering and downlink, aiming at multi-wavelength follow-up observations by the worldwide community. EP will enable systematic survey and characterization of high-energy transients with unprecedented sensitivity, spatial resolution, grasp, and monitoring cadence. Its scientific goals are mainly concerned with discovering new or rare types of transients, including tidal disruption events, supernova shock breakouts, high-redshift GRBs, and electromagnetic sources of gravitational wave events. EP is currently in Phase D (flight model phase) and is aimed for launch by the end of 2023.

Key words

X-ray all-sky monitor, Time-domain astronomy, High-energy astrophysics, X-ray transients

1 Mission Overview

The Einstein Probe (EP) is a mission of the Chinese Academy of Sciences (CAS) dedicated to time-domain high-energy astrophysics. Its primary goals are to discover high-energy transients and monitor variable objects. To achieve this, EP employs a very large instantaneous field-of-view (3600 square degrees), along with moderate spatial resolution (FWHM about 5 arcmin) and energy resolution. Its wide-field imaging capability is achieved by using established technology of novel lobster-eye optics, thereby offering unprecedentedly high sensitivity and large grasp, which would supersede previous and existing X-ray all-sky monitors. To complement this powerful capability to discover and monitor sources over a wide area, EP also carries a conventional X-ray focusing telescope with a larger effective area to perform follow-up characterization and precise

localization of newly-discovered transients. Public transient alerts will be issued rapidly to trigger multi-wavelength follow-up observations from the worldwide community. The satellite (see Fig. 1) has a weight of about 1400 kg and average power of about 825 W in total. In the normal survey mode, during one orbit of 97 minutes, three fields will be observed on the night-side of the sky with about 20 min each. Over three orbits almost the entire night sky will be sampled, with cadences ranging from several to a few ten revisits per day depending on the field location. The mission is aimed for launch by the end of 2023 with a nominal lifetime of 3 years (5 years as a goal).

The primary science objectives are: (i) Discover and characterize cosmic X-ray transients, particularly faint, distant and rare X-ray transients, in large numbers; (ii) discover and characterize X-ray outbursts from otherwise normally dormant black holes; (iii) search for



Fig. 1 Layout of the Einstein Probe spacecraft and scientific payloads, which include 12 modules of WXT aligned to mosaic the total 3600 square degrees field of view and 2 coaligned modules of FXT (credit: IMAC/CAS)

X-ray sources associated with gravitational-wave events and precisely locate them. These populations of cosmic high-energy transients will be characterized over a wide time scale and at high cadences, revealing new insights into a diverse set of systems including dormant black holes, neutron stars, supernova shock breakouts, active galactic nuclei, X-ray binaries, gamma-ray bursts, stellar coronal activity, and electromagnetic-wave sources and gravitational-wave events. Meanwhile, EP will also monitor the variability of various types of X-ray sources in large samples all over the sky. In light of the multi-messenger and multi-wavelength all-sky monitoring capability highly anticipated in the next decade, EP will produce a legacy data set in the X-ray band that is key to characterizing and understanding the nature of cosmic transients and variables, by working in synergy with the sky surveys by other facilities.

The mission will address some of the key questions in astrophysics and cosmology, and details of the physics that operates in extreme conditions of strong gravity. These include the prevalence of massive black holes in the Universe and how they formed and evolved; how black holes accrete mass and launch jets; the astrophysical origins and underlying processes of gravitational wave events; the progenitors and processes of supernovae; when and where did the first stars form in the early Universe and how they re-ionize the Universe. Fig. 2 showed the artist's impression of a stellar tidal disruption event by a massive black hole.

2 Background

The Einstein Probe is a mission managed by CAS in its Strategic Pilot Program for Space Science (2nd phase). The mission concept was proposed by scientists at the

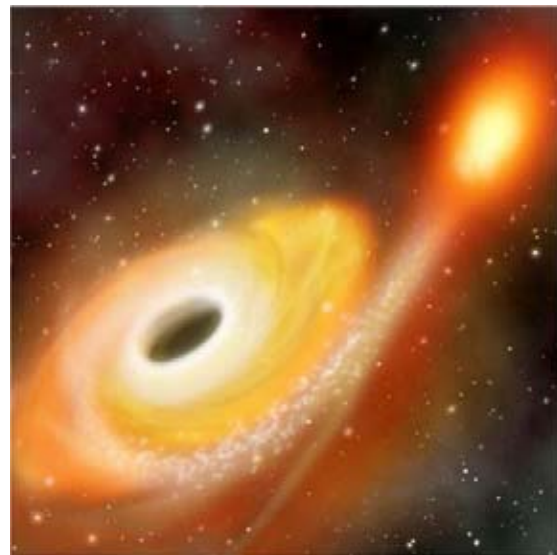


Fig. 2 Artist's impression of a stellar tidal disruption event by a massive black hole (credit: NASA)

National Astronomical Observatories of China (NAOC), in collaboration with scientists at the Institute of High-Energy Physics (IHEP) in 2013. The proposed mission was based on the progress of the lobster-eye micro-pore optics X-ray focusing technology developed at NAOC, CAS. In 2013 EP was selected and an “Advanced Study” program, funded by CAS, was carried out from January 2014 to May 2016 to develop and demonstrate the key technologies adopted and to study the science case.

The project was formally adopted at the end of 2017 by the CAS, and at the same time, the engineering implementation phase has initiated. The project passed the mission-level phase B conclusion review at the end of 2019, at which the base-line design of the payloads and the satellite had been achieved.

3 EP Mission Progress in Phase C

The EP satellite PDR (Preliminary Design Review) meeting was held on 28 April 2020, marking the official kicking-off of phase C of the project (see Fig. 3). The main tasks in Phase C include development of the Qualification Models (QM) of the payloads, the spacecraft and satellite AIT, as well as various tests and calibrations. Since the start of Phase C, tremendous progress has been made. The EP satellite qualification model was built, including the WXT QM and the FXT QM. A series of satellite-level tests (*e.g.*, thermal, mechanical, and EMC) were completed at IMAC, in

Shanghai. Calibration tests for the WXT and FXT QMs were performed at the IHEP 100 m X-ray beamline test facility. The calibration results confirmed that both the WXT QM and the FXT QM meet the performance requirements for EP science. Selected key project progress made in phase C is reported briefly below.

3.1 WXT QM Calibration

There are three WXT QMs built during phase C. In order to demonstrate the instrument performance, the WXT team conducted a series of calibration tests on the three WXT QMs (namely, QM2/QM5/QM4). The test and preliminary calibration of the first complete WXT QM module (QM2) started at the IHEP 100 m beamline facility on 18 June 2021 (see Fig. 4). The first light of WXT was obtained immediately, which was the first X-ray image achieved by a wide-field X-ray telescope with FoV over hundreds of degrees on the ground, as far as we are aware of (shown in Fig. 5). The WXT team completed detector mounting, optical alignment, thermal implementation, and overall integration of QM5 by



Fig. 3 Satellite PDR meeting held on 28 April 2020 (credit: NSSC, CAS).

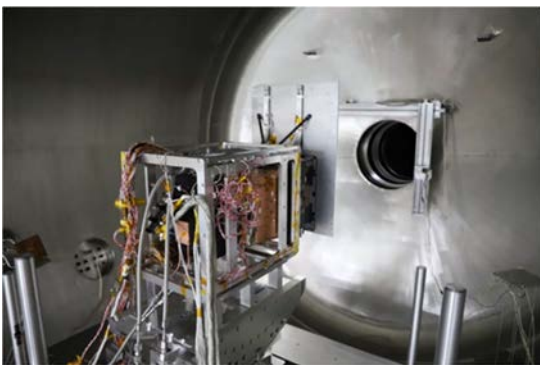


Fig. 4 WXT QM2 at test inside the 100 m beamline chamber at IHEP (credit: NAOC)

20 June 2021. Afterward, the test of QM5 was carried out at XIB (X-ray Imaging Beamline) at NAOC, CAS. An independent test for QM4 was carried out at Panter, MPE in Germany by the ESA/Leicester/MPE team in April 2021. After shipping back to China, the same module was tested again by the NAOC team at the IHEP 100m beamline facility.

Following the calibration for WXT-QM4, the WXT team completed most of the analysis of the calibration data. The calibration results show that the WXT QM meets the EP science requirements (see Fig. 6).

The principal goals of the tests were: (i) to demonstrate the WXT performance, which included PSF, effective area, location accuracy; and (ii) to optimize the calibration strategy for the WXT flight model. Both of these goals were accomplished in the calibration campaigns.

3.2 Development of the FXT QM

The development of FXT is led by an IHEP team with the participation of ESA and MPE *via* the provision of Mirror Modules and pnCCD detector modules. As an international collaborative effort, the development of FXT suffered from the impact of the Covid-19 pandemic. The mirror assembly was built at Media Lario in Milan, Italy, where the pandemic was rather severe. Nevertheless, the CAS and Europe teams and the contractor have made substantial efforts to ensure that the devices and instruments are delivered and tested in time.

The FXT Mirror Module Structural and Thermal Model (STM) was delivered to IHEP in July 2020. Following several months of mirror assembly, the IHEP team obtained the first light from the STM MM (see Fig. 7). MPE delivered pnCCD EM to IHEP in October

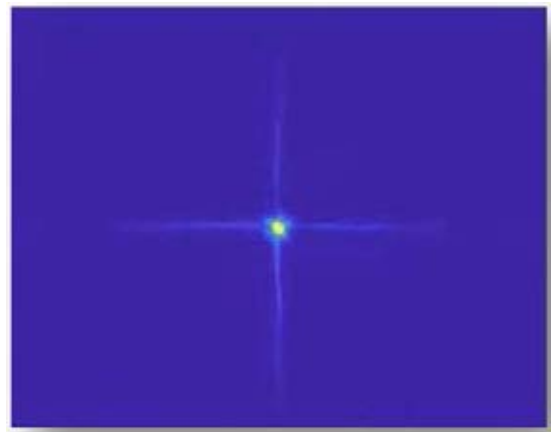


Fig. 5 First light of WXT (credit: NAOC)

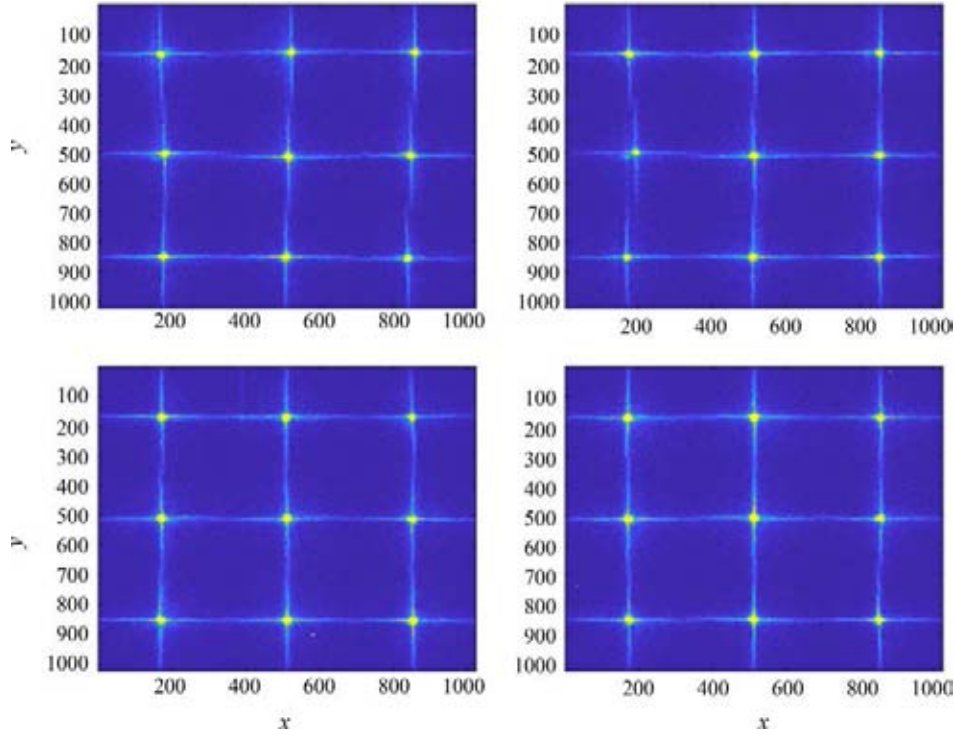


Fig. 6 Combined images of PSF scans at the Si Ka line energy over 4 sections for the QM4 module (credit: NAOC)

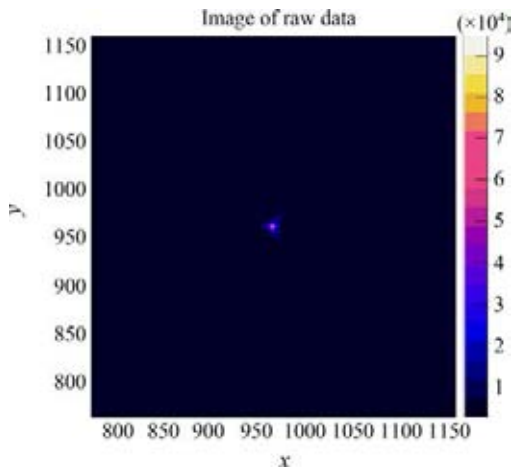


Fig. 7 First light image from the EP-FXT STM MM obtained at the Al-K energy of 1.49 keV, for all shells (credit: IHEP)



Fig. 8 FXT coated with multiple layers (credit: IHEP, CAS)

2020. As FXT QM (including QM pnCCD and STM MA) integration was completed, the FXT telescope was shipped to IMAC for satellite-level integration and tests in June 2021.

In general, FXT performed well during the satellite-level integration tests, including thermal, mechanical, and EMC tests. Fig. 8 showed the FXT coated with multiple layers. The FXT model (the STM MA incorporated with QM pnCCD) worked normally under all

working conditions of the thermal test. The reliability of the satellite structure design and the electromagnetic design was verified respectively during the mechanical test and the EMC test.

	requirement	goal	QM result	satisfaction
FOV	Diameter $\geq 38'$	-	1"	goal
Source upper limit	-	Image mode: ≥ 200 mCrab	200 mCrab	goal
		Timing mode: ≥ 5 Crab	10 Crab	goal
Eff area	$\geq 100\text{cm}^2@1.25$ keV, on axis	$\geq 600\text{cm}^2@1.25$ keV, on axis	STM 6 shells: 41.9cm^2 , (FMI: 332cm^2)	goal
Angular resolution	$\leq 2'$ HPD	$\leq 30''$, HPD	STM 6 shells: $30'' / 27.4''$	goal
Energy resolution	FWHM ≤ 170 eV@1.25 keV(Mg)	FWHM ≤ 120 eV@1.25 keV(Mg)	96.4eV@1.25 keV	goal
Energy range	0.5–8.0 keV	0.3–10.0 keV	0.2–13 keV	goal
Source location error	$< 20''$ (detector coordinate) 90% confidence level	$< 4''$ (detector coordinate) 68% confidence level	simulation, $11.8''$ (3 σ), $7.5''$ (90%), $5.2''$ (68%)	requirement

	requirements	measurements	satisfaction
Mass	≤ 276 kg	270 kg	yes
Power	FXT long time power ≤ 200 W	191 W	yes

Fig. 9 FXT QM meets all the mission requirements (credit: IHEP)



Fig. 10 Assembled satellite before thermal environment test (credit: IMAC)

After completing satellite-level integration tests, the FXT telescope was transported back to IHEP for re-testing in October 2021. Compared to the results before integration, no significant changes of effective area and focal length of FXT occurred. Following the successful performance tests, which demonstrated that the FXT QM meets all the mission requirements (see Fig. 9). FXT passed the conclusion review for Phase C on 9 December.

The final phase (phase D) of FXT development involves the FXT flight model design, MA FM and pnCCD FM delivery, FXT FM test and calibration. FXT has passed the critical design reviews in March 2022.

FXT calibration test will take place after mirror assembly following the delivery of MA FM and pnCCD FM.

3.3 Environmental Tests for EP Satellite QM

After twelve WXT modules (10 STM and 2 QMs) were delivered to IMAC, satellite integration was initiated in July 2021. After payload assembling and testing, the EP satellite QM (see Fig. 10) underwent its environmental testing sequence including thermal test, mechanical test and EMC test.

(1) The thermal test included the following three parts: low pressure discharge test, thermal balance test and thermal vacuum test. The thermal test was planned and implemented to qualify the design of thermal subsystem, and to verify thermal models of the satellite QM in the test facility. Fig. 11 showed the temperature of main equipment during the thermal balance test. The satellite thermal test was completed at IMAC, in Shanghai, in August 2021, which demonstrated that the operating temperature of satellite equipment was controlled meeting the mission requirements.

(2) The mechanical test was performed at IMAC, Shanghai, in September 2021. It was planned and implemented to verify the reliability of satellite structure design, during which acoustic and sine vibration tests were completed to test the satellite's endurance to the vibration during launch. Compared to the results of Phase B, the test results demonstrated that the response to the mirror assembly interface was improved (see Fig. 12). In addition, the solar array deployment test was completed, which demonstrated the reliability required by the mission (see Fig. 13).

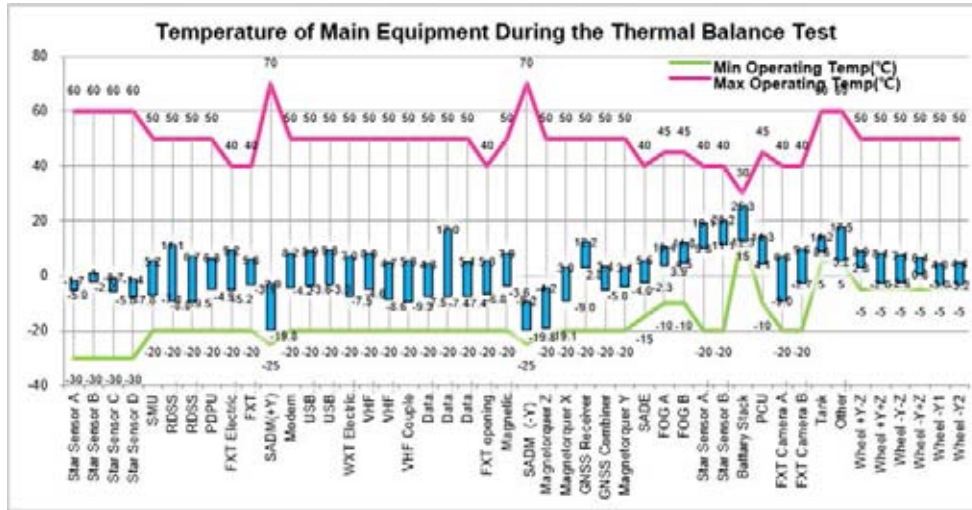


Fig. 11 Temperature of main equipment during the thermal balance test (credit: IMAC)

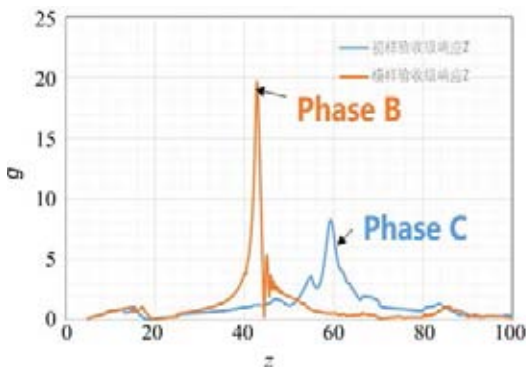


Fig. 12 Response of MA interface is better than Phase B (credit: IMAC)

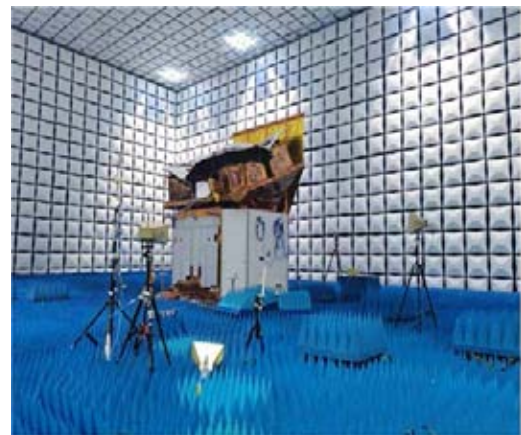


Fig. 14 Satellite EMC Test (credit: IMAC)



Fig. 13 Solar array deployment testing—panel unfolding (credit: IMAC)

(3) Finally, a comprehensive Electromagnetic Compatibility (EMC) test (see Fig. 14) was implemented in early October 2021, in which the electromagnetic emission and the satellite electromagnetic design were assessed. The test demonstrated that the payloads emissions would not interfere with the launch or flight communications systems, and conversely, that the electromagnetic

environment in flight will not interfere with WXT and FXT performance.

The satellite AIT process in Phase C was completed in October 2021. After the satellite environment test, the WXT and FXT payload performance re-tests were completed by the end of November 2021. With the completion of its environmental tests, the EP mission is one step further toward its next phase.

3.4 EP passed the Mission Critical Design Review (MCDR)

As one of the most significant mission milestones, the EP project passed the Mission Critical Design Review (MCDR) on 25 March 2022 (see Fig. 15). This milestone, to kick off the program of Phase D, signified the integrated observatory will meet all science and engineering requirements for its mission.



Fig. 15 EP MCDR meeting held on 25 March 2022 (credit: NSSC)

Progress Report on ASO-S*

GAN Weiqun

Key Laboratory of Dark Matter and Space Astronomy, Purple Mountain Observatory,
Chinese Academy of Sciences, Nanjing 210023

Abstract

The Advanced Space-based Solar Observatory (ASO-S) started officially its engineering phases at the beginning of 2018. In the past two years from 2020 to 2022 ASO-S completed smoothly the Phase-C study and is now undertaking the Phase-D study. The launch date is finally set in October of 2022. We here briefly summarize the progress of ASO-S from the late Phase-C to the current Phase-D studies, and plan the scientific affairs around the launch.

Key words

Space astronomy, Solar physics, Spacecraft

1 Introduction

ASO-S is the first comprehensive solar mission in China^[1], which was officially approved at the end of 2017 by the Chinese Academy of Sciences (CAS) via the Strategic Priority Research Program of Space Science. The scientific goals of ASO-S could be summarized as 1M2B, *i.e.*, on a single platform to observe simultaneously the solar magnetic field, solar flares, and Coronal Mass Ejections (CMEs), so as to investigate the origin mechanisms of solar magnetic field, solar flares and CMEs and possible causality among them. To fulfill these goals, three payloads were deployed, which are the Full-disc vector Magneto Graph (FMG), the Lyman-alpha Solar Telescope (LST), and the Hard X-ray Imager (HXI), respectively.

The details of ASO-S up to the end of Phase-B can be found in the special issue in the journal *Research in Astronomy and Astrophysics (RAA)*, which includes a total of 14 papers^[2–15], describing the general framework,

the scientific objectives, systematic designs, payload schemes, prototype models, engineering models, scientific systems, the synthetic studies, and so on. In 2020, a special issue in Chinese, as a supplement of that on RAA, was published in *Acta Astronomica Sinica*, which includes a total of 15 papers^[16–30], describing even more details like the designs for some key issues of the sub-systems.

In the last progress report^[31] two years ago, we briefly introduced the history of ASO-S, its scientific objectives, its payload deployments, the whole mission, as well as the Phase-B study and early Phase-C study. Here we continue along this way, but extend to the late Phase-C and Phase-D stages.

2 Late Phase-C Study

According to the last report^[31], the Phase-C study should have been finished in August 2020. But in practice the whole system finished the Phase-C study with a

* Supported by Chinese Academy of Sciences (XDA15052200) and by National Natural Science Foundation of China (11921003 and U1931138)

Received May 27, 2022

delay of almost one year. The COVID-19 epidemic was obviously one of the main reasons resulting in such a long delay. In addition, each payload has its own problems. For FMG, the original detector contractor was changed and then the newly-supplied detector (CMOS) was partially damaged in an environmental test. For HXI, the import of chip IDE 3381 in the electric control box took quite a long time and the beam test to check the behavior of fine grids needed a new X-ray source, which also took some time to satisfy the requirement. The longest delay was for LST. Due to the complexity of LST, the workload was much more than ever thought, especially on how to suppress the stray light. After a series of studies and simulations, finally both the original designs in hardware and software (like the exposure time modes) have to be changed, so as to meet the design objectives of the LST.

Based on the Phase-C pass of both HXI and FMG in April 2021 and LST in August 2021, the satellite system as a whole moved officially from Phase-C to Phase-D in September 2021 after all required tests were well made, like desktop joint commissioning, assembly performance, vibration, vacuum, thermal balance, thermal cycle, and so on.

3 Phase-D Study

Although the Phase-D was officially started only in September 2021, as a matter of fact, quite a number of Phase-D works had already been begun during the Phase-C study. This style of parallel working saves quite a lot of time required for the Phase-D study, which was set from September 2021 to August 2022. Then with over one month preparation for the transportation and all the works at the launch site, ASO-S is scheduled for launch in October 2022.

During the Phase-D study, there are almost no changes for all technical status. Everything goes smoothly as planned although it is always tense in time. No major harmful issues have appeared except for FMG which met again a damage of the detector in the environmental test of thermal-vacuum. The luck is that there is a backup of the detector. Up to March 2022, all the desktop debugs between each flight model of payloads and the platform, as well as that as a whole have been finished. In May 2022 the integration of the whole system will be undertaken and then the final environment, performance and communication tests will be made. If

everything goes as expected, the ASO-S will be transported to Jiuquan launch site at the beginning of September 2022.

4 Scientific Preparations

With approaching to the launch time, scientific preparations have become more and more important. In fact, with the initiation of the engineering phases, the scientific preparations had unfolded at the same time. There are two parallel aspects, one is so-called Science Operation and Data Center (SODC), as a part of mission engineering, supported by the Strategic Priority Research Program of Space Science, CAS; the other is the researches related directly to the usage of future ASO-S data, supported via grants from both the National Natural Science Foundation of China (NNSFC) and the CAS. Up to March 2022, SODC finished most of the work set in the four categories of scientific operation, data management, data analysis center, and user service. A major research project supported by a joint grant of NNSFC and CAS has been finished at the end of 2021. Now the science teams are working hard and try to complete the pipeline with version 1.0 (in which the basic functions should be wholly covered and operationable) in both the data production and data analysis tools by the end of May 2022. Then updating and improving will be kept on until to an advanced status that the team itself can work smoothly when the data are available and the users outside the team can make use of the data and tools without any difficulties.

Due to the influence of COVID-19 epidemic, the planned international workshop of ASO-S in 2021 has to be cancelled. How to arrange the following domestic and international cooperation is still under investigation. Anyway, to ensure a successful launch in 2022 is of primary importance. An open training course for the usage of the ASO-S data is planned to hold either in-person or in virtual forms at a suitable time between the launch and the open release of the data.

5 Conclusions

By now ASO-S is undertaking its Phase-D study. All the works look smooth and are on the track of the schedule, although the itinerary shows to be very tense. Let's express our best wishes for a successful launch in October 2022. Let's wish all the payloads working well

in orbit, and bringing us a series of exciting observations. Meanwhile we hope that more and more colleagues could be interested in ASO-S mission and make use of the data, in order to realize its scientific objectives.

References

- [1] GAN W Q, FENG L, SU Y. A Chinese solar observatory in space[J]. *Nature Astronomy*, 2022, **6**(1): 165
- [2] GAN W Q, DING M D, HUANG Y, et al. Preface: advanced space-based solar observatory (ASO-S)[J]. *Research in Astronomy and Astrophysics*, 2019, **19**(11): 155
- [3] GAN W Q, ZHU C, DENG Y Y, et al. Advanced space-based solar observatory (ASO-S): an overview[J]. *Research in Astronomy and Astrophysics*, 2019, **19**(11): 156
- [4] DENG Y Y, ZHANG H Y, YANG J F, et al. Design of the Full-disk MagnetoGraph (FMG) Onboard the ASO-S[J]. *Research in Astronomy and Astrophysics*, 2019, **19**(11): 157
- [5] LI H, CHEN B, FENG L, et al. The lyman-alpha solar telescope (LST) for the ASO-S Mission--I. Scientific objectives and overview[J]. *Research in Astronomy and Astrophysics*, 2019, **19**(11): 158
- [6] CHEN B, LI H, SONG K F, et al. The lyman-alpha solar telescope (LST) for the ASO-S Mission – II. Design of LST[J]. *Research in Astronomy and Astrophysics*, 2019, **19**(11): 159
- [7] ZHANG Z, CHEN D Y, WU J, et al. Hard X-ray imager (HXI) onboard the ASO-S mission[J]. *Research in Astronomy and Astrophysics*, 2019, **19**(11): 160
- [8] SU J T, BAI X Y, CHEN J, et al. Data reduction and calibration of the FMG onboard ASO-S[J]. *Research in Astronomy and Astrophysics*, 2019, **19**(11): 161
- [9] FENG L, LI H, CHEN B, et al. The lyman-alpha solar telescope (LST) for the ASO-S mission – III. Data and potential diagnostics[J]. *Research in Astronomy and Astrophysics*, 2019, **19**(11): 162
- [10] SU Y, LIU W, LI Y P, et al. Simulations and software development for the hard X-ray imager onboard ASO-S[J]. *Research in Astronomy and Astrophysics*, 2019, **19**(11): 163
- [11] HUANG Y, LI H, GAN W Q, et al. The science operations and data center (SODC) of the ASO-S mission[J]. *Research in Astronomy and Astrophysics*, 2019, **19**(11): 164
- [12] LI C, FANG C, LI Z, et al. Chinese H α Solar Explorer (CHASE)-A Complementary Space Mission to the ASO-S[J]. *Research in Astronomy and Astrophysics*, 2019, **19**(11): 165
- [13] VIAL J C. The synergy between the payloads on the ASO-S mission[J]. *Research in Astronomy and Astrophysics*, 2019, **19**(11): 166
- [14] KRUCKER S, HURFORD G J, SU Y, et al. Joint Hard X-ray Observations with ASO-S/HXI and SO/STIX[J]. *Research in Astronomy and Astrophysics*, 2019, **19**(11): 167
- [15] VOURLIDAS A. Ly α science from the LST aboard the ASO-S mission[J]. *Research in Astronomy and Astrophysics*, 2019, **19**(11): 168
- [16] HUAUG Y, CHEN P F, GAN W Q. ASO-S special issue in Chinese: preface[J]. *Acta Astronomica Sinica*, 2020, **61**(4): 32
- [17] CHEN B L, FANG Y X, DENG L, et al. High-precision and high-stability attitude control system based on guide telescope aboard the ASO-S[J]. *Acta Astronomica Sinica*, 2020, **61**(4): 33
- [18] ZHENG Z Y, WU Z, ZHANG H Y, et al. Research on the limb sensor for the FMG image stabilization system[J]. *Acta Astronomica Sinica*, 2020, **61**(4): 34
- [19] CHEN J Z, ZHANG H Y, ZHENG Z Y, et al. Design and simulation of a flexible-support tip/tilt mirror in the ASO-S/FMG image stabilization system[J]. *Acta Astronomica Sinica*, 2020, **61**(4): 35
- [20] CHEN C Y, LIN J B, BAI X Y, et al. Design and implementation of guiding and tracking system for ground-based experimental observation of FMG payload[J]. *Acta Astronomica Sinica*, 2020, **61**(4): 36
- [21] DUAN W, SONG Q, BAI X Y, et al. Application of CMOS image sensor in solar magnetic field observation[J]. *Acta Astronomica Sinica*, 2020, **61**(4): 37
- [22] LU L, LI H, HUANG Y, et al. The trigger and termination scheme for the event mode of the lyman-alpha solar telescope (LST) onboard the ASO-S mission[J]. *Acta Astronomica Sinica*, 2020, **61**(4): 38
- [23] LI J W, LI H, FENG L, et al. Influence of the flat field data acquisition interval on the lyman-alpha solar telescope flat field accuracy[J]. *Acta Astronomica Sinica*, 2020, **61**(4): 39
- [24] YU F, SU Y, ZHANG Z, et al. Research on the solar aspect system algorithm of ASO-S/HXI[J]. *Acta Astronomica Sinica*, 2020, **61**(4): 40
- [25] CHEN W, SU Y, ZHANG Z, et al. Tests and analysis of the arrangement configurations for ASO-S/HXI grids and their effect on imaging[J]. *Acta Astronomica Sinica*, 2020, **61**(4): 41
- [26] HUANG Y Y, MA T, ZHANG Y Q, et al. Calibration of the detector units of the spectrometer of the hard X-ray imager payload onboard the ASO-S mission[J]. *Acta Astronomica Sinica*, 2020, **61**(4): 42
- [27] WANG Q, ZHENG S, DENG Y Y, et al. Detection of polarity inversion line positions of active magnetic field in solar magnetograms based on support vector machine[J]. *Acta Astronomica Sinica*, 2020, **61**(4): 43
- [28] SHI G L, YING B L, FENG L, et al. Study of the streamer current sheet with white-light and UV observations[J]. *Acta Astronomica Sinica*, 2020, **61**(4): 44
- [29] SHAN J H, FENG L, YUAN H Q, et al. Automatic coronagraph image classification with machine learning methods[J]. *Acta Astronomica Sinica*, 2020, **61**(4): 45
- [30] GE Y Y, LI H, HUANG Y, et al. The database management analysis for the ASO-S science operation and data center[J]. *Acta Astronomica Sinica*, 2020, **61**(4): 46
- [31] GAN W Q. Status of the advanced space-based solar observatory[J]. *Chinese Journal of Space Science*, 2020, **40**(5): 704-706

Recent Advance in the Solar Wind Magnetosphere Ionosphere Link Explorer (SMILE) Mission*

WANG Chi¹, BRANDUARDI-RAYMONT Graziella², ESCOUBET C P³

1. State Key Laboratory of Space Weather, National Space Science Center, Chinese Academy of Sciences, Beijing 100190
2. Mullard Space Science Laboratory, University College London, London RH5 6NT
3. European Space Agency/European Space Research and Technology Centre, Noordwijk 2201 AZ

Abstract

The SMILE (Solar wind Magnetosphere Ionosphere Link Explorer) mission is a joint space science mission between the European Space Agency (ESA) and the Chinese Academy of Sciences (CAS), aiming to understand the interaction of the solar wind with the Earth's magnetosphere in a global manner. The mission was adopted by CAS in November 2016 and by ESA in March 2019 with a target launch date in the year 2024–2025. We report the recent progress of SMILE mission by May, 2022.

Key words

SMILE, Soft X-ray Imager (SXI), Ultra-Violet Imager (UVI), Light Ion Analyzer (LIA), MAGnetometer (MAG)

1 Introduction

The SMILE^[1] mission is a joint ESA and CAS space science mission, which aims at deepening our understanding of the interaction of the solar wind with the Earth's magnetosphere by making global images of the dayside magnetosheath and cusps of the magnetosphere, and the aurorae at the North Pole simultaneously, while monitoring the in-situ plasma environment. The mission was adopted by CAS in November, 2016 and by ESA in March 2019.

CAS is responsible for the development of satellite Platform (PF), Telecommand and Telemetry, Science Application System (SAS) as well as Ground Support

System (GSS), and provides MAGnetometer (MAG), Light Ion Analyzer (LIA) and Ultraviolet Imager (UVI) measurement instruments. ESA is responsible for the development of Payload Module (PLM), Launch Vehicle, Launch Site, and science operation and ground receiving station supports when necessary, and also the development of the Soft X-ray Imager (SXI), intensifiers, mirrors with coating and calibration of UVI.

The SMILE Mission will use novel soft X-ray imaging technology to obtain, for the first time, the global image of the large-scale structures of the geospace. This is critical to quantitatively analyzing and understanding of the global feature of the magnetosphere.

The interaction of the solar wind with the Earth's at-

* Supported by Strategic Priority Program on Space Science, CAS(XDA15350000), National Natural Science Foundation of China (41731070), Key Research Program of Frontier Sciences, CAS(QYZDJ-SSW-JSC028), and Strategic Pioneer Program on Space Science, CAS(XDA15052500)

Received May 27, 2022

mosphere leads to the formation of the large structures of the magnetosphere, including the bow shock, magnetopause, and the cusp regions. The position and shape of the magnetopause and cusps change constantly as the Earth's magnetosphere responds to the varying solar wind dynamic pressures and interplanetary magnetic field orientations. Both the fast and slow solar wind can be interrupted by large, fast-moving bursts of plasma called interplanetary Coronal Mass Ejections (CMEs). When a CME impacts the Earth's magnetosphere, it temporarily deforms the Earth's magnetic field, changing its direction and strength, and induces large electrical currents; this is called a geomagnetic storm and it is a global phenomenon. The southward interplanetary magnetic fields, as presented in a CME event, could induce magnetic reconnection in the Earth's magnetotail; this process accelerates protons and electrons downward toward the Earth's atmosphere, where they form the aurora, resulting in substorms.

The Scientific objectives of the SMILE mission are summarized as: (i) explore the fundamental modes of the dayside solar wind/magnetosphere interaction; (ii) understand the substorm cycle; (iii) determine how CME-driven storms arise and their relationship to substorms.

2 Modeling Update

The SMILE Modelling Working Group (MWG) performs studies on the predictions of X-ray signals and the reconstruction techniques from X-ray images to 3D magnetopause. Four approaches have been developed previously to derive the magnetopause position from X-ray images, including the Boundary Fitting Approach (BFA), Tangent Fitting Approach (TFA), Tangential Direction Approach (TDA), and Computed Tomography Approach (CTA). It is found that the 3D X-ray emissivity in the magnetosheath can be reconstructed based on the CTA, if tens of images are provided from different viewing geometries under the same or similar solar wind conditions (see Fig. 1)^[2]. To obtain the images required to better perform the CTA, 87 different orbit locations are considered during one year to allow wide-angle coverage resulting from orbital precession. However the assumption that the magnetopause position does not change during the one year is not valid, preventing the application of CTA. This problem can be solved by dividing the solar wind conditions into several

bins, and assuming that the magnetopause position corresponding to each solar wind bin is the same. An alternative way is through machine learning techniques^[3]. A 3D GAN network is applied to supplement 2D X-ray images collected at finite angles within limited orbital time during which the magnetopause is almost static. By deriving the information about cusps from the X-ray image, it is revealed that the tangent direction of the cusp boundary is the direction with the appreciable increase of local standard deviation in X-ray intensity^[4]. Instrument simulations are also performed to provide

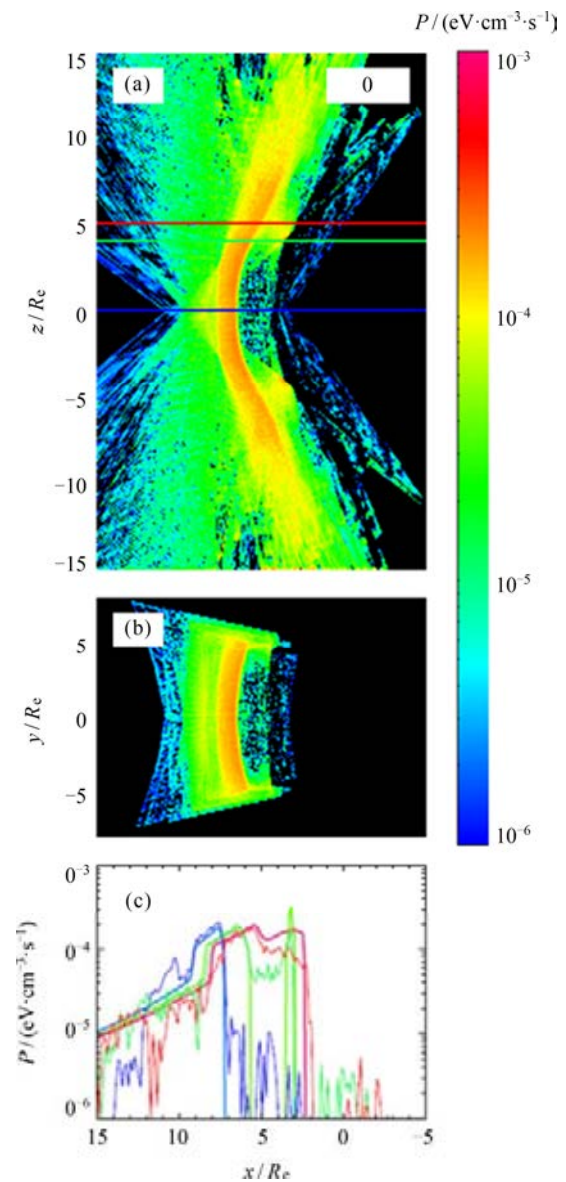


Fig. 1 Reconstructed X-ray emissivity on the noon-midnight meridian plane (a), equatorial plane (b), and along the three lines marked in the top panel (c) based on the CT Approach

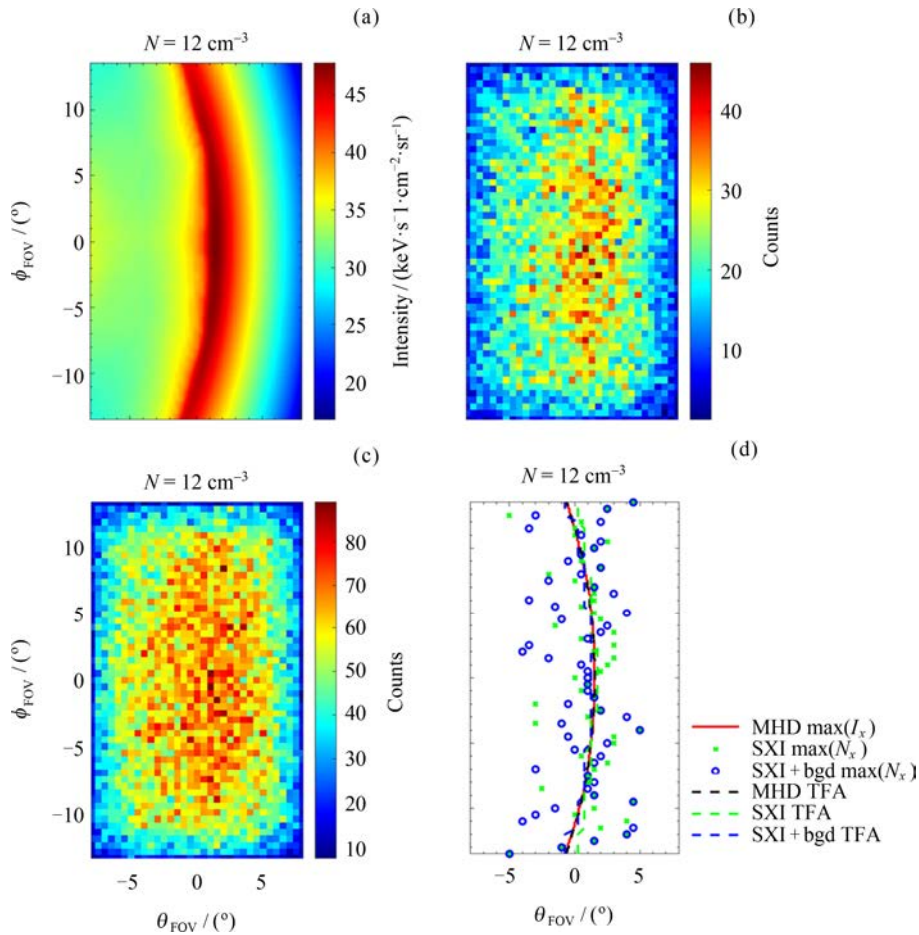


Fig. 2 Instrument simulations of the X-ray photon counts. (a) X-ray image inside field of view of SXI. (b) SXI photon counts image corresponding to (a) without sky background. (c) SXI image after adding the constant sky background. (d) The X-ray maximum intensity of MHD and SXI photon counts images, and their best match curves by using TFA

the photon counts images expected to be observed by the SXI instrument. The effectiveness of TFA is validated based on the simulated photon counts images (see Fig. 2)^[5].

3 Mission Update

3.1 Satellite System

The science orbit is a highly elliptical orbit with the apogee altitude of about $19 R_e$ and a perigee of about 5000 km. The inclination is 73° if launched with Vega-C as the baseline, or 98.2° with Ariane 62.

SMILE is a three-axis stabilized satellite which consists of Platform (PF) and Payload Module (PLM). The total mass of the satellite is less than 2250 kg including fuel that takes about 2/3 of the launch mass.

The science data will be downlinked by an X-band transmitter with a data volume of 47 Gbit per orbit. The

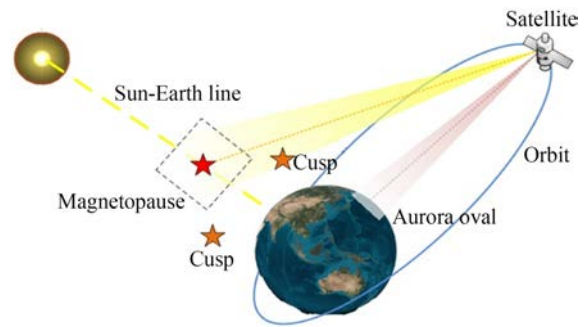


Fig. 3 SMILE satellite HEO orbit

telemetry and telecommand will go through Unified S-band TT&C system. The nominal life time is 3 years by launch and with the possibility to extend the mission another 2 years. Fig. 3 and Fig. 4 show SMILE satellite HEO orbit and structure.

SXI for imaging the magnetopause and cusps has passed Preliminary Design Review (PDR) and Structural

Model (STM) environment test. The SXI Critical Design Review is planned to begin in November 2022 (see Fig. 5).

Currently, the UVI instrument will image the Earth aurora is jointly developed by CAS and ESA. It is planned to begin CDR in December of 2022 (see Fig. 6).

MAG instrument will measure the magnetic field has finished PDR. MAG Engineering Model (EM) and MAG STM were delivered to Airbus for Assembly,



Fig. 4 Diagram of the satellite structure



Fig. 5 SXI STM on a shaker table at RALSpace, UK

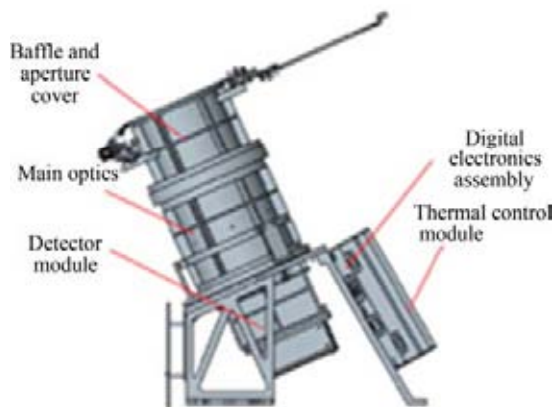


Fig. 6 UVI assembly

Integration and Test (AIT) in 2021. MAG BOOM Qualification Model (QM) has been successfully deployed under the control of PLM in ESTEC (see Fig. 7). It is planned to begin MAG CDR in June of 2022.

LIA instrument will monitor the in-situ plasma environment has passed PDR. LIA EM and Reduced EM (REM) have been delivered to PLM for the test (see Fig. 8). It is planned to begin LIA CDR in June of 2022.

Payload Module (PLM) which hosts SXI, UVI, MAG and X-band science downlink transmitter has finished PDR. PLM STM was integrated with instruments and has passed mechanical and thermal tests (see Fig. 9). PLM also has finished functional and electric tests with MAG and LIA. PLM STM was delivered to China in March of 2022. It is planned to begin PLM CDR at the beginning of 2023.

The Platform (PF) provides service for the whole satellite. PF also provides propellants and thruster for orbit maneuver from the insertion orbit to the HEO science orbit. PF also hosts two LIA sensors for 4π space measurement. All the PF QM units have been delivered to PF and have passed through electrical interface and functional tests (see Fig. 9). PF QM has been assembled and will pass the qualification level tests with PLM STM



Fig. 7 MAG BOOM deployment test in ESTEC



Fig. 8 LIA electrical interface test in Airbus

later (see Fig. 10). PF CDR is planned to begin in Oct. of 2022.

Satellite STM has passed environment test in China in 2020. From April of 2022, Satellite QM AIT campaign will start with PF QM and PLM STM in China. Satellite qualification level test will begin from April to August of 2022. After satellite qualification level test, we will begin fitness and separation tests with launch adapter in ESTEC in September 2022. It is also planned to do an electrical interface test in Madrid in Oct 2022. The mission CDR is scheduled to take place in March 2023. Fig. 11 showed satellite STM on the shaker.

3.2 Launch Vehicle

A single launch Vehicle is ESA’s responsibility. The baseline is single launching in Kourou with Vega-C. Vega-C is a solid launch vehicle. The launch capability is no less than 2250 kg for 700 km circular injection orbit or 2300 kg for 450 km×700 km injection orbit.

3.3 Launch Site

SMILE will be launched in Kourou. ESA is responsible for the Launch Site and Launch service, and will provide the ground segment support and logistics.

3.4 TC/TM

China Satellite Launch and Tracking Control General (CLTC) will be responsible for the TC/TM of SMILE satellite. European Space Operation Center (ESOC) will be responsible for the TC/TM before the satellite’s separation with the Launch Vehicle. In addition, ESA will also provide ground station support for orbit transfer from injection orbit to HEO science orbit and in case of emergency.

Satellite QM to ground S-band interface compatibility test was successful in 2020 (see Fig. 12).

3.5 Ground Support System (GSS)

GSS has been constructed in China during the 12th Five-Year Plan Period and it will undergo some modifications according to the new requirements of the space science missions during the 13th Five-Year Plan

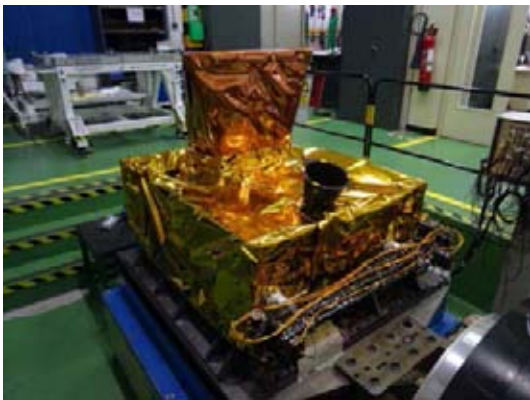


Fig. 9 PLM STM on shaker in ESTEC

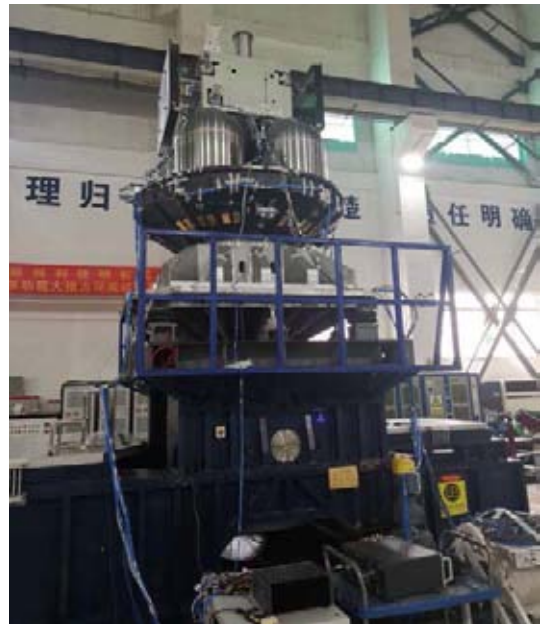


Fig. 11 Satellite STM on the shaker



Fig. 10 PF electrical interface test



Fig. 12 Satellite to ground S-band interface compatibility test

Period. It is mainly responsible for the operation and management of the payloads, scientific data receiving, processing and distribution to the science community.

GSS has finished PDR. Some core software has finished requirement analysis and design. It has started joint test the Docker operation environment. It is planned to start joint GS CDR in June of 2022.

3.6 Science Application System (SAS)

CAS will set up SAS located at NSSC, and ESA will set up Science Operation Center (SOC) located in European Space Astronomy Center (ESAC). Both parties will cooperate closely to make a scientific strategic plan and observation plan, monitor the execution of the plan, analyze the performance of the payloads in orbit, calibrate the payloads in orbit, produce quick look scientific data, and scientific data products.

SAS has finished PDR. Software is in the status of requirement analysis and design. A joint data products definition has been completed for SMILE.

4 Future Schedule

Based on Payload Instruments, PLM and PF PDRs, the joint Mission PDR was completed successfully in January 2020 in Netherlands, which is the third joint review of the SMILE mission, marking the kick-off of Phase C activities. PLM STM finished all the mechanical and the thermal tests and was shipped to IAMC for integration with QM Platform. The next step is S/C level QM test before the end of July 2022. All the scientific instruments, PLM and SC will finish CDR and a joint mission level CDR will be conducted in March 2023. SMILE satellite is planned to be launched around 2024–2025.

Acknowledgments

SMILE Mission is a joint project with support from CAS and ESA. Thanks for the great support of CAS Strategic Priority Research Program and the ESA science program. Also thanks go to the study and engineering teams for their cooperation and hard work: National Space Science Center, Innovation Academy for microsatellites of CAS, CLTC, Shanghai Institute of Space Propulsion, National Center for Space Weather, Polar Research Institute of China, *etc.* from Chinese side; University College London, University of Leicester, Bergen University, OEAW Space Research Institute, University of Liège, Institute National de Técnica Aeroespacial, Imperial College, Rutherford Appleton Laboratory, *etc.* from ESA side, as well as NASA Goddard Space Flight Center.

References

- [1] WANG C, BRANDUARDI-RAYMONT G. Update on the ESA-CAS joint solar wind magnetosphere ionosphere link explorer (SMILE) mission[J]. *Chinese Journal of Space Science*, 2020, **40**(5): 700-703. DOI: 10.11728/cjss2020.05.700
- [2] JORGENSEN A M, XU R, SUN T, *et al.* A theoretical study of the tomographic reconstruction of magnetosheath X-ray emissions[J]. *Journal of Geophysical Research: Space Physics*, 2022, **127**(4): e2021JA029948
- [3] WANG R, LI D, SUN T. Three-dimensional magnetospheric finite-angle integral projection complement and reconstruction method based on 3D GANs[J]. submitted to *Journal of Geophysical Research: Space Physics*, 2022
- [4] SUN T R, WANG X, WANG C. Tangent directions of the cusp boundary derived from the simulated soft X-ray image[J]. *Journal of Geophysical Research: Space Physics*, 2021, **126**(3): e2020JA028314. DOI: 10.1029/2020JA028314
- [5] GUO Y H, SUN T R, WANG C, *et al.* Deriving the magnetopause position from wide field-of-view soft X-ray imager simulation[J]. *Science China Earth Sciences*, 2022. DOI: 10.1007/s11430-021-9937-y

Research Advances of the Chinese Meridian Project in 2020–2021^{*}

WANG Chi, WANG Jiangyan, XU Jiyao

State Key Laboratory of Space Weather, National Space Science Center, Chinese Academy of Sciences, Beijing 100190

Abstract

The Chinese Meridian Project (CMP) is a major national science and technology infrastructure invested and constructed by the Chinese government. The project builds space environment observation stations, focusing on the monitoring of the space environment over China, so as to provide a monitoring basis for clarifying the regional characteristics of the space environment over China and its relationship with global change, and making important innovative scientific achievements. The first phase of the CMP passed the national acceptance in 2012. It has been running for nearly ten years and has accumulated more than 8TB monitoring data. These data are all available to all data users through the data center of the project. From 2020 to 2021, users of CMP data have completed a series of original works, which have solved current scientific problems in the field of space physics research. On the other hand, they also make us look forward to the completion of the second phase of CMP and its application benefits in national major strategic needs and cutting-edge scientific research.

Key words

Chinese Meridian Project (CMP), Space physics, Magnetosphere, Ionosphere, Middle and upper atmosphere

1 Overview of the Project

The Chinese Meridian Project (CMP) is a large-scale scientific facility funded by the Chinese government. The project is a joint effort of more than 10 institutions or universities in China, led by the National Space Science Center of Chinese Academy of Sciences. It is scheduled to be constructed in two phases. The first phase was under construction from 2008 to 2012 and has been in operation since 2012. The second phase was launched in 2019, and is expected to be completed by December 2023.

The first phase of CMP includes 15 ground-based observatories located roughly along the 120°E longitude and 30°N latitude. The longitudinal chain of observa-

tional stations starts from Mohe, the top north city of China. It runs south roughly through Beijing, Wuhan, Hainan within Chinese territory, and extends to China's Zhongshan station in the Antarctica. The latitudinal chain is constructed roughly following 30°N, spanning from Lhasa to Shanghai. 87 sets of monitoring instruments have been deployed at these stations to monitor the solar-terrestrial coupling and its influence on our planetary environment. Instruments include magnetometers, MST radar sets, meteor radar sets, high-frequency backscatter radar sets, incoherent scatter radar sets, traditional and digital ionosondes, lidars, Fabry-Perot interferometers, aurora spectrographs, *etc.*

Since 2012, the first phase of CMP has been run for ten years. It has continuously obtained more than 8TB

^{*} Supported by the Chinese Meridian Project.

Received May 27, 2022

monitoring data of China's space environment near 120°E and 30°N, and has made a series of original scientific achievements in space physics and space weather. This article mainly presents the research highlights of the past two years.

2 Major Scientific Achievements in 2020 and 2021

2.1 Study on Middle and Upper Atmosphere

2.1.1 Observations of Middle and Upper Atmosphere by Lidars

The first phase of CMP has deployed a Rayleigh-Sodium lidar chain near 120°E. The lidar chain of CMP provides scientists with a good tool to investigate the new features of the troposphere and the metal layers in the MLT region.

Cheng *et al.*^[1] observed 20 occasions of falling mixed-phase virga from a thin super cooled liquid cloud base at altitudes of 2.3–9.4 km using ground-based lidars at Wuhan, China. Polarization lidar profile (3.75 m) analysis reveals the vertical structures and phase states of both falling mixed-phase virga and their liquid parent cloud layers. Based on one year of polarization lidar measurements at Wuhan, China, Wang *et al.*^[2] studied geometrical and optical characteristics of cirrus clouds. They found that there is a positive correlation between the cirrus occurrence frequency and dust column mass density in seasons except summer. It was revealed that the formation processes of cirrus clouds are significantly impacted by the dust particles.

It has been widely confirmed that a close coupling exists between the lower and upper atmosphere. The activities at the lower atmosphere may produce a chain reaction in the middle-upper atmosphere. Based on the joint observations by an atmospheric electric mill, a fluxgate magnetometer, a temperature/wind lidar, an ionosonde, and the World Wide Lightning Location Network, Qiu *et al.*^[3] revealed a conjunction between the lower and upper atmosphere. The key interconnected processes could be suggested to be: lightning strokes → overturning of the electric field → ionospheric sporadic E (Es) generating a sodium layer (Nas).

The need of scientific research promotes the development of lidar techniques. Yanqing (40°N, 116°E) is one of the most important lidar stations in the lidar chain of CMP. In the past two years, this lidar station

has scored big points rapidly. A new Ni lidar has been designed and deployed there, which can effectively avoid the disturbances by Amplified Spontaneous Emission, and detect the Ni layer successfully. The nightly-averaged Ni densities observed by Yanqing lidar are similar to the results reported by Gerding *et al.*^[4]. Taking advantage of high-resolution detecting mode of Yanqing Na radar, Zou *et al.*^[5] successfully accomplished observations of the spectrum of a gravity wave in the turbulence region.

2.1.2 Dynamics and Planetary Waves in the Middle and Upper Atmosphere

Severe weather events in the lower atmosphere, such as thunderstorms, cyclones, tropical storms, typhoons *etc.*, produce waves by disturbing local atmosphere. These waves can propagate upward to the Mesosphere and Lower Thermosphere (MLT) region under appropriate conditions, exciting disturbances at these latitudes. It is an important coupling process between the lower atmosphere and the MLT region. The waves from the lower atmosphere bring energy and momentum to the MLT region, and then affect the dynamic structure of the whole atmosphere. The first phase of CMP has deployed multiple radio and optical instruments. It provides valuable first-hand experimental data for the in-depth study of dynamic processes and waves in the middle and upper atmosphere over China.

Based on the long-time observations of Wuhan MST radar and Beijing MST radar of CMP, Zhang *et al.*^[6] studied the statistical characteristics of the mesospheric vertical wind at mid-latitudes for the first time and described the diurnal, seasonal and annual variation characteristics of the vertical wind at Wuhan and Beijing. No prominent subdaily and seasonal variations are found. It was shown that there are differences between the summer vertical winds over Beijing and Wuhan. The differences are mainly related to the gravity wave activities.

Sudden Stratospheric Warming (SSWs) occur in the stratosphere of polar regions in the winter. It has a significant and severe impact on the atmosphere in all regions and latitudes (from the ground to hundreds of kilometers) of the world. Thanks to the observations with the meteor radar chain of CMP, some scientists have studied the variation characteristics of planetary waves and tidal waves in the middle and upper atmosphere during SSW events. Li *et al.*^[7] systematically analyzed the disturbance characteristics of atmospheric wind field

wind field and tidal waves in the MLT region during an SSW event in 2013. It was found that during this event, there was a sudden increase of northward wind in the latitudes of 18°N–53°N in China, and the diurnal tide and semidiurnal tide weakened first and then increased. There are obvious latitudinal differences in the response characteristics of MLT atmospheric wind field and atmospheric tide to the SSW event in 2013. Gong *et al.*^[8] presented that the Quarter Diurnal Tide (QDT) abnormally enhanced during the 2019 Arctic SSW event. Luo *et al.*^[9] found that the Quasi 10-Day Waves (Q10DWs) were enhanced during an SSW event in February 2018 as well. Ma *et al.*^[10] analyzed planetary-scale oscillations in the MLT region during SSW events. They revealed that the enhancement or generation of westward propagating quasi-16-day oscillation with wave number 1 is a common feature during SSWs over Mohe. They also analyzed a strong enhancement of the quasi-4-day oscillation during the 2018/2019 SSW, and presented the interpretation of formation mechanism. Their results not only showed that the amplified quasi-4-day oscillation in the MLT region is associated with the 2018/2019 SSW but also suggested that the amplification is originally generated around 60 km due to the instability caused by the drastic changes of local temperature and wind field and propagates upward to MLT region.

The atmospheric waves can also propagate upward, which are one of the main sources of ionospheric changes. Huang *et al.*^[11] found that there was a significant daytime TEC enhancement several days before the occurrence of SSW in 2017, with a range of 75%–160%; This event is a typical case of coupling between different atmospheric spheres and provides important evidence of lower atmosphere - ionosphere coupling. Liu *et al.*^[12], for the first time, described the response processes of the ionospheric parameters from the middle atmosphere to the top of ionosphere during SSW. From the point of view of the disturbance period, the quasi-16-day planetary wave scale disturbance in the ionosphere during SSW is related to semi diurnal and lunar tides. Mo *et al.*^[13] studied the multiscale planetary wave scale disturbance of the ionospheric Equatorial Anomaly Peak (EIA). It is found that the periodic disturbance of planetary waves in ionospheric EIA is obviously modulated by the semidiurnal tide in the lower atmosphere, indicating the role of tidal modulation in the planetary wave scale coupling process between the lower atmosphere and ionosphere.

The measurement of winds is one of the key data to study the dynamic process of the middle and upper atmosphere. At present, the detection of winds mainly depends on ground-based equipment and satellites. Jiang *et al.*^[14] compared the GOCE crosswind data with the horizontal winds measured by ground-based FPIs. It was found that during magnetically quiet periods the GOCE observations are in a good agreement with FPIs measurements in the magnitude and seasonal variations of winds. However, the GOCE and FPI derived winds have a lower agreement during geomagnetically active periods, which deserves further study. We all know that ground based observation has the advantage of continuous time coverage and satellite observation has the advantage of space coverage. Taking advantage of these two means comprehensively, Liu *et al.*^[15] obtained the global wind field information with a large vertical span from the stratosphere to the lower thermosphere and a large time span of 18 years, which meets the urgent demand for wind field data in the research and application of middle and upper atmospheric dynamics to a certain extent.

2.2 Study on Ionosphere

2.2.1 Variation Characteristics of Ionosphere

The Earth's ionosphere exhibits complex variation characteristics. One standard feature of the ionospheric variations is the diurnal variation, which is the fundamental of ionospheric empirical models. Liu *et al.*^[16] used the Qijing incoherent scatter radar in conjunction with ionosondes to investigate the feature of the enhancements of electron density in the ionospheric F region at low altitudes. The characteristic of decreasing $h_m F_2$ and increasing $N_m F_2$ may present at both nighttime and daytime. That is to say, the compression of the ionosphere certainly causes an increase in the low-latitude electron density and a lower peak height.

Another important feature is the day-to-day variability of the ionospheric electron density and its longitudinal gradient. Liu *et al.*^[17] reported a typical case of anomalous enhancement in ionospheric electron density and its longitudinal gradient during the period from 29 May to 2 June 2015. It is shown that electron density enhances strongly in the region around the northern crest of equatorial ionization anomaly; the increase in electron density depends on altitude, being stronger at higher altitudes; the electron density enhancement event is well correlated with an intensified equatorial electrojet.

The ionosphere presents complex changes under the control of dynamic processes. Sometimes the ionospheric electron density increases with local time under the action of dynamic processes. That is the nighttime enhancement. Li *et al.*^[18] statistically explored the feature and mechanism of the ionospheric nighttime enhancement at midlatitudes. The results showed that the dynamic process controlling the nighttime enhancement at midlatitudes in winter is obviously different from that in summer. In winter, the change of $h_m F_2$ has no significant effect on the characteristics of nighttime enhancement. Downward plasma influxes from the topside ionosphere and the conjugate summer hemisphere play a decisive role in the formation of nighttime enhancement.

2.2.2 Ionospheric Irregularities

Ionospheric irregularities refer to various scale ionized “clouds” or “wavy” structures floating in the normal ionospheric structure. The study of ionospheric irregularities not only helps to further understand the physical process of ionospheric disturbance and change, but also has important engineering and application value.

The special daytime E Region V-shaped echo pattern in Range-Time-Intensity (RTI) plots of VHF radar was investigated by two groups independently. Chen *et al.*^[19] presented the common features of V-shaped echoes by four cases studies. The V-shaped echoes usually occur between 10:00–15:00 LT in the daytime with the enhanced top frequency and blanketing frequency of Es layer ($f_{t,Es}$ and $f_{b,Es}$). Their left/right wings present negative/positive Doppler velocity. In another case study, Sun *et al.*^[20] connected the V-shaped radar echoes with the strong Es. The band-like strong Es structures with critical frequencies up to about 17 MHz were analyzed within the ionosonde and VHF radar fields-of-view, which caused unique V-shape backscatter radar echoes with negative (positive) Doppler velocity and range rate in the left (right) wing of the echo that was ascribed to the drift of the strong Es structure and wide beams of the radar sets.

Ionospheric F region bottom-type irregularity layer was first reported by Fuke and Sanya VHF radar observations in 2017. Hu *et al.*^[21] extended the bottom-type irregularity study with an eight-year observation by Sanya VHF radar during the equinoctial months of 2011–2018. The results showed the bottom-type irregularity layer occurred almost exclusively in the descend-

ing phase of the solar cycle (2015–2018). No clear correlation was found between the occurrences of bottom-type irregularity layer and plasma plume at low latitude.

Equatorial Plasma Bubble (EPB) and Medium-scale Traveling Ionospheric Disturbances (MSTIDs) are important ionospheric irregularities. The occurrences of EPB irregularities over Asian and American sectors often show different behaviors due to significantly different geometry of the geomagnetic field. Zhao *et al.*^[22] presented a comparative study of long-term occurrences of EPB kilometer-scale irregularities over the two longitude sectors. The two sectors showed significant differences in seasonal variability, solar activity dependency, latitudinal variation, and magnetic activity dependency of kilometer-scale irregularity occurrence rates. The findings will help in the design of experiments to better understand how EPB irregularities are generated in the future international meridian circle project.

Xie *et al.*^[23] reported that E region Quasi-Periodic (QP) echoes and F region MSTIDs were simultaneously observed at low latitudes. It was found that the QP echoes were clustered into groups coinciding with the periods of MSTIDs. They suggested that the E-F electrodynamic coupling could modulate the E region plasma instability, producing QP echoes at low latitudes. Hu *et al.*^[24] investigated the occurrence characteristics of periodic TEC perturbation associated with MSTIDs. The results showed that the latitudinal variations of periodic ionospheric disturbances show two occurrence peaks at higher and lower latitudes, with a minimum identified at latitudes centered around 30°N–33°N. It was surmised that the background electron density and perturbation source could play important roles in causing the latitudinal variation of MSTIDs along 110°E. Sun *et al.*^[25] investigated the effects of a post-evening Weddell Sea Anomaly (WSA)-like plasma patch on a southwestward propagating MSTID. They found some of WSA-like plasma patches moved northward from the EIA regions to midlatitudes, as they traveled westward into China. Over 50% of these structures were accompanied by concurrent MSTID and Es. They proposed that an intense Polarization Electric Field (PEF) associated with an MSTID/Es from the more northern regions of EIA could frequently drive these plasma patches poleward.

To better understand the evolution of EPB and MSTID, and the interaction between them, a ground-based airglow imager network across China that consists of 15 stations has been established (Xu *et al.*^[26]). Xinglong and Fuke of these stations are supported by the CMP. Based on the data from the airglow network, Wu *et al.*^[27] found oppositely MSTID in low latitudes during geomagnetically quiet night. Some MSTID structures of them propagated southwestward and others propagated northeastward. These MSTID structures encountered and interacted with each other. The interactive process of these MSTIDs should be related to their polarization electric fields. Wu *et al.*^[28] used observational data from two all-sky imagers, GPS, Swarm satellite, and a digisonde to study a special EPB event. They found that these EPBs occurred in the region of plasma depletion structure. These EPBs showed different zonal drifts within a narrow longitudinal zone which should be related to the zonal winds. Sun *et al.*^[29] investigated an interaction between an EMSTID and an EPB in the EIA crest region over China. Interaction could have polarized one depletion of the post-midnight EPB, inside which freshly-generated meter-scale irregularities caused activated radar echoes and enhanced Ranged Spread F (RSF) over Fuke station. The result showed how an electrical couple of EMSTID and EPB events can activate a post-midnight EPB depletion over low latitudes of China. Luo *et al.*^[30] reported a special MSTID event observed by multi-instruments over mid-latitude region of China. They found the inclination angles of MSTID bands were decreasing, resulting in the propagation direction changed from southwestward to nearly westward. The result showed the MSTIDs disappeared partly in the airglow observation when they propagated to lower latitudes (below 40°N) later. Based on the observations from the FPI and the simulations from the TIEGCM, they found that the variations of propagation direction and the disappearance of MSTIDs should be related to the variations of ionospheric neutral winds.

2.2.3 Characteristics of Sporadic E (Es)

The Es layer is a thin and dense layer composed of metallic ions in the altitude of 90–130 km of Earth's upper atmosphere. It was observed in the 1960s that there is seasonal variation in the Es layer. However, the mechanism driving the seasonal variation is still a big puzzle for us. Yu *et al.*^[31] reported that Es layer has an obvious meridional transportation from winter hemisphere to

summer hemisphere. This trans-hemispherical transportation of metallic ions within Es layer is mainly controlled by the lower thermospheric meridional circulation. Apart from the seasonal variation, Yu *et al.*^[32] presented that the change of metallic ions within Es layer has a strong 27 days' period, meaning that the Es layer is influenced by high-speed solar winds generated from persistent coronal holes on successive 27-day solar rotations and geomagnetic activities.

Based on the observations from GNSS TEC, Sun *et al.*^[33] investigated the morphology and dynamics of large-scale strong Es structures in the East/Southeast Asian sector. It was found that the large-scale strong Es structures mainly occur during summer months, with dominant horizontal azimuth in the east-west and north-west-southeast directions and dimensions of 1000–3000 km along the elongation. They predominantly drift southwestward at a speed of 30–210 m·s⁻¹. The main onset region for the large-scale Es structures over China is identified for the first time, which is around 20°N–45°N and 100°E–125°E. Furthermore, they proposed a High Temporal Resolution Rate-Of-TEC Index (HR-ROTI) based on the 1 s resolution TEC to characterize fine scale Es irregularity structures. It was found the typical scale size of Es embedded in the strong Es structures was down to about 7 km (Sun *et al.*^[34]).

Based on the observations from a longitudinal chain and a latitudinal chain of ionosondes including three ionosondes in CMP, Tang *et al.*^[35] investigated the Es occurrence rate and variation. It was found that the occurrence rate of Es at the American sector is lower than that at European and Asian sectors; the seasonal variations of Es occurrence and strength are related to the annual variation of meteor counts; aside from the impact of planetary waves in the MLT region, solar and geomagnetic activities can contribute to the periodic oscillations in the Es layer variations as well. Tang *et al.*^[36] used observations of ionosodes and meteor radars to study the mechanism of middle- and low-latitude Es layer formation. It is shown that Es layer can form at low-latitude non-wind shear points as well, and its formation can be affected by the turbo-pause at 90–105 km.

2.3 Observations and Researches on Polar Region Ionosphere

The Earth's polar region is its natural window to the space. The magnetic field lines are highly aggregated and nearly open to space vertically. Therefore, the

high-energy particles from solar wind can directly “hit” the atmosphere over the Earth’s north and south poles, where auroras light up. Various dynamic processes caused by the interaction between the solar wind and the Earth’s magnetosphere can be directly mapped to the polar ionosphere, which makes the processes of plasma precipitation and transportation in the polar ionosphere complex, and is accompanied by many irregular structures there. Polar cap patch is the most common irregularity in the polar ionosphere.

2.3.1 Space Hurricane

Zhang *et al.*^[37] discovered a hurricane-like phenomena above the ionosphere around the Earth’s magnetic north pole under low solar and otherwise low geomagnetic activity, and named it “space hurricane”. They found the space hurricane has similar characteristics to the typhoon or hurricane in the lower atmosphere: a coincident cyclone-shaped aurora, strong circular horizontal plasma flow with shears, a nearly zero-flow center, enhanced electron temperature, ion upflows, a circular magnetic field perturbation, and strong electron precipitations, *etc.* The observations and simulations revealed that the space hurricane is generated by steady high-latitude lobe magnetic reconnection and current continuity under extremely quiet conditions.

2.3.2 Observations of the Polar Ionosphere and Aurora

The monitoring instruments deployed by the CMP in the polar region provide effective means for the study of the polar ionosphere. Based on the satellite observations and the ground observations from Zhongshan Station in Antarctica, along with the 3D MHD simulation, Zhang *et al.*^[38] reported that unusually bright and multiple Transpolar Auroral Arcs (TPAs) appear in the polar cap region of Antarctica when the Interplanetary Magnetic Field (IMF) is northward and geomagnetic activity is quiet. These multiple TPAs are generated by precipitating energetic magnetospheric electrons within Field-Aligned Current (FAC) sheets. These FAC sheets are generated by multiple-flow shear sheets in both the magnetospheric boundary and the plasma sheet. Their study offers a new insight into the complex solar wind-magnetosphere-ionosphere coupling processes under a northward IMF.

There are many kinds of irregularities in the polar ionosphere. It is particularly important to investigate the formation mechanism and evolution characteristics of these large-scale irregularities. Wang *et al.*^[39] developed a new method named Total Electron Content (TEC) ke-

ogram based on a movie of TEC maps. A clear train of polar cap patches was identified from the TEC keogram and confirmed by SuperDARN radar observations. This tool offers a powerful tool for monitoring and studying large-scale plasma irregularities in the polar ionosphere. The structure and evolution of polar ionospheric irregularities show closely dependence on solar and geomagnetic activity. Zhang *et al.*^[40] presented a statistical survey of polar cap patches in relation to solar and geomagnetic activity. They found that the occurrence of cold patches is obviously dependent on solar and geomagnetic activity, while hot patches do not show such dependence. It was also found that the spatial size of both cold and hot patches decreases (increases) with solar (geomagnetic) activity. The poleward expansion of the active aurora region following substorm auroral onset is often associated with a bulge region that expands westward and forms the westward travelling surge. Ma *et al.*^[41] observed two surge events to study the relationship between the surge and ionospheric flows that likely have polar cap origin. They first demonstrated that the flow of polar cap origin, which maps to underlying processes in the magnetotail, may play a crucial role in the formation and development of the westward travelling surge.

2.4 Responses of Geospace to Solar Activities

2.4.1 Influence of Solar Radiation Variation on Magnetosphere

The solar wind plays an important role on the Earth’s magnetosphere, but it is unclear whether the same holds for solar flares. Liu *et al.*^[42] and Liu *et al.*^[43] have studied the effects of flares on the Earth’s magnetospheric dynamics and the magnetosphere-ionosphere electrodynamic coupling. Their studies showed that the ionospheric conductance sharply increases with the enhanced solar radiation. The increased ionospheric conductance reduces the efficiency of mechanical energy conversion in the dayside solar wind-magnetosphere interaction, resulting in less Joule heating of the Earth’s upper atmosphere, a reconfiguration of magnetosphere convection, as well as changes in dayside and nightside auroral precipitation. Their works demonstrate that solar flare effects extend throughout the geospace via electrodynamic coupling.

2.4.2 Influence of Solar and Geomagnetic Activities on Ionosphere

The mid and low latitude ionosphere shows complex

responses to the geomagnetic storm and solar flare. Using multiple measurements of Beidou Geostationary Orbit (GEO) satellite and MIT Madrigal Total Electron Contents (TECs), ionosondes, magnetometers, and Global Ultraviolet Imager, Li *et al.*^[44] reported that the daytime ionosphere displayed strong positive rather than negative storms at multiple longitude sectors in the mid- and low-latitudes during the recovery phase of August 2018 geomagnetic storm. They revealed that the enhanced upward vertical plasma drifts make an important contribution to the positive storm, while the drifts could not be driven by the common storm-induced source. Using aurora, high-latitude convection, potential data sets from DMSP satellite and SuperDARN radar combined with model simulation, Ren *et al.*^[45] further disclosed that high-speed solar wind stream was a possible but not the main driver to the mid- and low-latitude ionospheric positive storm during the August 2018 geomagnetic storm recovery phase. Using Beidou GEO TECs at 4 stations of the 120°E longitudinal chain of CMP, Jimoh *et al.*^[46] statistically disclosed the occurrence characteristics of the daytime TEC enhancements during geomagnetic storm and quiet geomagnetic conditions. The TEC enhancements displayed a preference for the September equinox and December solstice at the middle and low latitudes, respectively. Moreover, the occurrence during the main phase of geomagnetic storms was significantly above the TEC enhancement baselines, while it exhibited recurrence of TEC enhancements during the recovery phases. Owolabi *et al.*^[47] compared the global ionospheric currents in response to X9.33 disk and X8.28 limb solar flares, using the ground-based magnetometer data. They showed that the ionospheric currents displayed an asymmetrical pattern though the flares happened in equinox. The total current intensity changes are stronger in X8.28 than in X9.33 flare, although X9.33 flare has much more solar flux. The enhanced ionospheric conductance along with the associated electric field changes result in the observed ionospheric current variations during the flares. The longitudinal variations of the magnetic field and the seasonal effect could also play an important role.

2.4.3 Ionospheric Changes Caused by Solar Eclipse Sudden changes in solar radiation caused by instantaneous solar activities such as solar eclipses and solar flares will significantly affect the solar radiation reaching the Earth. The change of solar radiation is the most important driving force of ionospheric change. Chinese

scientists studied the responses of ionosphere to the annular eclipse on 21 June 2020. Zhang *et al.*^[48] investigated the ionospheric responses to the 21 June 2020 annular solar eclipse using the ionosondes and GNNS-TEC data from the CMP. The results revealed that the ionospheric responses to the eclipse are not only restricted in the Moon's shadow, but also in the conjugated hemisphere, which is suggested to be due to the coupling effect from the electric field, neutral wind, thermal conduction, and interhemispheric photoelectron transport. In addition, Huang *et al.*^[49] further investigated the low-latitude ionospheric responses to the annular solar eclipse using the Beidou GEO TEC and ionosondes data from the CMP and in-situ N_e and T_e in SWARM and CSES satellites. They found that the TEC evidently decreases with the obscuration and undergoes a considerable decrease in the EIA region in the conjugate hemisphere. The TEC and N_e at low latitudes showed a long-lasting response for over 7 h. after the eclipse. The relevant TEC and N_e changes could be attributed to the obscuration rate and the eclipse induced perturbations of dynamic processes.

2.4.4 Effects of Geomagnetic Storms on Ground-based Instruments

During geomagnetic storms, the drastic change of geomagnetic field induces an electric field on the ground, driving currents in long-distance conductive ground-based systems, such as power grids, pipelines, and railway systems. The currents are named as Geomagnetically Induced Currents (GICs). Large GICs can pose a threat to those ground-based instruments. The study of GICs events has become the research hotspot in space weather over recent years. The geomagnetic and geoelectric field data of the CMP provide powerful support to the GICs research including its measurement, modeling, forecasting, and hazards assessment, *etc.*

Zhang *et al.*^[50] studied the GICs characteristics at a Chinese low-latitude substation during geomagnetic storms. They then built a physical-based model to simulate the GICs at the low-latitude substation during storms. The model can capture the main active periods and strength of the GICs during the storms compared with the measurement. Its performance is better than the persistence model.

2.5 Progress on the Method of Detection and Data Processing

In recent years, a number of ground-based space envi-

ronment monitoring systems have been completed or put into construction (such as the second phase of CMP), which provide monitoring data support for the research of key scientific problems of space physics and the prediction of key parameters of space weather over China. In the last two years, with the rapid development of detection facilities, detection methods and data processing methods have also made remarkable progress. Based on the Ensemble Kalman filter data assimilation system, He *et al.*^[51] evaluated the effect of different radio observation systems on the nowcasting and forecasting of key ionospheric parameters (such as TEC and three-dimensional electron density) over China and the adjacent region. Xu *et al.*^[52] proposed a method for retrieving the Perceptible Water Vapor (PWV) along the line of sight toward the science target using the OH (8–3) band airglow spectrum. To verify the method of PWV retrieval, they made cross comparisons between the PWV retrieved from OH airglow and PWV from the standard star spectra of Ultraviolet and Visual Echelle Spectrograph (UVES). Kong *et al.*^[53] proposed a post-processing scheme to infer the electronic characteristic energy of the aurora based on the spectral data of ground-based auroral spectroscopic imager located in Antarctica Zhongshan station. In order to improve the inference rate, classical brute-force, recursive brute-force and self-consistent approximation strategies have been adopted successively. The inferred characteristic energies are compared to the average energies calibrated from the relevant electron data detected by the particle detectors SSJ5 on the DMSP satellite to prove the effectiveness of the inference model. These two energy estimations about auroral electrons show a strong linear relationship. It sheds light on further applications of the valuable aurora spectral data.

3 Summary and Prospect

In this report, we review the highlight studies done by scientists in the past two years using the monitoring data of the first phase of CMP. As the first and only national major scientific and technological infrastructure in the field of space environment monitoring in China, the CMP has already operated stably and efficiently for ten years, produced a series of high-quality monitoring data, met the major strategic needs of space weather forecasting for major space activities in China, and also provided strong support for the frontier scientific re-

search of space physics. In 2019, the Chinese government supported the construction of the second phase of CMP. The second phase is expected to be completed by the end of 2023 and put into formal operation. At that time, the first phase of the project will be fully integrated into the second phase. The CMP will operate as a whole, and continue to contribute to China's cutting-edge scientific and technological innovation in the field of space science and even interdisciplinary disciplines.

Acknowledgments

Thanks to WU Kun, HU Lianhuan, HUANG Fuqing, LI Qiaoling, and LIU Weijun for their helps.

References

- [1] CHENG C, YI F. Falling mixed-phase ice virga and their liquid parent cloud layers as observed by ground-based lidars[J]. *Remote Sensing*, 2020, **12**(13): 2094
- [2] WANG W, YI F, LIU F C, *et al.* Characteristics and seasonal variations of cirrus clouds from polarization lidar observations at a 30°N plain site[J]. *Remote Sensing*, 2020, **12**(23): 3998
- [3] QIU S C, WANG N, SOON W, *et al.* The sporadic sodium layer: a possible tracer for the conjunction between the upper and lower atmospheres[J]. *Atmospheric Chemistry and Physics*, 2021, **21**(15): 11927-11940
- [4] GERDING M, DALY S, PLANE J M C. Lidar soundings of the mesospheric nickel layer using Ni(³F) and Ni(³D) transitions[J]. *Geophysical Research Letters*, 2019, **46**(1): 408-415
- [5] ZOU X, WANG J H, LI F Q, *et al.* Atmospheric turbulence spectrum in high resolution mode detected by a high power-aperture sodium lidar over Yanqing, Beijing (40.47°N, 115.97°E)[J]. *Journal of Quantitative Spectroscopy and Radiative Transfer*, 2021, **270**: 107706
- [6] ZHANG W F, CHEN G, ZHANG S D, *et al.* Statistical study of the mid-latitude mesospheric vertical winds observed by the Wuhan and Beijing MST radars in China[J]. *Journal of Geophysical Research: Atmospheres*, 2020, **125**(18): e2020JD032776
- [7] LI N, LUAN X L, LEI J H, *et al.* Variations of mesospheric neutral winds and tides observed by a meteor radar chain over China during the 2013 sudden stratospheric warming[J]. *Journal of Geophysical Research: Space Physics*, 2020, **125**(5): e2019JA027443
- [8] GONG Y, XUE J W, MA Z, *et al.* Strong quarter diurnal tides in the mesosphere and lower thermosphere during the 2019 Arctic sudden stratospheric warming over Mohe, China[J]. *Journal of Geophysical Research: Space Physics*, 2021, **126**(10): e2020JA029066
- [9] LUO J H, GONG Y, MA Z, *et al.* Study of the quasi 10-day waves in the MLT region during the 2018 February SSW by a meteor radar chain[J]. *Journal of Geophysical Research: Space Physics*, 2021, **126**(3): e2020JA028367
- [10] MA Z, GONG Y, ZHANG S D, *et al.* Study of a Quasi 4-day oscillation during the 2018/2019 SSW over Mohe, China[J]. *Journal of Geophysical Research: Space Physics*, 2020, **125**(7): e2019JA027687

- [11] HUANG F Q, LEI J H, ZHANG R L, *et al.* Prominent daytime TEC enhancements under the quiescent condition of January 2017[J]. *Geophysical Research Letters*, 2020, **47**(14): e2020GL088398
- [12] LIU J, ZHANG D H, HAO Y Q, *et al.* Multi-instrumental observations of the quasi-16-day variations from the lower thermosphere to the topside ionosphere in the low-latitude eastern Asian sector during the 2017 sudden stratospheric warming event[J]. *Journal of Geophysical Research: Space Physics*, 2020, **125**(3): e2019JA027505
- [13] MO X H, ZHANG D H. Six-day periodic variation in equatorial ionization anomaly region[J]. *Journal of Geophysical Research: Space Physics*, 2020, **125**(11): e2020JA028225
- [14] JIANG G Y, XIONG C, STOLLE C, *et al.* Comparison of thermospheric winds measured by GOCE and ground-based FPIs at low and middle latitudes[J]. *Journal of Geophysical Research: Space Physics*, 2021, **126**(2): e2020JA028182
- [15] LIU X, XU J Y, YUE J, *et al.* Global balanced wind derived from SABER temperature and pressure observations and its validations[J]. *Earth System Science Data*, 2021, **13**(12): 5643-5661
- [16] LIU L, DING Z H, LE H J, *et al.* New features of the enhancements in electron density at low latitudes[J]. *Journal of Geophysical Research: Space Physics*, 2020, **125**(2): e2019JA027539
- [17] LIU L B, DING Z H, ZHANG R L, *et al.* A case study of the enhancements in ionospheric electron density and its longitudinal gradient at Chinese low latitudes[J]. *Journal of Geophysical Research: Space Physics*, 2020, **125**(5): e2019JA027751
- [18] LI W B, CHEN Y D, LIU L B, *et al.* A statistical study on the winter ionospheric nighttime enhancement at middle latitudes in the Northern Hemisphere[J]. *Journal of Geophysical Research: Space Physics*, 2020, **125**(7): e2020JA027950
- [19] CHEN G, WANG Z H, JIN H, *et al.* A case study of the daytime intense radar backscatter and strong ionospheric scintillation related to the low-latitude E-region irregularities[J]. *Journal of Geophysical Research: Space Physics*, 2020, **125**(7): e2019JA027532
- [20] SUN W J, NING B Q, HU L H, *et al.* The evolution of complex E_s observed by multi instruments over low-latitude China[J]. *Journal of Geophysical Research: Space Physics*, 2020, **125**(8): e2019JA027656
- [21] HU L H, ZHAO X K, SUN W J, *et al.* Statistical characteristics and correlation of low-latitude F region bottom-type irregularity layers and plasma plumes over Sanya[J]. *Journal of Geophysical Research: Space Physics*, 2020, **125**(8): e2020JA027855
- [22] ZHAO X K, XIE H Y, HU L H, *et al.* Climatology of equatorial and low-latitude F region kilometer-scale irregularities over the meridian circle around 120°E/60°W[J]. *GPS Solutions*, 2021, **25**(1): 20
- [23] XIE H Y, LI G Z, ZHAO X K, *et al.* Coupling between E region quasi-periodic echoes and F region medium-scale traveling ionospheric disturbances at low latitudes[J]. *Journal of Geophysical Research: Space Physics*, 2020, **125**(5): e2019JA027720
- [24] HU L H, LEI J H, SUN W J, *et al.* Latitudinal variations of daytime periodic ionospheric disturbances from Beidou GEO TEC observations over China[J]. *Journal of Geophysical Research: Space Physics*, 2021, **126**(3): e2020JA028809
- [25] SUN L C, XU J Y, ZHU Y J, *et al.* Interaction between a south-westward propagating MSTID and a poleward moving WSA-like plasma patch on a magnetically quiet night at midlatitude China region[J]. *Journal of Geophysical Research: Space Physics*, 2020, **125**(10): e2020JA028085
- [26] XU J Y, LI Q Z, SUN L C, *et al.* The ground-based airglow imager network in China: recent observational results[M]/WANG W B, ZHANG Y L, PAXTON L J. Upper Atmosphere Dynamics and Energetics. American Geophysical Union, 2021: 365-394
- [27] WU K, XU J Y, WANG W B, *et al.* Interaction of oppositely traveling medium-scale traveling ionospheric disturbances observed in low latitudes during geomagnetically quiet nighttime[J]. *Journal of Geophysical Research: Space Physics*, 2021, **126**(2): e2020JA028723
- [28] WU K, XU J Y, ZHU Y J, *et al.* Ionospheric plasma vertical drift and zonal wind variations cause unusual evolution of EPBs during a geomagnetically quiet night[J]. *Journal of Geophysical Research: Space Physics*, 2021, **126**(12): e2021JA029893
- [29] SUN L C, XU J Y, ZHU Y J, *et al.* Interaction between an EM-STID and an EPB in the EIA Crest Region over China[J]. *Journal of Geophysical Research: Space Physics*, 2021, **126**(8): e2020JA029005
- [30] LUO J, XU J Y, WU K, *et al.* The influence of ionospheric neutral wind variations on the morphology and propagation of medium scale traveling ionospheric disturbances on 8th August 2016[J]. *Journal of Geophysical Research: Space Physics*, 2021, **126**(6): e2020JA029037
- [31] YU B K, XUE X H, SCOTT C J, *et al.* Interhemispheric transport of metallic ions within ionospheric sporadic E layers by the lower thermospheric meridional circulation[J]. *Atmospheric Chemistry and Physics*, 2021, **21**(5): 4219-4230
- [32] YU B, SCOTT C J, XUE X H, *et al.* A signature of 27-day solar rotation in the concentration of metallic ions within the terrestrial ionosphere[J]. *The Astrophysical Journal*, 2021, **916**(2): 106
- [33] SUN W, ZHAO X, HU L, *et al.* Morphological characteristics of thousand-kilometer-scale Es structures over China[J]. *Journal of Geophysical Research: Space Physics*, 2021, **126**(2): e2020JA028712
- [34] SUN W J, HU L H, YANG Y Y, *et al.* Occurrences of regional strong E_s irregularities and corresponding scintillations characterized using a high-temporal-resolution GNSS network[J]. *Journal of Geophysical Research: Space Physics*, 2021, **126**(11): e2021JA029460
- [35] TANG Q, ZHAO J Q, YU Z B, *et al.* Occurrence and variations of middle and low latitude sporadic E layer investigated with longitudinal and latitudinal chains of ionosondes[J]. *Space Weather*, 2021, **19**(12): e2021SW002942
- [36] TANG Q, ZHOU C, LIU H X, *et al.* The possible role of turbopause on sporadic-E layer formation at middle and low latitudes[J]. *Space Weather*, 2021, **19**(12): e2021SW002883
- [37] ZHANG Q H, ZHANG Y L, WANG C, *et al.* A space hurricane over the Earth's polar ionosphere[J]. *Nature Communications*, 2021, **12**(1): 1207
- [38] ZHANG Q H, ZHANG Y L, WANG C, *et al.* Multiple transpolar auroral arcs reveal insight about coupling processes in the Earth's magnetotail[J]. *Proceedings of the National Academy of Sciences of the United States of America*, 2020, **117**(28): 16193-16198
- [39] WANG Y, ZHANG Q H, MA Y Z, *et al.* Polar ionospheric large-scale structures and dynamics revealed by TEC keogram extracted from TEC maps[J]. *Journal of Geophysical Research: Space Physics*, 2020, **125**(1): e2019JA027020
- [40] ZHANG D, ZHANG Q H, MA Y Z, *et al.* Solar and geomagnetic activity impact on occurrence and spatial size of cold and hot polar cap patches[J]. *Geophysical Research Letters*, 2021, **48**(18): e2021GL094526
- [41] MA Y Z, ZHANG Q H, LYONS L R, *et al.* Is westward travelling surge driven by the polar cap flow channels?[J]. *Journal of Geo-*

- physical Research: Space Physics*, 2021, **126**(8): e2020JA028498
- [42] LIU J, WANG W B, QIAN L Y, *et al.* Solar flare effects in the Earth's magnetosphere[J]. *Nature Physics*, 2021, **17**(7): 807-812
- [43] LIU J, QIAN L Y, MAUTE A, *et al.* Electrodynamical coupling of the geospace system during solar flares[J]. *Journal of Geophysical Research: Space Physics*, 2021, **126**(1): e2020JA028569
- [44] LI Q L, HUANG F Q, ZHONG J H, *et al.* Persistence of the long-duration daytime TEC enhancements at different longitudinal sectors during the August 2018 geomagnetic storm[J]. *Journal of Geophysical Research: Space Physics*, 2020, **125**(11): e2020JA028238
- [45] REN D X, LEI J H, ZHOU S, *et al.* High-speed solar wind imprints on the ionosphere during the recovery phase of the August 2018 geomagnetic storm[J]. *Space Weather*, 2020, **18**(7): e2020SW002480
- [46] JIMOH O, LEI J H, HUANG F Q. Investigation of daytime total electron content enhancements over the Asian-Australian sector observed from the Beidou geostationary satellite during 2016–2018[J]. *Remote Sensing*, 2020, **12**(20): 3406
- [47] OWOLABI C, LEI J H, BOLAJI O S, *et al.* Ionospheric current variations induced by the solar flares of 6 and 10 September 2017[J]. *Space Weather*, 2020, **18**(11): e2020SW002608
- [48] ZHANG R L, LE H J, LI W B, *et al.* Multiple technique observations of the ionospheric responses to the 21 June 2020 solar eclipse[J]. *Journal of Geophysical Research: Space Physics*, 2020, **125**(12): e2020JA028450
- [49] HUANG F Q, LI Q L, SHEN X H, *et al.* Ionospheric responses at low latitudes to the annular solar eclipse on 21 June 2020[J]. *Journal of Geophysical Research: Space Physics*, 2020, **125**(10): e2020JA028483
- [50] ZHANG J J, YU Y Q, WANG C, *et al.* Measurements and simulations of the geomagnetically induced currents in low-latitude power networks during geomagnetic storms[J]. *Space Weather*, 2020, **18**(8): e2020SW002549
- [51] HE J H, YUE X, HU L, *et al.* Observing system impact on ionospheric specification over China using EnKF assimilation[J]. *Space Weather*, 2020, **18**(10): e2020SW002527
- [52] XU J Y, LIU W J, BIAN J C, *et al.* Method for retrieval of atmospheric water vapor using OH airglow for correction of astronomical observations[J]. *Astronomy & Astrophysics*, 2020, **639**: A29
- [53] KONG W Q, HU Z J, WU J J, *et al.* A comparative study of estimating auroral electron energy from ground-based hyperspectral imagery and DMSP-SSJ5 particle data[J]. *Remote Sensing*, 2020, **12**(14): 2259

Progress of International Meridian Circle Program*

LIU William¹, MICHEL Blanc¹, WANG Chi¹, XU Jiyao¹,
LI Hui¹, REN Liwen¹, LIU Zhengkuan¹, ZHU Yajun¹,
LI Guozhu², LI Lei¹, ZEREN Zhima³, YANG Fang¹

1. National Space Science Center, Chinese Academy of Sciences, Beijing 100190
2. Institute of Geology and Geophysics, Chinese Academy of Sciences, Beijing 100083
3. National Institute of Natural Hazards, Ministry of Emergency Management of China, Beijing 100085

Abstract

Based on the Chinese Meridian Project (CMP), the International Meridian Circle Program (IMCP) aims to coordinate the deployment of a comprehensive ground-based monitoring network along the 120°E–60°W Great Meridian Circle to track the propagation and evolution of space weather events from the Sun to the Earth, as well as the imprints of other major natural and anthropic hazards on the ionosphere, the middle and upper atmosphere. Currently, we have completed the IMCP headquarters building in Beijing and established the China-Brazil Joint Laboratory for Space Weather in cooperation with Brazil. Meanwhile, the Chinese Meridian Project Phase II and different components of the IMCP observation system are under construction.

Key words

Chinese Meridian Project (CMP), Ionospheric observation, Middle and upper atmosphere, International Meridian Circle Program (IMCP)

1 Concept, Objectives and Implementation

The International Meridian Circle Program (IMCP) is a major international program led by the Chinese Academy of Sciences to deploy, integrate and operate a global network of monitoring instruments, primarily along the 120°E–60°W great meridian circle. This globally distributed network, coordinated with satellite observations, will provide a comprehensive three-dimensional representation of key geospace parameters across all

latitudes over each diurnal cycle, making it possible to investigate the imprints of energy inputs from the Sun into the Earth on the Ionosphere, Middle and Upper Atmosphere (IMUA), and to quantitatively assess the threats to the human society due to the different types of natural and anthropic hazards.

Based on the deployment of a globally distributed ground-based monitoring and research network observing the IMUA, the IMCP is to study Earth's geospace and its different coupled layers as a whole system. In this way, IMCP aims to reveal several key scientific questions: How do interplanetary disturbances (up-

* Supported by the International Partnership Program of Chinese Academy of Sciences (183311KYSB20200003)

Received May 27, 2022

stream disturbances) influence the solar-terrestrial environment? How do they disturb the atmospheric system at different altitudes and latitudes, and how do the responses in different atmospheric regions couple with each other? At the same time, how do disturbances generated internally in the Earth system (bottom disturbances, *e.g.*, long-term variations of the geomagnetic field and the climate, earthquakes, severe weather events) propagate to the IMUA? What characteristic imprints do they leave on it?

One of the major parts of the IMCP observing system is the Chinese Meridian Project, a ground-based space environment monitoring facility funded by the National Development and Reform Commission of China with 1.5 billion yuan whose construction started in 2008. In 2012, the first phase of the Chinese Meridian project started operation. By 2021, more than 8 TB of monitoring data with 64 kinds of space environment parameters have been collected. After the completion of the second phase of the Chinese Meridian Project in 2024, it will form a two-cross enhanced and more powerful space weather monitoring network over China.

The IMCP will also rely on a space-based satellite—the CAS-ESA Solar wind Magnetosphere Ionosphere Link Explorer (SMILE, scheduled to be launched in 2024). The cooperation of these two projects makes it possible to link the solar wind-magnetosphere interaction (driving source, observed by SMILE) to the ionospheric responses (observed by the ground-based IMCP), to follow the whole process of energy transfer from the interplanetary space to the geospace and to monitor the global responses of the terrestrial environment to solar energy inputs.

2 Major Achievements

We describe below several major achievements in IMCP development during the reporting period.

2.1 Western Hemisphere-Brazil

As the first step of the international cooperation of IMCP, the China-Brazil Joint Laboratory for Space Weather (CBJLSW) has passed the acceptance of the first-phase construction and started its second-phase construction.

Since Brazil is in the low-latitude region of the southern hemisphere and at 60° west longitude, joint detection and analysis of events by CBJLSW and CMP teams make it possible to investigate day-night and in-

ter-hemispheric contrasts in the response of the terrestrial environment to interplanetary disturbances.

So far, the CBJLSW has built a data center in South America with a storage capacity of up to 200 TB, as well as a Potassium-Sodium dual-wavelength Lidar, Digisonde, GPS-TEC ionospheric scintillator, and Magnetometer. In the second phase, a total of 16 sets of space environment monitoring equipment, including geomagnetic, radio, and optical, will be further deployed to detect geomagnetism and geoelectricity parameters, the density, temperature, and wind field of middle and upper atmospheric, ionospheric electron density and concentration, as well as solar wind events over South America, see Fig. 1. CBJLSW supports space science research in South America, revealing the characteristics of the atmosphere and ionosphere in the western hemispheres in low latitudes, and their relationship with global space weather processes.

At the same time, Both China and Brazil attach great importance to talent training and joint research, jointly training 27 postdoctoral fellows and publishing 64 scientific papers such as the JGR journal. The construction of the CBJLSW has been incorporated in the cooperation agreement between China and Brazil and listed as a key cooperation project in 2015 and 2018.

2.2 Eastern Hemisphere-Southeast Asia

Southeast Asia is at low geomagnetic latitudes, south of the CMP network along about 120°E. This region is characterized by strong convective weather and a special magnetic field configuration. Joint monitoring of space weather events by CMP and Southeast Asia networks makes it possible to track their propagation along this meridian.

At present, we cooperate with the National Astronomical Research Institute of Thailand, Telkom University (Indonesia), the Hydrographic Bureau of Laos, to build three observation networks: Ionospheric Observation Network for Irregularity and Scintillation in East/Southeast Asia (IONISE), China-Southeast Asia Upper Atmosphere Double Airglow Observation Network, and APSCO Geomagnetic Observation Network.

2.3 Ionospheric Observation Network for Irregularity and Scintillation in East/Southeast Asia (IONISE)

IONISE mainly includes three crossed chains of GNSS TEC/scintillation receivers, which can track Beidou



Fig. 1 CBJLSW Stations

geostationary satellite signals along 110°E, 23°N, and 40°N respectively, multi-static portable digital ionosondes (which can be operated to obtain Doppler ionograms with a time interval less than 1 min for vertical and oblique observations), and VHF radars equipped with beam steering and providing multi-baseline imaging observations (see Fig. 2).

The scientific objectives of IONISE are (i) to trace the occurrence and movements of ionospheric irregularities producing GNSS loss-of-lock and scintillations, (ii) to capture ionospheric disturbances of various scales produced by natural sources *e.g.*, low atmosphere activity, geomagnetic activity, and earthquakes, and (iii) to reveal extremely large gradients of background ionosphere over southern China and adjacent regions.

2.4 China-Southeast Asia Upper Atmosphere Double Airglow Observation Network

The double-layer airglow observation network of the middle and upper atmosphere is deployed mainly along

the 100°E meridian in Southeast Asia, starting from the equator to northward, and consists of 15 OH (87 km) airglow observation stations and 12 OI red-line (250 km) airglow observation stations (see Fig. 3).

The network provides an advantage for studying the propagation and evolution of atmospheric waves ranging from several kilometers to thousands of kilometers in the horizontal and vertical directions, as well as coupling processes of atmospheric waves between different regions of the atmosphere.

2.5 APSCO Geomagnetic Observation Network

The APSCO Geomagnetic Observation Network, mainly based on the APSCO seismic observation project, is to build several geomagnetic stations in seven APSCO member countries, namely Thailand, Bangladesh, Pakistan, Iran, Turkey, Mongolia, and Peru. Such a network can provide the geomagnetic data for comparative study with the magnetic field at the Sun-synchronous orbit by China Seismo-Electromagnetic Satellite (see Fig.4).

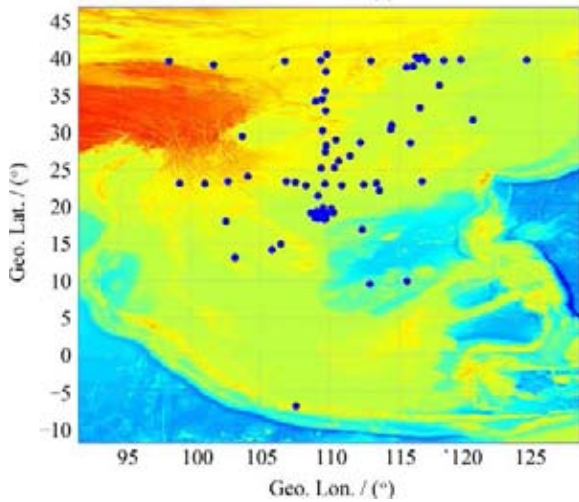


Fig. 2 IONISE stations

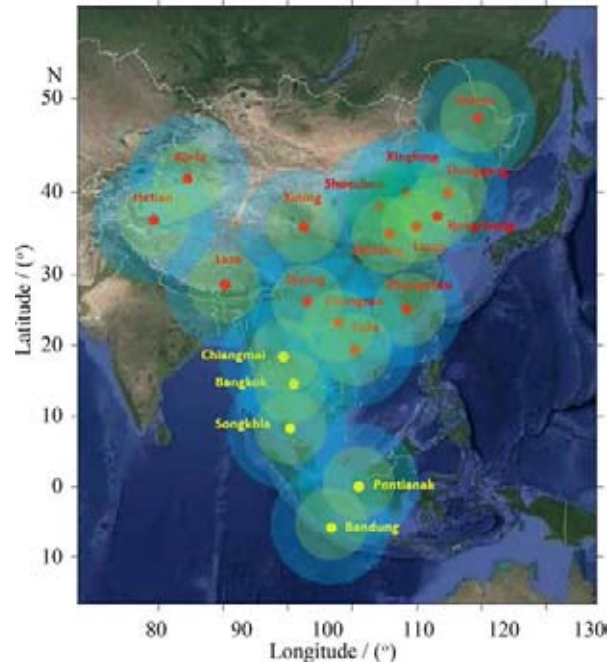


Fig. 3 China-Southeast Asia double-layer airglow observation network of the middle and upper atmosphere



Fig. 4 APSCO geomagnetic observation network

3 Conclusions and Perspectives

In the coming years, we will continue to focus on the 120°E–60°W meridian circle, its broad coverage of land facilitates and deployment of the instrument networks. In addition, we will also discuss and plan with additional international partners a secondary circle, *i.e.*, the 30°E–150°W meridian circle, to capture the significant longitudinal variations of hazard sources induced by land-ocean contrasts and by the geographic longitudinal asymmetries of the geomagnetic field.

References

- [1] LIU W, BLANC M and 34 co-authors. Science Objectives and Observation System for the International Meridian Circle Taikong IS-SI-Beijing[Z/OL]. 2020: 19. <https://www.issibern.ch/wp-content/uploads/2021/03/Taikong19.pdf>
- [2] LIU W L, WANG C, SHEN X H, et al. International meridian circle program[J]. *Chinese Journal of Space Science*, 2020, 40(5): 723-725
- [3] WANG C. New chains of space weather monitoring stations in China[J]. *Space Weather*, 2010, 8: S08001. DOI: 10.1029/2010SW000603
- [4] WANG C, BRANDUARDI-RAYMOND G. Progress of solar wind magnetosphere ionosphere link explorer (SMILE) mission[J]. *Chinese Journal of Space Science*, 2018, 38(5): 657-661
- [5] SUN W J, WU B Y, WU Z, et al. IONISE: an ionospheric observational network for irregularity and scintillation in east and southeast Asia[J]. *Journal of Geophysical Research: Space Physics*, 2020, 125(8): e2020JA028055. DOI: 10.1029/2020JA028055

Part IV: Research Progress of Space Science Disciplines

Space Astronomy

ZHANG Shuangnan, YI Shuxu

Institute of High Energy Physics, Chinese Academy of Sciences, Beijing 100049

Abstract

This chapter reports the recent progress on the space astronomy missions of China, including the following missions: currently operating in orbit, *e.g.*, DAMPE, Insight-HXMT, GECAM, PolarLight, GRID and Lobster-eye X-ray Satellite; approved and under development for launch in the next a couple of years, *e.g.*, SVOM and EP; planned experiments to be onboard China's Space Station in the next several years, *e.g.*, CSST, HERD, POLAR-2, DIXE and LyRIC; candidate missions that have passed the first round of review of Strategy Priority Program on space science (III) of the Chinese Academy of Sciences, *e.g.*, eXTP, DAMPE-2, Earth 2.0, DSL and CHES.

Key words

Space science, Space astronomy, Satellite, Space station

1 Introduction

This chapter reports the recent progress on the space astronomy missions of China. It covers the space astronomy projects in the following four categories: (i) missions currently operating in orbit; (ii) approved and under development for launch in the next a couple of years; (iii) planned experiments to be onboard China's Space Station in the next several years; (iv) candidate missions that have passed the first round of review of Strategy Priority Program on space science (III) of the Chinese Academy of Sciences. The brief introduction to each mission/project is summarized in Table 1.

2 DAMPE: DARK MATTER PARTICLE EXPLORER

Launch time: It was launched on 17 December 2015.

2.1 Scientific Goals

DAMPE is a high energy cosmic-ray and gamma-ray

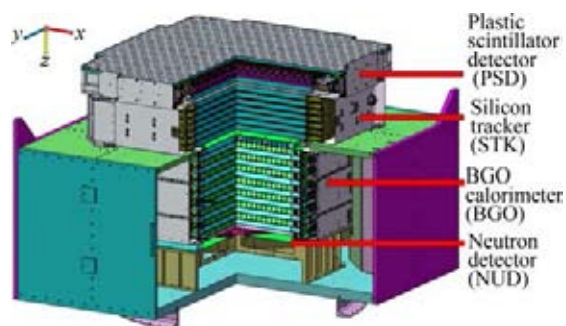
observatory aiming to study cosmic-ray physics, to probe the nature of dark matter, and to detect high energy gamma-ray emissions from astronomic sources.

2.2 DAMPE Detector

Fig.1 shows a schematic DAMPE detector, consisting of a Plastic Scintillator strip Detector (PSD), a Silicon-Tungsten tracker-converter (STK), a BGO imaging calorimeter and a Neutron Detector (NUD). The PSD provides charged-particle background rejection for gamma rays and measures the charge of incident cosmic rays; the STK measures the charges and the trajectories of charged particles, and allows to reconstruct the directions of incident gamma-rays that have been converted into electron/positron pairs mainly in the tungsten layers; the hodoscopic BGO calorimeter, with a total depth of about 32 radiation lengths, allows to measure the energy of incident particles with high resolution and to provide efficient electron/hadron identification; finally, the NUD provides a further improvement of the electron/hadron discrimination.

Table 1 Summary of space astronomy missions/projects of China. Phase A-Feasibility; Phase B-Preliminary Definition/Design; Phase C-Detailed Definition/Design; Phase D-Qualification and Flight Model

Name of project	Launch time	Status	Category
DAMPE	17 Dec. 2015	In orbit	1
Insight-HXMT	15 Jun. 2017	In orbit	1
GECAM	9 Dec. 2020	In orbit	1
PolarLight	29 Oct. 2018	In orbit	1
GRID	29 Oct. 2018 (GRID-01), 6 Nov. 2020 (GRID-02), 27 Feb. 2022 (GRID-03b and GRID-04)	In orbit	1
Lobster-eye X-ray Satellite	2020 Jul. 25	In orbit	1
SVOM	2023	Phase D	2
EP	2023	Phase D	2
CSST	2023/2024	Phase C	2
HERD	2027	Phase B	3
POLAR-2	2024 (European payload) 2025 (Chinese payload)	Early Phase D (European Payload) Phase B (Chinese Payload)	3
DIXE	–	Phase A	3
LyRIC	2025+	Phase A	3
eXTP	2027	Phase B	4
DAMPE-2	2025–2026 (suggested)	–	4
Earth2.0	TBD		4
DSL	2026	Phase A	4
CHES	TBD	–	4

**Fig. 1** Schematic drawing of the DAMPE detector (from Chang *et al.*^[1])

2.3 Main Scientific Results

(1) DAMPE has measured the Cosmic Ray Electron (CRE) plus positron spectrum in the energy range 25 GeV to 4.6 TeV with unprecedentedly high energy resolution and low background. The major part of the spectrum can be well fitted by a smoothly broken power-law model rather than a single power-law model. There is a sharp spectral break at about 0.9 TeV, which clarifies the behavior of the CRE spectrum at energies above 1 TeV and sheds light on the physical origin of the sub-TeV CREs^[2].

(2) DAMPE has directly measured the cosmic ray proton fluxes with kinetic energies from 40 GeV to 100 TeV. In addition to confirming the spectral hardening at about 300 GeV found by previous experiments, DAMPE reveals a softening at about 13.6 TeV, with the spectral index changing from 2.60 to 2.85, establishing the presence of a new spectral feature of cosmic rays at energies lower than the so-called knee^[3].

(3) With the 4.5 years of data recorded by DAMPE, the energy spectrum of cosmic ray helium nuclei from 70 GeV to 80 TeV has been obtained. A hardening of the spectrum is observed at about 1.3 TeV, similar to previous observations in space. In addition, a spectral softening at about 34 TeV is identified for the first time by big statistics with well controlled systematic uncertainties, with an overall significance of 4.3σ . Together with the proton spectral features revealed by DAMPE, we find a particle charge dependent softening energy, although with current uncertainties a dependence on the number of nucleons cannot be ruled out^[4].

(4) Thanks to its unprecedented high energy resolution, DAMPE is well suitable for searching for monochromatic and sharp gamma-ray structures in the GeV–TeV range. With five years of DAMPE data, we

do not find line signals or candidates between 10 and 300 GeV in the Galaxy. Compared to the previous Fermi-LAT results, though DAMPE has an acceptance smaller by a factor of about 10 and an exposure time shorter by a factor of about 2, similar constraints on the dark matter parameters are achieved and below 100 GeV the lower limits of the decay lifetime are even stronger by a factor of about 2^[5].

For further details, please refer to Ref. [1–5].

3 Insight-HXMT: Hard X-ray Modulation Telescope

Launch time: It was launched on 15 June 2017.

3.1 Scientific Goals

(i) To scan the Galactic Plane to find new transient sources and monitor the known variable sources; (ii) to observe X-ray binaries to study the dynamics and emission mechanism in the strong gravitational or magnetic fields; (ii) to monitor and study the Gamma-Ray Bursts and Gravitational Wave Electromagnetic counterparts.

3.2 Payloads

Insight-HXMT is China’s first X-ray astronomical satellite and is currently in service in an orbit of 550 km altitude and 43° inclination. *Insight-HXMT* carries three slat-collimated instruments: High Energy X-ray Telescope (HE), Medium Energy X-ray Telescope (ME), and Low Energy X-ray Telescope (LE). HE consists of 18 NaI/CsI phoswich modules (main detectors) with a total geometrical area of about 5000 cm² in 20–50 keV. ME takes 1728 Si-PIN pixels which cover an energy range of 5–30 keV and ends up with a total geometrical area of 952 cm². LE adopts the Swept Charge Device (SCD) its detectors, which is sensitive in 1–15 keV with a total geometrical area of 384 cm². For the details about the payloads see Table 2 and Fig. 2, and refer to Ref.[6].

3.3 Main Scientific Results

3.3.1 Discovery of Quasi-periodic Oscillation with the Highest Energy

Low-Frequency Quasiperiodic Oscillations (LFQPOs) are commonly found in black hole X-ray binaries, and their origin is still under debate. The properties of LFQPOs at high energies (above 30 keV) are closely



Fig. 2 Main payloads onboard *Insight-HXMT*. The 18 cylindrical NaI/CsI detectors located around the center are HE, the boxes on the lower left are LE and upper right ME

Table 2 Major characteristics of the *Insight-HXMT*

Detectors	LE: SCD, 384 cm ² ME: Si-PIN, 952 cm ² HE: NaI/CsI, 5000 cm ²
Energy range	LE: 1–15 keV ME: 5–30 keV HE: 20–250 keV
Time resolution	HE: 25 μs ME: 280 μs LE: 1 ms
Energy resolution	LE: 2.5% @ 6 keV ME: 14% @ 20 keV HE: 19% @ 60 keV
Field of view of one module	LE: 6°×1.6°; 6°×4°, 60°×3°, blind ME: 4°×1°, 4°×4°, blind HE: 5.7°×1.1°, 5.7°×5.7°, blind
Angular resolution (20σ source)	< 5'
Source location (20σsource)	< 1'
Sensitivity (3σ, in 105 s)	0.5 mCrab (only statistical uncertainties included)
Orbit	Altitude: 550 km
Attitude	Inclination: 43° Three-axis stabilized Control precision: 0.1° Measurement accuracy: 0.01°
Data rate	LE: 3 Mbit·s ⁻¹ ME: 3 Mbit·s HE: 300 kbit·s
Payload mass	1000 kg
Nominal mission lifetime	4 years
Working mode	Scan, pointing, GRB

related to the nature of the accretion flow in the innermost regions, and thus play a crucial role in critically testing various theoretical models. *Insight-HXMT* is capable of detecting emissions above 30 keV, and is

therefore an ideal instrument to do so. Insight-HXMT discovered LFQPOs above 200 keV in the new black hole MAXI J1820+070 in the X-ray hard state. The phase lag of the LFQPO is constant around zero below 30 keV, and becomes a soft lag above 30 keV. The soft lag gradually increases with energy and reaches about 0.9 s in the 150–200 keV band. The detection at energies above 200 keV, the large soft lag and the energy-related behaviors of the LFQPO pose a great challenge for most existing models, but suggest that the LFQPO probably originates from the precession of a small-scale jet^[7].

3.3.2 Discovery of Accelerating Jet During Outburst of a Black Hole X-Ray Binary System

A black hole X-ray binary produces hard X-ray radiation from its corona and disk when the accreting matter heats up. During an outburst, the disk and corona co-evolves with each other. However, such an evolution is still unclear in both its geometry and dynamics. Insight-HXMT detected an unusual decrease of the reflection fraction in MAXI J1820+070, which is the ratio of the coronal intensity illuminating the disk to the coronal intensity reaching the observer, as the corona is observed to contrast during the decay phase. With this discovery, a jet-like corona model is postulated, in which the corona can be understood as a standing shock where the material flowing through. In this dynamical scenario, the decrease of the reflection fraction is a signature of the corona's bulk velocity. These findings suggest that as the corona is observed to get closer to the black hole, the coronal material might be outflowing faster^[8].

3.3.3 Identification of Magnetar Counterpart of the Fast Radio Burst

Fast Radio Bursts (FRBs) are short pulses observed in the radio band from cosmological distances and remain a puzzle due to no identification of the counterpart in multi-wavelength.

Insight-HXMT detection of a non-thermal X-ray burst in the 1–250 keV energy band allows for the first identification of FRB 200428 from SGR J1935+2154^[9]. The X-ray burst showed two hard peaks with a separation of 34 milliseconds, broadly consistent with that of the two bursts in FRB 200428. The delay time between the double radio peak and the X-ray peaks is about 8.62 s, fully consistent with the dispersion delay of FRB 200428. The Insight-HXMT results suggest that the non-thermal X-ray burst and FRB 200428 share the same physical origin in an explosive event from SGR

J1935+2154, and thus provide the first identification of an FRB in multi-wavelength.

3.3.4 Discovery of the Cyclotron Resonant Scattering Feature with the Highest Energy

Insight-HXMT observed the outburst of high mass X-ray binary system GRO J1008-57 and detected a Cyclotron Resonant Scattering Feature (CRSF) line at around 90 keV with a significance of more than 70 sigmas^[10]. Such results provide for the first time the first firm detection of so far the highest centroid energy of CRSF and hence the strongest magnetic field ever measured directly from the NS system. Previous observations by a series of international X-ray telescopes reported only at most roughly 4 sigma due to their shortages in bandwidth and detector area for covering the hard X-rays.

For further details, please refer to Ref.[6–10].

4 GECAM: Gravitational Wave High-energy Electromagnetic Counterpart All-sky Monitor

Launch time: 9 December 2020.

4.1 Scientific Goals

GECAM is a dedicated all-sky monitor with a very large instantaneous field-of-view in the X-ray and soft gamma-ray band. The primary scientific objectives are: (i) monitor and characterize the high energy counterparts of Gravitational Waves (GWs), to reveal the underlying physics of neutron stars, black holes and merger process of them; (ii) monitor and characterize the high energy counterparts of Fast Radio Burst (FRBs), to reveal their origin and emission mechanism; (iii) discover various types of Gamma-Ray Bursts (GRBs) and Soft Gamma-Ray Repeaters (SGRs), to deepen our understanding of their burst physics.

4.2 GECAM Detectors

GECAM is composed of two microsatellites in the same Low Earth Orbit with opposite orbital phase (Fig.3), each of which is equipped with 25 Gamma-Ray Detectors (GRD) and 8 charged Particle Detectors (CPD) pointing to different directions to cover a very large field of view. All these detectors are based on SiPM technology which ensures the detector and satellite very compact and light-weighted but with good performance in detection. The specifications of GECAM are listed in Table 3.

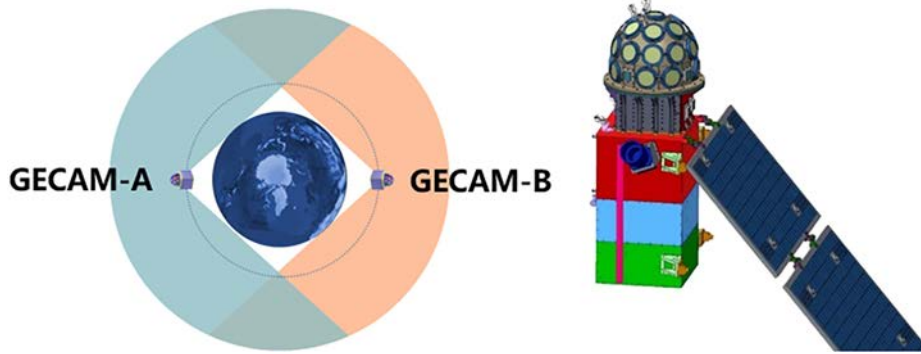


Fig. 3 Design of GECAM mission which is composed of two microsatellites (GECAM-A and GECAM-B) (left). Currently, only GECAM-B is working. Layout of the GECAM spacecraft and scientific payloads, which include 25 gamma-ray detectors and 8 charges (right)

Table 3 Specifications of GECAM

Parameters	Values	Notes
Orbit	600 km, 29°	/
Life time	3 years	Goal: 5 years
GRD energy range	15 keV–5 MeV	/
Field of view	~60% all-sky	For GECAM-B only
Burst Sensitivity	$<2 \times 10^{-8} \text{ erg}\cdot\text{cm}^{-2}\cdot\text{s}^{-1}$	20 s, 10–1000 keV
Burst localization accuracy	$<1^\circ$ (1 σ stat.)	Flux: $1 \times 10^{-6} \text{ erg}\cdot\text{cm}^{-2}\cdot\text{s}^{-1}$, 10 s
Absolute timing accuracy	$<3 \mu\text{s}$	/
Relative timing accuracy	0.1 μs	Between detectors
Time latency of trigger data	60 s	For the first BDS message

Due to the unexpected anomalies in the power supply system of both satellites, currently only GECAM-B can observe about 10 hours per day while GECAM-A has not been able to observe yet.

4.3 Main Scientific Results

GECAM-B has detected hundreds of transients in hard x-ray and soft gamma-ray, including Gamma-Ray Bursts (GRBs), Soft Gamma-Ray Repeaters (SGRs), bursts from X-Ray Binaries (XRB), Solar Flares and Terrestrial Gamma-ray Flashes (TGFs). GECAM-B also has been monitoring the potential gamma-ray counterparts of many Fast Radio Burst (FRBs). GECAM-B will seek for gamma-ray counterparts of Gravitational Waves (GWs) during the forthcoming O4 observation of LIGO/Virgo/KAGRA.

With the novel application of Beidou navigation System (BDS), GECAM-B has been able to downlink the trigger data nearly real-time (latency is about 60 s), and then guide other space-borne or ground-based telescopes to do follow-up observations of various bursts (See Fig.4). GECAM-B is the first Chinese space mission with the capability of sending prompt astronomical alert to the world-wide community.

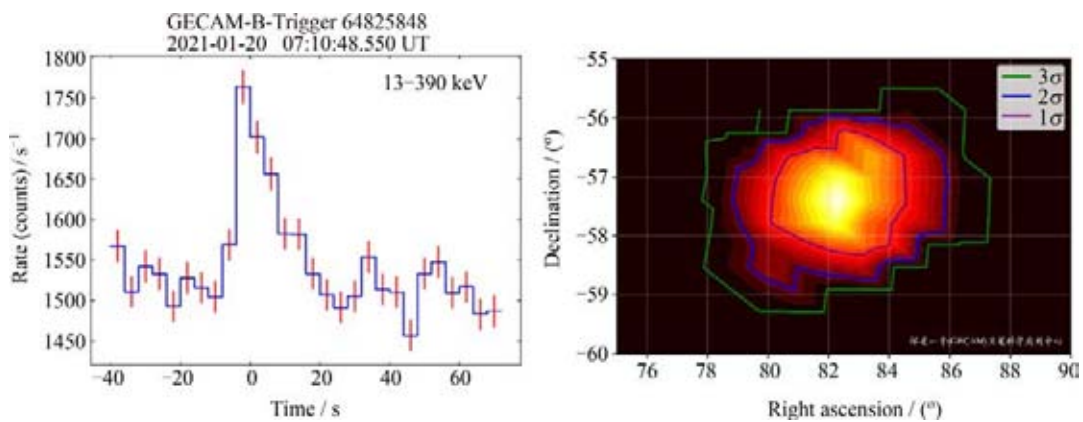


Fig. 4 GECAM real-time light curve of gamma-ray burst downlinked through the Beidou navigation system(left). The low-latency GECAM localization map of a gamma-ray burst (GRB 211105A, right)

For further details, please refer to Ref.[11].

5 PolarLight

Launch time: It was launched on 29 October 2018.

5.1 Scientific Goals

PolarLight is a collimated X-ray polarimeter observing the brightest X-ray sources in the sky in order to diagnose their magnetic field or accretion geometry.

5.2 Payload

The payload has a size of 1U (about 10 cm × 10 cm × 10 cm), containing three Printed Circuit Boards (PCBs) in an aluminum case. From top to bottom, the three PCBs respectively host the Gas Pixel Detector (GPD), the high voltage power supply, and the data acquisition system. A collimator is mounted on top of the GPD to avoid source confusion and reduce the diffuse background. The GPD is a 2D gas proportional counter using the Gas Electron Multiplier (GEM) with an ASIC pixel readout, filled with Dimethyl Ether (DME) at a pressure of 0.8 atm as the working gas. It enables us to measure the tracks of photoelectrons following the absorption of X-rays, and infer the polarization degree and angle from the emission angles of photoelectrons on the 2D plane (See Fig.5 and Table 4).

5.3 Main Scientific Results

Prior to PolarLight, the Crab nebula was the only astrophysical source with a significant polarimetric measurement in the keV band, performed in the 1970s with

the Bragg polarimeter onboard OSO-8 in narrow bands around 2.6 keV and 5.2 keV. The main scientific results with PolarLight are as follows.

In 2019, PolarLight revealed a possible variation in polarization (a sudden decrease in PF) coincident in time with the glitch of the Crab pulsar on July 23^[12]. The variation was found to have a significance of 3σ using different methods. This may suggest that the pulsar magnetosphere altered after the glitch. Then, the polarization recovered roughly 100 days after the glitch^[13]. With more data being accumulated, the PA measured with PolarLight from the total nebular emission was found to have a difference of $18.0^\circ \pm 4.6^\circ$ from that measured 42 years ago with OSO-8, indicating a secular evolution of polarization associated with either the Crab nebula or pulsar^[13]. The long-term variation in PA could be a result of multiple glitches in the history, magnetic reconnection in the synchrotron emitting regions in the nebula, or secular evolution of the pulsar magnetic geometry.

Sco X-1 is the brightest persistent extrasolar object in the keV sky, powered by accretion from a low-mass companion star onto a low-magnetic neutron star. OSO-8 observed the source and produced a non-detection in X-ray polarization around 2.6 keV, but obtained a 3σ detection around 5.2 keV. PolarLight yielded consistent results: a null-detection below 4 keV but a significant detection in 4–8 keV; the significance in the hard band is up to 5σ when the source shows the highest intensity^[14]. The PA measured with PolarLight is consistent with that obtained with OSO-8 within errors, and in line

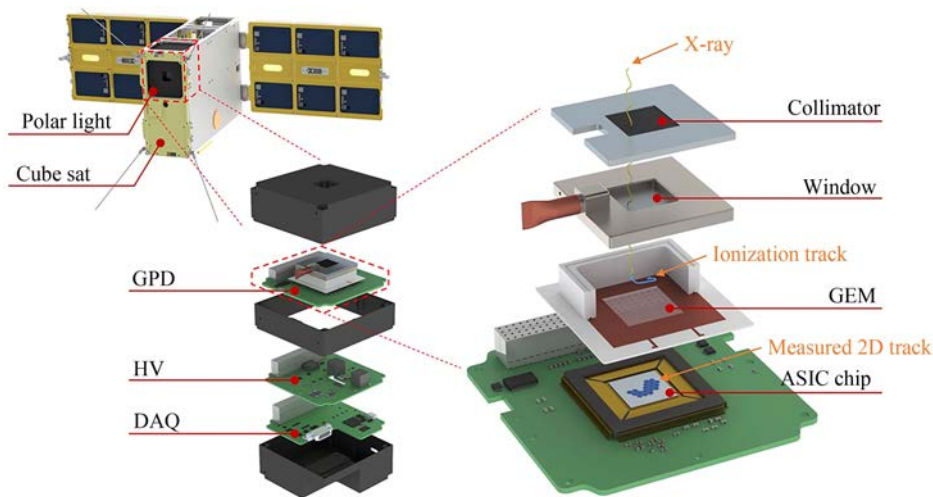


Fig. 5 Schematic drawing of PolarLight

Table 4 Specifications of PolarLight

Energy range	2–8 keV
Energy resolution	19% @ 6 keV
Field of view	2.3° FWHM or 5.7° FWZR
Gas mixture	pure DME at 0.8 atm, 1 cm thick
Window	100 μm beryllium
GEM	100 μm pitch and 100 μm thick
ASIC	50 μm pitch
Modulation factor	0.42 @ 3.74 keV
Weight	580 g
Power	2.2 W
Size	1U (about 10 cm × 10 cm × 10 cm)

with the orientation of the radio jet of Sco X-1 on the plane of the sky. The jet is supposed to be launched along the symmetry axis of the system. The results favor the scenario that an optically-thin corona is located in the transition layer of Sco X-1 under the highest accretion rates, and disfavor the accretion disk corona model.

For further details, please refer to Ref.[12–14].

6 GRID

Launch times: 29 Oct. 2018 (GRID-01), 6 Nov. 2020 (GRID-02), 27 Feb. 2022 (GRID-03b and GRID-04).

6.1 Scientific Goals

GRID is a project led by students, with multiple detectors deployed on low Earth orbits, to monitor the transient gamma-ray sky, with particular interests in identifying gamma-ray bursts associated with gravitational wave events and soft gamma-ray repeaters associated with fast radio bursts.

6.2 Payloads

GRID is a network of gamma-ray detectors on low Earth orbits. Each detector contains four GAGG crystals read out with Silicon Photomultipliers (SiPMs). Each crystal has a geometry of 3.8 cm × 3.8 cm × 1 cm, sensitive in the energy range from several tens of keV to about 2 MeV. The field of view is roughly half of the sky. The payload has a size of 0.5U (about 10 cm × 10 cm × 5 cm) with three print circuit boards, respectively for the SiPMs, preamplifiers, and data acquisition, from top to bottom. The GRID project is lead and operated by students. So far, four GRID payloads have been launched, all led by students from Tsinghua University.

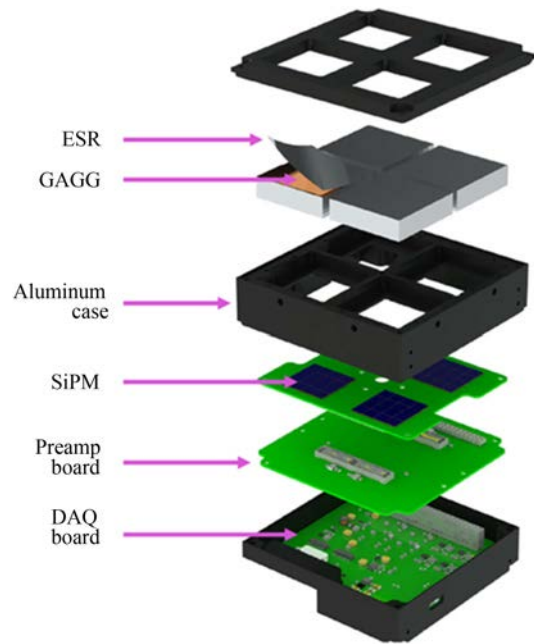


Fig. 6 Schematic drawing of the GRID payload

Table 5 Specifications of GRID

Energy range	20 keV–2 MeV
Energy resolution	20% FWHM @ 662 keV
Field of view	2π
Scintillator	Ce-doped $Gd_3(Al,Ga)_5O_{12}$ (GAGG)
SiPM	J-60035 manufactured by SensL
Payload size	0.5U (about 10 cm × 10 cm × 5 cm)

In the future, students from other universities will join the GRID collaboration and launch their own payloads (see Fig.6 and Table 5).

6.3 Main Scientific Results

GRID-01 was used for technical demonstration^[15]. GRID-02 started to produce scientific results^[16]. The first gamma-ray burst reported with GRID-02 is GRB 210121A^[17], which was jointly observed with Fermi GBM, HXMT, and GECAM. The burst is characterized by a hard low-energy spectral index, likely due to thermal origin, possibly a typical fireball burst from a host galaxy at $z = 0.319$. GRID-03b and GRID-04 were just launched as of this writing.

For further details, please refer to Ref.[15–17].

7 Lobster-eye X-ray Satellite

Launch time: It was launched on 25 July 2020.

7.1 Scientific Goal

To perform wide-field X-ray imaging of rich galaxy clusters, to detect early X-ray emissions from gamma-ray bursts, and to probe solar wind charge exchange X-ray emission from comets.

7.2 Mission

The “Lobster-eye X-ray Satellite” was developed by Nanjing University in a joint effort with the University of Hong Kong and the Beijing Institute of Space Mechanics and Electricity (BISME). Successfully launched on 25 July 2020 and operating to this date, the “Lobster-eye X-ray Satellite” is the first astronomical satellite equipped with the lobster-eye focused X-ray imaging technology, which was invented more than four decades ago^[18]. The key parameters and layout of the satellite are shown in Table 6 and Fig.7, respectively.

Table 6 Key parameters of “Lobster-eye X-ray Satellite”

Dimension	750mm×500mm×320mm (2840 mm with solar panel)
Power	30 W
Orbit	LEO
Optics	2×2 MPO ($f = 375 \text{ mm}, A = 4 \times 4 \text{ cm}^2$)
Detector	CCD 1024 pixel×1024 pixel
Field-of-view	2° (with detector)
Angular resolution	<0.2°
Energy range	1–6 keV (in-orbit)
Energy resolution	<200 eV

8 SVOM: Space-based Multiband Astronomical Variable Objects Monitor

Launch time: in 2023.

8.1 Scientific Goal

SVOM (Space-based multiband astronomical Variable Objects Monitor) is a mission dedicated to studying Gamma-Ray Bursts (GRBs)^[19].

8.2 Mission

The mission has been approved jointly by both Chinese and French space agencies. The satellite will have an orbit with an altitude of 600–650 km and an inclination of 29°. The system Critical Definition Review (CDR) was carried out by CNSA and CNES in July 2020. It had been planned to be in orbit in 2023.

GRBs are extremely luminous transient sources appearing when a newborn stellar mass black hole or magnetar emits an ultra-relativistic jet towards the Earth. Consequently, the study of GRBs not only has the potential to expand or revolutionize our understanding of key astrophysical issues on the mechanisms driving stellar explosions and the radiation processes of relativistic jets. In the next years, GRBs will also undoubtedly shed new light on the evolution of the young universe, particularly on the history of star formation, the metal

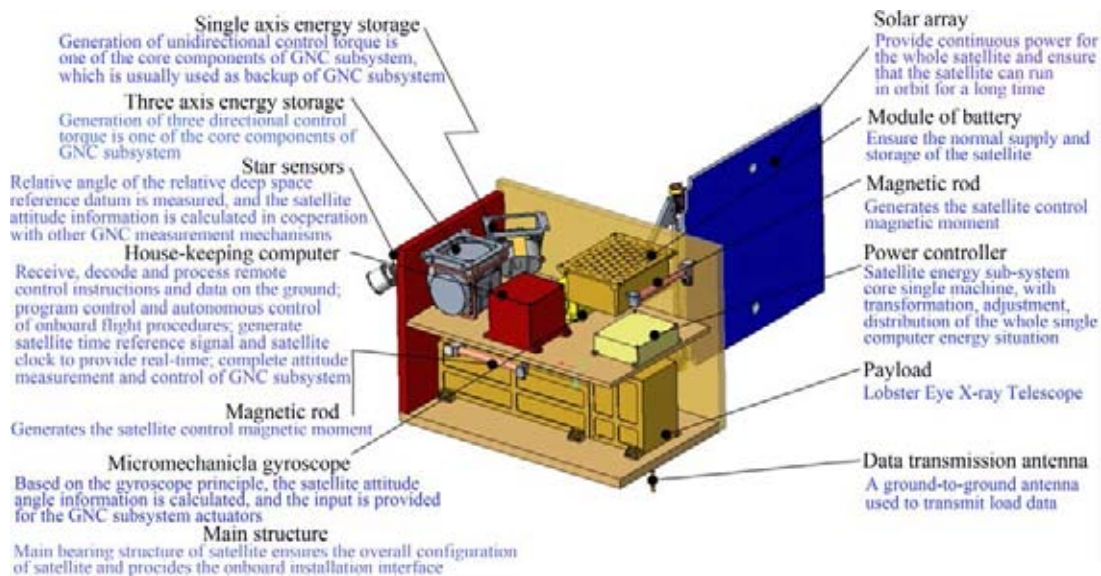


Fig. 7 Layout of the “Lobster-eye X-ray Satellite”

enrichment of galaxies, and the reionization of the intergalactic medium^[20]. GRB 170817A, a normal short GRB detected by Fermi-GBM, was the first confirmed counterpart of gravitational-wave transients, which made GRBs even hotter topic^[21].

The scientific objectives of SVOM put a special emphasis on two categories of GRBs: very distant GRBs at $z > 5$ which constitute exceptional cosmological probes, and faint/soft nearby GRBs which allow probing the nature of the progenitors and the physics at work in the explosion. These goals have a major impact on the design of the mission: the on-board hard X-ray imager is sensitive down to 4 keV and computes online image and rate triggers, and the follow-up telescopes on the ground are sensitive in the NIR.

In order to take advantage of the astrophysical potential of GRBs, SVOM is designed to (i) permit the detection of all known types of GRBs; (ii) provide fast, reliable GRB positions; (iii) measure the spectral shape of the GRB prompt emission from visible to MeV; (iv) measure the temporal properties of the GRB prompt emission from visible to MeV; (v) identify quickly the afterglows of detected GRBs at both X-ray and visible bands, including the ones that are highly redshifted ($z > 5$); (vi) measure the spectral shape of the early and late GRB afterglow from visible to X-rays; (vii) measure the temporal evolution of the early and late GRB afterglow from visible to X-rays.

SVOM mission by design consists of a set of scientific instruments to implement the synergy between space and ground observations. The space-based instruments include: (i) ECLAIRs, a wide field-of-view hard X-ray imager and spectrometer; (ii) GRM, a wide field-of-view soft gamma-ray spectrometer; (iii) MXT, a narrow field-of-view low-energy X-ray telescope; (iv) VT, a narrow field-of-view visible/near infrared (NIR) telescope. An artist view of the SVOM satellite is shown in Fig.8. And the ground-based instruments include: (i) GFTs, two follow-up telescopes (one of which featuring efficient NIR capabilities); (ii) GWAC, an array of wide field-of-view cameras in visible band. A network of about 45 VHF receiving stations, and a BeiDou short-message system as a supplement, are designed for real-time downlink communication.

SVOM is a unique multi-wavelength observatory with rapid slew capability and quick command up-link capability. Therefore, SVOM will also be a powerful target-of-opportunity observatory for the whole astronomy

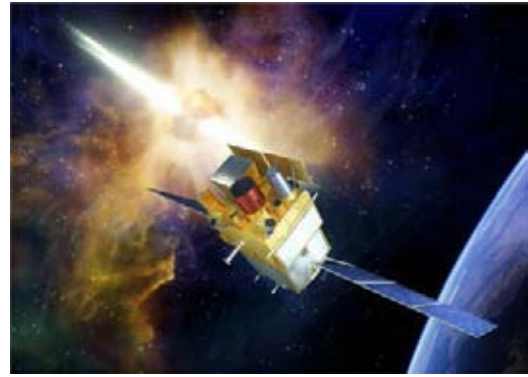


Fig.8 Artistic view of the SVOM satellite

community beyond the specific objectives linked to GRBs. For example, the SVOM mission has been conceived to promptly point to the celestial fields where sources have been detected by the wide field of view astronomical devices such as the upgraded generation of gravitational wave detectors (LIGO, VIRGO, GEO and KAGRA) and high-energy neutrino detectors (IceCube, KM3NeT).

For further details, please refer to Ref.[19–21].

9 Einstein Probe Mission

9.1 Expected Launch Time and Current Phase

The EP project is currently in Phase D (flight model phase) and the satellite is planned for launch by the end of 2023.

9.2 Scientific Goals

The Einstein Probe will carry out systematic sky monitoring surveys with a large instantaneous field-of-view in the soft X-ray band with the sensitivity and grasp one order of magnitude better than those currently in orbit. The primary science objectives are: (i) discover and characterize cosmic X-ray transients, to reveal their properties and gain insight into their nature and underlying physics; (ii) discover and characterize X-ray outbursts from otherwise quiescent black holes, for a better understanding of the demography of black holes and their origin and evolution, as well as accretion physics; (iii) search for X-ray sources associated with gravitational-wave events and precisely locate them.

9.3 EP

EP carries two scientific instruments: an X-ray monitoring instrument Wide-field X-ray Telescope (WXT)

with a large instantaneous FoV, and a narrow-field Follow-up X-ray Telescope (FXT). Some of the specifications of WXT and FXT are listed in Table 7.

To achieve both wide FoV and X-ray focusing, the novel micro-pore optics in the lobster-eye configuration is adopted for WXT. WXT consists of 12 identical modules with a 375 mm focal length. One WXT module includes the MPO mirror assembly, 4 scientific CMOS sensors and electronics units, optical baffle, structure and thermal control. The nominal detection bandpass of WXT is 0.5–4.0 keV. EP WXT has a large grasp (effective area times FoV) of the order of $10^4 \text{ cm}^2 \cdot (\text{°})^2$, which is the largest among all focusing telescopes in X-rays ever built. WXT has a nominal theoretical sensitivity of $10^{-11} \text{ erg} \cdot \text{s}^{-1} \cdot \text{cm}^{-2}$ for 1000 second exposure in the 0.5–4 keV band.

The FXT is composed of a pair of Wolter-I focusing mirror assemblies. For each of the telescope a CCD detector is mounted on the focal plane. FXT covers an

energy passband of 0.3–10 keV and has an effective area of about 300 cm^2 each at around 1 keV. EP is also capable of fast transient alerts triggering and downlinking, aiming at multi-wavelength follow-up observations by the world-wide community.

Fig.9 showed Layout of the Einstein Probe spacecraft and scientific payloads, which include 12 modules of WXT aligned with different directions and 2 coaligned modules of FXT

For further details, please refer to Ref.[22].

10 CSST: Chinese Survey Space Telescope/Chinese Space Station Telescope/Xuntian Space Telescope

Project name: Chinese Survey Space Telescope (CSST, also known as the Chinese Space Station Telescope or Xuntian Space Telescope). Launch: 2023/2024. Development phase: Phase C. An artist view of the CSST is showed in Fig. 10.

10.1 Science Goal

The CSST aims to explore the nature of dark energy and dark matter through precision measurements of gravitational lensing signal and galaxy clustering properties over its planned 17500 square degrees of high-resolution multiband imaging and slitless spectroscopy survey covering a wavelength range of 255 nm to 1000 nm. The same survey and observations of its versatile instruments will provide extremely rich data for a wide range of studies from the solar system to distant galaxies and beyond.

Table 7 Specifications of WXT and FXT

Parameters	WXT	FXT
Number of modules	12	2
Telescope optic	Lobster-eye MPO	Wolter-I
Detector	CMOS	CCD
Field of view	≥ 3600 square degrees	$\geq 38'$ (diameter)
Focal length/mm)	375	1600
Effective area @1.2 keV (cm^2)	2.7	300 (each module)
Spatial resolution (1 keV)	5'(FWHM)	30"(HPD)
Bandpass (keV)	0.5–4	0.3–10
E-resolution @1.25 keV (eV)	170	120
Sensitivity ($\text{erg} \cdot \text{s}^{-1} \cdot \text{cm}^{-2}$)	1×10^{-11} @ 1 ks	1×10^{-14} @ 10 ks



Fig. 9 Layout of the Einstein Probe spacecraft and scientific payloads, which include 12 modules of WXT aligned with different directions and 2 coaligned modules of FXT



Fig. 10 An artistic rendition of CSST in orbit (provided by Changchun Institute of Optics, Fine Mechanics and Physics, Chinese Academy of Sciences)

The CSST^[23] is a major science project of China Manned Space (CMS). It has a nominal mission lifetime of 10 years, which could be extended in principle. During normal observations, the CSST will fly independently in the same orbit as China's Tiangong space station while maintaining a large distance apart. It can dock with the space station for refueling and servicing as scheduled or as needed. With a Cook-type three-mirror anastigmatic design, the CSST can achieve superior image quality within a large Field of View (FoV), which gives it an advantage for survey observations. Being an off-axis telescope without obstruction, its Point Spread Function (PSF) does not have diffraction spikes from mirror support structures and is thus helpful for precision photometry, position, and shape measurements when properly sampled. The radius encircling 80% energy of the PSF within the CSST's central 1.1 square degrees of FoV is specified to be no more than 0.15", including all wavefront errors in the optics and instruments and dynamical effects such as the telescope's attitude control and vibration.

10.2 CSST

The CSST will be launched with 5 first-generation instruments including a Survey Camera, a Terahertz Receiver, a Multichannel Imager, an Integral Field Spectrograph, and a Cool Planet Imaging Coronagraph. The Survey Camera is equipped with 30 9000×9000 detectors for science observations, each with a filter or two grating elements mounted above, a defocused 9000×9000 detector for flux calibration in r band, eight 640×512 near-infrared detectors, two Fine Guide Sensors, and four Wavefront Sensors. It will take the Survey Camera roughly 7 years of operation accumulated

over 10 years of orbital time to image roughly 17,500 square degrees of the median-to-high galactic latitude and median-to-high ecliptic latitude sky in NUV, u, g, r, i, z, and y bands and take slitless spectroscopy of the same sky in 3 bands. The point-source 5 σ limiting magnitudes in g and r bands can reach 26th magnitude (AB mag) or higher. The spectral resolution ($R=\lambda/\Delta\lambda$) of the slitless spectrograph is specified to be on average no less than 200, and the wide-band-equivalent limiting magnitudes in GV (400–620 nm) and GI (620–1000 nm) bands will reach the 23rd magnitude or higher. In addition, a number of deep fields will be selected for more observations to reach at least one magnitude deeper than the wide-area survey. The Multichannel Imager plans to observe five ultra-deep fields of 300 square minutes in total to 30th magnitude in the visible.

Unlike the Survey Camera, the other four instruments all have a small FoV. They enable unique capabilities for detailed studies of individual objects or small fields. The Terahertz Receiver will be used to carry out spectral line surveys or mapping of star-forming regions of the Milky Way, nearby galaxies, late-type stars, and solar system objects. The Multichannel Imager can observe the same field in three bands simultaneously, capable of obtaining instantaneous color of fast varying objects such as fast transients, comets, and spinning asteroids. The Integral Field Spectrograph splits its 6"×6" FoV into 32×32 units and obtains 1024 spectra of these units. It can provide both two-dimensional spatial information and spectral information of the target, particularly helpful for investigations of the co-evolution of supermassive black holes and galaxies and star formation in the nearby universe. The Cool-Planet Imaging Coronagraph aims to realize 10⁻⁸ high-contrast direct

imaging of exoplanets in the visible. It plans to follow up exoplanets discovered by radial velocity observations, study planet formation and evolution, and probe protoplanet disks.

For further details, please refer to Ref.[23].

11 HERD: High Energy Cosmic Radiation Detection Facility

Expected launch time: in 2027. Current status: Phase B.

11.1 Scientific Goals

The primary scientific objectives of HERD are: dark matter search with unprecedented sensitivity in the energy spectra and anisotropy of high energy electrons from 10 GeV and in the gamma-ray spectrum from hundreds of MeV, precise cosmic ray spectrum and composition measurements up to PeV in order to determine the mechanism of the cosmic rays “knee” structure, as well as gamma-ray monitoring with a wide FOV and full sky survey with high sensitivity^[24].

11.2 Payload Description

HERD is an astronomy and particle astrophysics experiment onboard China’s Space Station. HERD is a China-led mission with a large European collaboration led by Italy. HERD is composed of five scientific instruments (see Fig.11). The primary instrument in the innermost is a deep 3D imaging Calorimeter (CALO)

with an innovative design that insures better e/p separation for particles and one order of magnitude larger geometrical factor than all previous experiments, by accepting particles impinging on its top face but also on the four lateral faces. Each sensitive face of CALO is instrumented from inside out with a Fiber Tracker (FIT), a Plastic Scintillation Detector (PSD) and a Silicon Charge Detector (SCD) to precisely measure the charges of cosmic rays. A Transition Radiation Detector (TRD) is located on one lateral side for the energy calibration of TeV nuclei. The total mass of HERD payload is about 4 tons^[25].

Table 8 shows HERD main specifications.

For further details, please refer to Ref.[24, 25].

12 POLAR-2: Gamma-Ray Burst Polarimetry on the China Space Station

Launch time: 2024 and 2025. There are two payloads of POLAR-2, which are European payload and Chinese payload, respectively. The two payloads are relatively independent and have their own scientific importance, although their joint observation in orbit will produce the best scientific observations for the whole project. Thus, the two payloads do not have to be launched at the same time. The European payload was proposed in 2018 and has been officially accepted in 2019 for execution with

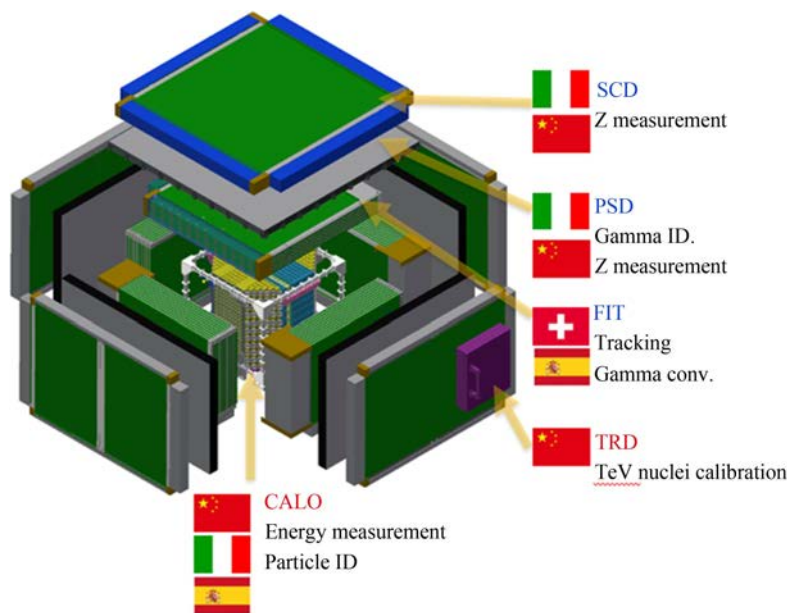


Fig. 11 HERD payload

Table 8 HERD main specifications

Energy range (e/ γ)	10 GeV–100 TeV (e); 0.5 GeV–100 TeV (γ)
Energy range (CR)	30 GeV–PeV
Angular resolution	0.1° @10 GeV
Charge resolution	0.1–0.3 c.u
Energy resolution (e)	1% @200 GeV
Energy resolution (p)	20% @100 GeV–PeV
e/p separation	$\sim 10^6$
G.F. (e)	$>3 \text{ m}^2\cdot\text{sr}@200 \text{ GeV}$
G.F. (p)	$>2 \text{ m}^2\cdot\text{sr}@100 \text{ TeV}$

an anticipated launch date of 2024. While for the Chinese payload, which was proposed in 2021, the launch is aimed at 2025.

12.1 Current Phase of the Project

For the European payload, it is at the end of Phase C and early Phase D. For the Chinese payload, it is in Phase B.

12.2 Scientific Goals

Following the important results of the POLAR experiment as the first major step toward understanding the details of the Gamma-Ray Burst (GRB) nature and the open questions raised according to POLAR's new findings^[26], the POLAR-2 experiment mainly aims to measure the linear polarization of GRBs prompt emissions and early X-ray flare with high precision, thus trying to answer the fundamental questions regarding the powering mechanism, jet characteristics, radiation physics and so on for GRBs and electromagnetic counterparts associated with the gravitational wave sources. The secondary scientific objective of POLAR-2 is to precisely measure the linear polarization of magnetar high-energy bursts, exploring the physical mechanism of their association with the fast radio bursts, which will make the key contribution to answering the questions of their origin.

12.3 POLAR-2 Payloads

The European payload of POLAR-2 will contain 100 High-energy Polarimeter Detector (HPD) modules by a factor of 4 compared to its predecessor POLAR. Each HPD module is composed of 64 Plastic Scintillator (PS) bars with optimized dimensions for Compton polarimetry purposes, which is the most effective way for polarization measurement in the 30 to 800 keV energy range of

hard X-rays to soft Gamma-rays. Different from POLAR which used the multi-anode photomultiplier tube device for reading out the fluorescence signals from the PS bars, a Silicon Photo Multiplier (SiPM) array will be used for each HPD module in order to increase the Photo-Detection Efficiency by about a factor of 2 and reduce the lower energy limit of the detector down to several keV, as well as to eliminate the cross-talk signals existed mostly among the neighboring PS bars in POLAR to a negligible level. More details of the HPD design are described in Ref.[27]. Although it is possible to localize GRBs and deduce their spectra roughly by making use of the HPD detector arrays, a better GRB localization and spectrum measurement precision is required in order to perform the polarization measurements with higher precision. Thus, a dozen of Broadband Spectrometer Detector (BSD) modules are proposed to enhance these two aspects. Each BSD module consists of the LaBr₃(Ce) crystal with a compact dimension as well as a SiPM array for the signal readout. A dual-channel design with different gains for each BSD module enables its detectable energy range from about 10 keV to several MeV. Besides, diverse pointing configurations for the BSD modules further increase the localization precision for GRBs. As it is vital to understand the radiation mechanism, geometry and magnetic field structure of the jet by observing comprehensively the polarization parameters during both the prompt and early afterglow emissions phases of GRB, a Low-energy Polarimeter Detector (LPD) was also proposed which consists of about eighteen independent modules. Each LPD module is filled with DME or Xenon mixture as the working gas to enable the soft X-ray polarization measurement from several keV to about 10 keV based on the photoelectric polarimetry. The signals will be collected by a gas multiplication microchannel panel and read out by customized ASIC electronics. Currently the design optimization for the two payloads is still ongoing, the CAD models are shown in Fig.12. A summary of the main anticipated features of the two payloads is listed in Table 9.

For further details, please refer to Ref.[26, 27].

13 DIXE: Diffuse X-ray Explorer

Status of project: Phase A.

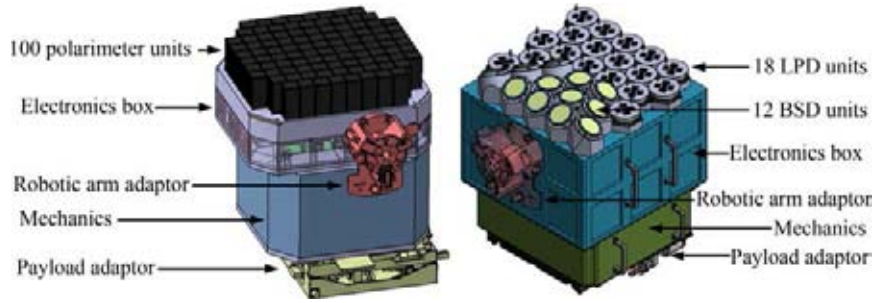


Fig. 12 Design of the POLAR-2 two payloads. On the left, the European payload CAD model is shown, while the Chinese payload CAD model is shown on the right

Table 9 Main anticipated technical performances of POLAR-2

Characteristics	Instrument		
	HPD	LPD	BSD
Detector sensitive material	Plastic scintillator bars array	DME or Xenon mixture	LaBr ₃ crystal
Energy range	30–800 keV	2–10 keV (potentially can be extended to 30 keV depending on the gas)	10–2000 keV
Detection area	2000 cm ²	≥290 cm ²	For each module ≥40 cm ²
Field of view	50% sky	90°×90°	50% sky
Energy resolution	–	≤25% @5.9 keV	≤18% @59.5 keV
Dimensions	590×664×700 mm ³	600×600×710 mm ³	

13.1 Scientific Goals

Bying conducting an all-sky survey with a high-resolution X-ray spectrometer, DIXE is expected to complement eROSITA with data of much improved spectral resolution. The primary scientific issues that DIXE hopes to address include the origin of the soft diffuse X-ray background, the nature of the “eROSITA Bubble”, and the physical state of the hot halo around the Milky Way. The issues are intimately related to some of the unsolved problems in understanding the ecosystem of galaxies.

13.2 Payload

The DIXE payload is to be installed on the Chinese Space Station. It employs a 10×10 array of microcalorimeters at the heart of its detector system. The microcalorimeters are based on superconducting Transition-Edge Sensor (TES) technology, promising to provide an energy resolution better than 6 eV, and are optimized for performance over the energy band of 0.1–5 keV (allowing an examination of the claimed 3.5 keV emission

Table 10 Key parameters of the preliminary payload design

Parameter	Value	Notes
Lower energy/keV	0.1	Goal
Upper energy/keV	5	Point of optimization
Energy resolution/eV	< 6	Goal: 2 eV at 1 keV
Field of view/(°) ²	100	With mechanical collimator
Effective area/cm ²	> 0.5	Goal: 1 cm ²
Grasp/[cm ² (°) ²]	> 50	Goal: 100 [cm ² (°) ²]
Power/W	800	Peak: 1000 W
Mass/kg	300	Goal: < 200 kg

line, which is speculated to be associated with dark matter). The detector is mechanically collimated to a field-of-view of about 100 square degrees. Table 10 shows the key parameters of the preliminary payload design.

To achieve the required energy resolution, the microcalorimeter array needs to be cooled to an operating temperature of about 50 mK. In the preliminary design, the cooling system consists of a two-stage cryocooler and a two-stage Adiabatic Demagnetization Refrigerator (ADR), with the cryocooler reaching down to 4.2 K and the ADR down to 50 mK. The microcalorimeter array is read out by multiplexing electronics.

From a technical point of view, DIXE serves as a pathfinder mission for the HUBS project^[28], hoping to advance the TRLs of key technologies including TES microcalorimeter, multiplexing readout electronics, cryocooler, and ADR.

For further details, please refer to Ref. [28].

14 LyRIC: Lyman Ultraviolet Radiation from Interstellar Medium and Circum-galactic Medium

Launch times: in 2025⁺. Current status: Phase A.

14.1 Scientific Goals

Accretion and feedback are of the frontiers in Astrophysics, as well as one of the important goals for the future space astronomical observatories. Circum-galactic Medium (CGM) is the best and hot target in this field. We propose an external scientific payload operating on Chinese Space Station: “LyRIC: Lyman ultraviolet Radiation from ISM and CGM”, to measure the LUV radiation of our Galaxy and nearby galaxies. LyRIC will fill in the unique LUV windows for the high-quality spectroscopic radiation measurements from CGM of nearby galaxies with a big angular size, HVCs in our Galaxy and M31, and the diffuse sources in our Galaxy and SMC/LMC for the first time. Such a scientific payload will also help us to verify our LUV technologies in space.

14.2 Payload

LyRIC is designed to take advantage of the mature technology, Long-Slit Spectrograph (LSS) operating on Chinese Space Station. Limited by the size and weight of the independent external payload operating on CSS, the new optimizations of LyRIC (the optical design, inside view and outlook, major specifications) are summarized in Fig.13. LyRIC will have a mirror with an aperture less than 30 cm, spectral resolution $R \approx 3000$, and spatial

resolution about 30 arcsec, working in the wavelength range of 91–115 nm for a lifetime longer than 5 years.

For further details, please refer to Ref.[29].

15 eXTP: The enhanced X-ray Timing and Polarimetry Mission

Expected launch time and current phase: Expected to be launched in 2027, currently in Phase B.

15.1 Scientific Goals

The three core objectives of eXTP aim at answering key open questions of fundamental physics: (i) the physical nature of cold ultra-dense matter; (ii) the behaviour of matter and light in the space-time shaped by strong-field gravity; (iii) the astrophysics and physics of the strongest magnetic fields in nature. The matter inside neutron stars (NSs), the space-time in the vicinity of the Black Hole (BH) horizon, and the extremely magnetized vacuum close to magnetars and accreting pulsars are uncharted territories of fundamental physics. NSs and BHs provide a unique arena for their exploration. The eXTP mission will revolutionize these fundamental areas of today’s research by high precision X-ray observations of NSs across the magnetic field scale and BHs across the mass scale.

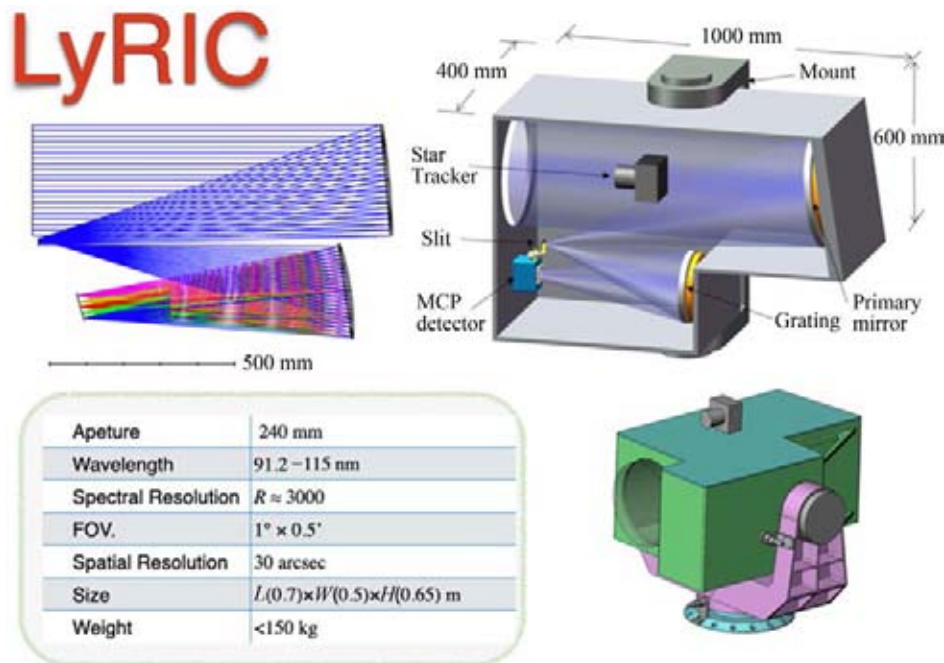


Fig. 13 Current optimizations of LyRIC: the optical design (upper left), the inside view (upper right); major specifications (lower left); the outlook (lower right). Taken from Ref.[29]

In addition to investigating questions of fundamental physics, eXTP will enable excellent observatory science opportunities, providing observations of unprecedented quality on a variety of galactic and extragalactic objects. eXTP’s wide field monitoring capabilities will also be crucial in the context of multi-messenger astronomy by detecting and monitoring the electromagnetic counterparts of gravitational waves and neutrino cosmic sources. eXTP will operate at the time of operation of major facilities in multi-messenger astronomy, such as the second generation of the GW interferometer network (*e.g.*, aLIGO, aVIRGO, KAGRA, LIGO-India), the neutrino observatories IceCube-Gen2 and KM3NeT, and other multiwavelength facilities including SKA, LOFAR and FAST (radio), HERD (GeV to TeV), CTA and LHAASO (from TeV to PeV), and ALMA (mm). eXTP observations will be of crucial interest to a very wide international community, well beyond the X-ray astronomy community. It is a goal of the Consortium to make data available to this community through a robust guest-observer programme and multi-messenger programmes coordinated through agreements with interna-

tional facilities.

15.2 eXTP

What makes eXTP unique in comparison to other existing X-ray missions, including those currently in development, is its unprecedented combination of broad-band large collecting area, polarimetric capability, and spectral resolution. Owing to this combination, eXTP is expected to open an entirely new window in X-ray observations: simultaneous spectral-timing-polarimetry, which requires innovative analysis tools that are already being developed. eXTP will thus be complementary to ATHENA in terms of science and payload. An artist view of eXTP is shown in Fig.14.

The current baseline of the scientific payload includes four science instruments: the Spectroscopy Focusing Array (SFA, China), the Large Area Detector (LAD, Europe), the Polarimetry Focusing Array (PFA, China), and the Wide Field Monitor (WFM, Europe). The instrument configuration and key specifications are summarized in Table 11.

For further details, please refer to Ref.[30].



Fig. 14 Artistic view of the eXTP satellite. The science payload consists of four instruments: the focused SFA and PFA telescopes arrays, the large area instrument LAD, and the WFM to monitor a large fraction of the sky.

Table 11 Instrument configuration and key specifications

Instrument	SFA	LAD	PFA	WFM
Configuration	9 telescopes	40 modules	4 telescopes	6 cameras
Optics or Collimator	Wolter-I, Nickel $F = 5.25$ m	capillary-plate collimators	Wolter-I, Nickel $F = 5.25$ m	Coded mask
Detector	19-pixel Silicon Drift Det. (SDD)	SDD	Gas Pixel Detector (GPD)	SDD
Energy range	0.5–10 keV	2–30 keV	2–8 keV	2–50 keV
Effective area or FoV	≥ 0.6 m ² @ 1–2 keV 0.4 m ² @ 6 keV	3.0 m ² at 8 keV	500 cm ² @ 2 keV 300 cm ² @ 3 keV	FoV ≥ 3.1 sr
Energy res. (FWHM)	180 eV @ 6 keV	260 eV @ 6 keV	25% @ 6 keV	≤ 500 eV @ 6 keV
Time res.	10 μ s	10 μ s	10 μ s	10 μ s
Remarks	Unprecedented effective area in the soft X-ray energy range	High throughput; effective area is a factor of 5–10 larger than any previous mission	About 5 times the area of IXPE, X-ray polar. Pathfinder by NASA; Min. Detectable Polarization about 3% in 2–8 keV range	Peak sensitivity: 1 Crab in 1s and 5 mCrab in 50 ks (5 σ source). Point source localization $\leq 1'$

16 DAMPE-2: DArk Matter Particle Explorer-2

Launch time: 2025–2026 (suggested).

Scientific Goals

Like DAMPE, the data sets of DAMPE-2 could be used to reveal the astrophysical origins of the gamma-ray emitters, to study the acceleration, propagation and radiation of high energy cosmic-rays, and to probe the nature of dark matter. The wide field-of-view gamma-ray flash monitors are appended to detect the sub-MeV outbursts. Moreover, the newly designed operation orbit and survey mode enable a quick coverage of the full sky in two orbits and a timely pointed observation. Therefore, DAMPE-2 provides the opportunity to monitor the violent sub-MeV and GeV-TeV transients for various purposes. It also serves as the pioneer of the proposing Very Large Area gamma-ray Space Telescope (VLAST) that is characterized by an acceptance of about $10 \text{ m}^2 \cdot \text{sr}$.

DAMPE-2 is a general-purpose high-energy gamma-ray and cosmic ray observatory. As a low-cost and rapid space mission benefited from the R&D and run experiences of DAMPE, the capabilities are enhanced with the “minimum” modification of the hardware. In comparison to DAMPE, DAMPE-2 is optimized in some sub-detectors, the trigger system, and the survey mode to considerably improve its performance in the detection of low-energy gamma-rays (see Fig.15) as well as very high energy cosmic rays.

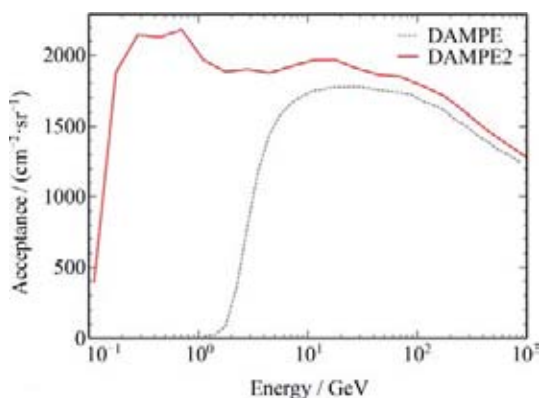


Fig. 15 Expected acceptance of DAMPE-2 on gamma-ray observation

17 DSL: Discovering the Sky at the Longest Wavelength/ The Hongmeng Project

Expected launch time and current phase: the Hongmeng project has completed the Intensive Study of Future Space Science Missions in the CAS Strategic Pioneer Program on Space Science, which is roughly equivalent to a phase A study. If selected as a flight mission, it can be developed in about 3 and half years and be launched in 2026.

17.1 Scientific Goals

The Hongmeng project has three main scientific goals.

(1) Reveal the dark ages and cosmic dawn with high-precision measurement of the low-frequency global spectrum. A measurement of the global spectrum on the lunar orbit can avoid systematics arising from the ionosphere, RFI and ground reflection, and achieve the ultimate high accuracy. The precisely measured spectrum will enable extraction of the 21 cm global signal from the cosmic dawn, which can provide us a unique probe of the early history of the Universe and reveal the nature of the first stars and galaxies.

(2) Open up the last unexplored electromagnetic window at 0.1–30 MHz. With the high-resolution sky map obtained at the ultra-long wavelength, we will discover for the first time what are the primary sources in this band, which may include stars and exoplanets, supernovae remnants, radio galaxies, and possibly even unknown and unexpected objects. These observations at the new wavelength may fundamentally change our understanding of many astrophysical processes. The absorption of the radio wave can also be exploited to reconstruct the three-dimensional structure of the interstellar medium, especially the local environment of the Solar system, and help resolving the problem of the origin and propagation of cosmic rays.

(3) Observing the Sun and planets to uncover the dynamics of the interplanetary space. Solar activity can cause severe disturbances in the solar-terrestrial space, and the radiation below 30 MHz comes mainly from the interplanetary space beyond $3\text{--}5 R_s$. By making quasi-imaging observations of solar radio bursts at low frequencies, we will be able to study the physical mechanism of the solar radio bursts, and the propagation,

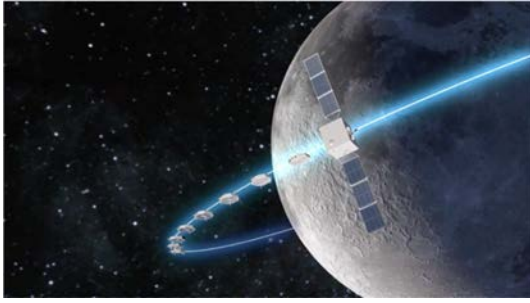


Fig. 16 Artistic concept of the DSL array

acceleration and evolution of the ejected plasma, and gain insights on the planetary magnetosphere.

17.2 DSL

The Hongmeng mission consists of one mother satellite and nine daughter satellites, which will be launched as an assembly by a single rocket, and released into a linear array along the same orbit^[31], as shown in Figure 13. The array will make astronomical observations when in the part of orbit that is shielded from the Earth, and communicate with the Earth when it is in view. The larger mother satellite at the front or end of the array is equipped with a high gain antenna for ground communication. It will collect the digital signals from each daughter satellite, process them and store the results, and transmit the data back to the Earth. Among the daughter satellites, one has a cone shaped antenna dedicated to make global spectrum measurement in the 30–120 MHz band. The other 8 daughter satellites have deployable tripole antennas on both sides. They form an array to make interferometric imaging observation as well as global spectrum measurement in the band 0.1–30 MHz, with baseline length up to 100 km. The satellites will move in the same circular orbit, at a height of about 300 km and an inclination angle of 30°. The precession of the orbital plane will generate a three-dimensional distribution of baselines, allowing the whole sky to be mapped without ambiguity.

For further details, please refer to Ref.[31].

18 CHES: Closeby Habitable Exoplanet Survey

18.1 CHES's Major Scientific Goals

To discover and explore habitable planets beyond our solar system, will provide essential answers to “Are we

alone in the universe?”, “Is the Earth unique?”, “How do planets become the cradle of life?” or “Is our solar system special?”. The in-depth understanding of the formation and evolution of planetary systems relies on the detection of the diverse exoplanets (especially habitable planets), which is of great significance to enriching human beings’ exploration of the unknown worlds, understanding the origin and evolution of life, and recognizing our status in the universe.

The CHES mission is proposed to discover Earth-like planets around the nearby solar-type stars via ultra-high-precision relative astrometry. The key scientific goals are: (i) to search for the terrestrial planets in habitable zones orbiting 100 FGK stars within 10 pc (the nearby stars), (ii) further to conduct a comprehensive survey and census on the nearby planetary systems.

CHES will offer the first direct measurements of true masses and inclinations of Earth Twins and super-Earths orbiting our neighbor stars based on micro-arcsecond astrometry from space. This will definitely enhance our understanding of the formation of diverse nearby planetary systems and the emergence of other worlds for nearby solar-type stars, and finally reflect the evolution of our own Solar system.

18.2 Scientific Instruments

The payload is a high-quality, low-distortion, high-stability telescope with the optical subsystem, camera subsystem and on-board calibration subsystem. The optical subsystem is a coaxial Three-Mirror Anastigmat (TMA) with a 1.2m-aperture, 0.44°×0.44° field of view and 500–900 nm working waveband. The camera focal plane is composed of 81 MOSAIC scientific CMOS detectors each with 4K×4K pixels. The on-board calibration subsystem consists of a metrology assembly. A heterodyne laser interferometric calibration technology is employed to ensure micro-arcsecond level (1 μas) relative astrometry precision that is required to detect the habitable Earth Twins orbiting our nearby stars.

The mission orbit of the CHES satellite travels about the Lagrange L2 point of the Sun and the Earth. The satellite is designed to have a lifespan of 5 years, during which the entire target stars will be extensively observed.

18.3 Scientific Additional Benefits

CHES will produce fruitful achievements not only in the Earth-like planets but also for cosmology, dark matter and black holes using this extreme relative astrometry

Table 12 Summary of CHES

Science case	Habitable exoplanets orbiting nearby stars
Science objectives	To discover habitable Earths about nearby solar-type stars To conduct a comprehensive survey and census on the nearby planetary systems Extended: cosmology, dark matter and black holes
Overview	Spacecraft at L2 for 5 years Optical telescope (500–900nm); Micro-arcsecond astrometry (1 μ as) Point and stare strategy to enable relative astrometry
What makes CHES unique	Ultra-high-precision relative astrometry simply reachable from space: 0.3 μ as (habitable Earths about the stars at 10 pc) To obtain true masses and orbital architecture (inclinations, <i>etc.</i>) of habitable-zone terrestrial planets and to conduct the census and characterization of nearby planetary systems Extended: Measurements of orbits and distances to reveal the interiors of neutron, <i>etc.</i>
Primary observational targets	closeby F, G, K stellar systems (100 stars with 10 pc) Extended: ultra-faint dwarf galaxies, neutron stars in X-ray binaries, <i>etc.</i>
Scientific Payload	Coaxial three-reflection TMA system Primary mirror: $D = 1.2$ m diameter Long focal length: $f = 36$ m FoV: $0.44^\circ \times 0.44^\circ$, with 6 to 8 reference stars; focal plane with 81 scientific CMOS detectors ($4K \times 4K$, ≥ 50 fps) Nyquist sampling of the PSF Metrology calibration of the Focal Plane Array (FPA): relative positions of pixels at the micro-pixel level for each detector, geometrical parameters of FPA
Spacecraft	Spacecraft dry mass with margin: 1,558 kg. Launch Mass: 2930 kg, fuel mass (990 kg + 382 kg) Attitude Control System: pointing accuracy of 0.07arcsec, pointing stability of 0.0036 arcsec/0.02sec Propulsion system: orbital maneuver engines: 490N+12 \times 10N, attitude control thrusters: 12 \times (1–50 μ N) + 12 \times 20 mN Thermal Control System: working temperature: $20 \pm 5^\circ$ and temperature stability of 45mK for payload; working temperature: -15 – $+45^\circ\text{C}$ for other instruments Telecommand: X-band, communication rate: 20 Mbit \cdot s $^{-1}$
Launcher and operations	CZ-3C: GTO (200 km \times 35958 km). Orbital maneuver to Halo orbit at L2. Launch in 2025 Nominal mission: 5 years. Launch site: Xichang

precision, which helps us better understand the philosophy, life and planet.

Acknowledgement

We acknowledge the contributions from the following colleagues on various missions.

DAMPE: FAN Yizhong (Purple Mountain Observatory).

Insight-HXMT: ZHANG Shu (Key Lab for Particle and Astrophysics, Institute of High Energy Physics).

GECAM: XIONG Shaolin (Key Lab for Particle and Astrophysics, Institute of High Energy Physics).

PolarLight: FENG Hua (Tsinghua University).

GRID: ZENG Ming (Tsinghua University), FENG Hug (Tsinghua University).

Lobster-eye X-ray Satellite: LI Zhiyuan (Nanjing University).

SVOM: WEI Jianyan (National Astronomical Observatories).

EP: YUAN Weimin (National Astronomical Observatories).

CSST: ZHAN Hu (Key Laboratory of Space Astronomy and Technology, National Astronomical Observatories, Chinese Academy of Sciences, Beijing 100101, China; Kavli Institute for Astronomy and Astrophysics, Peking University).

HERD: DONG Yongwei (Key Lab for Particle and Astrophysics, Institute of High Energy Physics).

POLAR-2: SUN Jianchao (Key Lab for Particle and As-

trophysics, Institute of High Energy Physics).

DIXE: CUI Wei (Tsinghua University).

LyRIC: JI Li (Purple Mountain Observatory).

eXTP: ZHANG Shuangnan and YI Shuxu (Key Lab for Particle and Astrophysics, Institute of High Energy Physics).

DAMPE-2: FAN Yizhong (Purple Mountain Observatory).

DSL: CHEN Xuelei (National Astronomical Observatories).

CHES: JI Jianghui (Purple Mountain Observatory).

References

- [1] CHANG J, AMBROSI G, AN Q, *et al.* The dark matter particle explorer mission[J]. *Astroparticle Physics*, 2017, **95**: 6-24
- [2] DAMPE Collaboration. Direct detection of a break in the teraelectronvolt cosmic-ray spectrum of electrons and positrons[J]. *Nature*, 2017, **552**(7683): 63-66
- [3] DAMPE Collaboration, AN Q, ASFANDIYAROV E, *et al.* Measurement of the cosmic ray proton spectrum from 40 GeV to 100 TeV with the DAMPE satellite[J]. *Science Advances*, 2019, **5**(9): eaax3793
- [4] ALEMANNO F, AN Q, AZZARELLO P, *et al.* Measurement of the cosmic ray helium energy spectrum from 70 GeV to 80 TeV with the DAMPE space mission[J]. *Physical Review Letters*, 2021, **126**(20): 201102
- [5] DAMPE Collaboration, LIANG Y F. Search for gamma-ray spectral lines with the DArk matter particle explorer[J]. *Science Bulletin*, 2022, **67**(7): 679-684

- [6] ZHANG S N, LI T P, LU F J, et al. Overview to the hard X-ray modulation telescope (*Insight-HXMT*) satellite[J]. *Science China Physics, Mechanics & Astronomy*, 2020, **63**(4): 249502
- [7] MA X, TAO L, ZHANG S N, et al. Discovery of oscillations above 200 keV in a black hole X-ray binary with insight-HXMT[J]. *Nature Astronomy*, 2021, **5**(1): 94-102
- [8] YOU B, TUO Y L, LI C Z, et al. Insight-HXMT observations of jet-like corona in a black hole X-ray binary MAXI J1820+070[J]. *Nature Communications*, 2021, **12**(1): 1025
- [9] LI C K, LIN L, XIONG S L, et al. HXMT identification of a non-thermal X-ray burst from SGR J1935+2154 and with FRB 200428[J]. *Nature Astronomy*, 2021, **5**(4): 378-384
- [10] GE M Y, JI L, ZHANG S N, et al. Insight-HXMT firm detection of the highest-energy fundamental cyclotron resonance scattering feature in the spectrum of GRO J1008-57[J]. *The Astrophysical Journal Letters*, 2020, **899**: L19
- [11] XIAO S, LIU Y Q, PENG W X, et al. On-ground and on-orbit time calibrations of GECAM[J]. *Monthly Notices of the Royal Astronomical Society*, 2022, **511**(1): 964-971
- [12] FENG H, LI H, LONG X Y, et al. Re-detection and a possible time variation of soft X-ray polarization from the Crab[J]. *Nature Astronomy*, 2020, **4**(5): 511-516
- [13] LONG X Y, FENG H, LI H, et al. X-ray polarimetry of the crab nebula with polar light: polarization recovery after the glitch and a secular position angle variation[J]. *The Astrophysical Journal Letters*, 2021, **912**(2): L28
- [14] LONG X Y, FENG H, LI H, et al. A significant detection of X-ray polarization in Sco X-1 with PolarLight and constraints on the corona geometry[J]. *The Astrophysical Journal Letters*, 2022, **924**(1): L13
- [15] WEN J X, LONG X Y, ZHENG X T, et al. GRID: a student project to monitor the transient gamma-ray sky in the multi-messenger astronomy era[J]. *Experimental Astronomy*, 2019, **48**(1): 77-95
- [16] GAO H Z, YANG D X, WEN J X, et al. On-ground calibrations of the GRID-02 gamma-ray detector[J]. *Experimental Astronomy*, 2022, **53**(1): 103-116
- [17] WANG X I, ZHENG X T, XIAO S, et al. GRB 210121A: a typical fireball burst detected by two small missions[J]. *The Astrophysical Journal*, 2021, **922**(2): 237
- [18] ANGEL J R P. Lobster eyes as X-ray telescopes[J]. *Astrophysical Journal*, 1979, **233**: 364-373
- [19] WEI J, CORDIER B, ANTIER S, et al. The deep and transient universe in the SVOM era: new challenges and opportunities—scientific prospects of the SVOM mission[J]. arXiv:1610.06892, 2016
- [20] GEHRELS N, RAMIREZ-RUIZ E, FOX D B. Gamma-ray bursts in the *Swift* era[J]. *Annual Review of Astronomy and Astrophysics*, 2009, **47**: 567-617
- [21] GOLDSTEIN A, VERES P, BURNS E, et al. An ordinary short gamma-ray burst with extraordinary implications: *Fermi*-GBM detection of GRB 170817A[J]. *The Astrophysical Journal Letters*, 2017, **848**(2): L14
- [22] YUAN W M, ZHANG C, LING Z X, et al. Einstein probe: a lobster-eye telescope for monitoring the x-ray sky[C]//Proceedings of SPIE 10699, Space Telescopes and Instrumentation 2018: Ultraviolet to Gamma Ray. Austin: SPIE, 2018: 1069925
- [23] ZHAN H. The wide-field multiband imaging and slitless spectroscopy survey to be carried out by the Survey Space Telescope of China manned space program[J]. *Chinese Science Bulletin*, 2021, **66**(11): 1290-1298 (詹虎. 载人航天工程巡天空间望远镜大视场多色成像与无缝光谱巡天[J]. 科学通报, 2021, **66**(11): 1290-1298)
- [24] ZHANG S N, ADRIANI O, ALBERGO S, et al. Introduction to the High Energy Cosmic-Radiation Detection (HERD) facility onboard China's future space station[C]//Proceedings of the 35th International Cosmic Ray Conference. Busan, Korea: PoS, 2017: 1077
- [25] DONG Y W, ZHANG S N. Overall status of the high energy cosmic radiation detection facility onboard the future China's space station[C]//Proceedings of the 36th International Cosmic Ray Conference. Madison, USA: PoS, 2019: 062
- [26] ZHANG S N, KOLE M, BAO T W, et al. Detailed polarization measurements of the prompt emission of five gamma-ray bursts[J]. *Nature Astronomy*, 2019, **3**(3): 258-264
- [27] De Angelis N, Burgess J M, Cadoux F, et al. Development and science perspectives of the POLAR-2 instrument: a large scale GRB polarimeter[C]//Proceedings of the 37th International Cosmic Ray Conference. Berlin: The International Union of Pure and Applied Physics (IUPAP), 2021
- [28] CUI W, BREGMAN J N, BRUIJN M P, et al. HUBS: a dedicated hot circumgalactic medium explorer[C]//Proceedings of SPIE 11444, Space Telescopes and Instrumentation 2020: Ultraviolet to Gamma Ray. SPIE, 2020: 114442S. DOI: 10.1117/12.2560871
- [29] JI L, LOU Z, ZHANG J L, et al. Mapping diffuse emission in Lyman UV band[C]//Proceedings of SPIE 11444, Space Telescopes and Instrumentation 2020: Ultraviolet to Gamma Ray. SPIE, 2020: 1144407
- [30] ZHANG S N, SANTANGELO A, FEROCI M, et al. The enhanced X-ray timing and polarimetry mission—eXTP[J]. *Science China Physics, Mechanics & Astronomy*, 2019, **62**(2): 29502
- [31] CHEN X L, YAN J Y, DENG L, et al. Discovering the sky at the longest wavelengths with a lunar orbit array[J]. *Philosophical Transactions of the Royal Society A*, 2021, **379**(2188): 20190566

Space Solar Physics in China: 2020–2022*

GAN Weiqun¹, FAN Quanlin²

1. Key Laboratory of Dark Matter and Space Astronomy, Purple Mountain Observatory, Chinese Academy of Sciences, Nanjing 210023
2. National Space Science Center, Chinese Academy of Sciences, Beijing 10090

Abstract

To follow up the last report two years ago, what happened from 2020 to 2022 deserves specially mentioning: CHASE was successfully launched on 14 October 2021; ASO-S will finish soon its Phase-D study and is scheduled for launch in October 2022; four solar mission candidates are being undertaken the engineering project evaluations; three solar mission proposals are being undertaken the background project evaluations; there are also quite a number of pre-study space solar physics projects getting either newly supported or finished. This paper describes in brief the status of all these related projects.

Key words

Space astronomy, Solar physics mission

1 Introduction

In order to see clearly the route of Chinese space solar physics, to read the series reports^[1–10] is recommended, especially to read the last report^[10] two years ago, so that one can better understand this report in the context of previous ones.

At first, Chinese H-alpha Solar Explorer (CHASE) was successfully launched on 14 October 2021. It was designed to spectrally image the whole Sun at lines of H-alpha (656.28 nm) and FeI (656.92 nm). A scheme of grating spectrometer plus scanning mirrors was used in its optical system. The first light and preliminary results look very nice and match well to the designed goals^[11]. Another remarkable progress is the ultraviolet (19.5 nm) and soft X-ray (0.6–8.0 nm) images of the Sun, obtained

by a payload on Fengyun-3E meteorological satellite, which was launched on 5 July 2021. The last most deserving of mention is ASO-S, the first Chinese comprehensive solar mission^[12], which overcame a series of challenges in manufactures in a strict epidemic-control social environment. The final launch is scheduled in October 2022.

The detailed progress reports for CHASE, solar observations by Fengyun-3E and ASO-S can be found in Ref. [13–15], respectively. Following we therefore pay attention to other solar mission candidates which are now being undertaken the engineering evaluations, solar mission proposals which are being undertaken the background evaluations, and some pre-study space solar physics projects either newly supported or finished in the past two years.

* Supported by Chinese Academy of Sciences (XDA15052200) and by National Natural Science Foundation of China (11921003 and U1931138)

Received May 27, 2022

2 Missions Under Engineering Evaluations

In the last report^[10], a total of 4 finished pre-study projects and 9 undertaking pre-study projects were described. Among them, two years later, there are four (in fact five) which are confidently ready to compete for the engineering projects. They are as follows.

(1) Solar Polar-orbiter Observatory (SPO): led by National Astronomical Observatories, SPO aims at pursuing both origins of solar magnetic field and high-speed solar wind, as well as numerical modeling of the global heliosphere. The payloads include: magnetograph, white-light coronagraph, heliosphere imager, in-situ particle package, low-frequency radio spectrometer, and X-ray imager. The total weight of payloads is over 200 kg. The maximum inclination angle of the orbit is designed to be 81° , with a perihelion of 0.9 AU and aphelion of 1.15 AU. Therefore, SPO could be the first mission which observes the polar magnetic field in more details.

(2) Global Observation with three Spacecrafts around the Sun (GOSS): led by University of Science and Technology of China, GOSS aims at imaging the global Sun, by proposing to launch a group of three spacecraft into the Earth orbit around the Sun, separating each other by 120° . The primary scientific objectives are to study the origins of solar activity cycle, solar eruptions and extremely space weather events. The payloads include: full-disk vector magnetograph, solar ultraviolet imager, high-energy radiation detector, wide-field white-light coronagraph, and a group of in-situ particle and field detectors.

(3) Solar-Terrestrial Mission at L2: led by National Space Science Center, this project plans to launch a mission working at L2, making use of the natural shelter of the Earth (in fact only partially occulted) to observe the solar corona. The main payloads are an imaging spectroscopic polarimetric coronagraph (in tradition) plus in-situ plasma analyzer and in-situ magnetometer, in order to study the origins and propagations of CMEs and the solar wind.

(4) Solar or Solar-Terrestrial Observatory at L5: there are in fact two independent projects, one is Solar-Terrestrial Environment Monitor (STEM) led by National Space Science Center, and the other is Solar Observatory at L5 (SO-L5) led by Nanjing University. Both aim at making full use of L5 advantage and get a

bird's view of the whole space from the Sun to the Earth and beyond. STEM pays more attention to the space weather domain while SO-L5 emphasizes more on solar physics. Both proposals are more or less similar in the payload deployments, including a couple of in-situ and remote-sensing instruments.

Above proposals (except SO-L5) joined the first-round meeting evaluations on 12 February 2022, organized by NSSC under the framework of CAS's Strategic Priority Program on Space Science. Projects (1), (2) and (3) seem to enter the next round evaluation, but it is obviously impossible to select all these three proposals to start the engineering phases finally. There will be fierce competition in the following steps. On the other hand, OS-L5 will try to pursue other channel, *i.e.*, to compete for support by Chinese National Space Administration, in late 2022. The OS-L5 team has some experience from this channel for the adoption of CHASE mission. In addition, as mentioned in the last report^[10], there was a proposal called Space Weather Mission at L1, which belongs to the National Satellite Meteorological Center and is still waiting for the start of engineering phases. Anyway, currently we do not know which one could be ultimately successful or maybe none is selected, since within a limited financial budget competition with other domains are obviously unavoidable.

3 Missions under Background Project Evaluations

Among the pre-study projects described in the last report^[10], besides above 5 projects which are being undertaken the engineering evaluations, there are still three projects which were recently submitted to apply for a background project, *i.e.*, an intensive study for clarifying some major scientific questions and making the project technically more feasible. Background study is in principle a necessary stage within the framework of CAS's Strategic Priority Program on Space Science if the project would like to go further into the engineering phases. These three projects are as follows.

(1) Close Observation on Solar Eruptions (COSE): led by Yunnan Astronomical Observatory, COSE aims at measuring the magnetic reconnection region directly and exploring the current sheet which results in solar flares and CMEs, with a group of instruments for energetic particles, ambient plasma, electric field, magnetic field, EUV imagers, and so on. The closest distance

from the Sun is designed to be 3 to 5 solar radius. To measure in-situ current sheet in such a close distance is really a great challenge both in technology and science, and needs a series of extensive studies to prove its feasibility.

(2) Solar and Stellar Coronal Explorer: led by Peking University, this project aims at combining both observations of the solar CMEs and the stellar CMEs on a single platform, comparing the difference of the solar CMEs from the stellar CMEs, and understanding the essence of CMEs. The proposed payloads include solar EUV spectrometer, solar EUV spectral coronagraph, stellar EUV spectrometer, stellar EUV telescope, and some other remote-sensing and in-situ instruments. This proposal is based on the pre-study project of Solar Transition region Observation and Research Mission (STORM, January 2018 to December 2019), but the revision is obvious and needs to be further studied.

(3) Formation-flying High Energy Solar Observatory: led by Purple Mountain Observatory, this project plans to launch two spacecraft separated about 100 meters. The front one is equipped with the focused grazing telescope, while the rear one is the detector, so as to get unprecedentedly high spatial resolution in solar hard X-ray imaging. Besides the focused grazing X-ray telescope, the updated project related to the original pre-study one includes also two other instruments, extremely high-spatial-resolved EUV and soft X-ray telescopes, and a solar gamma-ray imager. The extension of the instruments and the spacecraft itself need to be thoroughly investigated, so as to prove its advantage and feasibility.

At the moment, above three proposals are still awaiting to be evaluated in the soon-coming new round background project competitions. It is hard to say the results. Even one is selected, two to three years are needed to carry on. After background stage even if it could go smoothly into the engineering phases, other four to five years are necessary. So, for these background candidate projects the earliest date into the orbit would be around 2030.

4 Pre-study Projects: Newly-supported

During 2020–2022, there are a set of newly funded pre-study projects. Some have gotten further supports due to

their good behaviors in the first term of pre-studies, others are new proposals. We mention only part of them as follows.

(1) On key technologies of solar coronagraph in EV/EUV: it focuses on the design of raster with high resolution, suppress of stray light, detector with large dynamic range, and numerical discriminator of space and wavelength. Outcomes of the project could be applied to future missions.

(2) On key technologies of solar imaging at 46.5 nm: it focuses on the fabrication of a multi-filmed reflector, the property of CMOS under vacuum environment, and so on. Achievements of the project will serve directly the background candidate of Solar and Stellar Coronal Explorer or other missions.

(3) On heliosphere imager: it focuses on the design of a comprehensive heliosphere imager, stray-light model of optical system, fabrication of a prototype model, and the data processing method. Achievements of the project seem to have a wide application in future missions.

(4) High Resolution Solar Soft X-ray Telescope: it aims at proposing a novel scheme to realize a high resolution solar soft X-ray telescope.

5 Conclusions

We have seen from the above that in the past two years from 2020 to 2022 quite a lot of progress has been made, especially the zero-breakthrough of the first Chinese solar spacecraft CHASE was launched on 14 October 2021, and before the end of 2022 the first Chinese comprehensive solar mission ASO-S will also be launched. The researches based on the data from both CHASE and ASO-S will be used to promote substantially the progress of solar physics. Besides, there are five solar mission proposals which are now being undertaken the engineering evaluations, and three other solar mission proposals which have been submitted for the new round competitions of background projects. Optimistically, after the successful launch of ASO-S, we might expect one or two new solar missions which could get a green light either for engineering phases or for background stages, so that we solar community could make sustainable development.

References

- [1] ZHANG H Q. The progress on space astronomy in China during

- 2000-2002[J]. *Chinese Journal of Space Science*, 2002, **22**(S1): 14-20
- [2] GAN W Q, XUE S J. Space astronomy in China: 2002-2004[J]. *Chinese Journal of Space Science*, 2004, **24**(S1): 99-101
- [3] GAN W Q. Space astronomy in China during 2004-2006[J]. *Chinese Journal of Space Science*, 2006, **26**(S1): 76-78
- [4] GAN W Q. Space astronomy in China: 2006-2008[J]. *Chinese Journal of Space Science*, 2008, **28**(5): 424-425
- [5] GAN W Q, ZHANG S N, YAN Y H, et al. Space astronomy in China: 2008-2010[J]. *Chinese Journal of Space Science*, 2010, **30**(5): 424-426
- [6] ZHANG S N, YAN Y H, GAN W Q. China's space astronomy and solar physics in 2011-2012[J]. *Chinese Journal of Space Science*, 2012, **32**(5): 605-617
- [7] GAN W Q. Space solar physics in 2012-2014[J]. *Chinese Journal of Space Science*, 2014, **34**(5): 563-564
- [8] GAN W Q. Space solar physics in China: 2014-2016[J]. *Chinese Journal of Space Science*, 2016, **36**(5): 636-638
- [9] GAN W Q, FAN Q L. Space solar physics in China[J]. *Chinese Journal of Space Science*, 2018, **38**(5): 662-664
- [10] GAN W Q. Space solar physics in China[J]. *Chinese Journal of Space Science*, 2020, **40**(5): 726-728
- [11] LI C, FANG C, LI Z, et al. The Chinese Ha solar explorer (CHASE) mission: an overview[J]. arXiv: 2205.05962, 2022
- [12] GAN W Q, FENG L, SU Y. A Chinese solar observatory in space[J]. *Nature Astronomy*, 2022, **6**: 165
- [13] FANG C. Chinese H-alpha solar explorer (CHASE)[J]. *Chinese Journal of Space Science*, 2022, **42**(5). in press
- [14] ZHANG P. The progress of Fengyun meteorological satellite[J]. *Chinese Journal of Space Science*, 2022, **42**(5). in press
- [15] GAN W Q. Progress report on ASO-S[J]. *Chinese Journal of Space Science*, 2022, **42**(5). in press

A Brief Review of Interplanetary Physics Research Progress in Mainland China during 2020–2022*

ZHAO Xinhua¹, HE Jiansen², SHEN Chenglong³, FENG Shiwei⁴, JIANG Chaowei⁵, LI Huichao⁵, QIN Gang⁶, LUO Xi⁷

1. State Key Laboratory of Space Weather, National Space Science Center, Chinese Academy of Sciences, Beijing 100190
2. School of Earth and Space Sciences, Peking University, Beijing 100871
3. CAS Key Laboratory of Geospace Environment, Department of Geophysics and Planetary Sciences, University of Science & Technology of China, Hefei 230026
4. Shandong Provincial Key Laboratory of Optical Astronomy and Solar-Terrestrial Environment, School of Space Science and Physics, Shandong University at Weihai, Weihai 264209
5. Institute of Space Science and Applied Technology, Harbin Institute of Technology (Shenzhen), Shenzhen 518055
6. School of Science, Harbin Institute of Technology (Shenzhen), Shenzhen 518055
7. Shandong Institute of Advanced Technology, Jinan 250100

Abstract

Via independent research by the Chinese scientists or their international collaborations, great achievements have been made in interplanetary physics research in Mainland China during the past two years (2020–2022). More than 150 papers have been published in academic journals in this field during this period. These achievements can be grouped into the following areas, at least: (i) solar corona; (ii) solar and interplanetary transient phenomena; (iii) radio bursts; (iv) Magnetohydrodynamic (MHD) numerical modeling; (v) solar energetic particles and cosmic rays. These advances have greatly enriched our understanding of interplanetary physics, *i.e.* our knowledge of solar activities and solar eruptions, their propagation in the interplanetary space, and the corresponding geoeffects on the Earth. In the sense of application, they have also improved the forecasting of space weather. In this paper we will give a very short review about these advances.

Key words

Solar wind, Solar eruptions, Energetic particles, Interplanetary transients, Space weather

1 Solar Corona and Solar Wind

Coronal loops are building blocks of solar corona. Li *et*

al.^[1] reported that magnetic reconnection between loops could be accelerated by a nearby filament eruption. Hou *et al.*^[2] presented direct observational evidence for the

* Supported by the Strategic Priority Research Program of Chinese Academy of Sciences (XDB 41000000), NSFC grants (41531073, 41731067, 41861164026, 41874202, 41474153, and 42074183), the Youth Innovation Promotion Association of Chinese Academy of Sciences (2016133), and Pandeng Program of National Space Science Center, Chinese academy of Sciences

Received June 29, 2022

formation of coronal loops through magnetic reconnection as new magnetic fluxes emerge into the solar atmosphere.

Coronal jets are one type of pervasive and explosive phenomena on the Sun and are often observed in EUV and X-ray passbands in Active Regions (ARs) and Coronal Holes (CHs). Chen *et al.*^[3] reported some tornado-like mini-jets suspended in the corona, which were probably generated by fine-scale external or internal magnetic reconnections. In quiet-Sun regions, Hou *et al.*^[4] reported many smallest coronal jets ever observed with high-resolution observations from the High Resolution Telescopes of the Extreme Ultraviolet Imager (EUI) onboard Solar Orbiter (SO).

Recent high-resolution observations of EUI/SO revealed prevalent small-scale transient brightenings, named as campfires, appearing frequently in the corona above the quiet Sun. Using a numerical three-dimensional (3D) Magnetohydrodynamics (MHD) model, Chen *et al.*^[5] investigated the relation of brightenings to the magnetic field and the driven processes. They found that component reconnection between bundles of field lines at coronal heights could generate the majority of campfire events.

Significant progress has been made in the measurement of a coronal magnetic field. Using spectral observations, Yang *et al.*^[6,7] have firstly mapped the plane-of-sky component of the global coronal magnetic field. The field strengths in the corona were measured to be mostly 1–5 gauss from 1.05 to 1.35 solar radii. Based on the theory of gyrosynchrotron emission, Zhu *et al.*^[8] performed microwave diagnostics to measure the magnetic field strengths in solar flaring loops. Chen *et al.*^[9] performed a forward modeling with a 3D radiation MHD model of a solar AR and found that the magnetic-field-induced transition technique can provide reasonably accurate measurements of the coronal magnetic field.

Coronal wave-like phenomena have been extensively studied, which are generally associated with flares and CMEs. Their formation mechanisms, propagating properties and relation to other activities have been studied by Zhou *et al.*^[10], Zhou *et al.*^[11,12], Duan *et al.*^[13], and Hou *et al.*^[14]. In addition, Zhang *et al.*^[15–17] studied several events, in which oscillations of remote coronal loops could be triggered by flares or the eruption of a prominence-carrying flux rope.

Supra-arcade Downflows (SADs) appear as dark,

teardrop-shaped features descending toward flaring loop top, which might be the results of magnetic reconnection during solar flares. The thermodynamic properties of SADs have been studied by Xue *et al.*^[18] and Li *et al.*^[19]. Using EUV images, Samanta, Tian *et al.*^[20] found direct evidence of plasma heating to a temperature of 10–20 MK in flaring coronal loops collided by SADs and clear signatures of quasi-periodic enhancement in the full-Sun-integrated soft X-ray emission created by the interactions between flaring loops and SADs.

Quiescent coronal rain is generally observed to form along with both closed and open magnetic field structures. Recently, Li *et al.*^[21–23] proposed a new and alternative formation mechanism for quiescent coronal rain. They found that some quiescent coronal rain events could be generated by interchange magnetic reconnection between open and closed field lines. Filament formations and quasi-steady sunspot supersonic downflows were found to be associated with magnetic reconnection between two sets of loops, and the subsequent cooling and condensation processes of plasma by Li *et al.*^[24], Yang *et al.*^[25], and Chen *et al.*^[26].

Using Parker Solar Probe data, it is found for the solar wind turbulence that the proton-scale break frequency is controlled by the plasma β and the three-dimensional anisotropy and scaling properties exist in both the transition range and the ion-electron scales (Duan *et al.*^[27,28], Zhang *et al.*^[29]); the outward Alfvén mode dominates with a minority of outward fast mode and inward Alfvén mode at MHD scale, the kinetic Alfvén waves and Alfvén ion cyclotron waves co-exist at kinetic scale (Huang *et al.*^[30], Zhu *et al.*^[31]); the correlation between spectral index and magnetic helicity exists (Zhao *et al.*^[32]); the energy supply mechanism by low-frequency break sweeping for the solar wind turbulence supplies enough energy for the slow solar wind heating and the energy transfer rate is consistent with that from the traditional eddy decay mechanism (Wu *et al.*^[33,34]).

For the structures in the solar wind, it is found that the solar origin of the compressive Alfvénic spikes can be the guide-field discontinuity (He *et al.*^[35]); the large-amplitude fluctuations inside the switchbacks are the magnetic-velocity alignment structure, which is one of the main components in the slow solar wind within 0.1–0.3 AU (Wu *et al.*^[36], Wu *et al.*^[37]); the ion cyclotron waves are inside small-scale flux ropes with medium Alfvénicity (Shi *et al.*^[38]); the discontinuity oc-

currence and the occurrence ratio of the rotational and tangential discontinuity decrease with the heliocentric distance (Liu *et al.*^[39]); the duration longer, the depth deeper and the occurrence no clear variation with the increasing heliocentric distance for linear magnetic holes (Yu *et al.*^[40]).

For the waves and instabilities in the solar wind, Shi *et al.*^[41] exhibited the observational evidence of the non-linear interactions of the oblique ion acoustic wave or lower-hybrid wave and the electron Bernstein mode wave; Chen *et al.*^[42] found the electron cyclotron maser emission mechanism of type IIIb burst and the modulation of Alfvén waves to generate the fine striae structure.

Other than the Parker Solar Probe (PSP) observation, other missions keep producing new observations: the spectral indices at MHD scales vary from $-5/3$ in the near-Mercury solar wind to -1.3 within the Mercury magnetosheath (Huang *et al.*^[43]); the low-frequency break sweeping mechanism provides enough energy for the fast solar wind heating and the sign of the energy cascade rate relates to the large structures (Wu *et al.*^[44,45]); the solar activity level affects the magnetic field and the dynamic pressure in the solar wind upstream of Mars (Liu *et al.*^[46]); low-frequency whistler waves modulate electrons and generate higher-frequency whistler waves (Yao *et al.*^[47]). Using Wind data at 1 au, it is found that the scaling indices are isotropic with a stationary background local field (Wu *et al.*^[48]); the fluctuations in the slow wind are consistent with the magnetic-field directional turnings and magnetic-velocity alignment structures (Wang *et al.*^[49]); the solar wind temperature depends on the radial angle, alpha-proton differential flow vector and the magnetic helicity (Zhao *et al.*^[50], Zhao *et al.*^[51]); the stochastic heating depends on the plasma β and cyclotron damping of kinetic Alfvén waves leads to the proton perpendicular heating (Zhao *et al.*^[52]).

Based on the MMS observations in the magnetosheath, He *et al.*^[53] found the positive dispersion due to the Hall effect and the dominant parallel dissipation with energy transferred to electrons; Hou *et al.*^[54] found magnetic reconnection not the major contributor to energy dissipation; Luo *et al.*^[55] revealed the energy exchange between the electromagnetic energy, particle bulk kinetic energy and thermal energy; Wang *et al.*^[56] found that the anisotropies at sub-ion scales rose and fell as the scales decreased; Zhu *et al.*^[57] found the re-

markable differences of the intermittent properties between the magnetic and electric field from ion scales to sub-electron scales.

By analyzing the dispersion relation of fluctuating field components directly issued from the shock simulation, Yang *et al.*^[58] obtained key findings concerning wave excitations at the shock front: (i) at the leading edge of the foot, two types of Electrostatic (ES) waves are observed. (ii) From the middle of the foot all the way to the ramp, electrons can couple with both incident and reflected ions. Results shed new insight on the mechanism for the occurrence of ES wave excitations and possible electromagnetic wave emissions at young coronal mass ejection-driven shocks in the near-Sun solar wind.

Liu *et al.*^[59] reported on two small solar wind transients embedded in the corotating interaction region, characterized by surprisingly lower proton density compared with their surrounding regions. A synthesized picture for event One combining the observations by STEREO B, ACE, and Wind showed that this small solar transient has an independent magnetic field. Back-mapping links the origin of the small solar transient to a small coronal hole on the surface of the Sun. They concluded that such small solar wind transients may have originated from a small coronal hole at low latitudes.

Chen *et al.*^[60] performed a detailed analysis of the 2020 January 30 event and found the possible cause of the Macro Magnetic Hole (MMH) using coordinated remote sensing observations from STEREO A and PSP in situ measurements. The results indicate that an MMH represents a brief encounter with the rippled heliospheric current sheet. Out of the data from the first four orbits of PSP, they identified 17 MMHs and carried out a statistical analysis. These results suggest that MMHs are a frequent phenomenon that may shed light on the dynamics of the HCS and the origins and evolutions of the solar wind structures in the heliosphere.

Liu *et al.*^[61] presented an approach to determining the solar wind angular momentum flux based on observations from PSP. A flux of about 0.15×10^{30} dyn·cm·sr⁻¹ near the ecliptic plane and 0.7:1 partition of that flux between the particles and magnetic field is obtained by averaging data from the first four encounters within 0.3 au from the Sun. The angular momentum flux and its particle component decrease with the solar wind speed, while the flux in the field is remarkably constant. A

speed dependence in the Alfvén radius is also observed, which suggests a “rugged” Alfvén surface around the Sun. Substantial diving below the Alfvén surface seems plausible only for relatively slow solar wind given the orbital design of PSP. The large proton transverse velocity observed by PSP is perhaps inherent in the solar wind acceleration process, where an opposite transverse velocity is produced for the alphas with the angular momentum conserved.

Qi *et al.*^[62] calculated the propagation of small coronal hole winds and Alfvén waves using a simple two-dimensional solar wind model. Their results showed that the Alfvén waves are separated from the co-originated plasma during the propagation, leading to small coronal hole winds with low Alfvénicity and ordinary slow winds with high Alfvénicity. This result provides a new insight into the origin of the slow solar wind mystery.

Liu *et al.*^[63] did a Superposed Epoch Analysis (SEA) to investigate the plasma characteristics in the vicinity of switchbacks and their radial evolution. SEA is a good way to get the statistical average features of certain types of events that have obvious boundaries and different durations. For 55 events ranging from 1 to 30 min, the SEA results show that a small parcel of plasma is piling up in front of the reversed field, and that the trailing plasma density enhancement is much lower. This asymmetry can be explained in part by a fast ejecta and plasma piling up around it. The evolution of events at different distances from the Sun also supports that the switchbacks are related to the faster flow near the Sun. However, these features cannot rule out the possibility that these switchbacks and the related fast flows may be caused by the interchange reconnection near the surface of the Sun.

Meng *et al.*^[64] identified 242 switchbacks during the first two encounters of PSP. Statistics methods were applied to analyze the distribution and the rotation angle and direction of the magnetic field rotation of the switchbacks. Their main conclusions are as follows: (i) the rotation angles of switchbacks observed during the first encounter seem larger than those of the switchbacks observed during the second encounter in general; (ii) the tangential component of the velocity inside the switchbacks tends to be more positive (westward) than in the ambient solar wind; (iii) switchbacks are more likely to rotate clockwise than counterclockwise, and the number of switchbacks with clockwise rotation is

1.48 and 2.65 times those with counterclockwise rotation during the first and second encounters, respectively; (iv) the diameter of switchbacks is about 10^5 km on average and across five orders of magnitude (10^3 – 10^7 km).

2 Solar and Interplanetary Transient Phenomena

2.1 Large Scale Structures

In the study of large-scale interplanetary transients, a series of achievements have been made in the propagation of CMEs, the in-situ characteristics of CMEs and shocks, and the evolution of CMEs based on multi-point observations.

In terms of CME propagation, many methods for analyzing CME propagation properties based on multi-point observations have been established. Li *et al.*^[65] developed a new method called CORrelation-Aided Reconstruction (CORAR) to recognize and locate CMEs based on two simultaneous STEREO-A/B H_I images. This method does not presume any morphology of transients and can be run in an automated way. The accuracy of the reconstruction may be affected by the separation angle between the two spacecraft. Lyu *et al.*^[66] further indicated that the optimal separation angle should locate between 120° and 150° . In addition, Li *et al.*^[67] put forward a technique called maximum correlation-coefficient localization and cross-correlation tracking to reconstruct the radial velocity map of CMEs in 3D space based on 2D white-light images, and used it to estimate the expansion rate as well as some kinematic properties.

In terms of in-situ measurements of CME properties, some achievements have been made in the study of the southward magnetic fields in ICMEs. Shen *et al.*^[68] analyzed the origins of intense B_s in different types of ICMEs, finding that the ICME interaction events are more likely to carry extreme intense B_s and cause large geomagnetic storms. In particular, they indicated that some ICME interaction events, like the completely shocked ICME (ICME-in-sheath) or ICME cannibalism, could be classified as isolated ICME events. Liu *et al.*^[69] suggested that a geomagnetic storm with a minimum Dst of about -2000 nT could occur in principle if the ICME-in-sheath event on 23 July 2012 hit the Earth.

Besides, there has also been some work focusing on the magnetic flux rope structure of CMEs. Song *et al.*^[70]

conducted comparative statistics on several parameters, including the shock compression ratio, the sheath and ejecta sizes, the sheath-to-ejecta ratio, as well as the magnetic field strength in both sheath and ejecta regions of CMEs with and without magnetic flux ropes. Their analyses suggested that ICMEs without magnetic flux ropes mainly resulted from the spacecraft passing through the ICMEs from the leg flank. Zhao *et al.*^[71] made a statistical study of the azimuthal flux of flux ropes embedded within MCs near 5 AU, finding that the average azimuthal flux was less than 20% of that near 1 AU and the rope structure occupied from 30% to 100% of the magnetic cloud interval with an average of 69%. The results indicate that the rope structure of MCs still can be efficiently destructed as they move out beyond 1 AU.

The compositions of the ICMEs have also been analyzed. Song *et al.*^[72] conducted a statistical study on ion charge states and relative element abundances within ICMEs measured by ACE spacecraft from 1998 to 2011, and found that all the ICME compositions possess a solar cycle dependence. Huang *et al.*^[73] presented a comprehensive analysis of plasma and composition characteristics inside Magnetic Clouds (MCs). The results indicated that MCs of different speeds showed differences in composition and structure. The bimodal distribution of $\langle Q_{\text{Fe}} \rangle$ in both the fast and slow MCs suggests the existence of flux rope prior to the eruption. In addition, the distribution of iron charge state and some relevant element abundance ratio distribution inside fast MCs agrees with the “standard model” for CME/flares. Song *et al.*^[74] demonstrated that the helium abundance (A_{He}) in both ICMEs and slow wind exhibited a positive correlation with the sunspot numbers, indicating that the high A_{He} emanates from active regions as more ICMEs and slow wind originate from active regions around solar maximum. In the meantime, no high A_{He} data points existing in fast wind throughout a solar cycle imply that coronal holes do not emanate plasmas with enriched helium.

With the help of the recent planetary exploration missions, researches about the properties of ICMEs and shocks at other radial distances have been carried out. Based on the Venus Express (VEX) observation, Wang *et al.*^[75] established a list of 143 Fast Forward (FF) shocks near Venus covering the time period from 2006 to 2014. The shock occurrence at Venus shows a correlated variation with the solar cycle. On average, fast

forward shocks are stronger and less perpendicular near Venus than near Earth. Using the measurements from the Mars Atmosphere and Volatile Evolution (MAVEN) spacecraft, in orbit around Mars, Zhao *et al.*^[76] identified 24 ICMEs and examined the statistical properties of the ICMEs at Mars. Meanwhile, Huang *et al.*^[77] identified 52 fast shocks observed by MAVEN, including 39 FF shocks and 13 Fast Reverse (FR) shocks. Most (79%) of the FF shocks are driven by Stream Interaction Regions (SIRs) with only a few cases being driven by interplanetary coronal mass ejections, and all of the FR shocks are driven by SIRs.

In addition, studies of the CME evolution based on multipoint observation have been carried out. Chi *et al.*^[78] presented the “ghost front” model to combine remote observations from STEREO/SECCHI and in situ observations from the Wind and VEX spacecraft, and to derive the kinematics and propagation directions of the two CMEs left the Sun on 13–14 June 2012. Xu *et al.*^[79] report the formation process of the shock-ICME complex structure around 22 March 2011 based on the in-situ observations of two radial aligned spacecraft, VEX and STEREO-A. The interaction enhanced the magnetic field strength of the ICME by a factor of 2.3 and significantly shorten its duration.

2.2 Small Scale Structures

In the study of small-scale interplanetary transient structures, researches on the origin and evolution of small-scale magnetic flux ropes scientists have been carried out. In order to shed some light on the dispute of whether Small Flux Ropes (SFRs) are homologous to magnetic clouds, Xu *et al.*^[80] analyzed the properties of SFRs in ICMEs and SFRs outside the ICMEs. On the assumption that SFRs in ICMEs have the same origin as magnetic clouds, they compare the SFRs from several aspects, including magnetic field strength, expansion signatures, iron charge state, and counter streaming electrons. The results suggest that most of the SFRs near Earth have different origins from magnetic clouds. In addition, Feng *et al.*^[81] indicated that interchange reconnection and disconnection might be two important mechanisms changing the magnetic topology of the SFRs during their propagation in the interplanetary space.

3 Radio Bursts

Electron Cyclotron Maser Emission (ECME) is regarded

as a plausible source for coherent radio radiations from solar active regions (*e.g.*, solar radio spikes). Ning *et al.*^[82] presented a 2D3V fully kinetic electromagnetic particle-in-cell simulation to investigate the wave excitations and subsequent nonlinear processes induced by the energetic electrons in the loss-cone distribution. As a main result, they obtained strong emissions at the second-harmonic X mode (X2). While the fundamental X mode (X1) and the Z mode are amplified directly via the electron cyclotron maser instability, the X2 emissions can be produced by nonlinear coalescence between two Z modes and between Z and X1 modes. Ning *et al.*^[83] also studied the harmonic emissions generated by ECME driven by energetic electrons with the horseshoe distribution to solve the escaping difficulty of ECME for solar spikes. It is found that the horseshoe-driven ECME can lead to an efficient excitation of X2 and X3 with a low value of ω_{pe}/Ω_{ce} , providing novel means for resolving the escaping difficulty of ECME when applied to solar radio spikes. The simultaneous growth of X2 and X3 can be used to explain some harmonic structures observed in solar spikes.

On the basis of the ECMI-plasma emission mechanism, Li *et al.*^[84] examined the Double Plasma Resonance (DPR) effect and the corresponding plasma emission at both Harmonic (H) and Fundamental (F) bands using particle-in-cell simulations with various ω_{pe}/Ω_{ce} . They found that (i) the simulations reproduce the DPR effect nicely for the upper hybrid and Z modes, as seen from their variation of intensity and linear growth rate with ω_{pe}/Ω_{ce} , (ii) the intensity of the H emission is stronger than that of the F emission by ~ 2 orders of magnitude and varies periodically with increasing ω_{pe}/Ω_{ce} , while the F emission is too weak to be significant, (iii) the peak-valley contrast of the total intensity of H is ~ 4 , and the peak lies around integer values of ω_{pe}/Ω_{ce} (10 and 11) for the present parameter setup.

Ni *et al.*^[85] performed a fully kinetic, electromagnetic particle-in-cell simulation to investigate the proposed radiation process. They found that the electrostatic UH mode is the fastest-growing mode. Around the time when its energy starts to decline, the W mode grows to be dominant. During this stage, they observe significant F and H plasma emissions. They suggested that the F emission is caused by coalescence of almost counter propagating Z and W modes, while the H emission arises from a coalescence of an almost counter propagating UH mode at a relatively large wave number.

Thus the plasma emission investigated here is induced by a combination of wave growth due to ECMI and further nonlinear wave-coupling processes.

Li *et al.*^[86] performed 2.5-dimensional Particle-in-Cell (PIC) simulations to investigate the plasma emission excited by a relativistic electron beam using different pitch angles in the magnetized plasma. Langmuir waves at the fundamental and harmonic frequencies were excited via the energy dissipation of the electron beam. The backward Langmuir waves up to the third harmonic frequencies were reproduced in the cases of large pitch angles, likely arising from the reflecting and scattering of density fluctuations to the Langmuir waves during electron beam-plasma interaction.

Feng and Lü^[87] and Feng and Zhao^[88] presented recent progresses on observational studies of the fine structures of type II and type III radio bursts and outlined outstanding issues for future studies. These fine structures can be used to diagnose the coronal parameters, such as electron densities, atmospheric turbulences, energetic electron velocities, and magnetic field strength. It is of great importance to use data with high angular resolution available from newly-built radio heliographs in China for research.

Gao *et al.*^[89] investigated the reverse-drifting (RS) type-III bursts, intermittent sequence of type-U bursts, Drifting Pulsation Structure (DPS), and fine structures observed by the Yunnan Observatories Solar Radio Spectrometer (YNSRS). Their observations are consistent with previous numerical simulation results, support numerical simulations during the flare-impulsive phase, and are generally consistent with the results of numerical simulations.

Wan *et al.*^[90] performed a detailed statistical study of fiber bursts observed by the Chinese Solar Broadband Radio Spectrometers in Huairou (SBRS/Huairou) with high spectral-temporal resolutions in the frequency ranges of 1.10–2.06 GHz and 2.60–3.80 GHz during 2000–2006. The results indicate that most fiber bursts have a close temporal relation with energetic electrons. Tang *et al.*^[91] identified more than 600-millisecond microwave spikes which were also recorded by the SBRS/Huairou during an X3.4 solar flare on 2006 December 13 and presented a statistical analysis about their parametric evolution characteristic. They found that the spikes have nearly the same probability of positive and negative frequency drifting rates not only in the flare rising phase, but also in the peak and decay phase.

Zhang *et al.*^[92] presented the main observational results identified by MUSER from 2014 to 2019, including the quiet Sun and 94 solar radio burst events. They found that there are 81 events accompanied with Geostationary Operational Environmental Satellites (GOES) Soft X-ray (SXR) flares, among which the smallest flare class is B1.0. There are 13 events without accompanying any recorded flares, among which the smallest SXR intensity during the radio burst period is equivalent to level-A. The main characteristics of all radio burst events are presented, which shows the powerful ability of MUSER to capture the valuable information of the solar non-thermal processes and the importance for space weather.

Lu *et al.*^[93] reported Quasi-Periodic Pulsations (QPPs) with double periods during three solar flares. QPPs with double periods of about two minutes and one minute was first found in the Ly- α emission. They suggested that the two-minute QPP results from the periodic acceleration of nonthermal electrons during magnetic reconnections. Hong *et al.*^[94] also reported the analysis of multi-wavelength observations of QPPs during the impulsive phase of the C6.7 flare on 9 May 2019. Their observations suggest that the flare QPPs are possibly related to nonthermal electrons accelerated by the intermittent magnetic reconnection during the flare's impulsive phase.

Lü *et al.*^[95] presented an analysis on 34 stationary type IV solar radio bursts (IVSs) using two-dimensional imaging data provided by Nançay Radioheliograph (NRH) at 10 frequencies from 150 to 445 MHz. The main findings are: (i) In the majority of events (23/34) regular and systematic source dispersion with frequency can be clearly recognized. (ii) In most (31/34) events the maximum brightness temperature (T_{BM}^{E}) exceeds 10^8K , and exceeds 10^9K in 23 events. (iii) In most events (30/34) the sense of polarization remains unchanged and the numbers of events with right and left-handed polarization are comparable.

Zhang *et al.*^[96] performed ray-tracing simulations on radio wave transport in the corona and interplanetary region with anisotropic electron density fluctuations. It is found that position offsets due to wave scattering and refraction can produce the co-spatial of the fundamental and harmonic waves in the observation of some type III radio bursts. The visual speed due to the wave propagation effect can reach $1.5c$ for $\eta = 2.4 \times 10^{-4} \text{ km}^{-1}$ and $\alpha = 0.2$ for the fundamental emission in the sky plane,

accompanied with a large expansion rate of the source size. The direction of the visual speed is mostly identical to the direction of the offset, thus, for the observation aimed at obtaining the source position, the source centroid at the starting time is closer to the wave excitation site.

4 Magnetohydrodynamic (MHD) Numerical Modeling

MHD modeling of solar-interplanetary physics, such as solar eruptions, solar wind, and their interactions, has been witnessed with important progresses in recent two years. With an ultra-high accuracy MHD simulation, Jiang *et al.*^[97] established a fundamental mechanism of both simplicity and efficacy for solar eruptions initiated in a single bipolar configuration with no additional special topology. They found that through photospheric shearing motion alone, an electric CS forms in the highly sheared core field of the magnetic arcade during its quasi-static evolution. Once magnetic reconnection sets in at this internal CS, the whole arcade is expelled impulsively, forming a fast-expanding twisted MFR with a highly turbulent reconnecting region underneath. Bian *et al.*^[98] further demonstrated the robustness of this mechanism by carrying out a range of simulations with different magnetic flux distributions on the photosphere. In particular, it is found that the sheared bipolar fields with a stronger PIL can achieve more non-potentiality and their internal CS can form at a lower height and with a higher current density, by which the reconnection can be more efficient and thus produce larger eruptions. In addition, Bian *et al.*^[99] show that by the continuous shearing of the same PIL, the fundamental mechanism can effectively produce homologous CMEs by recurring formation and disruption of the internal CS.

The high-accuracy simulation of eruption has also been used to interpret the relevant phenomena in observations. For example, by quantifying the toroidal flux evolution of the MFR as formed during the simulated eruption, Jiang *et al.*^[100] reproduced an evolution pattern of increase-to-decrease of the toroidal flux as revealed in observations of variations in flare ribbons and transient coronal dimming^[101]. The increase of toroidal flux is owing to the flare reconnection in the early phase that transforms the sheared arcade to twisted field lines, while its decrease is a result of reconnection between field lines in the interior of the MFR in the later phase. Wang *et al.*^[102] analyzed the behavior of the peripheral

magnetic field lines of the simulated eruption and concluded that the often-observed peripheral coronal loop contraction and disappearance are caused by the reduction in magnetic pressure in the flaring core site (consistent with implosion conjecture^[103]) and the peripheral magnetic reconnection and the central eruption. Zhou *et al.*^[104] found that the evolution of the MFR formed during the simulated eruption compares favorably with a typical filament eruption (*e.g.*, the direction of filament rotation during eruption and its relationship with the filament chirality) and realized that the writhe of the MFR's axis decreases while the twist of its surrounding field lines increases, which challenges the conventional explanation of filament rotation based on ideal kink instability of MFR.

Some studies are focused on the development of turbulence as induced by reconnection during eruptions, using very high-resolution 2.5D MHD simulations, such as Ye *et al.*^[105]. Ye *et al.*^[106] found that the region immediately above the flare loop top is made more turbulent and hotter by multiple termination shocks and plasmoid collisions, and this turbulence region could be the source of the Quasi-Periodic Pulsations (QPPs) above the loop-top. They^[107] further studied the turbulence region at the bottom of the CME, and found that the interaction between the CS and the turbulence region can make a significant contribution to CME heating, and this region might also generate periodically coronal wave trains around the CME. Xie *et al.*^[108] found that the Rayleigh–Taylor instability inside the turbulence region below the CME can cause this region to oscillate locally, which also propagates downwards through the CS and leads to the CS oscillation. Mei *et al.*^[109–111] focused on the EUV disturbances during solar eruption by performing 3D MHD numerical simulations initialized with an analytic unstable MFR. They noticed a complex triple-layered leading edge of CME consisting of a fast shock in the front, a Helical Current ribbon/Boundary (HCB) behind, and a bright MFR within the HCB. Within these layers they also found a 3D Velocity Separatrix (VS) associated with slow shocks at the flanks of the CME bubble, and two types of 3D vortices near the VS, one with plasma converging toward the vortex center, and the other with plasma spreading out.

Important progresses have also been made in data-constrained and data-driven MHD simulations of solar eruptions. Jiang *et al.*^[112] developed a new model

of coronal magnetic field evolution with the bottom boundary self-consistently driven by a photospheric velocity field. Their model can efficiently reproduce the magnetic energy injection process from the photosphere into the corona. They have also tested the data-driven model using ground-truth data from a flux emergence simulation^[113,114], and found that the coronal field can be reliably reproduced if the input boundary data is sufficiently close to force-free. Using this model, He *et al.*^[115] simulated the formation and initiation of a large-scale preflare MFR in AR 12371, and suggested that tether-cutting reconnection plays a key role in building up the MFR until its initiation by torus instability. Using a data-driven zero- β MHD model, Zhong *et al.*^[116] reproduced a failed eruption of an MFR in a complex magnetic topology. They revealed that a particular Lorentz force component, which is related to the non-axisymmetry of the MFR's cross section, essentially constrains the erupting MFR. This component has been ignored in the theory of torus instability in which the confining force is thought to be coming only from the external strapping field. Guo *et al.*^[117] studied a long-duration flare with filament eruption using their zero- β MHD model with the initial condition of magnetic field determined by an advanced flux-rope insertion method that is based on regularized Biot-Savart laws. The data-driven model has also been extended to the very small scale dynamics, for example, recently a high-resolution (reaching spatial scale of 45 km) simulation^[118] reproduced the successive formation of mini flux ropes (*i.e.*, plasmoids in 2D) in the reconnection of a confined flare that matches the high resolution from New Vacuum Solar Telescope (NVST) and SDO.

Several studies have been devoted to developing advanced numerical techniques on corona and interplanetary MHD models to improve their robustness and accuracy in simulating ambient solar wind and CME. Feng *et al.*^[119] applied an effective implicit strategy, which resorts to the implicit lower-upper symmetric Gauss-Seidel method and keeps the sparse Jacobian matrix diagonally dominant, and show that this technique can robustly deal with the extremely low plasma β (about 10^{-7}) conditions with promising computational efficiency. Based on the MHD system of extended generalized Lagrange multiplier (EGLM) formulation with Galilean invariance, Li *et al.*^[120] developed a modified path-conservative HLLEM scheme that is shock-stable and can adaptively adjust diffusion according to the

smoothness of the physical flow. Furthermore, an auxiliary equation of entropy has been added to the EGLM formulation, along with a specially-designed spatial reconstruction to preserve the positiveness of pressure and solenoidality of a magnetic field, forming the EC-GLM MHD model^[121], which can cope with the high Mach number or low plasma β environment more handily and robustly. Meanwhile, other work that focuses on the comparison of the solenoidality-preserving methods is also carried out^[122].

The data of the solar surface, for example, the synoptic map of a photospheric radial magnetic field, is a key input for MHD models of solar wind. Based on the PFSS model, Li *et al.*^[123] compared that results of 2018 obtained from HMI, ADAPT and GONG maps with observation, and found those obtained from zero-point uncorrected GONG maps give significant deviation from others, which stresses cautions are needed when using these data in MHD modeling. Yang and Shen^[124] developed a new way to prescribe boundary conditions for interplanetary solar wind by utilizing multiple sets of observations and the machine learning technique. The modeling results of a few Carrington Rotations show improvements on their previous boundary conditions using only photospheric magnetic field observations.

As a critical step in the transition from research to application, an assessment suite for solar wind prediction results is established using multipoint observation in the interplanetary space. Assessment of CESE-HLLD model's results for 2008 reveal the two-stream structure observed near the ecliptic plane and the overall latitudinal variance observed by Ulysses are reproduced, but the differences among observations at L1 and the twin STEREO spacecraft are not caught by the model^[125]. Li *et al.*^[126] analyzed systematically the evolution of the north-south component B_z of the Interplanetary Magnetic Field (IMF) in the GSM coordinate system and indicates that the Russell-McPherron effect is the dominant mechanism that controls the large-scale evolution of B_z . Given proper boundary conditions at 0.1 AU, the MHD model can well reproduce the evolution of ambient B_z .

For the modeling of CME evolution, Shen *et al.*^[127,128] studied how the different CME initial parameters affect the results as seen by observers near different planets (*i.e.*, Earth and Mars) and the process of CME propagation in the interplanetary space. They found that with the initial mass of CME unchanged, the initial geomet-

ric thickness will have a different influence in the latitudinal and longitudinal directions. These two works confirm the importance of the initial geometric and physical parameters on the CME simulations. Zhang *et al.*^[129] compared simulation results for CME with and without radial compression for the 2007 November 15 event. It is found that CME without radial compression propagates in interplanetary space with a lower velocity and arrives at 1 AU later and tends to overestimate the radial extension and underestimate the magnetic field strength at 1AU. Yang *et al.*^[130] simulated the 2017 September 10 CME focus on the morphology and kinematics of the large shock and found several characteristics of the shock, especially the asymmetry of some shock properties.

5 Solar Energetic Particles and Cosmic Rays

Liu *et al.*^[131] proposed a pan-spectrum formula to examine energy spectrum of different suprathermal particle phenomena typically with a single energy break. Using this method, Wang *et al.*^[132] suggested that the upward-traveling electrons from an acceleration source high in the corona would form the Solar Energetic Electron (SEE) events, while their downward-traveling counterparts may undergo a secondary acceleration before producing HXRs via thick-target bremsstrahlung processes. Wang *et al.*^[133] also study SEE events observed in the Earth's cusp/ lobe regions by the Beida Image Electron Spectrometer on board a Beidou satellite in an inclined geosynchronous orbit, to show that interplanetary energetic electrons can enter the planet's cusp/lobe regions and get trapped.

Using test-particle simulations Kong *et al.*^[134] study the acceleration of suprathermal electrons at an ICME-driven shock event. In each energy channel the ratio of downstream to upstream intensities peaks at about 90-degree pitch angle, and the downstream electron energy spectral index is much larger than the theoretical index of diffusive shock acceleration, to show the importance of SDA in the acceleration of electrons by quasi-perpendicular shocks.

In reservoir phenomenon, solar energetic particle intensities of the decay phase observed by widely separated spacecraft present comparable intensities evolving similarly. Wang *et al.*^[135,136] find that the reservoir events could be observed in almost all longitudes in the ecliptic at 1 au; thus, the perpendicular diffusion in in-

terplanetary space is the most important mechanism to explain the uniform distribution of SEPs. Furthermore, they suggest that the effects of the magnetic boundary and/or the small diffusion coefficients in the sheath region of ICME could also help to form the reservoir phenomenon.

Ground-Level Enhancements (GLE) generally accompany fast ICMEs, and ICME driven shocks are sources of SEPs. Wu and Qin^[137] use numerical simulations to show that the sheath-MC structure reduced the proton intensities for about 2 days after the shock passed through the Earth, and the sheath contributed most of the decrease while the MC facilitated the formation of the second step decrease. In addition, Qin and Wu^[138] use simulations to study the effects of the Forbush Decrease with the magnetic cloud and sheath during the GLE events. It is suggested that the sheath plays an important role in the amplitude of the Fd while the MC contributes to the formation of the second step decrease and prolonged recovery time.

Diffusion is important for transport and acceleration of cosmic rays. There are different definitions for the spatial parallel diffusion coefficient. Wang and Qin^[139] proved that the Displacement Variance Definition (DVD) is invariant for the iterative transformation of the cosmic rays transport equation for focusing field. Therefore, for a spatially varying field, DVD is more appropriate than other definitions. In addition, Wang and Qin^[140] obtain the modified momentum diffusion due to the varying magnetic field.

The intensity of Galactic Cosmic Rays (GCRs) is modulated by solar activity on various timescales. Luo *et al.*^[141] have performed comprehensive numerical modeling of the solar rotational recurrent variation in GCRs caused by a Corotation Interaction Region (CIR). A newly developed Magnetohydrodynamic (MHD) numerical model is adapted to simulate the background solar wind plasma with a CIR structure present in the inner heliosphere. The simulated MHD inner heliosphere is extrapolated to the outer heliosphere by using the Parker interplanetary magnetic field model. The output of these plasma and magnetic field models is incorporated into a comprehensive Parker-type transport model for GCRs. The obtained solutions of this hybrid model, for studying the CIR effect, are as follows: (i) the onset of the decrease in the GCR intensity inside the CIR coincides with the increase of the solar wind speed with the intensity depression accompanied by a mag-

netic field and plasma density enhancement. Additionally, the CIR effect weakens with increasing heliocentric radial distance. (ii) This decrease in GCR intensity also appears at different heliolatitudes and varies with changing latitude; the amplitude of the GCR depression exhibits a maximum in the low-latitude region. (iii) The CIR affects GCR transport at different energy levels as well. Careful analysis has revealed a specific energy dependence of the amplitude of the recurrent GCR variation in the range of 30–2000 MeV.

With continuous measurements from space-borne cosmic-ray detectors such as AMS-02 and PAMELA, precise spectra of galactic cosmic rays over the 11 yr solar cycle have become available. Song *et al.*^[142] utilize proton and helium spectra below 10 GV from these missions from 2006 to 2017 to construct a cosmic-ray transport mode for a quantitative study of the processes of solar modulation. The Markov Chain Monte Carlo method is utilized to search the relevant parameter space related to the drift and the diffusion coefficients by reproducing and fitting the mentioned observed spectra. It is found that (i) when reproducing these observations the parameters required for the drift and diffusion coefficients exhibit a clear time dependence, with the magnitude of the diffusion coefficients anticorrelated with solar activity; (ii) the rigidity dependence of the resulting mean free paths varies with time, and their rigidity dependence at lower rigidity can even have a larger slope than at higher rigidity; (iii) using a single set of modulation parameters for each pair of observed proton and helium spectra, most spectra are reproduced within observational uncertainty; and (iv) the simulated proton-to-helium flux ratio agrees with the observed values in terms of its long-term time dependence, although some discrepancy exists, and the difference is mostly coming from the underestimation of proton flux.

Shen *et al.*^[143] developed a hybrid method to remove SEPs to obtain GCR background with the solar cycle variation characteristics of the 27-day GCR modulation. Shen *et al.*^[144] numerically study the latitudinal dependent GCR modulation to find that the latitudinal-dependent magnetic turbulence is crucial during the negative-polarity solar cycle, while the latitudinal diffusion coefficient and the reduced drift velocity in the polar region are more important during the positive-polarity solar cycle. In addition, Shen *et al.*^[145] established a predictive and empirical GCR model with a force field approach, to reproduce the 11 and 22 yr cy-

clie variations of GCRs.

The solar eruption on 10 September 2017 was accompanied by a fast coronal mass ejection (about 3000 km·s⁻¹) and produced a Ground-Level Enhancement (GLE) event at Earth. Zhu *et al.*^[146] determined the shock parameters by combining the 3D shock kinematics and the solar wind properties obtained from a global MHD simulation, in order to compare them with the characteristics of the Solar Energetic Particles (SEPs). They extracted the magnetic connectivities of the observers from the MHD simulation and found that L1 was magnetically connected to the shock flank (rather than the nose). The weak magnetic field and relatively dense plasma around the HCS result in a large Mach number of the shock, which leads to efficient particle acceleration even at the shock flank. They conclude that the interaction between the shock and HCS provides a potential mechanism for the production of the GLE event.

Acknowledgment

We are grateful to Dr. Huidong Hu at NSSC CAS for providing relevant information.

References

- [1] LI L P, PETER H, CHITTA L P, *et al.* Magnetic reconnection between loops accelerated by a nearby filament eruption[J]. *Astrophys. J.*, 2021, **908**: 213(13pp)
- [2] HOU Z Y, TIAN H, CHEN H C, *et al.* Formation of solar quiescent coronal loops through magnetic reconnection in an emerging active region[J]. *Astrophys. J.*, 2021, **915**: 39(10pp)
- [3] CHEN H D, ZHANG J, DE PONTIEU B, *et al.* Coronal mini-jets in an activated solar tornado-like prominence[J]. *Astrophys. J.*, 2020, **899**: 19(13pp)
- [4] HOU Z Y, TIAN H, BERGHMANS D, *et al.* Coronal microjets in quiet-sun regions observed with the extreme ultraviolet imager on board the solar orbiter[J]. *Astrophys. J. Lett.*, 2021, **918**: L20(11pp)
- [5] CHEN Y J, PRZYBYLSKI D, PETER H, *et al.* Transient small-scale brightenings in the quiet solar corona: a model for campfires observed with Solar Orbiter[J]. *A&A*, 2021, **656**: L7(12pp)
- [6] YANG Z H, BETHGE C, TIAN H, *et al.* Global maps of the magnetic field in the solar corona[J]. *Science*, 2020, **369**: 6504:694-697
- [7] YANG Z H, TIAN H, TOMCZYK S, *et al.* Mapping the magnetic field in the solar corona through magnetoseismology[J]. *Science China Technological Sciences*, 2020, **63**: 2357-2368
- [8] ZHU R, TAN B L, SU Y N, *et al.* Microwave diagnostics of magnetic field strengths in solar flaring loops[J]. *Science China Technological Sciences*, 2021, **64**: 169-178
- [9] CHEN Y J, LI W X, TIAN H, *et al.* Forward Modeling of Solar Coronal Magnetic-field Measurements Based on a Magnetic-field-induced Transition in Fe X[J]. *Astrophys. J.*, 2021, **920**: 116(15pp)
- [10] ZHOU G P, GAO G N, WANG J X, *et al.* Magnetic Reconnection invoked by sweeping of the CME-driven fast-mode shock[J]. *Astrophys. J.*, 2020, **905**: 150(10pp)
- [11] ZHOU X P, SHEN Y D, SU J T, *et al.* CME-driven and flare-ignited fast magnetosonic waves detected in a solar eruption[J]. *Solar Physics*, 2021, **296**: 169
- [12] ZHOU X P, SHEN Y D, TANG Z H, *et al.* Total reflection of a flare-driven quasi-periodic EUV wave train at a coronal hole boundary[J]. *A&A*, 2022, in press
- [13] DUAN Y D, SHEN Y D, ZHOU X P, *et al.* Homologous accelerated electron beams, a quasiperiodic fast-propagating wave, and a coronal mass ejection observed in one fan-spine jet[J]. *Astrophys. J. Lett.*, 2022, **926**: L39(9pp)
- [14] HOU Z Y, TIAN H, WANG J S, *et al.* Three-dimensional propagation of the global EUV wave associated with a solar eruption on 2021 October 28[J]. *Astrophys. J.*, 2022, in press
- [15] ZHANG Q M, DAI J, XU Z, *et al.* Transverse coronal loop oscillations excited by homologous circular-ribbon flares[J]. *A&A*, 2020, **638**: A32(5pp)
- [16] ZHANG Q M, Simultaneous transverse oscillations of a coronal loop and a filament excited by a circular-ribbon flare[J]. *A&A*, 2020, **642**: A159(7pp)
- [17] ZHANG Q M, CHEN J L, LI T, *et al.* Transverse coronal-loop oscillations induced by the non-radial eruption of a magnetic flux rope[J]. *Solar Physics*, 2022, **297**: 18
- [18] XUE J C, SU Y, LI H, *et al.* thermodynamical evolution of supra-arcade Downflows[J]. *Astrophys. J.*, 2020, **898**: 88(11pp)
- [19] LI Z F, CHENG X, DING M D, *et al.* Thermodynamic evolution of solar flare supra-arcade Downflows[J]. *Astrophys. J.*, 2021, **915**: 124(10pp)
- [20] SAMANTA T, TIAN H, CHEN B, *et al.* Plasma Heating induced by tadpole-like Downflows in the flaring solar corona[J]. *The Innovation*, 2021, **2**: 100083
- [21] LI L P, PETER P, CHITTLA L P, *et al.* Relation of coronal rain originating from coronal condensations to interchange magnetic reconnection[J]. *Astrophys. J.*, 2020, **905**: 26(13pp)
- [22] LI L P, PETER P, CHITTLA L P, *et al.* On-disk solar coronal condensations facilitated by magnetic reconnection between open and closed magnetic structures[J]. *Astrophys. J.*, 2021, **910**: 82(12pp)
- [23] LI L P, PETER P, CHITTLA L P, *et al.* Revisiting the formation mechanism for coronal rain from previous studies[J]. *RAA*, 2021, **21**: 255(16pp)
- [24] LI L P, PETER P, CHITTLA L P, *et al.* Formation of a solar filament by magnetic reconnection and coronal condensation[J]. *Astrophys. J. Lett.*, 2021, **919**: L21(8pp)
- [25] YANG B, YANG J Y, BI Y, *et al.* Formation of a solar filament by magnetic reconnection, associated chromospheric evaporation, and subsequent coronal condensation [J]. *Astrophys. J. Lett.*, 2021, **921**: L33(10pp)
- [26] CHEN H C, TIAN H, Li L P, *et al.* Coronal condensation as the source of transition region supersonic Downflows above a sunspot[J]. *A&A*, 2022, in press
- [27] DUAN D, HE J, WU H, *et al.* Magnetic energy transfer and distribution between protons and electrons for alfvénic waves at kinetic scales in wavenumber space[J]. *Astrophys. J.*, 2020, **896**: 47(8pp)
- [28] DUAN D, HE J, BOWEN T A, *et al.* Anisotropy of solar wind turbulence in the inner heliosphere at kinetic scales: Psp observa-

- tions[J]. *Astrophys. J. Lett.*, 2021, **915**: L8(7pp)
- [29] ZHANG J, HUANG S Y, HE J S, et al. Three-dimensional anisotropy and scaling properties of solar wind turbulence at kinetic scales in the inner heliosphere: Parker solar probe observations[J]. *Astrophys. J. Lett.*, 2022, **924**: L21(8pp)
- [30] HUANG S Y, ZHANG J, SAHRAOUI F, et al. Kinetic scale slow solar wind turbulence in the inner heliosphere: Coexistence of kinetic alfvén waves and alfvén ion cyclotron waves[J]. *Astrophys. J. Lett.*, 2020, **897**: L3(7pp)
- [31] ZHU X, HE J, VERSCHAREN D, et al. Wave composition, propagation, and polarization of magnetohydrodynamic turbulence within 0.3 au as observed by parker solar probe[J]. *Astrophys. J. Lett.*, 2020, **901**: L3(7pp)
- [32] ZHAO G Q, LIN Y, WANG X Y, et al. Two correlations with enhancement near the proton gyroradius scale in solar wind turbulence: Parker Solar Probe (PSP) and wind observations[J]. *Astrophys. J.*, 2022, **924**: 92(6pp)
- [33] WU H H, TU C Y, WANG X, et al. Energy supply for heating the slow solar wind observed by parker solar probe between 0.17 and 0.7 au[J]. *Astrophys. J. Lett.*, 2020, **904**: L8(6pp)
- [34] WU H H, TU C Y, HE J S, et al. Consistency of von karman decay rate with the energy supply rate and heating rate observed by parker solar probe[J]. *Astrophys. J.*, 2022, **926**: 16(5pp)
- [35] HE J, ZHU X, YANG L, et al. Solar origin of compressive alfvénic spikes/kinks as observed by parker solar probe[J]. *Astrophys. J. Lett.*, 2021, **913**: L14(8pp)
- [36] WU H H, TU C Y, WANG X, et al. Large amplitude switchback turbulence: Possible magnetic velocity alignment structures[J]. *Astrophys. J.*, 2021, **911**: 73(7pp)
- [37] WU H H, TU C Y, WANG X, et al. Magnetic and velocity fluctuations in the near sun region from 0.1–0.3 AU observed by parker solar probe[J]. *Astrophys. J.*, 2021, **922**: 92(7pp)
- [38] SHI C, ZHAO J S, HUANG J, et al. Parker solar probe observations of alfvénic waves and ion-cyclotron waves in a small-scale flux rope[J]. *Astrophys. J. Lett.*, 2021, **908**: L19(9pp)
- [39] LIU Y Y, FU H S, CAO J B, et al. Characteristics of interplanetary discontinuities in the inner heliosphere revealed by parker solar probe[J]. *Astrophys. J.*, 2021, **916**: 65(8pp)
- [40] YU L, HUANG S Y, YUAN Z G, et al. Characteristics of magnetic holes in the solar wind revealed by parker solar probe[J]. *Astrophys. J.*, 2021, **908**: 56(9pp)
- [41] SHI C, ZHAO J S, MALASPINA D M, et al. Multiband electrostatic waves below and above the electron cyclotron frequency in the near-sun solar wind[J]. *Astrophys. J. Lett.*, 2022, **926**: L3(8pp)
- [42] CHEN L, MA B, WU D J, et al. An interplanetary type iiib radio burst observed by parker solar probe and its emission mechanism[J]. *The Astrophys. J. Lett.*, 2021, **915**: L22(6pp)
- [43] HUANG S Y, WANG Q Y, SAHRAOUI F, et al. Analysis of turbulence properties in the mercury plasma environment using messenger observations[J]. *Astrophys. J.*, 2020, **891**: 159(6pp)
- [44] WU H H, TU C Y, WANG X, et al. Energy supply by low-frequency break sweeping for heating the fast solar wind from 0.3 to 4.8 AU[J]. *Astrophys. J.*, 2021, **912**: 84(6pp)
- [45] WU H H, TU C Y, HE J S, et al. The yaglom scaling of the third-order structure functions in the inner heliosphere observed by helios 1 and 2[J]. *Astrophys. J.*, 2022, **927**: 113(8pp)
- [46] LIU D, RONG Z J, GAO J W, HE J S, et al. Statistical properties of solar wind upstream of mars: maven observations[J]. *Astrophys. J.*, 2021, **911**: 113(10pp)
- [47] YAO S T, SHI Q Q, ZONG Q G, et al. Low-frequency whistler waves modulate electrons and generate higher-frequency whistler waves in the solar wind[J]. *Astrophys. J.*, 2021, **923**: 216(9pp)
- [48] WU H, TU C, WANG X, et al. Isotropic Scaling Features Measured Locally in the Solar Wind Turbulence with Stationary Background Field[J]. *Astrophys. J.*, 2020, **892**: 138(10pp)
- [49] WANG X, TU C Y, HE J S. Fluctuation amplitudes of magnetic-field directional turnings and magnetic-velocity alignment structures in the solar wind[J]. *Astrophys. J.*, 2020, **903**: 72(11pp)
- [50] ZHAO G Q, FENG H Q, WU D J, et al. Dependence of ion temperatures on alpha-proton differential flow vector and heating mechanisms in the solar wind[J]. *Astrophys. J. Lett.*, 2020, **889**: L14(7pp)
- [51] ZHAO G Q, FENG H Q, WU D J, et al. Dependence of ion temperatures on alpha-proton differential flow vector and heating mechanisms in the solar wind[J]. *Astrophys. J. Lett.*, 2020, **889**: L14(7pp)
- [52] ZHAO G Q, FENG H Q, WU D J, et al. On mechanisms of proton perpendicular heating in the solar wind: Test results based on wind observations[J]. *Research in Astronomy and Astrophysics*, 2022, **22**: 015009(8pp)
- [53] HE J S, ZHU X Y, VERSCHAREN D, et al. Spectra of diffusion, dispersion, and dissipation for kinetic alfvénic and compressive turbulence: Comparison between kinetic theory and measurements from mms [J]. *Astrophys. J.*, 2020, **898**: 43(12pp)
- [54] HOU C P, HE J S, ZHU X Y, et al. Contribution of magnetic reconnection events to energy dissipation in space plasma turbulence[J]. *Astrophys. J.*, 2021, **908**: 237(6pp)
- [55] LUO Q W, HE J S, CUI J, et al. Energy conversion between ions and electrons through ion cyclotron waves and embedded ion-scale rotational discontinuity in collisionless space plasmas[J]. *Astrophys. J.*, 2020, **904**: L16(6pp)
- [56] WANG T Y, HE J S, ALEXANDROVA O, et al. Observational quantification of three-dimensional anisotropies and scalings of space plasma turbulence at kinetic scales[J]. *Astrophys. J.*, 2020, **898**: 91(10pp)
- [57] ZHU X, HE J, WANG Y, et al. Difference of intermittency between electric field and magnetic field fluctuations from ion scale down to sub-electron scale in the magnetosheath turbulence[J]. *Astrophys. J.*, 2020, **893**: 124(11pp)
- [58] YANG Z W, LIU Y D, et al. PIC simulations of microinstabilities and waves at near-sun solar wind perpendicular shocks: Predictions for Parker Solar Probe and Solar Orbiter[J]. *Astrophys. J. Lett.*, 2020, **900**: L24(8pp)
- [59] LIU Y C M, QI Z H, et al. Unusually low density regions in the compressed slow wind: Solar wind transients of small coronal hole origin [J]. *A&A*, 2020, **635**: A49
- [60] CHEN C, LIU Y D, HU H D. Macro magnetic holes caused by ripples in Heliospheric Current Sheet from coordinated imaging and Parker Solar Probe observations[J]. *Astrophys. J.*, 2021, **921**: 15(10pp)
- [61] LIU Y D, CHEN C, STEVENS M L, LIU M Z. Determination of solar wind angular momentum and Alfvén radius from Parker Solar Probe observations[J]. *Astrophys. J. Lett.*, 2021, **908**: L41(7pp)
- [62] QI Z H, LIU Y, LIU R Y. The small coronal hole solar wind and Alfvén wave within the slow solar wind[J]. *Chinese J. Geophys. (in Chinese)*, 2021, **64(11)**: 3837-3845

- [63] LIU R Y, LIU Y C M, *et al.* Density compressions at magnetic switchbacks associated with fast plasma: A superposed epoch analysis[J]. *Journal of Geophysical Research: Space Physics*, 2022, **127**: e2022JA030382.
- [64] MENG M M, LIU Y D, CHEN C, WANG R. Analysis of the distribution, rotation and scale characteristics of solar wind switchbacks: Comparison between the first and second encounters of Parker Solar Probe[J]. *Research in Astronomy and Astrophysics*, 2022, **22**: 035018(8pp)
- [65] LI X L, WANG Y M, LIU R, *et al.* Reconstructing solar wind inhomogeneous structures from stereoscopic observations in white light: Solar wind transients in 3D[J]. *Journal of Geophysical Research (Space Physics)*, 2020, **125**: e2019JA027513, doi: 10.1029/2019JA027513
- [66] LYU S Y, WANG Y M, LI X L, GUO J N, WANG C B, ZHANG Q H. Three-dimensional reconstruction of coronal mass ejections by the correlation-aided reconstruction technique through different stereoscopic angles of the Solar Terrestrial Relations Observatory twin spacecraft[J]. *Astrophys. J.*, 2021, **909**: 182(11pp)
- [67] LI X L, WANG Y M, GUO J N, LIU R, ZHUANG B. Radial velocity map of solar wind transients in the field of view of STEREO/HI1 on 3 and 4 April 2010[J]. *A&A*, 2021, **649**: A58(13pp)
- [68] SHEN C L, CHI Y T, XU M J, WANG Y M. Origin of extremely intense southward component of magnetic field (Bs) in ICMEs[J]. *Front. Phys.*, 2021, **9**: 762488
- [69] LIU Y D, CHEN C, ZHAO X W. Characteristics and importance of “ICME-in-sheath” phenomenon and upper limit for geomagnetic storm activity[J]. *Astrophys. J. Lett.*, 2020, **897**: L11(7pp)
- [70] SONG H Q, ZHANG J, CHENG X, *et al.* Do all interplanetary coronal mass ejections have a magnetic flux rope structure near 1 au? *Astrophys. J. Lett.*, 2020, **901**: L21(7pp)
- [71] ZHAO Y, FENG H Q, LIU Q, *et al.* The flux of flux ropes embedded within magnetic clouds near 5 AU[J]. *Journal of Geophysical Research (Space Physics)*, 2021, **126**: e2020JA028594, doi: 10.1029/2020JA028594
- [72] SONG H Q, LI L P, SUN Y Y, *et al.* Solar cycle dependence of ICME composition[J]. *Sol. Phys.*, 2021, **296**: 111
- [73] HUANG J, LIU Y, FENG H Q, *et al.* A statistical study of the plasma and composition distribution inside magnetic clouds: 1998-2011[J]. *Astrophys. J.*, 2020, **893**: 136(12pp)
- [74] SONG H Q, CHENG X, LI L P, ZHANG J, CHEN Y. Comparison of helium abundance between ICMEs and solar wind near 1 AU[J]. *Astrophys. J.*, 2022, **925**: 137(6pp)
- [75] WANG C, XU M J, SHEN C L, CHI Y T, WANG Y M. Interplanetary shock candidates observed at Venus’s orbit[J]. *Astrophys. J.*, 2021, **912**: 85(12pp)
- [76] ZHAO D, GUO J P, HUANG H, *et al.* Interplanetary coronal mass ejections from MAVEN orbital observations at Mars[J]. *Astrophys. J.*, 2021, **923**: 4(12pp)
- [77] HUANG H, GUO J P, *et al.* Properties of interplanetary fast shocks close to the Martian environment[J]. *Astrophys. J.*, 2021, **914**: 14(15pp)
- [78] CHI Y T, SCOTT C, SHEN C L, *et al.* Using the “ghost front” to predict the arrival time and speed of CMEs at Venus and Earth[J]. *Astrophys. J.*, 2020, **899**: 143(14pp)
- [79] XU M J, SHEN C L, WANG C, *et al.* Multipoint analysis of the interaction between a shock and an ICME-like structure around 2011 March 22[J]. *Astrophys. J. Lett.*, 2022, **930**: L11(7pp)
- [80] XU M J, SHEN C L, HU Q, WANG Y M, CHI Y T. Whether small flux ropes and magnetic clouds have the same origin: A statistical study of small flux ropes in different types of solar wind[J]. *Astrophys. J.*, 2020, **904**: 122(10pp)
- [81] FENG H Q, ZHAO Y, WANG J M, LIU Q, ZHAO G Q. Observations of magnetic flux ropes opened or disconnected from the Sun by magnetic reconnection in interplanetary space[J]. *Front. Phys.*, 2021, **9**: 679780
- [82] NING H, CHEN Y, NI S L. *et al.* Harmonic Maser Emissions from Electrons with Loss-cone Distribution in Solar Active Regions[J]. *Astrophys. J. Lett.*, 2021, **920**: L40(8pp)
- [83] NING H, CHEN Y, NI S L. *et al.* Harmonic electron-cyclotron Maser Emissions Driven by Energetic Electrons of the Horseshoe Distribution with Application to Solar Radio Spikes[J]. *A&A.*, 2021, **651**: A118
- [84] LI C Y, CHEN Y, NI S L. *et al.* PIC Simulation of Double Plasma Resonance and Zebra Pattern of Solar Radio Bursts[J]. *Astrophys. J. Lett.*, 2021, **909**: L5(9pp)
- [85] NI S L, CHEN Y, LI C Y. *et al.* Plasma Emission Induced by Electron Cyclotron Maser Instability in Solar Plasmas with a Large Ratio of Plasma Frequency to Gyrofrequency[J]. *Astrophys. J. Lett.*, 2020, **891**: L25(8pp)
- [86] LI T M, LI C, CHEN P F. *et al.* Particle-in-cell Simulation of Plasma Emission in Solar Radio Bursts[J]. *A&A.*, 2021, **653**: A169
- [87] FENG S W, LÜ M S. Recent Observational Studies on the Fine Structures of Solar Type II Radio Bursts[J]. *PROGRESS IN ASTRONOMY*, 2021, **39**(2): 129-143
- [88] FENG S W, ZHAO F. Observational Study on the Fine Structures of Solar Type III Radio Bursts[J]. *Sci. China Technol. Sci.*, 2020, **51**(1): 35-45
- [89] GAO G N, CAI Q W, GUO S J, *et al.* Decimetric Type-U Solar Radio Bursts and Associated EUV Phenomena on 2011 February 9[J]. *Astrophys. J.*, 2021, **923**: 286(12pp)
- [90] WAN J L, TANG J F, TAN B L. *et al.* Statistical analysis of solar radio fiber bursts and relations with flares[J]. *A&A.*, 2021, **653**: A38
- [91] TANG J F, WU D J, WAN J L, *et al.* Evolution of Microwave Spike Bursts in a Solar flare on 2006 December 13[J]. *Res. Astron. Astrophys.*, 2021, **21**: 148(10pp)
- [92] ZHANG M H, ZHANG Y, YAN Y H, *et al.* Observational results of MUSER during 2014-2019[J]. *Res. Astron. Astrophys.*, 2021, **21**: 284(12pp)
- [93] LU L, LI D, NING Z J, *et al.* Quasi-periodic pulsations detected in α and nonthermal emissions during solar flares[J]. *Solar Phys.*, 2021, **296**: 130
- [94] HONG Z X, LI D, ZHANG M H, *et al.* Multi-wavelength observations of quasi-periodic pulsations in a solar flare[J]. *Solar Phys.*, 2021, **296**: 171
- [95] LV M S, CHEN Y, VASANTH V, *et al.* An observational revisit of stationary type IV solar radio bursts[J]. *Solar Phys.*, 2021, **296**: 38
- [96] ZHANG P J, WANG C B, KONTAR E P. Parametric Simulation Studies on the Wave Propagation of Solar Radio Emission: The Source Size, Duration, and Position[J]. *Astrophys. J.*, 2021, **909**: 195(11pp)
- [97] JIANG C W, FENG X S, LIU R, YAN X L, *et al.* A fundamental mechanism of solar eruption initiation[J]. *Nat. Astron.*, 2021, **5**: 1126-1138
- [98] BIAN X K, JIANG C W, FENG X S, *et al.* Numerical simulation

- of a fundamental mechanism of solar eruption with a range of magnetic flux distributions[J]. *A&A*, 2022, **658**, A174(13pp)
- [99] BIAN X K, JIANG C W, FENG X S, ZUO P B, WANG Y. Homologous coronal mass ejections caused by recurring formation and disruption of current sheet within a sheared magnetic arcade[J]. *Astrophys. J. Lett.*, 2022, **925**: L7(8pp)
- [100] JIANG C W, CHEN J, DUAN A Y, *et al.* Formation of magnetic flux rope during solar eruption. I. Evolution of toroidal flux and reconnection flux[J]. *Front. Phys.*, 2021, **9**, <https://doi.org/10.3389/fphy.2021.746576>.
- [101] XING C, CHENG X, Ding M D. Evolution of the toroidal flux of CME flux ropes during eruption[J]. *The Innovation*, 2020, **1**: 100059
- [102] WANG J T, JIANG C W, YUAN D, ZOU P. The causes of peripheral coronal loop contraction and disappearance revealed in a magnetohydrodynamic simulation of solar eruption[J]. *Astrophys. J.*, 2021, **911**: 1(12pp).
- [103] HUDSON H S. Global Properties of Solar Flares. *Space Sci Rev.*, 2011, **158**: 5–41
- [104] ZHOU Z J, JIANG C W, LIU R, *et al.* The rotation of magnetic flux ropes formed during solar eruption[J]. *Astrophys. J. Lett.*, 2022, **927**: L14 (7pp).
- [105] YE J, SHEN C, LIN J, MEI Z. An efficient parallel semi-implicit solver for anisotropic thermal conduction in the solar corona. *Astronomy and Computing*, 2020, **30**: 100341
- [106] YE J, CAI Q W, SHEN C C, *et al.* The role of turbulence for heating plasmas in eruptive solar flares[J]. *Astrophys. J.*, 2020, **897**: 64
- [107] YE J, CAI Q W, SHEN C C, *et al.* Coronal wave trains and plasma heating triggered by turbulence in the wake of a CME[J]. *Astrophys. J.*, 2021, **909**: 45(11pp)
- [108] XIE X Y, MEI Z X, SHEN C C, *et al.* Numerical experiments on dynamic evolution of a CME-flare current sheet[J]. *Monthly Notices of the Royal Astronomical Society*, 2021, **509**: 406–420 (2021).
- [109] MEI Z X, KEPPENS R, CAI Q W, *et al.* The triple-layered leading edge of solar coronal mass ejections[J]. *Astrophys. J. Lett*, 2020, **898**: L21
- [110] MEI Z X, KEPPENS R, CAI Q W, *et al.* 3D numerical experiment for EUV waves caused by flux rope eruption[J]. *Monthly Notices of the Royal Astronomical Society*, 2020, **493**: 4816–4829
- [111] MEI Z X, CAI Q W, YE J, *et al.* Velocity distribution associated with EUV disturbances caused by eruptive MFR[J]. *Front. Astron. Space Sci.*, 2021, **8**: 771882
- [112] JIANG C W, BIAN X K, SUN T T, FENG X S. MHD modeling of solar coronal magnetic evolution driven by photospheric flow. *Front. Phys.*, 2021, **9**: 646750
- [113] JIANG C W, TORIUMI S. Testing a data-driven active region evolution model with boundary data at different heights from a solar magnetic flux emergence simulation[J]. *Astrophys. J.*, 2020, **903**: 11(8pp)
- [114] TORIUMI S, TAKASAO S, CHEUNG M C M, JIANG C W. Comparative study of data-driven solar coronal field models using a flux emergence simulation as a ground-truth data set[J]. *Astrophys. J.*, 2020, **890**: 103(13pp)
- [115] HE W, JIANG C W, ZOU P, *et al.* Data-driven MHD simulation of the formation and initiation of a large-scale preflare magnetic flux rope in AR 12371. *Astrophys. J.*, 2020, **892**: 9 (10pp)
- [116] ZHONG Z, GUO Y, DING M D. The role of non-axisymmetry of magnetic flux rope in constraining solar eruptions. *Nat Commun*, 2021, **12**: 2734
- [117] GUO Y, *et al.* Data-constrained magnetohydrodynamic simulation of a long-duration eruptive flare[J]. *Astrophys. J.*, 2021, **919**: 39
- [118] YAN X, *et al.* Fast plasmoid-mediated reconnection in a solar flare. *Nat Commun* 2022, **13**: 640
- [119] FENG X S, WANG H P, XIANG C Q, *et al.* Magnetohydrodynamic modeling of the solar corona with an effective implicit strategy[J]. *Astrophys. J. Supplement Series*, 2021, **257**: 34 (23pp)
- [120] LI C X, FENG X S, LI H C, WEI F S. Modified path-conservative HLLEM scheme for magnetohydrodynamic solar wind simulations[J]. *Astrophys. J. Supplement Series*, 2021, **253**: 24 (20pp)
- [121] LI C X, FENG X S, WEI F S. An entropy-stable ideal EC-GLM-MHD model for the simulation of the three-dimensional ambient solar wind[J]. *Astrophys. J. Supplement Series*, 2021, **257**: 24 (22pp)
- [122] LIU C, SHEN F, LIU Y S, *et al.* Numerical study of divergence cleaning and coronal heating/acceleration methods in the 3D COIN-TVD MHD model[J]. *Frontiers in Physics*, 2021, **9**: 421
- [123] LI H C, FENG X S, WEI F S. Comparison of synoptic maps and PFSS solutions for the declining phase of solar cycle 24[J]. *Journal of Geophysical Research (Space Physics)*, 2021, **126**: e2020JA028870
- [124] YANG Y, SHEN F. Three-dimensional MHD modeling of interplanetary solar wind using self-consistent boundary condition obtained from multiple observations and machine learning[J]. *Universe*, 2021, **7**: 371
- [125] LI H C, FENG X S, WEI F S. Assessment of CESE-HLLD ambient solar wind model results using multipoint observation[J]. *Journal of Space Weather and Space Climate*, 2020, **10**: 44
- [126] LI H C, FENG X S, ZUO P B, WEI F S. Simulation of the interplanetary B_z using a data-driven heliospheric solar wind model[J]. *Astrophys. J.*, 2020, **900**: 76(13pp)
- [127] SHEN F, LIU Y S, YANG Y. Numerical research on the effect of the initial parameters of a CME flux-rope model on simulation results. II. Different locations of observers[J]. *Astrophys. J.*, 2021, **915**: 30(11pp)
- [128] SHEN F, LIU Y S, YANG Y. Numerical research on the effect of the initial parameters of a CME flux-rope model on simulation results[J]. *Astrophys. J. Supplement Series*, 2021, **253**: 12(13pp)
- [129] ZHANG M, FENG X S, SHEN F, YANG L P. Numerical study of two injection methods for the 2007 November 15 coronal mass ejection in the inner heliosphere[J]. *Astrophys. J.*, 2021, **918**: 35(12pp)
- [130] YANG L P, WANG H P, FENG X S, *et al.* Numerical MHD simulations of the 3D morphology and kinematics of the 2017 September 10 CME-driven shock from the sun to Earth[J]. *Astrophys. J.*, 2021, **918**: 31(14pp)
- [131] LIU Z X, WANG L H, *et al.* Pan-spectrum fitting formula for suprathermal particles[J]. *JGR: Space Physics*, 2020, **125**: e2020JA028702. <https://doi.org/10.1029/2020JA028702>
- [132] WANG W, WANG L H, *et al.* Solar energetic electron events associated with hard X-ray flares[J]. *Astrophys. J.*, 2021, **913**: 89(12pp)
- [133] WANG L H, ZONG Q G, SHI Q Q, *et al.* Solar energetic electrons entering the Earth's cusp/lobe[J]. *Astrophys. J.*, 2021, **910**: 12(7pp)
- [134] KONG F J, QIN G. Suprathermal electron acceleration by a quasi-perpendicular shock: Simulations and observations[J]. *Astrophys. J.*, 2020, **896**: 20(11pp)
- [135] WANG Y, LYU D, XIAO B X, QIN G, ZHONG Y S, LIAN L L.

- Statistical survey of reservoir phenomenon in energetic proton events observed by multiple spacecraft[J]. *Astrophys. J.*, 2021, **909**: 110(19pp)
- [136] WANG Y, LYU D, QIN G, XIAO B X. The effects of magnetic boundary on the uniform distribution of energetic particle intensities observed by multiple spacecraft[J]. *Astrophys. J.*, 2021, **913**: 66(8pp)
- [137] WU S S, QIN G. Magnetic cloud and sheath in the ground-level enhancement event of 2000 July 14. I. Effects on the solar energetic particles[J]. *Astrophys. J.*, 2020, **904**: 151(9pp)
- [138] QIN G, WU S S. Magnetic cloud and sheath in the ground-level enhancement event of 2000 July 14. II. Effects on the forrush decrease[J]. *Astrophys. J.*, 2021, **908**: 236(10pp)
- [139] WANG J F, QIN G. The invariance of the diffusion coefficient with iterative operations of the charged particle transport equation[J]. *Astrophys. J.*, 2021, **899**: 39(45pp)
- [140] WANG J F, QIN G. Study of momentum diffusion with the effect of adiabatic focusing[J]. *Astrophys. J. Supplement Series*, 2021, **257**: 44(34pp)
- [141] LUO X, ZHANG M, FENG X S, POTGIETER M S, SHEN F, BAZILEVSKAYA G. A numerical study of the effects of corotating interaction regions on cosmic-ray transport[J]. *Astrophys. J.*, 2020, **899**: 90 (12pp)
- [142] SONG X J, LUO X, POTGIETER M S, LIU X M, GENG Z K. Numerical Study of the Solar Modulation of Galactic Protons and Helium from 2006 to 2017[J]. *Astrophys. J. Supplement Series*, 2021, **257**: 48(13pp)
- [143] SHEN Z N, QIN G, ZUO P B, WEI F S, XU X J. A study of variations of galactic cosmic-ray intensity based on a hybrid data-processing method[J]. *Astrophys. J.*, 2020, **900**: 143(14pp)
- [144] SHEN Z N, QIN G, ZUO P B, WEI F S, XU X J. Numerical modeling of latitudinal gradients for galactic cosmic-ray protons during solar minima: Comparing with Ulysses observations[J]. *Astrophys. J. Supplement Series*, 2021, **256**: 18(19pp)
- [145] SHEN Z N, YANG H, ZUO P B, QIN G. Solar modulation of galactic cosmic-ray protons based on a modified force-field approach[J]. *Astrophys. J.*, 2021, **921**: 109(7pp)
- [146] ZHU B, LIU Y D, *et al.* Shock properties and associated characteristics of solar energetic particles in the 2017 September 10 ground-level enhancement event[J]. *Astrophys. J.*, 2021, **921**: 26(9pp)

Magnetospheric Physics in China: 2020–2021

CAO Jinbin, YANG Junying

Space Science Institute, School of Space and Environment, Beihang University, Beijing 100191
Key Laboratory of Space Environment Monitoring and Information Processing, Ministry of Industry and Information Technology, Beijing 100191

Abstract

In the past two years, many progresses were made in magnetospheric physics by using the data of OMNI, SuperMAG networks, Double Star Program, Cluster, THEMIS, RBSP, DMSP, DEMETER, NOAA, Van Allen Probes, GOES, Geotail, Swarm, MMS, BeiDa, Fengyun, ARTEMIS, MESSENGER, Juno, Chinese Mars ROVER, MAVEN, Tianwen-1, Venus Express, Lunar Prospector *e.g.*, or by computer simulations. This paper briefly reviews these works based on 356 papers published from January 2020 to December 2021. The subjects covered various sub-branches of Magnetospheric Physics, including solar wind-magnetosphere-ionosphere interaction, inner magnetosphere, outer magnetosphere, magnetic reconnection, planetary magnetosphere.

Key words

Solar wind-magnetosphere-ionosphere interaction, Inner magnetosphere, Outer magnetosphere, Magnetic reconnection, Planetary magnetosphere

1 Solar Wind-magnetosphere-ionosphere Interaction

Solar wind dynamic pressure (P_{dyn}) is the main driving factor that determines the intensity of a great geomagnetic storm^[1,2] and plays an important role in the wave evolution and particle dynamics in the inner magnetosphere^[3-5]. Xiang *et al.*^[6] confirmed that the solar wind speed has the greatest influence on the MeV electron flux variations, particularly at higher L , while the P_{dyn} has more influence at lower L . There were both electron dropout and enhancement drift echoes in some P_{dyn} decrease events^[7]. The magnetopause shadowing process in association with a sudden P_{dyn} pulse or a large geomagnetic storm may be the major loss mechanism during the initial phase of the storm at $L > 4.5$ ^[8]. Shi *et al.*^[9] re-

viewed how changing solar wind P_{dyn} produces the vortices, Ultralow Frequency (ULF) waves, and aurorae. Zhao *et al.*^[10] provided direct evidence of the scenario that magnetospheric flow vortices generated by a P_{dyn} pulse carry Field-Aligned Currents (FACs) into the ionosphere and thereby modulate auroral activity.

Zou *et al.*^[11] demonstrated that persistently enhanced P_{dyn} can modulate the radiation belt electron dynamics before the storm main phase. For energetic energy level, the occurrence rate of the pancake (butterfly) PADs does not clearly decrease (increase) with the enhancement of P_{dyn} at $L \leq 12$ ^[12]. About 5% time, protons with energies of 30–50 keV showed two distinct populations, having an additional field-aligned population overlapping with the original pancake population^[13]. Radiation belt electron butterfly PADs are well connected to the solar

wind condition, substorm activity, and magnetospheric wave distribution^[14].

Xiang *et al.*^[15] suggested that actual radial diffusion rates in the inner belt are lower than previous estimates in which cosmic ray albedo neutron decay contributions were not considered. Simulations showed that solar flares increased global daytime currents and reduced the eastward electric fields during the daytime from the equator to middle latitudes^[16]. The solar wind density plays a significant role in transferring solar wind energy into the magnetosphere, besides the southward magnetic field and the solar wind speed^[17].

Cai *et al.*^[18] reported the characteristics of the topside ionospheric O⁺ diffusive flux during both geomagnetically quiet and moderate times for solar minimum from 1970 to 2018. Statistical results show that the O⁺ density and its abundance (O⁺/H⁺) vary with SYM-H index and P_{dyn} exponentially^[19], and the H⁺ and O⁺ lifetimes generally increase with L shell^[20]. During the main phase, Ring Current (RC) ions with lower magnetic moments can penetrate into the deep inner magnetosphere^[21].

The global lightning can dominate the atmospheric noise^[22] and can generate whistler waves which can travel upward into the radiation belts during higher geomagnetic activities^[23]. The day-night difference of energetic electrons in the South Atlantic Anomaly (SAA) region depends not only on the electron energy but also on the geomagnetic activity levels^[24]. The subauroral polarization streams induced equatorial electrojet presented a semidiurnal pattern associated with the variations of the F₂-layer virtual height^[25] and flows westward and eastward in the daytime and dawn/dusk sectors, respectively^[26].

The statistical characteristics of the structures of giant undulations during geomagnetic storms were studied for the first time, based on aurora images during 2005–2019^[27]. He *et al.*^[28] showed direct observations of a plasmopause surface wave and its impacts during a geomagnetic storm. The electron density fluctuation events at the plasmopause mainly occur in the twilight sectors and the spatial distribution varies with MLT and geomagnetic activity^[29]. Li *et al.*^[30] suggested that the occurrence rate of an observed plasmaspheric plume in the inner magnetosphere is larger during stronger geomagnetic activity. The source population and the charge exchange losses along the drift paths play a very important role in the formation of the “finger” structure^[31].

The result of Ren *et al.*^[32] may explain previous ob-

servation that substorms frequently occur shortly after northward IMF turning. The statistical analysis shows that strong substorms ($AE > 1000$ nT) and super substorms ($AE > 2000$ nT) triggered by interplanetary shocks are most likely to occur under southward IMF and fast solar wind pre-conditions^[33]. Duan *et al.*^[34] indicated that characteristics of dipolarization with a large beginning elevation angle within the substorm onset region provide a new indicator to identify substorm onset location. Fu *et al.*^[35] suggested that there is an additional current wedge during intense substorms located near the dusk. Tang *et al.*^[36] reported local secondary magnetic reconnection at Earth's flank magnetopause, suggesting a new pathway for the entry of the solar wind into geospace. The magnetospheric energy deposition into the northern polar upper atmosphere has obvious longitudinal and seasonal variations^[37]. The ions with larger grazing angles would meander around the magnetopause without a full escape, whereas the meandering motion for those with smaller angles could be more easily to escape^[38]. Non-storm time super-substorm may also have a significant contribution to the RC^[39]. The reversed energy spectra of RC protons with distinct flux can be prevalent inside the plasmasphere^[40].

Wang *et al.*^[41] provided the first observational evidence that solar/interplanetary energetic electrons can directly and continuously enter the planet's cusp/lobe regions and get trapped there. Guo *et al.*^[42] found that during the northward IMF, high latitude magnetic reconnection both poleward and equatorward of the cusp can occur almost simultaneously. High solar wind density, low latitude magnetopause reconnection and positive dipole tilt are favorable conditions for high-density cusp events^[43]. Based on topology information, a new normalized statistical methodology is developed by Xiao *et al.*^[44] to organize the measurements of cusp crossings to obtain distributions of magnetic field and plasma parameters in the xz plane.

Xue *et al.*^[45] reported a simultaneous observation of two band Electromagnetic Ion Cyclotron (EMIC) waves and toroidal Alfvén waves by the Van Allen Probe mission. The original right-handed elliptically polarized Alfvén waves become linearly polarized, and eventually become right-handed and circularly polarized^[46]. Dipolarization Fronts (DFs) in the magnetosphere could couple the ionosphere with Alfvén waves^[47].

Chen *et al.*^[48] demonstrated that kinetic-scale FACs are significant in magnetosphere-ionosphere coupling

which can be generated by velocity shear shortly and locally^[49] between fast plasma flows associated with nightside magnetic reconnection and slower background magnetotail plasma flows^[50]. Ion upflow occurrence shows a dawn-dusk asymmetry distribution that matches well with the Region 1 FACs^[51]. Conjunctive observations of a downward FAC and ground data were made to investigate the generation of downward FAC^[52].

Yao *et al.*^[53] presented a new type of Kinetic-Scale Flux Rope (KFR) in the Earth's dayside magnetosheath boundary layer, which was possibly generated by a FAC, differing from typical dayside flux ropes usually observed within the current sheet where magnetic reconnection can occur. Pitkanen *et al.*^[54] statistically investigated how the rotation of the neutral sheet depends on the sign and magnitude of IMF B_y . Electrons can be non-adiabatic at the neutral sheet, which is able to scatter their PAD^[55].

The Transpolar Arcs (TPAs) presented by Park *et al.*^[56] were believed to be the result of both indirect and direct processes of solar wind energy transfer to the high-latitude ionosphere. Tang *et al.*^[57] suggested that the semiannual variation observed in the TPA incidence may be related to the Russell-McPherron effect due to the projection effect of the IMF B_y under northward IMF conditions. The observations and simulations reveal that these multiple TPAs are generated by precipitating energetic magnetospheric electrons within FAC sheets^[58].

Ma *et al.*^[59] suggest that the flow of polar cap origin may play a crucial role in auroral surges by feeding low entropy plasma into surge initiation and development. Li *et al.*^[60] suggested that the electron precipitation through the polar rain can be a main energy source of the polar wind during periods of high levels of solar activity. Polar cap cold patches occur more frequently during solar maximum years^[61]. The spatial size of cold and hot patches decreases with solar activity (increases with geomagnetic activity). Zhang *et al.*^[62] summarized the recent new progress in the formation and evolution of patches.

Zhang *et al.*^[63] presented the first statistical study on the Auroral Kilometric Radiation (AKR) electric field amplitude in the radiation belts. The first (higher) harmonic order of AKR contributes to diffusion coefficients at small (larger) pitch angles^[64].

Fujimoto and Sydora^[65] showed that the electron K-H instability plays a primary role in driving intense elec-

tromagnetic turbulence, and the high-energy electrons are efficiently scattered by the turbulences, leading to the dissipation and electron heating^[66]. The distribution of magnetosheath turbulence in the wavenumber space is dominantly transverse to the background magnetic field^[67]. The correlation (and Taylor) length scale of the solar wind turbulence is the largest along the magnetic field, and is the smallest in the field-perpendicular directions^[68]. The Taylor scale increases with the increasing sunspot number, indicating that the Taylor scale is positively correlated with the energy cascade rate^[69].

2 Inner Magnetosphere

Proton sustained gaps are predominantly distributed near the prenoon sector^[70], while the narrow gaps for oxygen ions are most frequently observed near the noon sector^[71]. Using the time-of-flight technique based on the pitch angle dependence of electron drift velocities, the "boomerang-shaped" stripes are inferred to originate from straight stripes^[72]. The particle tracing model suggests that the wedge-like structures originate from intermittent substorm injection, and it is the accessibility region of these injected ions that determines their shapes^[73]. These wedge-like structures are probably attributed to fresh substorm injections from the outer region^[74]. Li *et al.*^[75] found a clear MLT dependence of the number of stationary "nose-like" ion spectral structures. Ren *et al.*^[76] suggested that the wedge-like and nose-like spectral signatures are merely the manifestations of one single structure along different spacecraft trajectories.

The Very Low Frequency (VLF) transmitter signals have a slight influence on the loss of energetic electrons with pitch angles larger than 80° ^[77]. Xiang *et al.*^[78] suggested that the VLF transmitter signals in the inner magnetosphere mainly propagate along the magnetic field line across the station position. Hua *et al.*^[79] provided quantitative evidence that VLF transmitter emissions that leak from the Earth-ionosphere waveguide are primarily responsible for bifurcating the energetic electron belt. The bifurcation of the Earth's energetic electron belt (tens of keV) is mostly observed at 30–100 keV^[80].

Electron Cyclotron Harmonic (ECH) and chorus may not grow independently but competitively or collaboratively gain energy from hot electrons^[81] and nonlinear wave-wave interactions can redistribute the primary

ECH wave energy over a broader frequency range^[82]. Wu *et al.*^[83] demonstrated that the heating of cold electrons is negligible and non-resonant, different from previous conclusions, and suggested that the saturation of the ECH wave is caused by the filling of the loss cone of hot electrons. Lou *et al.*^[84] confirmed the significant role of ECH waves in driving the dayside diffuse aurora. ECH waves at Earth could exhibit frequency chirping^[85].

Wave trapping caused by field-aligned density irregularities (ducts) may account for whistler-mode waves^[86,87], which are found to be generated by the butterfly type PADs of electrons^[88], with field-aligned electron components acting as the energy source^[89]. The wave ducting effects at the plasmopause may lead to unusual and anomalous energetic pitch angle scattering^[90]. Lu *et al.*^[91] demonstrated that a continuous injection of energetic electrons caused by an azimuthal drift is essential for the repetitive emissions of chorus waves.

One-dimensional Particle-in-Cell (PIC) simulation can give a further understanding of the generation and propagation of rising-tone chorus waves^[92,93], *e.g.*, bidirectional chirping of whistler waves in a uniform magnetic field and falling-tone-only chirping in an inhomogeneous field^[92], a spectrum with a power gap around 0.5Ω ^[94]. The gap is found between two peaks of whistler-mode waves, which is caused by the mode splitting of beam-like electrons^[95].

Theoretical and numerical models of chorus waves were reviewed in Tao *et al.*^[96], focusing on the nonlinear wave particle interactions and the frequency chirping of rising tone chorus waves. The duration of whistler mode chorus waves increases and the chirping rate (Γ) decreases with increasing L -shell, although the dependence is weak^[97]. Liu *et al.*^[98] presented two unexpected chorus rising tone events within which the sub-elements exhibit unexpected clearly reversed, falling frequency-sweep. Statistically, lower-band chorus emissions exhibit higher wave occurrence rates and larger normalized peak wave frequencies in northern hemisphere but somehow stronger peak wave intensities in southern hemisphere^[99]. Tao *et al.*^[100] proposed a phenomenological model which could be applied to explain the fine structures of chorus waves, including subpackets and bandwidth.

The radial structures of seed electron Phase Space Density (PSD) should be considered when studying the

dynamics of the outer radiation belt^[101]. Chen *et al.*^[102] showed that electron PSD presents a peaked radial profile and power law energy spectrum, confirming that local acceleration plays an important role in the electron dynamics. Liu *et al.*^[103] reported that whistler waves can effectively trap/bunch thermal electrons and modulate electron phase space trajectories. Using a test particle simulation code, Cai *et al.*^[104] investigated effects of nonlinear resonance broadening on scattering of electrons and compare the results with a previous nonlinear theory. Wu *et al.*^[105] suggested that the loss and recovery processes developed first at higher L -shells. The “S-shaped” inner boundary is abruptly transformed from “V-shaped” in storm main phase but reoccurs in several days in the late recovery phase^[106].

Various frequency chorus waves have different effects on electron dynamics^[107]. ELF chorus can result in unusual loss of relativistic electrons while regular chorus contributes to the acceleration^[108]. By studying the Landau resonance between whistler mode waves and electrons, Kong *et al.*^[109] provided a better understanding of the formation of beam-like electron distribution in the Earth's magnetosphere. However, bounce resonance diffusion rates have slight energy dependence for >100 keV electrons while Landau-resonant scattering rates decrease significantly in the MeV energy range^[110]. Statistical electron PADs features observed in the whistler- and non-whistler waves are associated with the Landau resonance of whistler-mode waves and drift-shell splitting effect^[111]. Chen *et al.*^[112] demonstrated that the particle energy change might be underestimated in the conventional theories, as the Betatron acceleration induced by the curl of the wave electric field was often omitted.

The statistical studies of He *et al.*^[113] showed that incoherent hiss is widely distributed in dayside plasmasphere, with peak frequencies below 500 Hz; and intense coherent hiss occurs in outer plasmasphere of $L > 4$. Liu *et al.*^[114] presented the first comprehensive observations of hiss waves growing from the sub-storm-injected electron instability. Both hiss and ex-hiss waves have higher occurrence rates on the dayside (08:00–20:00 MLT) and are positively correlated^[115].

Hiss and chorus can simultaneously occur at the same electron drifting shells due to the irregular plasmasphere^[116]. Chorus wave is incoherent when the spatial extent is greater than 433 km or the time lag lasts about 10 s^[117]. Using high-quality Van Allen Probes meas-

urements, Gu *et al.*^[118] verified that chorus waves act as a critical candidate for relativistic electron acceleration and plasmaspheric hiss as a viable cause for relativistic electron loss. Fu *et al.*^[119] suggested that the hiss waves have different sources: low-frequency ($<0.18 f_{ce}$) hiss waves transmitted from chorus outside the plasmasphere and high-frequency ($>0.18 f_{ce}$) hiss waves locally amplified. Li *et al.*^[120] suggested that the enhanced electric field can significantly change the energetic electron distributions, which provide free energy for hiss wave amplification.

The gradual formation of “reversed energy spectrum” at $L \approx 3.5$ indicates that hiss scattering inside the plasmapause contributed to the fast decay of sub-MeV remnant belt^[121]. The collaborated effect of a low-frequency band and high-frequency band hiss can cause significant precipitation losses of energetic electrons of tens to several hundred keV within 2 days^[122] and Locally generated High-Frequency Plasmaspheric Hiss (LHFPH) could be a potential mechanism for the precipitation loss of suprathermal electrons of 0.1 keV to tens of keV^[123].

The competitive influences of different plasma waves on the PAD of energetic electrons depend on density of ambient plasmas and relative intensity of waves^[124]. Man-made VLF waves and naturally generated hiss or Lightning-Generated Whistlers (LGWs) play complementary and catalytic roles in the loss of radiation belt electrons^[125], and weaken the top hat Pitch Angle (PA) distribution^[126]. Mei *et al.*^[127] developed an empirical model of the energy-dependent boundaries of Earth's electron radiation belt slot region. Slot region electron loss timescales vary significantly from <1 day to several years^[128].

Hot plasma effects will modify the hiss dispersion relation^[129]. The cold plasma theory can become less reliable for plasmaspheric hiss waves under disturbed geomagnetic circumstances and the realistic wave dispersion is essential to better quantify the electron scattering effect of hiss waves^[130]. Wang *et al.*^[131] presented the first quantitative study on the evolution of suprathermal electrons under the competition between Landau heating by whistler mode hiss waves and Coulomb collisional cooling by background plasma inside a plasmaspheric plume. Fu *et al.*^[132] demonstrated that the cyclotron resonance is mainly responsible for the pitch angle scattering of electrons $<80^\circ$, while both Landau

and bounce resonances can affect the scattering of near-equatorially mirroring electrons. Li *et al.*^[133] found similarities and differences between sub-MeV and ultra-relativistic electrons three-belt events, providing a new perspective in three-belt structure study.

Strong storms and moderate storms can share in common a lot of features on the azimuthal mode structure and power spectrum of ULF waves^[134]. The generation of Pc4-5 ULF waves after interplanetary shock-induced electric fields is studied by Zhang *et al.*^[135]. Li *et al.*^[136] proposed that the shoulder-like pulsations which had been observed in many ULF wave events can be caused by monochromatic oscillations of the magnetic flux tubes in a ballooning-mirror mode structure, which are likely facilitated by the magnetic reconnection altering the state of plasma in the downstream plasma sheet^[137].

These toroidal ULF waves, like their poloidal counterparts, play an important role in magnetospheric particle dynamics^[138]. The seed (hundreds of keV) and core (≥ 1 MeV) electrons can resonate with ULF wave modes with distinctive values simultaneously^[139]. Resonant electrons can remain phase trapped by the low-m ULF waves under strong convection electric fields, whereas for high-m ULF waves, the electrons trajectories can be significantly modified^[140]. Zhao *et al.*^[141] suggested that localized ULF waves trapped in the plume may result in the preference of localized ULF wave-electron interactions in noon-to-dusk region. Liu *et al.*^[142] found the phase shift of ion flux oscillation across resonant pitch angles varies with time, when ULF wave growth and damping cannot be neglected. Li *et al.*^[143] suggested 180° phase shifts across pitch angle can also result from pitch angle-dependent bump-on-tail distributions.

During large AE, EMIC waves are mainly generated in the dusk sector and near the magnetic equator^[144]. Liu *et al.*^[145] highlighted the importance of solar wind conditions for the evolution of inner magnetospheric EMIC waves from a new perspective. Xiong *et al.*^[146] suggested that the inward extension of EMIC waves may be driven by the inward injection of anisotropic energetic protons from the dense plasma sheet.

However, H^+ and He^+ band EMIC waves can be simultaneously excited in the midnight sector under appropriate conditions^[147]. The maximum growth rate of H-band of EMIC waves appears in the dusk-to-midnight

sector near the plasmopause, while O-band is excited at a slightly outer region^[148]. The frequency of the H⁺ band EMIC wave triggered by anisotropic hot H⁺ drops quickly in the initial stage, and then, a narrow He⁺ band EMIC wave is excited^[149]. He⁺ band EMIC waves appeared to split into O²⁺ and He⁺ band emissions, providing insight into the generation of O²⁺ band EMIC waves^[150].

Wang *et al.*^[151] demonstrated for the first time the existence of the intense unguided L-mode EMIC waves in the radiation belt according to the polarization characteristics. The effects of super-thermal plasmas on EMIC wave instability growth have a strong dependence on the emission band, temperature anisotropy A_{hp} , and parallel beta β_{hp} of hot protons^[152]. Hot protons alter the refractive index of EMIC waves at a given wave frequency along latitude and thus modify resonance latitude^[153]. Polarization reversal of EMIC waves contributes significantly to the pitch angle diffusion coefficients at low pitch angles extending to the loss cone angle for various parameter sets^[154] or of H⁺ band-induced particles^[155].

Wang *et al.*^[156] revealed the important mechanism for the loss of RC protons, that is being scattered by EMIC waves^[157], and more important than the one due to field line curvature^[158,159], which mostly contributes to ion precipitation in outer regions ($L > 4-5$). When the intensity of EMIC waves is large, the cold protons (ions) having low-energies can be energized by the EMIC waves^[160].

Intense EMIC and Magnetosonic (MS) waves were simultaneously observed in the high-density regions and disappeared in low-density regions^[161]. The linear growth rates estimated for both these two waves are in good agreement with the observed wave frequency spectra^[162]. Huang *et al.*^[163] suggested that the complex unstable distribution in the velocity phase space of RC protons during the magnetic dip can trigger the simultaneous generation of EMIC and MS waves in the inner magnetosphere.

The MS wave occurrence rate and amplitude B_w increases with enhanced geomagnetic activity and decreasing magnetic latitude, and is strongest near the geomagnetic equator within the 08:00–20:00 MLT sector, both inside and outside the plasmopause, while the B_w can reach higher values inside the plasmopause than it does outside the plasmopause as the K_p index increases^[164,165]. This is different from the finding that

narrowband fast MS waves near the lower hybrid resonance frequency were observed mainly outside the plasmopause^[166], with a distinct boundary where energies of the low-harmonic fast MS waves cannot penetrate inward in the time-frequency domain^[167]. The electric/magnetic fields of MS waves decrease/increase rapidly when propagating across the plasmopause boundary layer from the outside^[168]. However, Huang *et al.*^[169] performed the first observations of high frequency MS waves with the frequencies of harmonics higher than the lower hybrid frequency in the Earth's magnetosphere. Zou *et al.*^[170] presented an unusual event of MS waves with more than six harmonics wavebands ($n = 1$ to 6). MS waves would be fully reflected near the cut-off point, since only evanescent waves are allowed in the cut-off regions^[171].

Sun *et al.*^[172] demonstrated that the background plasma density variation can modulate the MS waves and may play an important role in the spatial distribution of MS waves. Yu *et al.*^[173] indicated the validation of cold plasma approximation to estimate the electric field components of MS waves from their magnetic counterparts in the inner magnetosphere. Wu *et al.*^[174] illustrated a scenario that off-equatorial proton ring distributions could be a significant source of inner magnetosphere MS waves^[175], which can first appear at a distant region and then propagate to low L -shells^[176].

Gu *et al.*^[177] indicated that the MS waves associated with the density drop can cause considerable pitch angle and momentum diffusion for radiation belt electrons. Yuan *et al.*^[178] provided ionospheric signature of RC ions scattered by MS waves. Zhou *et al.*^[179] suggested that the electron butterfly distribution has important implications for revealing the combined scattering of MS wave-particle interactions. Fu and Ge^[180] demonstrated that the local acceleration of the RC protons by MS waves contributes to the dynamic evolution of Earth's RC.

3 Outer Magnetosphere

Liu *et al.*^[181] presented the first observational evidence for Magnetic Hole (MH) generation by electron mirror instability behind a DF. The reconstructed results of Liu *et al.*^[182] showed that the Electron-Scale Magnetic Holes (ESMHs) may have complex cross-section shapes (*e.g.*, saddle-like shapes) and comparable extension lengths in the parallel and perpendicular directions to

the magnetic field, which are inconsistent with the cylinder simplifications in previous studies. Kinetic-Scale Magnetic Holes (KSMHs) occur in the magnetosheath at rates far above their occurrence in the solar wind^[183]. Huang *et al.*^[184] identified whistler waves at the boundary of an ion scale magnetic hole, which should be locally excited rather than propagated from other regions.

Whistler waves were also observed in the Earth's foreshock^[185]. There is a clear decreasing trend between the size of foreshock cavitons and their velocity in the solar wind frame^[186]. Magnetic reconnection could occur in the foreshock region and heat/accelerate the electrons therein^[187]. A correlation between variations of magnetosheath hot ion fluxes and the transverse fluctuations of the ULF waves is found by Cai and Wei^[188]. Wang *et al.*^[189] for the first time found that the drift-bounce resonances played a major role in modulating the energy of ions with energy dispersions, during the interactions between the ions and the foreshock transient-driven Pc5 ULF wave. There are more than two resonant pitch angles at fixed energy, revealing a new drift-bounce acceleration mechanism in the dayside outer magnetosphere^[190].

A global MHD model is used by Lu *et al.*^[191] to study the energy transfer from solar wind to magnetosphere through magnetopause under radial IMFs, when the dayside of the bow shock is located closer to the Earth than the average^[192]. Wang *et al.*^[193] performed a series of 3D global Magnetohydrodynamic (MHD) simulations and demonstrated the quantitative effects of the IMF B_x component on the locations and shapes of the bow shock and magnetopause during northward IMF. Shang *et al.*^[194] demonstrated that the compressed magnetopause is sharply deflected at lunar distances in response to the shock and solar wind V - Y effects. Man *et al.*^[195] presented a comprehensive study of the intense current structures at the dayside magnetopause. There are obvious asymmetries on both flanks of the magnetopause and the dawn side magnetopause is thicker and more active^[196]. The statistical results reveal the important role of P_{dyn} in electron dynamics inside the magnetopause. The O^+ density in the duskside magnetopause boundary layer during the recovery phase is larger than that during the expansion phase^[197].

Zhu *et al.*^[198] provided key parameters to help understand how Hot Flow Anomalies (HFAs) disturb the magnetosphere. The electron velocity within the elec-

tron jets is much larger than the local Alfvén speed, implying that these jets belong to super-Alfvénic flows^[199]. At MHD scales, the spectral indices of the magnetic field and velocity spectra present a positive and negative correlation with Alfvén Mach number^[200]. When the IMF is southward and the Alfvén Mach number of solar wind is high, the bow shock indentation can be clearly determined^[201].

Guo *et al.*^[202] for the first time demonstrated the betatron-cooling effect beyond the Earth, which helps to understand the electron dynamics in the planetary magnetosphere. The donut-shaped PADs of magnetic cavity electrons were formed by the combined effects of betatron cooling, radial transport, and pitch angle variations^[203]. Based on the multipoint measurements from the Magnetospheric Multiscale (MMS) constellation, Li *et al.*^[204] developed a kinetic model which can utilize magnetic cavity observations by one MMS spacecraft to predict measurements from a second/third spacecraft. Liu *et al.*^[205] reported evidence of evolution of an identified microscale (*i.e.*, electron gyro-scale) magnetic cavity structure and reveal within it a unique energization process that does not adhere to prevailing adiabatic invariance theory. Observations from the MMS constellation^[206] have shown the existence of helical magnetic cavities characterized by the presence of azimuthal magnetic fields, which could not be reconstructed by the previous models.

Non-gyrotropic electron distributions can be generated by the finite electron gyration at an electron-scale boundary, and the electric field normal to this boundary usually contributes to the electron acceleration to make a gyrotropic distributions more apparent^[207]. The magnetic field line curvature in the turbulent magnetosheath plasma exhibits two power-law distributions: the low/large curvature follows the scaling of $\kappa^{0.33}/\kappa^{-2.16}$ ^[208]. Three kinds of PADs commonly observed in the magnetotail, Pancake, Rolling pin, and Cigar distributions, are formed in sequence during the propagation of the DFs^[209]. These electron pitch-angle distributions, as well as butterfly, are crucial to understanding electron dynamics in the magnetotail. For the first time, Liu *et al.*^[210] presented that they couldn't find any statistical correlation between magnetic structures and the rolling-pin distributions, different from previous studies suggesting a close connection between them.

Current sheets with widths of several ion inertial

lengths are produced in the magnetosheath after the upstream large-amplitude electromagnetic waves penetrate through the shock and are then compressed in downstream^[211]. Yang *et al.*^[212] shed new insight on the mechanism for electrostatic wave excitations and possible Electromagnetic wave emissions at young coronal mass ejection-driven shocks in the near-Sun solar wind. Wang *et al.*^[213] suggested that the ion-scale magnetic peaks are coherent structures associated with energy dissipation and electron heating in the magnetosheath. Magnetic reconnection can play a significant role for the energy dissipation in these magnetic peaks, which have been investigated by Lu *et al.*^[214] in the downstream of a quasi-perpendicular shock. Yang *et al.*^[215] provided direct evidence of shock self-reformation, and also shed light on energy dissipation and energetic particle acceleration at collisionless shocks throughout the universe.

Bipolar current densities exist in the cross section of two hole-like mirror-mode structures, referred to as Magnetic Dips (MDs)^[216]. Yao *et al.*^[217] identified four different types of MDs: “frozen-in,” “expanding,” “contracting,” and “stable-propagating.” MDs and the injected protons perform good agreement^[218]. The positive slope is responsible for the generation of high-frequency electrostatic wave in the magnetic dip ahead of the DF^[219].

Wei *et al.*^[220] reported that the wide-range of intense dB/dt (and dH/dt) variations are associated with a large-scale, substorm current system, driven by multiple Bursty Bulk Flows (BBFs). Zhang *et al.*^[221] suggested that the strong/weak vorticity field of the plasma bulk (convective) velocity within the BBF corresponds to the ion flux enhancement at high/ medium energy (above 10 keV/2–5 keV). Zhang *et al.*^[222] proposed a possible mechanism on the BBF deceleration, *i.e.*, “collision” with the tailward flow. Inside the BBFs, the strongest earthward electron flows are observed in the ion flow boundary, away from the current sheet center^[223]. Zhang *et al.*^[224] revealed that the cross-tail current sheet at the DF is rolled up, which could decelerate BBF and change the flow structure.

4 Magnetic Reconnection

Wang *et al.*^[225] provided the first dynamic picture of magnetic reconnection, demonstrating that the magnetic reconnection in space can develop rapidly during tens of milliseconds. The magnetotail reconnection is possible

to occur when the dawnside tail lobe contacts with the duskside tail lobe by a sudden increase of the IMF B_z component^[226] with significant B_y ^[227]. Huang *et al.*^[228] demonstrated that the asymmetric upstream plasma conditions during magnetic reconnection can be studied in the laboratory.

When the IMF clock angle is large, the flux ropes can coalesce and form new ones with larger diameters^[229]. Man *et al.*^[230] showed a typical ion-scale flux rope at the subsolar magnetopause. The energetic electron fluxes inside it were larger than those outside^[231]. Chen *et al.*^[232] presented the first observation of a Magnetic Flux Rope (MFR) inside an Electron Diffusion Region (EDR). The subion-scale MFRs host more intense plasma activity than the ion-scale MFR^[233]. Besides using four spacecraft with separation scale much smaller than the flux ropes, current density, curvature radius of the magnetic field, and the transverse size of flux ropes can also be inferred by a single-point method^[234].

Man *et al.*^[235] reported an MMS observation of magnetic reconnection occurring at the edge of a large-scale ($2 R_e$) MFR. Zhong *et al.*^[236] presented the first observational evidence for localized secondary reconnection at the separatrix surface of an MFR. Zhou *et al.*^[237] presented the first evidence that secondary reconnections occur in the turbulent outflow driven by a primary reconnection in the Earth’s magnetotail. Wang *et al.*^[238] presented direct evidence of secondary reconnection in the filamentary currents, which are plentiful in both primary flux ropes and the secondary flux ropes^[239]. Two re-reconnection processes increase the plasma energy and the magnetic flux connected to the Earth, which favors particle and energy transport toward the Earth’s magnetosphere^[240].

The particle acceleration processes around magnetotail DFs were reviewed by Fu *et al.*^[241]. As found a DF structure behind which energetic-electron fluxes are modulated by MS waves^[242] explained both the presence and absence of energetic electrons behind DFs. Liu *et al.*^[243] indicated that energy budgets at the DFs are dominated by electron physics, rather than ion dynamics suggested by previous studies. Betatron acceleration dominates at the DF^[244]. Only Fermi mechanism is contributory to suprathermal electron acceleration and presented a new explanation for its formation^[245].

Ma *et al.*^[246] suggested that plasma heating or temperature enhancements are related to both the flow vorticity/shear and current density, but more strongly with

flow vorticity/shear. By analyzing the velocity of the electrons, Jiang *et al.*^[247] found the first observation of electron vortex at the DF as far as they know. However, magnetic field perturbations induced by this electron vorticity are not significant^[248].

The curvature force continuously accelerates the DF moving outward, while the thermal pressure gradient force hinders the movement of the DF^[249]. Wang *et al.*^[250] suggested that the downstream magnetic energies of transient magnetic reconnections in the midtail may be transported to the near-Earth region by one DF event after another. Xu *et al.*^[251] found an intense current at the Anti-Dipolarization Fronts (ADFs), with the parallel current carried by a fast electron jet and the perpendicular current contributed by ion flow.

Electron current layer in the diffusion region splits into two sublayers at the electron inertial scale, not long after the triggering of reconnection^[252]. Zhong *et al.*^[253] reported a long EDR that extended at least 20 ion inertial lengths downstream of an X line at the Earth's magnetopause, suggesting that the EDR, where the reconnection electric field is directly proportional to the electron outflow speed^[254], probably plays more important roles in the energy conversion in magnetic reconnection than previously thought. Bai *et al.*^[255] suggested that the earthward moving flux rope was generated inside the HFA, implying that magnetic reconnection may have occurred inside the HFA.

Cold ions of ionospheric origin are widely observed in the lobe region of Earth's magnetotail and can enter the ion jet region after magnetic reconnection being triggered in the magnetotail. The cold-ion beams inside the explored jet could be accelerated by the Hall electric field in the cold ion diffusion region and the shrinking magnetic field lines through the Fermi effect^[256]. The large-amplitude unipolar can fill the entire EDR in the magnetosheath reconnection and thus dominates electron acceleration therein^[257]. The gyrotropic effect is more important than the nongyrotropic effect for the viscous dissipation in the diffusion region^[258].

A typical ion velocity distribution along the separatrix is found by Huang *et al.*^[259]: two counter-streaming populations in the perpendicular direction, with another two populations accelerated into distinct energy levels in the parallel direction. Chen *et al.*^[260] demonstrated that patchy magnetic reconnection has the potential to preserve the ion-to-electron temperature ratio under

certain conditions. Wu *et al.*^[261] reported the D-shaped velocity distribution of O^+ ions produced by the time-of-flight effect in the magnetotail reconnection.

Huang *et al.*^[262] quantitatively model the reduction of the reconnection rate and the maximum outflow speed observed in the short X-line limit. The distorted ion velocity distributions lead to a bipolar reversal in an off-diagonal element of the pressure tensor across the X-line, supporting an enhancement of the ion-scale reconnection electric field^[263]. But recent observations of Huang *et al.*^[264] proposed a new reconnection model: electron-only without ion coupling in an electron-scale current sheet. The spontaneous onset of collisionless magnetic reconnection is controlled by electron kinetics^[265]. However, magnetotail reconnection can start from electron reconnection in the presence of a strong external driver, then develops into ion reconnection^[266,267]. Tang *et al.*^[268] offered an insight into the Hall effect in collisionless magnetic reconnection. The Hall electric field could control the form of reconnection, producing either electron-only reconnection or traditional reconnection^[269].

Li *et al.*^[270] reported large-amplitude electron Bernstein waves at the electron-scale boundary of the hall current reversal. The flux pileup region hosts whistler waves because of the pancake distribution of electrons, whereas the DF boundary hosts lower hybrid drift waves due to the strong density and magnetic gradients statistically^[271]. On the magnetosphere side of reconnection, whistler waves are highly centered around the $1/2$ electron cyclotron frequency ω_e ^[272]. On the magnetosheath side of reconnection, whistler waves are mainly below $1/2 \omega_e$ and peaked around $0.2 \omega_e$. Yu *et al.*^[273] reported the whistler wave with a very narrow frequency band just above $1/2 \omega_e$ in the separatrix region, which was accompanied with the ECH waves. Tang *et al.*^[274] showed that the lower hybrid waves can also be found at the magnetosheath separatrix in asymmetric guide field reconnection.

Li *et al.*^[275] reported for the first time that the Upper-Hybrid (UH) waves were observed on both sides of the X line and may play an important role in controlling the reconnection rate. Shu *et al.*^[276] concluded that the reconnection rate can only represent the energy conversion at the reconnection site but not at the reconnection fronts for non-steady state magnetic reconnection. Yi *et al.*^[277] examined the energy conversion in multiple

X-line reconnection and found that the magnetic energy releases predominantly through primary islands and second at X-lines.

Two-dimensional Particle-in-Cell (PIC) simulations were performed by Chang *et al.*^[278] to investigate the characteristics of Electrostatic Solitary Waves (ESWs) in asymmetric magnetic reconnection. Fu *et al.*^[279] reported the first measurements of an electrostatic ESW's interior in a magnetotail reconnection jet and challenged the conventional belief that ESWs are efficient at particle acceleration. Using high-resolution MMS data, Guo *et al.*^[280] reported the observations of broadband electrostatic waves including electrostatic solitary waves and electron cyclotron waves associated with parallel electron temperature anisotropy ($T_{e\parallel} > T_{e\perp}$) behind a DF.

Yu *et al.*^[281] observed unique electron thermalization and associated electrostatic turbulence inside a special Dipolarizing Flux Tube (DFT) hosting both hot-tenuous and cold-dense electrons. While one-dimensional simulation helped Yu *et al.*^[282] to reproduce two types of waveforms similar to those observed in the EDR, implying that these electrostatic waves were generated by the bump-on-tail instabilities. Tang *et al.*^[283] suggested that the electrostatic waves generated by the fast-growing electron two-stream instability can contribute to the rapid isotropization of electron distributions in the reconnection exhaust, indicating that wave-particle interactions play an important role in electron dynamics.

5 Planetary Magnetosphere

Lai *et al.*^[284] studied the flux-return process, improving our understanding of the magnetic flux circulation in steady state at Saturn. Slow, global-scale flows resulting from transient noon-to-midnight electric fields^[285], which are associated with Saturnian zebra stripe^[286], are ultimately responsible for the bulk of the highest energy electrons trapped at Saturn. Using simultaneous measurements of the aurora, particles, magnetic fields, and energetic neutral atoms, Guo *et al.*^[287] revealed that a chain of paired currents is formed in Saturn's magnetosphere, which generates separated auroral patches.

Pan *et al.*^[288] showed a global picture of low-frequency waves while Long *et al.*^[289] performed a statistical analysis of ECH wave spatial distribution in Saturn's magnetosphere. Although a large anisotropy is generally

in favor of linear and nonlinear whistler-mode chorus wave growth in Saturn's inner magnetosphere, the nonlinear wave growth for a small anisotropy can still be generated^[290]. The occurrence frequency of Saturn radiation belt transient extensions indicates a possible role for corotating integration regions^[291]. At $3.5 < L < 6$, the PADs peak near 90° in Saturn's magnetosphere, while at $2.5 < L < 3.5$, the PADs transform to butterfly distributions^[292].

For the first time, Xu *et al.*^[293] found that the magnetic reconnection could also occur in the dayside magnetosphere of Saturn. Direct observations of plasmoids in Saturn's dayside magnetodisc were reported for the first time^[294].

A statistical model is constructed by Liu *et al.*^[295], providing us with a starting point for understanding the dynamics of the whole Jupiter's magnetosphere. High-resolution global simulations of Zhang *et al.*^[296] showed that the reconnection rate at the interface between the interplanetary and Jovian magnetic fields is too slow to generate a magnetically open, Earth-like polar cap. Wang *et al.*^[297] demonstrated the capabilities of their improved heliospheric MHD model in the prediction of the large-scale structures of the solar wind in the inner heliosphere of planets in the solar system such as Earth and Jupiter. Guo *et al.*^[298] suggested that the evolution of the double-arc structure of Jupiter is likely a consequence of the non-steady progress of magnetic reconnection. Simultaneous in situ satellite and space-based telescope Jupiter observations showed surprising similarities to terrestrial ion aurora^[299]. Yao *et al.*^[300] showed six clear examples displaying both Jupiter auroral dawn storms and auroral injection signatures, which could exist during intervals of either relatively low or high auroral activity. Wang *et al.*^[301] presented a new method combining Juno multi-instrument data (MAG, JADE, JEDI, UVS, JIRAM and Waves) and modeling tools to estimate these key parameters along Juno's trajectories.

The draping of IMF penetrates down to low altitudes and governs dynamics of the Martian ionosphere^[302]. Shan *et al.*^[303] demonstrated that periodic Martian shocks can perform the same functions as a single supercritical shock in a high-speed flow. Shan *et al.*^[304] showed an example of small-amplitude, sinusoidal MS waves at the proton gyro frequency upstream of the Martian bow shock. Using global MHD simulations, Wang *et al.*^[305] constructed a 3D parametric Martian

bow shock model that employs a generalized conic section function defined by seven parameters. The thermal pressure at the Martian Magnetic Pileup Boundary (MPB) plays a significant role in the compressed magnetic field^[306]. Small-scale Linear Magnetic Holes (LMHs) are ubiquitous in the Martian magnetosheath with an occurrence rate of approximately 1.5 events per hour^[307]. Gao *et al.*^[308] presented a new Spherical Harmonic (SH) model of the crustal magnetic field of Mars, finding that small-scale fields at low altitudes were underestimated by most previous models. The Chinese Mars ROVER Fluxgate Magnetometers (RoMAG) will implement the first mobile magnetic field measurements on the surface of Mars^[309].

Zhang *et al.*^[310] suggested that the plasma clouds of Mars might be the product of heating due to solar wind precipitation along the open field lines, generated by magnetic reconnection at the dayside Martian-induced magnetopause^[311]. Huang *et al.*^[312] presented the in situ detection of KSMHs in the Martian magnetosheath using Mars Atmosphere and Volatile Evolution (MAVEN) for the first time. Zou *et al.*^[313] described the scientific objectives and payloads of Tianwen-1, China's first exploration mission to Mars. The crustal magnetic fields can withstand the solar wind flows and effectively trap heavy ions below 1000 km^[314], and significantly attenuate the ion ionospheric motions and raise the flux of returning ions^[315]. Nearly 30% of the available nightside suprathermal electron spectra show clear photoelectron signatures in the Martian ionosphere^[316].

Sun *et al.*^[317] reviewed the research of Mercury's magnetosphere in the Post-MESSENGER era. Zhong *et al.*^[318] suggested that during extreme solar wind conditions multiple X-line reconnections may dominate the tail reconnection process and control the global dynamics of Mercury's magnetosphere. Jang *et al.*^[319] suggested that the near-cusp region of Mercury may trap energetic particles under particular conditions. Similar to Earth's magnetotail, there are two flapping types existent in Mercury's magnetotail, one is the kink-like flapping that can propagate as traveling waves, and the other one is the steady flapping that does not propagate^[320]. The proton density, pressure, and energy spectral index κ were higher on the dawnside plasma sheet of Mercury than on the duskside^[321]. A new Mercury magnetopause model gives a closed magnetopause for the nightside in most cases, and its flaring decreases

with the contraction of the magnetosphere. Zhong *et al.*^[322] concluded that Mercury's magnetopause is a natural plasma laboratory to study flux rope dynamics and evolution for the upcoming Bepi-Colombo mission. Spectral indices at MHD scales vary from about $-5/3$ in the near-Mercury solar wind (possibly the foreshock) to about -1.3 within the magnetosheath close to bow shock of Mercury^[323].

With 32 Hz magnetic field data of Venus Express from May 2006 to August 2012, the global spatial distributions of 1 Hz waves in the near-Venusian space were presented by Xiao *et al.*^[324]. The dayside Venusian induced magnetosphere boundary distance increases with solar activity, but decreases with increasing P_{dyn} and IMF cone angle^[325]. The statistical results of Xiao *et al.*^[326] suggested that the Venusian bow shock tends to modify the upstream spectra flatter to $1/f$ noise in the MHD regime and steeper to turbulence in the kinetic regime after the magnetic fluctuations crossing the bow shock. In the near-Venusian space, an energy cascade can be developed at the boundary between magnetosheath and wake^[327]. In terms of the spectral scaling features of Venus magnetic fluctuations, the day-side-nightside shock crossings exhibit a clear asymmetry^[328]. Gao *et al.*^[329] reported evidence of crossing the ion diffusion region of magnetic reconnection based on two cases recorded by Venus Express in the Venusian magnetotail.

Zhang *et al.*^[330] demonstrated that the solar-wind ions, reflected over the dayside lunar magnetic anomalies, have produced lunar wake magnetic and plasma asymmetries and periodical modulations. Behind the lunar terminator, the wake field reduction is also asymmetric^[331].

6 Theory and Technique

Dunlop *et al.*^[332] reviewed the range of applications and use of the curlometer technique, initially developed to analyze Cluster multi-spacecraft magnetic field data, but more recently adapted to other 2–5 spacecraft configurations. The normal field analysis method was presented by Shen *et al.*^[333] to determine the geometrical configurations of boundary surfaces in the space environment, based on multiple spacecraft measurements. Shen *et al.*^[334] presented a novel algorithm that can estimate the quadratic magnetic gradient as well as the complete

geometrical features of magnetic field lines, and another one for estimating both the linear and quadratic gradients of physical quantities^[335]. Zhu *et al.*^[336] gave a general description of the magnetometer onboard the Low Orbit Pearl Satellite.

Space plasmas are composed of charged particles that play a key role in electromagnetic dynamics. Three schemes for measuring charge densities in space are presented in^[337]. Li *et al.*^[338] reviewed some of the key results obtained from the wake technique helping us to understand how cold ionospheric outflow varies. Huang *et al.*^[339] applied the algebraic reconstruction technique and the minimization of the image total variation method to reconstruct plasmaspheric He⁺ density from simulated EUV images. Wang *et al.*^[340] demonstrated that the plasma flows at small scales are indeed linear, and thus the First-Order Taylor Expansion (FOTE) method can be applied to such flow fields. Fu *et al.*^[341] reviewed and compared the methods for finding magnetic nulls and reconstructing field topology. Tian *et al.*^[342] developed a new Grad-Shafranov solver which was applied to reconstruct a Pc5 compressional wave event. Yu *et al.*^[343] suggested the important role of the linear dispersion relation in the second-harmonic generation.

Li *et al.*^[344] developed a method which can effectively predict the geomagnetic disturbances during geomagnetic storms. The physical-based model in Zhang *et al.*^[345] is more applicable than the persistence model in prediction of GICs at low-latitude power grids during storms. Xu *et al.*^[346] used the Bagging ensemble-learning algorithm to predict the Dst index 1-6 h in advance. Using magnetic field observations from Van Allen Probe-A (VAP-A), Yang and Wang^[347] evaluated the performances of 13 widely used external magnetic field models in the Earth's outer radiation belt region in detail. The previous algorithm has been modified by Yu *et al.*^[348] to be capable of producing typical ripples in the electron diffusion coefficient maps, and could be applied to RC protons.

A lot of neural network models were developed to predict the global dynamic variation of the plasmopause location^[349], average daily flux of relativistic electrons^[350], and the electron number fluxes in the central plasma sheet^[351]. Radiation belt electron fluxes can also be simulated by an analytic model^[352] or a three-dimensional (3D) assimilation model^[353].

Guo *et al.*^[354] proposed to use the Moon as a platform to obtain a global view of Earth's magnetosphere by a lunar-based soft x-ray imager. Sun *et al.*^[355] introduced a new technique which can find the optimum match of tangent directions derived from the X-ray image and the parameterized magnetopause function. With reasonable assumptions, the large-scale cusp features can be clearly revealed by analyzing X-ray images^[356].

References

- [1] ZHAO M X, LE G M, LI Q, *et al.* Dependence of great geomagnetic storm ($\Delta SYM-H \leq -200$ nT) on associated solar wind parameters[J]. *Solar Physics*, 2021, **296**(4): 66. DOI: 10.1007/s11207-021-01816-2
- [2] LE G M, LIU G A, ZHAO M X. Dependence of major geomagnetic storm intensity ($Dst \leq -100$ nt) on associated solar wind parameters[J]. *Solar Physics*, 2020, **295**(8): 108. DOI: 10.1007/s11207-020-01675-3
- [3] XUE Z X, YUAN Z G, YU X D. Prompt emergence and disappearance of emic waves driven by the sequentially enhanced solar wind dynamic pressure[J]. *Geophysical Research Letters*, 2021, **48**(2): e2020GL091479. DOI: 10.1029/2020gl091479
- [4] PENG Q S, LI H M, TANG R X, *et al.* Variation of dayside chorus waves associated with solar wind dynamic pressure based on MMS observations[J]. *Advances in Space Research*, 2020, **65**(11): 2551-2558. DOI: 10.1016/j.asr.2020.03.006
- [5] SHANG X J, LIU S, CHEN L J, *et al.* ULF-modulation of whistler-mode waves in the inner magnetosphere during solar wind compression[J]. *Journal of Geophysical Research: Space Physics*, 2021, **126**(8): e2021JA029353. DOI: 10.1029/2021ja029353
- [6] XIANG Z, LI X L, KAPALI S, *et al.* Modeling the dynamics of radiation belt electrons with source and loss driven by the solar wind[J]. *Journal of Geophysical Research: Space Physics*, 2021, **126**(6): e2020JA028988. DOI: 10.1029/2020ja028988
- [7] MA X H, ZONG Q G, YUE C, *et al.* Energetic electron enhancement and dropout echoes induced by solar wind dynamic pressure decrease: the effect of phase space density profile[J]. *Journal of Geophysical Research: Space Physics*, 2021, **126**(3): e2020JA028863. DOI: 10.1029/2020ja028863
- [8] MA X, XIANG Z, NI B B, *et al.* On the loss mechanisms of radiation belt electron dropouts during the 12 September 2014 geomagnetic storm[J]. *Earth and Planetary Physics*, 2020, **4**(6): 598-610. DOI: 10.26464/epp2020060
- [9] SHI Q Q, SHEN X C, TIAN A M, *et al.* Magnetosphere response to solar wind dynamic pressure change: vortices, ULF waves, and aurorae[M]//ZENG Q G, ESCOUBET P, SIBECK D, *et al.* Dayside Magnetosphere Interactions. Washington: American Geophysical Union, 2020: 77-97
- [10] ZHAO J Y, SHI Q Q, TIAN A M, *et al.* Vortex generation and auroral response to a solar wind dynamic pressure increase: event analyses[J]. *Journal of Geophysical Research: Space Physics*, 2021, **126**(3): e2020JA028753. DOI: 10.1029/2020ja028753
- [11] ZOU Z Y, ZUO P B, NI B B, *et al.* Two-step dropouts of radiation belt electron phase space density induced by a magnetic cloud

- event[J]. *The Astrophysical Journal Letters*, 2020, **895**(1): L24. DOI: 10.3847/2041-8213/ab9179
- [12] LI H M, PENG Q S, TANG R X, et al. Statistical characteristics of electron pitch angle distributions inside the magnetopause based on MMS observations[J]. *Journal of Geophysical Research: Space Physics*, 2020, **125**(10): e2020JA028291. DOI: 10.1029/2020ja028291
- [13] YUE C, BORTNIK J, ZOU S S, et al. Episodic occurrence of field-aligned energetic ions on the dayside[J]. *Geophysical Research Letters*, 2020, **47**(2): e2019GL086384. DOI: 10.1029/2019gl086384
- [14] NI B B, YAN L, FU S, et al. Distinct formation and evolution characteristics of outer radiation belt electron butterfly pitch angle distributions observed by Van Allen probes[J]. *Geophysical Research Letters*, 2020, **47**(4): e2019GL086487. DOI: 10.1029/2019gl086487
- [15] XIANG Z, LI X L, TEMERIN M A, et al. On energetic electron dynamics during geomagnetic quiet times in earth's inner radiation belt due to atmospheric collisional loss and CRAND as a source[J]. *Journal of Geophysical Research: Space Physics*, 2020, **125**(2): e2019JA027678. DOI: 10.1029/2019ja027678
- [16] CHEN J J, LEI J H, WANG W B, et al. Ionospheric electrodynamic response to solar flares in September 2017[J]. *Journal of Geophysical Research: Space Physics*, 2021, **126**(11): e2021JA029745. DOI: 10.1029/2021ja029745
- [17] CHENG L B, LE G M, ZHAO M X. Sun-earth connection event of super geomagnetic storm on 2001 March 31: the importance of solar wind density[J]. *Research in Astronomy and Astrophysics*, 2020, **20**(3): 036. DOI: 10.1088/1674-4527/20/3/36
- [18] CAI Y H, WANG W B, ZHANG S R, et al. Climatology analysis of the daytime topside ionospheric diffusive O^+ flux based on incoherent scatter radar observations at millstone hill[J]. *Journal of Geophysical Research: Space Physics*, 2021, **126**(10): e2021JA029222. DOI: 10.1029/2021ja029222
- [19] ZENG C, WANG C, DUAN S P, et al. Statistical study of oxygen ions abundance and spatial distribution in the dayside magnetopause boundary layer: MMS observations[J]. *Journal of Geophysical Research: Space Physics*, 2020, **125**(7): e2019JA027323. DOI: 10.1029/2019ja027323
- [20] CHEN A, YUE C, CHEN H F, et al. Ring current decay during geomagnetic storm recovery phase: comparison between RBSP observations and theoretical modeling[J]. *Journal of Geophysical Research: Space Physics*, 2021, **126**(1): e2020JA028500. DOI: 10.1029/2020ja028500
- [21] HUANG Z, YUAN Z G, YU X D. Evolutions of equatorial ring current ions during a magnetic storm[J]. *Earth and Planetary Physics*, 2020, **4**(2): 131-137. DOI: 10.26464/epp2020019
- [22] GU X D, LI G J, PANG H, et al. Statistical analysis of very low frequency atmospheric noise caused by the global lightning using ground-based observations in China[J]. *Journal of Geophysical Research: Space Physics*, 2021, **126**(6): e2020JA029101. DOI: 10.1029/2020ja029101
- [23] GUO M Y, ZHOU Q H, XIAO F L, et al. Upward propagation of lightning-generated whistler waves into the radiation belts[J]. *Science China Technological Sciences*, 2020, **63**(2): 243-248. DOI: 10.1007/s11431-018-9486-9
- [24] LI L Y, ZHOU S P, WEI S H, et al. The day-night difference and geomagnetic activity variation of energetic electron fluxes in region of South Atlantic anomaly[J]. *Space Weather*, 2020, **18**(9): e2020SW002479. DOI: 10.1029/2020sw002479
- [25] CHEN G, LI Y X, ZHANG S D, et al. Multi-instrument observations of the atmospheric and ionospheric response to the 2013 sudden stratospheric warming over Eastern Asia region[J]. *IEEE Transactions on Geoscience and Remote Sensing*, 2020, **58**(2): 1232-1243. DOI: 10.1109/tgrs.2019.2944677
- [26] ZHANG K D, WANG H, YAMAZAKI Y, et al. Effects of subauroral polarization streams on the equatorial electrojet during the geomagnetic storm on June 1, 2013[J]. *Journal of Geophysical Research: Space Physics*, 2021, **126**(10): e2021JA029681. DOI: 10.1029/2021ja029681
- [27] ZHOU Y J, HE F, ZHANG X X, et al. Statistical characteristics of giant undulations during geomagnetic storms[J]. *Geophysical Research Letters*, 2021, **48**(13): e2021GL093098. DOI: 10.1029/2021gl093098
- [28] HE F, GUO R L, DUNN W R, et al. Plasmapause surface wave oscillates the magnetosphere and diffuse aurora[J]. *Nature Communications*, 2020, **11**(1): 1668. DOI: 10.1038/s41467-020-15506-3
- [29] WANG Yuyouting, ZHANG Xiaoxin, HE Fei, et al. A statistical analysis of the electron number density fluctuations near the plasmapause based on Van Allen Probes observations[J]. *Chinese Journal of Geophysics*, 2020, **63**(6): 2141-2148. DOI: 10.6038/cjg202000096 (王玉尤婷, 张效信, 何飞, 等. 基于 VAP 卫星的等离子体层顶电子密度波动统计分析[J]. 地球物理学报, 2020, **63**(6): 2141-2148. DOI: 10.6038/cjg202000096)
- [30] LI H M, FU T X, TANG R X, et al. Statistical study and corresponding evolution of plasmaspheric plumes under different levels of geomagnetic storms[J]. *Annales Geophysicae*, 2022, **40**(2): 167-177
- [31] WANG Y B, KISTLER L M, MOUIKIS C G, et al. Formation of the low-energy "finger" ion spectral structure near the inner edge of the plasma sheet[J]. *Geophysical Research Letters*, 2020, **47**(22): e2020GL089875. DOI: 10.1029/2020gl089875
- [32] REN G M, CAO J B, YANG J, et al. The response of plasma parameters and energy transport in the plasma sheet to interplanetary magnetic field B_z [J]. *Science China Technological Sciences*, 2021, **64**(7): 1528-1534
- [33] ZONG Q G, YUE C, FU S Y. Shock induced strong substorms and super substorms: preconditions and associated oxygen ion dynamics[J]. *Space Science Reviews*, 2021, **217**(2): 33. DOI: 10.1007/s11214-021-00806-x
- [34] DUAN S P, WANG C, LIU W W, et al. Characteristics of magnetic dipolarizations in the vicinity of the substorm onset region observed by themis[J]. *Earth and Planetary Physics*, 2021, **5**(3): 239-250. DOI: 10.26464/epp2021031
- [35] FU H B, YUE C, ZONG Q G, et al. Statistical characteristics of substorms with different intensity[J]. *Journal of Geophysical Research: Space Physics*, 2021, **126**(8): e2021JA029318. DOI: 10.1029/2021ja029318
- [36] TANG B B, LI W Y, WANG C, et al. Secondary magnetic reconnection at earth's flank magnetopause[J]. *Frontiers in Astronomy and Space Sciences*, 2021, **8**: 740560. DOI: 10.3389/fspas.2021.740560
- [37] YU C, ZHANG X X, WANG W B, et al. Longitudinal dependence of ionospheric Poynting flux in the northern hemisphere during quiet times[J]. *Journal of Geophysical Research: Space Physics*, 2021, **126**(10): e2021JA029717

- [38] ZHOU X Z, ZHANG X, LI J H, *et al.* On the species dependence of ion escapes across the magnetopause[J]. *Geophysical Research Letters*, 2021, **48**(8): e2021GL093115. DOI: 10.1029/2021gl093115
- [39] JANG E J, YUE C, ZONG Q G, *et al.* The effect of non-storm time substorms on the ring current dynamics[J]. *Earth and Planetary Physics*, 2021, **5**(3): 251-258. DOI: 10.26464/epp2021032
- [40] YI J, FU S, NI B B, *et al.* Global distribution of reversed energy spectra of ring current protons based on van Allen probes observations[J]. *Geophysical Research Letters*, 2021, **48**(4): e2020GL091559. DOI: 10.1029/2020gl091559
- [41] WANG L H, ZONG Q G, SHI Q Q, *et al.* Solar energetic electrons entering the earth's cusp/lobe[J]. *The Astrophysical Journal*, 2021, **910**(1): 12. DOI: 10.3847/1538-4357/abdb2b
- [42] GUO J, LU S, LU Q M, *et al.* Three-dimensional global hybrid simulations of high latitude magnetopause reconnection and flux ropes during the northward IMF[J]. *Geophysical Research Letters*, 2021, **48**(21): e2021GL095003. DOI: 10.1029/2021gl095003
- [43] XIAO Chao, LIU Wenlong, ZHANG Dianjun, *et al.* Formation of the high-density cusp[J]. *Chinese Journal of Geophysics*, 2020, **63**(9): 3231-3239 (肖超, 刘文龙, 张典钧, 等. 高密度极尖区的形成原因[J]. *地球物理学报*, 2020, **63**(9): 3231-3239)
- [44] XIAO C, LIU W L, ZHANG D J, *et al.* A normalized statistical study of Earth's cusp region based on nine years of Cluster measurements[J]. *Earth and Planetary Physics*, 2020, **4**(3): 266-273. DOI: 10.26464/epp2020031
- [45] XUE Z X, YUAN Z G, YU X D, *et al.* Formation of the mass density peak at the magnetospheric equator triggered by EMIC waves[J]. *Earth and Planetary Physics*, 2021, **5**(1): 32-41. DOI: 10.26464/epp2021008
- [46] YAO J S, ZHAO Y K, YE D F, *et al.* A simulation study of protons heated by left/right-handed Alfvén waves generated by electromagnetic proton-proton instability[J]. *Plasma Science and Technology*, 2021, **23**(12): 125301. DOI: 10.1088/2058-6272/ac11b0
- [47] QIN P F, GE Y S, DU A M, *et al.* Coupling between the magnetospheric dipolarization front and the earth's ionosphere by ultralow-frequency waves[J]. *The Astrophysical Journal Letters*, 2020, **895**(1): L13. DOI: 10.3847/2041-8213/ab8e48
- [48] CHEN Y Q, WU M, ZHANG T L, *et al.* Statistical characteristics of field-aligned currents in the plasma sheet boundary layer[J]. *Journal of Geophysical Research: Space Physics*, 2021, **126**(2): e2020JA028319. DOI: 10.1029/2020ja028319
- [49] ZHU Guangzhen, MA Yudian. Enhancement of field-aligned current during the azimuthal flow in the near-earth magnetotail[J]. *Chinese Journal of Space Science*, 2020, **40**(4): 493-504 (朱光振, 马玉端. 近地磁尾方位角流期间的场向电流增强[J]. *空间科学学报*, 2020, **40**(4): 493-504)
- [50] NOWADA M, ZONG Q G, HUBERT B, *et al.* North-south asymmetric nightside distorted transpolar arcs within a framework of deformed magnetosphere-ionosphere coupling: IMF- B_y dependence, ionospheric currents, and magnetotail reconnection[J]. *Journal of Geophysical Research: Space Physics*, 2020, **125**(10): 2020JA027991. DOI: 10.1029/2020ja027991
- [51] MA Y Z, ZHANG Q H, JAYACHANDRAN P T, *et al.* Statistical study of the relationship between ion upflow and field-aligned current in the topside ionosphere for both hemispheres during geomagnetic disturbed and quiet time[J]. *Journal of Geophysical Research: Space Physics*, 2020, **125**(9): e2019JA027538. DOI: 10.1029/2019ja027538
- [52] YUAN H Z, ZHANG H, LU J Y, *et al.* Flow vortex-associated downward field-aligned current retreating in the near-earth plasma sheet[J]. *Earth and Space Science*, 2020, **7**(2): e2019EA000916. DOI: 10.1029/2019ea000916
- [53] YAO S T, SHI Q Q, GUO R L, *et al.* Kinetic-scale flux rope in the magnetosheath boundary layer[J]. *The Astrophysical Journal*, 2020, **897**(2): 137. DOI: 10.3847/1538-4357/ab9620
- [54] PITKÄNEN T, KULLEN A, CAI L, *et al.* Asymmetry in the earth's magnetotail neutral sheet rotation due to IMF B_y sign?[J]. *Geoscience Letters*, 2021, **8**(1): 3. DOI: 10.1186/s40562-020-00171-7
- [55] WANG G Q, ZHANG T L, WU M Y, *et al.* Field-aligned currents originating from the chaotic motion of electrons in the tilted current sheet: MMS observations[J]. *Geophysical Research Letters*, 2021, **48**(9): e2020GL088841. DOI: 10.1029/2020gl088841
- [56] PARK J S, SHI Q Q, NOWADA M, *et al.* Transpolar arcs during a prolonged radial interplanetary magnetic field interval[J]. *Journal of Geophysical Research: Space Physics*, 2021, **126**(6): e2021JA029197. DOI: 10.1029/2021ja029197
- [57] TANG T, YANG J, SHI Q Q, *et al.* The semiannual variation of transpolar arc incidence and its relationship to the Russell-McPherron effect[J]. *Earth and Planetary Physics*, 2020, **4**(6): 619-626. DOI: 10.26464/epp2020066
- [58] ZHANG Q H, ZHANG Y L, WANG C, *et al.* Multiple transpolar auroral arcs reveal insight about coupling processes in the earth's magnetotail[J]. *Proceedings of the National Academy of Sciences of the United States of America*, 2020, **117**(28): 16193-16198. DOI: 10.1073/pnas.2000614117
- [59] MA Y Z, ZHANG Q H, LYONS L R, *et al.* Is westward travelling surge driven by the polar cap flow channels?[J]. *Journal of Geophysical Research: Space Physics*, 2021, **126**(8): e2020JA028498
- [60] LI K, FÖRSTER M, RONG Z J, *et al.* The polar wind modulated by the spatial inhomogeneity of the strength of the earth's magnetic field[J]. *Journal of Geophysical Research: Space Physics*, 2020, **125**(4): e2020JA027802. DOI: 10.1029/2020ja027802
- [61] ZHANG D, ZHANG Q H, MA Y Z, *et al.* Solar and geomagnetic activity impact on occurrence and spatial size of cold and hot polar cap patches[J]. *Geophysical Research Letters*, 2021, **48**(18): e2021GL094526. DOI: 10.1029/2021gl094526
- [62] ZHANG Q H, XING Z Y, WANG Y, *et al.* Formation and evolution of polar cap ionospheric patches and their associated upflows and scintillations: a review[M]//ZONG Q G, ESCOUBET P, SI-BECK D, *et al.* Dayside Magnetosphere Interactions. Washington: American Geophysical Union, 2020: 285-302.
- [63] ZHANG S, LIU S, LI W T, *et al.* A concise empirical formula for the field-aligned distribution of auroral kilometric radiation based on arase satellite and Van Allen probes[J]. *Geophysical Research Letters*, 2021, **48**(8): e2021GL092805. DOI: 10.1029/2021gl092805
- [64] ZHANG S, SHANG X J, HE Y H, *et al.* Dominant roles of high harmonics on interactions between AKR and radiation belt relativistic electrons[J]. *Geophysical Research Letters*, 2020, **47**(16): e2020GL088421. DOI: 10.1029/2020gl088421
- [65] FUJIMOTO K, SYDORA R D. Electromagnetic turbulence in the electron current layer to drive magnetic reconnection[J]. *The Astrophysical Journal Letters*, 2021, **909**(1): L15. DOI: 10.3847/2041-8213/abe877
- [66] FUJIMOTO K, CAO J B. Non-adiabatic electron heating in the magnetic islands during magnetic reconnection[J]. *Geophysical Research Letters*, 2021, **48**(19): e2021GL094431. DOI: 10.1029/2021gl094431
- [67] HUANG S Y, XIONG Q Y, YUAN Z G, *et al.* Multi-spacecraft

- measurement of anisotropic spatial correlation functions at kinetic range in the magnetosheath turbulence[J]. *Journal of Geophysical Research: Space Physics*, 2021, **126**(5): e2020JA028780. DOI: 10.1029/2020ja028780
- [68] ZHOU G, HE H Q. The solar-cycle variations of the anisotropy of Taylor scale and correlation scale in the solar wind turbulence[J]. *The Astrophysical Journal Letters*, 2021, **911**(1): L2. DOI: 10.3847/2041-8213/abef00
- [69] ZHOU G, HE H Q, WAN W. Effects of solar activity on Taylor scale and correlation scale in solar wind magnetic fluctuations[J]. *The Astrophysical Journal Letters*, 2020, **899**(2): L32. DOI: 10.3847/2041-8213/abaaa9
- [70] YUE C, LIU Y, ZHOU X Z, et al. MLT-dependence of sustained spectral gaps of proton and oxygen in the inner magnetosphere[J]. *Journal of Geophysical Research: Space Physics*, 2021, **126**(12): e2021JA029935. DOI: 10.1029/2021ja029935
- [71] YUE C, ZHOU X Z, BORTNIK J, et al. Sustained oxygen spectral gaps and their dynamic evolution in the inner magnetosphere[J]. *Journal of Geophysical Research: Space Physics*, 2021, **126**(4): e2020JA029092. DOI: 10.1029/2020ja029092
- [72] ZHAO X X, HAO Y X, ZONG Q G, et al. Origin of electron boomerang stripes: Localized ULF wave-particle interactions[J]. *Geophysical Research Letters*, 2020, **47**(17): e2020GL087960. DOI: 10.1029/2020gl087960
- [73] ZHOU X Z, REN J, YANG F, et al. On the formation of wedge-like ion spectral structures in the nightside inner magnetosphere[J]. *Journal of Geophysical Research: Space Physics*, 2020, **125**(12): e2020JA028420. DOI: 10.1029/2020ja028420
- [74] REN J, ZONG Q G, YUE C, et al. Simultaneously formed wedge-like structures of different ion species deep in the inner magnetosphere[J]. *Journal of Geophysical Research: Space Physics*, 2020, **125**(12): e2020JA028192
- [75] LI S Y, LUO H, KRONBERG E A, et al. Stationary "nose-like" ion spectral structures in the inner magnetosphere: observations by van Allen probes and simulations[J]. *Journal of Atmospheric and Solar-Terrestrial Physics*, 2020, **211**: 105390. DOI: 10.1016/j.jastp.2020.105390
- [76] REN J, ZHOU X Z, ZONG Q G, et al. The link between wedge-like and nose-like ion spectral structures in the inner magnetosphere[J]. *Geophysical Research Letters*, 2021, **48**(13): e2021GL093930. DOI: 10.1029/2021gl093930
- [77] LIU Yangxizi, XIANG Zheng, GUO Jianguang, et al. Scattering effect of very low frequency transmitter signals on energetic electrons in earth's inner belt and slot region[J]. *Acta Physica Sinica*, 2021, **70**(14): 149401. DOI: 10.7498/aps.70.20202029 (刘阳希子, 项正, 郭建广, 等. 甚低频台站信号对地球内辐射带和槽区能量电子的散射效应分析[J]. *物理学报*, 2021, **70**(14): 149401)
- [78] XIANG Zheng, LIN Xianhao, CHEN Wei, et al. Global morphology of NWC and NAA very-low-frequency transmitter signals in the inner magnetosphere: a survey using van Allen probes EMFISIS measurements[J]. *Chinese Journal of Geophysics*, 2021, **64**(11): 3860-3869 (项正, 林显浩, 陈薇, 等. 基于范阿伦双星 EMFISIS 观测数据的 NWC 和 NAA 人工甚低频台站信号的内磁层全球统计分布[J]. *地球物理学报*, 2021, **64**(11): 3860-3869)
- [79] HUA M, LI W, NI B B, et al. Very-low-frequency transmitters bifurcate energetic electron belt in near-earth space[J]. *Nature Communications*, 2020, **11**(1): 4847. DOI: 10.1038/s41467-020-18545-y
- [80] HUA M, NI B B, LI W, et al. Statistical distribution of bifurcation of Earth's inner energetic electron belt at tens of keV[J]. *Geophysical Research Letters*, 2021, **48**(3): e2020GL091242. DOI: 10.1029/2020gl091242
- [81] GAO Z L, SHANG X J, ZUO P B, et al. Lag-correlated rising tones of electron cyclotron harmonic and whistler-mode upper-band chorus waves[J]. *Physics of Plasmas*, 2020, **27**(6): 062903. DOI: 10.1063/5.0008812
- [82] GAO Z L, ZUO P B, FENG X S, et al. Evidence of nonlinear interactions between magnetospheric electron cyclotron harmonic waves[J]. *Geophysical Research Letters*, 2020, **47**(16): e2020GL088452. DOI: 10.1029/2020gl088452
- [83] WU Y F, TAO X, LIU X, et al. Particle-in-cell simulation of electron cyclotron harmonic waves driven by a loss cone distribution[J]. *Geophysical Research Letters*, 2020, **47**(9): e2020GL087649. DOI: 10.1029/2020gl087649
- [84] LOU Y Q, CAO X, NI B B, et al. Diffuse auroral electron scattering by electrostatic electron cyclotron harmonic waves in the day-side magnetosphere[J]. *Geophysical Research Letters*, 2021, **48**(5): e2020GL092208. DOI: 10.1029/2020gl092208
- [85] TENG S, WU Y, GUO R, et al. Observation of periodic rising and falling tone ECH waves at saturn[J]. *Geophysical Research Letters*, 2021, **48**(15): e2021GL094559. DOI: 10.1029/2021gl094559
- [86] CHEN R, GAO X L, LU Q M, et al. In situ observations of whistler-mode chorus waves guided by density ducts[J]. *Journal of Geophysical Research: Space Physics*, 2021, **126**(4): e2020JA028814. DOI: 10.1029/2020ja028814
- [87] KE Y G, CHEN L J, GAO X L, et al. Whistler-mode waves trapped by density irregularities in the earth's magnetosphere[J]. *Geophysical Research Letters*, 2021, **48**(7): e2020GL092305. DOI: 10.1029/2020gl092305
- [88] ZHANG H, ZHONG Z H, TANG R X, et al. Modulation of whistler mode waves by ultra-low frequency wave in a macroscale magnetic hole: MMS observations[J]. *Geophysical Research Letters*, 2021, **48**(22): e2021GL096056. DOI: 10.1029/2021gl096056
- [89] ZHAO D, FU S Y, PARKS G K, et al. Modulation of whistler mode waves by ion-scale waves observed in the distant magnetotail[J]. *Journal of Geophysical Research: Space Physics*, 2020, **125**(2): e2019JA027278. DOI: 10.1029/2019ja027278
- [90] CHEN R, GAO X L, LU Q M, et al. Observational evidence for whistler mode waves guided/ducted by the inner and outer edges of the plasmopause[J]. *Geophysical Research Letters*, 2021, **48**(6): e2021GL092652. DOI: 10.1029/2021gl092652
- [91] LU Q M, CHEN L J, WANG X Y, et al. Repetitive emissions of rising-tone chorus waves in the inner magnetosphere[J]. *Geophysical Research Letters*, 2021, **48**(15): e2021GL094979. DOI: 10.1029/2021gl094979
- [92] WU Y F, TAO X, ZONCA F, et al. Controlling the chirping of chorus waves via magnetic field inhomogeneity[J]. *Geophysical Research Letters*, 2020, **47**(10): e2020GL087791. DOI: 10.1029/2020gl087791
- [93] KE Y G, LU Q M, GAO X L, et al. Particle-in-cell simulations of characteristics of rising-tone chorus waves in the inner magnetosphere[J]. *Journal of Geophysical Research: Space Physics*, 2020, **125**(7): e2020JA027961. DOI: 10.1029/2020ja027961
- [94] CHEN H Y, GAO X L, LU Q M, et al. Gap formation around $0.5 \Omega_e$ of whistler-mode waves excited by electron temperature anisotropy[J]. *Journal of Geophysical Research: Space Physics*, 2021, **126**(2): e2020JA028631

- [95] CHEN H Y, SAUER K, LU Q M, *et al.* Two-band whistler-mode waves excited by an electron bi-Maxwellian distribution plus parallel beams[J]. *AIP Advances*, 2020, **10**(12): 125010. DOI: 10.1063/5.0026220
- [96] TAO X, ZONCA F, CHEN L, *et al.* Theoretical and numerical studies of chorus waves: a review[J]. *Science China Earth Sciences*, 2020, **63**(1): 78-92. DOI: 10.1007/s11430-019-9384-6
- [97] XIE Y, TENG S C, WU Y F, *et al.* A statistical analysis of duration and frequency chirping rate of falling tone chorus[J]. *Geophysical Research Letters*, 2021, **48**(19): e2021GL095349. DOI: 10.1029/2021gl095349
- [98] LIU S, GAO Z L, XIAO F L, *et al.* Observation of unusual chorus elements by van Allen probes[J]. *Journal of Geophysical Research: Space Physics*, 2021, **126**(7): e2021JA029258. DOI: 10.1029/2021ja029258
- [99] CHENG X W, GU X D, NI B B, *et al.* Hemispheric distribution of lower-band chorus waves observed by van Allen probes[J]. *Chinese Journal of Space Science*, 2020, **40**(2): 186-196
- [100] TAO X, ZONCA F, CHEN L. A "trap-release-amplify" model of chorus waves[J]. *Journal of Geophysical Research: Space Physics*, 2021, **126**(9): e2021JA029585. DOI: 10.1029/2021ja029585
- [101] LIU Z Y, ZONG Q G, BLAKE J B. On phase space density and its radial gradient of outer radiation belt seed electrons: MMS/FEPS observations[J]. *Journal of Geophysical Research: Space Physics*, 2020, **125**(4): e2019JA027711. DOI: 10.1029/2019ja027711
- [102] CHEN X R, ZONG Q G, ZOU H, *et al.* Distribution of energetic electrons in the near earth space: new observations from the BeiDa imaging electron spectrometer and the van Allen probes[J]. *Planetary and Space Science*, 2020, **186**: 104919. DOI: 10.1016/j.pss.2020.104919
- [103] LIU Z Y, WANG B, ZONG Q G, *et al.* Thermal electron behavior in obliquely propagating whistler waves: MMS observations in the solar wind[J]. *Geophysical Research Letters*, 2021, **48**(14): e2021GL094099. DOI: 10.1029/2021gl094099
- [104] CAI B, WU Y F, TAO X. Effects of nonlinear resonance broadening on interactions between electrons and whistler mode waves[J]. *Geophysical Research Letters*, 2020, **47**(11): e2020GL087991. DOI: 10.1029/2020gl087991
- [105] WU H, CHEN T, KALEGAEV V V, *et al.* Long - term dropout of relativistic electrons in the outer radiation belt during two sequential geomagnetic storms[J]. *Journal of Geophysical Research: Space Physics*, 2020, **125**(10): e2020JA028098
- [106] SHI X F, REN J, ZONG Q G. The dynamics of the inner boundary of the outer radiation belt during geomagnetic storms[J]. *Journal of Geophysical Research: Space Physics*, 2020, **125**(5): e2019JA027309. DOI: 10.1029/2019ja027309
- [107] HE J B, JIN Y Y, XIAO F L, *et al.* The influence of various frequency chorus waves on electron dynamics in radiation belts[J]. *Science China Technological Sciences*, 2021, **64**(4): 890-897. DOI: 10.1007/s11431-020-1750-6
- [108] LIU S, XIE Y Q, ZHANG S, *et al.* Unusual loss of van Allen belt relativistic electrons by extremely low-frequency chorus[J]. *Geophysical Research Letters*, 2020, **47**(18): e2020GL089994. DOI: 10.1029/2020gl089994
- [109] KONG Z Y, GAO X L, CHEN H Y, *et al.* The correlation between whistler mode waves and electron beam-like distribution: test particle simulations and THEMIS observations[J]. *Journal of Geophysical Research: Space Physics*, 2021, **126**(11): e2021JA029834. DOI: 10.1029/2021ja029834
- [110] GUO D Y, XIANG Z, NI B B, *et al.* Bounce resonance scattering of radiation belt energetic electrons by extremely low-frequency chorus waves[J]. *Geophysical Research Letters*, 2021, **48**(22): e2021GL095714. DOI: 10.1029/2021gl095714
- [111] MA X, TIAN A M, SHI Q Q, *et al.* Electron pitch angle distributions in compressional Pc5 waves by THEMIS-A observations[J]. *Geophysical Research Letters*, 2021, **48**(22): e2021GL095730. DOI: 10.1029/2021gl095730
- [112] CHEN X R, ZONG Q G, ZOU H, *et al.* Beida imaging electron spectrometer observation of multi-period electron flux modulation caused by localized ultra-low-frequency waves[J]. *Annales Geophysicae*, 2020, **38**(4): 801-813. DOI: 10.5194/angeo-38-801-2020
- [113] HE Z G, YU J, LI K, *et al.* A comparative study on the distributions of incoherent and coherent plasmaspheric hiss[J]. *Geophysical Research Letters*, 2021, **48**(7): e2021GL092902. DOI: 10.1029/2021gl092902
- [114] LIU N G, SU Z P, GAO Z L, *et al.* Comprehensive observations of substorm-enhanced plasmaspheric hiss generation, propagation, and dissipation[J]. *Geophysical Research Letters*, 2020, **47**(2): e2019GL086040. DOI: 10.1029/2019gl086040
- [115] WANG J L, LI L Y, YU J. Statistical relationship between exohiss waves and plasmaspheric hiss[J]. *Geophysical Research Letters*, 2020, **47**(5): e2020GL087023. DOI: 10.1029/2020gl087023
- [116] YU J, WANG J, LI L Y, *et al.* Electron diffusion by coexisting plasmaspheric hiss and chorus waves: multisatellite observations and simulations[J]. *Geophysical Research Letters*, 2020, **47**(15): e2020GL088753. DOI: 10.1029/2020gl088753
- [117] ZHANG S, RAE I J, WATT C E J, *et al.* Determining the global scale size of chorus waves in the magnetosphere[J]. *Journal of Geophysical Research: Space Physics*, 2021, **126**(11): e2021JA029569. DOI: 10.1029/2021ja029569
- [118] GU X D, XIA S J, FU S, *et al.* Dynamic responses of radiation belt electron fluxes to magnetic storms and their correlations with magnetospheric plasma wave activities[J]. *The Astrophysical Journal*, 2020, **891**(2): 127. DOI: 10.3847/1538-4357/ab71fc
- [119] FU H B, YUE C, MA Q L, *et al.* Frequency-dependent responses of plasmaspheric hiss to the impact of an interplanetary shock[J]. *Geophysical Research Letters*, 2021, **48**(20): e2021GL094810. DOI: 10.1029/2021gl094810
- [120] LI H M, LI W, MA Q L, *et al.* Attenuation of plasmaspheric hiss associated with the enhanced magnetospheric electric field[J]. *Annales Geophysicae*, 2021, **39**(3): 461-470. DOI: 10.5194/angeo-39-461-2021
- [121] HAO Y X, ZONG Q G, ZHOU X Z, *et al.* A short-lived three-belt structure for sub-MeV electrons in the van Allen belts: time scale and energy dependence[J]. *Journal of Geophysical Research: Space Physics*, 2020, **125**(9): e2020JA028031. DOI: 10.1029/2020ja028031
- [122] HE Z G, YAN Q, ZHANG X P, *et al.* Precipitation loss of radiation belt electrons by two-band plasmaspheric hiss waves[J]. *Journal of Geophysical Research: Space Physics*, 2020, **125**(10): e2020JA028157. DOI: 10.1029/2020ja028157
- [123] HE Z G, YU J, CHEN L J, *et al.* Statistical study on locally generated high-frequency plasmaspheric hiss and its effect on suprathermal electrons: van Allen probes observation and quasi-linear simulation[J]. *Journal of Geophysical Research: Space Physics*, 2020, **125**(10): e2020JA028526. DOI: 10.1029/2020ja028526
- [124] LI L Y, YU J, CAO J B, *et al.* Competitive influences of different plasma waves on the pitch angle distribution of energetic electrons inside and outside plasmasphere[J]. *Geophysical Research Letters*,

- 2022, **49**(1): e2021GL096062. DOI: 10.1029/2021gl096062
- [125] LI L Y, WANG Z Y, YU J, et al. Complementary and catalytic roles of man-made VLF waves and natural plasma waves in the loss of radiation belt electrons[J]. *Journal of Geophysical Research: Space Physics*, 2021, **126**(10): e2020JA028879. DOI: 10.1029/2020ja028879
- [126] XIANG Z, LI X L, NI B B, et al. Dynamics of energetic electrons in the slot region during geomagnetically quiet times: losses due to wave-particle interactions versus a source from cosmic ray albedo neutron decay (CRAND)[J]. *Journal of Geophysical Research: Space Physics*, 2020, **125**(9): e2020JA028042. DOI: 10.1029/2020ja028042
- [127] MEI Y, GE Y S, DU A M, et al. Energy-dependent boundaries of earth's radiation belt electron slot region[J]. *The Astrophysical Journal*, 2021, **922**(2): 246. DOI: 10.3847/1538-4357/ac25ec
- [128] ZHU Q, CAO X, GU X D, et al. Empirical loss timescales of slot region electrons due to plasmaspheric hiss based on van Allen probes observations[J]. *Journal of Geophysical Research: Space Physics*, 2021, **126**(4): e2020JA029057. DOI: 10.1029/2020ja029057
- [129] CAO X, NI B B, SUMMERS D, et al. Hot plasma effects on the pitch-angle scattering rates of radiation belt electrons due to plasmaspheric hiss[J]. *The Astrophysical Journal*, 2020, **896**(2): 118. DOI: 10.3847/1538-4357/ab9107
- [130] MA X, CAO X, NI B B, et al. Realistic dispersion of plasmaspheric hiss in the inner magnetosphere and its effect on wave-induced electron scattering rates[J]. *The Astrophysical Journal*, 2021, **916**(1): 14. DOI: 10.3847/1538-4357/abf4d6
- [131] WANG Z S, SU Z P, LIU N G, et al. Suprathermal electron evolution under the competition between plasmaspheric plume hiss wave heating and collisional cooling[J]. *Geophysical Research Letters*, 2020, **47**(19): e2020GL089649. DOI: 10.1029/2020gl089649
- [132] FU S Y, YI J, NI B B, et al. Combined scattering of radiation belt electrons by low-frequency hiss: cyclotron, Landau, and bounce resonances[J]. *Geophysical Research Letters*, 2020, **47**(5): e2020GL086963. DOI: 10.1029/2020gl086963
- [133] LI Y X, YUE C, HAO Y X, et al. The characteristics of three-belt structure of sub-MeV electrons in the radiation belts[J]. *Journal of Geophysical Research: Space Physics*, 2021, **126**(7): e2021JA029385. DOI: 10.1029/2021ja029385
- [134] LI L F, TU W C, DAI L, et al. Quantifying event-specific radial diffusion coefficients of radiation belt electrons with the PPMLR-MHD simulation[J]. *Journal of Geophysical Research: Space Physics*, 2020, **125**(5): e2019JA027634. DOI: 10.1029/2019ja027634
- [135] ZHANG D J, LIU W L, LI X L, et al. Relation between shock-related impulse and subsequent ULF wave in the earth's magnetosphere[J]. *Geophysical Research Letters*, 2020, **47**(23): e2020GL090027. DOI: 10.1029/2020gl090027
- [136] LI L, ZHOU X Z, ZONG Q G, et al. Origin of frequency-doubling and shoulder-like magnetic pulsations in ULF waves[J]. *Geophysical Research Letters*, 2021, **48**(23): e2021GL096532. DOI: 10.1029/2021gl096532
- [137] ZHANG Y C, DAI L, RONG Z J, et al. Observation of the large-amplitude and fast-damped plasma sheet flapping triggered by reconnection-induced ballooning instability[J]. *Journal of Geophysical Research: Space Physics*, 2020, **125**(9): e2020JA028218. DOI: 10.1029/2020ja028218
- [138] LI L, ZHOU X Z, OMURA Y, et al. Drift resonance between particles and compressional toroidal ULF waves in dipole magnetic field[J]. *Journal of Geophysical Research: Space Physics*, 2021, **126**(10): e2020JA028842. DOI: 10.1029/2020ja028842
- [139] HAO Y X, ZHAO X X, ZONG Q G, et al. Simultaneous observations of localized and global drift resonance[J]. *Geophysical Research Letters*, 2020, **47**(17): e2020GL088019. DOI: 10.1029/2020gl088019
- [140] LI L, OMURA Y, ZHOU X Z, et al. Roles of magnetospheric convection on nonlinear drift resonance between electrons and ULF waves[J]. *Journal of Geophysical Research: Space Physics*, 2020, **125**(6): e2020JA027787. DOI: 10.1029/2020ja027787
- [141] ZHAO X X, HAO Y X, ZONG Q G, et al. Origin of electron boomerang stripes: statistical study[J]. *Geophysical Research Letters*, 2021, **48**(11): e2021GL093377. DOI: 10.1029/2021gl093377
- [142] LIU Z Y, ZONG Q G, ZHOU X Z, et al. Pitch angle structures of ring current ions induced by evolving poloidal ultra-low frequency waves[J]. *Geophysical Research Letters*, 2020, **47**(4): e2020GL087203. DOI: 10.1029/2020gl087203
- [143] LI X Y, LIU Z Y, ZONG Q G, et al. Pitch angle phase shift in ring current ions interacting with ultra-low-frequency waves: van Allen probes observations[J]. *Journal of Geophysical Research: Space Physics*, 2021, **126**(4): e2020JA029025. DOI: 10.1029/2020ja029025
- [144] CHEN H Y, GAO X L, LU Q M, et al. Statistical evidence for EMIC wave excitation driven by substorm injection and enhanced solar wind pressure in the earth's magnetosphere: two different EMIC wave sources[J]. *Geophysical Research Letters*, 2020, **47**(21): e2020GL090275. DOI: 10.1029/2020gl090275
- [145] LIU N G, SU Z P, GAO Z L, et al. Can solar wind decompressive discontinuities suppress magnetospheric electromagnetic ion cyclotron waves associated with fresh proton injections?[J]. *Geophysical Research Letters*, 2020, **47**(17): e2020GL090296
- [146] XIONG Y, XIE L, FU S Y, et al. Non-storm erosion of MeV electron outer radiation belt down to $L^* < 4.0$ associated with successive enhancements of solar wind density[J]. *Earth and Planetary Physics*, 2021, **5**(6): 581-591
- [147] GUAN C Y, SHANG X J, XIE Y Q, et al. Generation of simultaneous H^+ and He^+ band EMIC waves in the nightside radiation belt[J]. *Science China Technological Sciences*, 2020, **63**(11): 2369-2374. DOI: 10.1007/s11431-019-1545-6
- [148] ZHU M H, YU Y Q, JORDANOVA V K. Simulating the effects of warm O^+ ions on the growth of electromagnetic ion cyclotron (EMIC) waves[J]. *Journal of Atmospheric and Solar-Terrestrial Physics*, 2021, **224**: 105737. DOI: 10.1016/j.jastp.2021.105737
- [149] YAO J S, ZHAO Y K, LI Y, et al. A new excitation mechanism of He^+ band electromagnetic ion cyclotron wave: hybrid simulation study[J]. *Physics of Plasmas*, 2021, **28**(1): 012903. DOI: 10.1063/5.0030265
- [150] YU X D, YUAN Z G, OUYANG Z H. First observations of O^{2+} band EMIC waves in the terrestrial magnetosphere[J]. *Geophysical Research Letters*, 2021, **48**(19): e2021GL094681
- [151] WANG G, GAO Z L, WU M Y, et al. Trapping and amplification of unguided mode EMIC waves in the radiation belt[J]. *Journal of Geophysical Research: Space Physics*, 2021, **126**(9): e2021JA029322. DOI: 10.1029/2021ja029322
- [152] CAO X, NI B B, SUMMERS D, et al. Effects of superthermal plasmas on the linear growth of multiband EMIC waves[J]. *The Astrophysical Journal*, 2020, **899**(1): 43. DOI: 10.3847/1538-4357/ab9ec4
- [153] YU J, LI L Y, CUI J, et al. Nonlinear interactions between relativ-

- istic electrons and EMIC waves in magnetospheric warm plasma environments[J]. *Journal of Geophysical Research: Space Physics*, 2020, **125**(12): e2020JA028089. DOI: 10.1029/2020ja028089
- [154] LOU Y Q, CAO X, NI B B, *et al.* Parametric dependence of polarization reversal effects on the particle pitch angle scattering by EMIC waves[J]. *Journal of Geophysical Research: Space Physics*, 2021, **126**(12): e2021JA029966. DOI: 10.1029/2021ja029966
- [155] CAO X, NI B B, SUMMERS D, *et al.* Effects of polarization reversal on the pitch angle scattering of radiation belt electrons and ring current protons by EMIC waves[J]. *Geophysical Research Letters*, 2020, **47**(17): e2020GL089718. DOI: 10.1029/2020gl089718
- [156] WANG Jie, YUAN Zhigang, YU Xiongdong, *et al.* Precipitation of ring current protons caused by wave-particle interactions with satellite conjugated observation[J]. *Chinese Journal of Geophysics*, 2020, **63**(6): 2131-2140. DOI: 10.6038/cjg2020N0313 (王杰, 袁志刚, 余雄东, 等. 波粒相互作用导致环电流质子沉降的卫星共轭观测[J]. *地球物理学报*, 2020, **63**(6): 2131-2140. DOI: 10.6038/cjg2020N0313)
- [157] SHREEDEVI P R, YU Y Q, NI B B, *et al.* Simulating the ion precipitation from the inner magnetosphere by H-band and He-band electromagnetic ion cyclotron waves[J]. *Journal of Geophysical Research: Space Physics*, 2021, **126**(3): e2020JA028553. DOI: 10.1029/2020ja028553
- [158] ZHU M H, YU Y Q, TIAN X B, *et al.* On the ion precipitation due to field line curvature (FLC) and EMIC wave scattering and their subsequent impact on ionospheric electrodynamics[J]. *Journal of Geophysical Research: Space Physics*, 2021, **126**(3): e2020JA028812. DOI: 10.1029/2020ja028812
- [159] YU Y Q, TIAN X B, JORDANOVA V K. The effects of field line curvature (FLC) scattering on ring current dynamics and isotropic boundary[J]. *Journal of Geophysical Research: Space Physics*, 2020, **125**(8): e2020JA027830. DOI: 10.1029/2020ja027830
- [160] ABID A A, LU Q M, GAO X L, *et al.* Energization of cold ions by electromagnetic ion cyclotron waves: magnetospheric multiscale (MMS) observations[J]. *Physics of Plasmas*, 2021, **28**(7): 072901. DOI: 10.1063/5.0046764
- [161] YUE C, MA Q L, JUN C W, *et al.* The modulation of plasma and waves by background electron density irregularities in the inner magnetosphere[J]. *Geophysical Research Letters*, 2020, **47**(15): e2020GL088855. DOI: 10.1029/2020gl088855
- [162] TENG S, LIU N, MA Q, *et al.* Direct observational evidence of the simultaneous excitation of electromagnetic ion cyclotron waves and magnetosonic waves by an anisotropic proton ring distribution[J]. *Geophysical Research Letters*, 2021, **48**(8): e2020GL091850. DOI: 10.1029/2020gl091850
- [163] HUANG Z, YUAN Z G, YU X D, *et al.* Simultaneous generation of EMIC and MS waves during the magnetic dip in the inner magnetosphere[J]. *Geophysical Research Letters*, 2021, **48**(18): e2021GL094842. DOI: 10.1029/2021gl094842
- [164] YAN L, CAO X, HUA M, *et al.* Statistics of magnetosonic waves in the slot region observed by van Allen probes[J]. *Geophysical Research Letters*, 2021, **48**(14): e2021GL094015. DOI: 10.1029/2021gl094015
- [165] YAO F, YUAN Z G, YU X D, *et al.* Analytical fast magnetosonic wave model based on observations of van Allen probe[J]. *Journal of Geophysical Research: Space Physics*, 2020, **125**(10): e2020JA028527. DOI: 10.1029/2020ja028527
- [166] OUYANG Z H, YUAN Z G, YU X D, *et al.* Narrowband magnetosonic waves near the lower hybrid resonance frequency in the inner magnetosphere: wave properties and excitation conditions[J]. *Journal of Geophysical Research: Space Physics*, 2021, **126**(1): 2020JA028158. DOI: 10.1029/2020ja028158
- [167] WANG G, WU M Y, WANG G Q, *et al.* Reflection of low-frequency fast magnetosonic waves at the local two-ion cutoff frequency: observation in the plasmasphere[J]. *Annales Geophysicae*, 2021, **39**(4): 613-625. DOI: 10.5194/angeo-39-613-2021
- [168] YU X D, YUAN Z G, OUYANG Z H, *et al.* Effects of the plasma-pause on the radial propagation of fast magnetosonic waves: an analytical approach[J]. *Journal of Geophysical Research: Space Physics*, 2021, **126**(3): e2020JA028330. DOI: 10.1029/2020ja028330
- [169] HUANG S Y, DENG D, YUAN Z G, *et al.* First observations of magnetosonic waves with nonlinear harmonics[J]. *Journal of Geophysical Research: Space Physics*, 2020, **125**(6): e2019JA027724. DOI: 10.1029/2019ja027724
- [170] ZOU Z Y, GAO Z L, ZUO P B, *et al.* Evidence of wave-wave coupling between frequency harmonic bands of magnetosonic waves[J]. *Physics of Plasmas*, 2021, **28**(12): 122903. DOI: 10.1063/5.0065582
- [171] YU X D, YUAN Z G, YAO F, *et al.* Radially full reflection of fast magnetosonic waves near the cut-off frequency[J]. *Journal of Geophysical Research: Space Physics*, 2021, **126**(8): e2021JA029508. DOI: 10.1029/2021ja029508
- [172] SUN J C, LU Q M, WANG X Y, *et al.* Modulation of magnetosonic waves by background plasma density in a dipole magnetic field: 2-D PIC simulation[J]. *Journal of Geophysical Research: Space Physics*, 2021, **126**(11): e2021JA029729. DOI: 10.1029/2021ja029729
- [173] YU X D, YUAN Z G, YAO F, *et al.* Electromagnetic characteristics of fast magnetosonic waves in the inner magnetosphere[J]. *Journal of Geophysical Research: Space Physics*, 2021, **126**(9): e2021JA029759. DOI: 10.1029/2021ja029759
- [174] WU Z Y, SU Z P, LIU N G, *et al.* Off-equatorial source of magnetosonic waves extending above the lower hybrid resonance frequency in the inner magnetosphere[J]. *Geophysical Research Letters*, 2021, **48**(6): e2020GL091830. DOI: 10.1029/2020gl091830
- [175] OUYANG Z H, YUAN Z G, YU X D, *et al.* Proton ring evolution and its effect on magnetosonic wave excitation: particle-in-cell simulation and linear theory[J]. *Geophysical Research Letters*, 2021, **48**(14): e2021GL092747. DOI: 10.1029/2021gl092747
- [176] ZHOU Q H, JIANG Z, YANG C, *et al.* Correlated observation on global distributions of magnetosonic waves and proton rings in the radiation belts[J]. *Journal of Geophysical Research: Space Physics*, 2021, **126**(1): e2020JA028354. DOI: 10.1029/2020ja028354
- [177] GU Xudong, HE Ying, NI Binbin, *et al.* Scattering of radiation belt electrons caused by wave-particle interactions with magnetosonic waves associated with plasma density drop[J]. *Chinese Journal of Geophysics*, 2020, **63**(6): 2121-2130. DOI: 10.6038/cjg2020N0384 (顾旭东, 何颖, 倪彬彬, 等. 伴随等离子体密度下降的磁声波与辐射带电子的波粒相互作用及其散射效应[J]. *地球物理学报*, 2020, **63**(6): 2121-2130. DOI: 10.6038/cjg2020N0384)
- [178] YUAN Z G, YAO F, YU X D, *et al.* Ionospheric signatures of ring current ions scattered by magnetosonic waves[J]. *Geophysical Research Letters*, 2020, **47**(16): e2020GL089032. DOI: 10.1029/2020gl089032
- [179] ZHOU R X, FU S, NI B B, *et al.* Parametric dependence of the formation of electron butterfly pitch angle distribution driven by magnetosonic waves[J]. *Journal of Geophysical Research: Space Physics*, 2020, **125**(10): e2020JA027967. DOI: 10.1029/2020ja027967
- [180] FU S, GE Y S. Acceleration of ring current protons driven by

- magnetosonic waves: comparisons of test particle simulations with quasilinear calculations[J]. *The Astrophysical Journal*, 2021, **908**(2): 203. DOI: 10.3847/1538-4357/abd2b3
- [181] LIU C M, FU H S, LIU Y Y, et al. Kinetics of magnetic hole behind dipolarization front[J]. *Geophysical Research Letters*, 2021, **48**(10): e2021GL093174. DOI: 10.1029/2021gl093174
- [182] LIU Y Y, FU H S, ZONG Q G, et al. First topology of electron-scale magnetic hole[J]. *Geophysical Research Letters*, 2020, **47**(18): e2020GL088374. DOI: 10.1029/2020gl088374
- [183] YAO S T, YUE Z S, SHI Q Q, et al. Statistical properties of kinetic-scale magnetic holes in terrestrial space[J]. *Earth and Planetary Physics*, 2021, **5**(1): 63-72. DOI: 10.26464/epp2021011
- [184] HUANG S Y, XU S B, HE L H, et al. Excitation of whistler waves through the bidirectional field-aligned electron beams with electron temperature anisotropy: MMS observations[J]. *Geophysical Research Letters*, 2020, **47**(14): e2020GL087515. DOI: 10.1029/2020gl087515
- [185] YAO S T, SHI Q Q, ZONG Q G, et al. Low-frequency whistler waves modulate electrons and generate higher-frequency whistler waves in the solar wind[J]. *The Astrophysical Journal*, 2021, **923**(2): 216. DOI: 10.3847/1538-4357/ac2e97
- [186] WANG M M, YAO S T, SHI Q Q, et al. Propagation properties of foreshock cavitons: cluster observations[J]. *Science China Technological Sciences*, 2020, **63**(1): 173-182. DOI: 10.1007/s11431-018-9450-3
- [187] JIANG K, HUANG S Y, FU H S, et al. Observational evidence of magnetic reconnection in the terrestrial foreshock region[J]. *The Astrophysical Journal*, 2021, **922**(1): 56. DOI: 10.3847/1538-4357/ac2500
- [188] CAI C L, WEI X H. Multipoint observations of magnetosheath response to foreshock transients[J]. *Journal of Geophysical Research: Space Physics*, 2020, **125**(2): e2019JA027416. DOI: 10.1029/2019ja027416
- [189] WANG B Y, ZHANG H, LIU Z Y, et al. Energy modulations of magnetospheric ions induced by foreshock transient-driven ultralow-frequency waves[J]. *Geophysical Research Letters*, 2021, **48**(10): e2021GL093913. DOI: 10.1029/2021gl093913
- [190] LI X Y, LIU Z Y, ZONG Q G, et al. Off-equatorial minima effects on ULF wave-ion interaction in the dayside outer magnetosphere[J]. *Geophysical Research Letters*, 2021, **48**(18): e2021GL095648. DOI: 10.1029/2021gl095648
- [191] LU J Y, ZHANG H X, WANG M, et al. Energy transfer across the magnetopause under radial IMF conditions[J]. *The Astrophysical Journal*, 2021, **920**(1): 52. DOI: 10.3847/1538-4357/ac15f4
- [192] WANG M, LU J Y, KABIN K, et al. Influence of the interplanetary magnetic field cone angle on the geometry of bow shocks[J]. *The Astronomical Journal*, 2020, **159**(5): 227. DOI: 10.3847/1538-3881/ab86a7
- [193] WANG J, HUANG C, GE Y S, et al. Influence of the IMF B_x on the geometry of the bow shock and magnetopause[J]. *Planetary and Space Science*, 2020, **182**: 104844. DOI: 10.1016/j.pss.2020.104844
- [194] SHANG W S, TANG B B, SHI Q Q, et al. Unusual location of the geotail magnetopause near lunar orbit: a case study[J]. *Journal of Geophysical Research: Space Physics*, 2020, **125**(4): e2019JA027401. DOI: 10.1029/2019ja027401
- [195] MAN H Y, ZHOU M, ZHONG Z H, et al. Statistics of the intense current structure in the dayside magnetopause boundary layer[J]. *Journal of Geophysical Research: Space Physics*, 2021, **126**(12): e2021JA029890. DOI: 10.1029/2021ja029890
- [196] LI Hongshuo, LÜ Jianyong, WANG Ming, et al. A statistical study of the relationship between the upstream plasma β and characteristic parameters such as magnetopause thickness and velocity based on satellite observations[J]. *Chinese Journal of Geophysics*, 2021, **64**(9): 3005-3020 (李宏硕, 吕建永, 王明, 等. 基于卫星观测的上游等离子体 β 与磁层顶厚度、速度等特征参数关系的统计研究[J]. *地球物理学报*, 2021, **64**(9): 3005-3020)
- [197] ZENG C, DUAN S P, WANG C, et al. Magnetospheric multiscale observations of energetic oxygen ions at the duskside magnetopause during intense substorms[J]. *Annales Geophysicae*, 2020, **38**(1): 123-135. DOI: 10.5194/angeo-38-123-2020
- [198] ZHU X Q, WANG M M, SHI Q Q, et al. Motion of classic and spontaneous hot flow anomalies observed by cluster[J]. *Journal of Geophysical Research: Space Physics*, 2021, **126**(11): e2021JA029418. DOI: 10.1029/2021ja029418
- [199] HUANG S Y, WEI Y Y, YUAN Z G, et al. Electron jets in the terrestrial magnetotail: a statistical overview[J]. *The Astrophysical Journal*, 2020, **896**(1): 67. DOI: 10.3847/1538-4357/ab8eb0
- [200] LI H, JIANG W C, WANG C, et al. Evolution of the earth's magnetosheath turbulence: a statistical study based on MMS observations[J]. *The Astrophysical Journal Letters*, 2020, **898**(2): L43. DOI: 10.3847/2041-8213/aba531
- [201] QU B H, LU J Y, WANG M, et al. Formation of the bow shock indentation: MHD simulation results[J]. *Earth and Planetary Physics*, 2021, **5**(3): 259-269. DOI: 10.26464/epp2021033
- [202] GUO Z Z, FU H S, CAO J B, et al. Betatron cooling of electrons in martian magnetotail[J]. *Geophysical Research Letters*, 2021, **48**(13): e2021GL093826. DOI: 10.1029/2021gl093826
- [203] LI J H, ZHOU X Z, ZONG Q G, et al. On the origin of donut-shaped electron distributions within magnetic cavities[J]. *Geophysical Research Letters*, 2021, **48**(2): e2020GL091613. DOI: 10.1029/2020gl091613
- [204] LI J H, YANG F, ZHOU X Z, et al. Self-consistent kinetic model of nested electron- and ion-scale magnetic cavities in space plasmas[J]. *Nature Communications*, 2020, **11**(1): 5616. DOI: 10.1038/s41467-020-19442-0
- [205] LIU J, YAO S T, SHI Q Q, et al. Electron energization and energy dissipation in microscale electromagnetic environments[J]. *The Astrophysical Journal Letters*, 2020, **899**(2): L31. DOI: 10.3847/2041-8213/abab92
- [206] LI J H, ZHOU X Z, YANG F, et al. Helical magnetic cavities: kinetic model and comparison with MMS observations[J]. *Geophysical Research Letters*, 2021, **48**(6): e2021GL092383. DOI: 10.1029/2021gl092383
- [207] GAO C H, TANG B B, LI W Y, et al. Effect of the electric field on the gyrotropic electron distributions[J]. *Geophysical Research Letters*, 2021, **48**(5): e2020GL091437. DOI: 10.1029/2020gl091437
- [208] HUANG S Y, ZHANG J, SAHRAOUI F, et al. Observations of magnetic field line curvature and its role in the space plasma turbulence[J]. *The Astrophysical Journal Letters*, 2020, **898**(1): L18. DOI: 10.3847/2041-8213/aba263
- [209] HUANG K, LU Q M, LU S, et al. Formation of pancake, rolling pin, and cigar distributions of energetic electrons at the dipolarization fronts (DFs) driven by magnetic reconnection: a two-dimensional particle-in-cell simulation[J]. *Journal of Geophysical Research: Space Physics*, 2021, **126**(10): e2021JA029939. DOI: 10.1029/

- 2021ja029939
- [210] LIU C M, FU H S, LIU Y Y, *et al.* Electron pitch-angle distribution in earth's magnetotail: pancake, cigar, isotropy, butterfly, and rolling-pin[J]. *Journal of Geophysical Research: Space Physics*, 2020, **125**(4): e2020JA027777. DOI: 10.1029/2020ja027777
- [211] LU Q M, WANG H Y, WANG X Y, *et al.* Turbulence-driven magnetic reconnection in the magnetosheath downstream of a quasi-parallel shock: a three-dimensional global hybrid simulation[J]. *Geophysical Research Letters*, 2020, **47**(1): e2019GL085661. DOI: 10.1029/2019gl085661
- [212] YANG Z W, LIU Y D, MATSUKIYO S, *et al.* PIC simulations of microinstabilities and waves at near-solar solar wind perpendicular shocks: predictions for parker solar probe and solar orbiter[J]. *The Astrophysical Journal Letters*, 2020, **900**(2): L24. DOI: 10.3847/2041-8213/abaf59
- [213] WANG S M, WANG R S, LU Q M, *et al.* Energy dissipation via magnetic reconnection within the coherent structures of the magnetosheath turbulence[J]. *Journal of Geophysical Research: Space Physics*, 2021, **126**(4): e2020JA028860. DOI: 10.1029/2020ja028860
- [214] LU Q M, YANG Z W, WANG H Y, *et al.* Two-dimensional particle-in-cell simulation of magnetic reconnection in the downstream of a quasi-perpendicular shock[J]. *The Astrophysical Journal*, 2021, **919**(1): 28. DOI: 10.3847/1538-4357/ac18c0
- [215] YANG Z W, LIU Y D, JOHLANDER A, *et al.* Mms direct observations of kinetic-scale shock self-reformation[J]. *The Astrophysical Journal Letters*, 2020, **901**(1): L6. DOI: 10.3847/2041-8213/abb3ff
- [216] WANG G Q, ZHANG T L, WU M Y, *et al.* Roles of electrons and ions in formation of the current in mirror-mode structures in the terrestrial plasma sheet: magnetospheric multiscale observations[J]. *Annales Geophysicae*, 2020, **38**(2): 309-318. DOI: 10.5194/angeo-38-309-2020
- [217] YAO S T, HAMRIN M, SHI Q Q, *et al.* Propagating and dynamic properties of magnetic dips in the dayside magnetosheath: MMS observations[J]. *Journal of Geophysical Research: Space Physics*, 2020, **125**(6): e2019JA026736. DOI: 10.1029/2019ja026736
- [218] YIN Z F, ZHOU X Z, ZONG Q G, *et al.* Inner magnetospheric magnetic dips and energetic protons trapped therein: multi-spacecraft observations and simulations[J]. *Geophysical Research Letters*, 2021, **48**(7): e2021GL092567. DOI: 10.1029/2021gl092567
- [219] WEI Y Y, HUANG S Y, YUAN Z G, *et al.* Observation of high-frequency electrostatic waves in the dip region ahead of dipolarization front[J]. *Journal of Geophysical Research: Space Physics*, 2021, **126**(11): e2021JA029408. DOI: 10.1029/2021ja029408
- [220] WEI D, DUNLOP M W, YANG J Y, *et al.* Intense dB/dt variations driven by near-earth bursty bulk flows (BBFs): a case study[J]. *Geophysical Research Letters*, 2021, **48**(4): e2020GL091781. DOI: 10.1029/2020gl091781
- [221] ZHANG L Q, LUI A T Y, BAUMJOHANN W, *et al.* Anisotropic vorticity within bursty bulk flow turbulence[J]. *Journal of Geophysical Research: Space Physics*, 2020, **125**(10): e2020JA028255. DOI: 10.1029/2020ja028255
- [222] ZHANG L Q, BAUMJOHANN W, KHOTYAINITSEV Y V, *et al.* BBF deceleration down-tail of $X < -15 R_E$ from MMS observation[J]. *Journal of Geophysical Research: Space Physics*, 2020, **125**(2): e2019JA026837. DOI: 10.1029/2019ja026837
- [223] ZHANG M, WANG R S, LU Q M, *et al.* Observation of the tailward electron flows commonly detected at the flow boundary of the earthward ion bursty bulk flows in the magnetotail[J]. *The Astrophysical Journal*, 2020, **891**(2): 175. DOI: 10.3847/1538-4357/ab72a8
- [224] ZHANG L Q, WANG C, DAI L, *et al.* MMS observation on the cross-tail current sheet roll-up at the dipolarization front[J]. *Journal of Geophysical Research: Space Physics*, 2021, **126**(4): e2020JA028796. DOI: 10.1029/2020ja028796
- [225] WANG Z, FU H S, VAIVADS A, *et al.* Monitoring the spatio-temporal evolution of a reconnection X-line in space[J]. *The Astrophysical Journal Letters*, 2020, **899**(2): L34. DOI: 10.3847/2041-8213/abad2c
- [226] WANG Z W, HU H Q, LU J Y, *et al.* Observational evidence of transient lobe reconnection triggered by sudden northern enhancement of IMF Bz[J]. *Journal of Geophysical Research: Space Physics*, 2021, **126**(9): e2021JA029410. DOI: 10.1029/2021ja029410
- [227] LI W H, WU L Y, GE Y S, *et al.* Magnetotail configuration under northward IMF conditions[J]. *Journal of Geophysical Research: Space Physics*, 2021, **126**(2): e2020JA028634. DOI: 10.1029/2020ja028634
- [228] HUANG K, LU Q M, CHIEN A, *et al.* Particle-in-cell simulations of asymmetric reconnection driven by laser-powered capacitor coils[J]. *Plasma Physics and Controlled Fusion*, 2021, **63**(1): 015010. DOI: 10.1088/1361-6587/abc600
- [229] GUO J, LU S, LU Q M, *et al.* Structure and coalescence of magnetopause flux ropes and their dependence on IMF clock angle: three-dimensional global hybrid simulations[J]. *Journal of Geophysical Research: Space Physics*, 2021, **126**(2): e2020JA028670. DOI: 10.1029/2020ja028670
- [230] MAN H Y, ZHONG Z H, LI H M. Internal structures of the ion-scale flux rope associated with dayside magnetopause reconnection[J]. *Astrophysics and Space Science*, 2020, **365**(5): 87. DOI: 10.1007/s10509-020-03803-8
- [231] ZHONG Z H, ZHOU M, TANG R X, *et al.* Direct evidence for electron acceleration within ion-scale flux rope[J]. *Geophysical Research Letters*, 2020, **47**(1): e2019GL085141. DOI: 10.1029/2019gl085141
- [232] CHEN Z Z, FU H S, WANG Z, *et al.* First observation of magnetic flux rope inside electron diffusion region[J]. *Geophysical Research Letters*, 2021, **48**(7): e2020GL089722. DOI: 10.1029/2020gl089722
- [233] HE R J, FU H S, LIU Y Y, *et al.* Subion-scale flux rope nested inside ion-scale flux rope in earth's magnetotail[J]. *Geophysical Research Letters*, 2021, **48**(23): e2021GL096169. DOI: 10.1029/2021gl096169
- [234] ZHANG C, RONG Z J, SHEN C, *et al.* Examining the magnetic geometry of magnetic flux ropes from the view of single-point analysis[J]. *The Astrophysical Journal*, 2020, **903**(1): 53. DOI: 10.3847/1538-4357/abba16
- [235] MAN H Y, ZHOU M, YI Y Y, *et al.* Observations of electron-only magnetic reconnection associated with macroscopic magnetic flux ropes[J]. *Geophysical Research Letters*, 2020, **47**(19): e2020GL089659. DOI: 10.1029/2020gl089659
- [236] ZHONG Z H, ZHOU M, DENG X H, *et al.* Three-dimensional electron-scale magnetic reconnection in earth's magnetosphere[J]. *Geophysical Research Letters*, 2021, **48**(1): 2020GL090946. DOI: 10.1029/2020gl090946
- [237] ZHOU M, MAN H Y, DENG X H, *et al.* Observations of secondary magnetic reconnection in the turbulent reconnection outflow[J]. *Geophysical Research Letters*, 2021, **48**(4): e2020GL091215. DOI: 10.1029/2020gl091215
- [238] WANG S M, WANG R S, LU Q M, *et al.* Direct evidence of sec-

- ondary reconnection inside filamentary currents of magnetic flux ropes during magnetic reconnection[J]. *Nature Communications*, 2020, **11**(1): 3964
- [239] JIANG K, HUANG S Y, YUAN Z G, et al. Statistical properties of current, energy conversion, and electron acceleration in flux ropes in the terrestrial magnetotail[J]. *Geophysical Research Letters*, 2021, **48**(11): e2021GL093458. DOI: 10.1029/2021gl093458
- [240] GUO J, LU S, LU Q M, et al. Re-reconnection processes of magnetopause flux ropes: three-dimensional global hybrid simulations[J]. *Journal of Geophysical Research: Space Physics*, 2021, **126**(6): e2021JA029388. DOI: 10.1029/2021ja029388
- [241] FU H S, GRIGORENKO E E, GABRIELSE C, et al. Magnetotail dipolarization fronts and particle acceleration: a review[J]. *Science China Earth Sciences*, 2020, **63**(2): 235-256. DOI: 10.1007/s11430-019-9551-y
- [242] FU H S, ZHAO M J, YU Y, et al. A new theory for energetic electron generation behind dipolarization front[J]. *Geophysical Research Letters*, 2020, **47**(6): e2019GL086790. DOI: 10.1029/2019gl086790
- [243] LIU C M, FU H S, YU Y Q, et al. Energy flux densities at dipolarization fronts[J]. *Geophysical Research Letters*, 2021, **48**(16): e2021GL094932. DOI: 10.1029/2021gl094932
- [244] MA W Q, ZHOU M, ZHONG Z H, et al. Electron acceleration rate at dipolarization fronts[J]. *The Astrophysical Journal*, 2020, **903**(2): 84. DOI: 10.3847/1538-4357/abb8cc
- [245] FU W D, FU H S, CAO J B, et al. Formation of rolling-pin distribution of suprathermal electrons behind dipolarization fronts[J]. *Journal of Geophysical Research: Space Physics*, 2022, **127**(1): e2021JA029642. DOI: 10.1029/2021ja029642
- [246] MA Y D, YANG J, DUNLOP M W, et al. Energy budget of high-speed plasma flows in the terrestrial magnetotail[J]. *The Astrophysical Journal*, 2020, **894**(1): 16. DOI: 10.3847/1538-4357/ab83fd
- [247] JIANG K, HUANG S Y, YUAN Z G, et al. Observations of electron vortex at the dipolarization front[J]. *Geophysical Research Letters*, 2020, **47**(13): e2020GL088448. DOI: 10.1029/2020gl088448
- [248] LIU C M, FU H S, LIU Y Y. Electron vorticity at dipolarization fronts[J]. *The Astrophysical Journal*, 2021, **911**(2): 122. DOI: 10.3847/1538-4357/abee1c
- [249] SONG L J, ZHOU M, YI Y Y, et al. Force and energy balance of the dipolarization front[J]. *Journal of Geophysical Research: Space Physics*, 2020, **125**(9): e2020JA028278. DOI: 10.1029/2020ja028278
- [250] WANG L, HUANG C, CAO X, et al. Magnetic energy conversion and transport in the terrestrial magnetotail due to dipolarization fronts[J]. *Journal of Geophysical Research: Space Physics*, 2020, **125**(10): e2020JA028568. DOI: 10.1029/2020ja028568
- [251] XU Y, FU H S, CAO J B, et al. Electron-scale measurements of antidipolarization front[J]. *Geophysical Research Letters*, 2021, **48**(6): e2020GL092232. DOI: 10.1029/2020gl092232
- [252] HUANG C, DU A M, GE Y S. Evolution of electron current layer during anti-parallel magnetic reconnection[J]. *Plasma Physics and Controlled Fusion*, 2020, **62**(5): 055014. DOI: 10.1088/1361-6587/ab7d49
- [253] ZHONG Z H, ZHOU M, TANG R X, et al. Extension of the electron diffusion region in a guide field magnetic reconnection at magnetopause[J]. *The Astrophysical Journal Letters*, 2020, **892**(1): L5. DOI: 10.3847/2041-8213/ab7b7c
- [254] HUANG K, LU Q M, WANG R S, et al. Spontaneous growth of the reconnection electric field during magnetic reconnection with a guide field: a theoretical model and particle-in-cell simulations[J]. *Chinese Physics B*, 2020, **29**(7): 075202. DOI: 10.1088/1674-1056/ab8da0
- [255] BAI S C, SHI Q Q, LIU T Z, et al. Ion-scale flux rope observed inside a hot flow anomaly[J]. *Geophysical Research Letters*, 2020, **47**(5): e2019GL085933. DOI: 10.1029/2019gl085933
- [256] LI Y X, LI W Y, TANG B B, et al. Quantification of cold-ion beams in a magnetic reconnection jet[J]. *Frontiers in Astronomy and Space Sciences*, 2021, **8**: 745264. DOI: 10.3389/fspas.2021.745264
- [257] WANG S M, WANG R S, LU Q M, et al. Large - scale parallel electric field collocated in an extended electron diffusion region during the magnetosheath magnetic reconnection[J]. *Geophysical Research Letters*, 2021, **48**(23): e2021GL094879
- [258] ZHOU M, MAN H Y, YANG Y, et al. Measurements of energy dissipation in the electron diffusion region[J]. *Geophysical Research Letters*, 2021, **48**(24): e2021GL096372. DOI: 10.1029/2021gl096372
- [259] HUANG H T, YU Y Q, CAO J B, et al. On the ion distributions at the separatrix during symmetric magnetic reconnection[J]. *Earth and Planetary Physics*, 2021, **5**(2): 205-217. DOI: 10.26464/epp2021019
- [260] CHEN C X. Preservation and variation of ion-to-electron temperature ratio in the plasma sheet in geo-magnetotail[J]. *Earth and Planetary Physics*, 2021, **5**(4): 337-347. DOI: 10.26464/epp2021035
- [261] WU T, FU S Y, XIE L, et al. Cluster observations on time-of-flight effect of oxygen ions in magnetotail reconnection exhaust region[J]. *Geophysical Research Letters*, 2020, **47**(3): e2019GL085200. DOI: 10.1029/2019gl085200
- [262] HUANG K, LIU Y H, LU Q M, et al. Scaling of magnetic reconnection with a limited X-line extent[J]. *Geophysical Research Letters*, 2020, **47**(19): e2020GL088147. DOI: 10.1029/2020gl088147
- [263] DAI L, WANG C, LAVRAUD B. Kinetic imprints of ion acceleration in collisionless magnetic reconnection[J]. *The Astrophysical Journal*, 2021, **919**(1): 15. DOI: 10.3847/1538-4357/ac0fde
- [264] HUANG S Y, XIONG Q Y, SONG L F, et al. Electron-only reconnection in an ion-scale current sheet at the magnetopause[J]. *The Astrophysical Journal*, 2021, **922**(1): 54. DOI: 10.3847/1538-4357/ac2668
- [265] LIU D K, LU S, LU Q M, et al. Spontaneous onset of collisionless magnetic reconnection on an electron scale[J]. *The Astrophysical Journal Letters*, 2020, **890**(2): L15. DOI: 10.3847/2041-8213/ab72fe
- [266] LU S, WANG R S, LU Q M, et al. Magnetotail reconnection onset caused by electron kinetics with a strong external driver[J]. *Nature Communications*, 2020, **11**(1): 5049. DOI: 10.1038/s41467-020-18787-w
- [267] LIU D K, HUANG K, LU Q M, et al. The evolution of collisionless magnetic reconnection from electron scales to ion scales[J]. *The Astrophysical Journal*, 2021, **922**(1): 51. DOI: 10.3847/1538-4357/ac2900
- [268] TANG S Y, ZHANG Y C, DAI L, et al. MMS observation of the hall field in an asymmetric magnetic reconnection with guide field[J]. *The Astrophysical Journal*, 2021, **922**(2): 96. DOI: 10.3847/1538-4357/ac31b1
- [269] WANG R S, LU Q M, LU S, et al. Physical implication of two types of reconnection electron diffusion regions with and without

- ion-coupling in the magnetotail current sheet[J]. *Geophysical Research Letters*, 2020, **47**(21): e2020GL088761. DOI: 10.1029/2020gl088761
- [270] LI W Y, GRAHAM D B, KHOTYAINTESEV Y V, *et al.* Electron Bernstein waves driven by electron crescents near the electron diffusion region[J]. *Nature Communications*, 2020, **11**(1): 141
- [271] CHEN G, FU H S, ZHANG Y, *et al.* An unexpected whistler wave generation around dipolarization front[J]. *Journal of Geophysical Research: Space Physics*, 2021, **126**(5): e2020JA028957. DOI: 10.1029/2020ja028957
- [272] REN Y, DAI L, WANG C, *et al.* Statistical characteristics in the spectrum of whistler waves near the diffusion region of dayside magnetopause reconnection[J]. *Geophysical Research Letters*, 2021, **48**(1): e2020GL090816. DOI: 10.1029/2020gl090816
- [273] YU X C, LU Q M, WANG R S, *et al.* Simultaneous observation of whistler waves and electron cyclotron harmonic waves in the separatrix region of magnetopause reconnection[J]. *Journal of Geophysical Research: Space Physics*, 2021, **126**(10): e2021JA029609. DOI: 10.1029/2021ja029609
- [274] TANG B B, LI W Y, GRAHAM D B, *et al.* Lower hybrid waves at the magnetosheath separatrix region[J]. *Geophysical Research Letters*, 2020, **47**(20): e2020GL089880. DOI: 10.1029/2020gl089880
- [275] LI W Y, KHOTYAINTESEV Y V, TANG B B, *et al.* Upper-hybrid waves driven by meandering electrons around magnetic reconnection X line[J]. *Geophysical Research Letters*, 2021, **48**(16): e2021GL093164. DOI: 10.1029/2021gl093164
- [276] SHU Y K, LU S, LU Q M, *et al.* Energy budgets from collisionless magnetic reconnection site to reconnection front[J]. *Journal of Geophysical Research: Space Physics*, 2021, **126**(10): e2021JA029712. DOI: 10.1029/2021ja029712
- [277] YI Y Y, ZHOU M, SONG L J, *et al.* Energy conversion during multiple X-lines reconnection[J]. *Physics of Plasmas*, 2020, **27**(12): 122905. DOI: 10.1063/5.0018269
- [278] CHANG C, HUANG K, LU Q M, *et al.* Particle-in-cell simulations of electrostatic solitary waves in asymmetric magnetic reconnection[J]. *Journal of Geophysical Research: Space Physics*, 2021, **126**(7): e2021JA029290. DOI: 10.1029/2021ja029290
- [279] FU H S, CHEN F, CHEN Z Z, *et al.* First measurements of electrons and waves inside an electrostatic solitary wave[J]. *Physical Review Letters*, 2020, **124**(9): 095101. DOI: 10.1103/PhysRevLett.124.095101
- [280] GUO Z Z, FU H S, CAO J B, *et al.* Broadband electrostatic waves behind dipolarization front: observations and analyses[J]. *Journal of Geophysical Research: Space Physics*, 2021, **126**(12): e2021JA029900. DOI: 10.1029/2021ja029900
- [281] YU Y, FU H S, CAO J B, *et al.* Electron thermalization and electrostatic turbulence caused by flow reversal in dipolarizing flux tubes[J]. *The Astrophysical Journal*, 2022, **926**(1): 22. DOI: 10.3847/1538-4357/ac42c5
- [282] YU X C, LU Q M, WANG R S, *et al.* Mms observations of broadband electrostatic waves in electron diffusion region of magnetotail reconnection[J]. *Journal of Geophysical Research: Space Physics*, 2021, **126**(3): e2020JA028882. DOI: 10.1029/2020ja028882
- [283] TANG B B, LI W Y, LE A, *et al.* Electron mixing and isotropization in the exhaust of asymmetric magnetic reconnection with a guide field[J]. *Geophysical Research Letters*, 2020, **47**(14): e2020GL087159. DOI: 10.1029/2020gl087159
- [284] LAI H R, JIA Y D, RUSSELL C T, *et al.* Magnetic flux circulation in the Saturnian magnetosphere as constrained by Cassini observations in the inner magnetosphere[J]. *Journal of Geophysical Research: Space Physics*, 2021, **126**(11): e2021JA029304. DOI: 10.1029/2021ja029304
- [285] HAO Y X, SUN Y X, ROUSSOS E, *et al.* The formation of Saturn's and Jupiter's electron radiation belts by magnetospheric electric fields[J]. *The Astrophysical Journal Letters*, 2020, **905**(1): L10. DOI: 10.3847/2041-8213/abca3f
- [286] SUN Y X, ROUSSOS E, HAO Y X, *et al.* Saturn's inner magnetospheric convection in the view of zebra stripe patterns in energetic electron spectra[J]. *Journal of Geophysical Research: Space Physics*, 2021, **126**(10): e2021JA029600. DOI: 10.1029/2021ja029600
- [287] GUO R L, YAO Z H, DUNN W R, *et al.* A rotating azimuthally distributed auroral current system on Saturn revealed by the Cassini spacecraft[J]. *The Astrophysical Journal Letters*, 2021, **919**(2): L25. DOI: 10.3847/2041-8213/ac26b5
- [288] PAN D X, YAO Z H, GUO R L, *et al.* A statistical survey of low-frequency magnetic fluctuations at saturn[J]. *Journal of Geophysical Research: Space Physics*, 2021, **126**(2): e2020JA028387. DOI: 10.1029/2020ja028387
- [289] LONG M Y, GU X D, NI B B, *et al.* Global distribution of electrostatic electron cyclotron harmonic waves in Saturn's magnetosphere: a survey of over-13-year Cassini RPWS observations[J]. *Journal of Geophysical Research: Planets*, 2021, **126**(4): e2020JE006800. DOI: 10.1029/2020je006800
- [290] ZHANG H, LI Q, TANG R X, *et al.* Background parameter effects on linear-nonlinear chorus wave growth in the planetary magnetosphere[J]. *The Astrophysical Journal*, 2020, **904**(2): 105. DOI: 10.3847/1538-4357/abbee
- [291] YUAN C J, ROUSSOS E, WEI Y, *et al.* Sustaining Saturn's electron radiation belts through episodic, global-scale relativistic electron flux enhancements[J]. *Journal of Geophysical Research: Space Physics*, 2020, **125**(5): e2019JA027621. DOI: 10.1029/2019ja027621
- [292] YUAN C J, ROUSSOS E, WEI Y, *et al.* Cassini observation of relativistic electron butterfly distributions in Saturn's inner radiation belts: evidence for acceleration by local processes[J]. *Geophysical Research Letters*, 2021, **48**(14): e2021GL092690. DOI: 10.1029/2021gl092690
- [293] XU S B, HUANG S Y, YUAN Z G, *et al.* Global spatial distribution of dipolarization fronts in the Saturn's magnetosphere: Cassini observations[J]. *Geophysical Research Letters*, 2021, **48**(17): e2021GL092701. DOI: 10.1029/2021gl092701
- [294] XU Y, GUO R L, YAO Z H, *et al.* Properties of plasmoids observed in Saturn's dayside and nightside magnetodisc[J]. *Geophysical Research Letters*, 2021, **48**(24): e2021GL096765. DOI: 10.1029/2021gl096765
- [295] LIU Z Y, ZONG Q G, BLANC M, *et al.* Statistics on Jupiter's current sheet with Juno data: geometry, magnetic fields and energetic particles[J]. *Journal of Geophysical Research: Space Physics*, 2021, **126**(11): e2021JA029710. DOI: 10.1029/2021ja029710
- [296] ZHANG B Z, DELAMERE P A, YAO Z H, *et al.* How Jupiter's unusual magnetospheric topology structures its aurora[J]. *Science Advances*, 2021, **7**(15): eabd1204. DOI: 10.1126/sciadv.abd1204
- [297] WANG Y X, GUO X C, WANG C, *et al.* MHD modeling of the background solar wind in the inner heliosphere from 0.1 to 5.5 AU: comparison with in situ observations[J]. *Space Weather*, 2020, **18**(6): e2019SW002262. DOI: 10.1029/2019sw002262
- [298] GUO R L, YAO Z H, GRODENT D, *et al.* Jupiter's double-arc aurora as a signature of magnetic reconnection: simultaneous ob-

- servations from HST and Juno[J]. *Geophysical Research Letters*, 2021, **48**(14): e2021GL093964. DOI: 10.1029/2021gl093964
- [299] YAO Z H, DUNN W R, WOODFIELD E E, et al. Revealing the source of Jupiter's x-ray auroral flares[J]. *Science Advances*, 2021, **7**(28): eabf0851. DOI: 10.1126/sciadv.abf0851
- [300] YAO Z H, BONFOND B, CLARK G, et al. Reconnection- and dipolarization-driven auroral dawn storms and injections[J]. *Journal of Geophysical Research: Space Physics*, 2020, **125**(8): e2019JA027663. DOI: 10.1029/2019ja027663
- [301] WANG Y X, BLANC M, LOUIS C, et al. A preliminary study of magnetosphere-ionosphere-thermosphere coupling at Jupiter: Juno multi-instrument measurements and modeling tools[J]. *Journal of Geophysical Research: Space Physics*, 2021, **126**(9): e2021JA029469. DOI: 10.1029/2021ja029469
- [302] DUBININ E, FRAENZ M, MODOLO R, et al. Induced magnetic fields and plasma motions in the inner part of the martian magnetosphere[J]. *Journal of Geophysical Research: Space Physics*, 2021, **126**(12): e2021JA029542. DOI: 10.1029/2021ja029542
- [303] SHAN L C, TSURUTANI B T, OHSAWA Y, et al. Observational evidence for fast mode periodic small-scale shocks: a new type of plasma phenomenon[J]. *The Astrophysical Journal Letters*, 2020, **905**(1): L4. DOI: 10.3847/2041-8213/abc02
- [304] SHAN L C, DU A M, TSURUTANI B T, et al. In situ observations of the formation of periodic collisionless plasma shocks from fast mode waves[J]. *The Astrophysical Journal Letters*, 2020, **888**(2): L17. DOI: 10.3847/2041-8213/ab5db3
- [305] WANG M, XIE L, LEE L C, et al. A 3D parametric martian bow shock model with the effects of Mach number, dynamic pressure, and the interplanetary magnetic field[J]. *The Astrophysical Journal*, 2020, **903**(2): 125. DOI: 10.3847/1538-4357/abbc04
- [306] WANG M, LEE L C, XIE L H, et al. Effect of solar wind density and velocity on the subsolar standoff distance of the martian magnetic pileup boundary[J]. *Astronomy & Astrophysics*, 2021, **651**: A22. DOI: 10.1051/0004-6361/202140511
- [307] WU M Y, CHEN Y J, DU A M, et al. Statistical properties of small-scale linear magnetic holes in the martian magnetosheath[J]. *The Astrophysical Journal*, 2021, **916**(2): 104. DOI: 10.3847/1538-4357/ac090b
- [308] GAO J W, RONG Z J, KLINGER L, et al. A spherical harmonic martian crustal magnetic field model combining data sets of MAVEN and MGS[J]. *Earth and Space Science*, 2021, **8**(10): e2021EA001860. DOI: 10.1029/2021ea001860
- [309] DU A M, ZHANG Y, LI H Y, et al. The Chinese mars ROVER fluxgate magnetometers[J]. *Space Science Reviews*, 2020, **216**(8): 135. DOI: 10.1007/s11214-020-00766-8
- [310] ZHANG C, RONG Z J, NILSSON H, et al. MAVEN observations of periodic low-altitude plasma clouds at mars[J]. *The Astrophysical Journal Letters*, 2021, **922**(2): L33. DOI: 10.3847/2041-8213/ac3a7d
- [311] WANG J, YU J, XU X J, et al. MAVEN observations of magnetic reconnection at martian induced magnetopause[J]. *Geophysical Research Letters*, 2021, **48**(21): e2021GL095426. DOI: 10.1029/2021gl095426
- [312] HUANG S Y, LIN R T, YUAN Z G, et al. In situ detection of kinetic-size magnetic holes in the martian magnetosheath[J]. *The Astrophysical Journal*, 2021, **922**(2): 107. DOI: 10.3847/1538-4357/ac2737
- [313] ZOU Y L, ZHU Y, BAI Y F, et al. Scientific objectives and payloads of Tianwen-1, China's first Mars exploration mission[J]. *Advances in Space Research*, 2021, **67**(2): 812-823. DOI: 10.1016/j.asr.2020.11.005
- [314] FAN K, FRAENZ M, WEI Y, et al. Deflection of global ion flow by the martian crustal magnetic fields[J]. *The Astrophysical Journal Letters*, 2020, **898**(2): L54. DOI: 10.3847/2041-8213/aba519
- [315] DUBININ E, FRAENZ M, PÄTZOLD M, et al. Impact of martian crustal magnetic field on the ion escape[J]. *Journal of Geophysical Research: Space Physics*, 2020, **125**(10): e2020JA028010. DOI: 10.1029/2020ja028010
- [316] CAO Y T, CUI J, WU X S, et al. A survey of photoelectrons on the nightside of mars[J]. *Geophysical Research Letters*, 2021, **48**(2): e2020GL089998. DOI: 10.1029/2020gl089998
- [317] SUN W J, DEWEY R M, AIZAWA S, et al. Review of mercury's dynamic magnetosphere: post-MESSENGER era and comparative magnetospheres[J]. *Science China Earth Sciences*, 2022, **65**(1): 25-74. DOI: 10.1007/s11430-021-9828-0
- [318] ZHONG J, LEE L C, WANG X G, et al. Multiple X-line reconnection observed in mercury's magnetotail driven by an interplanetary coronal mass ejection[J]. *The Astrophysical Journal Letters*, 2020, **893**(1): L11. DOI: 10.3847/2041-8213/ab8380
- [319] JANG E, ZHAO J T, YUE C, et al. Energetic ion dynamics near the cusp region of mercury[J]. *The Astrophysical Journal*, 2020, **892**(1): 10. DOI: 10.3847/1538-4357/ab74d1
- [320] ZHANG C, RONG Z J, GAO J W, et al. The flapping motion of mercury's magnetotail current sheet: MESSENGER observations[J]. *Geophysical Research Letters*, 2020, **47**(4): e2019GL086011. DOI: 10.1029/2019gl086011
- [321] ZHAO J T, ZONG Q G, SLAVIN J A, et al. Proton properties in mercury's magnetotail: a statistical study[J]. *Geophysical Research Letters*, 2020, **47**(19): e2020GL088075. DOI: 10.1029/2020gl088075
- [322] ZHONG J, WEI Y, LEE L C, et al. Formation of macroscale flux transfer events at mercury[J]. *The Astrophysical Journal Letters*, 2020, **893**(1): L18. DOI: 10.3847/2041-8213/ab8566
- [323] HUANG S Y, WANG Q Y, SAHRAOUI F, et al. Analysis of turbulence properties in the mercury plasma environment using messenger observations[J]. *The Astrophysical Journal*, 2020, **891**(2): 159. DOI: 10.3847/1538-4357/ab7349
- [324] XIAO S D, WU M Y, WANG G Q, et al. Survey of 1-Hz waves in the near-Venusian space: venus express observations[J]. *Planetary and Space Science*, 2020, **187**: 104933. DOI: 10.1016/j.pss.2020.104933
- [325] XU Q, XU X J, ZHANG T L, et al. The venus express observation of venus' induced magnetosphere boundary at solar maximum[J]. *Astronomy & Astrophysics*, 2021, **652**: A113. DOI: 10.1051/0004-6361/202141391
- [326] XIAO S D, WU M Y, WANG G Q, et al. The spectral scalings of magnetic fluctuations upstream and downstream of the Venusian bow shock[J]. *Earth, Planets and Space*, 2021, **73**(1): 13. DOI: 10.1186/s40623-020-01343-7
- [327] XIAO S D, WU M Y, WANG G Q, et al. Turbulence in the near-Venusian space: venus express observations[J]. *Earth and Planetary Physics*, 2020, **4**(1): 82-87. DOI: 10.26464/epp2020012
- [328] XIAO S D, ZHANG T L, VÖRÖS Z, et al. Turbulence near the Venusian bow shock: venus express observations[J]. *Journal of Geophysical Research: Space Physics*, 2020, **125**(2): e2019JA027190. DOI: 10.1029/2019ja027190
- [329] GAO J W, RONG Z J, PERSSON M, et al. In situ observations of

- the ion diffusion region in the Venusian magnetotail[J]. *Journal of Geophysical Research: Space Physics*, 2021, **126**(1): e2020JA028547. DOI: 10.1029/2020ja028547
- [330] ZHANG H, ZHONG J, ZHANG T X, *et al.* A meandering lunar wake produced by the pickup of reflected solar-wind ions[J]. *Geophysical Research Letters*, 2021, **48**(24): e2021GL096039. DOI: 10.1029/2021gl096039
- [331] ZHANG T X, ZHANG H, LAI H R, *et al.* Asymmetric lunar magnetic perturbations produced by reflected solar wind particles[J]. *The Astrophysical Journal Letters*, 2020, **893**(2): L36. DOI: 10.3847/2041-8213/ab8640
- [332] DUNLOP M W, DONG X C, WANG T Y, *et al.* Curlometer technique and applications[J]. *Journal of Geophysical Research: Space Physics*, 2021, **126**(11): e2021JA029538. DOI: 10.1029/2021ja029538
- [333] SHEN C, ZENG G, ZHANG C, *et al.* Determination of the configurations of boundaries in space[J]. *Journal of Geophysical Research: Space Physics*, 2020, **125**(9): e2020JA028163. DOI: 10.1029/2020ja028163
- [334] SHEN C, ZHANG C, RONG Z J, *et al.* Nonlinear magnetic gradients and complete magnetic geometry from multispacecraft measurements[J]. *Journal of Geophysical Research: Space Physics*, 2021, **126**(8): e2020JA028846. DOI: 10.1029/2020ja028846
- [335] SHEN C, ZHOU Y F, MA Y H, *et al.* A general algorithm for the linear and quadratic gradients of physical quantities based on 10 or more point measurements[J]. *Journal of Geophysical Research: Space Physics*, 2021, **126**(6): e2021JA029121. DOI: 10.1029/2021ja029121
- [336] ZHU Y, DU A M, LUO H, *et al.* The fluxgate magnetometer of the low orbit pearl satellites (LOPS): overview of in-flight performance and initial results[J]. *Geoscientific Instrumentation, Methods and Data Systems*, 2021, **10**(2): 227-243. DOI: 10.5194/gi-10-227-2021
- [337] SHEN C, ZHOU Y F, GAO L, *et al.* Measurements of the net charge density of space plasmas[J]. *Journal of Geophysical Research: Space Physics*, 2021, **126**(12): e2021JA029511. DOI: 10.1029/2021ja029511
- [338] LI K, ANDRÉ M, ERIKSSON A, *et al.* High-latitude cold ion outflow inferred from the cluster wake observations in the magnetotail lobes and the polar cap region[J]. *Frontiers in Physics*, 2021, **9**: 743316
- [339] HUANG Y, DAI L, WANG C, *et al.* A new inversion method for reconstruction of plasmaspheric He⁺ density from EUV images[J]. *Earth and Planetary Physics*, 2021, **5**(2): 218-222. DOI: 10.26464/epp2021020
- [340] WANG Z, FU H S, OLSHEVSKY V, *et al.* Extending the FOTE method to three-dimensional plasma flow fields[J]. *The Astrophysical Journal Supplement Series*, 2020, **249**(1): 10. DOI: 10.3847/1538-4365/ab95a0
- [341] FU H S, WANG Z, ZONG Q G, *et al.* Methods for finding magnetic nulls and reconstructing field topology: a review[M]//ZONG Q G, ESCOUBET P, SIBECK D, *et al.* Dayside Magnetosphere Interactions. Washington: American Geophysical Union, 2020: 153-172.
- [342] TIAN A M, XIAO K, DEGELING A W, *et al.* Reconstruction of plasma structure with anisotropic pressure: application to Pc5 compressional wave[J]. *The Astrophysical Journal*, 2020, **889**(1): 35. DOI: 10.3847/1538-4357/ab6296
- [343] YU X D, YUAN Z G, XUE Z X. Second-harmonic generation of electromagnetic emissions in a magnetized plasma: kinetic theory approach[J]. *Geophysical Research Letters*, 2021, **48**(5): e2020GL091762. DOI: 10.1029/2020gl091762
- [344] LI Mu, HE Fei, LIN Ruilin, *et al.* Prediction of the geomagnetic disturbances in high-latitude region with Weimer model[J]. *Chinese Journal of Geophysics*, 2020, **63**(6): 2159-2169. DOI: 10.6038/cjg2020N0379 (李沐, 何飞, 林瑞淋, 等. 基于 Weimer 模型的高纬地磁扰动预测[J]. *地球物理学报*, 2020, **63**(6): 2159-2169. DOI: 10.6038/cjg2020N0379)
- [345] ZHANG J J, YU Y Q, WANG C, *et al.* Measurements and simulations of the geomagnetically induced currents in low-latitude power networks during geomagnetic storms[J]. *Space Weather*, 2020, **18**(8): e2020SW002549. DOI: 10.1029/2020sw002549
- [346] XU S B, HUANG S Y, YUAN Z G, *et al.* Prediction of the dst index with bagging ensemble-learning algorithm[J]. *The Astrophysical Journal Supplement Series*, 2020, **248**(1): 14. DOI: 10.3847/1538-4365/ab880e
- [347] YANG X C, WANG L. A study of the performances of widely used external magnetic field models in the outer zone of the earth's radiation belts by comparing the field observations from van Allen probe-a and the model estimations[J]. *Space Weather*, 2021, **19**(12): e2021SW002722. DOI: 10.1029/2021sw002722
- [348] YU X D, YUAN Z G, YU J. Revisit the analytical approximation of transit-time scattering for fast magnetosonic waves[J]. *Geophysical Research Letters*, 2020, **47**(16): e2020GL088434. DOI: 10.1029/2020gl088434
- [349] GUO D Y, FU S, XIANG Z, *et al.* Prediction of dynamic plasma-pause location using a neural network[J]. *Space Weather*, 2021, **19**(5): e2020SW002622. DOI: 10.1029/2020sw002622
- [350] ZHANG H, FU S Y, XIE L, *et al.* Relativistic electron flux prediction at geosynchronous orbit based on the neural network and the quantile regression method[J]. *Space Weather*, 2020, **18**(9): e2020SW002445. DOI: 10.1029/2020sw002445
- [351] ZOU Z Y, SHPRITS Y Y, NI B B, *et al.* An artificial neural network model of electron fluxes in the Earth's central plasma sheet: a THEMIS survey[J]. *Astrophysics and Space Science*, 2020, **365**(6): 100. DOI: 10.1007/s10509-020-03819-0
- [352] WANG J Z, ZHU Q, GU X D, *et al.* An empirical model of the global distribution of plasmaspheric hiss based on van Allen probes EMFISIS measurements[J]. *Earth and Planetary Physics*, 2020, **4**(3): 246-265. DOI: 10.26464/epp2020034
- [353] ZHU Jia'nan, GUO Jianguang, NI Binbin, *et al.* Multi-dimensional data assimilation and analyses of earth's outer electron radiation belt[J]. *Chinese Journal of Geophysics*, 2021, **64**(5): 1496-1507 (朱佳楠, 郭建广, 倪彬彬, 等. 地球电子外辐射带的多数据同化建模与分析[J]. *地球物理学报*, 2021, **64**(5): 1496-1507)
- [354] GUO Y H, WANG C, WEI F, *et al.* A lunar-based soft X-ray imager (LSXI) for the earth's magnetosphere[J]. *Science China Earth Sciences*, 2021, **64**(7): 1026-1035. DOI: 10.1007/s11430-020-9792-5
- [355] SUN T R, WANG C, CONNOR H K, *et al.* Deriving the magnetopause position from the soft X-ray image by using the tangent fitting approach[J]. *Journal of Geophysical Research: Space Physics*, 2020, **125**(9): e2020JA028169. DOI: 10.1029/2020ja028169
- [356] SUN T R, WANG X, WANG C. Tangent directions of the cusp boundary derived from the simulated soft X-ray image[J]. *Journal of Geophysical Research: Space Physics*, 2021, **126**(3): e2020JA028314. DOI: 10.1029/2020ja028314

Ionospheric Investigations Conducted by Chinese Mainland Scientists in 2020–2021*

LIU Libo^{1,2,3}, LEI Jiuhou⁴, LIU Jing⁵

1. Key Laboratory of Earth and Planetary Physics, Institute of Geology and Geophysics, Chinese Academy of Sciences, Beijing 100029
2. Heilongjiang Mohe National Observatory of Geophysics, Institute of Geology and Geophysics, Chinese Academy of Sciences, Beijing 100029
3. College of Earth and Planetary Sciences, University of the Chinese Academy of Sciences, Beijing 100049
4. Chinese Academy of Sciences Key Laboratory of Geospace Environment, School of Earth and Space Sciences, University of Science and Technology of China, Hefei 230022
5. School of Space Science and Physics, Shandong Key Laboratory of Optical Astronomy and Solar-Terrestrial Environment, Institute of Space Sciences, Shandong University, Weihai 264209

Abstract

In this report, we outline works done by scientists from the Mainland of China on various ionospheric topics after the release of the National Report of China in 2020 on ionospheric research [Liu L and Wan W, 2020] to the Committee on Space Research (COSPAR). More than 180 papers were published in 2020–2021. The current report covers the following topics: ionospheric space weather, ionospheric structures and climatology, ionospheric dynamics and couplings, ionospheric irregularity and scintillation, modeling and data assimilation, and ionosphere and sounding techniques. Planetary ionospheres are included for the first time.

Key words

Ionospheric, Space weather, Planetary ionospheres

1 Ionospheric Space Weather

1.1 Transient Solar Irradiation Events

A solar eclipse transiently shields the solar ionizing radiation falling into the atmosphere of the Earth, providing a natural experiment to study the ionospheric disturbances due to the rapid solar input reduction. Zhang R L *et al.* (2020a) investigated the ionospheric responses to the 21 June 2020 solar eclipse using multi-instrument observations. During the eclipse, the Total Electron

Content (TEC) decreased slightly in the morning at 20°E–70°E and largely in the afternoon at 80°E–150°E. However, TEC depletion did not peak at the maximum obscuration but was close to the southern or northern edges of the running totality. Swarm observations recorded a drop in the electron temperature both in the eclipse region and in the conjugate hemisphere. The combined effect from the electric field, neutral wind, thermal conduction, and interhemispheric photoelectron transport might result in the complicated space and time variations of ionospheric responses to the eclipse (Fig.1).

* Supported by National Natural Science Foundation of China (42030202, 42188101, 42122031)

Received May 27, 2022

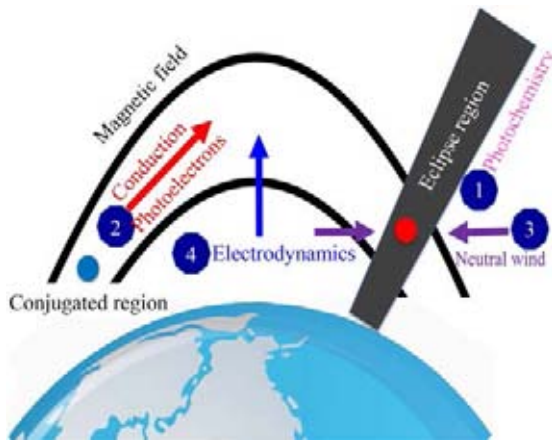


Fig. 1 Related physical processes during the eclipse, including the photochemistry, interhemispheric photoelectron transport, thermal conduction, neutral wind, and electrodynamics. After Zhang R *et al.* (2020a)

Both simulations of Le H J *et al.* (2020) and Dang T *et al.* (2020) studied the responses in the eclipse region and its conjugated region on 21 June 2020, when a solar eclipse passes East Asia. Le H J *et al.* (2020) reported that the TEC responses are not limited to the eclipse region, they also occur in the non-eclipse hemisphere. The variations in the conjugate region were considered to be mainly affected by heat conduction along the geomagnetic field lines, with the modulation of the trans-hemisphere photoelectron heating and global thermospheric wind change. Dang T *et al.* (2020) found a prominent TEC enhancement occurring in the Equatorial Ionization Anomaly (EIA) region, even still in the eclipse shadow. Further control simulations by Dang T *et al.* (2020) indicate the abnormal TEC increase results from eclipse-induced wind perturbations. The ionosphere-thermosphere system is nonlinear and transient in an eclipse, it is dynamically and energetically coupled.

Huang F *et al.* (2020b) further investigated the low-latitude ionospheric responses to the annular solar eclipse. They found that the TEC evidently decreases with the obscuration and in the EIA region in the conjugate hemisphere. The low latitude TEC changes during the eclipse are attributed to the obscuration rate and transport processes.

Solar eclipses can induce large-scale ionospheric and thermospheric disturbances. Sun Y Y *et al.* (2021b) reported a large-scale perturbation of TEC with a wavelength of about 2700 km and a period of about 3.5 hours propagating northwestward over East China after sunset.

It is beyond expectation that the perturbation persists to midnight. As the 21 August 2017 solar eclipse super-sonically approaches the American west coast, Sun Y Y *et al.* (2021a) found that the pre-existing traveling ionospheric disturbance (period about 40 min) gets shorter (period about 10 min), steepening, and breaking eventually. The wave becomes steep and propagates east-southward over Oregon and California. Yan M *et al.* (2021) investigated the characteristics of atmospheric perturbations triggered by solar eclipses. They found that the perturbations in neutral winds and temperature are superimposed on previously excited waves. As the eclipse progresses, the perturbations evolve from high-speed “bow waves” into freely propagating traveling atmospheric disturbances.

Solar flares are another typical type of transient solar irradiation events. Reduced daytime upward $E \times B$ drifts and weakened fountain effects in the equatorial ionosphere have been frequently observed during the initial stage of solar flares. Liu J, Qian L Y *et al.* (2021) explored the origin of this response by simulations of the coupled whole geospace model. They showed that both Prompt Penetration Electric Fields (PPEFs) and internal changes in the wind dynamo are responsible for the reduced upward ion drifts. PPEFs are caused by a reduction in the high-latitude potential as a result of flare-enhanced ionospheric conductance. The reduction of the dynamo-driven electric field was suggested to be a response to the flare enhancement of low-latitude Cowling conductance. Furthermore, Chen J *et al.* (2021a) conducted controlled numerical simulations and found that the wind-dynamo electric field reduction is primarily associated with the decrease of the ratio of the field line-integrated wind-driven currents to the conductance. Besides reducing daytime eastward electric fields, solar flares also increase global daytime currents, inducing westward equatorial electric fields and equatorial counter electrojets in the early morning.

The solar wind has major impacts on the whole geospace, but it is unclear whether the same holds for the transient solar irradiation events, such as solar flares and eclipses. The responses of the ionosphere, thermosphere, and even magnetosphere were investigated.

Liu J, Wang W *et al.* (2021) used a recently developed whole geospace model combined with observations during an X9.3 solar flare event to reveal solar flare effects on magnetospheric dynamics and on the coupling between the magnetosphere and ionosphere

(see Fig.2). A rapid and large increase in flare-induced photoionization of the polar ionospheric E-region reduces the efficiency of mechanical energy conversion in the dayside solar wind–magnetosphere interaction, resulting in less Joule heating of the upper atmosphere, a reconfiguration of magnetosphere convection, and changes in auroral precipitation. They revealed that solar flare effects extend throughout the geospace via electrodynamic coupling.

For the eclipse in the polar region, Chen X *et al.* (2021) showed that the solar eclipse across the arctic introduced significant disturbances in the high-latitudes currents, convections, and auroral activity. Surprisingly, the north polar eclipse impacts the whole geospace system, causing significant auroral disturbances in the unobscured Southern Hemisphere through the electrodynamic coupling of the magnetosphere-ionosphere system.

1.2 Geomagnetic Storms or Substorms

Geomagnetic storm effect on the ionosphere is always

an active research topic in the space physics. Ren D *et al.* (2020) used multiple observations to study the possible contributions from the High-Speed Solar wind (HSS) to the ionosphere during the recovery phase of the August 2018 geomagnetic storm. They found that the HSS could result in about 2-TECU enhancement of TEC at the auroral oval and low latitude. Therefore, the HSS was a possible driver of the ionospheric positive storm during the recovery phase, but the causes for the more than 10 TECU enhancement at low and middle latitudes during the recovery phase are still unknown.

In contrast to the common phenomenon of dayside plasma depletions during the storm recovery phase, Li Q *et al.* (2020) reported that the daytime TECs displayed large enhancements at multiple longitude sectors (Fig.3) during the recovery phase. They revealed that the enhanced upward vertical plasma drifts make an important contribution to the TEC responses, while the drifts could not be driven by the common storm-induced source (PPEF or ionospheric disturbance dynamo).

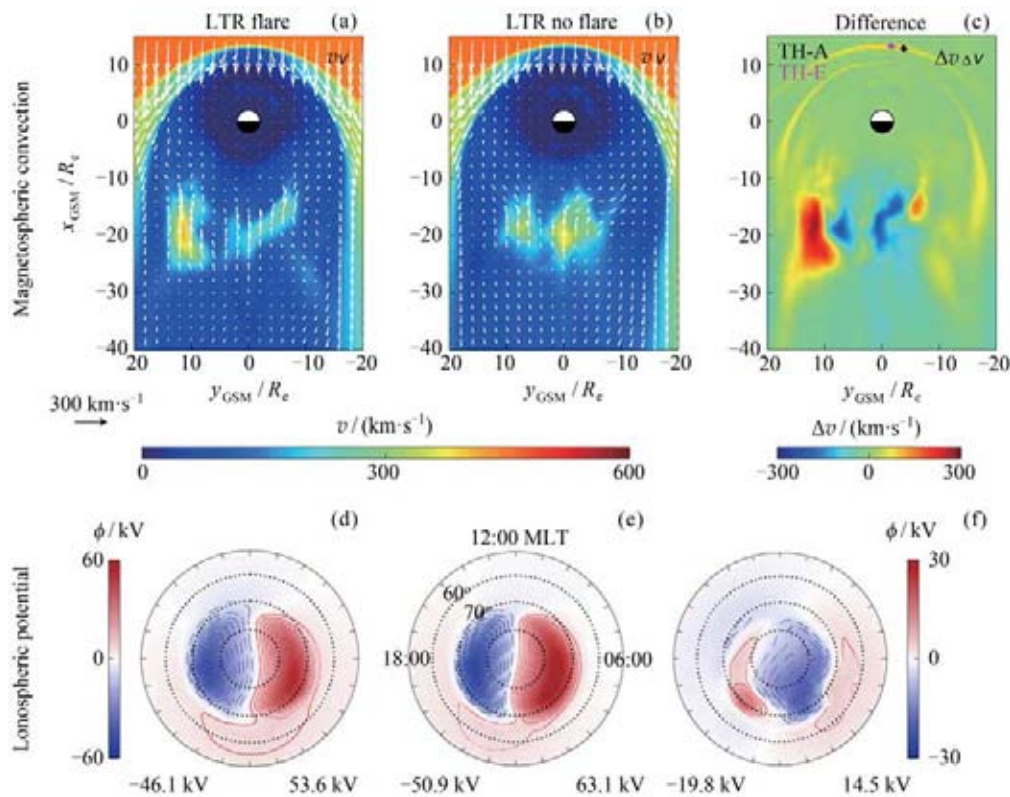


Fig. 2 Comparison of 50 min averages from the coupled geospace model simulations of magnetospheric and ionospheric states with and without the solar flare effects. Projections in GSM coordinates of the simulated magnetospheric convection velocity in the equatorial plane with (a) and without (b) the solar flare effects and their difference (c). High-latitude electric potential in the ionosphere with (d) and without (e) solar flare effects and their difference (f). After Liu J *et al.* (2021)

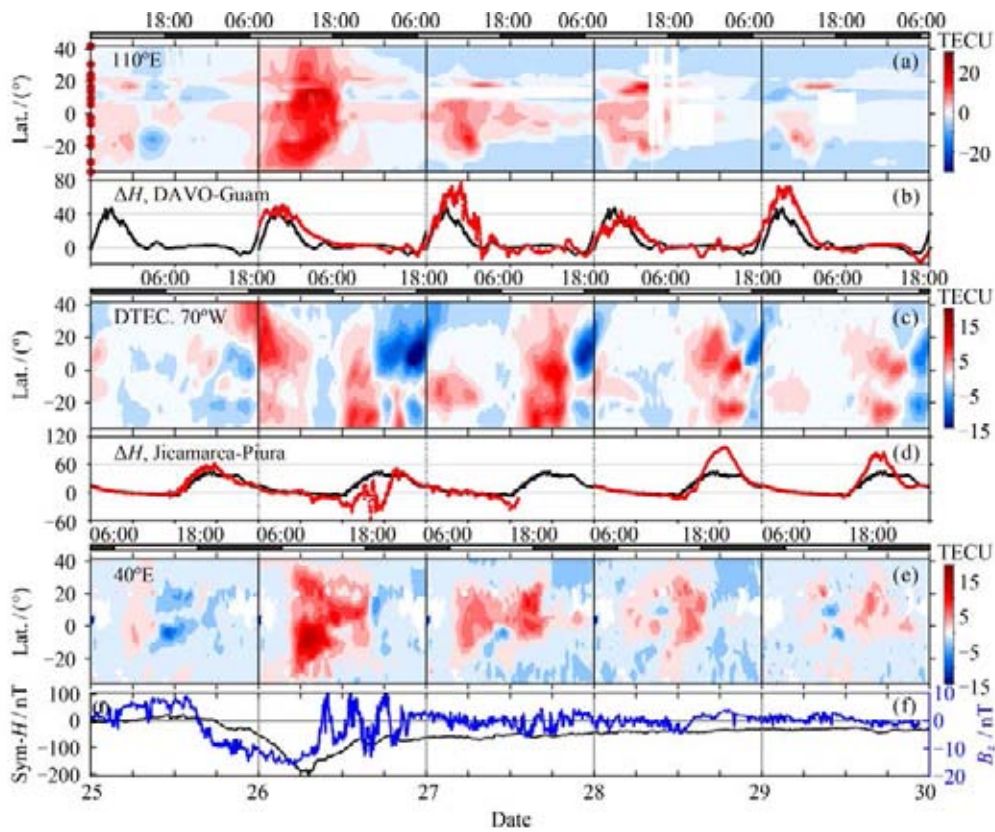


Fig. 3 Differential TEC (DTEC) provided by the Beidou GEO satellite and MIT Haystack Observatory at longitudes of (a) 110° E, (c) 70° W and (e) 40° E. The Equatorial Electrojet (EEJ) strength was calculated from differential geomagnetic horizontal component (ΔH) near 110° E and 70° W. Reorganized after Li Q *et al.* (2020)

The F₃ layer occurs frequently in the daytime equatorial and low latitude ionosphere in summer. Jin Y *et al.* (2021) found the inhibition of F₃ layer events and narrowing differences of virtual heights between the F₃ and F₂ layers in the recovery phase of 14 geomagnetic storms in 2012–2015. The inhibition of the F₃ layer can be an indicator to show how the magnetosphere-ionospheric coupling affects the low and equatorial ionosphere.

Wan X *et al.* (2021b) used Swarm and DMSP satellites to reveal a strip-like plasma density bulge at lower-middle latitudes during the 8–9 September 2017 geomagnetic storm. The strip-like bulge spanned over 150° in longitude but only 1°–5° in latitude. The structure can be identified at all local time sectors and last for more than 48 hours. The dominant ion composition is H⁺/He⁺, rather than O⁺. It is suggested that the combined effects from the plasmaspheric downwelling and disturbance neutral wind were responsible for the formation of strip-like bulges. Jiang C *et al.* (2021a) and Wei L *et al.* (2021a) investigated ionospheric irregularities associated with Spread F and spread Es at low and

middle latitudes by ionosonde, GNSS Receiver Network, and Swarm during the September 2017 storm event.

Zhai C *et al.* (2021a) investigated high-m Ultralow Frequency (ULF) waves during the recovery phase of a geomagnetic storm by using GPS TEC measurements. ULF wave signals in TEC data show high coherence and significant common power in the wavelet coherence and cross wavelet transform analyses with magnetic field radial component data from GOES-15. An automatic identification procedure is developed to identify ULF wave signatures in TEC data. The waves were mainly distributed on the dayside and post dusk sector from 64° to 71° magnetic latitudes.

Wang H *et al.* (2021a) explored the spatial and temporal distributions of ionospheric Electromagnetic Ion Cyclotron (EMIC) waves during magnetic storms from 2014 to 2018. There are obvious Magnetic Local Time (MLT) differences in the peak occurrence frequency of EMIC waves during storm phases. The enhanced solar wind dynamic pressure was favorable for dusk side EMIC waves. With an increased substorm activity, the wave occurrence rate peak shifted from the morning

side to the dusk-pre midnight sector. The storm time EMIC waves occur highest in the South Atlantic Anomaly region, which might be related to the drift shell splitting and the wave propagation effect in the weak magnetic field region.

2 Ionospheric Structures and Climatology

2.1 Spatial Structure

The ionospheric climatology was studied in EIA and mid-latitude trough regions (Liu J, Zhang D *et al.*, 2020b, 2021b; Mo & Zhang 2021; Mo *et al.*, 2021; He S C *et al.*, 2020). With ground-based TEC data in eastern Asian and American sectors from 2000 to 2011, Liu J, Zhang D *et al.* (2020) statistically studied the morphological difference of the EIA in these two sectors. The latitudinal location (Lc) of EIA in the American sector shows an annual variation that is more poleward in summer and more equatorward in winter, while Lc in the eastern Asian sector shows a semiannual variation that is more poleward around equinoxes and more equatorward around solstices. Additionally, in order to reveal the effect of the zonal electric field on the EIA morphological variation, the time delay between the EIA and the EEJ in these sectors is studied using TEC and magnetometer data during 2008–2018 (Liu J, Zhang D *et al.*, 2022). The prevailing seasonal pattern of the occurrence time of the delay most developed northern EIA crest is generally consistent in the two sectors. The solar cycle and longitudinal dependencies are probably due to the combined effects of the electric field, meridional wind, and geomagnetic field configuration. Ma H *et al.* (2021) investigated the longitudinal difference of electron temperature (T_e) at mid-latitudes in the topside ionosphere. The estimation of contributions to the longitudinal difference of T_e indicated that the magnetic declination modulation effect of neutral winds at mid-latitudes changed electron density (N_e), which indirectly changes the longitudinal difference in T_e .

Except for the F_2 layer, the EIA and latitudinal structures in the topside ionosphere are also studied. Li J C *et al.* (2021) used the DMSP F12-F15 measurements to examine EIA occurrence rate at ~ 840 km altitude in the dusk sector during solar maximum years 2000–2002. The results indicated that EIA can still be observed at DMSP heights. The EIA occurrence rate can reach 30%

at specific longitudes in equinox. The PRE of eastward electric field plays a significant role in the EIA formation at 840 km just after sunset, but the occurrence does not exactly represent the characteristics of the PRE of eastward electric field. Tian *et al.* (2021) investigated the latitudinal profile of the ionospheric plasma density, using the Planar Langmuir Probe observations of CHAMP. The occurrence of deep equatorial trough is attributed to $h_m F_2$ uplifted by the neutral winds at later local time. The neutral winds around the magnetic equator are particularly important, especially when the electric field forcing is weak or absent.

By utilizing CHAMP magnetic field measurements during the years 2001–2009, Zhou Y *et al.* (2020) found the night-time zonal ionospheric currents at F-region altitude exhibit an averaged height-integrated current density up to $10 \text{ mA} \cdot \text{m}^{-1}$. The amplitude varies quasi-linearly with $F_{10.7}$. During equinoxes, symmetric current systems at F-region altitude are found in the two hemispheres. After sunset, eastward currents dominate at low latitudes, fading away towards midnight. After midnight regions of eastward currents are observed at mid-latitude.

The ionosphere in the polar region also owns complex structures. Xiong C *et al.* (2020a, 2021) derived Field-Aligned Currents (FACs) from magnetometers onboard the DMSP satellites and GRACE Follow-On (GRACE-FO). They found that the largest displacement is found between the downward R1 current and ion flux peak at the dawn side. The auroral FACs can be classified into two groups: the small-scale ones, shorter than some tens of kilometers, dominated by kinetic Alfvén waves, are quite dynamic; and the large-scale ones, typically larger than 150 km, can be considered as quasi-static and persist longer than 1 min.

2.2 Temporal Variation (Enhancement/Bite-out)

Ionospheric electron density bite-out at noontime often occurs in the equatorial F_2 layer. Chen Y D *et al.* (2020) used ionosonde measurements to investigate the climatology of noontime bite-out. Noontime bite-out of $N_m F_2$ (peak electron density of the F_2 -layer) appears in all months at the dip equator. There is evident north-south asymmetry of the bite-out. However, it does not occur in the northern summer (winter) months at the equatorial north (south), where $N_m F_2$ enhances continuously in the early morning till late afternoon. Chen Y D *et al.* (2021) further investigated the climatology of mid-latitude F_2 -layer bite-out, which was less investigated, using

ionosonde measurements from EIA crest to mid-latitudes in the East Asia sector. The bite-out is more remarkable at solar minimum (maximum) than at solar maximum (minimum) at EIA latitudes (mid-latitudes).

Liu L *et al.* (2020a) presented a case study of the electron density enhancements in the low latitude F region. Common features in the cases demonstrate that N_mF_2 increases at low latitudes are characterized by a descent of the peak height (h_mF_2). As the Qujing radar observed, the electron density shows an increase in the bottom ionosphere and a depression at topside altitudes. It provides evidence that the enhancements in N_mF_2 are associated with a downwelling h_mF_2 . Liu L *et al.* (2020b) conducted a case study of the anomalous daytime enhancements in ionospheric electron density. The enhancements are found in the region around the northern EIA crest. During the anomalous enhancement, the increase in electron density over Qujing is stronger at higher altitudes. Strong longitudinal gradients are present in TEC in the regions during the course of the enhancements.

Kuai J *et al.* (2021) investigated the geomagnetic quiet time variations of the ionosphere at middle and low latitudes. TEC has multiple prominent enhancements in the Asian-Australian and American sectors. TEC depletions also occur repeatedly in the Asian-Australian sector. A mid-latitude band structure appears continuously at all local times in the North American sector. The low-latitude electric fields vary significantly, attributed to the modulation of the notably changing tides.

Chen J. *et al.* (2020b) explored the physical mechanisms responsible for the sunrise enhancement of equatorial upward vertical drifts using model simulations. Numerical experiments reveal that the equatorial sunrise enhancement at solar minimum is primarily driven by the E region zonal wind dynamo at middle latitudes rather than by the local dynamo effect in the equatorial region (Fig.4). Chen J *et al.* (2021b) further explored the physical processes by which the longitude-dependent geomagnetic field drives the longitudinal variations of the sunrise enhancement of the zonal electric fields at the dip equator near the June solstice. Simulations show the longitudinal differences of the sunrise equatorial zonal electric fields are mainly related to the longitudinal variations of $U \times B$ and conductance, which are caused primarily by the direct influence of the longitudinal structures of magnetic field declination and strength.

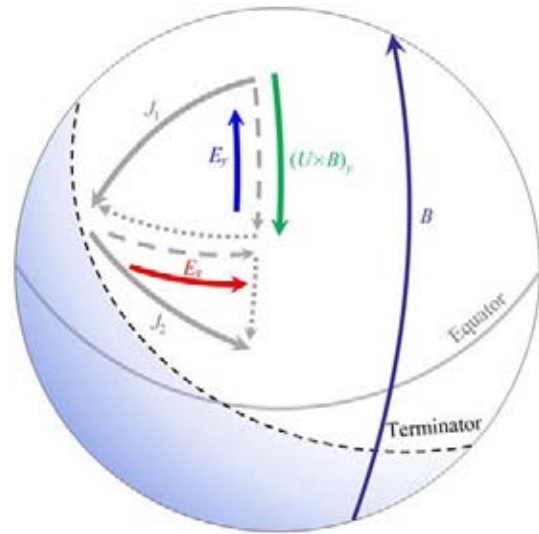


Fig. 4 A schematic diagram of the physical mechanism of eastward enhancement of magnetically zonal electric fields caused by the zonal wind dynamo at middle latitudes near sunrise. After Chen J *et al.* (2020b)

Wang Y H *et al.* (2021) investigated the ionospheric Diurnal Double-Maxima (DDM) patterns over the Asian-Australian sector during 2016-2018 by using the TEC observations from the Beidou GEO satellites. The occurrence rate of DDM was higher around June solstice in both the northern and southern hemispheres and had an anti-correlation with the background TEC.

Yearly and monthly averaging are basic preprocessing methods of ionospheric data to smooth out the cyclic variations. Adopting the two methods, Huang J *et al.* (2020) constructed a linear regression model of the ionospheric dependence on the solar EUV flux, to examine the hysteresis phenomenon (different N_mF_2 EUV relation in the solar rising and declining phase) and long-term trends in the ionosphere. The fundamental cause is the ionospheric sensitivity to the solar EUV irradiance varying with the season. The monthly average method is then suggested to be a better choice for accurate estimation of the hysteresis and long-term trends in the ionosphere.

3 Ionospheric Dynamics and Couplings

3.1 Sudden Stratosphere Warming and Lower Atmospheric Forcing

Based on the observed ionospheric parameters, the iono-

spheric response to SSW or planetary and the ionospheric morphology were studied. These studies mainly focused on: (i) the coupling processes or mechanism from the troposphere to the ionosphere and from high latitude to low latitude or even interhemispheric coupling; (ii) the importance of the planetary wave, solar and lunar tides, and mean wind on the above coupling processes or mechanism; (iii) the morphology of the ionospheric variations, which parameters to control these changes.

Zhang R *et al.* (2020b) used the Communication/Navigation Outage Forecasting System satellite measurements, for the first time, to present the responses of the field-aligned drift during the 2009 Sudden Stratosphere Warming (SSW). The observations (Fig.5) show that the field-aligned drift presents a southward disturbance in the morning sector and a large northward disturbance in the afternoon sector and gradually shifts to later local time during the SSW. Further, this new finding of semidiurnal disturbance in field-aligned drift can well explain the hemispheric differences in the responses of the TEC to the SSW.

Huang F *et al.* (2020a) reported remarkable en-

hancements in the TEC from the Beidou GEO satellites during the quiescent geophysical condition of January 2017 prior to the arrival of the SSW. The daytime TEC increased by 75%–160% around the EIA region and lasted for several days. The meteorological forcing is suggested as the source of the great ionospheric changes before the SSW arrival.

Recent studies showed that there are strong signatures of planetary waves or semidiurnal lunar tides during the SSW. Liu J, Zhang D *et al.*, (2020a) reported simultaneous variations with (about 14.5 days) periods detected in the parameters from the E region to the topside ionosphere. Liu J, Zhang D *et al.* (2021) focused on fundamental vertical coupling processes associated with the latitudinal extent and hemispheric asymmetry of the semilunar tide (M2) signatures using TECs from the American sector. Mo and Zhang (2020a, 2020b) studied the perturbations in the EIA region during the SSWs, using the location of EIA crests derived from GNSS observations and the Equatorial Electrojet (EEJ) estimated by the geomagnetic field. They examined the variations of quasi-6-day and 10-day oscillations in the ionosphere. Tang Q *et al.* (2020) found that f_0E_s during

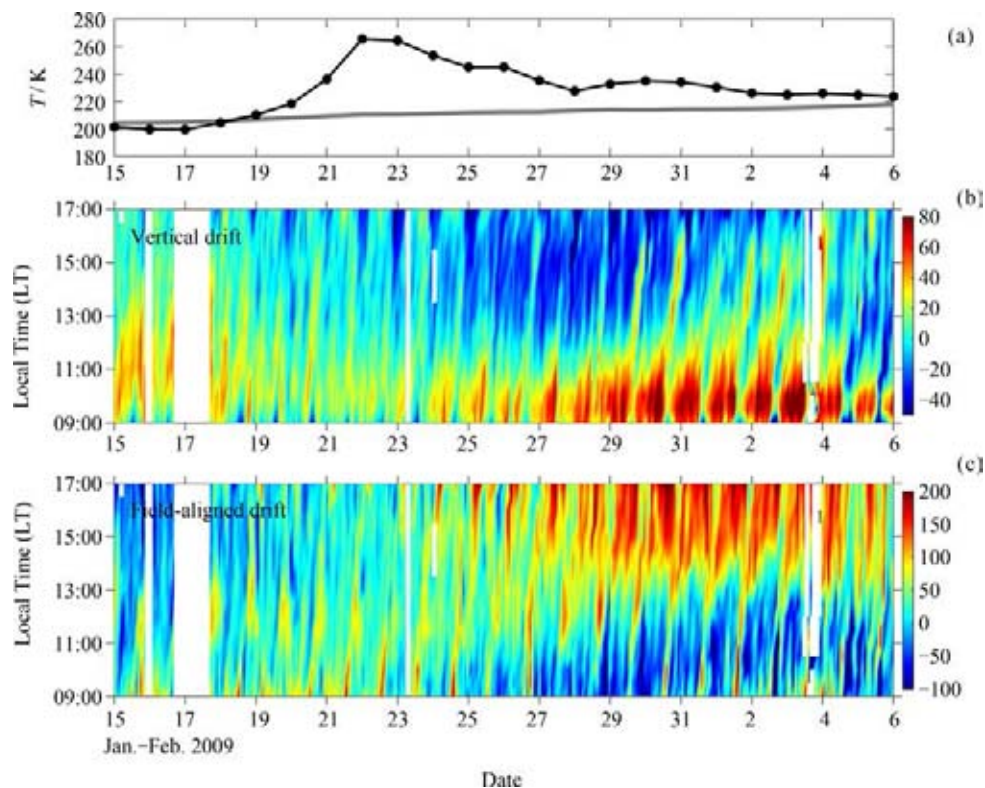


Fig. 5 Stratospheric temperature at 90°N and 10 hPa and the C/NOFS observations of the vertical and field-aligned drifts from 15 January to 6 February 2009. Gray line indicates its 40-year mean. After Zhang R *et al.* (2020b)

two SSW events exhibit noticeably enhanced 14.5-day modulations, which resembles the lunar semimonthly period. The observational evidence reveals that the semimonthly lunar period of 14.5-day can be a contributing factor to the disturbance of Es layers during SSW events.

Li N *et al.* (2020, 2021) investigated the responses of the ionosphere and the neutral winds in the mesospheric and lower thermospheric region to two SSWs, respectively. The amplitudes of solar and lunar semidiurnal tides in winds are greatly enhanced during the SSW. Tang Q *et al.* (2021b) reported a later lunar tide modulation in the summer hemisphere than that in the winter hemisphere, which can be explained by the planetary wave penetrating across the winter to summer hemisphere during SSW.

Yu T *et al.* (2020) and Ye H L *et al.* (2021) investigated the F layer scintillation related to ionospheric irregularities during SSW events by using the Constellation Observing System for Meteorology, Ionosphere, and Climate Radio Occultation (COSMIC) data. They reported that the occurrence frequency and altitude of ionospheric F-layer scintillation were obviously suppressed over the American sector during SSW periods. Ye *et al.* (2021) found that an SSW event under low solar activity can affect the generation of ionospheric irregularities.

In addition, other lower atmospheric activities can also introduce ionospheric disturbances. Liu Y *et al.* (2020a) explored the responses of ionosphere on quasi-6-day wave events from the lower atmosphere at low and middle latitudes during 2014–2015. Zhou X *et al.* (2021b) investigated the responses of atmospheric carbon dioxide (CO₂) density to geomagnetic secular variation using the WACCM-X. Their simulation results demonstrate that the impact of geomagnetic variation on atmospheric CO₂ distribution is noticeable on a time scale of decades. Based on the TEC data, Liu J, Wang W *et al.* (2020) found some latitudinal and longitudinal characteristics of ionospheric terdiurnal tide, and suggested these variations are likely related to the nonlinear interaction between diurnal and semidiurnal tides.

3.2 Dynamics

The equatorial electrojet or zonal electric field occasionally becomes westward in the afternoon sector during quiet times. Zhang R *et al.* (2020c) present the first analysis of the dependence of the afternoon downward

plasma drifts on the season, longitude, solar activity, and lunar phase using the ROCSAT-1 observations during 1999–2004. There are about 20% of downward plasma drifts at 13:00–17:00 LT. The downward plasma drift occurs most frequently around the full moon in the afternoon sector. The geomagnetic declination induces the hemispheric differences in the dynamo current in the conjugate regions and controls the occurrence of the westward electric fields.

Wang H *et al.* (2020) investigated the diurnal and longitudinal patterns of EEJ using data from CHAMP satellite and simulations from TIEGCM. The tides were important in causing the later local time occurrence of the EEJ peak in the Peruvian sector, and they favored the occurrence of the morning Counter Electrojet (CEJ) in the frame of the IGRF. The difference in the EEJ peak intensity between the Peruvian and Indian stations was enhanced due to the tidal effect.

Li W *et al.* (2020) performed a statistical study on the Ionospheric Nighttime Enhancement (INE) at the mid-latitude using observation data from ionosondes, FPI, and the Jet Propulsion Laboratory TEC. Fig.6 displays the distribution of INE events with different h_mF_2 variation pattern. It can be seen that h_mF_2 could both rise and decline during winter INE. This feature is different from the summer INE which h_mF_2 mostly presents increased. Changes in h_mF_2 had no significant effect on the amplitude and duration of winter INE. The downward transport of plasma causes electron density to accumulate near the peak height of F₂ layer, resulting in the thinning of ionospheric plate and the formation of INE. This downward transport could imply the importance of ionosphere-plasmasphere coupling to ionospheric nighttime behavior.

Chen J *et al.* (2020a) explored a strong anticorrelation between temporal variations of field-aligned upward plasma velocity ($V_{i||}$) and field-perpendicular poleward plasma drift ($V_{i\perp N}$) in midlatitude F₂ region using numerical simulations. The anticorrelation between the diurnal variations of $V_{i||}$ and $V_{i\perp N}$ is associated with the neutral wind dynamo. The anticorrelation between short-term temporal disturbances of $V_{i||}$ and $V_{i\perp N}$ is mainly caused by ion drag, in response to high-latitude convection electric field force. Furthermore, ambipolar diffusion plays a significant role in modulating the relationship between $V_{i||}$ and $V_{i\perp N}$.

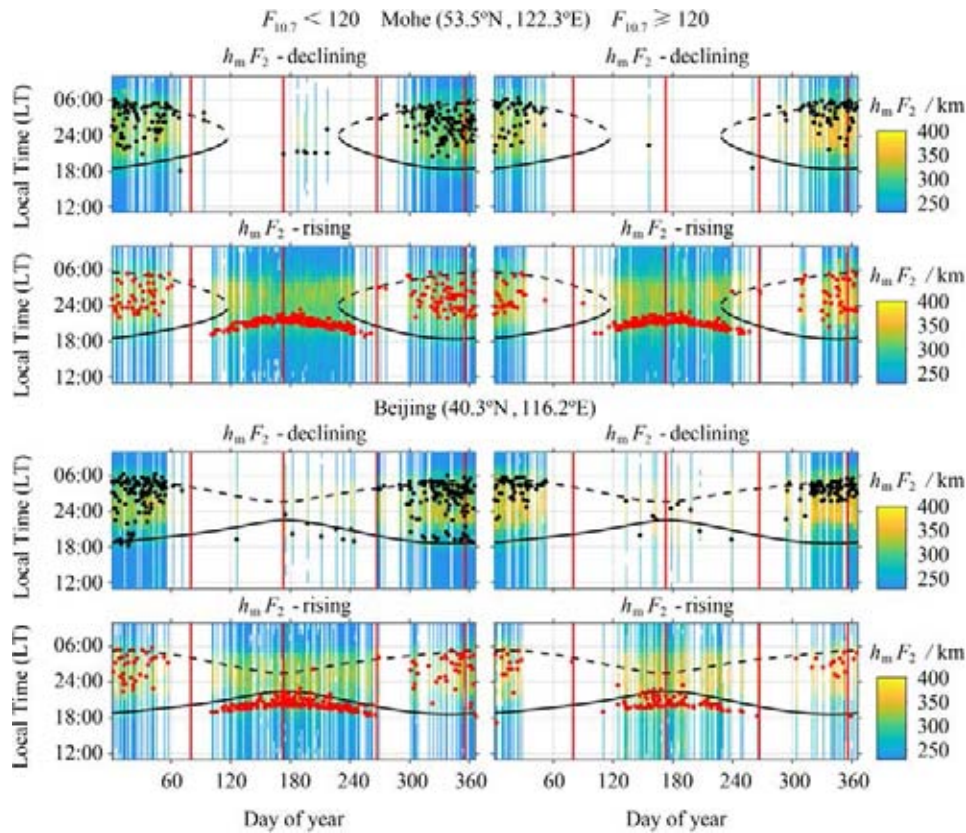


Fig. 6 $h_m F_2$ as functions of Day of Year (DOY) and Local Time (LT) at Mohe and Beijing. The black solid (dashed) lines plot the sunset (sunrise) terminator at 400 km. The vertical red lines indicate the equinox and solstice days. After Li W B *et al.* (2020)

Jiang C *et al.* (2020a) investigated midlatitude peaks in TEC using the model simulations to explore its possible mechanisms driving. They found that the latitudinal variations of the downwards-moving plasma ambipolar diffusive flux can play a significant role in forming nighttime midlatitude ionospheric peaks and their latitudinal structures. Cai Y *et al.* (2021) reported the characteristics of the topside ionospheric O^+ diffusive flux using incoherent scatter radar observations at Millstone Hill for solar minimum from 1970 to 2018. The diffusive flux partially characterizes plasma mass exchange between the upper and lower part of the topside ionosphere through diffusion and sometimes serves as upper boundary conditions for ionosphere-thermosphere models.

To investigate day-to-day variability of equatorial vertical drift under quiet-time conditions, Zhou X *et al.* (2020) analyzed ROCSAT-1 observations and performed simulations using the WACCM-X model. The day-to-day variability of equatorial vertical drift had a strong dependence on local time, largest around dawn and dusk. Modeling results revealed that the day-to-day

variability of dawn drift is larger during solar minimum than maximum condition. Short-term variability of E-region winds is found to be the primary driver to produce the day-to-day variability of dawn drift, and F-region winds play a secondary role. Ionospheric conductivities could modulate the drift variability response to E-region wind variability and thus affect the strength of day-to-day variability of dawn drift and determine its seasonal and longitudinal variations.

Zhou X *et al.* (2021a) examined the day-to-day variability of $N_m F_2$ from both observational and modeling perspectives. The coupled whole atmospheric model reproduces the observed local-time dependence of the day-to-day variability of $N_m F_2$ in 2012, which was large by night and small by day, and favorably agrees with the daytime day-to-day variability in 2009. However, the stand-alone model without considering the lower atmospheric variability does not reproduce the observed features, especially under solar minimum conditions and during the nighttime, possibly due to the absence of day-to-day changes in the lower atmosphere in the

simulations. The effects of lower atmospheric perturbations on the ionospheric day-to-day variability were proposed to be more important in solar minimum.

Wang H and Lühr H (2021) investigated the effects of solar illumination and the substorm process on the auroral electrojets using 10 years of CHAMP high-resolution magnetic field data. The eastward electrojet was found to be proportional to the ionospheric conductance over the whole day. More notably, a stronger westward current was detected in times of lower flux tube-integrated conductance in both hemispheres. The results provide observational evidence of the increased efficiency of the Cowling channel in the nighttime during substorm periods and contribute to our understanding of the formation mechanism of the auroral electrojet.

By using 4 years of CHAMP zonal wind observations and model simulations, Wang H *et al.* (2021b) investigated the longitudinal and seasonal variations of thermospheric superrotation at geomagnetic equator. The superrotation shows longitudinal structures. The superrotation is stronger in December than in June solstice, and stronger in March than in September equinox.

3.3 Lithosphere-ionosphere Coupling

The earthquakes could induce ionospheric electron density disturbance. Subsequently the electromagnetic field observed on the ground and Low Earth Orbit satellite could change due to the ionospheric disturbance. Zhao S *et al.* (2020a) constructed a full-wave model to simulate the influence of the ionospheric disturbance on the electromagnetic field. The result shows the electromagnetic field at the satellite altitude changes obviously when the wave encounters an ionospheric disturbance. The electromagnetic field increases with the amplitude and scale of the ionospheric disturbance. However, the influence of the ionospheric F layer disturbance just has a local effect on the electromagnetic field.

Chen C H *et al.* (2021) reported a novel system for monitoring vibrations and perturbations (MVP) in the LAI (MVP-LAI) (<http://geostation.top/>). The MVP-LAI system was established in the countryside of Leshan City, Sichuan Province, China, at the end of 2021. Fourteen different types of instruments were set within an area of 50 m × 50 m. The VHF coherent scattering radar and Meteor radar were installed about 20 km away from the system to avoid interference. These instruments routinely monitor the changes in the geophysical parameters with short sampling intervals, available for

capturing waves propagating from the subsurface to the ionosphere (Fig.7).

Using the TEC data, Hao *et al.* (2021), investigated the seismo-ionospheric disturbances after the 2011 Tohoku earthquake. The two-dimensional structure of large-scale TEC variations caused by far-field Rayleigh waves was revealed. The zonal band structures have wave fronts oriented in the northwest-southeast direction at mid-latitude, and then rotate to east-west at lower latitudes. The rotation is expected due to the neutral-ion coupling, which effectively drives plasma motion along geomagnetic field lines in favor of southward propagation of the ionospheric disturbances.

Tariq *et al.* (2021) analyzed Pre-Earthquake Ionospheric Anomalies (PEIAs) with TEC data within seismogenic zones of three earthquakes from GPS stations in Pakistani regions. Zhao S *et al.* (2020b) studied how these ionospheric disturbances at different altitudes affect the VLF signals observed by ground and LEO satellites through joint observation from ground receivers and satellite.

The combination of the observations with the machine learning technique is widely applied to explore the earthquake effect on the ionosphere. Jointly with the Swarm satellite earthquake research team of INGV, Italy, the study proposes a deep learning model called SafeNet for identifying pre-earthquake electromagnetic anomaly signals based on the ESA Swarm satellite three-component magnetic field, Ne and other observations from April 2014 to April 2020 (Xiong P *et al.*, 2020, 2021b). Xiong P *et al.* (2021a) proposed a deep learning framework called SeqNetQuake, which combines one-dimensional convolutional layer and BiLSTM (bi-directional long and short-term memory layer) models to obtain classification results through fully connected layers and Softmax classifier, which improves the accuracy and reduces the false alarm rate of the system.

The linkage between the earthquake and VLF/ULF wave activity was also explored. For instance, Zhao S *et al.* (2020c) showed that SNR (Signal to Noise ratio) over the epicenter of the Yushu earthquake especially in the southwestern region decreased before the main shock, and a TEC anomaly accompanied, which implies that the decrease in SNR might be caused by the enhancement of TEC. Ouyang *et al.* (2020) examined the relationship between earthquakes and ULF wave activity in the nighttime ionosphere based on the electric field data in the DC/ULF range observed by the DEMETER

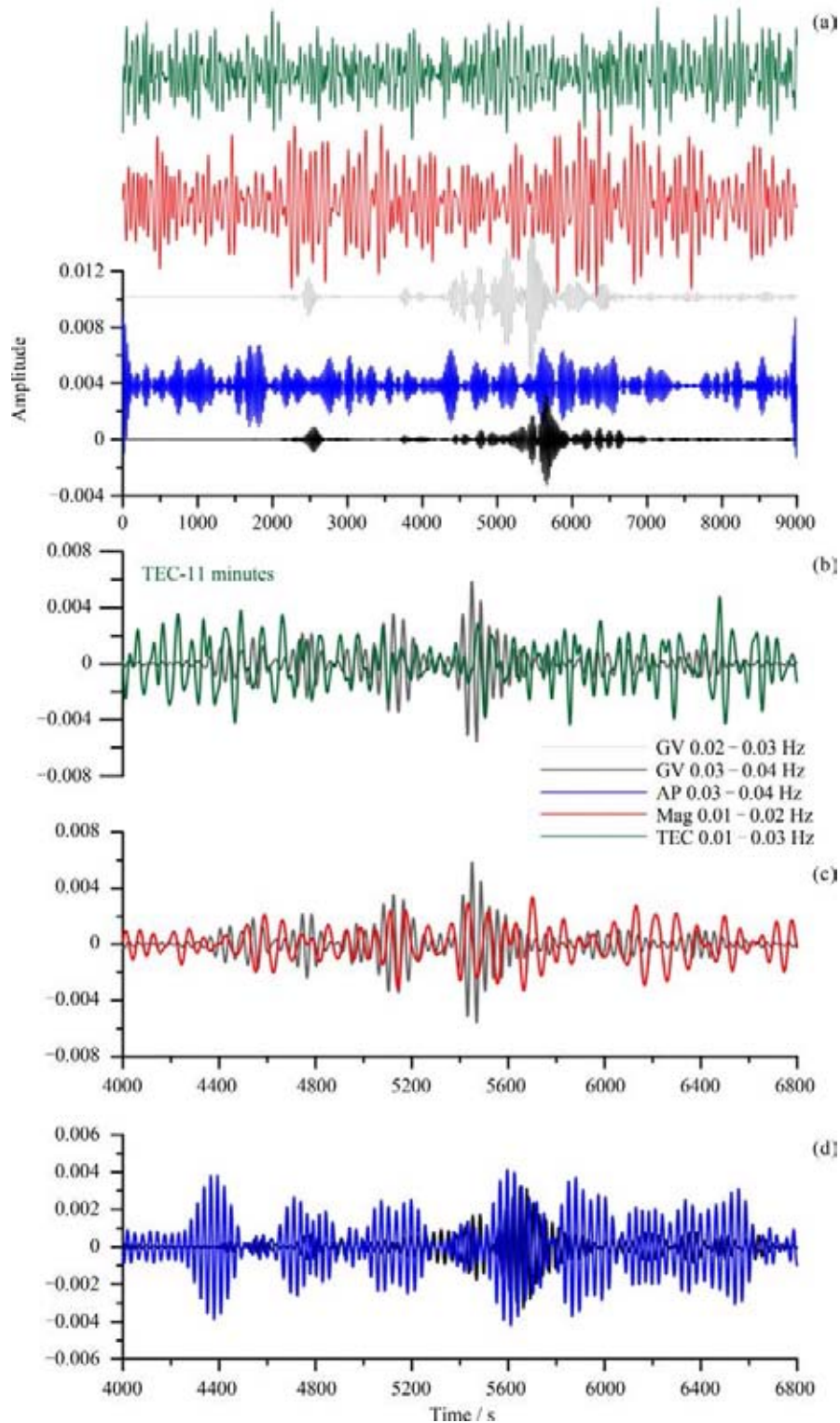


Fig. 7 Filtered data associated with the arrival of seismic waves from 20:00 LT to 23:30 LT on 10 February 2021. See the details in Chen C H *et al.* (2021)

satellite over an about 5.5-year period from May 2005 to November 2010. Moreover, on the basis of CSES, the ionospheric perturbations in VLF transmitters were in-

vestigated around the 2018 Ms 6.9 Indonesia earthquake, combined with the multi parameters of the plasma and electromagnetic field (Zhang X *et al.*, 2020b).

There are plenty of the Quasiperiodic waves (QP) in the ELF/VLF range. Zhima *et al.*, (2021) found the QP waves accompanied by simultaneous energetic electron precipitations in the high-latitude ionosphere from the observations of the sun-synchronous circular orbit satellite CSES. The new features of QP waves observed by CSES are the well-pronounced rising-tone structures and very short repetition periods which are not often reported by previous studies.

3.4 Solar Wind-magnetosphere-polar Ionosphere Coupling

In low atmosphere, hurricanes are destructive due to their great size, strong spiral winds with shears, and intense rain/precipitation (Fig.8). However, disturbances re-

sembling hurricanes have not been detected in the upper atmosphere. Zhang Q H *et al.* (2021) reported a long-lasting space hurricane in the polar ionosphere and magnetosphere during low solar and otherwise low geomagnetic activity. This hurricane shows strong circular horizontal plasma flow with shears, a nearly zero-flow center, and a coincident cyclone-shaped aurora caused by strong electron precipitation associated with intense upward magnetic field-aligned currents.

The hurricane imparted large energy and momentum deposition into the ionosphere despite otherwise extremely quiet conditions. A distinct class of aurora, called Transpolar Auroral Arc (TPA) appears in the extremely high-latitude ionosphere of the Earth when IMF is northward. Zhang Q

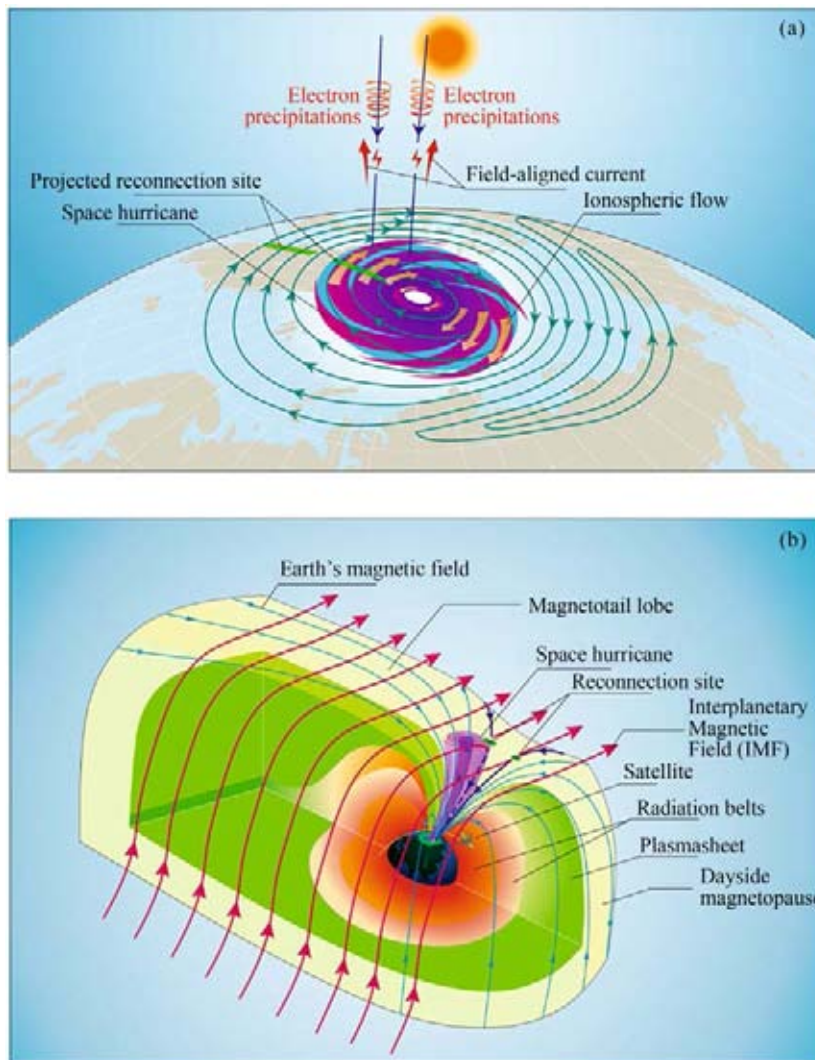


Fig. 8 (a) Schematic of a space hurricane in the northern polar ionosphere. The magenta cyclone-shaped auroral spot with brown thick arrows of circular ionospheric flows represents the space hurricane. (b) The 3D magnetosphere when a space hurricane happened. After Zhang Q H *et al.* (2021)

H *et al.* (2020) report a mechanism identified from multiple-instrument observations of unusually bright, multiple TPAs and simulations from a high-resolution 3D global MHD model. The observations and simulations show an excellent agreement and reveal that these multiple TPAs were generated by precipitating energetic magnetospheric electrons within FAC sheets. These FAC sheets are generated by multiple-flow shear sheets in both the magnetospheric boundary produced by Kelvin-Helmholtz instability between supersonic solar wind flow and magnetosphere plasma, and the plasma sheet generated by the interactions between the enhanced earthward plasma flows from the distant tail (less than $-100 R_e$) and the enhanced tailward flows from the near tail (about $-20 R_e$).

Liu Y Y *et al.* (2021) analyzed the evolution characteristics of the two auroras by using the observation data of the high-resolution All-Sky Imagers at the Yellow River Station, together with solar wind and IMF observations. PMAFs mainly occurred in the poleward of dayside auroral oval equatorial boundary, were distributed along the east-west direction, and extended to the high latitude after brightening. Throat auroras were distributed along the north-south direction, which extended to low latitude from equatorward of the discrete auroral oval and moved to the west after brightening, usually existed near the PMAFs. The formation processes of the two auroral events are relatively independent, and there may be no mutual triggering relationship.

Yang Z *et al.* (2020) explored the responses of cross-polar cap potential (ϕ_{pc}) to the Solar Wind (SW) density under northward IMF by using the three-dimensional magnetohydrodynamic model. Simulation results show that ϕ_{pc} has a complicated response to the SW density depending on the magnitude of IMF. For weak IMF, ϕ_{pc} increases linearly due to the enhancement of the viscously-induced electric field in the equatorial magnetosphere. The ϕ_{pc} may be insensitive to SW density increasing at moderate or intense IMF B_z under large-density conditions. The different behavior of SW density in regulating ϕ_{pc} is mainly due to the competing effects that originated from viscous interaction and magnetic reconnection.

The energy deposition or the momentum changes associated with geomagnetic activity can further alter the status of the upper atmosphere and the ionosphere. Ma Y Z *et al.* (2021) showed all-sky imager and Poker Flat Advanced Modular Incoherent Scatter Radar observa-

tions of two surge events to investigate the relationship between the surge and ionospheric flows that likely have polar cap origin. By using DMSP satellite observations from 2010–2013, Ma Y Z *et al.* (2020) performed a statistical study of ion upflow and FACs in the topside ionosphere of both hemispheres for magnetic quiet and disturbed times. Ion upflow occurrence shows a dawn–dusk asymmetry distribution that matches well with the Region 1 FACs.

Based on the observations from SuperDARN radar and DMSP satellites, Wang Z W *et al.* (2021) found that short-term sunward ionospheric flow bursts in the poleward of the cusp showed one-to-one correspondence with the sudden increase of the IMF B_z , and a cusp auroral spot, together with an inverse ion energy dispersion, was observed in association with one of the flow bursts. They suggest that the lobe reconnections can be triggered by a sudden increase of the IMF B_z component.

Zhang K *et al.* (2021a) investigated the dynamic evolution of the double Tongue of Ionization (TOI) into a single TOI at 400 km altitude during the geomagnetic storm of 7 September 2015 by using DMSP observations and model simulations. The double TOIs occurred in the presence of increased southward IMF B_z and weak positive IMF B_y , and transit to single TOI due to both the northward turning of IMF B_z and duskward turning of IMF B_y . Further studies showed that the equatorial thermospheric wind jet can be formed in response to the temporal oscillation of IMF B_z (Zhang K *et al.*, 2021b), and the nighttime poleward wind shows a remarkable UT variation during the Subauroral Polarization Streams (SAPS) period (Zhang K *et al.*, 2021c). Also, the Disturbance Dynamo Electric Field (DDEF) induced by SAPS can modulate the variations of the EEJ and CEJ (Zhang K *et al.*, 2021d).

4 Ionospheric Irregularity and Scintillation

Through the interactions between the magnetosphere-ionosphere/thermosphere, a large number of ionospheric plasma irregularities and waves are usually generated, which often produce the ionospheric scintillations and Geomagnetically Induced Current (GIC) and more.

4.1 Es

Based on comprehensive observation measurements,

our understanding on the plasma irregularity of sporadic-E layer at the middle and high latitude has fruitfully extended. Sun W J *et al.* (2020a, 2021a, 2021b) investigated the occurrence, morphology and dynamics of large-scale strong Es structures in the East/Southeast Asian sector, and proposed a High temporal Resolution Rate-of-TEC Index (HR-ROTI) to characterize strong Es irregularity structures. The statistical results of large-scale strong Es structures are shown in Fig.9. It is found that the large-scale strong Es structures mainly occur during summer months, with dominant horizontal azimuth in the east-west and northwest-southeast directions and dimensions of 1000–3000 km along the elongation. They predominantly drift southwestward at the speed of 30–210 m·s⁻¹. The main onset region for the large-scale

Es structures is identified around 20°N–45°N and 100°E–125°E. It is surmised that gravity waves could play an important role in the generation of large-scale Es structures.

The climatology of the Es occurrence over China and its underlying mechanisms were recently revisited (Tang Q *et al.*, 2021a, 2021c). It was demonstrated that planetary waves in the MLT region cannot fully explain the seasonal variations of the periodic disturbance of Es. Solar and geomagnetic activities can also result in periodic variations of the Es. Further numerical simulations suggested that the turbopause plays an important role in forming low-altitude Es layer in the middle and low latitude region.

Xu T *et al.* (2020) presented a physical model of Es

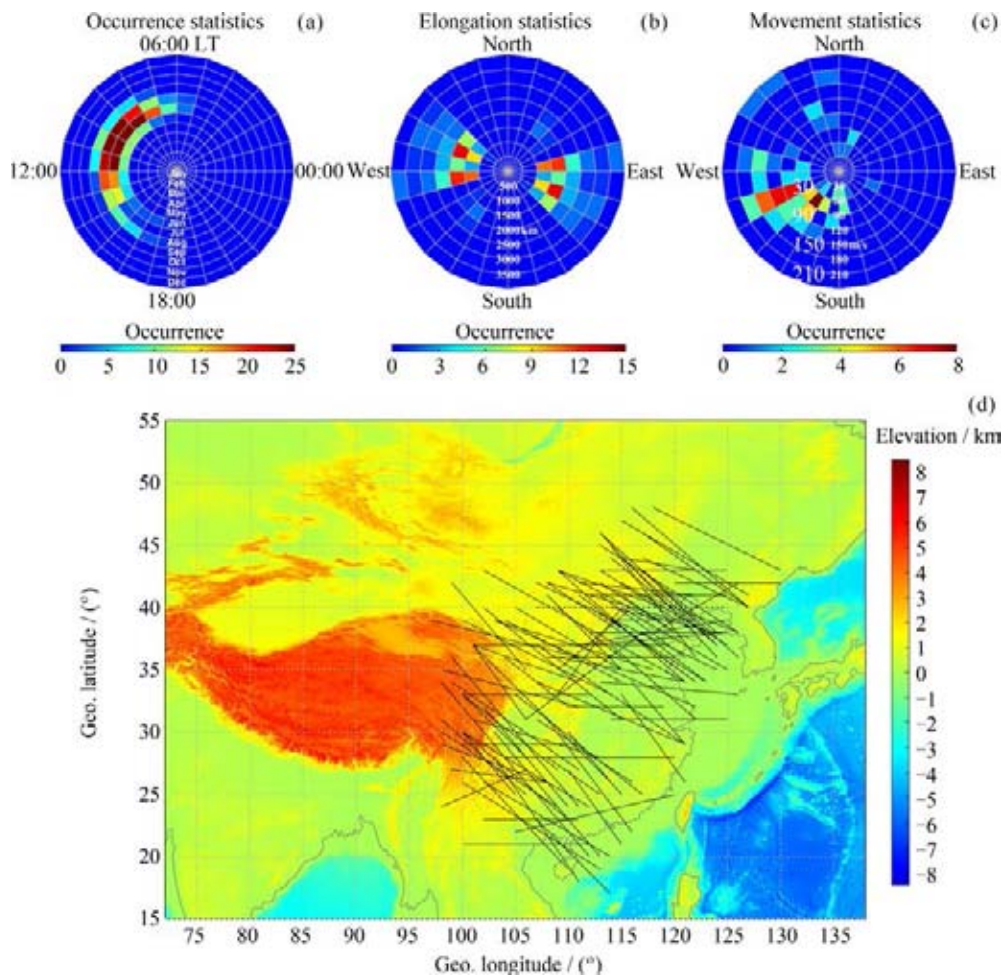


Fig. 9 Occurrence of large-scale strong Es structures during 2017–2019 binned into (a) local time and month, (b) the elongation azimuth and dimension, and (c) the horizontal drifting direction and average velocity. (d) The onset locations of all the cases of large-scale Es structures observed during 2017–2019 on a map of topography elevation height. Each black solid line illustrates the location, dimension and elongating direction at the onset of each large-scale Es case. After Sun W J *et al.* (2021a)

layers at middle latitudes based on wind shear theory to re-examine the influence of seismogenic electric fields on Es layers. The results show that zonal electric fields of several $\text{mV}\cdot\text{m}^{-1}$ can influence the formation of higher Es layers. However, by comparing the altitude variation profiles of vertical ion convergence intensity derived from HWM14 model and Es-layer parameters obtained from COSMIC, Qiu L H *et al.* (2021a) showed that their maxima appeared at different altitudes. The Es traces and the wind shear nodes are not completely overlapped in the vertical direction (Qiu L H *et al.*, 2021b). Further investigation is required on the formation of Es associated with wind shear.

It has been widely proposed that Es layers play an important role in the formation of Sporadic Sodium Layers (SSL), but detailed studies of their dynamic process and evolution are still lacking. To clarify the dynamic properties of Es/SSL, an SSL associated with a strong Es layer was studied by Chen X C *et al.* (2021), based on measurements of sodium density, atmospheric wind field, and temperature from the three-frequency Sodium resonance fluorescence Doppler lidar at Zhongshan. The temporal/spatial sodium density variations strongly indicate that the formation and perturbation of SSLs are related to the evolution of Es layers due to varied electric fields and atmospheric gravity waves, while it is advected by the horizontal wind.

Wang J *et al.* (2021a) analyzed the response of the Es to the annular solar eclipse over Eastern China on 21 June 2020. The Es can be multilayered during the solar eclipse, which is mainly distributed at much higher altitudes (130–190 km). Moreover, it is interesting to find that the Es layer is being uplifted significantly over the center path of the moon shadow near the maximum obscuration of the solar eclipse. The results suggested that the occurrence of the small-scaled Atmospheric Gravity Waves (AGWs) and the transport process mainly control the Es behaviors over eastern China during the 2020 annular solar eclipse.

Wang Y *et al.* (2021b) carried out a comprehensive study of the polar cap Es layer associated with GPS TEC variations and scintillations with multiple measurements at Resolute, Canada. According to the joint-observations, the polar cap Es layer is a thin patch-structure with variously high electron density, which is gradually developing into the lower E-region and horizontally extending >200 km. The TEC variations pro-

duced by the polar cap Es layer are pulse-like enhancements, followed by smaller but rapid TEC perturbations.

4.2 TID

MSTIDs at middle latitudes are widely studied, but their sources and their causes are not fully understood. Wang J *et al.* (2021b) analyzed the far-field ionospheric disturbances related to the 2011 tsunamigenic earthquake using the oblique-incidence ionosonde detection network located in North China. T_h MSTIDs induced by the tsunamigenic earthquake could transport more than 2000 km westward away from the epicenter and be captured by the network located in North China. The far-field inland observations of the ionospheric disturbances illustrated how efficiently wave energy could be transported and suggested the remote sensing ability of the ionosonde network for the ionospheric disturbances.

Deng Z X *et al.* (2021) investigated the mechanism of MSTID triggering Spread-F in the low latitude using ionosonde and GNSS-TEC measurements. Although it is widely acknowledged that MSTID is normally accompanied by polarization electric fields which can trigger Rayleigh-Taylor (RT) instability and consequently excite Spread-F, the statistical analysis of 13 months of MSTID and spread-F occurrence showed that there is an inverse seasonal occurrence rate between MSTID and spread-F. Thus, only MSTID with specific properties can trigger spread-F occurrence. The MSTID at night has a high possibility to trigger Spread-F.

Huang F *et al.* (2021a) investigated the variations and relationships of ionospheric irregularities and MSTIDs simultaneously at mid-latitudes over central China based on high-fidelity observations of the TEC from a Beidou GEO satellite during 2016–2017. The ionospheric irregularities and MSTIDs both had evident seasonal and temporal variations. The nighttime ionospheric irregularities were generally associated with MSTIDs after sunset but the situations during the daytime were different. Using TEC data from a chain of GNSS receivers along about 110°E during 2016–2019, Hu L H *et al.* (2021) investigated the local time, seasonal and latitudinal occurrence characteristics of periodic TEC perturbation associated with MSTIDs.

Chen G. *et al.* (2020) investigated the propagation features of three groups of multiple LSTIDs on 22 June 2015 over China using the TEC data. The observations imply that the propagation of mid- and low-latitude

LSTIDs is more complicated than previously reported.

Whereas there have been many studies on the simultaneous occurrence of E region QP echoes and F region MSTIDs at middle latitudes, there are few events reported at low latitudes. Xie H *et al.* (2020a) present simultaneous observations of nighttime E region QP echoes and Es layers from the VHF radar and digisonde collocated at Fuke, and MSTIDs derived from GNSS TEC measurements at low latitudes. The QP echoes in radar height-time intensity maps were clustered into groups, coinciding with the periods of MSTIDs and strong Es layer (Fig.10). The MSTIDs had phase fronts elongating in the northwest-southeast direction and propagated southwestward from middle to low latitudes. Similar to the propagation direction of MSTIDs, the low-latitude Es layers also propagated southwestward. For the QP echoing clusters, a westward drift was seen from the radar multi-beam observations. The Doppler

velocities of QP echoes show beam dependence, with significantly enhanced positive values in the westernmost beam. When the MSTIDs coming from middle latitudes approach low latitudes, the polarization electric fields associated with the MSTIDs could modulate the E region plasma instability producing QP echoes at low latitudes through the E-F region electrodynamic coupling.

4.3 EPBs

As summarized in Li *et al.* (2021), the current knowledge of EPBs and ionospheric scintillations in the East and Southeast Asia, including their generation mechanism and occurrence morphology, has been greatly advanced. The current observing capabilities, future new facilities and campaign observations in the East and Southeast Asia provided a good opportunity to address the short-term variability of EPBs and ionospheric scintillations.

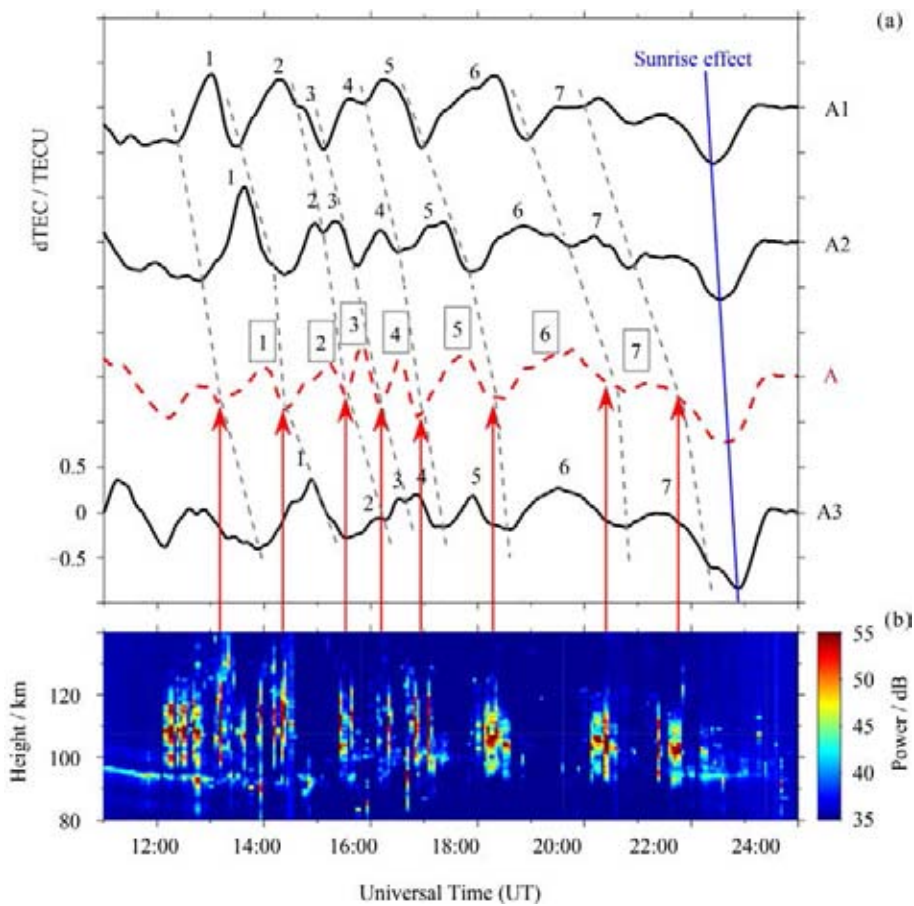


Fig. 10 (a) Black solid lines show the Beidou TEC perturbations from fixed IPPs. Red dashed line shows the estimated TEC perturbations in the region connected with radar E region by field lines. (b) HTI map of backscatter echoes for beam 4 of the Fuke VHF radar. After Xie H *et al.* (2020a)

Ionospheric F region bottom-type irregularity layers and plasma plumes observed by Sanya VHF radar during the equinoctial months of 2011–2018 show different occurrence pattern with that of magnetic equator. No clear correlation is found between the occurrences of bottom-type irregularity layer and plasma plume at low latitude. During the days when bottom-type irregularity layers occur, the $h'F$ was relatively lower. It is surmised that besides gravity waves, the background F layer height could, oppositely, play a negative role in the generation of bottom-type irregularity layer at low latitude (Hu L *et al.*, 2020).

The occurrences of EPB irregularities over Asian and American sectors often show different behavior due to significantly different geometry of the geomagnetic field. By using the GPS TEC observations over equatorial and low latitudes sectors of Asia and America during 1997–2018, Zhao X K *et al.* (2021a) presented a comparative study of long-term occurrences of EPB kilometer-scale irregularities over the two longitude sectors. Seasonal variations, solar activity dependencies, latitudinal variation, and magnetic activity dependencies of kilometer-scale irregularity occurrence rates were found to differ significantly between the two sectors. The results will help in designing experiments to understand better the generation of EPB irregularities under the future international meridian circle project.

Xie H Y *et al.* (2020b) conducted experiments to observe F-region echoes at daytime by using the Sanya VHF radar, showing that the daytime F-region echoing structures could appear at any time. Radar interferometry and ICON satellite in situ results reveal that these daytime echoes were from field-aligned irregularities, which are shown as plume structures in the topside ionosphere. The results indicate that the EPBs could maintain their vertically elongated structures and meter-scale irregularities at F-region topside for much longer time than previously thought and have important implications for understanding their dynamics.

Ajith *et al.* (2020) reported a case of intense and periodic EPBs that occurred during 8–9 April 2013 at Kototabang, Indonesia. The periodic EPBs separated by about 200–250 km were initiated before sunset. The presunset onset and development of these periodic EPBs were discussed in the light of the Gravity Waves (GWs) excited in connection with the deep convection due to the Tropical Cyclone (TC) Victoria. The GW signatures

at ionospheric altitudes were also observed from the Ionosonde observations over magnetic equator, and medium-scale GWs were observed from the GPS-TEC data near to the magnetic equator and cyclone center. They surmised that the secondary GWs generated by the dissipation of primary GWs associated with TC Victoria could have served as a seeding source on the generation of periodic EPBs during the two consecutive days.

The EPB irregularities can be significantly modulated by geomagnetic activity. Huang F *et al.* (2021b) showed that the sunrise EPBs and enhanced post-sunset EPBs were observed in the geomagnetic storm main phase, whereas they were absent throughout the recovery phase. The storm-induced electric field variations could be the primary causal factor that produced the different EPB variations during the storm. Wan X *et al.* (2021a) compared the general ionospheric responses, as well as the nighttime Equatorial Plasma Irregularities (EPIs) activities between the two geomagnetic storms that happened on 7–8 September 2017 and 25–26 August 2018. It is found that the dusk side ionospheric response could be affected by the daytime ionospheric plasma density/TEC variations during the recovery phase of geomagnetic storms, which further modulates the vertical plasma drift and plasma gradient. As a result, the growth rate of post-sunset EPIs will be enhanced or inhibited. Liu Y *et al.* (2021) revealed that the particle precipitation is the dominant mechanism for the dayside MIT region irregularities, while nightside MIT region irregularities are strongly related with the temperature gradient drift instability.

Liu Y *et al.* (2020b) investigated the nighttime ionospheric E-F coupling and interhemispheric coupling at middle latitudes from 2006–2018 using COSMIC Radio Occultation data. Significant increases in concurrence rate of ionospheric irregularities in E and F regions were shown during the summer hemisphere. The F region irregularity concurrence at the conjugate hemispheres reached a maximum during the winter hemisphere. Their analysis shows that the E-F coupling and inter-hemispheric coupling were proposed to play the important role in triggering nighttime ionospheric irregularity at middle latitudes.

4.4 Polar Cap Patches

Zhang Q H *et al.* (2020) summarized the recent new progress in the formation and evolution of patches as

well as their impact on the M-I-T coupling processes and space weather. The dayside reconnection and bursty sunward return flows produced by the modulation of nightside reconnection are confirmed as the dominant mechanisms which separate the entering ionization into islands (patches). The patches evolve along streamlines of the Dungey convection cycle from the dayside to the nightside and exit the polar cap modulated by pulsed nightside reconnection. Rapidly moving patches are associated with clear ion upflows and the patches often produce significant scintillations at their edges.

Zhang D *et al.* (2021) statistically analyzed the polar cap patches in relation to solar and geomagnetic activity. The statistical results indicated that the occurrence of cold patches is clearly dependent on solar and geomagnetic activity, but hot patches do not show such dependence. Cold and hot patches preferably appear in winter. The spatial size of cold and hot patches decreases (increases) with solar (geomagnetic) activity.

Wang Y *et al.* (2020) developed a new method named TEC keogram for continuous monitoring and studying of large-scale plasma irregularities in the polar ionosphere. The keogram is developed from a movie of TEC maps along various meridian lines from the day-side to the nightside across the magnetic pole. The identification and the motion speed of polar cap patches are confirmed by SuperDARN radar observations. The occurrences of fully-tracked patches on months and UT hours are consistent with previous reports. Besides, the dependence of the patch occurrences on IMF B_z indicates that the magnetic reconnection is probably the main mechanism in the patch formation.

4.5 Scintillations

The ionospheric irregularities could cause scintillation at both high and lower latitudes. Wang Y *et al.* (2021a) reported a unique example that a polar cap arc producing clear amplitude and phase scintillations in GPS L-band signals, using observations from an all-sky imager and a GPS receiver at Resolute Bay and the SuperDARN Inuvik radar. During the southward Interplanetary Magnetic Field (IMF) condition, the polar cap arc moved quickly from the dusk-side to the midnight auroral oval at a speed of about $700 \text{ m}\cdot\text{s}^{-1}$, as revealed by all-sky 557.7 nm and 630.0 nm images. When it intersected the ray path of GPS signals, both amplitude and phase scintillations appeared, which is very different from previous results. They proposed that the strong

TEC enhancement (about 6 TECU) and flow shears in association with the polar cap arc under the southward IMF condition were creating the scintillations.

Geng W *et al.* (2020) produced the amplitude scintillation index maps in terms of GPS scintillation data in South China. The scintillation map can be used as a routine product for the now-casting and warning of scintillation events over Southern China. Geng W *et al.* (2021) analyzed the temporal and spatial characteristics of cycle slip events using the data from Chinese 260 GPS observations during the period of the year 2015–2018. The cycle slips have dependence on the local time, seasons, solar activity, and latitude. The cycle slip occurrence has a strong correlation with solar activity and ionospheric scintillation.

Xiong C *et al.* (2020b) provided the comparison of the GPS signal amplitude degradations from receivers on board low Earth orbiting satellites at different altitudes. Intense carrier phase variations but almost no amplitude fades (less than $2 \text{ dB}\cdot\text{Hz}$) are observed when the spaceborne receiver lies right inside the ionospheric plasma irregularities, like the case for the Swarm (see Fig.11) and CHAMP satellites flying at about 400–500 km. Zhao W H *et al.* (2022) presented the phenomenon of loss of lock of satellite signal at the middle latitude region by using a ground-based GNSS ionospheric TEC and scintillation receiver at Weihai, China, during a period of 2018–2019.

Jiang C *et al.* (2020c) studied the effect of ionospheric irregularities on the propagation of radio waves and reproduced spread F on the ionograms when ionospheric irregularities occurred in the ionosphere.

Numerical simulations were also used to investigate the scintillation associated with artificial technique. Gao J F *et al.* (2020) presented the high-resolution numerical simulation of ionospheric instability triggered by chemical release. The upwelling, pinching, penetrating, and bifurcating processes of artificial instability are produced with electron density patterns generated by using this model. Zhao H S *et al.* (2020) presented a simulation model for the vaporized samarium release in the ionosphere and the redundancy reaction, inversion and the photochemical reactions were all taken into account. The model results were consistent with experimental observations. Due to the geomagnetic field and neutral wind, the shape of artificial plasma clouds changes significantly. The error of the spherically symmetric reflection model is large. According to the density distribution

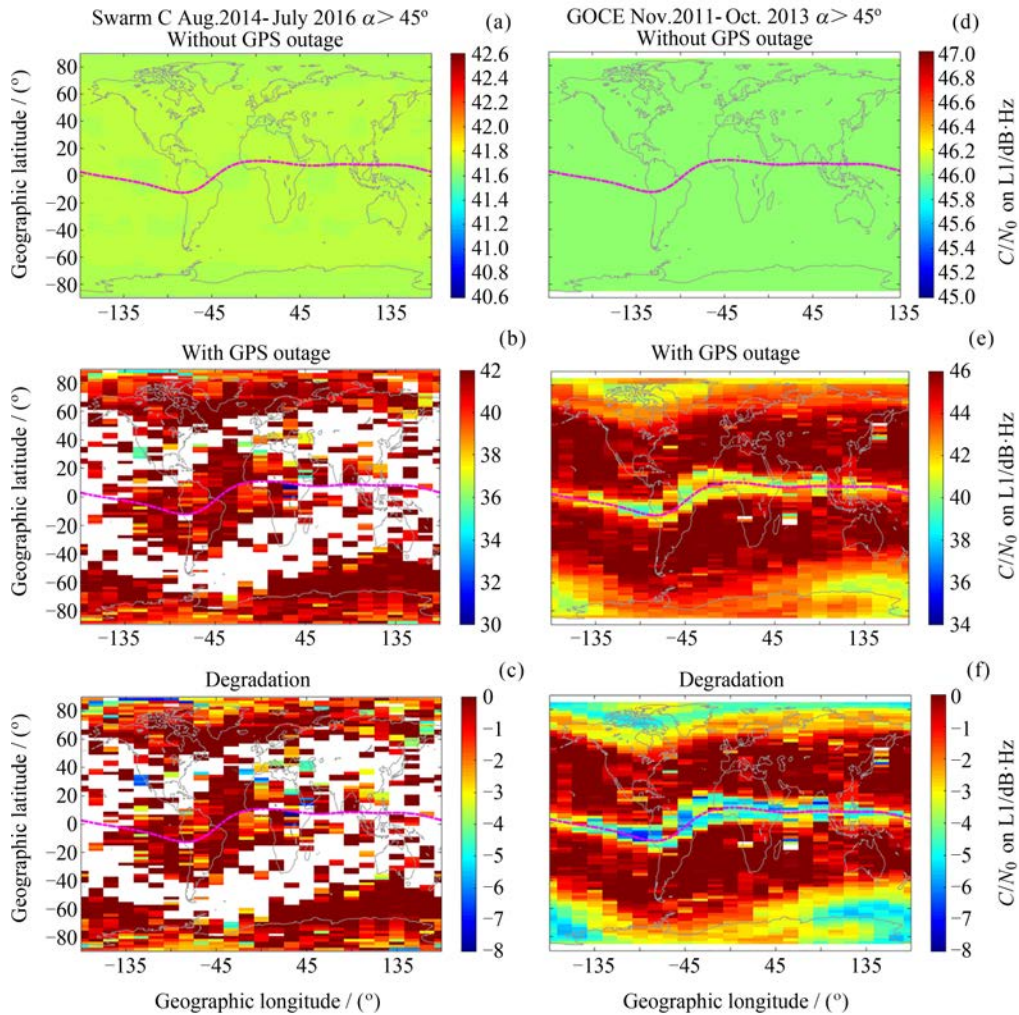


Fig. 11 Global distributions of received GPS signal amplitude for Swarm C and GOCE satellite. See the details in Xiong C *et al.* (2020b)

of plasma clouds, the Geometric Theory of Diffraction (GTD) is introduced here in dealing with the electromagnetic scattering. The GTD-based scattering model has been established and used to study the time-space evolution of the ground received power patterns in this paper.

5 Modeling and Data Assimilation

5.1 Theoretical and Empirical Models

Theoretical numerical model and empirical model as well are important tools in the study of the ionosphere and upper atmosphere variations. With regards to theoretical model, Dang T *et al.* (2021) developed a post-processing technique with an averaging-reconstruction (ring average) algorithm to solve the singularity problem in a spherical coordinate with the finite-difference

method (Fig.12). The algorithm is implemented in a community upper-atmospheric model, the TIEGCM, with a finer horizontal resolution in geographic longitude-latitude coordinates, which enables the capability of resolving critical mesoscale structures. Moreover, the ring average scheme has also been implemented in other community models to enable high-spatial-resolution self-consistent simulations of the whole geospace from the ground to the magnetosphere.

Li Z *et al.* (2021) developed an ESF model and presented an effective analysis on some key issues surrounding the modeling of ESF. The model includes flexible adjustments of advection schemes and resolutions, which provides the capability to examine the effects of grid resolution and numerical diffusion on ESF simulation. It was found that advection schemes with the total variation diminishing property are preferred for

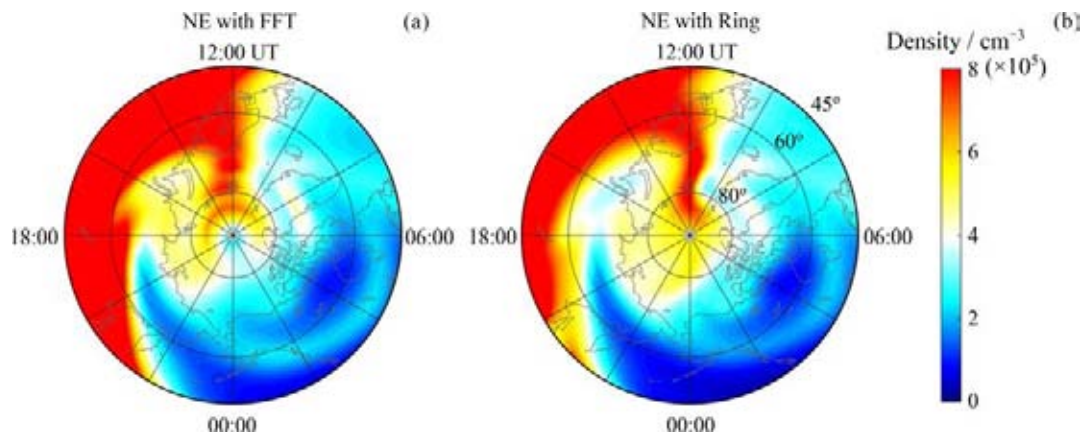


Fig. 12 Simulated polar maps of electron densities using (a) an FFT filter and (b) ring average at 10:50 UT on 17 March 2013 as a function of geographic latitude and local time. From Dang *et al.* (2021)

preventing spurious oscillations which occur near the steep density gradients in the ESF. On the other hand, schemes with low diffusion are also desirable to model complicated dynamic structures of the ESF. Moreover, numerical experiments suggest that some of the secondary instabilities in idealized ESF simulations, although with morphological similarities, are possibly initiated by numerical seeding, which may differ from the observed evolution of secondary ESF.

Empirical model is an efficient tool in the ionospheric research. Li Q *et al.* (2021) constructed a new empirical model of N_e profile in F region ionosphere, using 13-year N_e profiles from COSMIC radio occultation. They used five parameters of the α -Chapman function to describe the N_e profiles, and then built the model by applying algorithms of Empirical Orthogonal Function (EOF) analysis and Fourier expansion to each parameter. The model captures well the key temporal-spatial variations of the F region electron density and makes up the descriptive shortcomings (EIA, mid-latitude trough) of IRI-2016. Huang H *et al.* (2021) evaluated the three options embedded in IRI-2016 for the $h_m F_2$ estimation under low and high solar flux levels. They compare the modeled $h_m F_2$ with observations of digisonde and COSMIC ionospheric radio occultation. They proposed that the performance of the three options do not vary much with solar condition, while they differ greatly with location.

Using the long-term ground-based GNSS receiver and ionosonde data collected in the Brazilian longitude sector during 2012–2020, Zhao *et al.* (2021b) developed an ionospheric strong scintillation prediction model based on the gradient boosting algorithms XGBoost,

LightGBM and CatBoost. A comparison of daily scintillation occurrence from the modeled and observed results during 2014 and 2020 shows that the gradient boosting algorithms are effective for predicting strong scintillations over low latitude, with a prediction accuracy of about 85%.

5.2 Data Assimilation and Machine Learning

With advances in observations and modellings, techniques of data assimilation and machine learning are being applied in the ionospheric modelling and forecasting. Accurate ionospheric specification for the current and future is one of the key tasks in operational space weather.

A series of studies by He J H *et al.* (2020a, 2020b, 2021) observed that simultaneously assimilating different observation types can greatly improve the quality of ionosphere specification. Updating the thermospheric state variables in the coupled thermosphere-ionosphere forecast model in the assimilation step plays an important role in improving the ionosphere forecasting. Also, the ionosphere forecast quality could be enhanced by optimizing the thermospheric neutral components *via* the EnKF method. The ionosphere electron density forecast accuracy can be improved by at least 10% for 24 h.

Furthermore, He and Yue (2021) investigated the impact of perturbing different model external forcing parameters on ensemble generation and forecast capability of ionosphere and thermosphere. Better ensemble members of ionosphere and thermosphere states can be generated if two additional model forcing parameters are perturbed, so that the forecast capability of the ionosphere and thermosphere variables can be further

enhanced.

In the past decade, with the increase of space observation data, machine learning has been applied to space weather modeling, especially where the physical relationship is still not very clear from modeling perspective, machine learning and big data intervention can improve the applicability of the model. Based on Ultraviolet Imager (UVI) data of Polar satellite, Hu Z J *et al.* (2020, 2021) constructed two auroral models by using the Generalized Regression Neural Network (GRNN), and the Conditional Generation Adversarial Network (CGAN). See Fig. 13 for the comparison.

5.3 Laboratory and GNSS Modelling

Yuan *et al.* (2019) developed a new global ionospheric broadcast model known as the BDGIM model which maintained a good correction accuracy regardless of the

ionospheric effect and had been formally applied to the BDS-3 navigation system. The BDS-3 BDGIM coefficients are available to GNSS users for providing ionospheric corrections. Zhang W *et al.* (2021) adjusted the ionospheric global index IG12 using GNSS to calibrate the IRI-2016 model TEC, and the different interpolation strategies for the updated IG12 index were investigated to improve the TEC accuracy in China. Differential Code Bias (DCB) is a significant error source in ionosphere modeling. Liu M *et al.* (2020) applied Low Earth Orbit (LEO) spaceborne GPS data to estimate GPS satellite DCB, receiver DCB and LEO-based vertical TEC parameters, simultaneously. Li M *et al.* (2020) analyzed the dependence of the receivers' DCB variations on the ambient temperature, and showed that the temperature dependence of DCB varies among different satellite systems and frequency bands.

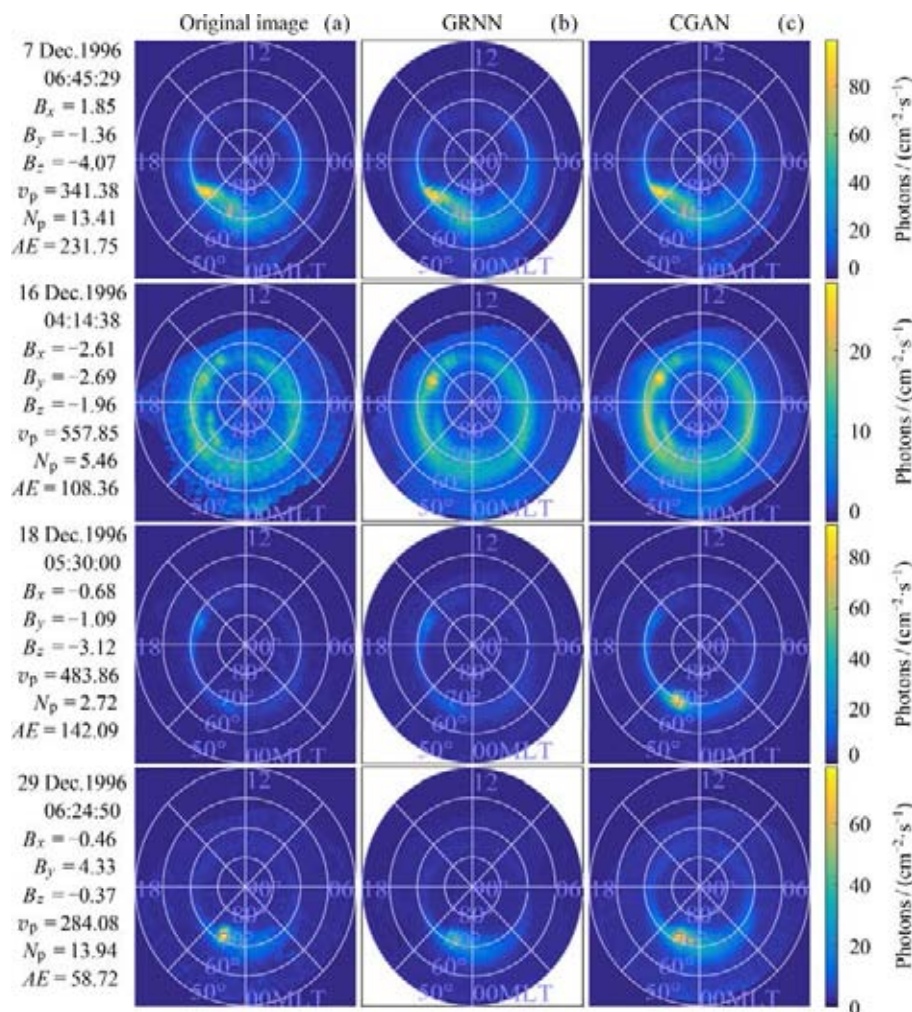


Fig. 13 Image of polar UVI (a) and the results of GRNN (b) and CGAN (c) models under the same space environment parameters (Hu *et al.*, 2021)

The Differential Code Bias (DCB) caused by the GNSS satellite transmitter and receiver hardware is one of the main error sources in TEC retrieval. She *et al.* (2020) independently solved TEC and DCBs with the hypothesis of local spherical symmetry imposed on the dual-frequency observations from only one individual station. Zhong J *et al.* (2020) assessed both the long-term and short-term variations of the GPS DCBs and receiver DCBs, and confirmed that the long-term variations of the DCBs are primarily attributed to the GPS satellite replacement, rather than the ionospheric variability. The short-term variations of the GPS DCBs are associated with the GPS draconic year, as the Sun's illumination changes the hardware thermal status of the GPS satellite in a regular period.

Based on the TEC data solved from the GPS data of the tectonic environment monitoring network in mainland China, a long/short-term memory network model (ED-LSTM) with encoding-decoding with convolutional optimization was built by selecting 15 uniformly distributed GPS stations in China, using the data covering one solar cycle from 2006 to 2018, and taking into account the spatial environmental index K_p and other information. Using this model, a new method for ionospheric TEC prediction is developed. The application shows the model prediction performance is better than that of NeQuick and IRI international ionospheric reference models under different geographical locations, seasons, and geomagnetic activities (Xiong P *et al.*, 2021c).

The laboratory experiment is an alternative way to study the physical mechanisms involved in the ionospheric plasma. Recently, a method was developed to study the generation and evolution of instability in the ionosphere-like plasma in a laboratory environment (Ling Y *et al.*, 2021). It was further demonstrated that, under different experimental conditions, the frequency matching relations of the high-frequency-wave mode, low-frequency-wave mode and the pump waves were always satisfied, which confirmed the onset of the parametric decay instability in the ionosphere-like plasma. In addition, the existing background wave mode could significantly decrease the excitation threshold of the parametric instability, indicating that the parametric decay instability can be much more easily excited.

6 Ionosphere Sounding Techniques

Ground-based observation Chains in China were built

up under the support of Chinese Academy of Sciences, and Chinese Meridian Project, and National Natural Science Foundation. An Ionospheric Observational Network for Irregularity and Scintillation in East and Southeast Asia (IONISE) was also developed (Sun W *et al.*, 2020b). The IONISE network mainly includes three crossed chains of GEO TEC/scintillation receivers along 110°E, 23°N and 40°N respectively, multi-static portable digital ionosondes, and bi-static very high-frequency radars. The scientific objectives of the IONISE were to trace the occurrence and movements of ionospheric irregularities producing GNSS loss-of-lock and scintillations; capture ionospheric disturbances of various scales by natural sources, *e.g.*, low atmosphere activity, geomagnetic activity and earthquake; and reveal extremely large gradients of background ionosphere over China and adjacent regions.

Optical observation system for meteor and ionospheric irregularity had been developed by Yang S *et al.* (2021). This system consists of several video cameras at Sanya and Ledong, separated by about 70 km. It can capture meteor optical trail and spectrum and save it as video format file. The corresponding methods for identifying emissions from meteor and atmospheric species, and calculating the meteor velocity, trajectory and orbital parameters were also developed. This information may help us to study how the meteoroids gain entry into the Earth's atmosphere and effect changes on the ionosphere throughout the combining radio observation.

Yue *et al.* (2020) reported the preliminary experimental results from the state-of-the-art phased-array ISR at Sanya. A smart iterative strategy based on trust region method for ionospheric parameter extraction from ISR detection was developed. Tests and comparisons between the smart strategy and the conventional strategy, which is based on the Levenberg-Marquardt method, show that the efficiency of the smart iterative strategy is much higher than the conventional strategy. A software incoherent scattering radar has been designed and fabricated under the grant of National High Technology Research and Development Program (Li Y *et al.* 2021). Ionospheric detection experiments have been carried out to test this software radar.

Li W B *et al.* (2021) introduced the new Fabry-Perot Interferometer (FPI) at Mohe. The climatological feature of the thermospheric wind was carried out and an empirical model was developed. The study shows that, when examining regional differences in the ionosphere,

more focus should be placed on the effect of regional changes of thermospheric winds.

Jiang C *et al.* (2020b) carried out a statistical study of autoscaled data from ionograms by the IonoScaler to verify its performance for space weather. They found that the autoscaled data by the IonoScaler were accurate enough for space weather if the quality of ionograms is good.

Progress has been achieved in the past two years to use the European Incoherent Scatter Scientific Association (EISCAT) to explore ionospheric processes. Feng T *et al.* (2021) developed an algorithm for the automatic extraction of naturally enhanced Plasma Lines (PLs). The results show that the occurrence time of PLs strongly depends on the magnetic local time and correlates with the geomagnetic and solar activities. Wu J *et al.* (2021) presented an observation of altitude descents in High-Frequency enhanced Ion Line (HFIL) and Plasma Line (HFPL). Feng T *et al.* (2020) presented the evidence of X-mode suppressing O-mode heating by analyzing ionospheric heating experiments. It was found that TPI was inhibited by X-mode heating because of the increase in electron temperature.

Yang J T *et al.* (2020) present observations of ELF waves received on the satellite and on the ground simultaneously, which were excited in the EISCAT modulation heating experiment carried out alternately in the AM and BW modes. Lu H *et al.* (2021) present the results of the first ELF/VLF communication experiments being conducted at Tromsø, where the EISCAT HF facility is located. The ELF/VLF waves from the ionosphere are modulated by Quaternary Phase Shift Keying (QPSK) and used for communication. ELF communication signals generated by the amplitude modulation heating of the ionosphere have been successfully received by the satellite and the ground-based receiver. These experimental results confirm that the ELF/VLF waves radiated by amplitude modulation heating of the auroral electrojet can be used for long-distance communication in the future.

The CSES was successfully launched on 2 February 2018. Not only the satellite mission but also many scientists were concerned on the quality of observation data. Liu J, Guan Y *et al.* (2021) carried out the data comparison of electron density between CSES and DEMETER satellite, Swarm constellation and IRI model, and they found that the patterns of electron density for CSES can exactly exhibit the shape of iono-

spheric variation. Yan R *et al.* (2020) comprehensively compared in situ Ne and temperature (T_e) measured by Langmuir Probe (LAP) on board CSES and other techniques/models. It reveals that the global distributions and their relative variations of N_e/T_e from CSES and Swarm are quite consistent during conjunction periods of the two satellites.

In 2018, a total of 17 SURA-CSES experiments have been carried out and analyzed in multiple parameters detected in the topside ionosphere at an altitude of 507 km from CSES (Zhang X *et al.*, 2020a). X mode emitted HF waves excited a filamentary structure on the existing VLF transmitters at 19 kHz in local daytime, being different from those in O-mode HF waves to enhance the VLF transmitter signals and widen their frequency band in local nighttime. The higher conductivity in E region, the self-focused instability, and strong heating of HF waves on lower ionosphere are considered to be the possible mechanism for these overlapped and enhanced VLF transmitters.

The observations from CSES were further used to study the ionospheric disturbance and also the temporal and spatial distributions of ELF/VLF wave activities, as well as the energetic electron fluxes in the ionosphere during intense storm periods (Zhima *et al.*, 2021; Yang Y Y *et al.*, 2020; Liu D P *et al.*, 2021). The storm events excited some significant ELF/VLF waves and enhanced the energetic electron flux.

7 Planetary Ionosphere

Yang N *et al.* (2021) present a concept simulation for the measurement of Martian atmospheric winds using the Doppler Michelson interferometry technique. The simulation is based on the satellite instrument initially designed for the Dynamic Atmosphere Mars Observer (DYNAMO) project to measure vertical profiles of winds from the 1.27 μm airglow observations in the Martian atmosphere. A comprehensive DYNAMO measurement simulation forward model is developed using the Michelson equation. The agreement between the derived atmospheric signals from the simulated interferogram without altitude inversion and the input parameters used to initiate the forward model confirms the validity of the forward model.

By using MAVEN and photochemistry models, the characteristics of the Martian photoelectrons, and their impact on the Martian upper atmosphere have been stu-

studied extensively (Wu X *et al.*, 2020a, 2020b; Cao Y *et al.*, 2020a, 2020b, 2021). Many new results were obtained. For instance, it was found that for nightside photoelectrons, their occurrence rate declined rapidly near and beyond the terminator; their velocities were more likely parallel to the ambient magnetic field lines; and they were less likely observed under high solar wind dynamic pressures.

Also, Niu D *et al.* (2020) investigated systematically the variations of the occurrence of suprathermal electron depletions in the nightside Martian ionosphere and revealed that depletions were more easily observed in regions with near horizontal magnetic fields and under low Solar Wind (SW) dynamic pressures. Niu D *et al.* (2021a) reported that in situ nightside neutral heating was dominated by exothermic chemistry and Maxwell interaction with thermal ions for regions with depletion, and by direct SW impact for regions without. Collisional quenching of excited state species produced from a variety of channels, such as electron impact excitation, dissociation, and ionization, as well as O_2^+ dissociative recombination, made a substantial contribution to neutral heating, except during depletion. For comparison, nightside ion heating was mainly driven by energetic ion production under all circumstances.

In addition to the photoelectron in Martian ionosphere, Cao Y *et al.* (2020c) presented a statistical survey of ionospheric photoelectrons at Titan. The spatial distribution of photoelectrons was consistent with the scenario of photoelectron transport along the magnetic field lines. The analysis also revealed the presence of a photoelectron gap in the deep nightside ionosphere where it was very difficult for photoelectrons to travel

to this region.

The ionospheric compositional variations of Mars were examined in the unprecedented details, including the dominant O^{++} production and destruction channels, CO_2^{++} distribution, and the modulation of the Martian topside ionosphere by the upstream solar wind condition (e.g., Gu H *et al.*, 2020a, 2020b; Huang J *et al.* 2020; Wu X *et al.*, 2021; Niu D *et al.*, 2021c).

The Martian ionosphere has close relationship with the background atmosphere. The species-dependent variations of the dayside Martian ionosphere were presented during the global dust storm period (Niu D *et al.* 2021b). It was suggested that the variation of ionospheric species during a global dust storm was closely linked to the variation of neutral species in the thermosphere during the same event. In addition, the H_2 distribution is important for a thorough understanding of hydrogen escape and climate evolution on Mars. Cui J *et al.* (2020) reported that several species presented an abnormal dawn enhancement above the exobase where they were mainly produced by ion-neutral reactions involving H_2 , as shown in Fig.14. Such a peculiarity was indicative of a dawn bulge of H_2 present in the Martian upper atmosphere and corona, which was driven by subsidence in regions of horizontal wind convergence and the subsequent buildup of minor atmospheric species with large vertical scale heights.

Aside the data analysis, a numerical model was also used to explore the generation of the ionospheric irregularities at Mars. Jiang C *et al.* (2021b) carried out nonlinear simulation of small-scale ionospheric irregularities at Mars seeding by perturbation zonal neutral wind. Results show that the associated perturbation magnetic

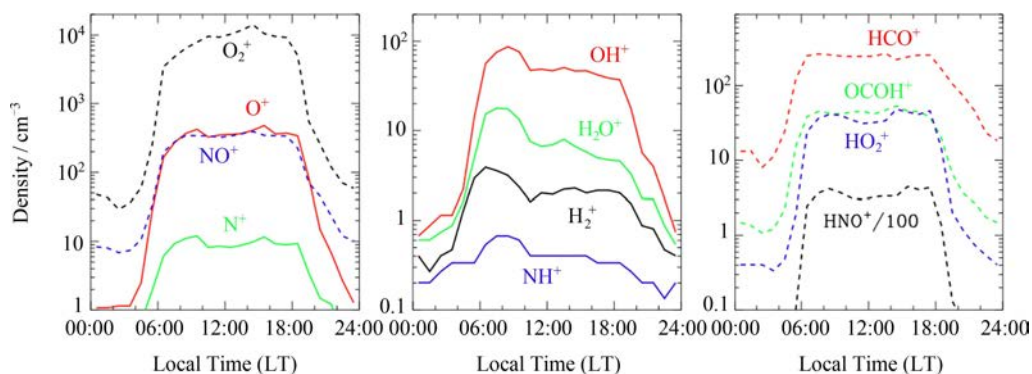


Fig. 14 Density variations of the same species as a function of local time and at fixed altitudes, either 300 km (solid) or 180 km (dashed) depending on whether a distinctive layer structure is observable over the altitude range examined in this study. A strong dawn enhancement is observed for each species in the middle panel. Note that the HNO^+ density has been everywhere divided by 100 to improve visibility (Cui *et al.*, 2020)

field and electric field, induced by the gradient drift instability, can cause the velocity shear of the plasma, which induced the Kelvin-Helmholtz instability. Then, Kelvin-Helmholtz instabilities furthermore lead to smaller-scale irregularities in plasma density, magnetic field, and electric field in the Martian ionosphere.

Acknowledgments

The authors would like to express their gratitude to all colleagues for kindly providing articles and pictures in the course of the preparation for this national report.

Reference

- [1] AJITH K K, LI G Z, TULASI RAM S, et al. On the seeding of periodic equatorial plasma bubbles by gravity waves associated with tropical cyclone: a case study[J]. *Journal of Geophysical Research: Space Physics*, 2020, **125**(10): e2020JA028003. DOI: 10.1029/2020JA028003
- [2] CAI Y H, WANG W B, ZHANG S R, et al. Climatology analysis of the daytime topside ionospheric diffusive O^+ flux based on incoherent scatter radar observations at millstone hill[J]. *Journal of Geophysical Research: Space Physics*, 2021, **126**(10): e2021JA029222. DOI: 10.1029/2021JA029222
- [3] CAO Y T, CUI J, NI B B, et al. Bidirectional electron conic observations for photoelectrons in the Martian ionosphere[J]. *Earth and Planetary Physics*, 2020, **4**(4): 403-407. DOI: 10.26464/epp2020037
- [4] CAO Y T, CUI J, WU X S, et al. A survey of photoelectrons on the nightside of mars[J]. *Geophysical Research Letters*, 2021, **48**(2): e2020GL089998. DOI: 10.1029/2020GL089998
- [5] CAO Y, CUI J, WU X, et al. Photoelectron pitch angle distribution near Mars and implications on cross terminator magnetic field connectivity[J]. *Earth and Planetary Physics*, 2020, **4**(1): 17-22. DOI: 10.26464/epp2020008
- [6] CAO Y T, WELLBROCK A, COATES A J, et al. Field-aligned photoelectron energy peaks at high altitude and on the nightside of titan[J]. *Journal of Geophysical Research: Planets*, 2020, **125**(1): e2019JE006252. DOI: 10.1029/2019je006252
- [7] CHEN C H, SUN Y Y, LIN K, et al. A new instrumental array in Sichuan, China, to monitor vibrations and perturbations of the lithosphere, atmosphere, and ionosphere[J]. *Surveys in Geophysics*, 2021, **42**(6): 1425-1442. DOI: 10.1007/s10712-021-09665-1
- [8] CHEN G, DING F, WAN W X, et al. Structures of multiple large-scale traveling ionospheric disturbances observed by dense Global Navigation Satellite System networks in China[J]. *Journal of Geophysical Research: Space Physics*, 2020, **125**(2): e2019JA027032. DOI: 10.1029/2019JA027032
- [9] CHEN J J, LEI J H, WANG W B, et al. Ionospheric electrodynamic response to solar flares in September 2017[J]. *Journal of Geophysical Research: Space Physics*, 2021, **126**(11): e2021JA029745. DOI: 10.1029/2021JA029745
- [10] CHEN J J, LEI J H, ZHANG S R, et al. A simulation study on the relationship between field-aligned and field-perpendicular plasma velocities in the ionospheric F region[J]. *Journal of Geophysical Research: Space Physics*, 2020, **125**(1): e2019JA027350. DOI: 10.1029/2019JA027350
- [11] CHEN J J, WANG W B, LEI J H. Longitudinal variations of equatorial ionospheric electric fields near sunrise[J]. *Journal of Geophysical Research: Space Physics*, 2021, **126**(5): e2020JA028977. DOI: 10.1029/2020JA028977
- [12] CHEN J J, WANG W B, LEI J H, et al. The physical mechanisms for the sunrise enhancement of equatorial ionospheric upward vertical drifts[J]. *Journal of Geophysical Research: Space Physics*, 2020, **125**(8): e2020JA028161. DOI: 10.1029/2020JA028161
- [13] CHEN X C, HUANG W T, BAN C, et al. Dynamic properties of a sporadic sodium layer revealed by observations over Zhongshan, Antarctica: a case study[J]. *Journal of Geophysical Research: Space Physics*, 2021, **126**(11): e2021JA029787. DOI: 10.1029/2021JA029787
- [14] CHEN X T, DANG T, ZHANG B Z, et al. Global effects of a polar solar eclipse on the coupled magnetosphere-ionosphere system[J]. *Geophysical Research Letters*, 2021, **48**(23): e2021GL096471. DOI: 10.1029/2021GL096471
- [15] CHEN Y D, LIU L B, LE H J, et al. Equatorial north-south difference of noontime electron density bite-out in the F_2 layer[J]. *Journal of Geophysical Research: Space Physics*, 2020, **125**(8): e2020JA028124. DOI: 10.1029/2020JA028124
- [16] CHEN Y D, LIU L B, LE H J, et al. Latitudinal dependence of daytime electron density bite-out in the ionospheric F_2 -Layer[J]. *Journal of Geophysical Research: Space Physics*, 2021, **126**(1): e2020JA028277. DOI: 10.1029/2020JA028277
- [17] CUI J, REN Z P, WU Z P, et al. Abnormal dawn-dusk asymmetry of protonated ions in the Martian ionosphere[J]. *Astrophysical Journal Letters*, 2020, **895**(2): L43. DOI: 10.3847/2041-8213/ab930c
- [18] DANG T, LEI J H, WANG W B, et al. Prediction of the thermospheric and ionospheric responses to the 21 June 2020 annular solar eclipse[J]. *Earth and Planetary Physics*, 2020, **4**(3): 231-237. DOI: 10.26464/epp2020032
- [19] DANG T, ZHANG B Z, LEI J H, et al. Azimuthal averaging-reconstruction filtering techniques for finite-difference general circulation models in spherical geometry[J]. *Geoscientific Model Development*, 2021, **14**(2): 859-873. DOI: 10.5194/gmd-14-859-2021
- [20] DENG Z X, WANG R, LIU Y, et al. Investigation of low latitude spread-F triggered by nighttime medium-scale traveling ionospheric disturbance[J]. *Remote Sensing*, 2021, **13**(5): 945. DOI: 10.3390/rs13050945
- [21] FENG T, LIU M R, XU B, et al. Auroral-enhanced plasma lines by suprathermal electrons observed by EISCAT[J]. *Journal of Geophysical Research: Space Physics*, 2021, **126**(3): e2020JA028495. DOI: 10.1029/2020JA028495
- [22] FENG T, ZHOU C, WANG X, et al. Evidence of X-mode heating suppressing O-mode heating[J]. *Earth and Planetary Physics*, 2020, **4**(6): 588-597. DOI: 10.26464/epp2020068
- [23] GAO J F, GUO L X, XU Z W, et al. Simulation of plasma instabilities artificially induced in the equatorial ionosphere[J]. *Physics of Plasmas*, 2020, **27**(9): 092902. DOI: 10.1063/5.0013329
- [24] GENG W, HUANG W G, LIU G Q, et al. Generation of iono-

- spheric scintillation maps over southern China based on kriging method[J]. *Advances in Space Research*, 2020, **65**(12): 2808-2820. DOI: 10.1016/j.asr.2020.03.035
- [25] GENG W, HUANG W G, LIU G Q, *et al.* The distribution characteristics of GPS cycle slip over the China mainland and adjacent region during the declining solar activity (2015-2018) period of solar cycle 24[J]. *Radio Science*, 2021, **56**(5): e2020RS007196. DOI: 10.1029/2020RS007196
- [26] GU H, CUI J, HE Z G, *et al.* A MAVEN investigation of O⁺⁺ in the dayside Martian ionosphere[J]. *Earth and Planetary Physics*, 2020, **4**(1): 11-16. DOI: 10.26464/epp2020009
- [27] GU H, CUI J, NIU D D, *et al.* Observation of CO₂⁺⁺ dication in the dayside Martian upper atmosphere[J]. *Earth and Planetary Physics*, 2020, **4**(4): 396-402. DOI: 10.26464/epp2020036
- [28] HAO Yongqiang, LI Quanhan, GU Jianguang, *et al.* Imaging of the large-scale ionospheric disturbances induced by seismic waves using GPS network in China[J]. *Chinese Journal of Geophysics*, 2021, **64**(11): 3925-3932 (郝永强, 李泉翰, 郭建广, 等. 利用中国 GPS 站网对地震波引发的大尺度电离层扰动的观测[J]. *地球物理学报*, 2021, **64**(11): 3925-3932)
- [29] HE J H, YUE X A, HU L H, *et al.* Observing system impact on ionospheric specification over China using EnKF assimilation[J]. *Space Weather*, 2020, **18**(10): e2020SW002527. DOI: 10.1029/2020SW002527
- [30] HE J H, YUE X A, LE H J, *et al.* Evaluation on the quasi-realistic ionospheric prediction using an ensemble Kalman filter data assimilation algorithm[J]. *Space Weather*, 2020, **18**(3): e2019SW002410. DOI: 10.1029/2019SW002410
- [31] HE J H, YUE X A, REN Z P. The impact of assimilating ionosphere and thermosphere observations on neutral temperature improvement: Observing system simulation experiments using EnKF[J]. *Space Weather*, 2021, **19**(10): e2021SW002844. DOI: 10.1029/2021SW002844
- [32] HE J H, YUE X A. The impact of perturbing eddy diffusion and upper boundary on the ionosphere EnKF assimilation system[J]. *Journal of Geophysical Research: Space Physics*, 2021, **126**(8): e2021JA029366. DOI: 10.1029/2021JA029366
- [33] HE Shichuang, ZHANG Donghe, HAO Yongqiang, *et al.* Statistical study on the occurrence of the ionospheric mid-latitude trough and the variation of trough minimum location over northern hemisphere[J]. *Chinese Journal of Geophysics*, 2020, **63**(1): 31-46. DOI: 10.6038/cjg2020M0564 (何世闯, 张东和, 郝永强, 等. 北半球电离层中纬槽发生率及其槽极小位置变化的统计研究[J]. *地球物理学报*, 2020, **63**(1): 31-46. DOI: 10.6038/cjg2020M0564)
- [34] HU L H, LEI J H, SUN W J, *et al.* Latitudinal variations of daytime periodic ionospheric disturbances from Beidou GEO TEC observations over China[J]. *Journal of Geophysical Research: Space Physics*, 2021, **126**(3): e2020JA028809. DOI: 10.1029/2020JA028809
- [35] HU L H, ZHAO X K, SUN W J, *et al.* Statistical characteristics and correlation of low - latitude F region bottom - type irregularity layers and plasma plumes over Sanya[J]. *Journal of Geophysical Research: Space Physics*, 2020, **125**(8): e2020JA027855. DOI: 10.1029/2020JA027855
- [36] HU Z J, HAN B, ZHANG Y S, *et al.* Modeling of ultraviolet aurora intensity associated with interplanetary and geomagnetic parameters based on neural networks[J]. *Space Weather*, 2021, **19**(11): e2021SW002751. DOI: 10.1029/2021SW002751
- [37] HU Zejun, HAN Bing, LIAN Huifang *et al.* Modeling of ultraviolet auroral intensity based on generalized regression neural network associated with IMF/solar wind and geomagnetic parameters[J]. *Chinese Journal of Geophysics*, 2020, **63**(5): 1738-1750. DOI: 10.6038/cjg2020N0151 (胡泽俊, 韩冰, 连慧芳. 基于广义回归神经网络的行星际/太阳风参数和地磁指数的紫外极光强度建模[J]. *地球物理学报*, 2020, **63**(5): 1738-1750. DOI: 10.6038/cjg2020N0151)
- [38] HUANG F Q, LEI J H, OTSUKA Y, *et al.* Characteristics of medium-scale traveling ionospheric disturbances and ionospheric irregularities at mid-latitudes revealed by the total electron content associated with the Beidou geostationary satellite[J]. *IEEE Transactions on Geoscience and Remote Sensing*, 2021, **59**(8): 6424-6430. DOI: 10.1109/Tgrs.2020.3032741
- [39] HUANG F Q, LEI J H, XIONG C, *et al.* Observations of equatorial plasma bubbles during the geomagnetic storm of October 2016[J]. *Earth and Planetary Physics*, 2021, **5**(5): 416-426. DOI: 10.26464/epp2021043
- [40] HUANG F Q, LEI J H, ZHANG R L, *et al.* Prominent daytime TEC enhancements under the quiescent condition of January 2017[J]. *Geophysical Research Letters*, 2020, **47**(14): e2020GL088398. DOI: 10.1029/2020GL088398
- [41] HUANG F Q, LI Q L, SHEN X H, *et al.* Ionospheric responses at low latitudes to the annular solar eclipse on 21 June 2020[J]. *Journal of Geophysical Research: Space Physics*, 2020, **125**(10): 2020JA028483. DOI: 10.1029/2020JA028483
- [42] HUANG H, MOSES M, VOLK A E, *et al.* Assessment of IRI-2016 hmF2 model options with digisonde, COSMIC and ISR observations for low and high solar flux conditions[J]. *Advances in Space Research*, 2021, **68**(5): 2093-2103. DOI: 10.1016/j.asr.2021.01.033
- [43] HUANG J P, HAO Y Q, ZHANG D H, *et al.* The use of monthly mean average for investigating the presence of hysteresis and long-term trends in ionospheric NmF2[J]. *Journal of Geophysical Research: Space Physics*, 2020, **125**(1): e2019JA026905. DOI: 10.1029/2019JA026905
- [44] HUANG J P, CUI J, HAO Y Q, *et al.* Solar and magnetic control of minor ion peaks in the dayside Martian ionosphere[J]. *Journal of Geophysical Research: Space Physics*, 2020, **125**(8): e2020JA028254. DOI: 10.1029/2020JA028254
- [45] JIANG C H, WANG W B, YANG G B, *et al.* An investigation of mid-latitude ionospheric peak in TEC using the TIEGCM[J]. *Journal of Atmospheric and Solar-Terrestrial Physics*, 2020, **211**: 105480. DOI: 10.1016/j.jastp.2020.105480
- [46] JIANG C H, WEI L H, LAN T, *et al.* A statistical study of auto-scaled data at the northern equatorial ionization anomaly during the year 2016[J]. *Radio Science*, 2020, **55**(2): e2019RS006898. DOI: 10.1029/2019RS006898
- [47] JIANG C H, WEI L H, YANG G B, *et al.* Large-scale ionospheric irregularities detected by ionosonde and GNSS receiver network[J]. *IEEE Geoscience and Remote Sensing Letters*, 2021, **18**(6): 940-943. DOI: 10.1109/Lgrs.2020.2990940
- [48] JIANG C H, WEI L H, YANG G B, *et al.* Numerical simulation of the propagation of electromagnetic waves in ionospheric irregularities[J]. *Earth and Planetary Physics*, 2020, **4**(6): 565-570. DOI: 10.26464/epp2020059
- [49] JIANG C H, YOKOYAMA T, WEI L H, *et al.* Nonlinear simulation of ionospheric irregularities at mars[J]. *Astrophysical Journal*, 2021, **909**(1): 47. DOI: 10.3847/1538-4357/abdc1d
- [50] JIN Y Y, ZHAO B Q, LI G Z, *et al.* Inhibition of F3 layer at low

latitude station Sanya during recovery phase of geomagnetic storms[J]. *Journal of Geophysical Research: Space Physics*, 2021, **126**(12): e2021JA029850. DOI: 10.1029/2021JA029850

- [51] KUAI J W, LI Q L, ZHONG J H, et al. The ionosphere at middle and low latitudes under geomagnetic quiet time of December 2019[J]. *Journal of Geophysical Research: Space Physics*, 2021, **126**(6): e2020JA028964. DOI: 10.1029/2020JA028964
- [52] LE H J, LIU L B, REN Z P, et al. Effects of the 21 June 2020 solar eclipse on conjugate hemispheres: a modeling study[J]. *Journal of Geophysical Research: Space Physics*, 2020, **125**(11): e2020JA028344. DOI: 10.1029/2020JA028344
- [53] LI G Z, NING B Q, OTSUKA Y, et al. Challenges to equatorial plasma bubble and ionospheric scintillation short-term forecasting and future aspects in East and Southeast Asia[J]. *Surveys in Geophysics*, 2021, **42**(1): 201-238. DOI: 10.1007/s10712-020-09613-5
- [54] LI J C, CHEN Y D, LIU L B, et al. Occurrence of Ionospheric Equatorial Ionization Anomaly at 840 km height observed by the DMSP satellites at solar maximum dusk[J]. *Space Weather*, 2021, **19**(5): e2020SW002690. DOI: 10.1029/2020SW002690
- [55] LI M, YUAN Y B, ZHANG X, et al. A multi-frequency and multi-GNSS method for the retrieval of the ionospheric TEC and intraday variability of receiver DCBs[J]. *Journal of Geodesy*, 2020, **94**(10): 102. DOI: 10.1007/s00190-020-01437-w
- [56] LI M Z, YUE X A, WAN W X, et al. Characterizing ionospheric effect on GNSS radio occultation atmospheric bending angle[J]. *Journal of Geophysical Research: Space Physics*, 2020, **125**(6): e2019JA027471. DOI: 10.1029/2019JA027471
- [57] LI M Z, YUE X A. Statistically analyzing the effect of ionospheric irregularity on GNSS radio occultation atmospheric measurement[J]. *Atmospheric Measurement Techniques*, 2021, **14**(4): 3003-3013. DOI: 10.5194/amt-14-3003-2021
- [58] LI N, LUAN X L, LEI J H, et al. Variations of mesospheric neutral winds and tides observed by a meteor radar chain over China during the 2013 sudden stratospheric warming[J]. *Journal of Geophysical Research: Space Physics*, 2020, **125**(5): e2019JA027443. DOI: 10.1029/2019JA027443
- [59] LI N, LEI J H, HUANG F Q, et al. Responses of the ionosphere and neutral winds in the mesosphere and lower thermosphere in the Asian-Australian sector to the 2019 southern hemisphere sudden stratospheric warming[J]. *Journal of Geophysical Research: Space Physics*, 2021, **126**(10): e2020JA028653. DOI: 10.1029/2020JA028653
- [60] LI Q L, HUANG F Q, ZHONG J H, et al. Persistence of the long-duration daytime TEC enhancements at different longitudinal sectors during the August 2018 geomagnetic storm[J]. *Journal of Geophysical Research: Space Physics*, 2020, **125**(11): e2020JA028238. DOI: 10.1029/2020JA028238
- [61] LI Q L, LIU L B, HE M S, et al. A global empirical model of electron density profile in the F region ionosphere basing on COSMIC measurements[J]. *Space Weather*, 2021, **19**(4): e2020SW002642. DOI: 10.1029/2020SW002642
- [62] LI W B, CHEN Y D, LIU L B, et al. Variations of thermospheric winds observed by a Fabry–Perot interferometer at Mohe, China[J]. *Journal of Geophysical Research: Space Physics*, 2021, **126**(2): e2020JA028655. DOI: 10.1029/2020JA028655
- [63] LI W B, CHEN Y D, LIU L B, et al. A statistical study on the winter ionospheric nighttime enhancement at middle latitudes in the Northern Hemisphere[J]. *Journal of Geophysical Research: Space Physics*, 2020, **125**(7): e2020JA027950. DOI: 10.1029/2020JA027950
- [64] LI Y, YUAN K, YAO M, et al. The prototype incoherent scatter radar system of Nanchang university[J]. *IEEE Geoscience and Remote Sensing Letters*, 2021, **18**(7): 1184-1188. DOI: 10.1109/LGRS.2020.2994082
- [65] LI Z Z, LEI J H, ZHANG B Z. Numerical considerations in the simulation of equatorial spread F[J]. *Journal of Geophysical Research: Space Physics*, 2021, **126**(10): e2021JA029622. DOI: 10.1029/2021JA029622
- [66] LING Y M, LIU Y, LEI J H, et al. Laboratory evidence of a pre-existing instability that can enhance the ionospheric heating efficiency[J]. *Geophysical Research Letters*, 2021, **48**(9): e2021GL092560. DOI: 10.1029/2021GL092560
- [67] LIU D P, ZEREN Z, SHEN X H, et al. Typical ionospheric disturbances revealed by the plasma analyzer package onboard the China seismo-electromagnetic satellite[J]. *Advances in Space Research*, 2021, **68**(9): 3796-3805. DOI: 10.1016/j.asr.2021.08.009
- [68] LIU J, GUAN Y B, ZHANG X M, et al. The data comparison of electron density between CSES and DEMETER satellite, Swarm constellation and IRI model[J]. *Earth and Space Science*, 2021, **8**(2): e2020EA001475. DOI: 10.1029/2020EA001475
- [69] LIU J, QIAN L Y, MAUTE A, et al. Electrodynamical coupling of the geospace system during solar flares[J]. *Journal of Geophysical Research: Space Physics*, 2021, **126**(1): e2020JA028569. DOI: 10.1029/2020JA028569
- [70] LIU J, WANG W B, QIAN L Y, et al. Solar flare effects in the Earth's magnetosphere[J]. *Nature Physics*, 2021, **17**(7): 807-812. DOI: 10.1038/s41567-021-01203-5
- [71] LIU J, WANG W B, ZHANG X M. The characteristics of terdiurnal tides in the ionosphere[J]. *Astrophysics and Space Science*, 2020, **365**(9): 155. DOI: 10.1007/s10509-020-03874-7
- [72] LIU J, ZHANG D H, GONCHARENKO L P, et al. The latitudinal variation and hemispheric asymmetry of the ionospheric lunitidal signatures in the American sector during major sudden stratospheric warming events[J]. *Journal of Geophysical Research: Space Physics*, 2021, **126**(5): 2020JA028859. DOI: 10.1029/2020JA028859
- [73] LIU J, ZHANG D H, HAO Y Q, et al. Multi-instrumental observations of the quasi-16-day variations from the lower thermosphere to the topside ionosphere in the low-latitude eastern Asian sector during the 2017 sudden stratospheric warming event[J]. *Journal of Geophysical Research: Space Physics*, 2020, **125**(3): e2019JA027505. DOI: 10.1029/2019JA027505
- [74] LIU J, ZHANG D H, HAO Y Q, et al. The time delay between the equatorial ionization anomaly and the equatorial electrojet in the eastern Asian and American sectors[J]. *Advances in Space Research*, 2022, **69**(1): 187-196. DOI: 10.1016/j.asr.2021.10.004
- [75] LIU J, ZHANG D H, MO X H, et al. Morphological differences of the northern equatorial ionization anomaly between the eastern Asian and American sectors[J]. *Journal of Geophysical Research: Space Physics*, 2020, **125**(3): e2019JA027506. DOI: 10.1029/2019JA027506
- [76] LIU L B, DING Z H, LE H J, et al. New features of the enhancements in electron density at low latitudes[J]. *Journal of Geophysical Research: Space Physics*, 2020, **125**(2): e2019JA027539. DOI: 10.1029/2019JA027539
- [77] LIU L B, DING Z H, ZHANG R L, et al. A case study of the en-

- hancements in ionospheric electron density and its longitudinal gradient at Chinese low latitudes[J]. *Journal of Geophysical Research: Space Physics*, 2020, **125**(5): e2019JA027751. DOI: 10.1029/2019JA027751
- [78] LIU L B, WAN W X. Recent ionospheric investigations in China (2018-2019)[J]. *Earth and Planetary Physics*, 2020, **4**(3): 179-205. DOI: 10.26464/epp2020028
- [79] LIU M M, YUAN Y B, HUO X L, *et al.* Simultaneous estimation of GPS P1-P2 differential code biases using low earth orbit satellites data from two different orbit heights[J]. *Journal of Geodesy*, 2020, **94**(12): 121. DOI: 10.1007/s00190-020-01458-5.
- [80] LIU Y, TANG Q, CHEN G Y, *et al.* Quasi-6-day wave effects in ionospheric E and F region during the recent solar maximum 2014-2015[J]. *Earth Planets and Space*, 2020, **72**(1): 190. DOI: 10.1186/s40623-020-01319-7
- [81] LIU Y W, XIONG C, WAN X, *et al.* Instability mechanisms for the F-region plasma irregularities inside the midlatitude ionospheric trough: swarm observations[J]. *Space Weather*, 2021, **19**(7): e2021SW002785. DOI: 10.1029/2021SW002785
- [82] LIU Y, ZHOU C, XU T, *et al.* Investigation of midlatitude nighttime ionospheric E-F coupling and interhemispheric coupling by using COSMIC GPS radio occultation measurements[J]. *Journal of Geophysical Research: Space Physics*, 2020, **125**(3): e2019JA027625. DOI: 10.1029/2019JA027625
- [83] LIU Yingyu, XING Zanyang, FENG Huiting, *et al.* Comparative analysis of optical observation characteristics between PMAFs and throat aurora[J]. *Journal of Space Science*, 2021, **41**(5): 737-745. DOI: 10.11728/cjss2021.05.737 (刘映妤, 邢赞扬, 冯惠婷, 等. 极向运动极光结构和喉区极光光学观测特征的对比分析[J]. *空间科学学报*, 2021, **41**(5): 737-745. doi: 10.11728/cjss2021.05.737)
- [84] LU H, YANG J T, LI Q L, *et al.* ELF/VLF communication experiment by modulated heating of ionospheric auroral electrojet at EISCAT[J]. *IEEE Transactions on Antennas and Propagation*, 2021, **69**(4): 2267-2273. DOI: 10.1109/TAP.2020.3026872
- [85] MA H, LIU L B, CHEN Y D, *et al.* Longitudinal differences in electron temperature on both sides of zero declination line in the mid-latitude topside ionosphere[J]. *Journal of Geophysical Research: Space Physics*, 2021, **126**(2): e2020JA028471. DOI: 10.1029/2020JA028471
- [86] MA Y Z, ZHANG Q H, JAYACHANDRAN P T, *et al.* Statistical study of the relationship between ion upflow and field-aligned current in the topside ionosphere for both hemispheres during geomagnetic disturbed and quiet time[J]. *Journal of Geophysical Research: Space Physics*, 2020, **125**(9): e2019JA027538. DOI: 10.1029/2019JA027538
- [87] MA Y Z, ZHANG Q H, LYONS L R, *et al.* Is westward travelling surge driven by the polar cap flow channels?[J]. *Journal of Geophysical Research: Space Physics*, 2021, **126**(8): e2020JA028498. DOI: 10.1029/2020JA028498
- [88] MO X H, ZHANG D H. Quasi-10d wave modulation of an equatorial ionization anomaly during the Southern Hemisphere stratospheric warming of 2002[J]. *Annales Geophysicae*, 2020, **38**(1): 9-16. DOI: 10.5194/angeo-38-9-2020
- [89] MO X H, ZHANG D H. Six-day periodic variation in equatorial ionization anomaly region[J]. *Journal of Geophysical Research: Space Physics*, 2020, **125**(11): e2020JA028225. DOI: 10.1029/2020JA028225
- [90] MO X H, ZHANG D H. A comparative study of the northern and southern equatorial ionization anomaly crests in the East-Asian sector during 2006-2015[J]. *Advances in Space Research*, 2021, **68**(3): 1461-1472. DOI: 10.1016/j.asr.2021.04.003
- [91] MO X H, ZHANG D H, LIU J, *et al.* Lunar tidal effect on equatorial ionization anomaly region in China low latitude[J]. *Journal of Geophysical Research: Space Physics*, 2021, **126**(11): e2021JA029845. DOI: 10.1029/2021JA029845
- [92] NIU D D, CUI J, GU H, *et al.* In situ heating of the Nightside Martian upper atmosphere and ionosphere: the role of solar wind electron precipitation[J]. *The Astrophysical Journal*, 2021, **909**(2): 108. DOI: 10.3847/1538-4357/abdbb0
- [93] NIU D D, CUI J, GU H, *et al.* Energetic electron depletions in the Nightside Martian upper atmosphere revisited[J]. *Journal of Geophysical Research: Space Physics*, 2020, **125**(4): e2019JA027670. DOI: 10.1029/2019JA027670
- [94] NIU D D, CUI J, WU S Q, *et al.* Species-dependent response of the Martian ionosphere to the 2018 global dust event[J]. *Journal of Geophysical Research: Planets*, 2021, **126**(2): e2020JE006679. DOI: 10.1029/2020JE006679
- [95] NIU D D, GU H, CUI J, *et al.* Effects of the solar wind dynamic pressure on the martian topside ion distribution: implications on the variability of bulk ion outflow[J]. *The Astrophysical Journal*, 2021, **922**(2): 231. DOI: 10.3847/1538-4357/ac2bfc
- [96] OUYANG X Y, PARROT M, BORTNIK J. ULF wave activity observed in the nighttime ionosphere above and some hours before strong earthquakes[J]. *Journal of Geophysical Research: Space Physics*, 2020, **125**(9): e2020JA028396. DOI: 10.1029/2020JA028396
- [97] QIU L H, YU T, YAN X X, *et al.* Altitudinal and latitudinal variations in ionospheric sporadic-E layer obtained from FORMOSAT-3/COSMIC radio occultation[J]. *Journal of Geophysical Research: Space Physics*, 2021, **126**(9): e2021JA029454. DOI: 10.1029/2021JA029454
- [98] QIU L H, ZUO X M, YU T, *et al.* The characteristics of summer descending sporadic E layer observed with the ionosondes in the China region[J]. *Journal of Geophysical Research: Space Physics*, 2021, **126**(3): e2020JA028729. DOI: 10.1029/2020JA028729
- [99] REN D X, LEI J H, ZHOU S, *et al.* High-speed solar wind imprints on the ionosphere during the recovery phase of the august 2018 geomagnetic storm[J]. *Space Weather*, 2020, **18**(7): e2020SW002480. DOI: 10.1029/2020SW002480
- [100] SHE C L, YUE X A, HU L H, *et al.* Estimation of ionospheric total electron content from a multi-GNSS station in China[J]. *IEEE Transactions on Geoscience and Remote Sensing*, 2020, **58**(2): 852-860. DOI: 10.1109/TGRS.2019.2941049
- [101] SUN W J, NING B Q, HU L H, *et al.* The evolution of complex E_s observed by multi instruments over low - latitude China[J]. *Journal of Geophysical Research: Space Physics*, 2020, **125**(8): e2019JA027656. DOI: 10.1029/2019JA027656
- [102] SUN W J, WU B Y, WU Z, *et al.* IONISE: an ionospheric observational network for irregularity and scintillation in East and Southeast Asia[J]. *Journal of Geophysical Research: Space Physics*, 2020, **125**(8): e2020JA028055. DOI: 10.1029/2020JA028055
- [103] SUN W J, ZHAO X, HU L, *et al.* Morphological characteristics of thousand-kilometer-scale E_s structures over China[J]. *Journal of Geophysical Research: Space Physics*, 2021, **126**(2): e2020JA028712. DOI: 10.1029/2020JA028712
- [104] SUN W J, HU L H, YANG Y Y, *et al.* Occurrences of regional strong E_s irregularities and corresponding scintillations character-

- ized using a high-temporal-resolution GNSS network[J]. *Journal of Geophysical Research: Space Physics*, 2021, **126**(11): e2021JA029460. DOI: 10.1029/2021JA029460
- [105] SUN Y Y, SHEN M M, TSAI Y L, *et al.* Wave steepening in ionospheric total electron density due to the 21 August 2017 total solar eclipse[J]. *Journal of Geophysical Research: Space Physics*, 2021, **126**(3): e2020JA028931. DOI: 10.1029/2020JA028931
- [106] SUN Y Y, CHEN C H, QING H, *et al.* Nighttime ionosphere perturbed by the annular solar eclipse on June 21, 2020[J]. *Journal of Geophysical Research: Space Physics*, 2021, **126**(9): e2021JA029419. DOI: 10.1029/2021JA029419
- [107] TANG Q, ZHAO J Q, YU Z B, *et al.* Occurrence and variations of middle and low latitude sporadic E layer investigated with longitudinal and latitudinal chains of ionosondes[J]. *Space Weather*, 2021, **19**(12): e2021SW002942. DOI: 10.1029/2021SW002942
- [108] TANG Q, ZHOU C, LI Z S, *et al.* Semi-monthly lunar tide oscillation of foF2 in Equatorial Ionization Anomaly (EIA) crests during 2014-2015 SSW[J]. *Journal of Geophysical Research: Space Physics*, 2021, **126**(2): e2020JA028708. DOI: 10.1029/2020JA028708
- [109] TANG Q, ZHOU C, LIU H X, *et al.* The possible role of turbopause on sporadic-E layer formation at middle and low latitudes[J]. *Space Weather*, 2021, **19**(12): e2021SW002883. DOI: 10.1029/2021SW002883
- [110] TANG Q, ZHOU C, LIU Y, *et al.* Response of sporadic e layer to sudden stratospheric warming events observed at low and middle latitudes[J]. *Journal of Geophysical Research: Space Physics*, 2020, **125**(2): e2019JA027283. DOI: 10.1029/2019JA027283
- [111] TARIQ M A, SHAH M, LI Z S, *et al.* Lithosphere ionosphere coupling associated with three earthquakes in Pakistan from GPS and GIM TEC[J]. *Journal of Geodynamics*, 2021, **147**: 101860
- [112] TIAN Y Y, HAO Y Q, LI Q H, *et al.* The role of strong meridional neutral winds in the formation of deep equatorial ionization trough in CHAMP observations[J]. *Journal of Geophysical Research: Space Physics*, 2021, **126**(8): e2021JA029319. DOI: 10.1029/2021JA029319
- [113] WAN X, XIONG C, GAO S Z, *et al.* The nighttime ionospheric response and occurrence of equatorial plasma irregularities during geomagnetic storms: a case study[J]. *Satellite Navigation*, 2021, **2**(1): 23. DOI: 10.1186/s43020-021-00055-x
- [114] WAN X, ZHONG J H, XIONG C, *et al.* Persistent occurrence of strip-like plasma density bulges at conjugate lower-mid latitudes during the September 8-9, 2017 geomagnetic storm[J]. *Journal of Geophysical Research: Space Physics*, 2021, **126**(5): e2020JA029020. DOI: 10.1029/2020JA029020
- [115] WANG H, HE Y F, LÜHR H, *et al.* Local time and longitudinal differences in the occurrence frequency of ionospheric EMIC waves during magnetic storm periods[J]. *Journal of Geophysical Research: Space Physics*, 2021, **126**(2): e2020JA028878. DOI: 10.1029/2020JA028878
- [116] WANG H, LÜHR H. Effects of solar illumination and substorms on auroral electrojets based on CHAMP observations[J]. *Journal of Geophysical Research: Space Physics*, 2021, **126**(2): e2020JA028905. DOI: 10.1029/2020JA028905
- [117] WANG H, LÜHR H, ZHANG K D. Longitudinal variation in the thermospheric superrotation: CHAMP observation and TIE-GCM simulation[J]. *Geophysical Research Letters*, 2021, **48**(18): e2021GL095439. DOI: 10.1029/2021GL095439
- [118] WANG H, ZHENG Z, ZHANG K, *et al.* Influence of nonmigrating tides and geomagnetic field geometry on the diurnal and longitudinal variations of the equatorial electrojet[J]. *Journal of Geophysical Research: Space Physics*, 2020, **125**(6): e2019JA027631. DOI: 10.1029/2019JA027631
- [119] WANG J, ZUO X M, SUN Y Y, *et al.* Multilayered sporadic-E response to the annular solar eclipse on June 21, 2020[J]. *Space Weather*, 2021, **19**(3): e2020SW002643. DOI: 10.1029/2020SW002643
- [120] WANG J, CHEN G, YU T, *et al.* Middle-scale ionospheric disturbances observed by the oblique-incidence ionosonde detection network in north China after the 2011 Tohoku Tsunamigenic earthquake[J]. *Sensors*, 2021, **21**(3): 1000. DOI: 10.3390/s21031000
- [121] WANG Y, CAO Z, XING Z Y, *et al.* GPS scintillations and TEC variations in association with a polar cap arc[J]. *Journal of Geophysical Research: Space Physics*, 2021, **126**(3): e2020JA028968. DOI: 10.1029/2020JA028968
- [122] WANG Y, JAYACHANDRAN P T, THEMENS D R, *et al.* A case study of polar cap sporadic-E layer associated with TEC Variations[J]. *Remote Sensing*, 2021, **13**(7): 1324. DOI: 10.3390/rs13071324
- [123] WANG Y, ZHANG Q H, MA Y Z, *et al.* Polar ionospheric large-scale structures and dynamics revealed by TEC Keogram extracted from TEC maps[J]. *Journal of Geophysical Research: Space Physics*, 2020, **125**(1): e2019JA027020. DOI: 10.1029/2019JA027020
- [124] WANG Y H, HUANG F Q, LEI J H, *et al.* Ionospheric diurnal double-maxima patterns observed by the TEC from Beidou geostationary satellites in the Asian-Australian sector during 2016-2018[J]. *Journal of Geophysical Research: Space Physics*, 2021, **126**(1): e2020JA028578. DOI: 10.1029/2020JA028578
- [125] WANG Z W, HU H Q, LU J Y, *et al.* Observational evidence of transient lobe reconnection triggered by sudden northern enhancement of IMF Bz[J]. *Journal of Geophysical Research: Space Physics*, 2021, **126**(9): e2021JA029410. DOI: 10.1029/2021JA029410
- [126] WEI L H, JIANG C H, HU Y G, *et al.* Ionosonde observations of spread F and Spread Es at low and middle latitudes during the recovery phase of the 7-9 September 2017 geomagnetic storm[J]. *Remote Sensing*, 2021, **13**(5): 1010. DOI: 10.3390/rs13051010
- [127] WEI L H, JIANG C H, LAN T, *et al.* Observations of unusual daytime range spread F at middle latitude during the afternoon hours[J]. *Space Weather*, 2021, **19**(11): e2021SW002870. DOI: 10.1029/2021SW002870
- [128] WU J, BLAGOVESHCHENSKAYA N F, WU J, *et al.* Altitude descents in high-frequency enhanced plasma and ion lines during ionospheric heating at EISCAT[J]. *Journal of Atmospheric and Solar-Terrestrial Physics*, 2021, **212**: 105425. DOI: 10.1016/j.jastp.2020.105425
- [129] WU X S, CUI J, CAO Y T, *et al.* Response of photoelectron peaks in the Martian ionosphere to solar EUV/X-ray irradiance[J]. *Earth and Planetary Physics*, 2020, **4**(4): 390-395. DOI: 10.26464/ep2020035
- [130] WU X S, CUI J, NIU D D, *et al.* Compositional variation of the dayside Martian ionosphere: inference from photochemical equilibrium computations[J]. *The Astrophysical Journal*, 2021, **923**(1): 29. DOI: 10.3847/1538-4357/ac24fe
- [131] WU X S, CUI J, YELLE R V, *et al.* Photoelectrons as a tracer of planetary atmospheric composition: application to CO on mars[J]. *Journal of Geophysical Research: Planets*, 2020, **125**(7):

- e2020JE006441. DOI: 10.1029/2020JE006441
- [132] XIE H Y, LI G Z, ZHAO X K, *et al.* Coupling between *E* region quasi - periodic echoes and *F* region medium-scale traveling ionospheric disturbances at low latitudes[J]. *Journal of Geophysical Research: Space Physics*, 2020, **125**(5): e2019JA027720. DOI: 10.1029/2019JA027720
- [133] XIE H Y, YANG S P, ZHAO X K, *et al.* Unexpected high occurrence of daytime *F* - region backscatter plume structures over low latitude Sanya and their possible origin[J]. *Geophysical Research Letters*, 2020, **47**(22): e2020GL090517. DOI: 10.1029/2020GL090517
- [134] XIONG C, STOLLE C, ALKEN P, *et al.* Relationship between large-scale ionospheric field-aligned currents and electron/ion precipitations: DMSP observations[J]. *Earth, Planets and Space*, 2020, **72**(1): 147. DOI: 10.1186/s40623-020-01286-z
- [135] XIONG C, STOLLE C, MICHAELIS I, *et al.* Correlation analysis of field-aligned currents from the magnetic measurements of GRACE follow-on mission[J]. *Earth, Planets and Space*, 2021, **73**(1): 206. DOI: 10.1186/s40623-021-01540-y
- [136] XIONG C, XU J S, STOLLE C, *et al.* On the occurrence of GPS signal amplitude degradation for receivers on board LEO satellites[J]. *Space Weather*, 2020, **18**(2): e2019SW002398. DOI: 10.1029/2019SW002398
- [137] XIONG P, LONG C, ZHOU H Y, *et al.* Pre-earthquake ionospheric perturbation identification using CSES data via transfer learning[J]. *Frontiers in Environmental Science*, 2021, **9**: 779255
- [138] XIONG P, LONG C, ZHOU H Y, *et al.* Identification of electromagnetic pre-earthquake perturbations from the DEMETER data by machine learning[J]. *Remote Sensing*, 2020, **12**(21): 3643.
- [139] XIONG P, MARCHETTI D, DE SANTIS A, *et al.* SafeNet: SwArm for earthquake perturbations identification using deep learning networks[J]. *Remote Sensing*, 2021, **13**(24): 5033
- [140] XIONG P, ZHAI D L, LONG C, *et al.* Long short - term memory neural network for ionospheric total electron content forecasting over China[J]. *Space Weather*, 2021, **19**(4): e2020SW002706
- [141] XU T, HU Y L, DENG Z X, *et al.* Revisit to sporadic *E* layer response to presumably seismogenic electrostatic fields at middle latitudes by model simulation[J]. *Journal of Geophysical Research: Space Physics*, 2020, **125**(3): e2019JA026843. DOI: 10.1029/2019JA026843
- [142] YAN M D, DANG T, LEI J H, *et al.* From bow waves to traveling atmospheric disturbances: thermospheric perturbations along solar eclipse trajectory[J]. *Journal of Geophysical Research: Space Physics*, 2021, **126**(4): e2020JA028523. DOI: 10.1029/2020JA028523
- [143] YAN R, ZHIMA Z, XIONG C, *et al.* Comparison of electron density and temperature from the CSES satellite with other space-borne and ground-based observations[J]. *Journal of Geophysical Research: Space Physics*, 2020, **125**(10): e2019JA027747. DOI: 10.1029/2019JA027747
- [144] YANG N, XIA C L, YU T, *et al.* Measurement of Martian atmospheric winds by the O₂ 1.27 μm airglow observations using Doppler Michelson interferometry: a concept study[J]. *Science China-Earth Sciences*, 2021, **64**(11): 2027-2042. DOI: 10.1007/s11430-020-9814-7
- [145] YANG J T, LI Q L, LU H, *et al.* CSES observations of ELF wave radiation excited by the EISCAT heater[J]. *Physics of Plasmas*, 2020, **27**(12): 122903. DOI: 10.1063/5.0022474
- [146] YANG S P, WU Z, DUBS M, *et al.* MIOS optical subsystem for determining physical and chemical properties of meteors producing plasma irregularities[J]. *Advances in Space Research*, 2021, **68**(3): 1556-1567. DOI: 10.1016/j.asr.2021.03.031
- [147] YANG Y Y, ZHIMA Z R, SHEN X H, *et al.* The first intense geomagnetic storm event recorded by the China Seismo-Electromagnetic Satellite[J]. *Space Weather*, 2020, **18**(1): e2019SW002243. DOI: 10.1029/2019SW002243
- [148] YANG Z Y, ZHANG B Z, LEI J H, *et al.* Nonlinear response of the cross polar cap potential to solar wind density under northward interplanetary magnetic field[J]. *Geophysical Research Letters*, 2020, **47**(8): e2020GL087559. DOI: 10.1029/2020GL087559
- [149] YE H L, XUE X H, YU T, *et al.* Ionospheric *F*-layer scintillation variabilities over the American sector during sudden stratospheric warming events[J]. *Space Weather*, 2021, **19**(8): e2020SW002703. DOI: 10.1029/2020SW002703
- [150] YU T, YE H L, LIU H X, *et al.* Ionospheric *F* layer scintillation weakening as observed by COSMIC/FORMOSAT-3 during the major sudden stratospheric warming in January 2013[J]. *Journal of Geophysical Research: Space Physics*, 2020, **125**(9): e2019JA027721. DOI: 10.1029/2019JA027721
- [151] YUAN Y B, WANG N B, LI Z S, *et al.* The BeiDou global broadcast ionospheric delay correction model (BDGIM) and its preliminary performance evaluation results[J]. *Navigation*, 2019, **66**(1): 55-69. DOI: 10.1002/navi.292
- [152] YUE X A, WAN W X, XIAO H, *et al.* Preliminary experimental results by the prototype of Sanya Incoherent Scatter Radar[J]. *Earth and Planetary Physics*, 2020, **4**(6): 579-587. DOI: 10.26464/epp2020063
- [153] ZHAI C Z, LU G, YAO Y B, *et al.* 3-D tomographic reconstruction of SED plume during 17 March 2013 Storm[J]. *Journal of Geophysical Research: Space Physics*, 2020, **125**(11): e2020JA028257. DOI: 10.1029/2020JA028257
- [154] ZHAI C Z, SHI X L, WANG W B, *et al.* Characterization of High-m ULF wave signatures in GPS TEC data[J]. *Geophysical Research Letters*, 2021, **48**(14): e2021GL094282. DOI: 10.1029/2021GL094282
- [155] ZHAI C Z, YAO Y B, KONG J. Three-dimensional reconstruction of seismo-traveling ionospheric disturbances after March 11, 2011, Japan Tohoku earthquake[J]. *Journal of Geodesy*, 2021, **95**(7): 77. DOI: 10.1007/s00190-021-01533-5
- [156] ZHANG D, ZHANG Q H, MA Y Z, *et al.* Solar and geomagnetic activity impact on occurrence and spatial size of cold and hot polar cap patches[J]. *Geophysical Research Letters*, 2021, **48**(18): e2021GL094526. DOI: 10.1029/2021GL094526
- [157] ZHANG K D, WANG H, LIU J, *et al.* Dynamics of the tongue of ionizations during the geomagnetic storm on September 7, 2015[J]. *Journal of Geophysical Research: Space Physics*, 2021, **126**(6): e2020JA029038. DOI: 10.1029/2020JA029038
- [158] ZHANG K D, WANG H, WANG W B. Equatorial nighttime thermospheric zonal wind jet response to the temporal oscillation of solar wind[J]. *Journal of Geophysical Research: Space Physics*, 2021, **126**(8): e2021JA029345. DOI: 10.1029/2021JA029345
- [159] ZHANG K D, WANG H, WANG W B, *et al.* Nighttime meridional neutral wind responses to SAPS simulated by the TIEGCM: a universal time effect[J]. *Earth and Planetary Physics*, 2021, **5**(1): 52-62. DOI: 10.26464/epp2021004
- [160] ZHANG K D, WANG H, YAMAZAKI Y, *et al.* Effects of subauroral polarization streams on the equatorial electrojet during the geomagnetic storm on June 1, 2013[J]. *Journal of Geophysical Re-*

- Research: Space Physics*, 2021, **126**(10): e2021JA029681. DOI: 10.1029/2021JA029681
- [161] ZHANG Q H, MOEN J, LOCKWOOD M, et al. Polar cap patch transportation beyond the classic scenario[J]. *Journal of Geophysical Research: Space Physics*, 2016, **121**(9): 9063-9074. DOI: 10.1002/2016JA022443
- [162] ZHANG Q H, XING Z Y, WANG Y, et al. Formation and evolution of polar cap ionospheric patches and their associated upflows and scintillations[M]//ZONG Q G. ESCOUBET P, SIBECK D, et al. Dayside Magnetosphere Interactions. Wiley, 2020. DOI: 10.1002/9781119509592.ch16
- [163] ZHANG Q H, ZHANG Y L, WANG C, et al. Multiple transpolar auroral arcs reveal insight about coupling processes in the Earth's magnetotail[J]. *Proceedings of the National Academy of Sciences of the USA*, 2020, **117**(28): 16193-16198. DOI: 10.1073/pnas.2000614117
- [164] ZHANG Q H, ZHANG Y L, WANG C, et al. A space hurricane over the Earth's polar ionosphere[J]. *Nature Communications*, 2021, **12**(1): 1207. DOI: 10.1038/s41467-021-21459-y
- [165] ZHANG R L, LE H J, LI W B, et al. Multiple technique observations of the ionospheric responses to the 21 June 2020 solar eclipse[J]. *Journal of Geophysical Research: Space Physics*, 2020, **125**(12): e2020JA028450. DOI: 10.1029/2020JA028450
- [166] ZHANG R L, LIU L B, LIU H X, et al. Interhemispheric transport of the ionospheric F region plasma during the 2009 sudden stratosphere warming[J]. *Geophysical Research Letters*, 2020, **47**(6): e2020GL087078. DOI: 10.1029/2020GL087078
- [167] ZHANG R L, LIU L B, YU Y, et al. Westward electric fields in the afternoon equatorial ionosphere during geomagnetically quiet times[J]. *Journal of Geophysical Research: Space Physics*, 2020, **125**(12): e2020JA028532. DOI: 10.1029/2020JA028532
- [168] ZHANG W, HUO X L, YUAN Y B, et al. Algorithm research using GNSS-TEC data to calibrate TEC calculated by the IRI-2016 Model over China[J]. *Remote Sensing*, 2021, **13**(19): 4002. DOI: 10.3390/rs13194002
- [169] ZHANG X M, FROLOV V, SHEN X H, et al. The electromagnetic emissions and plasma modulations at middle latitudes related to SURA-CSES experiments in 2018[J]. *Radio Science*, 2020, **55**(8): e2019RS007040. DOI: 10.1029/2019RS007040
- [170] ZHANG X M, WANG Y L, BOUDJADA M Y, et al. Multi-experiment observations of ionospheric disturbances as precursory effects of the Indonesian Ms6.9 earthquake on August 05, 2018[J]. *Remote Sensing*, 2020, **12**(24): 4050. DOI: 10.3390/rs12244050.
- [171] ZHAO H S, XU Z W, TANG W, et al. Electromagnetic scattering by artificial plasma clouds in the ionosphere[J]. *IEEE Transactions on Antennas and Propagation*, 2020, **68**(6): 4810-4819: DOI: 10.1109/TAP.2020.2972608
- [172] ZHAO S F, SHEN X H, ZHOU C, et al. The influence of the ionospheric disturbance on the ground based VLF transmitter signal recorded by LEO satellite – Insight from full wave simulation[J]. *Results in Physics*, 2020, **19**: 103391. DOI: 10.1016/j.rinp.2020.103391
- [173] ZHAO S F, SHEN X H, LIAO L, et al. Investigation of precursors in VLF subionospheric signals related to strong earthquakes (M>7) in Western China and possible explanations[J]. *Remote Sensing*, 2020, **12**(21): 3563. DOI: 10.3390/rs12213563
- [174] ZHAO S F, SHEN X H, ZHIMA Z, et al. The very low-frequency transmitter radio wave anomalies related to the 2010 Ms7.1 Yushu earthquake observed by the DEMETER satellite and the possible mechanism[J]. *Annales Geophysicae*, 2020, **38**(5): 969-981. DOI: 10.5194/angeo-38-969-2020
- [175] ZHAO Weihua, ZHANG Qinghe, WANG Cheng, et al. Preliminary study on loss of lock of satellite signal at the mid-latitude region in China[J]. *Chinese Journal of Radio Science*, 2022, **37**(3): 1-8. DOI: 10.12265/j.cjors.2021076 (赵伟华, 张清和, 王成, 等. 我国中纬地区卫星信号失锁现象初步研究[J]. 电波科学学报, 2022, **37**(3): 1-8. DOI: 10.12265/j.cjors.2021076)
- [176] ZHAO X K, XIE H Y, HU L H, et al. Climatology of equatorial and low-latitude F region kilometer-scale irregularities over the meridian circle around 120°E/60°W[J]. *GPS Solutions*, 2021, **25**(1): 20. DOI: 10.1007/s10291-020-01054-2
- [177] ZHAO X K, LI G Z, XIE H Y, et al. The prediction of day-to-day occurrence of low latitude ionospheric strong scintillation using gradient boosting algorithm[J]. *Space Weather*, 2021, **19**(12): e2021SW002884. DOI: 10.1029/2021SW002884
- [178] ZHIMA Z M, HU Y P, SHEN X H, et al. Storm-time features of the ionospheric ELF/VLF waves and energetic electron fluxes revealed by the China Seismo-electromagnetic satellite[J]. *Applied Sciences*, 2021, **11**(6): 2617. DOI: 10.3390/app11062617
- [179] ZHIMA Z R, HUANG J P, SHEN X H, et al. Simultaneous observations of ELF/VLF rising-tone quasiperiodic waves and energetic electron precipitations in the high-latitude upper ionosphere[J]. *Journal of Geophysical Research: Space Physics*, 2020, **125**(5): e2019JA027574. DOI: 10.1029/2019ja027574
- [180] ZHONG J H, LEI J H, YUE X A et al. Correlation between ionospheric TEC and the DCB stability of GNSS receivers from 2014 to 2016. *Remote Sens.* 2019, **11**, 2657[J]. *Remote Sensing*, 2020, **12**(21): 3496. DOI: 10.3390/rs12213496
- [181] ZHOU X, LIU H L, LU X, et al. Quiet - time day - to - day variability of equatorial vertical E×B drift from atmosphere perturbations at dawn[J]. *Journal of Geophysical Research: Space Physics*, 2020, **125**(4): e2020JA027824. DOI: 10.1029/2020JA027824
- [182] ZHOU X, YUE X A, LIU H L, et al. A comparative study of ionospheric day-to-day variability over Wuhan based on ionosonde measurements and model simulations[J]. *Journal of Geophysical Research: Space Physics*, 2021, **126**(3): e2020JA028589. DOI: 10.1029/2020JA028589
- [183] ZHOU X, YUE X A, LIU H L, et al. Response of atmospheric carbon dioxide to the secular variation of weakening geomagnetic field in whole atmosphere simulations[J]. *Earth and Planetary Physics*, 2021, **5**(4): 327-336. DOI: 10.26464/ep2021040
- [184] ZHOU Y L, LÜHR H, ALKEN P. Average ionospheric middle and low latitudes nighttime zonal currents deduced from CHAMP[J]. *Journal of Geophysical Research: Space Physics*, 2020, **125**(8): e2019JA027702. DOI: 10.1029/2019JA027702

CHEN Zeyu, XU Jiyao, CHEN Hongbin, CHEN Wen, REN Rongcai, HU Xiong, ZHU Yajun, XUE Xianghui, LU Gaopeng, ZHANG Shaodong, HUANG Kaiming, TIAN Wenshou, ZHANG Jiankai, HU Dingzhu, RAO Jian, HU Yongyun, XIA Yan. Advances in the Researches of the Middle and Upper Atmosphere in China in 2020–2022. *Chinese Journal of Space Science*, 2022, 42(4). DOI:10.11728/cjss2022.04.yg20

Advances in the Researches of the Middle and Upper Atmosphere in China in 2020–2022

CHEN Zeyu^{1,9}, XU Jiyao^{2,9}, CHEN Hongbin^{1,9}, CHEN Wen^{1,9}, REN Rongcai^{1,9}, HU Xiong^{2,9}, ZHU Yajun^{2,9}, XUE Xianghui³, LU Gaopeng^{3,8}, ZHANG Shaodong⁴, HUANG Kaiming⁴, TIAN Wenshou⁵, ZHANG Jiankai⁵, HU Dingzhu⁶, RAO Jian⁶, HU Yongyun⁷, XIA Yan⁷

1. Institute of atmospheric physics, Chinese Academy of Sciences, Beijing 100029
2. National Space Science Center, Chinese Academy of Sciences, Beijing 100190
3. School of Earth and Space Sciences, University Science and Technology of China, Hefei 230026
4. School of Electronic Information, Wuhan University, Wuhan 430072
5. College of Atmospheric Science, Lanzhou University, Lanzhou 730000
6. Nanjing University of Information Science and Technology, Nanjing 210044
7. Peking University, Beijing 100871
8. Key Laboratory of Atmospheric Optics, Anhui Institute of Optics and Fine Mechanics, HFIPS, Chinese Academy of Sciences, Hefei, Anhui Province, 230031
9. University of the Chinese Academy of Sciences, Beijing 100049

Abstract

This report reviews the researches for the middle and upper atmosphere in 2020–2022 by Chinese scientists. The report consists of four parts introducing primarily the results from the aspects of the development of infrastructure, the structure and composition, the climate and modeling, and the dynamics for the middle and upper atmosphere, respectively.

Key words

Middle and upper atmosphere, Structure and composition, Climate, Dynamics

1 Development of Infrastructure

The development of the daytime lidar at Yanqing station was reported by Xia *et al.*^[1]. This lidar can permit full-diurnal-cycle observation of the metal Na layer. In order

to suppress the skylight background during daytime effectively with less signal losses, a dual-channel Faraday filtering unit was implemented in the lidar receiver. Based on the diurnal Na lidar system, a good number of continuous observational results that lasted more than

120 h with a good signal-to-noise ratio were obtained, demonstrating its reliability. The lidar will provide valuable observational support for investigating the rapid production and disappearance mechanisms of Na atoms.

A dual-wavelength tunable lidar system that simultaneously detects the Ca and Ca⁺ layers has been established at Yanqing Station (Wu *et al.*^[2]). The lidar system implements a pulsed Nd: YAG laser that simultaneously pumps two dye lasers, which reduces the hardware configuration of the lidar system. Three nights of preliminary simultaneous observations of Ca and Ca⁺ layers are reported.

Du *et al.*^[3] reported that a Na-K lidar was built in 2016 at são José dos Compose, Brazil, by the joint work of NSSC and INPE. This system realized simultaneously observation of the potassium and sodium metal layer, and this is the first time of potassium layer detection in South America. The detection capability of potassium lidar is high, compared with the available detection results of Germany potassium layer.

A new Ni lidar has been designed and deployed at Yanqing station (Wu *et al.*^[4]). The Ni lidar has good stability, and makes continuous Ni measurements over an extended period, enabling the first investigation of night-time and seasonal density variation of the Ni layer. For the first time, we used the high altitude Ni lidar to determine the branching ratios of three different optical transitions from Ni in the 3d9(2D)4s3D3 state (excited at 341 nm), and showed that these branching ratios are very close to the theoretical values.

The first nighttime meteor observation by MF radar in mid-latitude China was reported by Cai *et al.*^[5]. The observation period was 12:00–22:00 (UT) and the observation range was 78–150 km. By using broad vertical beams, totally 94 meteor echoes were obtained with the mean height of 106.5 km and the majority of them were distributed from 97 km to 115 km. Ambipolar diffusion coefficient, angle of arrival and some relevant parameters were simultaneously analyzed using the raw data. Initial bi-hourly and nightly averaged wind profiles were calculated, which are well fitted to the wind estimations by co-located VHF meteor radar at the altitude of 100–110 km. On the other side, echoes around 140 km are successfully detected in the observation.

Ban *et al.*^[6] reported a Rayleigh scattering lidar for measuring the atmospheric density and temperature has been deployed at Zhongshan Station (69.4°S, 76.4°E), Antarctica. Lidar transmitter was a frequency doubled

Nd: YAG laser with about 400 mJ pulse energy and a 30 Hz repetition rate. A telescope with a 0.8 m diameter pointing to the zenith direction served as the lidar receiver. This lidar was capable of profiling the density and temperature in the Upper Stratosphere and Lower Mesosphere (USLM) region. At the vertical resolution of 300 m and the temporal resolution of 30 min, the lidar measurement uncertainties, mainly due to the photon noise, were calculated to be within 1.5% and 1 K for density and temperature, respectively. Since March 2020, this lidar has been routinely operated at Zhongshan station for exploring the atmospheric density and temperature variations and wave propagation characteristics in the polar USLM region.

Chen *et al.*^[7] reported that a sodium Doppler lidar system with three-directional measurements of sodium density, atmospheric wind field, and temperature was established at Zhongshan (69.4°S, 76.4°E), Antarctica. On 14 November 2019, a Sporadic Sodium Layer (SSL) was observed at an altitude range of 93–103 km. The temporal/spatial sodium density variations of this SSL are associated with a strong sporadic E (Es) layer at nearly the same height, which is modulated by the convective electric field. By considering the structures and the time lags of the SSL's growth at three positions, the SSL appears to have a horizontal advection in an approximately westward direction with a velocity of the order of 80 m·s⁻¹. This is consistent with the zonal wind velocity derived from the lidar system itself. The temporal/spatial sodium density variations strongly indicate that the formation and perturbation of SSLs are related to the evolution of ES layers due to varied electric fields and atmospheric gravity waves, while it is advected by the horizontal wind.

Tian *et al.*^[7] presented the Beijing Mesosphere Stratosphere and Troposphere (MST) radar, established at Xianghe Observatory of Whole Atmosphere (39.75°N, 116.96°E) by the Institute of Atmospheric Physics, Chinese Academy of Sciences, with the support of the Chinese Meridian Project. It was put into route operation in late 2011. It has been verified that the horizontal wind profiles are in good agreement with the nearest radiosonde observations. The dataset of atmospheric horizontal wind speed and direction from 3 to 25 km with a vertical resolution of 600 m and a sampling interval of 30 min was provided based on the Beijing MST radar observation in 2012. This high temporal and spatial resolution horizontal wind dataset can play a

unique role in atmospheric dynamics and processes in the troposphere and lower stratosphere.

Chen *et al.*^[8] have improved the power spectral density data processing algorithms to obtain higher quality MST radar data such as horizontal wind, vertical wind, and spectral width. It has been proved to be effective and reliable after comparing the derived data with the original data, radiosonde data and ERA5 reanalysis data.

2 Structure and Composition in the Middle Atmosphere

Wu *et al.*^[9] reported an unusual equatorial plasma bubble during the recovery phase of a geomagnetic storm. The results showed the EPB occurred after sunset and drifted westward, which is different from previous EPB. The EPBs dissipated at about one hour after sunrise and its lifetime is about three hours. Based on the simulations of the Thermosphere-Ionosphere-Electrodynamics General Circulation Model (TIEGCM), they found that the rapid uplift of the ionospheric should be the main reason for triggering the EPBs. Wu *et al.*^[10] used observational data from two all-sky imagers, GPS, Swarm satellite, and a digisonde to study a special EPB event. They found that these EPBs occurred in the region of plasma depletion structure. Then, the plasma depletion structure disappeared with time. Around sunrise, new plasma depletion appeared and might merge with those EPBs. In addition, these EPBs showed special zonal drifts within a narrow longitudinal zone. An EPB drifted eastward and other remained stationary. Based on TIEGCM simulation, they found that the different zonal drifts of these EPBs should be related to the zonal winds. Sun *et al.*^[11] used observations by multiple ground-based instruments to investigate the physical processes accompanied by an EPB event that occurred at low latitudes over China. They provided observational evidence that an enhanced equatorward wind associated with a substorm could have re-initiated the Rayleigh-Taylor Instability (RTI) that forced several depletions to surge poleward by nearly 9° two hours before midnight, after a stay of nearly three hours at near 10° magnetic latitude. Accompanied by the growing phase of the EPB were two airglow-type blobs generated in the downwelling regions of a Large-Scale Wave-Like Structure (LSWS). They proposed a mechanism of LSWS-blob connection in which a westward polarization electric field inside the

LSWS was likely to have compressed plasma downward, inducing the two airglow-type blobs in the bottom side ionosphere. During the decay phase, an enhanced poleward wind associated with a passing-by Brightness Wave (BW) was likely to have transported plasma to fill the airglow depletions, which finally evolved into brightness airglow structures.

The nighttime O₂ auroral emission in winter was extracted based on the Sounding of the Atmosphere using Broadband Emission Radiometry (SABER) observation over 18 years (Gao *et al.*^[12]). The horizontal structure of O₂ aurora zone and the vertical profile of O₂ auroral volume emission rate were studied. The results indicated that the O₂ auroral intensity, peak emission rate, and peak height were respectively in the ranges of 0.14–5.97 kR, 0.97×10^2 – 41.01×10^2 photons cm⁻³·s⁻¹, and 104–112 km under the condition of *Kp* Levels 1–5. The peak height was negatively correlated with the auroral intensity and peak volume emission rate. The intensity and peak emission rate were positively related to *Kp* index but the peak height was negatively related to *Kp* index. The O₂ auroral intensity and peak volume emission rate (peak height) under solar maximum conditions were less (higher) than those under solar maximum conditions.

The SABER OH(9–7, 8–6) (2.0 μm) and OH(5–3, 4–2) (1.6 μm) airglow measurements are simulated by an OH airglow forward model using OH (4–2, 5–2, 8–5, 9–6) airglow data measured by SCIAMACHY (Zhu *et al.*^[13]). The study shows that SABER “unfiltered” data are about 40% at 1.6 μm and about 20% at 2.0 μm larger than the related simulations using the SCIAMACHY data. Deviations can be reduced by about 50% when considering the SABER interference filter characteristics and the latest HITRAN OH Einstein coefficients. The rest differences may be related to model parameter uncertainties and the SABER radiometric calibration. Yu *et al.*^[14,15] compared the observations of the sporadic E (Es) layer from global 25 ionosondes including five digisondes under the Chinese Meridian Project and the GNSS Radio Occultation (RO) satellite measurements. Their analysis indicates that there is a universal connection between the *S*₄ max index retrieved from GNSS RO measurements and the critical frequency of Es layers (*f*_{0E_s). The *S*₄max between 90 and 130 km altitude can be used as a proxy for the intensity of the Es layer. Yu *et al.*^[16] found a large-scale}

winter-to-summer transport of long-lived metallic ions within Es layers driven by the lower thermospheric meridional circulation, which can account for the long-standing mystery of the seasonal variability of the Es layer. To quantitatively investigate the global distribution of metal ions and the formation mechanisms of the ionospheric Es layer, Wu *et al.*^[17] extended the high-altitude chemistry-climate model to incorporate the full life cycle of multiple meteoric ions and atoms (Mg, Na, and Fe). The model with full ion transport significantly improves the simulation of global distribution and seasonal variations of meteoric ions. In order to help design a multistate meteor radar system, Zhong *et al.*^[18] numerically simulated the measurement errors that affect the spatial resolution and obtain the spatial-resolution distribution in three-dimensional space for the first time. Moreover, they estimated the accuracy of retrieved horizontal wind parameters.

Xia *et al.*^[18] investigated the variation in stratospheric water vapor using data from observations of the Microwave Limb Sounder on the Aura satellite (MLS), ERA-Interim reanalysis (ERA-I), and simulations by the Whole Atmosphere Community Climate Model (WACCM). It is found that the differences of annual-mean stratospheric water vapor among these datasets may be partly caused by the differences in vertical transports. Using budget analysis, they found that the upward transport of water vapor at 100 hPa is mainly located over the Pacific warm pool region and South America in the equatorial tropics in boreal winter and over the southeast of the South Asian high and south of North America in boreal summer. Temperature averaged over regions with upward transport is a better indicator of interannual variability of tropical mean stratospheric water vapor than the tropical mean temperature. It seems that the distributions of the seasonal cycle amplitude of lower stratospheric water vapor in the tropics can also be impacted by the vertical transport. The radiative effects of the interannual changes in water vapor in the lowermost stratosphere are underestimated by approximately 29% in both ERA-I and WACCM compared to MLS, although the interannual variations of water vapor in the lowermost stratosphere are dramatically overestimated in ERA-I and WACCM. The results here indicate that the radiative effect of long-term changes in water vapor in the lowermost stratosphere may be underestimated in both ERA-I and WACCM simulations.

Xia *et al.*^[18] investigated Na layer diurnal variations from the Na lidar at Yanqing station (40.5°N, 116.0°E). Considerable diurnal variation in Na density on the layer top and bottom are clearly revealed on a logarithmic scale. Intriguingly, larger height-scale nighttime extensions on the Na layer topside have been frequently observed from early summer to autumn. These observational results can provide valuable evidence for studying solar effect on the metal layer variation, atmospheric dynamical and chemical processes in the mesosphere and lower thermosphere region.

Xia *et al.*^[19] reported a statistical analysis of Sporadic Sodium Layers (SSLs) observed by the diurnal Na lidar at Yanqing station. SSLs occurred more frequently around 03:00–04:00 LT during nighttime and 16:00–17:00 LT during daytime, while rarely around midday. Diurnal variation of SSL occurrence is related to tidal-modulated Es height and photochemistry and ionization reactions. The possible explanations for the diurnal and seasonal variations of SSLs characteristics are discussed, and the key role of the evolution of Es layer height modulated by semidiurnal tide in the local time variation of SSL is highlighted.

Hu *et al.*^[20] found that the ozone level in the Arctic stratosphere at 100–150 hPa during 1998–2018 exhibits a decreasing trend of pre-decade -0.12 ± 0.07 ppmv from MERRA2, suggesting a continued depletion during this century. About 30% of this ozone depletion is contributed by the second leading mode of Sea Surface Temperature Anomalies (SSTAs) over the North Pacific with one month leading and therefore is dynamical in origin. The North Pacific SSTAs associated with this mode tends to result in a weakened Aleutian low, a strengthened Western Pacific pattern and a weakened Pacific-North American pattern, which impede the upward propagation of wavenumber-1 waves into the lower stratosphere. The changes in the stratospheric wave activity may result in decreased ozone in the Arctic lower stratosphere through weakening the Brewer-Dobson circulation.

Liu *et al.*^[21] investigated the sub-seasonal relationship between the AO and stratospheric ozone over the Arctic in each boreal winter month during 1980–2017 that is independent on the El Niño-Southern Oscillation and Quasi-Biennial Oscillation signals using Modern-Era Retrospective Analysis for Research and Applications version 2 reanalysis data sets. Results showed

that the positive AO phases correspond to two negative anomalous ozone centers located in the middle stratosphere (about 30 hPa) and upper troposphere-lower stratosphere over the Arctic in each month. There is an in-phase relationship between the AO and the Arctic ozone at 70–100 hPa in December, which is opposite to the out-of-phase relationship between these two metrics in mid-to-late winter. In December, the subtropical jet in the Pacific under the positive AO phase shifts poleward with strengthened planetary wavenumber-2 waves in the lower stratosphere. The strengthened wavenumber-2 wave flux contributes to the positive ozone anomalies at 70–100 hPa via modifying the asymmetric component of polar vortex. However, in January and February, the subtropical jet weakens during the positive AO years, along with fewer planetary wavenumber-1 waves propagating into the Arctic lower stratosphere. This weakened wavenumber-1 wave tends to result in the negative ozone anomalies via weakening the downwelling branch of Brewer-Dobson circulation and strengthening the stratospheric Arctic vortex.

Liu *et al.*^[22] compare the relationship between the Arctic Oscillation (AO) and ozone concentration in the lower stratosphere over the Arctic during 1980–1994 (P1) and 2007–2019 (P2) in January and February using reanalysis datasets. The out-of-phase relationship between the AO and ozone in the lower stratosphere is significant in January during P1 and February during P2, but it is insignificant in January during P2 and February during P1. The variable links between the AO and ozone in the lower stratosphere over the Arctic in January and February are not caused by changes in the spatial pattern of AO but are related to the anomalies in the planetary wave propagation between the troposphere and stratosphere. The upward propagation of the planetary wave in the stratosphere related to the positive phase of AO significantly weakens in January during P1 and in February during P2, which may be related to negative buoyancy frequency anomalies over the Arctic. When the AO is in the positive phase, the anomalies of planetary waves further contribute to the negative ozone anomalies via weakening the Brewer-Dobson circulation and decreasing the temperature in the lower stratosphere over the Arctic in January during P1 and in February during P2.

Xu *et al.*^[23] studied the effects of the stationary and transient transport of ozone in the Upper Troposphere

and Lower Stratosphere (UTLS) on the Ozone Valley over the Tibetan Plateau (OVTP) in summer using the daily ERA-Interim reanalysis dataset for the time period 1979–2016. They used the Lorenz circulation decomposition method to separate the stationary and transient transport of ozone into terms related to either the mean flow or eddies. The decrease in the total ozone concentration in summer is associated with the transport of ozone, which, in turn, reinforces the OVTP. The zonal (meridional) transport of ozone, which combines stationary and transient transport, strengthens (weakens) the ozone valley. The stationary zonal (meridional) transport of ozone strengthens (weakens) the ozone valley. The transient zonal (meridional) transport of ozone weakens (strengthens) the ozone valley, but this effect is weaker than that of stationary transport. The mean flow has the dominant role, especially in the stationary component. The effect of eddies on the zonal transient transport of ozone is as strong as that of the mean flow. For stationary transport, the zonal deviation of ozone transported by the zonal mean flow in the zonal (meridional) direction $C(\overline{O_3[u]})(C(\overline{O_3[v]}))$ dominates total zonal (meridional) change of ozone $C(\overline{O_3\bar{u}})(C(\overline{O_3\bar{v}}))$, which strengthens (weakens) the ozone valley. The transient transport of the zonal mean ozone by eddies $(C(\overline{[O_3] u^{*r}}))$, the zonal deviation of ozone by the zonal mean flow $(C(\overline{[O_3] u^{*r}}))$ and the zonal deviation of ozone by eddies $(C(\overline{[O_3] u^{*r} u^{*r}}))$ all have a strong effect on the ozone valley. By contrast, the transient transport of the zonal mean ozone by eddies in the meridional direction $(C(\overline{[O_3] v^{*r}}))$ has a much weaker and the smallest effect. Both the zonal deviation of ozone by the zonal mean flow and by eddies in the meridional direction $(C(\overline{[O_3] v^{*r}}))$ and $(C(\overline{[O_3] v^{*r} v^{*r}}))$ have major roles in transient meridional transport, but their roles are the opposite of each other. The contributions of stationary and transient transport to zonal transport are consistent, whereas their contributions to meridional transport are the opposite of each other. The influence of transient transport on the formation and maintenance of OVTP is not negligible.

Using Equatorial Electric Field (EEF) data observed by Swarm satellites, Liu *et al.*^[24] investigated the main

wave sources of the longitudinal structures of the EEF (LSEEF) in all seasons for the first time. They found that there existed a prominent one-peaked structure in all seasons, with a peak at 90°E–120°E and trough at 30°W–70°W, which was neglected in the past. Furthermore, they determined the main wave sources of the LSEEF in different seasons and their contributions. That is, DW2 (DE3 and DE2, DE3, DW2 and SW4) were the main wave sources of the LSEEF in spring (summer; autumn; winter) with contributions exceeding 15%.

Yang *et al.*^[25] analyzed a Gigantic Jet (GJ) event at about 22:43:30 BJT (Beijing Time = UTC+8) on 13 August 2016 which was captured by two amateur astronomers in Shikengkong, Guangdong Province, and Jiahe County, Hunan province, respectively. Using optical images, Doppler weather radar data, lightning detection network data, magnetic field, ECMWF reanalysis, sounding data, and the infrared weather maps of MTSAT (Multi-Function Transport Satellite), they analyzed the meteorological background environment, characteristics of the parent thunderstorm, and lightning activity by using multiple data. In addition, three interesting NBEs have been found in a time window containing the GJ, and the characteristics of NBEs were also analyzed. The research shows that the GJ was associated with strong vertical development of the thunderstorm and the GJ occurred near the thunderstorm's strong convection region (overshooting top). The negative cloud-to-ground flashes dominated during the thunderstorm evolution. Three positive Narrow Bipolar Events (NBEs) were detected within 30 s before and after the GJ. It indicates that the NBEs occurred in the upper and middle layers of the thunderstorm (at an altitude of 11–13 km) with radar reflectivity of 30–35 dBz.

Liu *et al.*^[26] examined the optical emissions observed by the Atmosphere-Space Interactions Monitor (ASIM) on the International Space Station associated with narrow bipolar events from thunderstorm clouds penetrating into the stratosphere. The spectral measurements were obtained for such emissions related to nine negative and three positive NBEs observed by a ground-based array of receivers. It is found that both polarities NBEs are associated with emissions at 337 nm with weak or no detectable emissions at 777.4 nm, suggesting that NBEs are associated with streamer breakdown. The rise times of the emissions for negative NBEs are about 10 μ s, consistent with source locations at cloud

tops where photons undergo little scattering by cloud particles, and for positive NBEs are about 1 ms, consistent with locations deeper in the clouds. For negative NBEs, the emission strength is almost linearly correlated with the peak current of the associated NBEs. This finding reveals the optical emissions of NBEs, which would provide a new means to measure the occurrences and strength of cloud-top discharges near the tropopause by ground-based radio signals.

Liu *et al.*^[27] reported on two mid-latitude thunderstorms in which the outbreaks of negative NBEs produced 13 blue discharges. Using the ISUAL observations, VLF/LF sferic data from a ground-based array, infrared brightness temperatures from satellites, and the reflectivity data of an S-band radar, the meteorological conditions and charge structures of two thunderstorms were investigated. In these two thunderstorms, blue discharges always occurred in the vicinity of the coldest cloud top (195 K) and clustered within a bounded area near the convective surge, leading to the overshooting thundercloud top (reaching about 18 km) into the stratosphere. The parent thunderstorms were normally electrified with a main midlevel negative and an upper positive charge layer centered at about 15 km as inferred from source heights of NBEs. The associated negative NBEs near the tropopause indicated that they are upward positive discharges initiated between the upper positive charge layer and the negative screening layer at the cloud top. These results also suggest that blue discharges are preferred to occur in selective thunderstorms associated with strong convective surges. These intense updrafts induce a high and therefore create favorable charge structures for initiating upward positive blue discharges.

Liu *et al.*^[28] reported that on the analyses of two-midnight thunderstorms in East China that were both characterized by outbreaks of negative NBEs. Combining with the VLF/LF radio signal measured by Jianghuai Area Sferic Array (JASA), S-band Doppler radar observation and balloon sounding data, two mid-latitude thunderstorms with outbreaks of negative NBEs at midnight in East China were analyzed. The comparison with the vertical radar profile shows that the bursts of negative NBEs occurred near thunderclouds with overshooting tops higher than 18 km. Manifestation of negative NBEs is observed with a relatively low spectrum width near thundercloud tops. The work findings sug-

gested that the outbreak of negative NBEs in both parent thunderstorms was produced near the overshooting tops with an intense convection surge region where the significant updrafts drove the cloud top to penetrate above the tropopause. The relatively low values of spectrum width ($<5 \text{ m}\cdot\text{s}^{-1}$) around the outbreak of negative NBEs indicate that negative NBEs tend to occur under the relatively low mixing between the upper positive charge layer and screening charge layer at thundercloud tops. Further research showed that the outbreak of negative NBEs is usually associated with overshooting tops of thunderclouds.

Ren *et al.*^[29] examined the detailed development of halo/sprite events by comparing the high-speed video observation and broadband sferic measurements. Using an intensified high-speed camera, a low-light-level video camera (SpriteCam), several radio-frequency magnetic sensors, and the National Lightning Location Network (NLDN), a total of 51 sprites have been recorded over an MCS in the central United States. They selected two sprites with halo features to study. The first event was the brightest sprites observed on that night, while the second event was a dancing sprite event containing three sprite elements all following a single +CG. The lightning-induced E-field at halo and sprite altitudes is calculated to separate the static component generated from the charge displacement and the induction term generated by the movement of charge with the TL model, and they analyzed the lightning-induced E-field perturbation at the altitude of halo initiation. It is found that the E-field generated by the current pulse of charge transfer may be more important than that generated by the charge relocation for the initiation of halos. Furthermore, the traditional electrostatic field theory has been significantly supplemented.

Wang *et al.*^[30] reported the ground-based observation of negative sprites over a tropical thunderstorm as the embryo of Hurricane Harvey (2017). Using the ground-based observations provided by an amateur photographer, Frankie Lucena, and ultralow-frequency (ULF, $<1\text{--}400 \text{ Hz}$)/very-low-frequency to low-frequency (VLF-LF, $0.5\text{--}470 \text{ kHz}$) magnetic field measured in Duke Forest, they examined six red sprites produced by negative Cloud-to-Ground (CG) lightning strokes in a tropical thunderstorm that later evolved into Hurricane Harvey (2017), and analyzed these parent strokes characteristics. Most of the sprite-parent CG strokes occurred at the edge of deep convection cores (as inferred from

cold cloud tops and high lightning density). It was found that tropical marine meteorological systems, such as tropical disturbances, depressions, and thunderstorms are more likely to be the main production systems of negative sprites. The frequent occurrence of 18 GJs produced by the same thunderstorm further indicates that the thundercloud charge structures of sprite-producing oceanic thunderstorms are significantly different from that of continental thunderstorms.

Wang *et al.*^[31] reported the space-born observation of a negative sprite with an unusual signature of associated sprite current. With the observations from ISUAL and the WWLLN, they found an extremely rare case of negative sprite where the event is near the northern border of Bogotá, Colombia. Although the sprite observations associated with negative Cloud-to-Ground (CG) strokes are very rare, it contains a distinct “sprite current” feature. Since the unusual red sprite was unrelated to the parent stroke and the atypical structure of CG, we analyzed the charge transfer time. It was found that the extraordinarily long charge transfer time (5.25 ms) after the parent negative CG stroke might play a critical role in the formation of the intense sprite current and the formation condition of the unusual sprite may also be attributed to the plasma irregularities in the mesosphere.

Zhang *et al.*^[32] reported nine TGF events related to NBEs with concurrent LF sferics and lightning location data. The LF data examined in this work were acquired respectively at multiple stations. The analyses of these TGFs found that the occurrence of NBEs was preceded by a minimum of 60 μs to 13.5 ms, and no other fast leader discharge was found within 20 ms before the TGF. Further research showed that the NBE preceding TGFs bear a harder energy spectrum with a larger proportion of high-energy photons than EIP related TGFs produced in association with the lightning leader on a statistical basis indicate. The results indicated that the NBE-related TGFs were produced by the large-scale thunderstorm E-field, supporting the relativistic feedback mechanism of TGF generation. That is, the high E-field between the two major charge layers in the thundercloud is also capable of producing TGFs, and the TGF-producing process could contribute to generating NBEs.

Zhang *et al.*^[33] analyzed the role of chemical processes in the QBO impact on stratospheric ozone in the tropics and Northern Hemisphere during winter and early spring. During easterly QBO phases, tropical

ozone concentrations decrease in the lower stratosphere and middle stratosphere but increase in the transition region between 15 and 40 hPa compared to westerly phases. Although the contributions of chemical processes to the ozone QBO signal are less than those of dynamical processes, the role of chemical processes is non-negligible. Xie *et al.*^[34] revealed that the joint effect of El Niño-Southern Oscillation (ENSO) and QBO on stratospheric ozone is approximately equal to the linear superposition of their independent impacts because the phases of wave-1 and wave-2 planetary waves anomalies related to ENSO activities are broadly similar to those of QBO phases.

Wang *et al.*^[35] found that the anomalously large Antarctic ozone hole in late austral spring is related to the weakened residual circulation and anomalous planetary wave reflection from late October to mid-November. They also showed that the anomalously large ozone loss in August is not a precondition for the anomalously large Antarctic ozone hole in late spring.

Zhang *et al.*^[36] evaluated long-term changes in Total Column Ozone (TCO) and the ozone valley over the Tibetan Plateau (TP) from 1984 to 2100 using Coupled Model Inter comparison Project Phase 6 (CMIP6) and found that most of the CMIP6 models can capture the TP ozone valley. Further analysis revealed that coupled chemical-radiative-dynamical processes play a key role in the simulation of the TP ozone valley. Multi-model mean predicts that the TP ozone valley in summer will deepen in the future.

Xie *et al.*^[37] pointed out that SST warming in the past 100 years has caused an increase in stratospheric water vapor. SST warming over the tropical Indian Ocean and the western Pacific has resulted in a drier stratosphere. However, tropical Atlantic Ocean warming has resulted in a significantly wetter stratosphere and is the main contributor to the increasing trend of water vapor in the past 100 years. The responses of Rossby and Kelvin waves over the Indian Ocean and western Pacific to Atlantic warming have led to a warmer tropopause temperature, resulting in more water vapor entering the stratosphere.

By deploying a UV radiometer aboard a stratospheric balloon released at Qaidam (QDM) during the Asian Summer Monsoon (ASM) period in 2019, Zhang *et al.*^[38] provided in situ measurement of the UV profiles from the surface to the upper troposphere and lower strato-

sphere over the Tibetan Plateau (TP), China, for the first time. Based on two in situ UV profiles accompanied by four ozonesonde measurements, the study exhibited detailed variations of downwelling UV and vertical ozone distributions over the TP during the ASM period. The UV differences between the surface and stratospheric balloon flight altitudes were 16.7, 15.8, 12.6 and 18.0 $W \cdot m^{-2}$ during the four ozonesonde launches. Due to the diurnal variations in photochemical production and the stratosphere-troposphere exchange, the integrated ozone columns below 30 km ranged from 184.4 to 221.6 DU from four ozonesonde measurements. A positive correlation between UV attenuation and ozone column was exhibited under low cloud cover and clear sky conditions.

The ozone profile in the troposphere and lower stratosphere over Beijing has been observed since 2002 by ozonesondes developed by the Institute of Atmospheric Physics. As more observations are now available, Zhang *et al.*^[39] used these data to analyze the long-term variability of ozone over Beijing during the whole period from 2002 to 2018. It is found that the ozonesondes measured increasing concentrations of ozone from 2002 to 2012 in both the troposphere and lower stratosphere. There was a sudden decrease in observed ozone between 2011 and 2012. After this decrease, the increasing trend in ozone concentrations slowed down, especially in the mid-troposphere, where the positive trend became neutral. They also used the Chemical Lagrangian Model of the Stratosphere (CLaMS) to determine the influence of the transport of ozone from the stratosphere to the troposphere on the observed ozone profiles. CLaMS simulations showed a weak increase in the contribution of stratospheric ozone before the decrease in 2011–2012 and a much more pronounced decrease after this time. Because there is no tropospheric chemistry in CLaMS, the sudden decrease simulated by CLaMS indicates that a smaller downward transport of ozone from the stratosphere after 2012 may explain a significant part of the observed decrease in ozone in the mid-troposphere and lower stratosphere.

Li *et al.*^[40] have reported the processes of dehydration and low ozone in the tropopause layer over the Asian monsoon caused by tropical cyclones based on the Lagrangian transport calculations using ERA-Interim and ERA5 reanalysis data. Ma *et al.*^[41] investigated the mixing characteristics within the tropopause transition

layer over the Asian summer monsoon region based on ozone and water vapor sounding data.

Dai *et al.*^[42] used a Rayleigh lidar has been to study the middle atmosphere at Golmud (36.25°N, 94.54°E), Qinghai, located in the northeastern part of the Tibetan Plateau. Mesospheric density profiles from 50 to 90 km were retrieved based on 205 nights of lidar observation from Aug. 2013 to Oct. 2015, with a total of 1616 hours of operation. They compared our lidar density measurements with SABER observations onboard TIMED satellite and MSIS-00 model data. The results showed that the annual mean density measured by lidar agreed well with SABER data, but both were lower than that of MSIS-00. All datasets exhibited dominant annual oscillation in the mesosphere. From 63 to 85 km, the annual amplitude of lidar density is larger than those of SABER and MSIS-00. PDD (Percentage of Density Difference) was calculated to investigate the mesospheric density climatology. The largest density variations of lidar, MSIS-00, and SABER occurred at around 72 km. Both lidar and SABER PDD reached their maximum in May, about one month earlier than the MSIS-00; while the minimum PDD appeared in late December for all datasets.

3 Climate and Modeling

Jiao *et al.*^[43] gave the full seasonal cycles of the Ni layer and Na layer, based upon the Yanqing lidar observations. The Ni and Na layers exhibit a similar annual cycle, increasing by a factor of about 3 from a mid-summer minimum to a midwinter maximum. The mean Na: Ni ratio is 8.1, which is significantly larger than their CI chondritic ratio of 1.2. This is explained by the more efficient ablation of Na from cosmic dust particles by a factor of 3, and the more rapid neutralization of Na⁺ between 90 and 100 km, where the measured Na⁺:Ni⁺ ratio is only 2.2. The Ni layer peak occurs around 84 km, 8 km below that of Na. These features are simulated satisfactorily by the Whole Atmosphere Community Climate Model (WACCM) and are explained by significant differences in the neutral chemistry of the two metals below 90 km and their ion-molecule chemistry between 90 and 100 km.

Zhou and Chen^[44] documented the possible influence of the 11-year solar cycle on the onset of the South China Sea Summer Monsoon (SCSSM) based on the reanalysis dataset and observational Sunspot Number

(SSN) from 1948–2017. They found that the SSN is significantly correlated to the SCSSM with stronger (weaker) solar activity corresponding to later (earlier) outbreak of the SCSSM. Further composite analysis revealed that during the peak (valley) years of SSN, an anomalous anticyclone (cyclone) appears around the Philippines in May, concurrent with the westward-shifting (eastward-shifting) and intensified (declined) western Pacific Subtropical High. This can be attributed to the change of the local meridional circulation related to the convective activity over the maritime continent south of equator and the variations of the Walker circulation over the tropical Indo-Pacific region. And the solar signals on the SCSSM are suggested to originate from the temperature responses in the stratosphere. With the enhancement of solar irradiance, the upper-troposphere to the lower-stratosphere over the entire southern hemisphere is warmer in March and April. Through modulating the mean meridional circulation, there is a negative Antarctic Oscillation pattern in the lower troposphere induced by the redistribution of the atmosphere mass. The subsequent cyclonic circulation anomalies in the mid-latitudes delay the establishment of the Somali cross equatorial flows when the solar activity is stronger and the SASSM onset tends to occur later accordingly. Zhou and Chen^[45] also investigated possible linkages between Antarctic sea ice and the 11-year solar cycle as well as related physical processes by using NCEP-DOE reanalysis datasets, sea ice concentration data from the Hadley Center and sunspot number data. In years with high solar activity, sea ice concentration is low in the vicinity of the Ross Sea and high in the Weddell Sea near the Antarctic Peninsula. And the Antarctic Sea Ice Dipole (SID) index is significantly negatively correlated with the Antarctic Oscillation (AAO), possibly through the mediation of the westerly jet. When the AAO is strong, the westerly stream turns southward around the Antarctic Peninsula-Weddell Sea, and northward near the Ross Sea, resulting in negative SID anomalies as warm air enters the Antarctic Peninsula-Weddell Sea region and cold air intrudes over the Ross Sea. Sea ice and circulation anomalies are reversed when the AAO is weak. These findings extend earlier ones by emphasizing the possible impact from solar cycle, which has practical use for climate prediction.

Zou *et al.*^[46] report a statistical study on the effects of strong geomagnetic activity on the mesopause temperature over the auroral region from 2002 to 2018. They

found the energetic electron precipitation was significantly enhanced in the 55°–70° geomagnetic latitude band. At the same time, the mesopause temperature increased about 4 K at 95 km immediately in the mesopause region, together with a descent of the mesopause of about 0.5–2 km. They suggested that mesopause is mainly influenced by electrons in the energy range of 30–100 keV.

Wu *et al.*^[47] analyzed a long-term simulation of the Whole Atmosphere Community Climate Model with the chemistry of three metals (Na, K, and Fe), and presented the response of the meteoric metal layers in the mesosphere and lower thermosphere regions to the 27-day solar rotational cycle. The altitude-dependent correlation and sensitivity of the metal layers to the solar spectral irradiance demonstrate that there is a significant increase in sensitivity to solar rotational cycle with increasing altitude.

Xia *et al.*^[48] found that the poleward expansion of the Hadley circulation in autumn is closely related to the increase of Stratospheric Water Vapor (SWV) under greenhouse warming. The SWV increase radiatively cools the stratosphere, especially in the polar lower stratosphere, which consequently leads to widening of the Hadley cell in autumn. The SWV effect is affirmed in a set of “SWV-locking” experiments. It is found that the SWV increase leads to a poleward expansion of the Hadley circulation in autumn in both Hemispheres, which contributes about 30% of the total expansion due to quadrupling CO₂ in autumn.

Record ozone loss was observed in the Arctic stratosphere in spring 2020. Xia *et al.*^[49] found that the extreme Arctic ozone loss was likely caused by record-high Sea Surface Temperatures (SSTs) in the North Pacific. It is found that the record Arctic ozone loss was associated with the extremely cold and persistent stratospheric polar vortex over February–April, and the extremely cold vortex was a result of anomalously weak planetary wave activity. Further analysis reveals that the weak wave activity can be traced to anomalously warm SSTs in the North Pacific. Both observations and simulations show that warm SST anomalies in the North Pacific could have caused the weakening of wavenumber-1 wave activity, colder Arctic vortex, and lower Arctic ozone. These results suggest that for the present-day level of ozone-depleting substances, severe Arctic ozone loss could form again, as long as certain dynamic conditions are satisfied.

Rao *et al.*^[50] assessed four Chinese models and found that the SSW frequency in most CMIP6 models is underestimated. SSWs mainly appear in midwinter in observations, but one-month climate drift is simulated in the models. The contrasting difference in the intensity for displacement and split events are well simulated by Chinese models. Rao and Garfinkel^[51] included more CMIP5/6 models in their study to assess the possible future change in the SSW under a moderate emission scenario (RCP45/SSP245) and a strong emissions scenario (RCP85/SSP585). An insignificant (though positive) change in the SSW frequency from historical simulations to RCP45/SSP245 and then to RCP85/SSP585 is consistently projected by CMIP5 and CMIP6 multimodel ensembles. Further, they emphasized that the troposphere-stratosphere coupling strength during SSWs is nearly unchanged in the future scenario simulations. With the same models, Rao and Garfinkel^[52] examined the possible future changes of Stratospheric Final Warming (SFW) events. Most CMIP5/6 models project a delay of SFWs in the two future scenarios in the Northern Hemisphere. In the Southern Hemisphere, the SFW date is largely unchanged as ozone recovers through the end of the century.

Xia *et al.*^[53] calculated the Stratospheric Water Vapor (SWV) climate feedback using the 150-year CO₂ forcing (1pct CO₂) simulations in the CMIP6 ensemble of models. All models robustly show a moistening of the stratosphere, causing a positive radiative feedback to surface warming. It is found that the stratospheric moistening rate and the SWV feedback both increase with surface warming. The moistening occurs at a rate of 0.9 ± 0.1 ppmv·K⁻¹ and its radiative feedback measured by the fixed-dynamical-heating method is 0.11 ± 0.02 W·m⁻²·K⁻¹ in the first 50 model years; the moistening rate increases to 1.2 ± 0.2 ppmv·K⁻¹ and the feedback increases to 0.16 ± 0.03 W·m⁻²·K⁻¹ in the last 50 model years when the global mean surface temperature is 3.3 K warmer. These increases are found to be caused by an amplified rate of tropical tropopause warming with respect to surface warming, which is 0.6 K/K and 1.1 K/K for the two 50-year periods, respectively. They concluded that the SWV feedback is strengthening with surface warming, which can contribute to increasing climate sensitivity in the future under global warming.

Zhang *et al.*^[54] reported the correlation of the Low Frequency (LF) lightning sferics of two Terrestrial

Gamma ray Flashes (TGFs), including one TGF associated lightning discharge at only about 28 km range. The LF lightning sferics associated with TGFs detected by Fermi Gamma-ray Burst Monitor (GBM) over equatorial thunderstorms have been recorded at a station in Melaka, Malaysia, in 2017 and 2018. By means of the lightning detection data of the WWLLN, and Vaisala's Global Lightning Dataset (GLD360), the paper analyzed TGFs are related to the strongest pulse during the initial stage of their parent Intracloud (IC) lightning. It shows on a statistical basis that TGF related lightning is mostly located in the strong convection of equatorial thunderstorms at the mature stage, and nearly half TGFs are not produced in the strongest convection region.

Zhang *et al.*^[55] provided evidence from both observations and model simulations that zonally asymmetric stratospheric ozone depletion gives a significant feedback on the position of the polar vortex and further favors the stratospheric polar vortex shift toward Siberia in February for the period 1980–99. However, the polar vortex shift is not significant in the experiment forced by zonal mean ozone fields.

Xie *et al.*^[56] investigated the effects of global and regional SST warming from the Industrial Revolution to the present on the stratosphere using a climate model, and estimated the relative contributions of SST warming in different regions. They found that the observed global SST warming and 1-K uniform global SST warming have opposite effects on the high-latitude stratosphere in both hemispheres: 1-K uniform global SST warming results in warmer and weaker stratospheric zonal circulations and a corresponding increase in ozone, and vice versa for observed global SST warming.

Cheng *et al.*^[57] described the density correction of the NRLMSISE-00 using more than 15 years (2002–2016) of TIMED/SABER satellite atmospheric density data from the middle atmosphere (20–100 km). A bias correction factor dataset is established based on the density differences between the TIMED/SABER data and NRLMSISE-00. Seven height nodes are set in the range between 20 and 100 km. The different scale oscillations of the correction factor are separated at each height node, and the spherical harmonic function is used to fit the coefficients of the different timescale oscillations to obtain a spatiotemporal function at each height node. The evaluation results show that the spatiotemporal correction function proposed in this paper achieves a good correction effect on the atmospheric density of

NRLMSISE-00. The ability of the model to characterize the mid-atmosphere (20–100 km) is significantly improved compared with the pre-correction performance.

Based on the atmospheric density observed by TIMED/SABER satellite from 2002–2018, the grid data of monthly average and standard deviation were calculated statistically by Cheng *et al.*^[58]. Driving by the grid data, the atmospheric density is characterized as the sum of the monthly average and the large-scale disturbances and small-scale disturbances. The large-scale perturbations and small-scale perturbations are characterized by cosine functions and first-order autoregressive models, respectively. By comparing the simulated values of the model with the observations of the lidar in Dunhuang, the results show that the model values have a good agreement with the observations, which verifies that the modeling method is feasible. In addition, Monte Carlo method can be used to reproduce all possible states of atmospheric density on a given trajectory. The model can be used as a tool to provide density data for aerospace design and reentry trajectories simulations.

4 Dynamics in the Middle Atmosphere

4.1 Meteorological Process

The Gravity field and steady-state Ocean Circulation Explorer (GOCE) cross-track wind data (version 2.0, dusk side) have been compared with winds measured by four ground-based FPIs at low and middle latitudes (PAR, Arecibo, CAR and XL), and the time span is from 2010 to 2013 (Jiang *et al.*^[59]). The results showed that during geomagnetically quiet periods, GOCE crosswinds are 1.37–1.69 times larger than the ground-based FPIs winds, and the GOCE crosswind has typical seasonal variations with the largest speed around December and lowest speed around June, which is consistent with the ground-FPI measurements. The correlation coefficients between the four stations and GOCE crosswind data all reach around 0.6. During geomagnetically active periods, the relation between the GOCE and FPI derived winds are generally poorer, with average ratios of 0.85 for the Asian station (XL) and about 2.15 for the other three American stations (PAR, Arecibo and CAR). The discrepancies of absolute wind values from the GOCE accelerometer and ground-based FPIs should be mainly due to the different measurement principles of

the two techniques. The results also suggested that XL FPI can provide reliable wind observations in the same quality as from established FPIs in the American sector.

Wu *et al.*^[60] found oppositely Medium-Scale Traveling Ionospheric Disturbances (MSTID) in low latitudes during a geomagnetically quiet night. These MSTIDs showed the wave-fronts aligned from northwest to southeast. Some MSTID structures of them propagated southwestward and others propagated northeastward. In addition, these MSTID structures encountered and interacted with each other. The interactive process of these MSTIDs should be related to their polarization electric fields. Sun *et al.*^[61] investigated the interaction between a midlatitude MSTID and a poleward moving Weddell Sea Anomaly (WSA)-like plasma patch. They provided observational evidence that Polarization Electric Field (PEF) inside passing-by MSTID or its seeding Es could frequently drive plasma patches from the Equatorial Ionization Anomaly (EIA) poleward to cause the Midlatitude Summer Nighttime Anomaly Structures (MSNAs) over China. This kind of MSNA in turn interacted with the MSTID, causing some poleward extending C-shaped airglow depletions/enhancements of the MSTID in a transition region where the ionosphere changed from a collapse region to an uplifted one. Sun *et al.*^[62] investigated an interaction between an EMSTID and an EPB in the EIA crest region over China. The interaction changed the phase elongations and drifting velocities of both the EMSTID and EPB when they encountered. Moreover, interaction could have polarized one depletion of the postmidnight EPB, inside which freshly-generated meter-scale irregularities caused activated radar echoes and enhanced Ranged Spread F (RSF) over Fuke station. An observational evidence was provided that how an electrical couple of EMSTID and EPB events can activate a postmidnight EPB depletion over low latitudes of China. Luo *et al.*^[63] reported a special MSTID (medium-scale traveling ionospheric disturbance) event observed by multi-instruments over mid-latitude region of China. The airglow results showed that the inclination angles of MSTID bands were decreasing, resulting in the propagation direction changed from southwestward to nearly westward. It was also found that the MSTIDs disappeared partly in the airglow observation when they propagated to lower latitudes (below 40°N) in the later times. Both the observations from the FPI (Fabry-Perot Interferometer) and the simulations from the TIEGCM (Thermosphere-Ion-

osphere-Electrodynamics General Circulation Model) indicated that the variations of ionospheric neutral winds might be related to the variations of propagation direction and the disappearance of MSTIDs.

Shang *et al.*^[64] found ionospheric irregularities measured with different instruments have obvious morphological differences at Hainan station after midnight, where the larger the scale of the irregularities, the slower its attenuation. Compared with the magnetic equator, the ionospheric irregularities near equatorial abnormal peaks can last until near dawn. The occurrence of ionospheric irregularities in Hainan and Southeast Asia is obviously related to the quasi-periodic structure of plasma bubbles observed by the C/NOFS satellite passing through the region, indicating that the seeding of atmospheric gravity waves may play an important role in the generation of ionospheric irregularities, even in the second half of the night.

Yi *et al.*^[65] present the climatology of mesopause temperatures using high- and middle-latitude meteor radars. The daily mesopause temperatures are estimated using ambipolar diffusion coefficient data from the meteor radars at Davis Station (68.6°S, 77.9°E), in Antarctica, Svalbard (78.3°N, 16°E), Tromsø (69.6°N, 19.2°E) in the Arctic, and Mohe (53.5°N, 122.3°E) and Beijing (40.3°N, 116.2°E) in the northern middle latitudes. The seasonal variations in the meteor radar-derived temperatures are in good agreement with the SABER and MLS temperatures.

Yi *et al.*^[65] report the response of tides in neutral atmospheric mesospheric winds observed by meteor radar and medium frequency radar to recurrent geomagnetic activity over Antarctica. The zonal component of the daily prevailing winds showed a westward increase as the geomagnetic activity increased. In addition, the zonal and meridional semidiurnal tides both showed a clear upward propagating phase but responded differently to geomagnetic activity.

Yu *et al.*^[66] reported the observations of the 27-day and its harmonic 13.5-day periodic oscillations in the Es layers associated with the 27-day solar rotation period. The spectral analyses show that the 27-day periodic oscillations of Es layers are due to the recurrent geomagnetic activities.

By utilizing reanalysis data, Huang *et al.*^[67] studied the climatology of the eastward and westward traveling 10-day waves from the surface to the middle mesosphere. The westward propagating wave with zonal

wavenumber 1 and eastward propagating waves with zonal wavenumbers 1 and 2 are identified as the dominant traveling ones. Li *et al.*^[68] analyzed global characteristics of the westward propagating quasi 16-day wave (Q16DW) with zonal wavenumber 1 in the troposphere and stratosphere from December 2012 to November 2013. During the 2012/2013 Stratospheric Sudden Warming (SSW), the strong wave likely provides a forcing on the splitting of the displaced polar vortex. Tang *et al.*^[69] investigated the climatological features of W1 Q16DW. The wave amplitude is stronger in the NH than in the SH. The Quasi-Biennial Oscillation (QBO) signatures of the wave are mainly located in the stratosphere at low latitudes, no significant responses to ENSO and solar activity are observed; and the linear trends are generally positive, especially in the mid-upper stratosphere. Using the dataset from an incoherent scatter radar at Arecibo, Gong *et al.*^[70] present a long-term statistical analysis of thermospheric tides in an altitude range from 150 to 400 km, including their climatological mean and seasonal variations and their response to solar activities.

Gong *et al.*^[71] present an analysis of a quarter diurnal tide during the 2019 Arctic SSW event based on meteor radar data at Mohe. Applying meteor radar measurement, Ma *et al.*^[72] studied the excitation of quasi-6-day waves (Q6DWs) in both hemispheres during the September 2019 Antarctic SSW. The equatorward propagation induced by the SSW is the main reason for the enhanced Q6DWs in the upper MLT at mid-latitudes in the SH, and the main source of the Q6DWs in the NH is the seasonal variability. Besides, interhemispheric propagations also contribute to the amplification of Q6DWs during the 2019 Antarctic SSW. Ma *et al.*^[73] also investigated the variations of planetary waves in the MLT during 2019/2020 Arctic winter. Quasi 10-day waves are enhanced following three of these warmings in the zonal winds in the MLT region over Mohe, but unusually weak after the SSW in February 2020, which is due to largely inhibited by the extremely strong polar vortex and a lack of mesospheric instability.

As the number of models that can simulate the QBO increases, some new progresses for the QBO studies have been achieved in the past two years. For example, Rao *et al.*^[74] investigates the impact of the QBO on the northern winter stratosphere with CMIP5/6 outputs. Regardless of biases in QBO periodicity (25–31 months in observation *vs.* 20–40 months in models), the Hol-

ton-Tan relationship can be well simulated in CMIP5/6 models with more planetary wave convergence in the polar stratosphere in easterly QBO winters. An Eliassen-Palm (E-P) flux divergence dipole (with poleward E-P flux) is simulated in midlatitude upper stratosphere by most models during QBO easterlies around 30 hPa. Rao *et al.*^[75] further evaluated three dynamical pathways for impacts of the QBO on the troposphere, including the Holton-Tan effect and the northern annular mode, the subtropical zonal wind downward arching over the Pacific, and changes in local convection over the Maritime Continent and Indo-Pacific Ocean. More than half of the models can reproduce at least one of the three pathways, but few models can reproduce all of the three routes. Based on two emission pathways, Rao *et al.*^[76] indicated an enhanced surface response to the QBO via a strengthened Holton-Tan relationship in the future. Using the Model of an Idealized Moist Atmosphere (MiMA) capable of spontaneously generating the QBO, Rao *et al.*^[77] explored the gradual establishment of the extratropical response to the QBO. When easterly QBO winds maximized around 30 hPa are relaxed, an Eliassen-Palm (E-P) flux divergence dipole quickly forms in the extratropical middle stratosphere as a direct response to the tropical meridional circulation, in contrast to the Holton-Tan mechanism. No detectable changes in upward propagation of waves in the midlatitude lowermost stratosphere are evident for at least 20 days after branching, with the first changes only evident after 20 days in perpetual midwinter and season-varying runs, but after 40 days in perpetual November runs.

Hu *et al.*^[78] found that the Antarctic stratospheric planetary wave activity in September has weakened significantly since the year 2000. Further analysis indicates that the September Sea Surface Temperature (SST) trend over 20°N–70°S induces a reduction in the tropospheric wave source, and subsequently leads to weakening in the stratospheric wave flux and Brewer-Dobson circulation, while the ozone recovery since 2000 has a minor contribution.

Quan *et al.*^[79] reported the variation characteristics of D region in the lower ionosphere from 62 km to 82 km based on Langfang Medium Frequency (MF) radar. They focused on multiple C-level and M-level solar flare events before and after the large-scale flare event at 11:53 UT on 6 September 2017. The results show that it is difficult to detect the electron density over 70 km in Langfang during solar flares, but the electron density

value can be obtained as low as 62 km, and the stronger the flare intensity, the lower the detectable electron density height. Besides, the equal electron density height, the received power of X and O waves will also be significantly reduced during the flares, and the reduction of equal electron density height has a weak linear relationship with flare intensity.

Cai *et al.*^[80] analyzed the dependence of the 11-year solar cycle on horizontal winds in the local mesosphere and lower thermosphere. They found that the zonal wind is positively correlated with solar activity during spring at 80–84 km, and during summer at 80–82 km; the meridional wind is positively correlated with solar activity during spring at 84–88 km and during summer at 84–90 km. They explained the correlations in terms of the changes in stratospheric temperature and the net flux of gravity waves during solar activities. In addition, annual and semiannual oscillations of the zonal/meridional wind were found by using the least squares fitting method on daily horizontal winds, which show negative correlations with solar activity at heights of 80–90 km.

Tian *et al.*^[81] reported the momentum flux of short-period (less than 2 h) Gravity Waves (GWs) in the mesosphere and lower thermosphere (MLT), using meteor radar data collected over Langfang, China. They found that seasonal variations in GW momentum flux exhibited Annual Oscillation (AO), Semiannual Oscillation (SAO), and quasi-4-month oscillation. The mean flow acceleration of zonal winds, estimated from the divergence of this flux, was in the same direction as the observed acceleration of zonal winds for quasi-4-month oscillation winds, with GWs contributing more than 69%. In addition, the estimated acceleration due to Coriolis forces to the zonal wind was opposite to the estimated acceleration of high-frequency GWs for quasi-4-month oscillation winds.

Tian *et al.*^[82] showed the diurnal and seasonal variations in atmospheric short-period (less than 2 h) Gravity Waves (GWs) in the Mesosphere and Lower Thermosphere (MLT). They found that GW activity was strong over a 24-hour period, above the 95% confidence level, during almost every month of the year. A 12-hour period of particularly high activity was also evident in April and October for zonal wind variance, as well as in January, April, May, and December for meridional wind variance. Additional periods were observed for the first time, including 4-, 6-, and 8-hour cycles with confidence intervals greater than 95%. These results suggest

the possibility that GW activity could be modulated by solar-heating tidal wave harmonics.

Shi *et al.*^[83] analyzed a case of CGWs detected simultaneously by the AIRS (Atmospheric Infrared Sounder) and the VIIRS/DNB (Day/Night Band of the Visible Infrared Imager Radiometer Suite) in the stratosphere and mesosphere. Results showed that Gravity Waves (GWs) were generated by the collocated Hurricane Bejisa on the island of Mauritius. The AIRS data showed arc-like phase fronts of GWs with horizontal wavelengths of 190 and 150 km at 21:08 Coordinated Universal Time(UTC) on 1 January 2014 and at 10:00 UTC on 2 January 2014, whereas the DNB observed arced GWs with horizontal wavelengths of 60 and 150 km in the same geographic regions at 22:24 UTC. The characteristics of CGW parameters in the stratosphere (about 40 km) and the mesosphere (about 87 km), such as the vertical wavelength, intrinsic frequency, and intrinsic horizontal phase speed, were first derived together with the background winds from ERA5 reanalysis data and Horizontal Wind Model data through the dispersion relationship of GWs and the wind-filtering theory.

Guo *et al.*^[84] analyzed the global distribution of stratospheric gravity wave activity intensity and occurrence frequency using the 79th channel's observation data of the AIRS in January and July between 2012 and 2014. The study shows that the gravity wave intensity varies significantly with latitude. In the low latitude area (0–30°), the value of the gravity wave intensity in winter hemisphere is low, but is high in summer hemisphere. In the middle and high latitudes, winter hemisphere has strong gravity waves activity but the summer hemisphere gravity wave is weak. In January, there are four prominent hot spots in the global range, located at 50° north latitude, the continental and Atlantic intersections, and the North American and Atlantic intersections, and at 20° south latitude, the South American and Atlantic intersections, and Africa. Intersection with the Indian Ocean. In July, the gravity wave activity was prominent in Patagonia to Antarctic Peninsula region and the Indian Ocean region near 50° south latitude and 75° east longitude.

4.2 Influence of Lower Atmospheric Perturbation on the Thermosphere/Ionosphere

Sun *et al.*^[85] further analyzed the effect of the MJO on the Northern Hemisphere (NH) mesosphere. Both ob-

servations and simulations suggest the anomalous PWs lagging MJO P4 by 25 days lead to the weaker eastward zonal wind in the upper stratosphere and lower mesosphere approximately 5 days later. Due to critical-level filtering, the mesosphere meridional circulation is suppressed due to both anomalous PWs and GWs, and this suppression causes polar mesospheric cooling in 10 days. The interaction between PWs, zonal wind and GWs results in the 15-day lag between the stratospheric and mesospheric response. Yang *et al.*^[86] revealed the effect of the MJO on springtime Antarctic ozone variations for the first time from multi-satellite reanalysis and model simulations. Twenty to 30 days after MJO Phase 8 (P8), Antarctic Total Column Ozone (TCO) anomalies significantly decrease by up to -15 DU, associated with a wave -1 response at around 60°S . The MJO suppressed the upward and poleward propagation of Planetary Waves (PWs) and lead to weakened Brewer-Dobson circulation in the SH stratosphere. This in turn results in less ozone transport from midlatitudes into the polar region and thus a negative polar TCO response. Dynamical transport plays a dominant role rather than chemical processes in modulating the Antarctic TCO after MJO P8.

By using meteor radar, radiosonde observations and reanalysis data, Cheng *et al.*^[87] reported a dynamical coupling from the tropical lower atmosphere to the Mesosphere and Lower Thermosphere (MLT) through a quasi-27-day intraseasonal oscillation. Ma *et al.*^[88] studied an enhancement of a quasi-27-day wave during recurrent geomagnetic storms in the autumn of 2018 based on the zonal wind observations in the Mesosphere and Lower Thermosphere (MLT) region over Beijing. Combining radiosonde and satellite observations and reanalysis data, Bai *et al.*^[89] investigated anomalous changes in temperature and ozone QBOs from the lower to middle stratosphere. Anomalous changes of temperature and ozone QBOs due to unexcepted QBO zonal wind variation are well explained according to thermal wind balance and thermodynamic balance. Du *et al.*^[90] reported an extremely negative anomaly of atmospheric water vapor in the tropical western Pacific during the super El Niño winter of 2015/16, and revealed the contributions of the anomalies in the Hadley, Walker and monsoon circulations to the observed water vapor anomalies in the eastern-Pacific and central-Pacific El Niño events.

Using the high-precision wind and temperature ob-

servations from lidar, Huang *et al.*^[91] and Li *et al.*^[92] investigated the fundamental features of three-dimensional wind and temperature spectra. The wavenumber spectral slopes of the horizontal winds and temperature are systematically less negative than -3 , and their frequency spectrum slopes have more or less deviated from the universal spectral index of $-5/3$. In the saturated spectrum region, the frequency and vertical wavenumber spectra of the vertical wind have the shallower slopes than those of the horizontal winds. In the spectral tail region, the frequency and wavenumber spectrum slopes are far steeper relative to their saturated spectrum slopes. Although the vertical wind spectrum is almost always separable, the horizontal wind spectra are separable only at high frequencies. Based on the wind measurements from MST radar at Xianghe, Ning *et al.*^[93] statistically analyzed the Inertia-Gravity Wave (IGW) activity in the troposphere and lower stratosphere, and estimate directly the intensity of wave momentum flux. The annual average of momentum flux indicates that the IGWs in the lower stratosphere can apply a persistent eastward drag on the background flow at higher altitudes through momentum transported by these waves.

Using the temperature profiles measured by the SABER instrument (2002–2021), Liu *et al.*^[94] derived the global GW action and its scale height and identified a persistent layer of enhanced GW dissipation centered at 80–85 km with a vertical extent of 8–20 km. The possible mechanisms of enhanced dissipation include wave refraction, wind filtering, and reduced static stability. According to the dispersion and polarization relations of linear GWs and the SABER temperature data, Liu *et al.*^[95] proposed a method of deriving GW-perturbed wind shears and showed that the magnitudes of the GW-perturbed shears agreed with the lidar and sounding rocket observations in mesosphere and lower thermosphere. Liu *et al.*^[96] studied the global atmospheric static stability in the middle atmosphere and its relation to GWs. They found that the correlation coefficients between static stability and GW amplitudes was about 0.8 and indicated that large static stability supported large-amplitude GWs. The background wind is difficult to be measured in the stratosphere and mesosphere. To fill this gap, Liu *et al.*^[97] developed a dataset of the monthly mean zonal wind in the height range of 18–100 km and at latitudes of 50°S – 50°N from 2002 to 2019, derived from the gradient balance wind theory and the temperature and pressure observed by the

SABER instrument.

Zou *et al.*^[98] gave the spectrum of a gravity wave in the turbulence region, by using the high-resolution data of Yanqing Lidar. This is the first report on the properties of the turbulence spectrum and their seasonal variations in the northern hemisphere over China. The observed gravity wave turbulence spectra well fitted with the theoretical prediction. These results achieved new field detections, which will lead us to further discover the nature and essence of a gravity wave and deeply study the behavior of upper atmosphere circulation on a large scale.

5 Coupling between Stratosphere and Troposphere

He *et al.*^[99] showed that the mixing ratio of carbon monoxide (CO) within the Asian Summer Monsoon Anticyclone (ASMA) is significantly higher at both 100 hPa and 147 hPa in the easterly phase of QBO than the westerly phase of QBO, which is related to the variations of location and strength of the ASMA. Additionally, the enhanced ascending motions over the Tibetan Plateau favor the high CO at 100 hPa during easterly QBO.

Wang *et al.*^[100] found that a decrease of Arctic stratospheric ozone in March favors anomalous tropospheric cyclones and negative sea surface temperature anomalies over the western North Pacific in early summer via influencing the tropospheric circulation and air-sea interaction processes. These results suggested that the Arctic stratospheric ozone signal in March has implications for the predictions of the circulation and SST variations over the western North Pacific in early summer.

Zhang *et al.*^[101] found that the stratospheric Quasi-Biennial Oscillation (QBO) plays an important role in the mid-latitude surface temperature variations through modifying the stratospheric polar vortex. The downward extension of stratospheric negative northern annular mode signals is more than twice as large during the easterly phase of the QBO as those during the westerly phase of the QBO. The effects of QBO on stratospheric polar vortex are carried out through both the tropospheric and stratospheric paths.

Xu *et al.*^[102] found that the tropospheric and stratospheric pathways contribute roughly equally to the late-winter cooling over Eurasia induced by the Barents-Kara Seas (BKS) sea-ice loss. Their study further identified the underlying mechanisms responsible for the

two pathways: for tropospheric pathway, the reduced sea-ice could strengthen the Siberian High and induce two cold air-mass streams over Eurasia; for a stratospheric pathway, a sea-ice-induced extension of stratospheric polar vortex toward Eurasia could intensify the Eurasian cooling. Xu *et al.*^[103] found that the sea ice loss over Barents-Kara Seas (BKS) could lead to a deepened East Asian trough (EAT) in late winter, while the EAT axis tilt is not sensitive to the BKS sea ice reduction. Their analysis indicates that stratosphere-troposphere coupling contributes to around 70% of the sea-ice-induced deepening of EAT, while the remaining 30% is from tropospheric processes.

Ma *et al.*^[104] found that the East Asian Winter Monsoon (EAWM) in the early winter months (November-December) is weaker in the easterly phase of the QBO (EQBO) than in the westerly phase of the QBO (WQBO). During EQBO, the northerly monsoon flow is weakened, and anomalously warm temperatures occur over East Asia. Moreover, components of the EAWM circulation system, including the Siberian High, Aleutian Low, East Asian trough, and East Asian jet stream, are all weakened. The QBO is suggested to influence the EAWM directly via a subtropical pathway. The EQBO tends to weaken the East Asian jet stream and shift it poleward, and the changes in the East Asian jet stream lead to a weakened EAWM. The activities of planetary waves are also changed in association with the QBO. Examinations of individual zonal Wavenumbers (WNs) of planetary waves in the SLP field reveal that WN 1 is strengthened while WNs 2 and 3 are weakened during EQBO. Specifically, the anomalous WN 2 leads to weakening of the Siberian High, Aleutian Low, and East Asian trough, and the anomalous WN 3 reduces the pressure gradient between the East Asia landmass and the western Pacific. The changes in WN 2 and WN 3 associated with the QBO play a dominant role in anomalous EAWM.

Chen *et al.*^[105] further found that the relationship between the spring NAO and the following EASM varied with the 11-year solar cycle. The analysis of the time-lag relationship between the NAO in May and the following summer rainfall indicates that during the low solar activity (LS) summers, a more robust relationship is established, with below-normal rainfall anomalies in South China and the Sunda Islands in relation to a positive NAO. And the May NAO-related atmospheric circulation anomalies during boreal summer over East and

Southeast Asia may well explain the distinct rainfall difference. The possible mechanism for this solar modulation is attributed to the changes in structure of the spring NAO and associated tripole SST anomalies in the North Atlantic. On the other hand, Xue *et al.*^[106] revealed the solar cycle modulation of the connection between boreal winter ENSO and following summer South Asia High (SAH). For El Niño accompanied by a low solar cycle (EL&LS) or La Niña accompanied by a low solar cycle (LA&LS), the boreal winter ENSO prominently affects the following summer's SAH variation. The SAH is enhanced (weakened) and expanded (narrowed) in the meridional and zonal directions in the EL&LS (LA&LS) phase. The composite difference in the SAH between El Niño and La Niña events is obviously stronger in the low solar cycle phase. Further investigation based on longer historic data also ensures that the 11-year solar cycle modulates the ENSO-SAH connection, with a more robust connection in the low solar cycle phase.

Huangfu *et al.*^[107] investigated the process by which the QBO modulates tropospheric circulation and convection during summer (between July and October), when Tropical Cyclone (TC) activities enter their peak period. Concurrent with the western phase of the QBO (QBOW), significant tripole pattern modulations over the tropical Indo-Pacific Ocean are regressed onto the residual part of U70 after removing the ENSO signal, with enhanced convection observed over its central branch (0°–10°N, 120°E–180°) and the inactive convection branches located to both sides. A ventilation opening-like effect is exerted on the monsoon trough, which is shifted southward under the QBOW phase. According to the QBO-associated changes in the circulations over the tropical Western North Pacific (WNP), equatorial environments tend to be favorable for TC genesis. Consequently, the off-equatorial TC tracks show a significantly decreased occurrence frequency in the northern monsoon trough region. In addition, Wang *et al.*^[108] identified the significant modulation of the QBO on the winter Tropical Cyclone Precipitation (TCP) in the coastal regions of the Western North Pacific (WNP). In the westerly QBO winter, the zonal wind vertical shear anomalies in the stratosphere strengthen (weaken) convective activities around the East China Sea (the Philippines) and cause middle-level easterly (westerly) anomalies of the middle (low) latitudes in the troposphere, leading to more (less) TC activities around the

East China Sea (the Philippines). Consequently, a TCP dipole pattern can be observed. The TCP increases in East China, Korean peninsula, Japan and Russian Far East, but decreases in Indo-China Peninsula, South China and the Philippines. These results not only improve the knowledge of QBO-TC activity relationship but also provide a potential indicator for the seasonal prediction of the TC variation around the WNP due to the high predictability of the QBO.

Lu *et al.*^[109] investigated the impact of the stratospheric polar vortex shift on the tropospheric Arctic Oscillation (AO) in winter. Their results showed that a shift in the stratospheric polar vortex toward the Eurasian continent is favorable for the occurrence of the negative phase of the AO, the extension of duration of AO events and enhancement in the AO intensity. The polar vortex shift leads to changes in the intensity and position of the three action centers in the AO spatial pattern.

Zhang *et al.*^[110] analyzed the impacts of Arctic Stratospheric Polar Vortex (SPV) on wintertime precipitation over the Northern Hemisphere. They found that the SPV-induced changes in precipitation over the North Atlantic are stronger than those over the North Pacific. The convective (large-scale) precipitation changes play a major role in the total precipitation changes over the southern (northern) parts of middle latitudes associated with SPV changes.

Hu *et al.*^[111] showed that the interannual relationship between the SAV (Stratospheric Arctic Vortex) in early winter and the AO (Arctic Oscillation) in late winter during 1958–2018 is unsteady and has experienced a remarkable interdecadal change around the 2000s, with large and statistically significant positive correlations before the 2000s but small and insignificant correlations after the 2000s. The weakened linkage between the SAV and AO after the 2000s is possibly caused by (i) the weakened downward effect of SAV on the North Atlantic and polar sectors of AO, and (ii) the opposite signs of Sea Level Pressure (SLP) in the North Pacific and North Atlantic. The links of SAV-AO are enforced (weakened) when AO-related SLP anomalies over the North Pacific are the same (opposite) signs of those over the North Atlantic before (after) the 2000 s. Differences in the tropospheric state over the North Pacific during two periods might be jointly contributed by the SAV and the SAV-related significant (insignificant) sea surface temperature anomalies over central North Pa-

cific in the earlier (latter) period.

Huang *et al.*^[112] investigated the impact of the first two tropical Indian Ocean SST modes on the stratospheric water vapor and stratospheric polar vortex. It is found that the first (second) Indian Ocean SST mode servers to dry (moisten) the tropical stratosphere on the annual average and the responses are seasonally dependent. Both modes enhance (weaken) northern (southern) stratospheric polar vortex in boreal winter (austral spring).

Huang *et al.*^[113] provided corroborative evidence that weak polar vortex conditions in the lower stratosphere substantially increase the risk of severe Cold Air Outbreaks (CAOs) over most continental regions of the Northern Hemisphere, as compared to moderate CAOs. By analyzing the stream of polar cold air mass, this study showed that the polar vortex affects severe cold air outbreaks by modifying the inter-hemispheric transport of cold air mass, which sheds light on the spatial and temporal response of CAOs following anomalous stratospheric conditions. Huang *et al.*^[114] explored the stratospheric influence on the synoptic development of the 2018 later winter European cold air outbreak by running a regional Weather Research and Forecasting (WRF) model. Based on a set of nudged WRF simulations, they showed that capturing the evolution of the stratospheric child vortex over northeastern Canada, particularly in the lowermost stratosphere, is of great importance for predicting this CAO, since it substantially affects the strength and location of the Atlantic ridge that in turn determines the evolution and severity of this CAO.

Liang *et al.*^[115] separated the dry and moist components of the moist isentropic mass circulation (MIMC) on a daily timescale and investigates their relationships with extratropical surface temperature changes in winter (November to February). Results from ERA5 reanalysis data set (1979–2018) show that the MIMC is composed of a poleward warm branch in the upper layers and an equatorward cold branch below. The Warm Branch (WB) is dominated by the moist component in the mid-latitude troposphere, but by the dry component in other regions. The stronger moist component of WB at 50°N–70°N (WB_M) is a better precursory indicator than the dry component (WB_D) for the Arctic surface warming as a result of its dominant role in modifying the downward longwave radiation via water-vapor-

related processes. The stronger WB_D is coupled with a negative Arctic Oscillation and a stronger, longer-lasting equatorward transport of colder air, therefore a better precursory indicator of mid-latitude cold events.

Liu *et al.*^[116] examined the relationship between Sea Surface Temperatures (SSTs) in the North Pacific and the concentration of stratospheric ozone in the northern hemisphere in February–March from 1980 to 2017 using reanalysis and satellite datasets. Our results show that the concentration of stratospheric ozone can be modulated by the principal mode of the North Pacific SSTs that is, there are negative and zonally asymmetrical ozone anomalies in the Arctic stratosphere, but positive ozone anomalies in the lower stratosphere at midlatitudes during the positive phases of the North Pacific SSTs. The North Pacific SST anomalies account for about 20% of the linear variance of ozone concentrations in the lower stratosphere over the Arctic. Negative SST anomalies in the central North Pacific tend to result in a strengthened Western-Pacific-like teleconnection, which favors the propagation of more planetary wave-number-1 and -2 waves into the stratosphere. The North Pacific SSTs-related upwelling branch of the Brewer-Dobson circulation in the midlatitude stratosphere strengthens, but its downwelling branch in the Arctic stratosphere weakens. This results in decreased ozone anomalies in the lower stratosphere over the Arctic and increased ozone anomalies in the lower stratosphere at mid-latitudes. The zonally asymmetrical distribution of ozone related to the positive phase of SSTs over the North Pacific may be related to the shifting and strengthening of the stratospheric Arctic vortex.

Xia *et al.*^[117] found that Arctic ozone loss may lead to a decrease in surface Ultraviolet (UV) radiation over the Siberian Arctic in spring using ERA5 reanalysis. It is found that Arctic ozone loss is associated with an increase in high clouds by modifying static stability in the upper troposphere. Stratospheric ozone loss allows more UV radiation to reach the surface. On the contrary, the increase in high clouds results in a reduction of surface UV radiation. Interestingly, a composite analysis suggests that this cloud masking effect is found to be stronger than that from stratospheric ozone loss over the Siberian Arctic in spring. These results suggest that more attention should be paid to the high-ozone events which would lead to more surface UV radiation by the cloud effects.

Xia *et al.*^[118] showed that the anomalous surface warming in the Siberian Arctic in spring 2020 was likely related to the severe stratospheric ozone loss. The dramatic Arctic ozone loss in March was shifted to Siberia in April and May, which largely cools the lower stratosphere and leads to an increase of high clouds by modifying the static stability in the upper troposphere. This further results in an increase of longwave radiation at the surface which likely contributes to surface warming. Multiple linear regression demonstrates that ozone loss contributes most of the surface warming in April, while the Arctic Oscillation and ice-albedo feedback play a minor role. In May, both ozone loss and ice-albedo feedback contribute to the surface warming. These results support that surface warming in the Siberian Arctic could occur in April and May when severe ozone loss occurs in March.

That SSW tends to follow certain phases of the Madden-Julian Oscillation (MJO) was documented. Ma *et al.*^[119] investigated the modulation of El Niño-Southern Oscillation (ENSO) on the relationship between the MJO and major SSW in the Northern Hemisphere winter. They found that there is a much stronger MJO-SSW relationship during La Niña winters than El Niño winters. Further analysis indicates that ENSO influences the MJO-related geopotential height anomalies in middle to high latitudes of the upper troposphere, which leads to an increase in wavenumber 2 in La Niña winters. And wavenumber 2 plays a key role in generating the strong heat flux anomalies in the stratosphere. The results may help explain that, although the stratospheric polar vortex is stronger on a seasonal mean timescale during La Niña winters, some extreme events, such as SSWs, may not decrease as suggested in observational studies. Xu *et al.*^[120] further identified two leading modes of SSWs by using height-time domain Empirical Orthogonal Function (EOF) analysis. They found that the EOF1 is associated with polar vortex state before the occurrence of SSW, and the EOF2 indicates the intensity of the SSW. And those SSWs with weak initial polar vortex or stronger warming intensity may lead to evident surface pressure anomalies of negative North Atlantic Oscillation pattern, whereas the SSWs with strong initial polar vortex or weaker warming intensity tend not to exert influence on the surface. Different activity of planetary waves leads to discrepancy among SSWs. These results could help to better predict the tropospheric response following SSWs.

Koval *et al.*^[121] analyzed the changes in the vertical and meridional Residual Mean Meridional Circulation (RMC) velocity components at different stages of SSW events with ensemble simulation of the atmospheric general circulation at altitudes up to the lower thermosphere. Their obtained statistically significant results on the evolution of RMC and eddy circulation at different SSW stages at altitudes up to the lower thermosphere may provide a better understanding of the mechanisms of planetary wave impacts on the mean flow and for the diagnostics of the transport of conservative tracers in the atmosphere.

Ma *et al.*^[122] systematically studied the stratospheric and tropospheric evolutions during the lifecycle of both strong and weak Stratosphere Polar Vortex events (SPV and WPV events, respectively) based on the reanalysis data for the period of 1958–2017. Moreover, the atmospheric circulation and dynamical characteristics of two types of WPV events, namely events with and without SSW, have also been analyzed. The results show that the formation of SPV event follows a slow development and then a rapid intensification stage, while a WPV event is established dramatically. Compared with the SPV events, the WPV events are stronger and have a higher anomaly center when they reach a peak. And the occurrence of SPV and WPV events is closely related to the positive feedback of wave–mean flow interaction. In addition, for the WPV events with SSW, enhanced upward wave-1 Eliassen-Palm (EP) flux in the stratosphere occurs in the growth stage. Through the positive feedback of wave–mean flow interaction, both the upward propagating wave-1 and wave-2 EP fluxes are increased, which leads to the breakdown of the polar vortex. For the WPV events without SSW, the upward propagating wave-1 EP flux is weak in the growth stage, while the wave-2 flux plays an important role. Hence, the total upward propagating planetary waves are much smaller than the WPV events with SSW. And the tropospheric influence of the WPV events with SSW is not robust, and the magnitude of induced AO index in the troposphere is much smaller than that for the WPV events without SSW.

Wei *et al.*^[123] further investigated the longitudinal asymmetry of planetary wave propagation and its role in stratosphere-troposphere dynamical coupling, since three-dimensional (3D) planetary wave analysis can provide more regionalized information on stratospheric-tropospheric dynamic interactions. They found

that the upward wave flux from the troposphere to the stratosphere is maximized above northeastern Eurasia, and the downward flux occurs mainly over the North America and North Atlantic (NANA) region, which is much stronger during mid-to-late winter. The upward wave flux anomalies in early winter are negatively correlated with the strength of the Stratospheric Polar Vortex (SPV). During the mid-to-late winter months, the strength of the SPV is positively correlated with the first mode of the 3D wave flux and has a leading relationship of approximately one month. The stronger SPV corresponds to a stronger upward wave flux above northern Eurasia and a stronger downward flux over the NANA region. The interannual variations in wave flux during early winter are closely associated with the Scandinavian wave train pattern. In contrast, the wave flux variations are related to the circulation anomaly corresponding to the Arctic Oscillation during mid-to-late winter, which causes climate anomalies across the Northern Hemisphere, especially coherent temperature changes in northern Europe, eastern United States and northeastern China. Wei *et al.*^[124] also suggested that stratosphere may amplify the global climate effect of wildfires and volcano eruptions. In the Earth's long historical evolution, large-scale wildfires, active volcanic activities, meteorites that hitting the Earth, are likely to inject aerosol particles such as black carbon and sulfate into the stratosphere. The dynamical stability and horizontal circulation in the stratosphere can spread aerosols globally, and extend the lifetime of aerosols in the stratosphere, affecting the radiation balance of the Earth system on a global scale. Therefore, the stratosphere can be an “amplifier” of climate change events. They called on that the scientific community needs to pay more attention to the stratospheric process, since there are still many problems related to aerosol radiation, photochemistry and transport dynamics in the stratosphere that need further study.

Lu *et al.*^[125] explored a Sudden Stratospheric Warming (SSW) in January 2021, its favorable conditions, and the near surface impact. Wavenumbers 1 and 2 alternately contributed to the total eddy heat flux from mid-December 2020 to late January 2021, and the wavenumber 2 during the onset period nearly split the stratospheric polar vortex. In mid-December 2020 and during the 2021 New Year period (1–5 January 2021), a blocking developed over the Urals, which enhanced the local ridge and the climatological wavenumber 2.

Composite results confirm that the Arctic sea ice loss in autumn and La Niña favor the deepening of the high latitude North Pacific low and the increase of the Urals height ridge, which together enhance the planetary waves and hence disturb the stratospheric polar vortex. However, the Madden-Julian Oscillation (MJO) in the tropics was dormant in mid-to-late December 2020 and early January 2021, and the well-established statistical relationship between the MJO convection over the western Pacific and the SSW is not applicable to this special case. The cold air outbreak in China during the 2021 New Year period before the January 2021 SSW onset is not explained by the SSW signal which developed in the stratosphere. In contrast, the downward-propagating signal reached the near surface in mid-February 2021, which may contribute to the cold air outbreak in US and may help to explain the extreme coldness of Texas in middle February.

Rao *et al.*^[126] analyzes the prediction of the downward propagation and surface impact of the 2018 and 2019 SSWs by using the real-time predictions from 11 subseasonal models. These two SSWs differed both in their morphology types and magnitudes, with the former more splitting in the vortex shape and stronger in the westerly wind deceleration. With abundant samples, they also showed that the strength of the SSW is more important than the vortex morphology and wavenumbers to determine the magnitude of its downward impact. Strong SSWs are more likely and easily to propagate downward than weak SSWs. The multimodel ensemble analysis supports that the observed strong SSW in February 2018 had a stronger and more continuous downward impact than the January 2019 SSW. For another SSW event during January 2021, predictability^[127] of the event was investigated by adopting reanalysis, observations; and subseasonal to seasonal forecasts of the event was conducted concurrently. They found that this SSW occurred under the tropical westerly Quasi-Biennial Oscillation (QBO) and weak convection over tropical Pacific. Alternate wave pulses by the wavenumber 1 and 2 finally led to the January 2021 SSW onset. Due to an unfavorable condition in the tropics with QBO westerlies, the predictability for the occurrence of the January 2021 SSW is not beyond two weeks with the required hit ratio >50%. The observed Arctic sea ice loss since the autumn in 2020 is unlikely to extend the predictability of this event in subseasonal models. For the Southern Hemisphere (SH) SSW event in September

2021, Rao *et al.*^[128] found that the predictive limit to this SSW is around 18 days in some S2S models with favorable tropical forcing conditions.

In addition to weak polar vortex events such as SSWs, Rao and Garfinkel^[129] also compared the possible maximum predictability of strong polar vortex events in early spring coupled to evident ozone loss in the Arctic. Three ozone loss events in springs of 1997, 2011, and 2020 were accompanied by an extremely strong and cold polar vortex. Rao and Garfinkel^[130] further adopted real-time forecasts and found that the strong stratospheric polar vortex in March 2020 coupled with Arctic ozone loss is related to the anomalously weak wave activities. Weakened Brewer-Dobson circulation contributed around 40% of the total Arctic ozone loss in March. The empirical model using the S2S outputs tends to underestimate the Arctic total ozone. Yu *et al.*^[131] further explored the possible impact of Arctic ozone loss coupled with a strong polar vortex on the Eurasia.

The cancelling effect of the tropical Indian Ocean forcing on the stratospheric ENSO signal traditionally attributed to the Pacific force has been well understood in recent years. Rao and Ren^[132] further revealed the destructive interference of the sea surface temperature forcing in the southern winter stratosphere between the tropical Indian and Pacific Oceans by designing sensitivity experiments with WACCM4. The Southern Hemisphere zonal wind responses to the tropical SST forcings from the Indian and Pacific Oceans exhibit a dipole pattern. Specifically, a warm Pacific SST forcing favors an equatorward shift of the polar jet, while a warm Indian Ocean SST forcing induces a poleward shift. Therefore, no significant observed ENSO signal in the southern winter stratosphere is mainly caused by the destructive interference from the tropical Indian Ocean. In the Southern Hemisphere, warm Pacific forcing excites a positive Pacific–South America (PSA)-like pattern, while warm Indian Ocean forcing induces a negative PSA circulation pattern.

Ren *et al.*^[133] and Xia *et al.*^[134] found that the Eastern Asian (EA) topographic forcing has a dominant weakening effect on the stratospheric polar vortex, while the North American (NA) topography has a trivial or an even opposite effect. By designing sensitivity experiments with WACCM4, they proved the dominant role of the EA topography in its interference with the NA. The joint effects of EA and NA topography, rather than being a linear superimposition of their independent ef-

fects, are largely dominated by the effects of EA. Yu *et al.*^[135] continued to investigate the topographic dynamical effect of EA and NA on the winter isentropic meridional mass circulation and further confirmed the dominant role of the EA as compared with NA topography.

Xie *et al.*^[136] diagnosed the dynamics for the February 2018 SSW event and analyzed its possible impact on the weather over North America. They found that the ridge over Alaska and the trough over the northeastern North America are the prominent tropospheric precursors before the SSW. A cold wave occurs in the northwestern North America within 10 days after the 2018 SSW.

Huang *et al.*^[137] showed that a PM_{2.5} diffusion event in December 2015–January 2016 includes two stages: rapid diffusion stage (22–28 December 2015) and persistent diffusion stage (1–23 January 2016), controlled by different tropospheric and stratospheric meteorological conditions. The stratosphere-troposphere coupling effectively favors and extends the duration of PM_{2.5} diffusion, and the weakening of SPV provides a 1–2 week lead information to the meteorological diffusion condition.

Lu *et al.*^[138] compared the PM_{2.5} concentration in Beijing–Tianjin–Hebei during two SSWs (11 February 2018 and 2 January 2019). They found that the PM_{2.5} concentration in the pre-SSW period, SSW-occurrence period, and post-SSW period is different. The February 2018 SSW shows stronger downward propagating signals in the post-SSW period, which favors weakening of the pressure contrast between Arctic and midlatitudes and strengthening of the East Asian winter monsoon systems in the middle troposphere, resulting in diffusion and dilution of the pollutants. In contrast, the PM_{2.5} concentration is still high in the post-SSW period during the 2019 non-downward propagating event.

Chen *et al.*^[139] used the WRF model to simulate the typical case of a cut-off low over northeast Asia, and then applied the output of the WRF model to drive a FLEXPART-WRF model to carry out both forward and backward simulations. They revealed the detailed trajectories and sources of air masses within the cut-off lows. Their trajectories illustrate the multi-time scale deep intrusion processes in the upper troposphere and lower stratosphere caused by the cut-off low. The processes of air intrusion from the lower stratosphere to the middle troposphere can be divided into three stages: a slow descent stage, a rapid intrusion stage and a rela-

tively slow intrusion stage. The ozone-rich air in the COL primarily originated from an extratropical cyclone over central Siberia and from the extratropical jet stream.

Xiao *et al.*^[140] found that surface nitrogen oxides (NO_x) emissions in East Asia can be transported to the tropics and East Asian upper troposphere and lower stratosphere (UTLS) region during summer and autumn. In summer, the south Asia anticyclone can transport the NO_x in the East Asian UTLS region to the lower latitudes. In the UTLS regions, with the increase of surface NO_x emissions in East Asia, ozone concentration increases in the lower latitudes while ozone concentration decreases in the middle latitudes.

Tian *et al.*^[141] investigated the anomalous signals near the tropopause before the overshooting convective system onset over the Tibetan Plateau. They found that the tropopause height is stable at the maximum height seven and five days before the onset of overshooting convection. It then decreases significantly one day before and on the day of the onset. The upward motion in the troposphere is the strongest five days before the onset. From one day before and after the onset, there are strong ascending motions at 500–300 hPa but weak descending motions near the tropopause.

References

- [1] XIA Y, CHENG X, LI F, *et al.* Sodium lidar observation over full diurnal cycles in Beijing, China[J]. *Applied Optics*, 2020, **59**(6): 1529-1536. DOI.org/10.1364/AO.382077
- [2] WU F, ZHENG H, CHENG X, *et al.* Simultaneous Detection of the Ca and Ca⁺ layers by a dual-wavelength tunable lidar system[J]. *Applied Optics*, 2020, **59**: 4122-4130 DOI.org/10.1364/AO.381699
- [3] DU L, JIAO J, LI F, *et al.* The technical optimization of Na-K lidar and to measure mesospheric Na and K over Brazil[J]. *Journal of Quantitative Spectroscopy and Radiative Transfer*, 2021, **259**, 107383. DOI.org/10.1016/j.jqsrt.2020.107383
- [4] WU F, ZHENG H, YANG Y, *et al.* Lidar observations of the upper atmospheric nickel layer at Beijing (40°N, 116°E). *Journal of Quantitative Spectroscopy and Radiative Transfer*, 2021, **260**, 107468. DOI.org/10.1016/j.jqsrt.2020.107468
- [5] CAI Bing, XU Qingchen, HU Xiong, YANG Junfeng, HU Xiong. Initial results of meteor wind with Langfang medium frequency radar[J]. *Atmosphere*, 2020, **11**(5): 507
- [6] BAN C, PAN W, WANG R, *et al.* Initial results of Rayleigh scattering lidar observations at Zhongshan station, Antarctica[J]. *Infrared and Laser Engineering*, 2021, **50**(3): 20210010, DOI: 10.3788/IRLA20210010
- [7] TIAN Yufang, CHEN Ze, LÜ Daren, A dataset of Beijing MST radar horizontal wind fields at Xianghe Station in 2012[J]. *China Scientific Data*, 2021: 6(2). DOI: 10.11922/csdata.2020.0078.zh
- [8] CHEN Ze, TIAN Yufang, LÜ Daren. Improving the processing algorithm of Beijing MST radar power spectral density data[J]. *Journal of Applied Meteorological Science*, 2020, **31**: 694-705
- [9] WU K, XU J, YUE X, *et al.* Equatorial plasma bubbles developing around sunrise observed by an all-sky imager and GNSS network during the storm time[J]. *Annales Geophysicae*, 2020, **38**, 163-177. <https://doi.org/10.5194/angeo-2019-122>
- [10] WU K, XU J, ZHU Y, *et al.* Ionospheric plasma vertical drift and zonal wind variations cause unusual evolution of EPBs during a geomagnetically quiet night[J]. *Journal of Geophysical Research: Space Physics*, 2021a, 126, e2021JA029893. <https://doi.org/10.1029/2021JA029893>
- [11] SUN L C, XU J Y, ZHU Y J, *et al.* Case study of an equatorial plasma bubble event investigated by multiple ground-based instruments at low latitudes over China[J]. *Earth Planet. Phys.*, 2021, **5**(5): 1-15. DOI.org/10.26464/epp2021048
- [12] GAO H, XU J, CHEN G, *et al.* Statistical structure of nighttime O2 aurora from SABER and its dependence on geomagnetic and solar activities in winter[J]. *Journal of Geophysical Research: Space Physics*, 2020, 125, e2020JA028302. DOI.org/10.1029/2020JA028302
- [13] ZHU Y, KAUFMANN M, CHEN Q, *et al.* A comparison of OH nightglow volume emission rates as measured by SCIAMACHY and SABER[J]. *Atmos. Meas. Tech.*, 2020, **13**: 3033-3042. DOI.org/10.5194/amt-13-3033-2020
- [14] YU B, SCOTT C J, XUE X *et al.* Derivation of global ionospheric Sporadic E critical frequency (*f*_oE_s) data from the amplitude variations in GPS/GNSS radio occultations[J]. *Roy. Soc. Open Sci.*, 2020, **7**, 200320. DOI: 10.1098/rsos.200320
- [15] YU B, SCOTT C J, XUE X *et al.* Using GNSS radio occultation data to derive critical frequencies of the ionospheric sporadic E layer in real time[J]. *GPS Solut.*, 2021, **25**(1): 1-11. DOI: 10.1007/s10291-020-01050-6
- [16] YU B, XUE X, SCOTT C J, *et al.* Interhemispheric transport of metallic ions within ionospheric sporadic E layers by the lower thermospheric meridional circulation[J]. *Atmos. Chem. Phys.*, 2021, **21**(5): 4219-4230 DOI: 10.5194/acp-21-4219-2021
- [17] WU J, FENG W, LIU HL, *et al.* Self-consistent global transport of metallic ions with WACCM-X[J]. *Atmos. Chem. Phys.*, 2021, **21**: 15619-15630. <https://doi.org/10.5194/acp-21-15619-2021>
- [18] XIA Y, CHENG X, LI F, *et al.* (2020a). Diurnal variation of atmospheric metal Na layer and nighttime top extension detected by a Na lidar with narrowband spectral filters at Beijing[J]. *Chinese Journal of Quantitative Spectroscopy and Radiative Transfer*, **255**, 107256. DOI.org/10.1016/j.jqsrt.2020.107256
- [19] XIA Y, NOZAWA S, JIAO J, *et al.* Statistical study on Sporadic Sodium Layers (SSLs) based on diurnal sodium lidar observations at Beijing, China (40. 5°N, 116°E)[J]. *Journal of Atmospheric and Solar-Terrestrial Physics*, 2021, 212, 105512. DOI.org/10.1016/j.jastp.2020.105512
- [20] HU D, GUAN Z, LIU M, *et al.* Dynamical mechanisms for the recent ozone depletion in the arctic stratosphere linked to north pacific sea surface temperatures[J]. *Climate Dynamics*, 2021, **1**: 17
- [21] LIU M, HU D. Contrast relationships between arctic oscillation and ozone in the stratosphere over the arctic in early and mid-to-late

- winter[J]. *Journal of Geophysical Research: Atmospheres*, 2021, **126**(5): 1-16
- [22] LIU M, HU D. Different relationships between arctic oscillation and ozone in the stratosphere over the arctic in January and February[J]. *Atmosphere*, 2021, **12**(2): 1-14
- [23] XU W, SONG Q, LI Y, *et al.* Effects of Stationary and Transient Transport of Ozone On the Ozone Valley Over the Tibetan Plateau in Summer[J]. *Frontiers in Earth Science*, 2021, **9**: 1-11
- [24] LIU Y, XU J, XIONG C, *et al.* Main wave sources of the longitudinal structures of equatorial electric field[J]. *Geophysical Research Letters*, 2021, **48**, e2021GL092426. DOI.org/10.1029/2021GL092426
- [25] Yang, J., X. Qie, L. Zhong, Q. He, **G. Lu**, Z. Wang, ... and F. Liu (2020), Analysis of a gigantic jet in southern China: morphology, meteorology, storm evolution, lightning and narrow bipolar events[J]. *J. Geophys. Res.: Atmos.*, <https://doi.org/10.1029/2019JD031538>
- [26] LIU F, ZHU B, ZHU G, *et al.* Meteorological and electrical conditions of two mid-latitude thunderstorm producing blue discharges[J]. *J. Geophys. Res.: Atmos.*, 2021, **126**, e2020JD033648, DOI: 10.1029/2020JD033648
- [27] LIU F, **LU G**, NEUBERT T, *et al.* Optical emissions associated with narrow bipolar events in radio signals from thunderstorm clouds penetrating into the stratosphere[J]. *Nature Communications*, 2021, **12**: 6631, DOI.org/10.1038/s41467-021-26914-4
- [28] LIU F, ZHU B, LU G, *et al.* Outbreak of negative narrow bipolar events in two mid-latitude thunderstorms featuring overshooting tops[J]. *Remote Sensing.*, 2021c, **13**, 5130; <https://doi.org/10.3390/rs13245130>
- [29] REN H, **LU G**, CUMMER S A, *et al.* Comparison between high-speed video observation of sprites and broadband sferic measurements[J]. *Geophys. Res. Lett.*, 2021, **48**, e2021GL093094. DOI: 10.1029/2021GL093094
- [30] Wang, Y., **G. Lu**, S. A. Cummer, F. Lucena, M. Cohen, H. Ren, Z. Cheng, and S. Zhang (2021a), Ground observation of negative sprites over a tropical thunderstorm as the embryo of Hurricane Harvey (2017), *Geophys. Res. Lett.*, **48**, e2021GL094032. DOI. org/10.1029/2021GL094032
- [31] WANG Y, **LU G**, PENG K M, *et al.* Space-based observation of a negative sprite with an unusual signature of associated sprite current[J]. *J. Geophys. Res.: Atmos.*, 2021, **126**, e2020JD033686. DOI. org/10.1029/2020JD033686
- [32] Zhang, H., **G. Lu**, F. Lyu, S. Xiong, *et al.* (2021), On the terrestrial gamma-ray flashes preceding narrow bipolar events produced in tropical thunderstorms[J]. *Geophys. Res. Lett.*, **48**, e2020GL092160, doi: 10.1029/2020GL092160
- [33] Zhang JK, Zhang CY, Zhang KQ, Xu M, Duan JK, Chipperfield MP, Feng WH, Zhao SY, Xie F. The role of chemical processes in the Quasi-Biennial Oscillation (QBO) signal in stratospheric ozone[J]. *Atmospheric Environment*, 2021, **244**: 117906
- [34] Xie F, Zhang JK, Li XT, Li J, Wang T, Xu M. Independent and joint influences of eastern Pacific El Niño–southern oscillation and quasi-biennial oscillation on Northern Hemispheric stratospheric ozone[J]. *International Journal of Climatology*, 2020a, **40**(12): 5289-307
- [35] Wang Z, Zhang JK, Wang T, Feng WH, Hu YH, Xu XR. Analysis of the Antarctic Ozone Hole in November[J]. *Journal of Climate*, 2021, **34**(16): 6513-6529
- [36] Zhang KQ, Duan JK, Zhao SY, Zhang JK, Keeble J, Liu HW. Evaluating the Ozone Valley over the Tibetan Plateau in CMIP6 Models[J]. *Advances in Atmospheric Sciences*, 2021, DOI: 10.1007/s00376-021-0442-2
- [37] Xie F, Tian WS, Zhou X, *et al.* Increase in lower stratospheric water vapor in the past 100 years related to tropical atlantic warming[J]. *Geophysical Research Letters*, 2020, **47**(22): e2020GL090539
- [38] ZHANG J, XIA X, WU X. First in situ UV profile across the UTLS accompanied by ozone measurement over the Tibetan Plateau[J]. *Journal of Environmental Sciences*, 2020, **98**: 71-76. DOI.org/10.1016/j.jes.2020.05.020, 2020
- [39] ZHANG Y, TAO M, TAO M, *et al.* Long-term variations in ozone levels in the troposphere and lower stratosphere over Beijing: observations and model simulations[J]. *Atmospheric Chemistry and Physics*. 2020, **20**(21): 13343-13354
- [40] LI D, VOGEL B, MÜLLER R, *et al.* Dehydration and low ozone in the tropopause layer over the Asian monsoon caused by tropical cyclones: Lagrangian transport calculations using ERA-Interim and ERA5 reanalysis data[J]. *Atmos. Chem. Phys.*, 2020: **20**: 4133-4152. <https://doi.org/10.5194/acp-20-4133-2020>
- [41] MA D, BIAN J, LI D, *et al.* Mixing characteristics within the tropopause transition layer over the Asian summer monsoon region based on ozone and water vapor sounding data[J]. *Atmospheric Research*, 2022, **271**, 106093. DOI. org/10.1016/j.atmosres.2022.106093
- [42] DAI Y, PAN W, QIAO S, *et al.* Seasonal variations of mesospheric densities observed by Rayleigh Lidar at Golmud, Qinghai[J]. *Journal of Space Science*, 2020, **40**(2): 207-214. doi:10.11728/cjss2020.02.207
- [43] JIAO J, FENG W, WU F, *et al.* A Comparison of the midlatitude nickel and sodium layers in the mesosphere: Observations and modeling[J]. *Journal of Geophysical Research: Space Physics*, 2022, **127**, e2021JA030170. DOI.org/10.1029/2021JA030170
- [44] ZHOU Q, CHEN W. Possible influences of the solar cycle on the onset of South China Sea summer monsoon[J]. *Journal of Tropical Meteorology* (in Chinese), 2020, **36**(1): 25-31
- [45] Zhou Q, Chen W. Possible linkages between the 11-year solar cycle and Antarctic sea ice variability[J]. *Chinese Journal of Polar Research* (in Chinese), 2020, **32**(3): 290-300
- [46] ZOU Z, XUE X, YI W *et al.* Response of the high-latitude upper mesosphere to energetic electron precipitation[J]. *Astrophys. J.*, 2020, **893**(1): 55. DOI.org/10.3847/1538-4357/ab7eb0
- [47] WU J, FENG W, XUE X, *et al.* The 27-day solar rotational cycle response in the mesospheric metal layers at low latitudes[J]. *Geophysical Research Letters*, 2019, **46**: 7199-7206. <https://doi.org/10.1029/2019GL083888>
- [48] XIA Y, WANG Y, HUANG Y, *et al.* Significant contribution of stratospheric water vapor to the poleward expansion of the hadley circulation in autumn under greenhouse warming[J]. *Geophysical Research Letters*, 2021, **48**: e2021GL094008
- [49] XIA Y, HU Y, ZHANG J, *et al.* Record arctic ozone loss in spring 2020 is likely caused by north pacific warm sea surface temperature

- anomalies[J]. *Advances in Atmospheric Sciences*, 2021, **1**: 14
- [50] RAO Jian, LIU Siming, CHEN Yuanhao. Northern Hemisphere sudden stratospheric warming and its downward impact in four Chinese CMIP6 models[J]. *Adv. Atmos. Sci.*, 2021, **38**(2): 187-202
- [51] RAO Jian, GARFINKEL C I. CMIP5/6 models project little change in the statistical characteristics of sudden stratospheric warmings in the 21st century[J]. *Environ. Res. Lett.*, 2021, **16**(3): 034024
- [52] RAO Jian, GARFINKEL C I. Projected changes of stratospheric final warmings in the Northern and Southern Hemispheres by CMIP5/6 models[J]. *Climate Dyn.*, 2021, **56**(9/10): 3353-3371
- [53] XIA Y, HUANG Y, HU Y. Robust acceleration of stratospheric moistening and its radiative feedback under greenhouse warming[J]. *Journal of Geophysical Research: Atmospheres*, 2020, 125: e2020JD033090
- [54] ZHANG H, LU G, LYU F, et al. First measurements of low-frequency sferics associated with Terrestrial Gamma-Ray Flashes produced by equatorial thunderstorms[J]. *Geophys. Res. Lett.*, 2020, **47**, e2020GL089005, <https://doi.org/10.1029/2020GL089005>
- [55] ZHANG J K, TIAN W S, XIE F, et al. The influence of zonally asymmetric stratospheric ozone changes on the Arctic polar vortex shift[J]. *Journal of Climate*, 2020, **33**(11): 4641-4658
- [56] XIE F, ZHANG J K, Huang Z, et al. An Estimate of the Relative Contributions of Sea Surface Temperature Variations in Various Regions to Stratospheric Change[J]. *Journal of Climate*, 2020, **33**(12): 4993-5011
- [57] CHENG Xuan, YANG Junfeng, XIAO Cunying, HU Xiong. Density Correction of NRLMSISE-00 in the middle atmosphere (20–100 km) based on TIMED/SABER density data[J]. *Atmosphere*, 2020, **11**(4), 341
- [58] CHENG Xuan, XIAO Cunying, YANG Junfeng, et al. A modeling method and its application of global atmospheric density in near space[J]. *Journal of Beijing University of Aeronautics and Astronautics*, 2020, **46** (12): 2227-2235
- [59] JIANG G, XIONG C, STOLLE C, et al. Comparison of thermospheric winds measured by GOCE and ground-based FPIs at low and middle latitudes[J]. *Journal of Geophysical Research: Space Physics*, 2021, **126**, e2020JA028182. <https://doi.org/10.1029/2020JA028182>
- [60] WU K, XU J, WANG W, et al. Interaction of oppositely traveling medium-scale traveling ionospheric disturbances observed in low latitudes during geomagnetically quiet nighttime[J]. *Journal of Geophysical Research: Space Physics*, 2021, 126, e2020JA028723, DOI.org/10.1029/2020JA028723
- [61] SUN L, XU J, ZHU Y, et al. Interaction between a southwestward propagating MSTID and a poleward moving WSA-like plasma patch on a magnetically quiet night at midlatitude China region[J]. *Journal of Geophysical Research: Space Physics*, 2020, 125, e2020JA028085. DOI.org/10.1029/2020JA028085
- [62] SUN L, XU J, ZHU Y, et al. Interaction between an MSTID and an EPB in the EIA Crest Region of China[J]. *Journal of Geophysical Research: Space Physics*, 2021, e2020JA028085. DOI.org/10.1029/2020JA028085
- [63] LUO J, XU J, WU K, et al. The Influence of Ionospheric Neutral Wind Variations on the Morphology and Propagation of Medium Scale Traveling Ionospheric Disturbances on 8th August 2016[J]. *Journal of Geophysical Research: Space Physics*, 2021, **126**, e2020JA029037
- [64] SHANG S, SHI J, WANG G, et al. Analysis of the long lasting events of ionospheric irregularities near the equatorial region of East Asia based on various observations[J]. *Advances in Space Research*, 2021, **68**: 2244-2255. <https://doi.org/10.1016/j.asr.2020.12.026>
- [65] YI W, REID I M, XUE X, et al. First observations of Antarctic mesospheric tidal wind responses to recurrent geomagnetic activity[J]. *Geophysical Research Letters*, 2021, **48**, e2020GL089957. DOI.org/10.1029/2020GL089957
- [66] YU B, SCOTT C J, XUE X, et al. A Signature of 27 day solar rotation in the concentration of metallic ions within the terrestrial ionosphere[J]. *Astrophys. J.*, 2021, **916**(2): 106. DOI: 10.3847/1538-4357/ac0886
- [67] HUANG C, LI W, ZHANG S, et al. Investigation of dominant traveling 10-day wave components using long-term MERRA-2 database[J]. *Earth, Planets and Space*, 2021, **73**: 85. DOI.org/10.1186/s40623-021-01410-7
- [68] LI W, HUANG C, LI W, et al. Global characteristics of the westward-propagating quasi-16-day wave with zonal wavenumber 1 and the connection with the 2012/2013 SSW revealed by ERA-Interim[J]. *Earth, Planets and Space*, 2021, **73**: 113. DOI.org/10.1186/s40623-021-01431-2
- [69] TANG W T, ZHANG S D, HUANG C M, et al. Latitudinal- and height-dependent long-term climatology of propagating quasi-16-day waves in the troposphere and stratosphere[J]. *Earth, Planets and Space*, 2021, **73**: 210. DOI.org/10.1186/s40623-021-01544-8
- [70] GONG Y, LV X, ZHANG S, et al. Climatology and seasonal variation of the thermospheric tides and their response to solar activities over Arecibo[J]. *Journal of Atmospheric and Solar-Terrestrial Physics*, 2021, **215**. DOI:10.1016/j.jastp.2021.105592
- [71] GONG Y, XUE J, MA Z, et al. Strong quarterdiurnal tides in the mesosphere and lower thermosphere during the 2019 Arctic sudden stratospheric warming over Mohe, China[J]. *Journal of Geophysical Research: Space Physics*, 2021, **126**, e2020JA029066. DOI.org/10.1029/2020JA029066
- [72] MA Z, GONG Y, ZHANG S, et al. Understanding the excitation of quasi-6-day waves in both hemispheres during the September 2019 Antarctic SSW[J]. *Journal of Geophysical Research: Atmospheres*, 2022, **127**, e2021JD035984. DOI.org/10.1029/2021JD035984
- [73] MA Z, GONG Y, ZHANG S, et al. First observational evidence for the role of polar vortex strength in modulating the activity of planetary waves in the MLT region[J]. *Geophysical Research Letters*, 2022, **49**, e2021GL096548. DOI.org/10.1029/2021GL096548
- [74] RAO Jian, GARFINKEL C I, WHITE I P. Impact of the quasi-biennial oscillation on the northern winter stratospheric polar vortex in CMIP5/6 models[J]. *J. Climate*, 2020, **33**(11): 4787-4813
- [75] RAO Jian, GARFINKEL C I, WHITE I P. How does the quasi-biennial oscillation affect the boreal winter tropospheric circulation in CMIP5/6 models[J]. *J. Climate*, 2020, **33**(20): 8975-8996
- [76] RAO Jian, GARFINKEL C I, WHITE I P. Projected strengthening of the extratropical surface impacts of the stratospheric quasi-biennial oscillation[J]. *Geophys. Res. Lett.*, 2020, **47**(20): e2020GL089149
- [77] RAO Jian, GARFINKEL C I, WHITE I P. Development of the ex-

- tratospheric response to the stratospheric quasi-biennial oscillation[J]. *J. Climate*, 2021, **34**(17): 7239-7255
- [78] HU YH, TIAN WS, ZHANG JK, *et al.* Weakening of Antarctic stratospheric planetary wave activities in early austral spring since the early 2000s: a response to sea surface temperature trends[J]. *Atmospheric Chemistry and Physics*, 2022, **22**(2): 1575-1600
- [79] QUAN Lin, CAI Bing, HU Xiong, *et al.* Study of ionospheric D region changes during solar flares using MF radar measurements[J]. *Journal of Advances in Space Research*, 2021, **67**(2): 715-721
- [80] CAI Bing, XU Qingchen, HU Xiong, *et al.* Analysis of the correlation between horizontal wind and 11-year solar activity over Langfang, China[J]. *Earth and Planetary Physics*, 2021, **5**(3): 270-279
- [81] TIAN Caixia, HU Xiong, LIU Yurong, *et al.* Seasonal variations of high-frequency gravity wave momentum fluxes and their forcing toward zonal winds in the mesosphere and lower thermosphere over Langfang, China (39. 4°N, 116. 7°E)[J]. *Atmosphere*, 2020, **11**(11), 1253
- [82] TIAN Caixia, HU Xiong, YAN Zhaoai, *et al.* Diurnal and seasonal variation in gravity wave activity at ~40°N by Langfang meteor radar[J]. *Journal of Advances in Space Research*, 2021, **68**(3): 1341- 1355
- [83] SHI Guochun, HU Xiong, YAO Zhigang, *et al.* Case study on stratospheric and mesospheric concentric gravity waves generated by deep convection[J]. *Earth and Planetary Physics*. 2021, **5**(1): 79-89
- [84] GUO Wenjie, YAO Zhigang, HU Xiong, YANG Junfeng. Research on global stratospheric gravity wave characteristics by AIRS observation data[J]. *Chines Journal of Space Science*, 2021, **41**(4): 609-616
- [85] SUN C, YANG C, LI T. Dynamical influence of the Madden-Julian oscillation on the Northern Hemisphere mesosphere during the boreal winter[J]. *Science China Earth Sciences*, 2021, **64**. DOI.org/10.1007/s11430-020-9779-2
- [86] YANG, C., SMITH, A. K., LI, T *et al.* (2020). Can the Madden-Julian Oscillation affect the Antarctic total column ozone[J]. *Geophysical Research Letters*, **47**, e2020GL088886. A. org/10.1029/2020GL088886
- [87] CHENG H, HUANG K M, LIU A Z, *et al.* A quasi-27-day oscillation activity from the troposphere to the mesosphere and lower thermosphere at low latitudes[J]. *Earth Planets and Space*, 2021, **73**: 183. DOI.org/10.1186/s40623-021-01521-1
- [88] MA Z, GONG Y, ZHANG S, *et al.* Study of a quasi-27-day wave in the MLT region during recurrent geomagnetic storms in autumn 2018[J]. *Journal of Geophysical Research: Space Physics*, 2021, **126**, e2020JA028865. <https://doi.org/10.1029/2020JA028865>
- [89] BAI X Y, HUANG K M, ZHANG S D, *et al.* Anomalous changes of temperature and ozone QBOs in 2015–2017 from radiosonde observation and MERRA-2 reanalysis[J]. *Earth Planetary Physics*, 2021, **5**(3): 1-10. DOI.org/10.26464/epp2021028
- [90] DU M K, HUANG K M, ZHANG S D, *et al.* Water vapor anomaly over the tropical western Pacific in El Niño winters from radiosonde and satellite observations and ERA5 reanalysis data[J]. *Atmospheric Chemistry and Physics*, 2021, **21**: 13553-13569. DOI.org/10.5194/acp-21-13553-2021
- [91] HUANG K M, LIU H, LIU A Z, *et al.* Investigation on spectral characteristics of gravity waves in the MLT using lidar observations at Andes[J]. *Journal of Geophysical Research: Space Physics*, 2021, **126**, e2020JA028918. DOI.org/10.1029/2020JA028918
- [92] LI, Q., ZHANG, S. D., HUANG, C. M., Huang, K. M., Gong, Y., Gan, Q., *et al.* (2021a). Statistical spectral characteristics of three-dimensional winds in the mesopause region revealed by the Andes lidar. *Journal of Geophysical Research: Atmospheres*, **126**, e2021JD035586. <https://doi.org/10.1029/2021JD035586>
- [93] NING W H, HUANG K M, ZHANG S D, *et al.* A statistical investigation of inertia gravity wave activity based on MST radar observations at Xianghe (116. 9°E, 39. 8°N)[J]. *China. Journal of Geophysical Research: Atmospheres*, 2021, **127**, e2021JD035315. DOI.org/10.1029/2021JD035315
- [94] LIU X, XU J, YUE J, *et al.* Persistent layers of enhanced gravity wave dissipation in the upper mesosphere revealed from SABER observations[J]. *Geophysical Research Letters*, 2022, 1-11. DOI.org/10.1029/2021gl097038
- [95] LIU X, XU J, YUE J, *et al.* Gravity-wave-perturbed wind shears derived from SABER temperature observations[J]. *Atmospheric Chemistry and Physics*, 2020, **20**(22), 14437-14456. <https://doi.org/10.5194/acp-20-14437-2020>
- [96] LIU X, XU J, YUE J. Global static stability and its relation to gravity waves in the middle atmosphere[J]. *Earth and Planetary Physics*, 2020, **4**(5): 504-512. DOI.org/10.26464/epp2020047
- [97] LIU X, XU J, YUE J, *et al.* Global balanced wind derived from SABER temperature and pressure observations and its validations[J]. *Earth Syst. Sci. Data*, 2021, **13**(12): 5643-5661. <https://doi.org/10.5194/essd-13-5643-2021>
- [98] ZOU X, YANG G, *et al.* Atmospheric turbulence spectrum in high resolution mode detected by a high power-aperture sodium lidar over Yanqing, Beijing (40. 47°N, 115. 97°E)[J]. *Journal of Quantitative Spectroscopy and Radiative Transfer*, 2021
- [99] HE X, LUO J L, XU X, *et al.* The effect of QBO on CO distribution in the UTLS over the Asian monsoon region during boreal summer[J]. *Frontiers in Earth Science*, 2021, **9**: 1-10
- [100] WANG T, TIAN W S, ZHANG J K, *et al.* Connections between Spring Arctic Ozone and the Summer Circulation and Sea Surface Temperatures over the Western North Pacific[J]. *Journal of Climate*, 2020, **33**(7): 2907–2923
- [101] ZHANG R H, TIAN W S, WANG T. Role of the quasi-biennial oscillation in the downward extension of stratospheric northern annular mode anomalies[J]. *Climate Dynamics*, 2020, **55**(3): 595-612
- [102] XU M, TIAN W S, ZHANG J K, *et al.* Distinct tropospheric and stratospheric mechanisms linking historical Barents-Kara sea-ice loss and late winter Eurasian temperature variability[J]. *Geophysical Research Letters*, 2021, **48**(20): e2021GL095262
- [103] XU M, TIAN W S, ZHANG J K, *et al.* Impact of sea ice reduction in the barents and kara seas on the variation of the east asian trough in late winter[J]. *Journal of Climate*, 2021b, **34**(3): 1081-1097
- [104] MA T, CHEN W, HUANGFU J, *et al.* The observed influence of the Quasi-Biennial Oscillation in the lower equatorial stratosphere on the East Asian winter monsoon during early boreal winter[J]. *International Journal of Climatology*, 2021, **41**: 6254-6269. DOI: 10.1002/joc. 7192
- [105] CHEN W, ZHOU Q, XUE X. Solar cycle modulation of the relationship between the boreal spring Northern Atlantic Oscillation

- and the East and Southeast Asian summer climate[J]. *Meteorology and Atmospheric Physics*, 2020, **132**: 287-295. DOI: 10. 1007/s00703-019-00687-4
- [106] XUE X, CHEN W, ZHOU Q. Solar cycle modulation of the connection between boreal winter ENSO and following summer South Asian high[J]. *Journal of Atmospheric and Solar-Terrestrial Physics*, 2020, **211**, 105466. DOI: 10. 1016/j. jastp. 2020. 105466
- [107] HUANGFU J, TANG Y, MA T, *et al.* Influence of the QBO on tropical convection and its impact on tropical cyclone activity over the western North Pacific[J]. *Climate Dynamics*, 2021, **57**, 657-669. DOI: 10. 1007/s00382-021-05731-x
- [108] WANG L, WANG L, CHEN W, HUANGFU J. Modulation of winter precipitation associated with tropical cyclone of the western North Pacific by the stratospheric Quasi-Biennial oscillation[J]. *Environmental Research Letters*, 2021, **16**, 054004, <https://doi.org/10.1088/1748-9326/abf3dd>
- [109] LU Y J, TIAN W S, ZHANG J K, *et al.* The Impact of the Stratospheric Polar Vortex Shift on the Arctic Oscillation[J]. *Journal of Climate*, 2021, **34**(10): 4129-4143
- [110] ZHANG J K, ZHENG H Y, XU M, *et al.* Impacts of stratospheric polar vortex changes on wintertime precipitation over the northern hemisphere[J]. *Climate Dynamics*, 2022, DOI: 10. 1007/s00382-021-06088-x
- [111] Hu D, Guan Z, Liu M, Wang T. Is the Relationship Between Stratospheric Arctic Vortex and Arctic Oscillation Steady[J]. *Journal of Geophysical Research: Atmospheres*, 2021, **126**(19): 1-20
- [112] HUANG R, TIAN W S, QIE K, *et al.* Contrasting effects of Indian Ocean basin and dipole modes on the stratosphere[J]. *Journal of Geophysical Research: Atmospheres*, 2021, 126: e2021JD035156
- [113] HUANG J L, HITCHCOCK P, MAYCOCK A C, *et al.* Northern hemisphere cold air outbreaks are more likely to be severe during weak polar vortex conditions[J]. *Communications Earth & Environment*, 2021, **2**(1): 1-11
- [114] HUANG J L, HITCHCOCK P, TIAN W S, SILLIN J. Stratospheric influence on the development of the 2018 late winter European cold air outbreak[J]. *Journal of Geophysical Research: Atmospheres*, 2022, 127(5): e2021JD035877
- [115] LIANG R, YU Y, SHI C, GUAN Z. Role of the Moist and Dry Components of Moist Isentropic Mass Circulation in Changing the Extratropical Surface Temperature in Winter[J]. *Geophysical Research Letters*, 2021, **48**(3): 1-10
- [116] LIU M, HU D, ZHANG F. Connections Between Stratospheric Ozone Concentrations Over the Arctic and Sea Surface Temperatures in the North Pacific[J]. *Journal of Geophysical Research: Atmospheres*, 2020, **125**(4): 1-18
- [117] XIA Y, HU Y, HUANG Y, *et al.* Stratospheric ozone loss-induced cloud effects lead to less surface ultraviolet radiation over the siberian arctic in spring[J]. *Environmental Research Letters*, 2021, **16**: 084057
- [118] XIA Y, HU Y, HUANG Y, *et al.* Significant contribution of severe ozone loss to the siberian-arctic surface warming in spring 2020[J]. *Geophysical Research Letters*, 2021, **48**: e2021GL092509
- [119] MA J, CHEN W, NATH D, LAN X. Modulation by ENSO of the relationship between stratospheric sudden warming and the Madden-Julian oscillation[J]. *Geophysical Research Letters*, 2020, **47**, e2020GL088894. DOI: 10. 1029/2020GL088894
- [120] XU Q, CHEN W, SONG L. Two leading modes in the evolution of major sudden stratospheric warmings and their distinctive surface influence[J]. *Geophysical Research Letters*, 2022, **49**, e2021GL095431. DOI.org/10.1029/2021GL095431
- [121] KOVAL A V, CHEN W, DIDENKO K A, *et al.* Modelling the residual mean meridional circulation at different stages of sudden stratospheric warming events[J]. *Annales Geophysicae*, 2021, **39**, 357-368. <https://doi.org/10.5194/angeo-39-357-2021>
- [122] MA J, CHEN W, LAN X. Comparative analysis of the evolution processes of the strong and weak stratosphere polar vortex events in boreal winter. Chinese Journal of Atmospheric Sciences (in Chinese), 2020b, 44(4): 726-747, doi: 10. 3878/j. issn. 1006-9895. 1906. 19110
- [123] WEI K, MA J, CHEN W, VARGIN P. Longitudinal peculiarities of planetary waves-zonal flow interactions and their role in stratosphere-troposphere dynamical coupling[J]. *Climate Dynamics*, 2021, **57**: 28431-2862. DOI: 10. 1007/s00382-021-05842-5
- [124] WEI K, CHEN W, XU L, ZHOU C. Stratosphere amplifies the global climate effect of wildfires. *Science China Earth Sciences*, 2020, **63**: 309-311. DOI: 10. 1007/s11430-019-9560-3
- [125] LU Q, RAO J, LIANG Z, *et al.* The Sudden Stratospheric Warming in January 2021[J]. *Environmental Research Letters*, 2021, **16**(8): 1-9
- [126] RAO Jian, GARFINKEL C I, WHITE I P. Predicting the downward and surface influence of the February 2018 and January 2019 sudden stratospheric warming events in subseasonal to seasonal (S2S) models[J]. *J. Geophys. Res. Atmos.*, 2020, **125**(2): e2019JD031919
- [127] RAO Jian, GARFINKEL C I, WU Tongwen, *et al.* The January 2021 sudden stratospheric warming and its prediction in subseasonal to seasonal models[J]. *J. Geophys. Res. Atmos.*, 2021, **126**(21): e2021jd035057
- [128] RAO Jian, GARFINKEL C I, WHITE I P, *et al.* The Southern Hemisphere minor sudden stratospheric warming in September 2019 and its predictions in S2S models[J]. *J. Geophys. Res. Atmos.*, 2020, **125**(14): e2020jd032723
- [129] RAO Jian, GARFINKEL C I. Arctic Ozone loss in March 2020 and its seasonal prediction in CFSv2: a comparative study with the 1997 and 2011 cases[J]. *J. Geophys. Res. Atmos.*, 2020, **125**(21): e2020jd033524
- [130] RAO Jian, GARFINKEL C I. The strong stratospheric polar vortex in March 2020 in sub-seasonal to seasonal models: implications for empirical prediction of the low Arctic total ozone extreme[J]. *J. Geophys. Res. Atmos.*, 2021, **126**(9): e2020jd034190
- [131] YU Shuyang, RAO Jian, GUO Dong. Arctic ozone loss in early spring and its impact on the stratosphere-troposphere coupling[J]. *Earth and Planetary Physics*, 2022, **6**(2): 177-190
- [132] RAO Jian, REN Rongcai. Modeling study of the destructive interference between the tropical Indian Ocean and eastern Pacific in their forcing in the southern winter extratropical stratosphere during ENSO[J]. *Climate Dyn.*, 2020, **54**(3/4): 2249-2266
- [133] REN Rongcai, XIA Xin, RAO Jian. Topographic forcing from east Asia and North America in the northern winter stratosphere and their mutual interference[J]. *J. Climate*, 2020, **32**(24): 8639-8658
- [134] XIA Xin, REN Rongcai, YU Yueyue. Dynamical role of the Rocky

- Mountain controlled by East Asian topographies in modulating the tropospheric westerly jet in northern winter[J]. *Atmos. Ocean. Sci. Lett.*, 2020, **12**(1): 66-72
- [135] YU Yueyue, REN Rongcai, XIA Xin, *et al.* A dissection of the topographic effects from Eurasia and North America on the isentropic meridional mass circulation in northern winter[J]. *Climate Dyn.*, doi: 10.1007/s00382-021-06055-6
- [136] XIE Jincai, HU Jinggao, XU Haiming, *et al.* Dynamic diagnosis of stratospheric sudden warming event in the boreal winter of 2018 and its possible impact on weather over North America[J]. *Atmosphere*, 2020, **11**(5): 438
- [137] HUANG Wei, Yu Yueyue, YIN Zhicong, *et al.* Appreciable role of stratospheric polar vortex in the abnormal diffusion of air pollutant in North China in 2015/2016 winter and implications for prediction[J]. *Atmos. Environ.*, 2021, **259**: 118549
- [138] LU Qian, RAO Jian, GUO Dong, *et al.* Downward propagation of sudden stratospheric warming signals and the local environment in the Beijing-Tianjin-Hebei region: A comparative study of the 2018 and 2019 winter cases[J]. *Atmos. Res.*, 2021, **254**: 105514
- [139] CHEN Dan, ZHOU Tianjiao, GUO Dong, GE Shuhao. Simulation of the multi-timescale stratospheric intrusion processes in a typical cut-off low over Northeast Asia[J]. *Atmosphere*, 2022, **13**(1): 68
- [140] XIAO N, ZHANG J K, TIAN W S, *et al.* Effects of Nitrogen Oxide Emissions over East Asia on Ozone and Temperature in UTLS Region of the Northern Hemisphere[J]. *Plateau Meteorology*, 2020, **39**(2): 402-415 (in Chinese)
- [141] TIAN H Y, XU XR, CHEN H B, *et al.* Analysis of the Anomalous Signals near the Tropopause before the Overshooting Convective System Onset over the Tibetan Plateau[J]. *Advances in Meteorology*, 2020, 2020: 8823446

Recent Progress of Earth Science Satellite Missions in China

SHI Jiancheng¹, LÜ Daren², WANG Yu³, DU Yan⁴, PANG Yong⁵, YANG Dongxu², WANG Xin², DONG Xiaolong¹, YANG Xiaofeng³

1. National Space Science Center, Chinese Academy of Sciences, Beijing 100190
2. Institute of Atmospheric Physics, Chinese Academy of Sciences, Beijing, 100029
3. Aerospace Information Research Institute, Chinese Academy of Sciences, Beijing 100094
4. South China Sea Institute of Oceanology, Chinese Academy of Sciences, Guangzhou 510301
5. Institute of Forest Resource Information Technique, Chinese Academy of Forestry, Beijing 100091

Abstract

Earth Science from Space is an interdisciplinary discipline that studies the interactions, mechanisms, and evolution of the Earth system through space observation. In China, the national medium- to long-term civilian space infrastructure development plan and the space-science pilot project from the Chinese Academy of Sciences are two programs associated with advancing the Earth science from space. This paper reports recent scientific findings, developments and the status of the six missions. It is organized as the following sections: Introduction, two satellite missions that are already in orbit—the TanSat-1 for atmospheric CO₂ and the LuTan-1 for global surface deformation, a Terrestrial Ecosystem Carbon Inventory Satellite to be launched in 2022, and three missions that passed the Phase II study and planned for near future—the Ocean Surface Current multiscale Observation, the Terrestrial Water Resources Satellite. Climate and Atmospheric Components Exploring Satellites (CACES), followed by the conclusion.

Key words

Earth science from space, Earth observation, Energy and water cycle, Carbon cycle, Human activity

1 Introduction

Earth science is a fundamental discipline with strong practicality, and experiments and observations play an important role in promoting the development of the domain. For a long time, the observation of the earth can only be limited to a few points or a small area, which has a substantial limitation for a comprehensive, comprehensive and overall study of the earth. Small-scale conclusions usually cannot be mechanically extrapolated to large-scale. The development of satellite earth

observation technology has presented the earth in a complete form to scientists and the public for the first time. China is one of the few nations that has been successful in developing a comprehensive Earth observation system. Since 2020, China has developed and launched several new satellites to support Earth Science studies.

2 TanSat-1

Since CO₂ has been recognized as the most important

anthropogenic greenhouse gas owing to its significant impact on global warming and climate change, there are a substantial number of studies that have focused on investigating the status of CO₂ in the atmosphere in the past and present, and how it will change in the future. In support of the upcoming global stocktake in 2023, we require a new method to verify how much human emissions impact the global carbon cycle and climate change.

The first Chinese carbon dioxide monitoring satellite mission, TanSat, which was supported by the Ministry of Science and Technology of China, the Chinese Academy of Sciences, and the China Meteorological Administration, was launched in December 2016 to monitor carbon dioxide (CO₂) concentrations in the atmosphere over the globe.

2.1 A New TanSat XCO₂ Data Product

The first TanSat global map of CO₂ dry-air mixing ratio (XCO₂) measurements over land was released as version 1 data product^[1] with an accuracy of 2.11 ppmv (parts per million by volume)^[2,3]. Unfortunately, it is not accurate enough to support estimation of anthropogenic CO₂ emissions in cities due to it has a 1–1.5 ppm gradient across the urban regions as has been shown from ground-based measurement in Paris. On TanSat 4th birthday coming this year, we introduce a new (version 2) TanSat global XCO₂ product that is approached by the Institute of Atmospheric Physics Carbon dioxide retrieval Algorithm for Satellite remote sensing (IAP-CAS), and the European Space Agency (ESA) Climate Change Initiative plus (CCI⁺) TanSat XCO₂ product by University of Leicester Full Physics (UoL-FP) retrieval algorithm^[4]. The new TanSat XCO₂ data product is now retrieved by the Institute of Atmospheric Physics Carbon dioxide retrieval Algorithm for Satellite remote sensing (IAPCAS) using the O₂ A-band and CO₂ weak band together, after a new approach has been developed to improve the retrieval accuracy by optimizing the TanSat measured spectrum. The TanSat v2 XCO₂ data product can be obtained from the CASA TanSat data and science service (<http://www.chinageoss.cn/tansat/index.html>). The inter-comparison of TanSat XCO₂ retrieval between the two algorithms shows a good agreement for all TCCON overpass measurements with 34 699 individual measurements. The dispersion between the two data products has a standard deviation of 1.28 ppmv, and there is a –0.35 ppmv overall bias between both, and this systematic error^[5].

2.2 Global Carbon Flux Distribution Derived from TanSat-1

The new version of TanSat XCO₂ data has been applied to drive the TanSat's first estimates of the global distribution of carbon surface fluxes inferred from dry-air CO₂ column (XCO₂), by using an Ensemble Transform Kalman Filter (ETKF) data assimilation system coupled with the GEOS-Chem global chemistry transport model to optimally fit model simulations with the TanSat XCO₂ observations^[6]. High posterior error reduction (30%–50%) compared with a priori fluxes indicates that assimilating satellite XCO₂ measurements provides highly effective constraints on global carbon flux estimation. The impacts of TanSat XCO₂ observations are also highlighted by significant spatiotemporal shifts in flux patterns over regions critical to the global carbon budget, such as tropical South America and China. An integrated global land carbon net flux of 6.71 ± 0.76 Gt C·yr⁻¹ over 12 months (May 2017–April 2018) is estimated from the TanSat XCO₂ data, which is generally consistent with other inversions based on satellite data, such as the JAXA GOSAT and NASA OCO-2 XCO₂ retrievals. Further study attempts to estimate terrestrial Net Ecosystem Exchange (NEE) using TanSat XCO₂ retrievals based on the GEOS-Chem 4D-Var data assimilation system and infer the global NEE from April 2017 to March 2018 using TanSat XCO₂ retrievals^[7]. The estimates global NEE at –3.46 PgC·yr⁻¹, evidently higher than the prior estimate and giving rise to an improved estimate of global atmospheric CO₂ growth rate.

2.3 SIFs Derived from TanSat-1

Solar-induced chlorophyll Fluorescence (SIF) is emitted during plant photosynthesis, and it is recognized as the ideal proxy for terrestrial Gross Primary Productivity (GPP) according to many laboratory and field experiments. In recent years, a large number of studies have shown that SIF can effectively improve the estimation of GPP and then promote the quantitative research of the global carbon sink. The first TanSat SIF map was obtained by the SVD method^[8]. A new TanSat SIF product is retrieved by a physical-based algorithm (IAPCAS/SIF), and this algorithm is based on the IAPCAS. The new TanSat SIF product is retrieved from two micro-windows in the O₂ A-band, representing the SIF emission at 757nm and 771nm^[9]. The new TanSat SIF data product can be obtained from the the Cooperation

on the Analysis of carbon SATellites data (CASA) TanSat data and science service*. Comparing global distributions of SIF retrieved by IAPCAS/SIF from TanSat and OCO-2 shows the same spatial pattern for all seasons with gridded SIF difference less than $0.3 \text{ W}\cdot\text{m}^{-2}\cdot\mu\text{m}^{-1}\cdot\text{sr}^{-1}$ ^[10]. The global distributions also agree well with the official OCO-2 SIF product with a difference less than $0.2 \text{ W}\cdot\text{m}^{-2}\cdot\mu\text{m}^{-1}\cdot\text{sr}^{-1}$. The retrieval uncertainty of seasonally gridded TanSat IAPCAS/SIF is less than $0.03 \text{ W}\cdot\text{m}^{-2}\cdot\mu\text{m}^{-1}\cdot\text{sr}^{-1}$ whereas the uncertainty of each sounding ranges from 0.1 to $0.6 \text{ W}\cdot\text{m}^{-2}\cdot\mu\text{m}^{-1}\cdot\text{sr}^{-1}$.

3 LuTan-1

LuTan-1 mission (referred as LT-1) is an innovative space borne Earth observation constellation. It contains two identical satellites that both carry an advanced full polarimetry L-band Synthetic Aperture Radar (SAR). The LT-1A was successfully launched by the Long March-4C carrier rocket on 26 January 2022, from the Jiuquan Satellite Launch Center (China). The LT-1B was launched successfully on 27 February 2022. LT-1 is the first launched satellite mission in the “China National Civil Space Infrastructure Long-Term Development Plan (2015–2025)”. The main tasks of LT-1 are global surface deformation measurement and Digital Elevation Model (DEM) acquisition. The data of LT-1 can also serve many industries such as land, earthquake, mapping, environment, disaster mitigation, forestry, etc.

The scientific objectives of LT-1 include global DEM acquirement, surface deformation measurement, biomass observation, and geological hazards monitoring and assessment. To meet the requirements of scientific objective, the satellite is designed to be in a sun-synchronous orbit with a high inclination of 97.8° at an altitude of around 607 km. The LT-1A and LT-1B satellites can work independently, and can also be used for dual-satellite collaborative imaging and Interferometric SAR (InSAR) applications. Each satellite equips an L-Band SAR as the main payload. It can provide an all-weather, day-and-night supply of images of the Earth’s surface. The L-Band SAR operates in six imaging modes (Table 1) with different resolutions (down to 3 m) and coverages (up to 400 km). It provides the multi-polarization capability and very short revisit times. The revisit time of a single satellite of LT-1 is 8 days. The two-satellite constellation can offer a 4 days exact

repeat cycle. Wide swath coverage and efficient revisit frequency will significantly facilitate the acquisition of time series images. In addition, the L-band has excellent coherence maintenance capability, which is of great significance for emergency management of disasters such as earthquakes and landslides.

The two satellites are expected to operate for 8 years in orbit. The duration of the mission is divided into two phases. In phase I, two satellites fly in a formation with a variable baseline, and the bistatic InSAR strip map mode is utilized to acquire the global digital elevation and terrain models with high accuracy and spatial resolution. In phase II, two satellites shall share the common reference orbit with a 180° orbital phasing difference. Land deformation with millimeter accuracy at a large scale can be measured using the differential InSAR technique. For high-precision interferometric measurement, LT-1 needs high accurate synchronization to guarantee the same working state of the two satellites in the data acquisition process, especially phase synchronization. An advanced non-interrupted phase synchronization scheme is proposed for LuTan-1^[11,12]. The synchronization pulses are exchanged immediately after the ending time of the radar echo receiving window and before the starting time of the next pulse repetition interval, which will not interrupt the regular SAR operation and realize the high-accuracy phase synchronization. Moreover, LT-1 achieves a very high phase synchronization accuracy. To solve the contradiction between the short working time and the urgent need for large-scale global monitoring, a Non-linear wide-band FM (NLFM) transmit signal was proposed^[13]. A satellite signal generator capable of generating arbitrary NLFM waveforms in orbit is equipped on LT-1, which can increase the working time of satellites in a single orbit cycle by 22%^[14].

SAR satellites have to sacrifice imaging swath width to achieve full polarization imaging capability, which reduces observation efficiency typically. To solve this problem, a series of new technologies such as multi-mode hybrid polarization and a new beamforming scheme have been proposed. SAR satellites’ multi-polarization observation efficiency has improved, boosting the quantitative remote sensing capabilities of businesses like land, disaster relief, surveying and mapping, and forestry. Besides, a large number of promising observation products will be available, such as the single-pass

* <http://www.chinageoss.cn/tansat/index.html>

Table 1 Imaging modes of LT-1. The achievable polarization, swath width, resolution and range of incidence angles are given in the description of each mode

Mode	Strip 1	Strip 2	Strip 3	Strip 4	Strip 5	Scan	
Polarization	Single/Dual Pol, Compact Pol	Single/Dual Pol, Compact Pol	Quad Pol, Hybrid Pol	Quad Pol, Hybrid Pol	Single/Dual Pol, Compact Pol	Single/Dual Pol, Compact Pol	
SAR mode	Strip (Dual channel)	Strip (Single channel)	Strip (Dual channel)	Strip (Single channel)	Strip (Single channel)	Scan (Dual channel)	
Resolution	3 m×3 m (Nominal)	12 m×12 m (Nominal)	3 m×3 m (Nominal)	6 m×6 m (Nominal)	24 m×24 m (Nominal)	30 m×30 m (Nominal)	
Swath width	50 km	100 km	50 km	30 km	160 km	400 km	
Incidence Angle	Imaging	20°–53°(Imaging) 10°–60°(Extended)	20°–53°	10°–60°	13°–21°	15.7–30°	20°–49°
	InSAR	20°–46°	20°–46°				

polarimetry InSAR (Pol-InSAR) for forestry application, the hybrid polarimetric for land classification, *etc.* LT-1 will become the first SAR mission in the world with single-pass Pol-InSAR imaging capability. For example, forest biomass measurement is one of its most common applications, which provides an appropriate technological measurement for carbon cycle monitoring and further supports China's Carbon Dioxide Peaking and Carbon Neutrality plan.

Currently, LuTan-1 is undergoing on-orbit testing. Independent imaging experiments were performed for both LT-1A and LT-1B. The flight formation of Phase I is now in the process of being constructed, and it will be completed in three months. After LT-1 is put into use, it will provide a large amount of Earth observation data for scientific applications. It will drive the development of SAR system for acquiring multi-dimensional information on Earth's dynamic processes and monitoring the global environment.

4 Terrestrial Ecosystem Carbon Monitoring Satellite (TECMS)

Forest plays a crucial role in the carbon cycle and Earth system processes. Remote sensing is vital in quantifying forest carbon through different sensing capabilities (optical, radar, and LiDAR). According to the Application System Plan and Design of National Space Infrastructure (2015–2025), the Chinese Terrestrial Ecosystem Carbon Monitoring Satellite (TECMS) will be launched in the summer of 2022. TECMS is the first Chinese scientific satellite dedicated to comprehensively monitoring carbon storage in terrestrial ecosystems. It aims to monitor terrestrial ecosystems and provide measurements for major national ecological program evaluation.

TECMS has an orbit of 506 km with a 10:30 am op-

eration time. The data coverage capacity is from -80° south to 80° north latitude. TECMS contains LiDAR and multi-angle optical (BRDF) sensors on board. There are 3 large footprint lasers with another 2 lasers as back-ups (see Fig. 1). These five laser systems have a nominal footprint of 25 m. The full waveform data with 1 ns interval will be recorded. Each laser has a 35 Hz repeat frequency. The cross orbit distance among two adjacent laser footprints is about 8 km. The multi-angle optical (BRDF) observations consist of five VNIR cameras. Each camera contains 5 spectral bands with a 20 km swath. The nominal observation angles are 0° , $\pm 28^\circ$, and $\pm 50^\circ$. The spatial resolution is about 8 m.

The combination of multi-angle optical (BRDF) observations with waveform LiDAR remote sensing is unprecedented on board the same satellite. These laser waveforms provide detailed vertical structure information of forests as discrete footprints. The optical BRDF-imager extrapolates the laser height profiles to wall-to-wall biophysical vegetation maps. This innovative mission will significantly improve the capacity of forest carbon estimation.

5 Ocean Surface Current Multiscale Observation Mission (OSCOM)

Ocean Surface Current multiscale Observation Mission (OSCOM), is a satellite mission proposed to the Strategic Priority Program of Space Science (Phase III). The intensive study as a candidate mission has been supported by Chinese Academy of Sciences since 2020, and is under selection review now.

Motion is the essential state of the ocean. Ocean current is a primary physical parameter to describe the motion of the ocean. Global Ocean Surface Currents (OSC, including both speed and direction) play an important

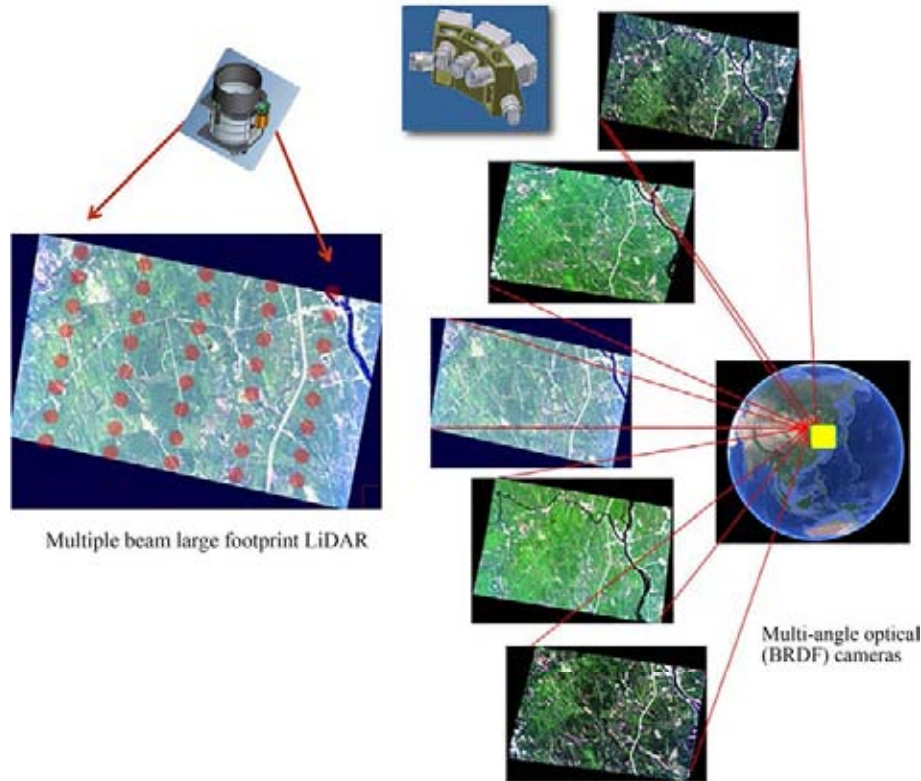


Fig. 1 LiDAR and multi-angle optical cameras configuration of the Chinese Terrestrial Ecosystem Carbon Monitoring Satellite (TECMS)

role in the momentum and energy coupling of multiscale ocean dynamics^[15,16], air-sea exchange and interaction^[17,18], ocean mass and energy transport and balance^[19], global oceanic biochemical processes^[20,21], and their effects on global changes^[22–24]. The complete understanding of the spatial and temporal variation of multiscale ocean dynamics is a frontier to the development of ocean dynamics, air-sea interaction, marine ecological dynamics, biogeochemistry, and earth system modelling.

Firstly, ocean near-surface current has enormous energy, involving processes in multiple spatial and temporal scales (Fig. 2)^[25]. Nearly 90% of ocean kinetic energy clusters in mesoscale and sub-mesoscale, including near-inertial oscillations, fronts, mesoscale eddies, and sub-mesoscale processes^[15]; secondly, OSC is a key element of the ocean water cycle, since it dramatically impacts the distribution and balance of the ocean temperature and salinity^[26,27]; thirdly, feedback of the surface currents to the air-sea exchange through heat transports affects ocean surface fluxes and thermal equilibrium^[28]; and fourthly, the surface currents determine the ocean nutrient transport, pollutant dispersion, sea ice

drift, etc.^[29–31], which seriously affects the biogeochemical cycle and ecosystem balance^[20,21].

Satellite remote sensing is the most powerful tool for global ocean observations and monitoring. Presently, OSC is mainly derived from satellite altimeter data through the geostrophic equilibrium theory, only available to resolve quasi-geostrophic current at large- to meso-scale (>100 km) in the off-equatorial open oceans^[32]. The quasi-geostrophic current in the middle and high latitudes, and, the ageostrophic and non-equilibrium processes and OSC in the equatorial and near-shore regions, especially in meso- to submeso-scales, are still rarely available globally^[33]. This becomes a bottleneck impeding our understanding of the ocean dynamic processes.

Since the 2010s, there has been a consensus among international scientific communities on the direct observation of the surface vector fields from space^[24]. Scientific communities optimistically estimate that, by 2025, one and last most essential ocean environment measurement may become available—total ocean surface currents^[34].

OSCOM will implement simultaneous observation of

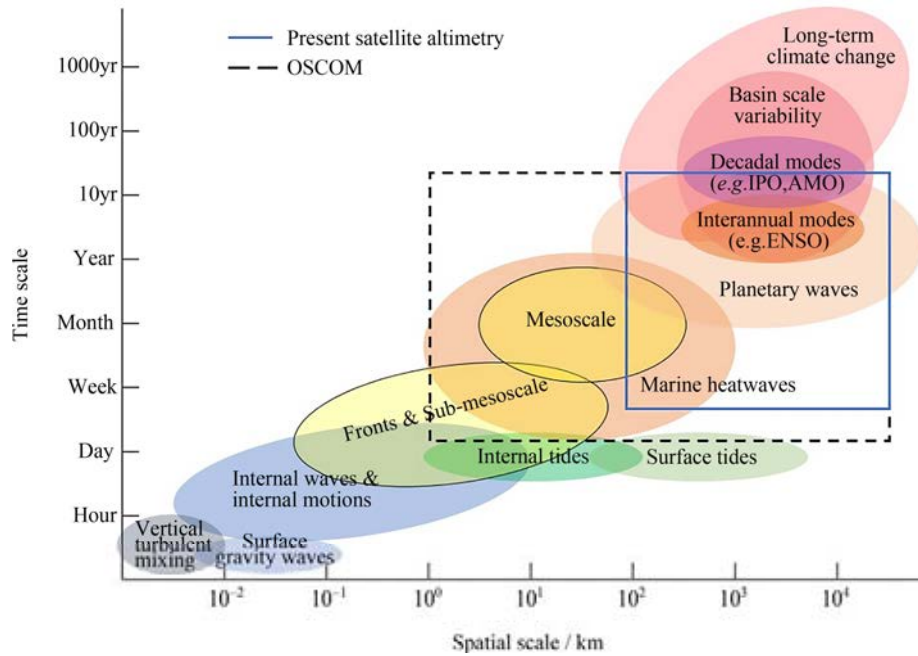


Fig. 2 Schematic diagram of multiscale ocean dynamics (updated from Chelton, 2001)

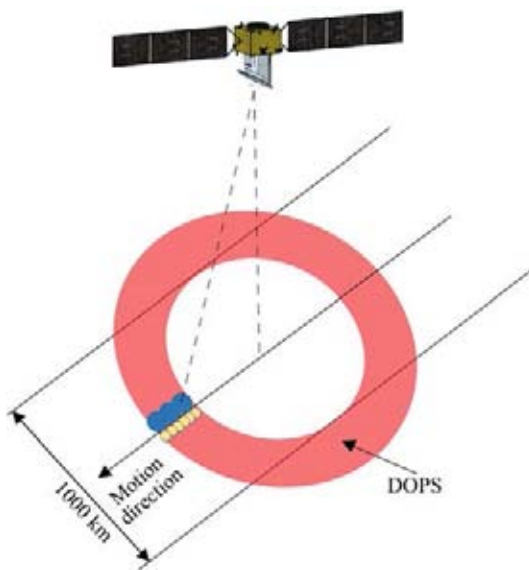


Fig. 3 Schematic diagram of the wide-swath OSCOM surface observations. The swath of OSCOM at the Earth's surface exceeds 1000 km in 650 km high orbit

OSC, Ocean Surface Vector Winds (OSVW), and Ocean Surface Wave Spectrum (OSWS) by a Doppler Scatterometer (DOPS) (Fig. 3). DOPS is a real-aperture radar with a dual-frequency (Ka+Ku) conically scanned rotating multi-pencil-beam antenna. By developing and exploiting combined ocean surface Doppler spectral, roughness spectral, and slope spectral models, OSC with high precision is to be retrieved from the measured Doppler frequency of backscattered signals (Table 2).

Table 2 Expected Performances of OSCOM

Variables	Spatial resolution	Accuracy/precision		Swath/temporal coverage
		Speed accuracy	Direction accuracy	
OSC	5 km	0.1 m·s ⁻¹	15°	>1000 km <3 days
OSVW	5 km	1.5 m·s ⁻¹	15°	globally, mid-to-high latitude
OSWS	10 km	10% @50–500 m wavelength		daily

The direct observation of the global OSC, OSVW, and OSWS, combined with other satellite observations (e.g., high-resolution temperature and ocean color), will further facilitate the investigation and understanding of ocean surface heat flux, carbon budget, and ocean biogeochemical cycle, and provide a novel pathway to data assimilation, coupling of General Circulation Models, and earth system modeling for ocean prediction and climate change.

5.1 Scientific Objectives

To directly observe global OSC at km scale (5–10 km), filling the gap of OSC observation in the space measurements.

To advance the research of ocean sub-mesoscale dynamics, multiscale processes, mass/energy exchanges between ocean and atmosphere, and biogeochemical cycles, promoting the development of theoretical research on ocean science and climate change.

To establish the foundation for numerical simulation

of ocean non-equilibrium processes, providing theoretical and technical support for earth system modeling and earth observation applications.

5.2 Expected Breakthroughs and Innovations

OSCOM will achieve a breakthrough in observing the global ocean's meso- and sub-mesoscale structures/processes from space directly, dedicated to the frontier of ocean multiscale dynamics and energetics based on satellite Doppler oceanography.

OSCOM will set a technical scheme to integrate OSC-OSVW-OSWS detection and inversion. Based on the sea surface Doppler velocity spectrum model, roughness spectrum model, and slope spectrum model, OSCOM will achieve simultaneous observations for a complete portrayal of ocean dynamic structure with a wide swath.

OSCOM will promote the development of many branches of Earth System Science, including physical oceanography, meteorology, biogeochemistry, climate dynamics, and geospatial information science, and improve the ability of earth system modeling to forecast global climate changes.

5.3 Key Technologies

OSCOM has been supported by an intensive pre-study project of candidate missions for Strategic Priority Program on Space Science II since 2020 for in-depth study and demonstration of scientific objectives, development of observation technologies, and retrieval models and techniques. Numerous projects have supported the research and development of the concept and technologies of DOPS since 2012, and an airborne technology verification campaign was completed in the summer of 2020.

The key enabling technologies include: integrated OSC-OSVW-OSWS measurement and retrieval models and techniques; space borne Ka-band power amplifier; and high-precision pointing measurement and determination. Pre-study and development of these technologies satisfy the TRL requirements to start the engineering phase of the mission.

6 Water Cycle Observatory from Space

The water cycle is the continuous movement of water within lands, oceans, and atmosphere. Terrestrial water

cycle is a dynamic component of the global water cycle that exerts important controls over water, energy, and carbon fluxes at the land-atmosphere interface, where humans primarily operate, thereby playing an important role in water resources conservancy, meteorology and climatology, agriculture, ecology, and environment^[35]. Space-based observations have been providing an unprecedented capacity in monitoring different components of the water cycle, such as the Global Precipitation Measurement (GPM) for precipitation^[36], the Soil Moisture Ocean Salinity (SMOS) and Soil Moisture Active Passive (SMAP) for soil moisture^[37,38], the Advanced Technology Microwave Sounder (ATMS) onboard NOAA-20 for water vapor^[39], the Gravity Recovery and Climate Experiment (GRACE) for ground water storage^[40], and the Surface Water and Ocean Topography (SWOT) for water surface elevations^[41]. Such global observations from space should be secured and continued for the development of long-term consistent data record governing the terrestrial water cycle.

Since 2009 with the successful launch of the SMOS mission, it has been a golden age for the development of L-band radiometry from space, with the Aquarius launched in 2011 and SMAP launched in 2015. It has been proved that L-band radiometer and radar is an essential tool for monitoring soil moisture, vegetation water content, and landscape freeze-thaw processes. However, Aquarius is gone, and both SMOS and SMAP are aging. The Terrestrial Water Resources Satellite (TWRS) is a new Chinese mission under development focusing on space-based observation of terrestrial water components, that includes water stored in soil and vegetation, surface waters (rivers and inland water bodies), and solid waters (snow and ice), thus in support of estimation of terrestrial evapotranspiration. Initially, it is designed to have four payloads for the TWRS mission, including the L-band active-passive microwave imager, the multi-angle thermal infrared imager, the wide-swath multispectral camera, and the wide-swath programmable hyperspectral camera (see Table 3 for details). The TWRS mission is designed in Sun synchronous orbit, passing over the equator at 14:00 with an altitude of 680 km, thus, capturing the maximum evapotranspiration, which usually happens in early afternoon.

The L-band active-passive microwave imager is mainly used for the global mapping of soil moisture and its freeze-thaw status with a targeted spatial resolution about 5 km. Unlike the SMOS and SMAP missions, the

Table 3 Initial payload configuration of the Terrestrial Water Resources Satellite

L-band active-passive microwave imager		
Parameters	L-band radiometer	L-band radar
Frequency	1.413 GHz	1.26 GHz
Polarization	H, V, and T3	HH, VV, HV, and VH
Range of incidence angle	0°–40° or 30°–52° (to be adopted)	
Antenna	Parabolic cylinder antenna (12 m × 10 m)	
Spatial resolution	18 km	1.5 km
Swath width	1000 km	
Wide-swath multispectral camera		
Parameters	Visible bands	Near-infrared bands
Spectral range	0.4–0.67 μm	0.85–0.97 μm
Spatial resolution	16 m	
Swath width	800 km	
Wide-swath programmable hyperspectral camera		
Parameters	Visible and near-infrared bands	Short-wave infrared bands
Spectral range	0.4–1.0 μm	1.0–1.68 μm
Spectral bands	128/64	80/40
Spatial resolution	25 m	
Swath width	120 km	
Multi-angle thermal infrared imager		
Spectral range	10.5–12.5 μm	
View angles	+48°, 0°, –31°	
Spatial resolution	100 m	
Swath width	1000 km	

L-band radiometer of TWRS is based on the one-dimensional synthetic aperture technology, which can reduce the complexity as compared to a two-dimensional radiometer of SMOS and avoid the risk of large antenna rotating (SMAP) to obtain high resolution observations in the cross-track direction. A synthetic aperture radar with higher spatial resolution than the radiometer is designed to share the reflector antenna towards soil moisture downscaling based on the synergy between active and passive microwave observations. However, this concept with incidence angle varying along the cross-track direction, raises new challenges including how to perform brightness temperature downscaling at variant incidence angles and how to reduce the dependence of soil moisture retrieval errors on incidence angle. This mission concept has been demonstrated in the Soil Moisture Experiment in the Luan River^[42] focusing on specific challenges with the TWRS mission through an airborne simulator^[43]. The active-passive approach for brightness temperature downscaling is found to be fea-

ible with the airborne simulated observations of TWRS, the uncertainties caused by variant incidence angles can be suppressed by a downscaling method of spectral analysis^[44]. It is indicated that the soil moisture retrieval is expected to have a satisfactory accuracy within 0.04 m³/m³ under the incidence angle ranging from 30° to 50°, which would be adopted for the TWRS mission^[45]. A novel soil moisture retrieval algorithm^[46] is developed to enable the use of different combinations of microwave channels in terms of polarization, frequency, and incidence angles, and the algorithm for the TWRS mission would rely on polarization information with many other options including single-channel algorithm, dual-channel algorithm as adopted for the SMAP mission. In addition, the simultaneously retrieved vegetation optical depth has been found to be a good indicator of vegetation water content and water potential. With its multiple optical sensors including visible, near infrared, short wave infrared, and thermal infrared bands, the microwave-derived soil moisture can be further down-scaled to an even higher spatial resolution for a much broader application.

The multi-angle thermal infrared imager allows retrieval of component temperatures of the land surface, which can improve the modeling of heat exchanges at the land-atmosphere interface. Component temperatures are essential for a better estimation of terrestrial evapotranspiration that deeply affects the water resources availability. The wide-swath multispectral camera is in support of mapping of dynamic changes of surface waters including rivers, lakes, and reservoirs, which are one of the most important resources for human survival and development. It can also be used for detecting the snow cover and glaciers due to the large difference in reflectance in the visible, near infrared and shortwave infrared regions of the spectrum. The programmable hyperspectral camera can be further used to estimate water quality parameters like sediment and carbon concentration and their spatial dynamics over water bodies. Therefore, the TWRS mission can provide a quite comprehensive observation of terrestrial water resources except for the water in the atmosphere and underground.

Based on the planned TWRS mission, combined with China's existing Fengyun satellites and Haiyang satellites, it is expected to form an integrated capability of water cycle observatory from space with active-passive, multi-band remote sensing measurements.

7 Climate and Atmospheric Components Exploring Satellites (CACES)

Global climate change is one of the significant challenges of our time. A deeper understanding of how Greenhouse Gases (GHGs) impact and respond to climate change is one of the urgent scientific questions in Earth system science. Therefore, expanding the observational foundation for climate change studies with accurate, long-term, and consistent benchmark data is a fundamental need of climate science. The mission CACES, Climate and Atmospheric Components Exploring Satellites, focuses on benchmark climate variables and atmospheric composition observations from space to provide the essential atmospheric datasets for scientific research of global climate change.

The CACES satellite constellation consists of two Low-Earth-Orbit (LEO-LEO) satellites in sun-synchronous orbits: one transmitting (Tx) and one receiving (Rx) satellite (see Fig. 4). The orbit altitudes for the Tx and Rx satellites are 500 km and 550 km, respectively. The Tx satellite actively sends signals through the atmosphere to the Rx satellite while the two types of satellites are counter-rotating to implement LEO-LEO occultation measurements. The satellites are designed to support autonomous on-orbit operations. The orbit information is exchanged through low-speed microwave communication between satellites, which supports the independent calculation of the occultation events during the satellites' rendezvous, the antenna or lens aiming of the Tx satellite and the Rx satellite is achieved through orbit attitude maneuver.

CACES combines the microwave occultation (LMO) and the infrared-laser occultation (LIO) techniques by making breakthroughs in essential detection techniques for occultation measurements in the X/K microwave band and Short-Wave Infrared (SWIR) band. It employs an LEO-to-LEO Microwave Occultation detection System (LMOS) and an Infrared-laser Occultation detection System (LIOS) on the constellation.

The LMOS is composed of a Transmitter (LMOS-T) instrument, a Receiver (LMOS-R) instrument, and a Precise Orbit Determination (POD) system. The LMOS is designed to employ X/K band signals to detect altitude and thermodynamic variables. The LMOS-T onboard the Tx satellite sends microwave signals through the atmosphere to the LMOS-R onboard the Rx satellite, during which the excess phases and the amplitude attenuations at different heights are measured. Based on these measurements, vertical profiles of refractivity and absorption are derived. This method can solve the temperature-humidity ambiguity and retrieve the temperature, pressure, and humidity profiles without auxiliary background information. The performance estimation of this 4-frequency LMOS has been conducted using quasi-realistic end-to-end simulations, and the results show that the retrieved temperature, pressure, and humidity profiles are generally unbiased and with minor standard deviations. The POD is the supporting payload for timing and navigation, which is also for the benefit of the LIOS payload.

The LIOS is also composed of a Transmitter (LIOS-T) and a Receiver (LIOS-R) instrument, which use infrared laser signals in the SWIR spectral region within the 2.0–2.5 μm band to provide profiling of GHG based on differential absorption measurements and species and

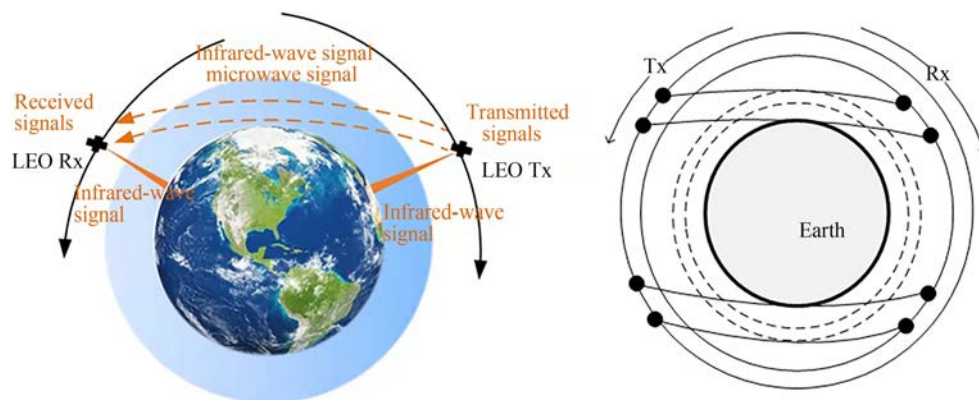


Fig. 4 Schematic view of the measurement concept of CACES, comprising the LIO, LMO components and the hyperspectral imager

further retrieve Line-of-sight (LOS) wind from through the spectral Doppler frequency shift. The infrared occultation system adopts the frequency stabilization technology of optical frequency combs to ensure the precision of laser wavelengths. The spatial heterodyne spectrometer in LIOS-R can achieve extremely high spectral resolution in a narrow field of view. Thus, the Earth's atmosphere is scanned from top to bottom, which enables high precision retrieval of vertical profiles of the atmospheric variables.

In practice, both the Tx and Rx satellites are equipped with a Fabry-Perot Interferometer (FPI)-based hyperspectral imager to fulfill local high-resolution monitoring of GHGs concentration (CO₂ and CH₄). The hyperspectral imager adopts a large-aperture transmission optical system, and the FPI enables high spectral resolution spectroscopy, which is featured by advantageous high spectral resolution, high spatial resolution, high throughput, lightweight, and miniaturization. Therefore, CACES can measure three-dimensional GHGs (CO₂, CH₄, H₂O, *etc.*) concentrations and LOS wind, simultaneously with thermodynamic variables (pressure, temperature, humidity), which also guarantees self-calibration and independence of the mission.

According to preliminary performance simulations, the CACES, when fulfilling its system requirements, can deliver its atmospheric profiles well within observational requirements and in most cases within target requirements. These results underline the potential of the CACES to provide benchmark measurements of unprecedented quality for addressing the climate and other science objectives. If implemented, CACES will provide all-day, accurate, and long-term stable data of essential climate variables with a high vertical resolution and achieve the great leap forward from one-dimensional measurements of GHGs column densities to three-dimensional detections. It will significantly drive the development of many branches of Earth system science research, thereby improving the ability of global change trends projection and a better understanding of the forcing and feedbacks that strongly link the atmosphere, human activities, and climate change. CACES will also provide a solid support for the carbon emission calculation in 2028 and China's targets of achieving a carbon peak by 2030 and carbon neutrality by 2060.

8 Conclusion

Currently, China has operated the second largest earth

observation satellites in the world, and its satellite observation system of meteorology, oceanography, resources, environmental disaster reduction, and surveying/ mapping has been continuously improved. In 2030, China will have around 30 Earth observation satellites in orbit, which may surpass the United States to become the world's largest. Space infrastructure development has laid the foundation for the development of space Earth Science from space. Space borne observations have been widely used in various branches of Earth science, and have played a role that fundamentally changing the way of Earth science research. With the implementation of Earth science satellite missions, China will develop and cultivate a group of international frontiers. The progress of Earth Science from Space will continue to improve our understanding of climate change and comprehensively support the sustainable economic and social development goals.

References

- [1] YANG D X, LIU Y, CAI Z, *et al.* First global carbon dioxide maps produced from TanSat measurements[J]. *Advances in Atmospheric Sciences*, 2018, **35**(6): 621-623
- [2] LIU Y, WANG J, YAO L, *et al.* The TanSat mission: preliminary global observations[J]. *Science Bulletin*, 2018, **63**(18): 1200-1207
- [3] LIU Y, WANG J, YAO L, *et al.* TanSat mission achievements: from scientific driving to preliminary observations[J]. *Chinese Journal of Space Science*, 2018, **38**(5): 627-639
- [4] YANG D, BOESCH H, LIU Y, *et al.* Toward high precision XCO₂ retrievals from tansat observations: retrieval improvement and validation against TCCON measurements[J]. *Journal of Geophysical Research: Atmospheres*, 2020, **125**(22): e2020JD032794
- [5] YANG D X, LIU Y, BOESCH H, *et al.* A new TanSat XCO₂ global product towards climate studies[J]. *Advances in Atmospheric Sciences*, 2021, **38**(1): 8-11
- [6] YANG D X, LIU Y, FENG L, *et al.* The first global carbon dioxide flux map derived from TanSat measurements[J]. *Advances in Atmospheric Sciences*, 2021, **38**(9): 1433-1443
- [7] WANG H M, JIANG F, LIU Y, *et al.* Global terrestrial ecosystem carbon flux inferred from TanSat XCO₂ retrievals[J]. *Journal of Remote Sensing*, 2022, 2022: 9816536
- [8] DU S S, LIU L Y, LIU X J, *et al.* Retrieval of global terrestrial solar-induced chlorophyll fluorescence from TanSat satellite[J]. *Science Bulletin*, 2018, **63**(22): 1502-1512
- [9] YAO L, YANG D X, LIU Y, *et al.* A new global solar-induced chlorophyll fluorescence (SIF) data product from TanSat measurements[J]. *Advances in Atmospheric Sciences*, 2021, **38**(3): 341-345
- [10] YAO L, LIU Y, YANG D X, *et al.* Retrieval of solar-induced chlorophyll fluorescence (SIF) from satellite measurements: comparison of SIF between TanSat and OCO-2[J]. *Atmospheric Measurement Techniques*, 2022, **15**(7): 2125-2137
- [11] JIN G D, LIU K Y, LIU D C, *et al.* An advanced phase synchronization scheme for LT-1[J]. *IEEE Transactions on Geoscience and*

Remote Sensing, 2020, **58**(3): 1735-1746

- [12] LIANG D, LIU K Y, ZHANG H, et al. The processing framework and experimental verification for the noninterrupted synchronization scheme of LuTan-1[J]. *IEEE Transactions on Geoscience and Remote Sensing*, 2021, **59**(7): 5740-5750
- [13] WANG W, WANG R, ZHANG Z M, et al. First demonstration of airborne SAR with nonlinear FM chirp waveforms[J]. *IEEE Geoscience and Remote Sensing Letters*, 2016, **13**(2): 247-251
- [14] JIN G D, DENG Y K, WANG R, et al. An advanced nonlinear frequency modulation waveform for radar imaging with low side-lobe[J]. *IEEE Transactions on Geoscience and Remote Sensing*, 2019, **57**(8): 6155-6168
- [15] FERRARI R, WUNSCH C. Ocean circulation kinetic energy: reservoirs, sources, and sinks[J]. *Annual Review of Fluid Mechanics*, 2009, **41**: 253-282
- [16] CHEN R, FLIERL G R, WUNSCH C. A description of local and nonlocal eddy-mean flow interaction in a global eddy-permitting state estimate[J]. *Journal of Physical Oceanography*, 2014, **44**(9): 2336-2352
- [17] NAKAMURA H, SAMPE T, GOTO A, et al. On the importance of midlatitude oceanic frontal zones for the mean state and dominant variability in the tropospheric circulation[J]. *Geophysical Research Letters*, 2008, **35**(15): L15709
- [18] SU Z, WANG J B, KLEIN P, et al. Ocean submesoscales as a key component of the global heat budget[J]. *Nature Communications*, 2018, **9**(1): 775
- [19] BOCCALETTI G, FERRARI R, ADCROFT A, et al. The vertical structure of ocean heat transport[J]. *Geophysical Research Letters*, 2005, **32**(10): L10603
- [20] LEGECKIS R, BROWN C W, BONJEAN F, et al. The influence of tropical instability waves on phytoplankton blooms in the wake of the Marquesas Islands during 1998 and on the currents observed during the drift of the Kon-Tiki in 1947[J]. *Geophysical Research Letters*, 2004, **31**(23): L23307
- [21] YODER J A, DONEY S C, SIEGEL D A, et al. Study of marine ecosystems and biogeochemistry now and in the future: examples of the unique contributions from space[J]. *Oceanography*, 2010, **23**(4): 104-117
- [22] DOHAN K, MAXIMENKO N. Monitoring ocean currents with satellite sensors[J]. *Oceanography*, 2010, **23**(4): 94-103
- [23] DOHAN K. Ocean surface currents from satellite data[J]. *Journal of Geophysical Research: Oceans*, 2017, **122**(4): 2647-2651
- [24] LEE T, HAKKINEN S, KELLY K, et al. Satellite observations of ocean circulation changes associated with climate variability[J]. *Oceanography*, 2010, **23**(4): 70-81
- [25] TALLEY L D, PICKARD G L, EMERY W J, et al. Descriptive Physical Oceanography: An Introduction[M]. 6th ed. Boston: Academic Press, 2011
- [26] GORDON C, COOPER C, SENIOR C A, et al. The simulation of SST, sea ice extents and ocean heat transports in a version of the Hadley Centre coupled model without flux adjustments[J]. *Climate Dynamics*, 2000, **16**(2/3): 147-168
- [27] YU L S. A global relationship between the ocean water cycle and near-surface salinity[J]. *Journal of Geophysical Research: Oceans*, 2011, **116**(C10): C10025
- [28] YU L S, WELLER R A. Objectively analyzed air-sea heat fluxes for the global ice-free oceans (1981-2005)[J]. *Bulletin of the American Meteorological Society*, 2007, **88**(4): 527-540
- [29] LETSCHER R T, PRIMEAU F, MOORE J K. Nutrient budgets in the subtropical ocean gyres dominated by lateral transport[J]. *Nature Geoscience*, 2016, **9**(11): 815-819
- [30] MAES C, GRIMA N, BLANKE B, et al. A surface "superconvergence" pathway connecting the South Indian Ocean to the subtropical South Pacific gyre[J]. *Geophysical Research Letters*, 2018, **45**(4): 1915-1922
- [31] VAN SEBILLE E, GRIFFIES S M, ABERNATHEY R, et al. Lagrangian ocean analysis: fundamentals and practices[J]. *Ocean Modelling*, 2018, **121**: 49-75
- [32] CHELTON D B, SCHLAX M G, SAMELSON R M. Global observations of nonlinear mesoscale eddies[J]. *Progress in Oceanography*, 2011, **91**(2): 167-216
- [33] QIU B, CHEN S M, KLEIN P, et al. Reconstructing upper-ocean vertical velocity field from sea surface height in the presence of unbalanced motion[J]. *Journal of Physical Oceanography*, 2020, **50**(1): 55-79
- [34] FREEMAN A, ZLOTNICKI V, LIU T, et al. Ocean measurements from space in 2025[J]. *Oceanography*, 2010, **23**(4): 144-161
- [35] GIROTTO M, RODELL M. Terrestrial water storage[M]/MAGGIONI Y, MASSARI C. Extreme Hydroclimatic Events and Multivariate Hazards in A Changing Environment: A Remote Sensing Approach. Amsterdam: Elsevier, 2019: 41-64
- [36] SMITH E A, ASRAR G, FURUHAMA Y, et al. International global precipitation measurement (GPM) program and mission: an overview[M]/LEVIZZANI V, BAUER P, TURK F J. Measuring Precipitation from Space: EURAINSAT and the Future. Dordrecht: Springer, 2007: 611-653
- [37] KERR Y H, WALDTEUFEL P, WIGNERON J P, et al. The SMOS mission: new tool for monitoring key elements of the global water cycle[J]. *Proceedings of the IEEE*, 2010, **98**(5): 666-687
- [38] ENTEKHABI D, NJOKU E G, O'NEILL P E, et al. The soil moisture active passive (SMAP) mission[J]. *Proceedings of the IEEE*, 2010, **98**(5): 704-716
- [39] WENG F Z, YANG H, ZOU X L. On convertibility from antenna to sensor brightness temperature for ATMS[J]. *IEEE Geoscience and Remote Sensing Letters*, 2013, **10**(4): 771-775
- [40] TAPLEY B D, BETTADPUR S, RIES J C, et al. GRACE measurements of mass variability in the Earth system[J]. *Science*, 2004, **305**(5683): 503-505
- [41] BIANCAMARIA S, LETTENMAIER D P, PAVELSKY T M. The SWOT mission and its capabilities for land hydrology[M]/CAZENAVE A, CHAMPOLLION N, BENVENISTE J, et al. Remote Sensing and Water Resources. Cham: Springer, 2016: 117-147
- [42] ZHAO T J, SHI J C, LV L Q, et al. Soil moisture experiment in the Luan River supporting new satellite mission opportunities[J]. *Remote Sensing of Environment*, 2020, **240**: 111680
- [43] SUN Yanlong, ZHAO Tianjie, LI Enchen, et al. Radiometer calibration of airborne L-band active and passive microwave detector[J]. *National Remote Sensing Bulletin*, 2021, **25**(4): 918-928
- [44] GUO P, ZHAO T J, SHI J C, et al. Assessing the active-passive approach at variant incidence angles for microwave brightness temperature downscaling[J]. *International Journal of Digital Earth*, 2021, **14**(10): 1273-1293
- [45] ZHAO T J, HU L, SHI J C, et al. Soil moisture retrievals using L-band radiometry from variable angular ground-based and airborne observations[J]. *Remote Sensing of Environment*, 2020, **248**: 111958
- [46] ZHAO T J, SHI J C, ENTEKHABI D, et al. Retrievals of soil moisture and vegetation optical depth using a multi-channel collaborative algorithm[J]. *Remote Sensing of Environment*, 2021, **257**: 112321

Progress of Fengyun Meteorological Satellites Since 2020*

ZHANG Peng, XU Zhe, GUAN Min, XIE Lizi, XIAN Di, LIU Chang

Key Laboratory of Radiometric Calibration and Validation for Environmental Satellites, Beijing 100081
National Satellite Meteorological Center (National Center for Space Weather), Beijing 100081
Innovation Center for Fengyun Meteorological Satellite (FYSIC) China Meteorological Administration, Beijing 100081

Abstract

China's efforts to develop Fengyun meteorological satellites have made major strides over the past 50 years, with the polar and geostationary meteorological satellite series achieving continuously stable operation to persistently provide data and product services globally. By the end of 2021, 19 Chinese self-developed Fengyun meteorological satellites have been launched successfully. Seven of them are in operation at present, the data and products are widely applied to weather analysis, numerical weather forecasting and climate prediction, as well as environment and disaster monitoring. Since the last COSPAR report, FY-4B, the first new-generation operational geostationary satellite, and FY-3E, the first early-morning orbit satellite in China's polar-orbiting meteorological satellite family have been launched in 2021. The characteristics of the two latest satellites and the instruments onboard are addressed in this report. The status of current Fengyun Satellites, product and data service and international cooperation and supporting activities has been introduced as well.

Key words

Fengyun meteorological satellite, Early morning orbit, Product and data service, International co-operation and supporting

1 Introduction

After half a century's development, China has become one of the few countries that maintain both polar and geostationary meteorological satellites operationally in the world. Currently, there are 7 Fengyun Meteorological Satellites in orbit, include 3 polar-orbit satellites and 4 geostationary satellites. Fig. 1 shows the present operational Fengyun satellites in space^[1,2].

In 2021, two satellites have been added to Fengyun

Meteorological Satellites family. FY-4B, the first operational geostationary satellite in FY-4 series, was launched on 3 June 2021, and positioned over the equator at 133° east longitude on 12 April 2022. FY-3E, which is the world's first early-morning-orbit meteorological satellite for civil use was launched successfully on 5 July 2021^[3]. FY-3B was out of service in 2021 after more than ten years' service. The details of them will be introduced in Chapter 2.

The status of current Fengyun polar orbiting or Low

* Supported by the National Key Research and Development Program of China (2018YFB0504900, 2018YFB0504905) and the National Project on Fengyun Meteorological Satellite Development

Received May 27, 2022

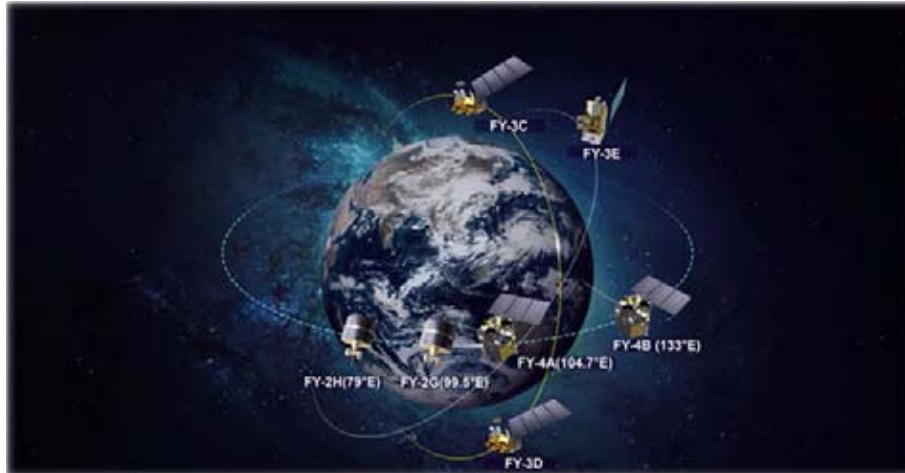


Fig. 1 Operating Fengyun satellites in space

Earth Observation (FY-LEO), and Fengyun Geostationary (FY-GEO) meteorological satellites are updated in Chapter 3. The data service performance and international cooperation activities of Fengyun satellites will be introduced in Chapter 4 and Chapter 5.

2 Update on Fengyun Satellite Program

2.1 FY-3E

FY-3E, which is the first early-morning orbit satellite in China’s polar-orbiting meteorological satellite family, was launched on 5 July 2021. It is the first satellite of the third batch of Chinese second-generation polar-orbiting meteorological satellite series FY-3, and it is also the world’s first civilian early-morning orbiting meteorological satellite. The design life of FY-3E is 8 years. It is equipped with 11 sets of remote sensing instruments (Table 1), including: MERSI (medium-resolution spectral imager), HIRAS (hyper-spectral infrared atmospheric sounder), MWTS (Micro-Wave Temperature Sounder), MWHS (Micro-Wave Humidity Sounder), GNOS (GNSS Occultation Sounder), WindRad (Wind radar), SIM (Solar Irradiance Monitor), SSIM (Solar Spectral Irradiance Monitor), XEUVI (Solar X-ray and Extreme Ultraviolet Imager), IPM (Triple-angle Ionospheric PhotoMeter), and SEM (Space Environment Monitor), among which WindRad, SSIM and XEUVI are new instruments, the MWHS is an inherited payload, and the performances of 7 instruments including HIRAS have been improved^[4].

Table 1 Instruments onboard FY-3E

No.	Instruments	Statuses
1	Dual-frequency wind radar (WindRAD)	new
2	Solar spectral irradiance monitor (SSIM)	
3	Solar X-EUV Imagers (XEUVI)	
4	MERSI-L	
5	MWTS-III	
6	HIRAS-II	
7	GNOS-II	improved
8	SIM-II	
9	SEM	
10	Tri-IPM	
11	MWHS-II	inherited

There are 4 capacities in the FY-3E series, including: High-precision optical and microwave combined atmospheric temperature and humidity sounding capability; Active microwave wind field accurate remote sensing capability; High-efficiency global optical imaging capability in the low light condition with 250 m spatial resolution; Comprehensive detection capability of the sun and space environment.

With the global imaging and atmospheric sounding observation on the polar-orbiting meteorological satellites, the FY-3E focuses to meet the requirement of numerical weather forecasting as the first priority. And FY-3E has unique advantages in weather forecasting, meteorological disaster warning, climate monitoring, as well as solar and space weather observation in the early-morning orbit. After FY-3E was successfully launched and operated in orbit, it has been completed to construct the three orbital polar constellation of Fen-

gyun, *i.e.*, early-morning, mid-morning and afternoon orbits. The global observation frequency of FY-3 can reach every 4 hours. The number of instruments assimilated in the national NWP model GRAPES has increased from 11 to 18, the amount of assimilated FY-3 satellite data has increased by 50%, and the forecast period has been extended by about 12 hours.

2.2 FY-4B

FY-4B, which is the first operational geostationary satellite in FY-4 series, was successfully launched from the Xichang Satellite Launch Center at 00:17 LT on 3 June 2021, and was successfully positioned over the equator at 123.5° east longitude at 17:07 LT on 10 June 2021, repositioned to the equator at 133° east longitude on 12 April 2022. There are 4 instruments on the FY-4B (Table 2), Advanced Geostationary Radiation Imager (AGRI), Geostationary Interferometric Infrared Sounder (GIIRS), Geostationary High Speed Imager (GHI), and Space Environment Package (SEP)^[5].

Table 2 Instruments onboard FY-4B

No.	Instruments	Statuses
1	Advanced Geostationary Radiation Imager (AGRI)	inherited
2	Geostationary Interferometric Infrared Sounder (GIIRS)	inherited
3	Geostationary High Speed Imager (GHI)	new
4	Space Environment Package (SEP)	inherited

The main observation capabilities are similar to those of FY-4A, with significant improvement in the on-orbit performances. The main application objectives of FY-4B are: to monitor high-impacted weather systems such as typhoons and strong convection, and provide services for meteorological and disaster prediction; to obtain regional atmospheric temperature and humidity profiles through high-frequency monitoring of the atmosphere and clouds; to monitor Earth radiation, ice and snow cover, sea surface temperature, aerosol and ozone, *etc.*, and provide services for short-term climate prediction and climate change prediction; to provide information services for ecological and environmental monitoring through real-time monitoring of floods, high temperatures, cold waves, droughts, snow cover, vegetation, and sandstorms; to obtain space weather monitoring data and apply it to space weather forecasting to ensure satellite security, communication, navigation and space activities; to generate various atmospheric physical parameters and products to provide services for ecological

environment, transportation, agriculture, forestry, ocean, energy and other industries, as well as national emergency and national defense security.

3 Status of Current Fengyun Satellites

At present, FY-3 LEO (Low Earth observation) meteorological satellites have realized early-morning, morning and afternoon three orbital observations to obtain global data four times a day. The operational LEO satellites in orbit contain FY-3C since 2013, FY-3D since 2017 and FY-3E since 2021.

FY-2 and FY-4 geostationary meteorological satellites are positioned over the Equator and can carry out continuous minute-scale high frequency observation of the fixed area covering one third of the Earth. The operational GEO (Geostationary) satellites in orbit contain FY-2G, FY-2H, FY-4A and FY-4B.

Among them, FY-4B and FY-3E have completed the on-orbit commission testing, and are scheduled for operational service in June 2022.

3.1 Status of Current LEO

FY-3B stopped operation on 9 December 2021. There are two LEO satellites for operational use by 1 May 2022, which are FY-3C and FY-3D. FY-3C is in partial operation with 5 payloads. FY-3D is in normal operations with 9 payloads^[6]. Satellites and payloads information are shown in Table 3.

Information about the main instruments carried on Fengyun LEO satellite.

VIRR (Visible and Infra-Red Radiometer), flying on FY-3A/B/C, 10-channel VIS/IR radiometer for multi-purpose imagery, resolution 1.1 km, swath 2800 km.

MERSI (Medium Resolution Spectral Imager), flying on FY-3A/B/C, 20-channel radiometer (19 in VIS/NIR/SWIR and one in TIR at 10.0–12.5 μm) for ocean color and vegetation indexes. Resolution 250 m for 4 VIS/NIR and one TIR channel, 1 km for other channels; swath 2800 km. Since FY-3D, the MERSI is evolved to MERSI-2, which has 25 channels (19 in VIS/NIR/SWIR and 6 in TIR from 3.7–12.5 μm).

MWRI (Micro-Wave Radiation Imager), flying on FY-3A/B/C/D, 5-frequencies/10 channels (all frequencies in double polarization) for multi-purpose MW imagery. Conical-scanning radiometer, resolution 9.5 km×15 km at

Table 3 Current Fengyun LEO satellites (as of 1 May 2022)

Orbit type (Local time of descending node/ascending node)	Satellites currently in orbit	Equatorial crossing time (design specifications)	Equatorial crossing time (present)	Launch date	Status	Main instruments
Morning orbit (07:00–12:00 LT)/ (19:00–24:00 LT)	FY-3C	10:00 LT	07:39 LT	23 Sept. 2013	Primary operation	VIRR (O) MERSI (S) IRAS (S) MWRI (S) MWTS-2 (S) MWHS-2 (O) TOU (O) SIM (S) ERM (O) GNOS (O) SEM (S)
Afternoon orbit (12:00–17:00 LT)/ (00:00–05:00 LT)	FY-3D	14:00 LT	13:45 LT	15 Nov. 2017	Primary operation	MERSI-II (O) HIRAS (O) MWTS-II (O) MWHS-II (O) MWRI (O) GAS (T) GNOS (O) WAI (O) IPM (O) SEM (O)

Note (O) means the instruments working operationally, (T) means the instruments are working for testing, (S) means the instruments are shut down.

90 GHz, 30 km×50 km at 19 GHz, swath 1400 km.

IRAS (Infra-Red Atmospheric Sounder), flying on FY-3A/B/C, 26-channel IR radiometer (including one VIS) for temperature/humidity sounding, resolution 17 km, swathe 2250 km.

MWTS (Micro-Wave Temperature Sounder), flying on FY-3A/B, 4-channel MW radiometer for nearly-all-weather temperature sounding, 54 GHz band, resolution 70 km, cross-track scanning, swath 2200 km.

MWTS-2 (Micro-Wave Temperature Sounder), flying on FY-3C/D, 13-channel MW radiometer for nearly-all-weather temperature sounding, 54 GHz band, resolution 70 km, cross-track scanning, swath 2200 km.

MWHS (Micro-Wave Humidity Sounder), flying on FY-3A/B, 4-frequency/5-channel (one frequency in double polarization) MW radiometer for nearly-all-weather humidity sounding. 183 GHz band, resolution 15 km, cross-track scanning, swath 2700 km.

MWHS-2 (Micro-Wave Humidity Sounder), flying on FY-3C/D, 15-channel MW radiometer for nearly-all-weather humidity sounding. 183 GHz band, resolution 15 km, cross-track scanning, swath 2700 km.

TOU/SBUS (Total Ozone Unit and Solar Backscatter Ultraviolet Sounder), flying on FY-3A/B/C, a suite of two UV spectro-radiometers, one (TOU) with 6 channels

in the 308–360 nm range, resolution 50 km, swath 3000 km, for total ozone; the other one (SBUS) with 12 channels in the range 252–340 nm, resolution 200 km, nadir viewing, for ozone profile.

ERM (Earth Radiation Measurement), flying on FY-3A/B/C, 2 broad-band channels radiometer for Earth reflected solar flux and Earth emitted thermal flux over total (0.2–50 μm) and short (0.2–4.3 μm) waveband; resolution 28 km, cross-track scanning with 2° NFOV, swath 2300 km, nadir viewing with 120° WFOV.

SIM (Solar Irradiance Monitor), flying on FY-3A/B/C, 3-channel radiometer over 0.2–50 μm waveband for the total incident solar flux; viewing the Sun near the north pole area.

GNOS (GNSS Occultation Sounder), flying on FY-3C/D, receives the signal from GPS or China Beidou satellites; observing over 1000 occultation events per day.

GAS (Greenhouse gases Absorption Spectrometer), flying on FY-3D, has four narrow bands with center wavelength located at 0.76 μm, 1.6 μm, 2.1 μm and 2.3 μm, which observes infrared light reflected from the Earth's surface and the atmosphere. Column abundances of CO₂ and CH₄ are calculated from the observational data.

SEM (Space Environment Monitor), flying on FY-

3A/B/C/D, for in-situ observation of charged particles in the proximity of satellite.

WAI (Wide-field Auroral Imager), flying on FY-3D, for remote sensing imaging the N₂ Lyman-Birge-Hopfield (LBH) auroral bands.

IPM (Ionospheric PhotoMeter), flying on FY-3D, for nadir remote sensing the airglow intensity of the OI 135.6 nm and N₂ Lyman-Birge-Hopfield (LBH) bands.

HIRAS-1 (Hyperspectral Infrared Atmospheric Sounder-I), flying on FY-3D, 1370 channels, for temperature/humidity sounding, spatial resolution 16 km.

3.2 Status of Current GEO

There are three GEO satellites for operational use by 1 May 2022, which are FY-2G, FY-2H, and FY-4A. Satellites and payloads information are shown in Table 4. As planned, FY-2F stopped service on 1 April 2022.

The information about the main instruments carried on Fengyun GEO satellites^[7] is listed as follows.

VISSR (Visible and Infrared Spin Scan Radiometer): The version for FY-2A/B had three VIS/IR channels (0.55–1.05 μm, 6.2–7.6 μm, and 10.5–12.5 μm), the improved version for FY-2C/D/E/F/G/H splits the IR channels into two and adds a 3.5–4.0 μm channels. The spatial-resolution is slightly improved from 5.76 km (IR) and 1.44 km (VIS), to 5.0 km (IR) and 1.25 (VIS). The image cycle is 30 min.

SEM (Space Environment Monitor): A space particle monitor and an X-ray monitor are mounted on FY-2 to detect the space environment in the proximity of the satellite, the solar activities, and relevant space phenomena. The SEM data is transmitted *via* telemetry to the ground system.

AGRI (Advanced Geosynchronous Radiation Imager): to fly on FY-4A, multispectral imager with two independent mirrors scanning in north-south and east-west directions respectively; 216 sensors in 14 bands from

visible to long-wave infrared (0.45–13.8 μm); on-board calibration for all bands, full optic length of radiation considered in calibration. Spatial resolutions: 1 channel in 1 km, 2 channels in 500 m, 4 channels in 2 km, 8 channels in 4 km. Sensitivity: S/N 90–200, $NE \Delta T$ 0.2–0.7 K at 300 K. Full-disk scanning time: 15 min.

GIIRS (Geo. Interferometric Infrared Sounder): to fly on FY-4A, two independent mirrors scanning in north-south and east-west directions respectively; 32×4 plane arrays for mid-wave (375 S/MIR channels) and long-wave infrared bands (538 LWIR channels). Spatial resolution 16 km; active and radiant coolers; radiometric calibration accuracy 1.5 K. Temporal resolution: mesoscale area 35 min (1000 km×1000 km); China area 67 min (5000 km×5000 km).

LMI (Lightning Mapping Imager): to fly on FY-4A, two tubes for observation to achieve more spatial coverage. Central wave-length 777.4 nm; sensitivity $S/N \geq 6$; spatial resolution 7.8 km; temporal resolution 2 ms.

SEP (Space Environment Package): to fly on FY-4A, a suite that contains a magnetometer for magnetic field vector, an energetic particle detector detecting high-energy electron storms (1–165 MeV, and >165 MeV) and proton events (0.4–4 MeV), and space weather effect detectors for the impact of space weather on the spacecraft.

4 Product and Data Service

4.1 Data Resources

NSMC Data Service Center is responsible for Fengyun series satellite data management and long-term storage. NSMC is also one of three national satellite data centers as the Atmospheric Remote Sensing Satellite Data Center. By the end of 2021, NSMC has stored data volume

Table 4 Current Fengyun GEO satellites (as of 1 May 2022)

Satellites currently in orbit	Location	Launch date	Status	Main instruments
FY-2G	99.5°E	31 Dec. 2014	Primary operation for full disk scan	VISSR (O) SEM (O)
FY-4A	104.7°E	11 Dec. 2016	Primary operation for full disk scan	AGRI (O) GIIRS (O) LMI (O) SEP (O)
FY-2H	79°E	5 Jun. 2018	Primary operation for full disk scan since 1 Jan. 2019	VISSR (O) SEM (O)

Note (O) means the instruments working operationally, and (S) means the instruments are shut down.

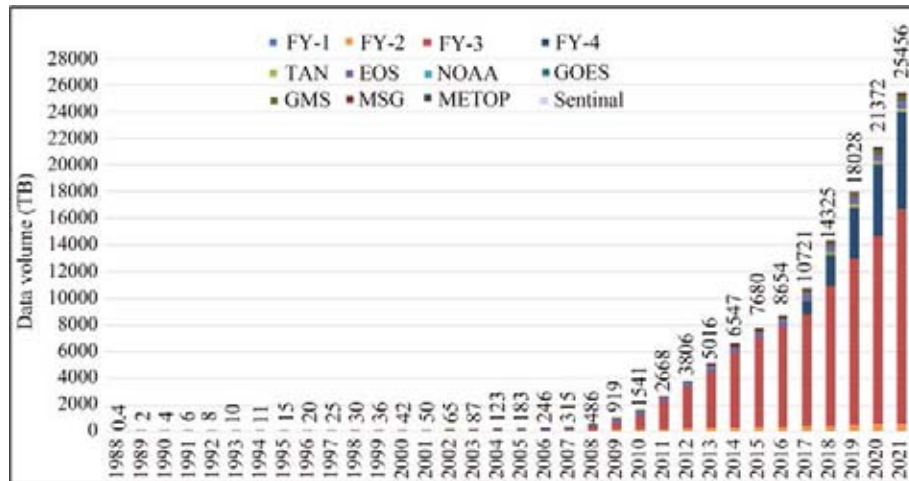


Fig. 2 Cumulative annual archive data volume in NSMC

up to near 25PB from 50 satellites, 92% of the archive is Fengyun series satellite data. The cumulative annual archive data volume from 1988 to 2021 in NSMC are shown in Fig. 2. Data and products specification and details can be found on NSMC web portal (<http://www.nsmc.org.cn>).

4.2 Data Service

Fengyun Meteorological Satellites data are shared globally in real-time and open to global users. There exist several ways for global community to get Fengyun meteorological satellite data. Direct broadcasting users can directly receive real-time data with appropriate receiving antenna and pre-processing software package. The CMACast users can receive data and product with DVB-S equipment near real-time. The full Fengyun meteorological satellite dataset, both real-time and historical data are available on NSMC satellite data service website in Chinese and English version (<http://data.nsmc.org.cn>). Users can search and download data after registration^[8].

By the end of 2021, more than 120 thousand users registered at NSMC satellite data service website. Near 9PB satellite data have been delivered to the domestic and international users in 2021. NSMC satellite data service website has processed near 140 thousand orders and retrieved 501 TB satellite data for users.

World Meteorological Organization (WMO) released a publication “RA II and RA V Survey on the Use of Satellite Data” in 2020. The purpose of the survey is to collect up-to-date information on WMO Members’ ca-

pabilities and needs regarding the use of satellite data in meteorological, climate, water and related environmental applications. Fig. 3 shows a survey result for general-purpose polar-orbiting satellite products, including the well-known and widely used Fengyun Satellite Data Center^[9].

5 International Co-operation and Supporting

5.1 International and Regional Cooperation

Fengyun meteorological satellites play important roles in the global space programs of World Meteorological Organization (WMO). NSMC keeps close cooperation with WMO, CGMS, CEOS, GEO, APSCO and other international organizations and EUMETSAT, NOAA and other satellite providers on instrument development, remote sensing application, data exchange and applications related to weather monitoring and forecasting. From 1 to 5 November 2021, the 11th Asia-Oceania Meteorological Satellite User Conference (AOMSUC-11) hosted by the China Meteorological Administration (CMA) was held in Beijing *via* the internet. In order to further strengthen exchanges and cooperation with international users of Fengyun Meteorological Satellites in remote sensing applications, improve the international service capabilities of Fengyun Meteorological Satellites, and also to further promote the sharing and application of Fengyun Meteorological Satellites in countries and regions along the “Belt and Road”, The 2021 Fengyun Meteorological Satellite International

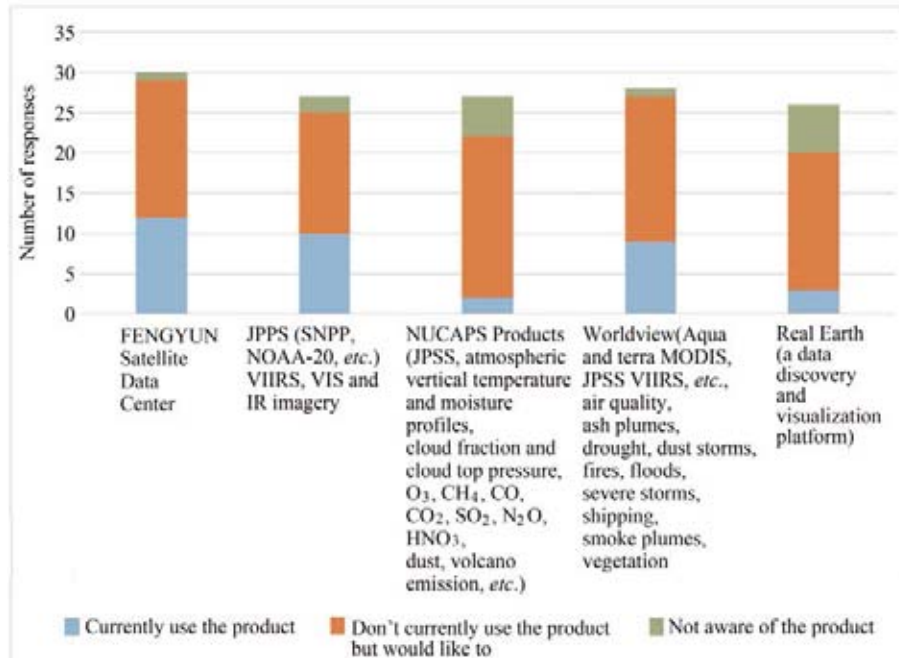


Fig. 3 WMO Survey Result: General-purpose polar-orbiting satellite products

User Conference (FYSUC-2021) co-hosted by CMA and CNSA was held concurrently with AOMSUC-11. This conference attracted representatives from more than 50 countries, regions and international organizations, with a total of 80 oral presentations and 1386 participants. The themes of the conference include the status and future development of global meteorological satellites, satellite data and products, numerical weather forecast and now weather forecasting, land-ocean-atmosphere products, space weather, climate, and the application and service of Fengyun meteorological satellites.

Meanwhile, CMA is deepening bilateral cooperation with international organizations and “Belt and Road” countries on Fengyun meteorological satellite application. Several online workshops were held to enhance remote sensing capabilities and data exchange. EUMETSAT and NSMC have built a long-term mechanism on remote sensing technologies. On 16 November 2021, China-Russia Consortium Global Space Weather Center (CRC) was inaugurated. CRC is co-built by China Meteorological Administration (CMA), Civil Aviation Administration of China (CAAC), and the Russian Federal Service for Hydrometeorology and Environmental Monitoring (Roshydromet). It is the first global center in China’s civil aviation meteorology field that is approved by International Civil Aviation Organization (ICAO).

This center is the fourth global space weather center.

5.2 Disaster Mitigation

Since CMA introduced the Emergency Support Mechanism of Fengyun satellite (FY_ESM) in 2018, there are 29 countries registered for this mechanism. FY-3D, FY-4A and FY-2H have officially become on-duty satellites of International Charter “Space and Major Disasters”. They have already provided relevant data service and monitoring service products for countries and territories like Madagascar, Mozambique and Malawi. In recent years, as on-duty satellites of CHARTER, Fengyun satellites have played increasingly significant roles in global meteorological disaster readiness, and serving “Belt and Road” construction.

NSMC has provided 19 international emergency support services in 2021 (Table 5). The international emergency responses involve meteorological disasters such as dam break, volcanic eruption, heavy rainfall, tropical cyclone, and flood and oil spill.

5.3 “Belt and Road” Services

Several kinds of services have been implemented by NSMC to support “Belt and Road” users. NSMC has provided FY-2, FY-3 and FY-4 data for the “Belt and Road” countries and regions including Eswatini, India,

Table 5 List of Fengyun satellite international disaster support cases in 2021

No.	Date	Country	Disaster
1	28 Jan. 2021	Swaziland	Tropical cyclone and flood
2	8 Feb. 2021	India	Flash flood
3	23 Feb. 2021	Philippines	Tropical cyclone and flood
4	7 Apr. 2021	Indonesia	Flash flood
5	8 Apr. 2021	East Timor	Tropical cyclone
6	13 Apr. 2021	St Vincent	Volcano eruption
7	24 May 2021	Congo	Volcano eruption
8	7 Jun. 2021	Sri Lanka	Sea oil spill
9	7 Jun. 2021	Sri Lanka	Flash flood
10	22 Jul. 2021	Russia	Wildfire
11	29 Jul. 2021	Tunisia and Algeria	Wildfire
12	9 Aug. 2021	Russia	Flash flood
13	15 Aug. 2021	Russia	Wildfire
14	9 Sept. 2021	Republic of Togo	Flash flood
15	3 Oct. 2021	United Arab Emirates	Tropical cyclone
16	4 Oct. 2021	Oman	Tropical cyclone
17	13 Nov. 2021	Sri Lanka	Flash flood
18	7 Dec. 2021	Indonesia	Volcano eruption
19	9 Dec. 2021	Micronesia	Flash flood

Philippines, Indonesia, East Timor, Saint Vincent, Congo, Sri Lanka, Russia, Togo, Arabia, United Arab Emirates, Oman and Micronesia during 2021. The monitoring service products provided to international users include satellite remote sensing monitoring map, monitoring thematic map, change monitoring map, dynamic map, quantitative statistical data and satellite remote sensing monitoring service report. At the same time, NSMC has strengthened the construction of a remote sensing application service platform. We have completed the testing of global fire monitoring system and atmospheric environment monitoring platform, upgraded the “cloud + client” international remote sensing application platform, and had SWAP and SMART platform ready to support the newly launched FY-3E and FY-4B. The cloud data acquisition software, which also has been upgraded with 33 products in total, is providing cloud services for the new data and products of Fengyun satellites. The online version of SWAP has 94 international users in 2021.

NSMC has continued to provide technical support including CMACAST, FY-3 satellite software package, Fengyun satellite data cloud client, green channel FTP, SMART, SWAP and other Fengyun satellite remote sensing application platforms in 2021 according to the requirements of international users. FY-3 meteorological satellite software package has 55 users from 29

countries, the green channel FTP has 106 users in 42 countries, and the international users of swap platform have reached 94 countries. NSMC provided 12 technical support services for Fengyun satellite data and various application software platforms to 8 countries including Laos, Iran, Maldives, Belarus, Bangladesh, Seychelles, Papua New Guinea and Singapore, and remotely guided and assisted in remote application fault resolution of swap platform in 2021. At the meantime, NSMC has provided Fengyun satellite preprocessing software support services for Britain, Australia, Norway, Germany and Belarus for 5 times, and assisted users in upgrading FY-3 preprocessing software package, updating calibration coefficient, user login, data acquisition and processing, *etc.*

6 Summary

At present, FY-3 polar-orbiting meteorological satellites have completed the early-morning, morning and afternoon three orbital constellation observations to obtain the global observation data four times a day which have been used in a number of the global Numerical Weather Prediction (NWP) models worldwide. FY-2 and FY-4 geostationary meteorological satellites are positioned over the Equator and can carry out continuous minute-scale high frequency observations of the fixed area cov-

ering one third of the Earth. FY satellites have made a positive contribution to improving the accuracy of global weather forecasting.

FY meteorological satellite system become one of the major components in the World Meteorological Organization (WMO)'s Space-based Observing System as well as the International Charter on Space and Major Disaster. CMA will continue to implement the open sharing data policy. Global users can obtain FY meteorological satellite data through several service channels.

China plans to launch five more meteorological satellites during the country's 14th Five-Year Plan period (2021–2025) and upgrade the third generation Fengyun satellite observation system by 2035, to better serve users around the world.

References

- [1] ZHANG P, CHEN L, XIAN D, *et al.* Update on Fengyun meteorological satellite program and development[J]. *Chinese Journal of Space Science*, 2020, **40**(5): 884-897
- [2] ZHANG P, LU Q F, HU X Q, *et al.* Latest progress of the Chinese meteorological satellite program and core data processing technologies[J]. *Advances in Atmospheric Sciences*, 2019, **36**(9): 1027-1045
- [3] ZHANG P, HU X Q, LU Q F, *et al.* FY-3E: The first operational meteorological satellite mission in an early morning orbit[J]. *Advances in Atmospheric Sciences*, 2022, **39**(1): 1-8
- [4] National Satellite Meteorological Center. Fengyun3-03 User Requirement Specification[R]. Beijing: National Satellite Meteorological Center, 2015
- [5] National Satellite Meteorological Center. Fengyun4-02 Requirement Specification[R]. Beijing: National Satellite Meteorological Center, 2019
- [6] YANG Z D, ZHANG P, GU S Y, *et al.* Capability of *Fengyun-3D* satellite in Earth system observation[J]. *Journal of Meteorological Research*, 2019, **33**(6): 1113-1130
- [7] YANG J, ZHANG Z Q, WEI C Y, *et al.* Introducing the new generation of Chinese geostationary weather satellites, Fengyun-4[J]. *Bulletin of the American Meteorological Society*, 2017, **98**(8): 1636-1658
- [8] XIAN D, ZHANG P, GAO L, *et al.* Fengyun meteorological satellite products for Earth system science applications[J]. *Advances in Atmospheric Sciences*, 2021, **38**(8): 1267-1284
- [9] WMO. RA II and RA V Survey on the Use of Satellite Data[R]. Geneva: World Meteorological Organization, 2020

Current Status and Main Application Achievements of Ocean Satellites

LIN Mingsen, ZHANG Youguang

National Satellite Ocean Application Service, Beijing 10081

Abstract

Ocean satellites have realized multi-satellite networked operation. The HY-1D satellite launched in June 2020 realized networked with HY-1C satellite, and completed the construction of ocean color satellite constellation. The HY-2D satellite launched in May 2021 is networked with the on orbit HY-2B and HY-2C satellites to complete the construction of marine dynamic environment satellite constellation. The 1mC-SAR satellite 01 launched in November 2021 is networked with GF-3, which initially forms the marine monitoring satellite constellation. This year, the networking of 1mC-SAR satellite 02 with satellite 01 and GF-3 is realized, and the construction of marine monitoring satellite constellation is completed. At present, the ocean satellites have the operational application capabilities of remote sensing investigation, monitoring, evaluation and supervision of marine ecology, marine disaster prevention and reduction, global oceans and Polar Regions, Sea Islands, rights and interests maintenance.

Key words

Ocean color satellite, Ocean dynamic environment satellite, Ocean monitoring satellite, Satellite networking

1 Introduction

Since the launch of the first ocean satellite on 15 May 2002, 10 ocean satellites have been launched, including HY-1A/1B/1C/1D, HY-2A/2B/2C/2D, CFOSAT, GF-3 and C-SAR satellites. At present, HY-1A/1B have stopped working, HY-2A has degraded, and the rest of the satellites work normally in orbit, as shown in Fig. 1.

The ocean satellite has realized networking operation of multiple satellites. The HY-1D satellite launched in June 2020 realized networked with HY-1C satellite, and completed the construction of ocean color satellite constellation. The HY-2D satellite launched in May 2021 realized networked with the on orbit HY-2B and HY-2C satellites, and completed the construction of ocean dynamic environment satellite constellation. In November 2021, 1mC-SAR satellite 01 was launched to

form a network with GF-3, initially forming an ocean monitoring satellite constellation. This year, the networking of 1mC-SAR satellite 01, 02 and GF-3 was completed, and the construction of ocean monitoring satellite constellation was completed. At the same time, the quality of ocean satellite data products has also been steadily improved. Among them, the quality of sea surface height data of HY-2 series satellites has also been fully recognized by foreign scientific research institutions. After many evaluations, scientists of the CNES believe that the sea surface height data obtained by HY-2 series satellites has high precision, at the same precision level as that of satellites in Europe and America. The numerical prediction products provided by Eumetsat to users around the world are recognized as the highest quality marine and atmospheric data products, in which the initial information required for model

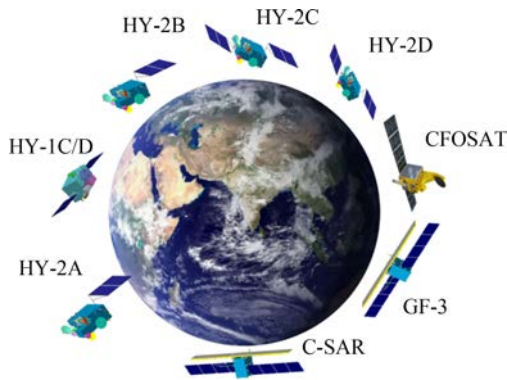


Fig. 1 Ocean satellites currently in orbit

operation is contributed by the sea surface wind field data of HY-2 series satellites^[1-3].

In addition, a new generation of polar orbit ocean dynamic environment satellite, salinity satellite, high orbit ocean and coastal zone environment monitoring satellite, a new generation of ocean color satellite and HY-2E/F satellite will be launched to further enrich and improve the ocean satellite observation system.

2 Function of on Orbit Ocean Satellite

Ocean satellites are designed according to the detection technical capabilities and characteristics of different elements, time and space resolution, coverage and monitoring frequency requirements. They are divided into three categories according to their uses, including ocean color environment, ocean dynamic environment and marine monitoring series.

HY-1 series satellites are used for ocean color, ocean temperature and coastal zone observation. HY-1A/1B are experimental satellites, equipped with ocean water color and water temperature scanner and coastal zone imager. HY-1C/1D is an operational satellite, equipped with ocean color and temperature scanner, coastal zone imager, ultraviolet imager, calibration spectrometer and ship automatic identification system. They are networked for land and sea observations in the morning and afternoon sectors. The payloads have the advantages of multiple spatial resolution, high signal-to-noise ratio, high dynamic range and wide swath.

HY-2 series satellites are used to monitor various marine dynamic environmental parameters such as all-weather global sea surface wind field, wave height,

sea surface height and sea surface temperature, directly provide measured data for early warning and prediction of disastrous sea conditions, and provide support services for marine disaster prevention and reduction, maintenance of marine rights and interests, development of marine resources, marine environmental protection, marine scientific research and national defense. The payloads are radar altimeter, microwave scatterometer, microwave radiometer, dual frequency global positioning system, ship automatic identification system, data collection system, two-way data communication, *etc.* HY-2A is the experimental satellite, and HY-2B/2C/2D have realized operational networked observation.

Marine Surveillance and monitoring series satellites are used for all-weather monitoring of the global marine and land information. The payload is a C-band multipolar synthetic aperture radar. They are used in many fields such as marine, disaster reduction, water conservancy and meteorology. They are an important technical support for China's implementation of marine development, land environmental resources monitoring and emergency disaster prevention and reduction. The experimental satellite is GF-3 satellite, one follow-up satellite, 1m C-SAR-02, to be networked with GF-3 and 1m C-SAR-01 satellite, will be launched in 2022.

International cooperative experimental satellite: CFOSAT is a scientific research experimental satellite cooperated by China and France. China provides a scatterometer and France provides an ocean spectrometer. Its main task is to obtain global sea surface wave spectrum, sea surface wind field and polar sea ice information, and further strengthen the scientific understanding of the rules of marine dynamic environmental change; to improve the accuracy and timeliness of forecasting catastrophic sea conditions such as huge waves, marine tropical storms and storm surges; at the same time, to obtain the relevant data of polar ice sheet to provide basic information for the study of global climate change.

2.1 Satellite Payload Configuration, Orbit and Working Mode

The satellite payloads are configured according to mission requirements, detection means and constraints. The configured payloads include ocean color and temperature scanner, coastal zone imager, ultraviolet imager, calibration spectrometer, radar altimeter, microwave scatterometer, microwave radiometer, correction radi-

ometer, synthetic aperture radar, ocean spectrometer, global positioning system, ship automatic identification system, etc. The detection means cover ultraviolet, visible light, near infrared, infrared and active and passive microwave remote sensing. There are many varieties to achieve high quantitative accuracy.

The on orbit ocean satellites HY-1C/1D, HY-2B, CFOSAT and GF-3 are in solar synchronous orbits. The local time for global exploration is basically the same every day. They pass through China's sea areas in the early morning and evening. Each satellite works 24 hours a day and flies 14 or 15 times around the north and south poles every day. HY-2C/2D satellite is in Non solar synchronous orbit and is networked with HY-2B to improve the observation timeliness of marine dynamic environmental parameters.

All satellites work 24 hours, and most of the payloads have the capabilities to realize the detection of the world, north and south poles, coastal zones and islands. The coverage width of each payload is 10–3000 km, and the coverage period is 1–3 days. The coverage period of a remote sensing payload with large scanning width is short, while the coverage period of a remote sensing payload with small scanning width is long. The widest coverage is the ocean color and ocean temperature scanner, with a scanning width of 3000 km. It covers the whole world every day and night. The scatterometer has a width of 1300–1750 km, and it observes once in the morning and evening to realize the observation of the whole world once every two days.

2.2 Ocean Satellite Can Also Be Used for Large-scale Land Monitoring

Ocean satellites can not only monitor the ocean, but also obtain rich information when passing through the land. GF-3 satellite itself is a satellite for both land and sea, which can monitor water and land surface all day. HY-1C/1D satellite has large payload scanning width and short data acquisition cycle. It is designed for water body, with a large dynamic range, high signal-to-noise ratio and good radiation performance. It is also a powerful tool for a general survey of land natural resources, ecological environment, flood disaster and forest fire monitoring.

2.3 Integrated Management of Satellite Ground System, Fast Data Acquisition

The operation of ocean satellites is under the unified

responsibility of the national satellite ocean application service, which is responsible for the whole process of satellite exploration planning and control, real-time data reception of multiple ground stations, data communication transmission, standard product production, data calibration and product validation, product archiving and distribution. The multi-satellite operational production chain is complete. The integrated satellite ground operation system of the ocean satellites is becoming more and more perfect, and the operational capability of ocean satellite network is basically formed. In the process of ocean satellite processing, for the domestic detection data, the product production shall be completed within one hour after receiving the data; overseas data is processed through delayed playback, with a delay of between 2 hours and 12 hours.

3 Typical Application Results

3.1 Seas Surface Fields and Significant Wave Height Networked Observation

3.1.1 Radar Altimeter Networking

HY-2B, HY-2C and HY-2D radar altimeters have realized three-satellite networked observation, and the spatial coverage and timeliness have been synchronously improved. Fig. 2–3 show the joint observation of significant wave height and sea surface wind speed by HY-2D and its joint HY-2B and HY-2C radar altimeters during typhoon IN-FA on 24 July 2021. In the figure, it can see the local area with extreme value of wind and wave caused by typhoon in Northeast Taiwan.

3.1.2 Microwave Scatterometer Networking

The microwave scatterometer of HY-2B, HY-2C and HY-2D satellites realizes networked observation. The average observation area of each satellite is 1500 km. In typhoon observation, it has the advantage of a larger observation area than similar satellites (e.g. MetOp Series). This network can cover 80% of the globe in 6 hours, as shown in Fig. 4–7. It should be pointed out that the microwave scatterometers carried on HY-2C and HY-2D are the only non-solar synchronization satellite scatterometers in orbit in the world. which make complementary observations together with HY-2B satellite scatterometer in the polar orbit, conducive to calibration and validation.

3.2 Polar Observation

Ocean satellite is one of the effective tools for polar

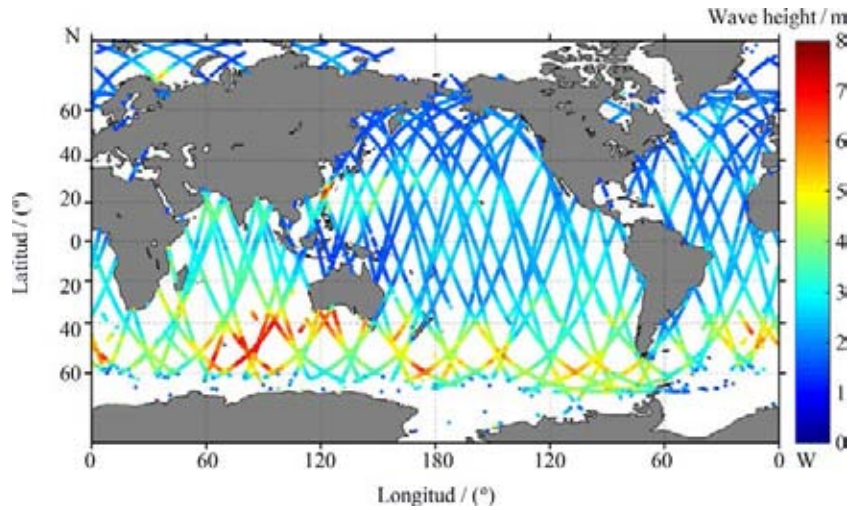


Fig. 2 Significant wave height by HY-2B, HY-2C and HY-2D altimeters on 24 July 2021

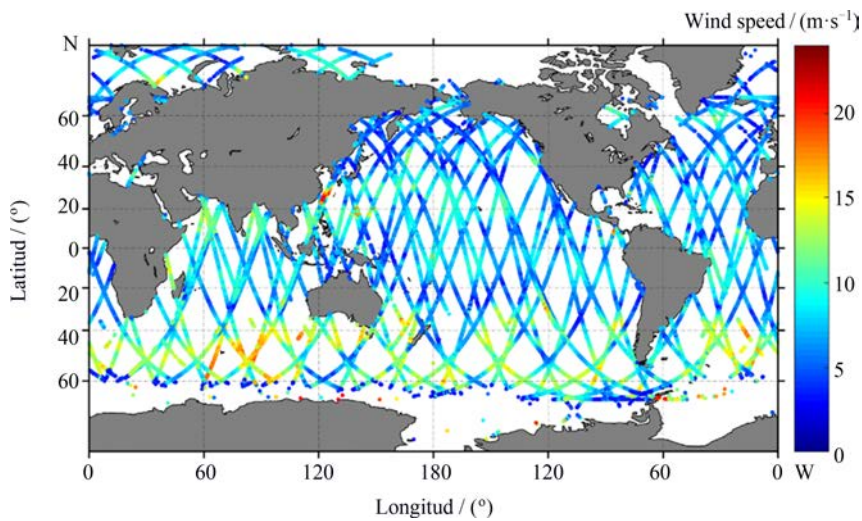


Fig. 3 Sea surface wind speed by HY-2B, HY-2C and HY-2D altimeters on 24 July 2021

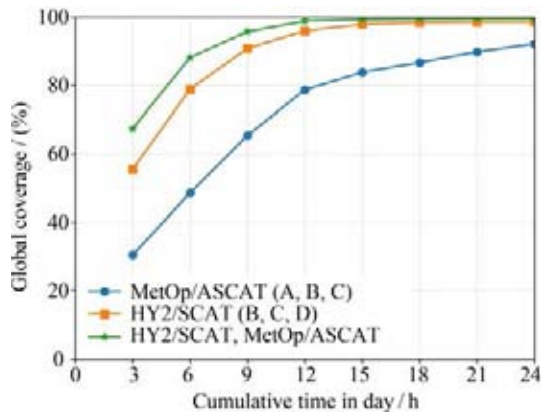


Fig. 4 Observation coverage of HY-2 satellite and MetOp satellite Scatterometer

monitoring and research. Since the launch of HY-1 C/D satellite into orbit, 13694 images with a spatial resolu-

tion of 50 m between 66.5° and 86.0° north latitude in the Arctic Circle have been obtained, each with an image size of 1000 km×360 km. Among them, HY-1C satellite has 9341 images and HY-1D satellite has 4353 images, which are used to recognize, discover and study the landform, ice sheet, glacier, sea ice, iceberg, and river. The distribution and daily, monthly and seasonal variation of characteristic parameters such as ocean color, snow cover and cloud system provide a new data source. In some areas, the annual variation characteristics of some parameters in recent three years can also be analyzed.

Measured from the obtained ocean satellite remote sensing images, the actual area of the young pioneer island is about 1535 square kilometers and the circumference is about 219 km. As can be seen from the

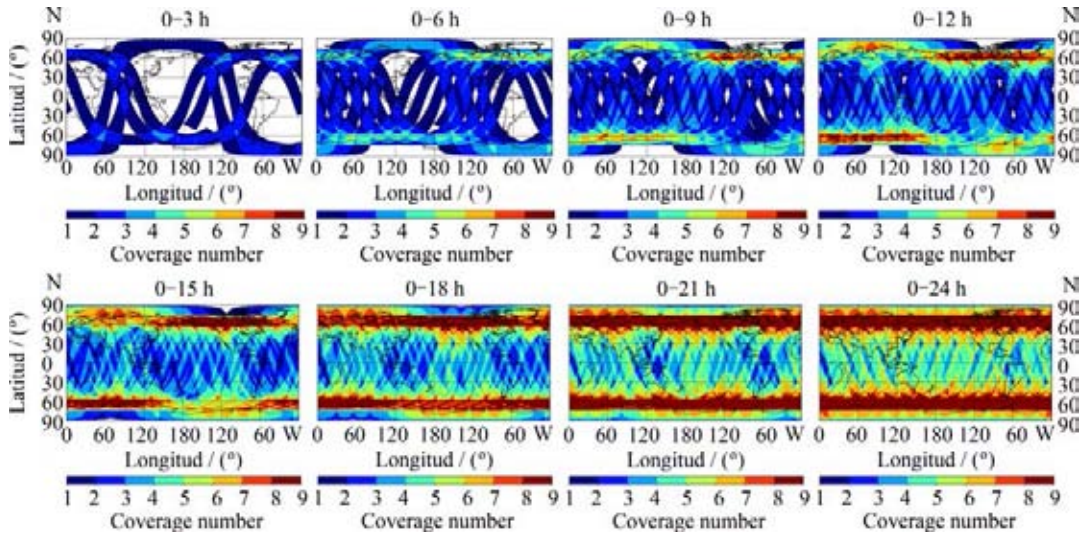


Fig. 5 observation coverage area of HY-2B/C/D scatterometer in different periods

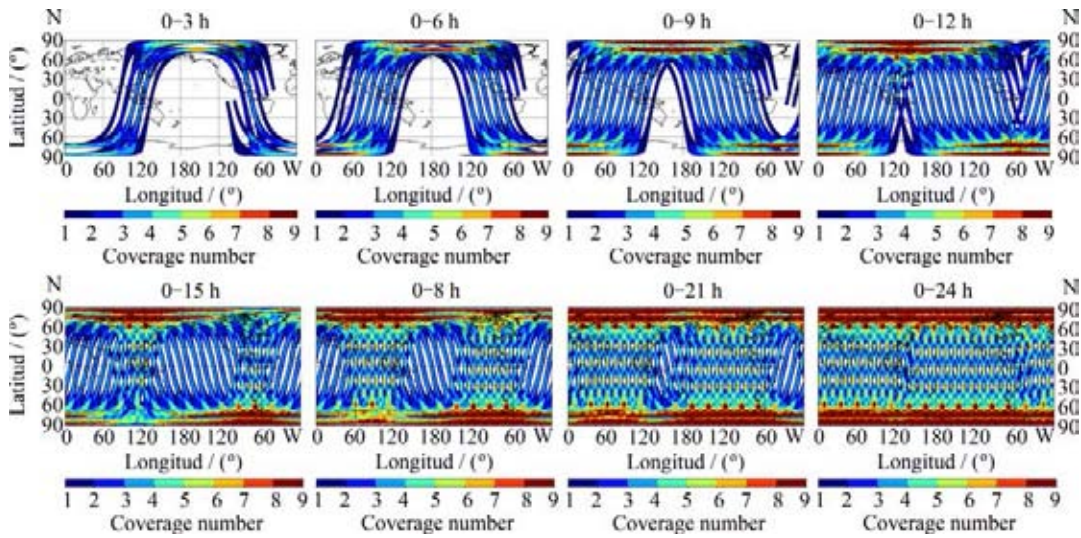


Fig. 6 Observation coverage area of MetOp ASCAT-A/B/C/scatterometer in different periods

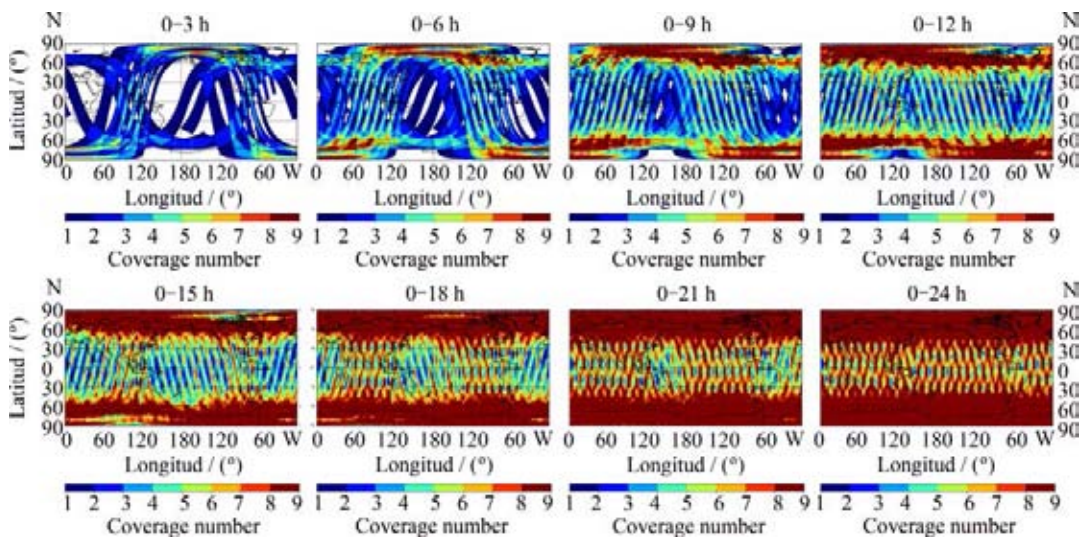


Fig. 7 Observation coverage area of HY-2B/C/D and MetOp ASCAT-A/B/C scatterometer in different periods

image on 1 August 2020 in Fig. 8, except for the glacier on the young pioneers Island, all the land ice and snow

on the island have melted, and the frozen soil layer is exposed. Its shape and color are similar to that

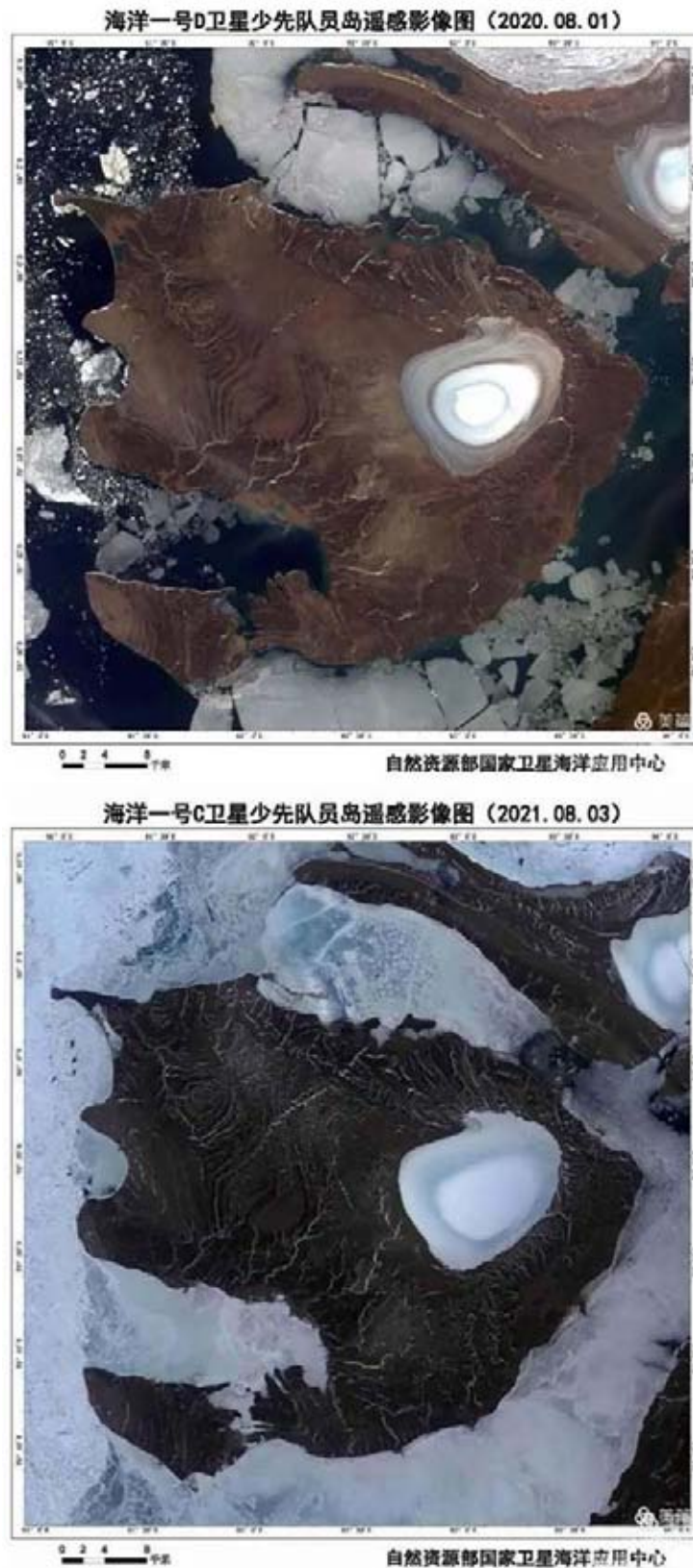


Fig. 8 Remote sensing images of young pioneer Island observed by HY-1C and HY-1D satellites

of a copper carving board inlaid with a piece of jewelry or a piece of chocolate, or a large oil cake superimposed with a fried egg. The sea ice around the young pioneers island is gradually decreasing. In mid and late August, the surrounding sea ice almost completely melted, and some land began to be covered with snow in late September. The image of April 2021 shows that the whole island is white and covered with snow. The ice cap on the island is raised. The frozen soil layer begins to appear in June, and the snow continues to decrease in July. By 3 August 2021, some ice and snow on the land will melt, but the snow area of the ice cap on the island has not decreased compared with last year.

3.3 Typhoon Observation

The visible light, near infrared, thermal infrared channels and ultraviolet channels of the HY-1C/D satellite ocean color water temperature scanner can obtain the global distribution of surface vegetation and clouds. The multi-satellite network can obtain the typhoon wind field, cloud rainfall distribution, change state, influence range and moving path many times a day. At 01:25 LT on 22 July 2021, the Typhoon In-Fa was observed by the thermal infrared channel of ocean color and water temperature scanner of HY-1D satellite, the typhoon eye is very clear, and the typhoon intensity reaches level 14 in Fig. 9.

3.4 Hurricane Observation

Ocean satellites can also observe hurricanes at high frequencies. On 29 August 2021, hurricane Ida landed in Louisiana in the southern United States, with a maximum wind speed of about $240 \text{ km}\cdot\text{h}^{-1}$. HY-2B/ 2C/2D network continuously observed the hurricane landing process and corresponding wind field information from 28th to 29th. From 28 to 29 August, HY-2B/ 2C/2D observed 8 times in total, including 3 times of HY-2B, 2 times of HY-2C and 3 times of HY-2D, as shown in Fig. 10.

3.5 Land Water Monitoring

During the period from 29 March to 31 May 2012, the HY-1C/D Satellite coastal zone imager took 42 photos of Poyang Lake area in Jiangxi Province in Fig. 11 (left). Three times were sunny on 9 April, 30 April and 1 May, with a clear sky accounting for less than 10%, and more than 90% of the time was cloudy and rainy. After being included in GF-3 satellite, two times of all-weather and all-time Synthetic Aperture Radar (SAR) data were obtained in Fig. 11 (right). HY-1C/D satellite, GF-3 satellite remote sensing thematic map and relevant data provide a strong basis for rapid response to floods.

3.6 Marine Ecological Environment Monitoring

Land-based pollution emissions, marine production and

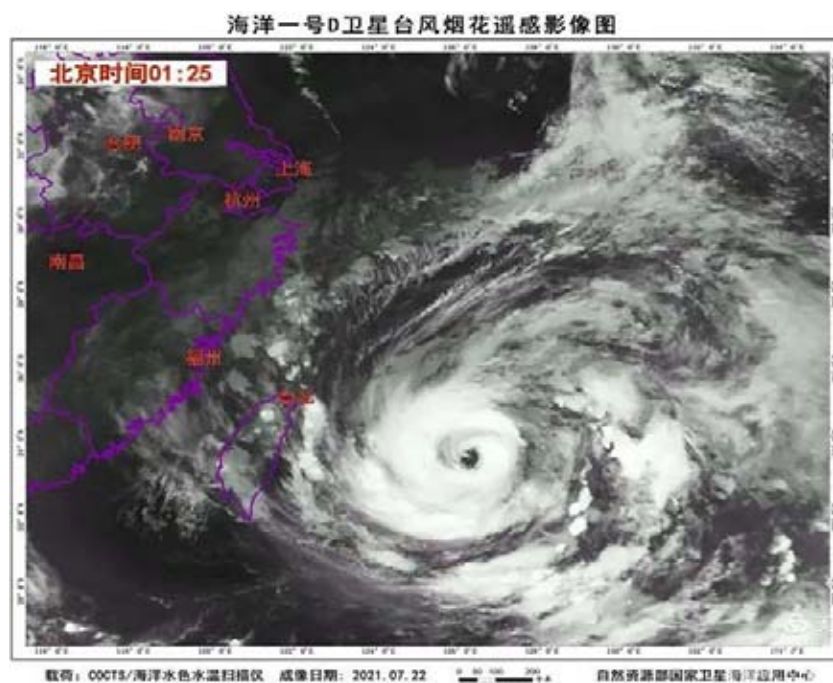


Fig. 9 Typhoon In-Fa thermal infrared cloud image of ocean color water temperature scanner

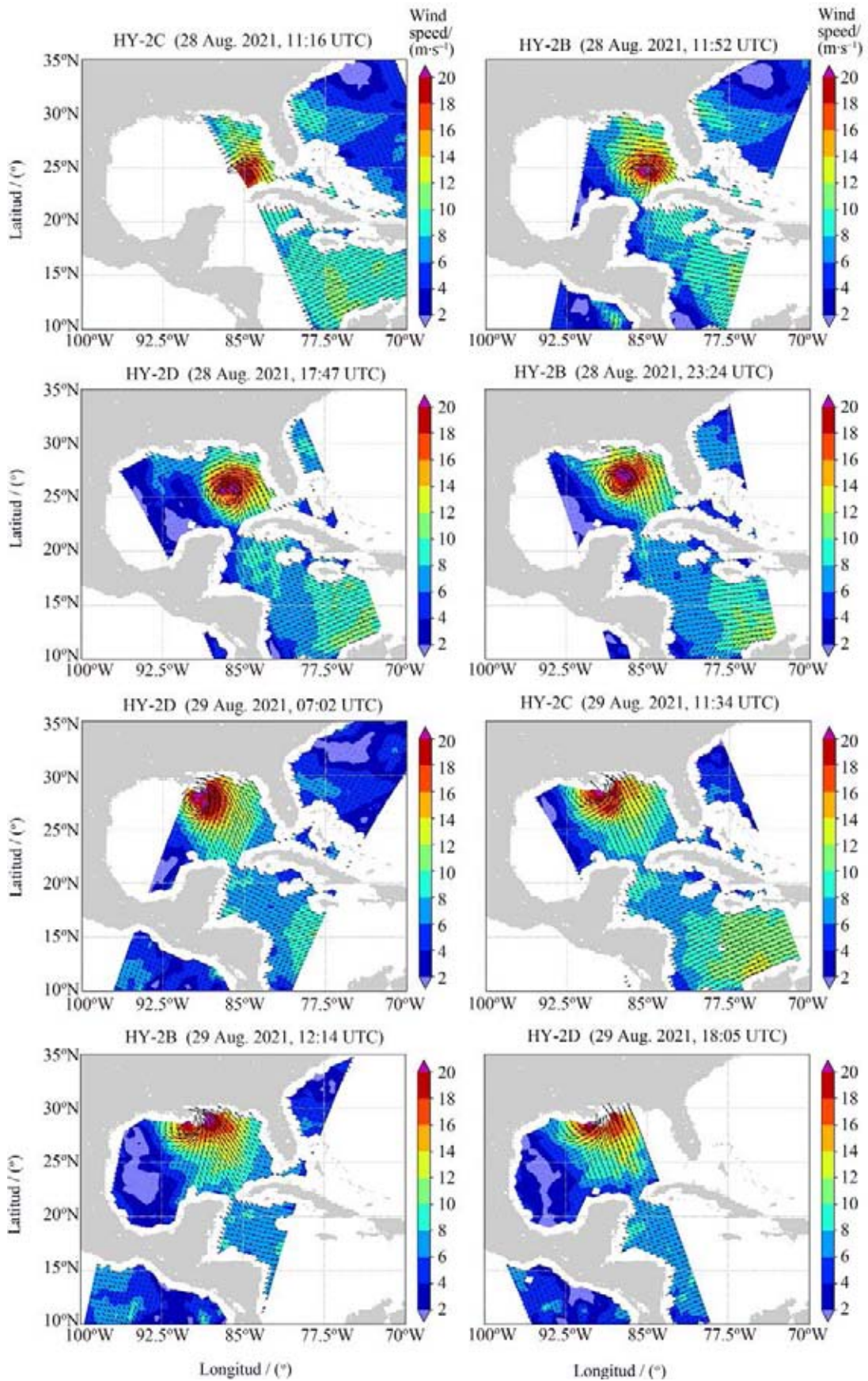


Fig. 10 HY-2B/2C/2D joint observation of Hurricane Ida

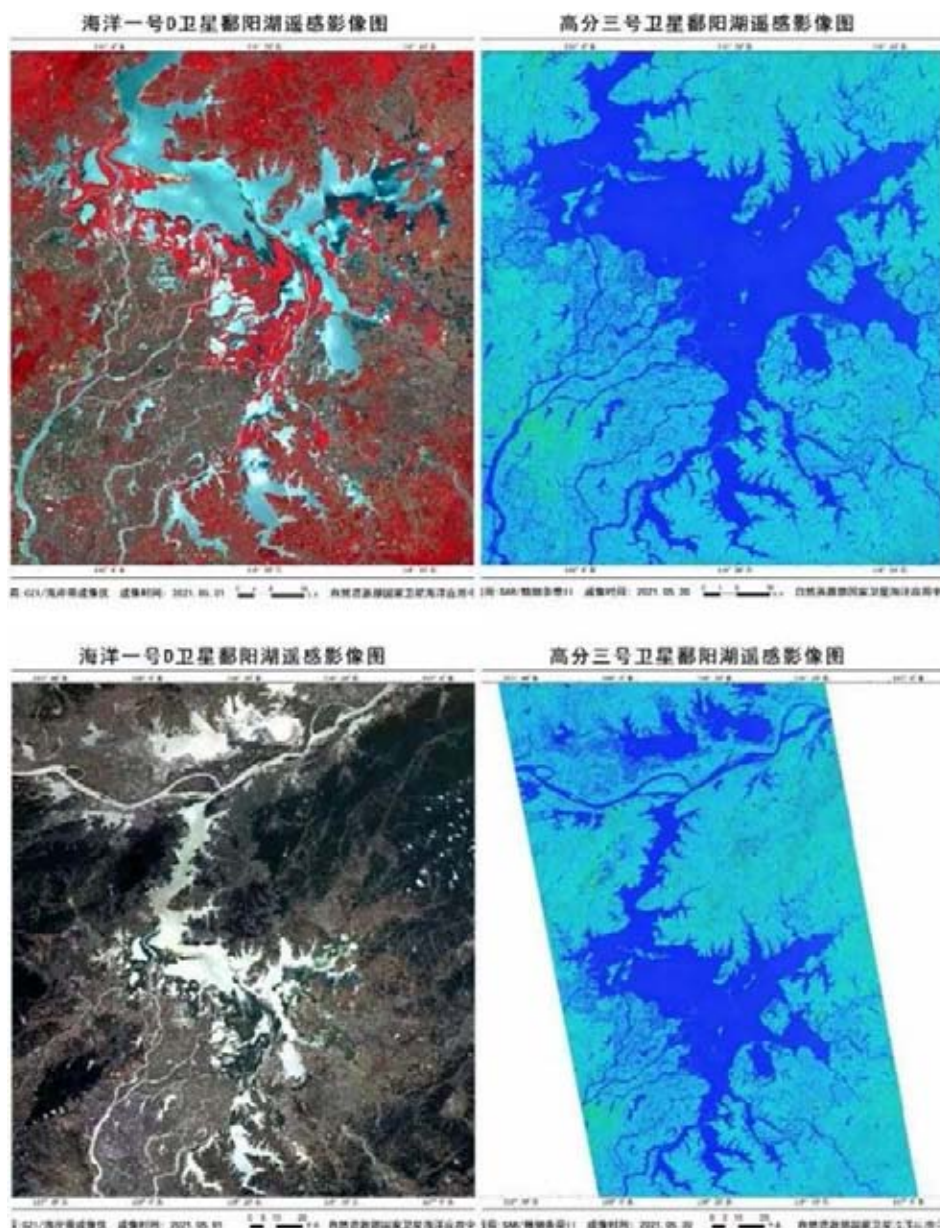


Fig. 11 Multi-satellite monitoring of water changes in Poyang Lake

operation activities, oil exploitation and transportation have led to changes in the marine ecological environment, and some endanger the marine ecological security. The impact can be continuously observed by multiple marine satellites.

3.6.1 Red tide Monitoring

Red tide is a marine ecosystem anomaly that occurs frequently in China's offshore waters. The explosive and rapid reproduction of plankton in the ocean causes the sea water to show different colors such as yellow, green, brown and red. In recent years, HY-1C and HY-1D satellites have been used to monitor many red tide events in the Bohai Sea, Yellow Sea, East China Sea and South

China Sea, and their locations and the area of influence and other important information shall be provided to relevant application departments. An example of red tide observation in Beibu Gulf is shown in Fig. 12.

3.6.2 Green Tide Monitoring

Since the outbreak of green tide in Qingdao in 2008, green tide monitoring has become an operational monitoring work. The information of green tides in the Yellow Sea and the East China Sea has been extracted by using a variety of satellite data such as HY-1/B/C/D, MODIS and GF series satellites, which has realized the early detection and whole process tracking and monitoring of green tide disasters, and provided accurate and

timely information services for the prediction of green tide drift path and disaster prevention and reduction. An example of multi-satellite monitoring of green tide in Daqiao Bay is shown in Fig. 13.

3.6.3 Oil Spill Pollution Monitoring

Oil spill pollution does great harm to the marine environment, marine ecology and human economic life.

Marine oil spill can be detected by microwave sensing, optical remote sensing, thermal infrared, ultraviolet and other remote sensors. The 50m coastal zone imager of HY-1C and HY-1D satellites and GF-3 satellite were used to monitor multiple oil spills in the Bohai Sea, the South China Sea and the East China Sea. An example of HY-1C satellite monitoring of oil spill in offshore

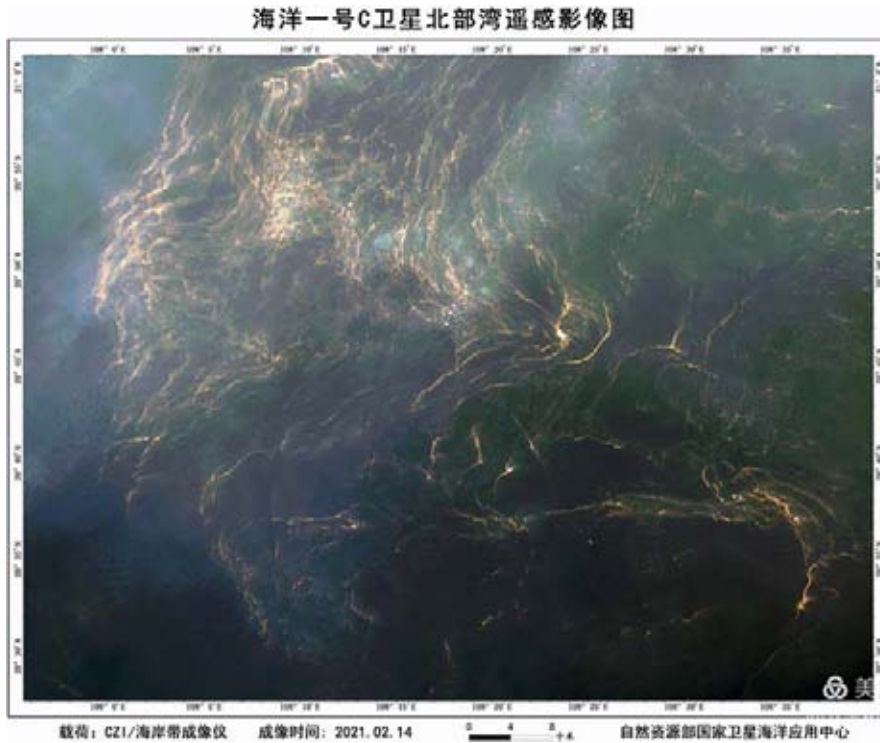


Fig. 12 Red tide in Beibu Gulf

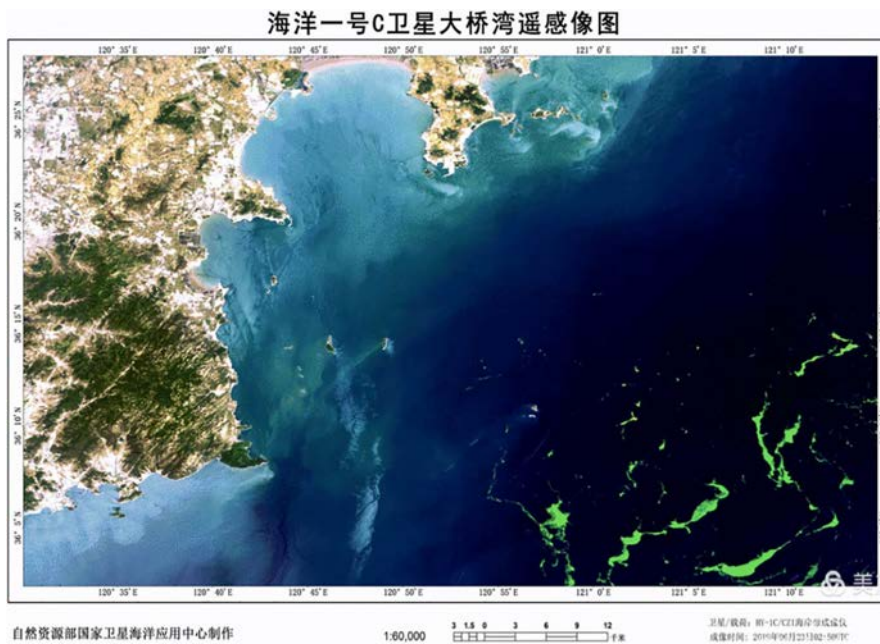


Fig. 13 Multi-satellite green tide monitoring

Indonesia is shown in Fig. 14.

3.7 Forest Fire Monitoring

Taking advantage of the short revisit period of HY-1C/D Satellite and the high signal-to-noise ratio of coastal zone imager, effective monitoring and analysis have been carried out on forest fires in Russia, Australia, Brazil, the United States, Myanmar, Ukraine, India, Indonesia and many other countries. In China, such as Qingdao,

Shanxi, Guangdong, Sichuan, Yunnan, Jiangxi and Beijing, the thematic map of fire was obtained by analyzing the vegetation change and smoke direction of multi-time images during and after the disaster, and was pushed to the Emergency Management Department and the front headquarters of relevant provinces at the first time, providing effective and powerful services for emergency relief. An example of HY-1C satellite forest fire monitoring of Laojun Mountain in Lijiang is shown in Fig. 15.

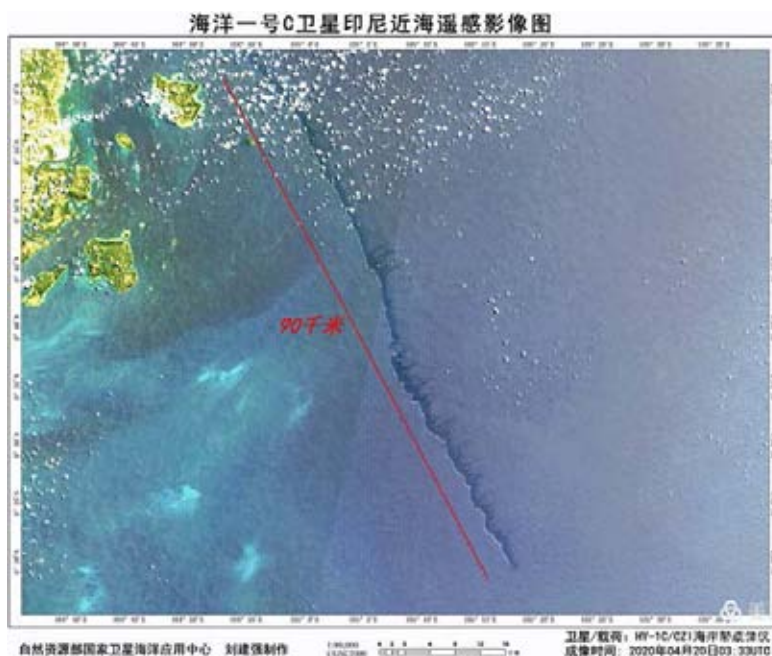


Fig. 14 HY-1C-satellite monitoring of oil spill pollution



Fig. 15 HY-1C Satellite Forest Fire Monitoring

3.8 Volcano Monitoring

From the image of HY-1C/D Satellite coastal zone imager on 28 February 2022 in Fig. 16, it is found that the volcano of Suwanosejima in Japan erupted. From the comparative analysis of the image, there are no obvious changes in the islands themselves, but the volcanic ash cloud is clearly visible. The volcanic ash cloud emitted

from Suwanosejima has obvious characteristics, showing white and striped cloud system, from dense to sparse distribution, the length of volcanic ash cloud is more than 100 km. From the comparative analysis of the time series images in the morning and afternoon, the volcanic ash cloud drifts towards the southeast, and a small amount of floating objects can be seen on the sea surface, but it is not sure whether it is pumice.

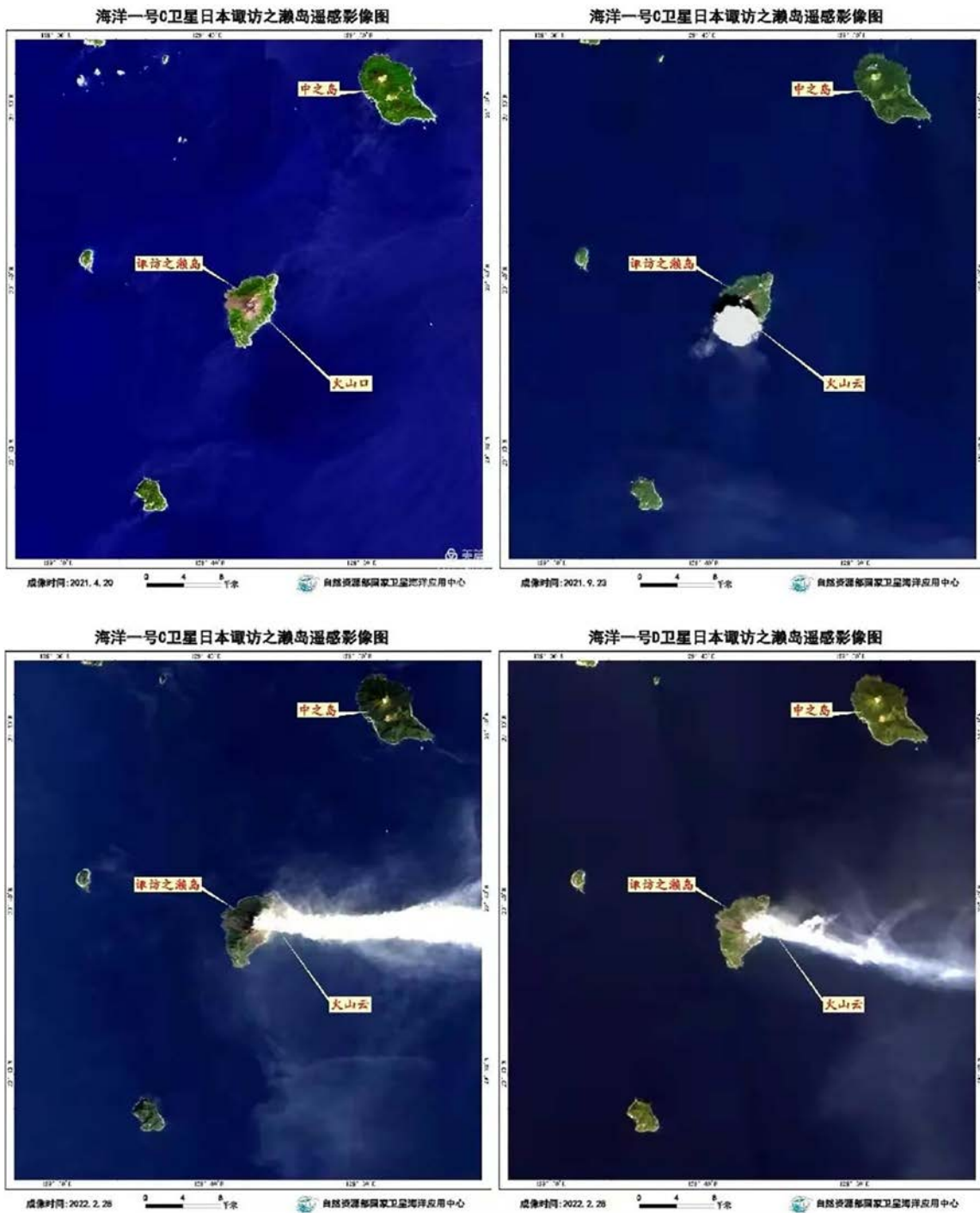


Fig. 16 HY-1C/D satellite Volcano monitoring

4 Conclusion

Ocean satellites have realized multi-satellite networked operation. The HY-1D satellite launched in June 2020 realized networked with HY-1C satellite, and completed the construction of ocean color satellite constellation. The HY-2D satellite launched in May 2021 is networked with the on orbit HY-2B and HY-2C satellites to complete the construction of marine dynamic environment satellite constellation. The 1m C-SAR satellite 01 launched in November 2021 is networked with GF-3, which initially forms the marine monitoring satellite constellation. This year, the networking of 1m C-SAR satellite 02 with satellite 01 and GF-3 is realized, and the construction of marine monitoring satellite constellation is completed. At present, ocean satellite has the operational application capabilities of satellite remote sensing investigation, monitoring, evaluation and supervision of marine ecology, marine disaster prevention and reduction, global oceans and Polar Regions, Sea Islands and rights and interests maintenance.

In the follow-up development of ocean satellites,

while providing services in many fields, it is also necessary to continue to improve the monitoring capacity and expand the application service capacity in terms of satellite observation accuracy, spatial resolution and timeliness. Build a complete space-based ocean observation system with high and low orbit coordination, solar and non-solar synchronous satellites, and low, medium and high-resolution observation capabilities, so as to realize the synchronous acquisition of large, medium and small-scale marine environment information and the synchronous observation capability of the marine surface, subsurface and seafloor.

References

- [1] HY-2C satellite in orbit test report[M]. National Satellite Ocean Application Service, 2021
- [2] HY-2D satellite in orbit test report[M]. National Satellite Ocean Application Service, 2022
- [3] KNAFF J A, SAMPSON C R, KUCAS M E, *et al.* Estimating tropical cyclone surface winds: Current status, emerging technologies, historical evolution, and a look to the future[J]. *Tropical Cyclone Research and Review*, 2021, **10**(3): 125-150

Space Environment Measurements and Applications on the Tianhe Core Module of China Space Station

LIU Siqing^{1,2,3}, SUN Yueqiang^{2,3}, ZHONG Qiuzhen^{1,2,3}, WEI Fei^{2,3},
LI Yongping^{2,3}, ZHANG Xianguo², LIN Ruilin^{1,2}, LI Zhitao^{1,2},
REN Tingling^{1,2}, LUO bingxian^{1,2,3}, CHANG Zhen², WANG Chunqin²,
PENG Songwu², AI Jiangzhao²

1. State Key Laboratory of Space Weather, National Space Science Center, Chinese Academy of Sciences, Beijing 100190
2. Key Laboratory of Science and Technology on Environmental Space Situation Awareness, Chinese Academy of Sciences, Beijing 100190

Abstract

Tianhe Core Module of China Space Station (CSS) equips a set of instruments consisting of a Particle Fluxes and Solar Activity Detector (PFSAD) and two Atmospheric Density Multi-directional Detectors (ADMDs). The PFSAD is to measure X-rays from the Sun and energetic particles in the low-latitude and low altitude regions, including electrons, protons, and helium ions. The ADMDs are to measure thermospheric atmospheric density. The instruments provide real-time data of the orbital space environment, including solar flares, energetic particle variation and thermospheric density enhancement. All the data contribute to the CSS space weather service for mission control and astronaut's safety. The paper gives preliminary analyses of the space environment measurements from the PFSAD and the ADMDs. By further analysis, the 1024-channel fine spectra of the solar X-ray can be used to study the mechanism of solar flares and their impacts on the Earth's atmosphere. Data accumulation will be helpful for analyzing mid-term and long-term variations of the South Atlantic Anomaly and atmosphere density. Furthermore, the data is useful to calibrate previous empirical models and establish new models to study the space environment.

Key words

Space environment, Tianhe core module, China Space Station (CSS)

1 Introduction

The radiation environment of Low Earth Orbit (LEO) is dependent on altitude and inclination of the spacecraft's orbit and changes with the solar activity. Tianhe, the

core module of China Space Station (CSS), was launched into an orbit with 350–400km altitude and about 42° inclination on 29 April 2021. The radiation particles from Galactic Cosmic Radiation (GCR), the Earth's inner radiation belts and occasional Solar Parti-

cle Events (SPEs), as well as secondary particles, are capable of entering Tianhe. As a result, the exposure the crew receives during an extended spaceflight significantly exceeds exposure limits for terrestrial radiation workers^[1]. Since the early times of human spaceflight, space radiation, especially its heavy ion component, has been recognized as a main health concern for human space missions^[2-3]. Usually several astronauts reside in Tianhe for a few months, and carry out the Extravehicular Activities (EVAs) missions. Thus the need for radiation monitoring on the CSS for purposes of crew safety has been apparent.

In LEO the air drag force is considered to be the predominant perturbing force^[4]. The uncertainties in the upper atmosphere modeling may significantly degrade the mission performance in many LEO orbit activities, such as satellite and debris impact risk evaluation, collision avoidance maneuver planning, spacecraft lifetime and re-entry time evaluation^[5]. The drag force on satellites increases when the Sun is active. For the CSS, the precise estimate of thermosphere neutral density is vital to the mission control.

Tianhe equips a Particle Fluxes and Solar Activity Detector (PFSAD) and two Atmospheric Density Multi-directional Detectors (ADMDs) which provide in-situ measurements of radiation particles, solar X-ray flux and thermospheric atmosphere density. CSS will be in orbit for 10 to 15 years, therefore in-situ measurements can describe space environment disturbances in both short- and mid-term scales, and even variations in long-scale spanning over one solar cycle. The observations are key to CSS orbital space weather forecast, and moreover can effectively improve the accuracy of the thermospheric density models and radiation belt models.

2 Space Environment Detectors

2.1 Particle Flux and Solar Activity Detector

The PFSAD consists of three components. The unit of high-energy proton monitor is made of five pieces of silicon semiconductor sensors with 12 mm in diameter and 500 micron to 1mm in thickness. The unit of high-energy electron monitor uses six pieces of silicon semiconductor sensors with 8 mm to 12 mm in diameter and 300 micron to 1 mm in thickness, and the unit of solar X-ray monitor uses two Silicon Drift Sensors (SDD). PFSAD is mounted outside the Tianhe Core Module.

The PFSAD measures solar X-ray and energetic particles in the low-latitude regions, including electrons, protons, and helium ions. It has 9 channels for electrons with 0.2–2.0 MeV and ≥ 2.0 MeV, 6 channels for protons with 4.0–165 MeV and ≥ 165 MeV, and 3 channels for helium ions with 4.0–16.4 MeV and ≥ 16.4 MeV. The full-angle circular conical FOV (field-of-view) for electrons, protons and helium ions are 40°, 60° and 60°, respectively. The PFSAD was turned on 2 days after launch and provides the data of particle count rates with 2 seconds resolution since 1 May 2021, which can be converted to particle unidirectional integral fluxes by geometry factors. The details of particle channels and X-ray channels of the PFSAD instrument are listed in Table 1 and Table 2, respectively.

2.2 Atmospheric Density Multi-directional Detectors (ADMDs)

The Tianhe Core Module was equipped two same At

Table 1 Information of energetic particle channels of PFSAD

Particle species	Protons	α ion	Electrons
Energetic particle channels	P1: 4–9MeV	I1: 4–12.5MeV/u	E1: 0.2–0.3MeV
	P2: 9–15MeV	I2: 12.5–16.4MeV/u	E2: 0.3–0.4MeV
	P3: 15–40MeV	I3: ≥ 16.4 MeV/u	E3: 0.4–0.5MeV
	P4: 40–80MeV		E4: 0.5–0.6MeV
	P5: 80–165MeV		E5: 0.6–0.8MeV
	P6: ≥ 165 MeV		E6: 0.8–1.0MeV
			E7: 1.0–1.5MeV
			E8: 1.5–2.0 MeV
			E9: ≥ 2.0 MeV

Table 2 information of Solar X-ray channels of PFSAD

Channels	energy threshold/keV
Main channels	Main channel 1: 1.5–12.4 (Corresponding wavelength: 1–8Å)
	Main channel 2: 3.1–24.8 (Corresponding wavelength: 0.5–4Å)
10 fine channels	R1: 1.5–3.1
	R2: 3.1–4.0
	R3: 4.0–6.0
	R4: 6.0–8.0
	R5: 8.0–10.0
	R6: 10.0–12.4
	R7: 12.4–15.0
	R8: 15.0–18.0
	R9: 18.0–21.0
	R10: 21.0–24.8
1024 fine channels (solar flare mode)	1.5–24.8 divided in 1024 channels

mospheric Density Multi-directional Detectors (ADMDs). The ADMD-1 and ADMD-2 are symmetrically mounted at the II-III and I-IV quadrant of the large column section outside the core module. The design can adapt to the different flight attitude of the CSS and achieve the full-direction atmospheric density data. The measurement atmospheric density is in the range of $5 \times 10^{-15} - 5 \times 10^{-10} \text{ kg} \cdot \text{m}^{-3}$. Sampling chamber pressure and temperature are in the ranges of $5 \times 10^{-7} - 1 \times 10^{-3} \text{ Pa}$ and -20 to $+70 \text{ }^\circ\text{C}$, respectively.

3 Data Processing

3.1 Energetic Particle Flux Data Processing

Data processing requires the physical quantity conversion and orbital position matching to generate the energetic particle fluxes including the electrons, protons and heavy ions from the original count rates.

The energetic particle flux conversion function is as follows:

$$J = R_C / G_i \quad (1)$$

Here the flux unit is $\text{cm}^{-2} \cdot \text{s}^{-1} \cdot \text{sr}^{-1}$, R_C represents count rate, and G_i represents the geometric factors of various channels which are listed in Table 3.

3.2 Solar X-ray Flux Data Processing

The data processing of solar X-ray flux mainly includes three steps: the first is to remove background noise, the second is to calculate the X-ray effective area and the transmission efficiency, and the third is to transform the X-ray flux into the standard unit (in unit of $\text{W} \cdot \text{m}^{-2}$ or $\text{J} \cdot \text{s}^{-1} \cdot \text{m}^{-2}$).

Environmental background noise mainly comes from the cosmic X-ray and energetic particles in the South Atlantic Anomaly (SAA). The temperature of the PFSAD in operation can change the background noise level as well, which should be calibrated according to the temperature, and be deducted in the data processing. When

the PFSAD passes through the SAA, energetic particles may directly enter the sensor or interact with collimator and materials surrounding the detector, producing the background counts. The noise level caused by the SAA is generally less than a C2-level solar flare. In the current data processing, the data of X-ray flux will be marked when the PFSAD flies through the SAA.

The effective area and transmission efficiency of the solar X-ray mainly depend on the incidence angle and the transmission path of the X-ray into the SDD sensors. After unifying the PFSAD and the sun in the same coordinate system, we could determine whether the X-ray irradiation is in the observing FOV and the SDD number and the irradiation area according to the angle between the solar X-ray incident direction and the normal directions of the two SDD sensors. The solar X-ray is first penetrating the 1mm Be window, then reaching the SDD sensor and penetrating 20 μm Be film, and finally be absorbed by the 450 μm Si sensor. According to the solar X-ray incidence angle and the actual path, the total X-ray transmission efficiency is calculated.

The integration time of data is 1s in normal mode, when in event mode the integration time of each data packet is 5 s. Eq.(2) gives the conversion between X-ray proton counts and flux value.

$$\phi = \frac{N \cdot E}{A_{\text{eff}} \cdot t \cdot \eta_{\text{total}}} \times C \quad (2)$$

Here, N is the photon counts after removing X-ray channel noise; E represents photon energy in unit eV; A_{eff} is the effective irradiation area of X-ray on the SDD sensor in unit of m^2 ; t is the integral time in unit of s; η_{total} is the total transmission efficiency of X-ray; and C is equal to $1.602 \times 10^{-19} \text{ J}$, corresponding to the energy of 1 eV.

3.3 Thermospheric Atmosphere Density Data Processing

According to the gas molecular dynamics theory, the

Table 3 Geometric factors of various channels of different particles

Particle species	Geometric factor / ($\text{cm}^2 \cdot \text{sr}^{-1}$)								
Electrons	E1	E2	E3	E4	E5	E6	E7	E8	E9
	0.139	0.125	0.065	0.072	0.104	0.115	0.146	0.166	0.254
Protons	P1	P2	P3	P4	P5	P6	-	-	-
	1.587	1.117	0.969	0.740	0.857	1.022	-	-	-
α ions	I1	I2	I3	-	-	-	-	-	-
	1.093	0.864	0.680	-	-	-	-	-	-

thermospheric atmosphere density can be directly obtained by the pressure and temperature measurements in the sampling chamber. Therefore, when the gas molecules (atoms) enter the sampling chamber with the regulating plate through the standard measuring hole, the incoming gas molecules (atoms) undergo collision with the sampling chamber wall and the regulating plate, and its temperature is adjusted to approximate the wall temperature. The thermospheric atmosphere mass density is calculated by Eq.(3) and Eq.(4).

$$N_a = P_g (2\pi k m_1)^{-\frac{1}{2}} \left(\frac{1}{T_g} \right)^{\frac{1}{2}} \frac{1}{V \cos \theta}, \quad (3)$$

$$\rho = N_a \times m_2. \quad (4)$$

Here, ρ is the free atmospheric mass density in unit of $\text{kg}\cdot\text{m}^{-3}$; N_a is the number density of free atmosphere in unit of $\text{counts}\cdot\text{m}^{-3}$; P_g is the gas atmospheric pressure in the sensor in unit of Pa; T_g is the gas temperature in the sensor in unit of K; m_1 is the average mass of gas molecules in the sensor in unit of kg; m_2 is the average molecular mass outside the sensor gas in unit of kg; k is the Boltzmann constant (dimensionless); V is the speed of core module or assembly in unit of $\text{m}\cdot\text{s}^{-1}$; θ is the angle between the outside normal vector of sampling hole and core module velocity vector, called the angle of attack in unit of degree.

Data processing steps are as follows.

(a) Determine the working situation of the main filament or backup filament by detecting the voltage value of the sensor filament, and then convert the L1 level scientific data (pressure voltage value and temperature voltage value from sampling chamber) into the corresponding physical quantity through the ground calibration data.

(b) Solve the speed and angle of attack of the core module, and select the sensor on the windward side according to the calculated angle of attack.

(c) Calculate the orbital atmospheric density by Eq. (3) and (4) using the pressure and temperature obtained from the sensor on the windward side selected in Step 2.

4 Data analysis and Applications

4.1 Solar X-ray Flux Data Analysis and Application

Solar X-Ray Sensors (SRS) measure the full-disk total solar flux in two main channels, ten fine channels and

1024 fine channels in flare mode with flux threshold of C5-X30 flare. The Tianhe Core Module orbits the Earth every 90 min passing through the insolation zone and the earth shadow zone periodically. The effective X-ray flux observation window is 40–60 min in inertial attitude, and 20–40 min in 3-axis stabilized attitude within one orbital period. The lifetime of solar flares is usually less than one hour. Thus solar flares are fully visible or partially visible, even invisible to the solar X-ray sensor due to the discontinuity of the observed FOV.

Usually PFSAD provides solar X-ray flux of two main channels and ten fine channels. It also provides 1024 channels X-ray flux when solar flares erupt. To evaluate the data detected by PFSAD, GOES-16 satellite was selected to make a comparison with solar X-ray flux. Fig. 1 gives the solar X-ray flux from two main channels of PFSAD (solid lines) and from GOES-16 satellite (dotted lines) on 28 October 2021. PFSAD observed peak flux with $1.02 \times 10^{-4} \text{ W}\cdot\text{m}^{-2}$ in the 1–8 Å and with $1.78 \times 10^{-5} \text{ W}\cdot\text{m}^{-2}$ in the 0.5–4 angstrom at 15:32 UTC. GOES-16 observed peak flux with $1.0 \times 10^{-4} \text{ W}\cdot\text{m}^{-2}$ in the 1–8 Å and with $1.66 \times 10^{-5} \text{ W}\cdot\text{m}^{-2}$ in the 0.5–4 Å at 15:34 UTC. The values of peak flux from both satellites are very close. However, in the early and late stages of the flare, the X-ray flux monitored by PFSAD is slightly lower than that by GOES-16 satellite. The possible reason was the deviations in the low-energy channels of PFSAD.

GOES-16 satellite screens the stray light through multilayer filters, thus the low energy X-ray, especially below 1.5 keV, also can be monitored and collected. The hardware condition of PFSAD determines that X-ray below 1.5 keV will be cut off. Meanwhile, the

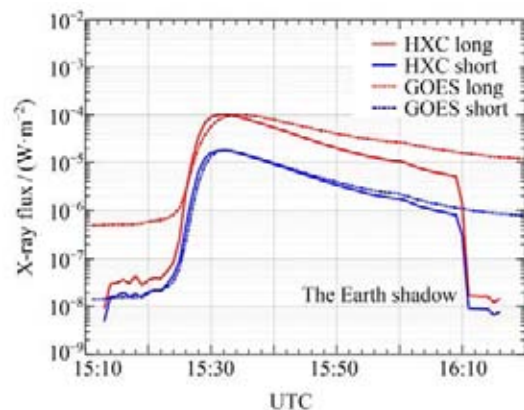


Fig. 1 X-ray flux (1-minute data) on 28 October 2021

X-ray flux in the lower energy channels is higher, so the X-ray flux in the flare early outbreak and decline phase is relatively low. Fig. 2 gives X-ray flux in the ten fine passbands of the same X1.0 flare. It can be seen as the energy passbands rise, the peak flux gradually decreases.

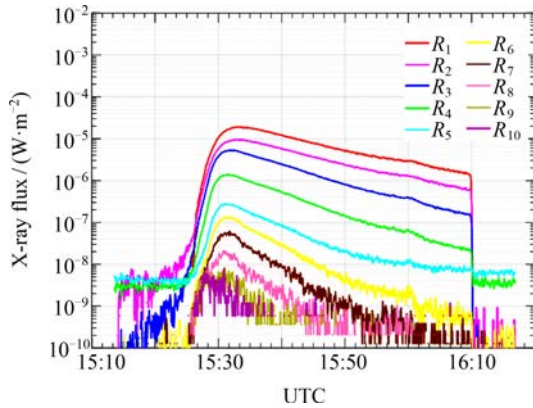


Fig. 2 X-ray flux in ten fine passbands of X1.0 flare on 28 October 2021

X-ray flux in high energy passbands rises and decreases more steeply than that in lower energy passbands.

Due to the discontinuity of the FOV, part of the flares can be detected by PFSAD. From 1 May 2021 to 18 April 2022, PFSAD observed 20 M-class flares and 2 X-scale flares whose peaks were fully visible among total 61 M-class and 4 X-class flares which were monitored by GOES-16 satellite. Table 4 shows the X-ray peak flux of these 22 flare events. The absolute deviation of solar X-ray peak flux between PFSAD and GOES satellite is from 1.00×10^{-7} to $2.4 \times 10^{-5} \text{ W} \cdot \text{m}^{-2}$, and the average value is $4.0 \times 10^{-6} \text{ W} \cdot \text{m}^{-2}$. The peak flux of solar X-ray flares from two satellites are very close.

The solar X-ray flux observed by Tianhe Core Module reflects the solar activity and provide effectively warn of solar erupting, such as solar proton events and coronal mass ejections. The fine channels data can help to study the solar X-ray flare bursts and their mechanisms.

Table 4 Peak flux of 22 X-ray flares from May 2021 to April 2022 (1–8 angstrom)

Number	Time (UT)	GOES/(W·m ⁻²)	Tianhe/(W·m ⁻²)	Absolute difference/(W·m ⁻²)
1	2021-05-22 21:36	1.49×10^{-5}	1.48×10^{-5}	-1.00×10^{-7}
2	2021-05-23 11:08	1.19×10^{-5}	1.31×10^{-5}	1.20×10^{-6}
3	2021-10-26 15:57	1.02×10^{-5}	1.19×10^{-5}	1.70×10^{-6}
4	2021-10-28 07:40	1.42×10^{-5}	1.40×10^{-5}	-2.00×10^{-7}
5	2021-10-28 15:34	1.00×10^{-4}	1.02×10^{-4}	2.00×10^{-6}
6	2021-10-29 02:42	1.56×10^{-5}	1.77×10^{-5}	2.10×10^{-6}
7	2021-12-17 00:51	1.29×10^{-5}	1.50×10^{-5}	2.10×10^{-6}
8	2022-01-14 02:03	1.84×10^{-5}	1.92×10^{-5}	8.00×10^{-7}
9	2022-01-20 06:01	5.51×10^{-5}	6.50×10^{-5}	9.90×10^{-6}
10	2022-01-29 23:32	1.14×10^{-5}	1.04×10^{-5}	-1.00×10^{-6}
11	2022-03-02 17:39	2.02×10^{-5}	2.13×10^{-5}	1.10×10^{-6}
12	2022-03-15 22:46	1.59×10^{-5}	1.68×10^{-5}	9.00×10^{-7}
13	2022-03-28 11:29	4.06×10^{-5}	6.46×10^{-5}	2.40×10^{-5}
14	2022-03-29 01:11	2.22×10^{-5}	2.09×10^{-5}	-1.30×10^{-6}
15	2022-03-31 18:35	9.67×10^{-5}	1.08×10^{-4}	1.13×10^{-5}
16	2022-04-02 02:56	2.91×10^{-5}	3.59×10^{-5}	6.80×10^{-6}
17	2022-04-02 13:55	3.94×10^{-5}	4.37×10^{-5}	4.30×10^{-6}
18	2022-04-15 11:49	2.21×10^{-5}	1.96×10^{-5}	-2.50×10^{-6}
19	2022-04-17 02:11	1.89×10^{-5}	2.04×10^{-5}	1.50×10^{-6}
20	2022-04-17 03:34	1.16×10^{-4}	1.12×10^{-4}	-4.00×10^{-6}
21	2022-04-18 07:48	1.36×10^{-5}	2.23×10^{-5}	8.70×10^{-6}
22	2022-04-18 10:27	1.19×10^{-5}	1.30×10^{-5}	1.10×10^{-6}

4.2 Energetic Particle Flux Data Analysis and Application

The China's space station passes through the SAA several times each day. The PFSAD onboard it detects the energetic electrons, protons, and helium ions in the most regions of SAA in these altitudes, except for some high-latitude regions, and monitors the variations of energetic particle intensities and the boundary of SAA in real time. For strong solar proton events, some solar protons can be detected by the PFSAD when the magnetic latitudes of the CSS exceed a certain value.

Fig. 3 shows the unidirectional integral fluxes of 0.2–0.3 MeV electrons, 4–9 MeV protons and 4–12.5 MeV/u helium ions from the PFSAD and the orbit altitudes between 1 May 2021 and 8 May 2022. The data of Kp index in Fig. 3(e) are from GFZ German Research Centre. The upper bounds in Fig. 3(a), 3(b) and 3(c) roughly represent the peak intensities of energetic electrons, protons, and helium ions in the SAA, respectively.

It is shown that the data of energetic particles are basically continuous from 1 May 2021, the peak intensities of energetic electrons vary obviously and sometimes change by more than 2 orders of magnitude on time scales ranging from minutes to days, especially when geomagnetic storms occur, and the peak intensities of energetic protons and helium ions are relatively stable, only several fold variation at most.

In order to get the whole shape and distribution of SAA at the altitudes of CSS, the data from PFSAD between 1 January 2022 and 8 May 2022 are used to create the dataset of latitude and longitude grids with 0.5 degree intervals. The average unidirectional integral fluxes of electrons, protons, helium ions in each grid are plotted in the longitude-latitude coordinates, shown in Fig. 4 and 5, and the SAA of electron, proton and helium ion radiation belts are clearly outlined. Both figures illustrate that the proton and electron intensities of SAA changes with energy, and their boundaries are also related to the particle energy.

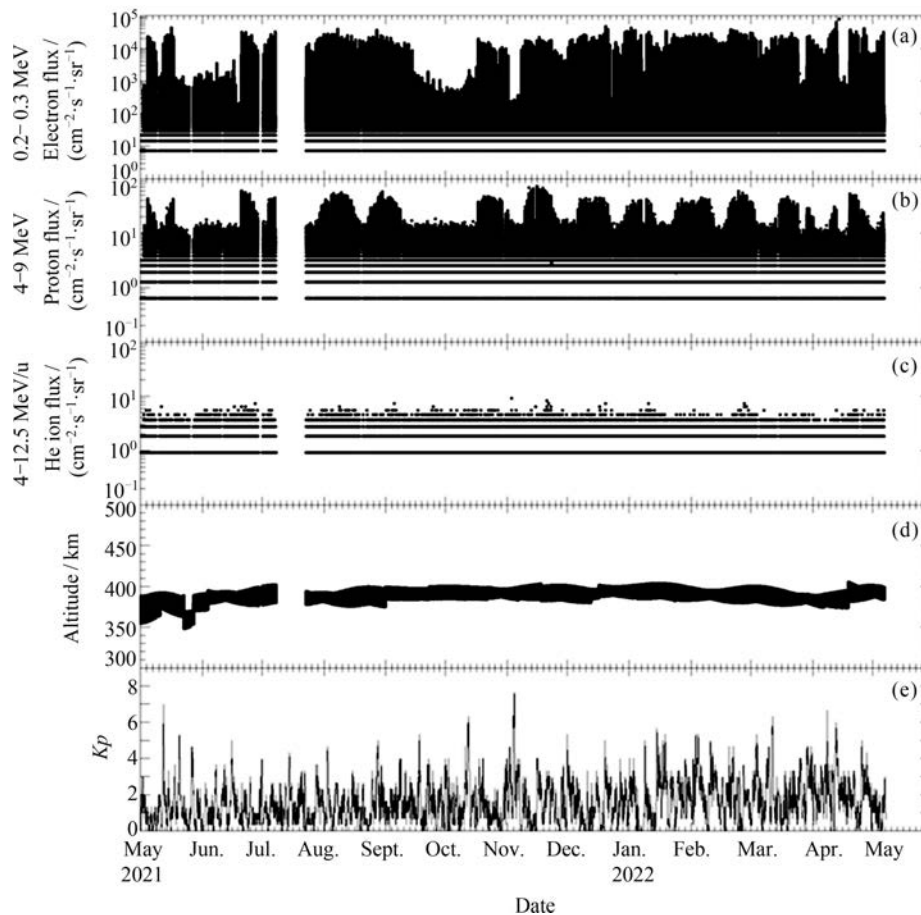


Fig. 3 Unidirectional integral fluxes of 0.2–0.3 MeV electrons, 4–9 MeV protons and 4–12.5 MeV/u helium ions from CSS and the orbit altitudes between 1 May 2021 and 8 May 2022

When the electron energies are less than 1.0 MeV, the electron intensities and the area of SAA decrease with increasing energy. The results are the same as the protons of SAA. However, the results are just the opposite when the electron energies are larger than 1.0 MeV. According to the result of Li *et al.*^[6] and Fennell *et al.*^[7], there are no significant fluxes of MeV electrons in the inner radiation zone, so the E7, E8 and E9 channels of the PFSAD are likely polluted by the unforgiving penetration of the highly energetic protons (tens of MeV to GeV). In the E1 and E2 channels, a small amount of electrons polluted by the cosmic rays are detected near the 40° north and south latitudes outside the SAA. For these polluted data of electrons, further data processing is required. In Fig. 5(h) and 5(i), there are no significant fluxes of helium ions. It proves that the integral fluxes of ≥ 12.5 MeV/u helium ions are less than $1 \text{ cm}^{-2} \cdot \text{s}^{-1} \cdot \text{sr}^{-1}$, below the lower detection limit of the PFSAD.

In summary, the data of energetic particles from CSS can be used to alert the SAA crossings of satellites with altitudes about 400 km, and to analyze the influence of radiation belts particles on spacecraft or astronauts. The data can also participate in the radiation belts modeling to improve the prediction in the low altitude region.

4.3 Atmospheric Density Data Analysis and Application

The observed densities were recorded with a high temporal resolution of 2 seconds, and they were mostly consecutive except on some occasions such as orbital maneuvers, spacecraft dockings and extravehicular activities, when the ADMDs were powered off for instrument protection purpose. In the past year, several geomagnetic storm cases had happened, and this made it applicable to evaluate the performance of these observed density under different geomagnetic conditions. NRLMSISE-00 was selected as the baseline model to make the comparison, and both geomagnetic quiet and storm event cases were considered.

Fig. 6 gives the comparison of results on 2–3 March 2022, when the geomagnetic condition is mostly quiet ($Kp < 3$) except the last segment of 3h for unsettled ($Kp = 3$). The thin red and black curves in the top panel represent NRLMSISE-00 and observed densities, respectively. The bold curves represent the mean density values averaged over two orbit circles. Geomagnetic Kp index values are shown in the bottom panel. It's evident that the outline and magnitude of both of the thin and

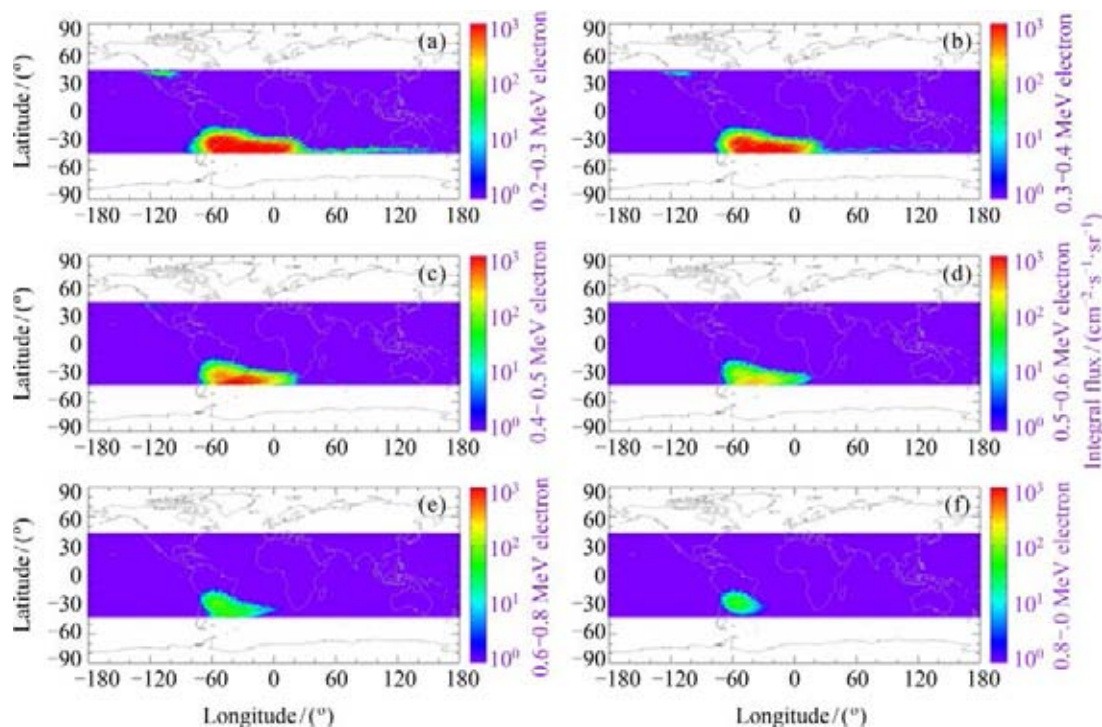


Fig. 4 Distribution of 0.2–1.0 MeV electrons with 6 channels measured by China Space Station between 1 January 2022 and 8 May 2022

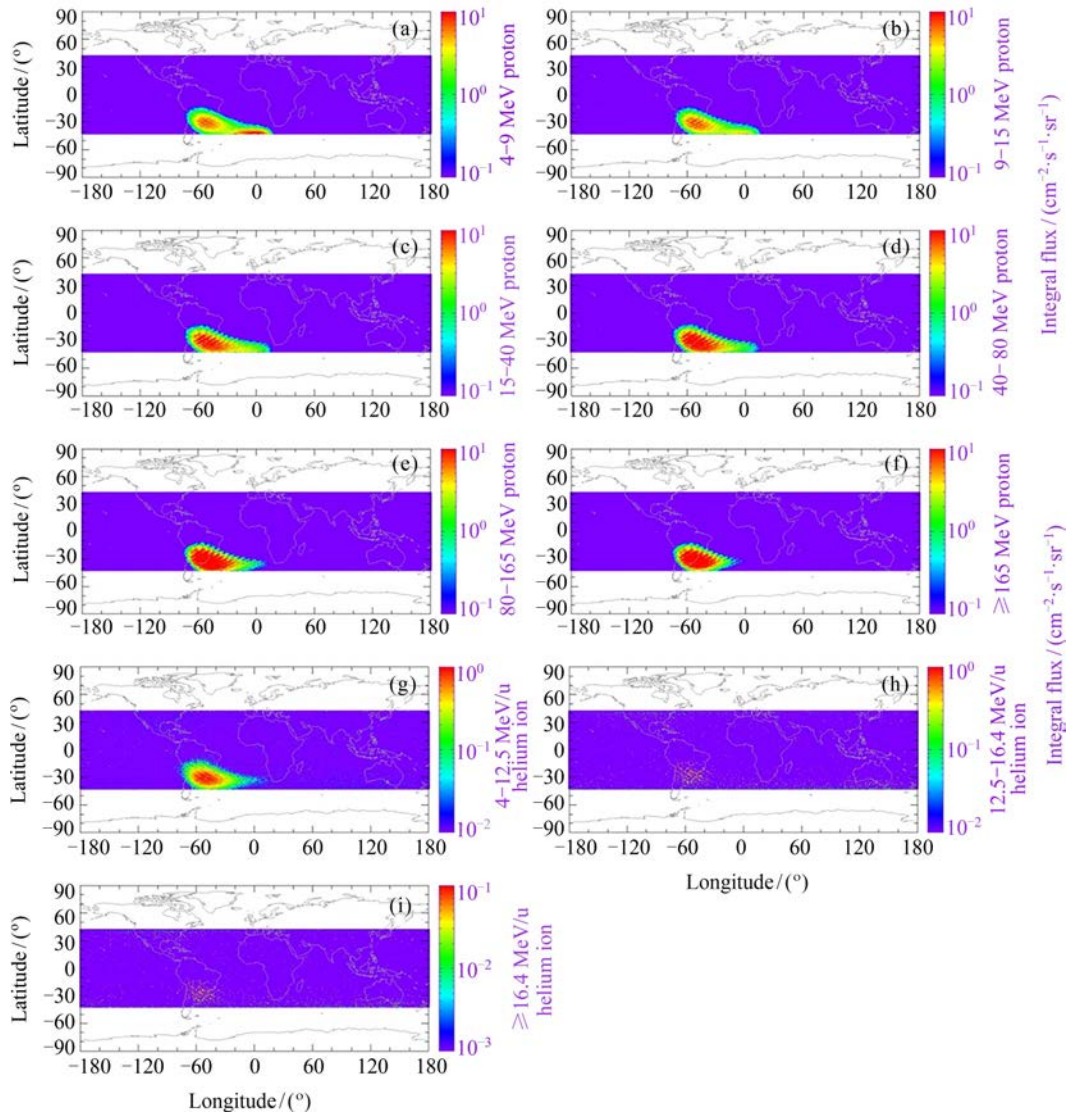


Fig. 5 Distribution of ≥ 4.0 MeV protons with 6 channels and ≥ 4.0 MeV/u helium ions with 3 channels measured by China Space Station between 1 January 2022 and 8 May 2022

bold curves conform well, implying that the observed values could give a reasonable description of the atmospheric densities under geomagnetic quiet conditions.

Fig. 7 gives the comparison results on 13–14 March 2022. A consecutive geomagnetic storm periods including moderate storm levels ($Kp=6$) for 12 hours and minor storm levels ($Kp=5$) for 3 hours were recorded. It indicates that the observed and model densities conform well either. However, there are some apparent differences between the observed and model densities. For example, result shows that the observed densities increased about 48% during the intensified geomagnetic activities while the model densities increased about 31%. Meanwhile, when geomagnetic storm happened, the mean

observed densities increased with a higher rate than the mean model densities, and it decreased also more quickly after the geomagnetic conditions recovered to quiet levels.

Fig. 8 gives another example for geomagnetic storm event on 4–6 March 2022. The geomagnetic field was quiet to unsettled on the first day, followed by isolated minor storm and active levels for 12 hours, respectively, throughout the last two days. The observed and model densities conform well, the same as results on 2–3 March 2022, but the mean observed densities increased with an apparent higher rate than the mean model densities. To be specific, the density increased about 49% for the observed value, while about 36% for NRLMSISE-00 model.

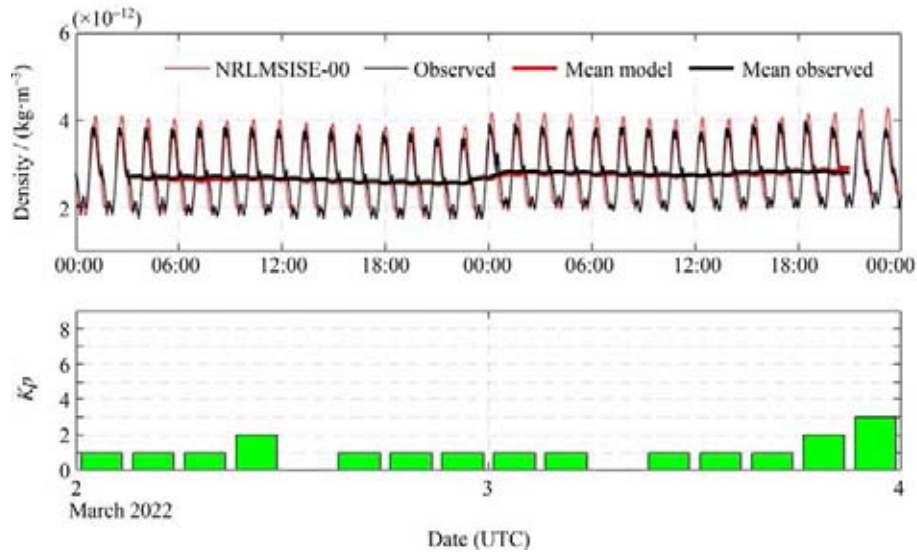


Fig. 6 Comparison between observed (black line) and NRLMSISE-00 model (red line) densities (top panel) on 2–3 March 2022. The bold lines represent the mean values averaged over two orbit circles. Geomagnetic Kp index values were also given in the bottom panel

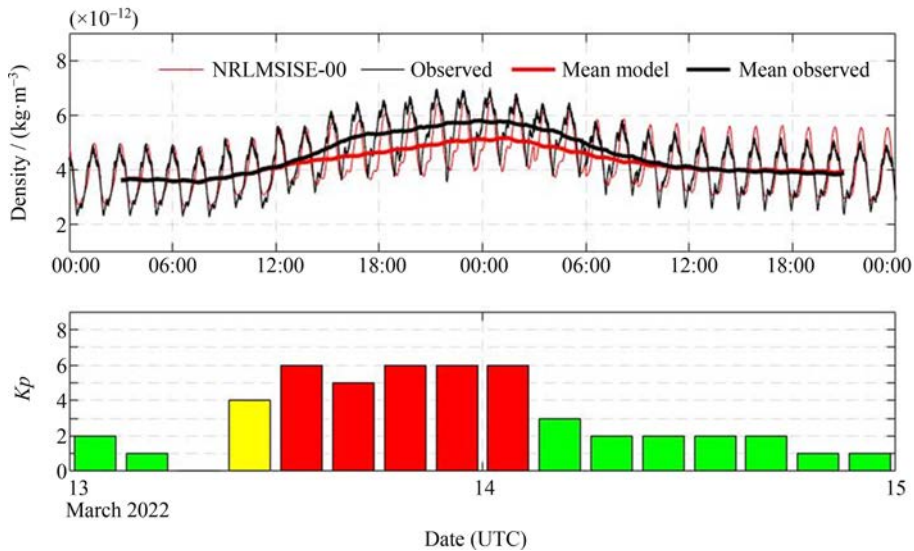


Fig. 7 Comparison between observed (black line) and NRLMSISE-00 model (red line) densities (top panel) on 13–14 March 2022

The result of the two geomagnetic storm cases implied that the observed densities may react more sensitive with the geomagnetic conditions than those from NRLMSISE-00 model. However, it should be note that more storm cases should be added in the following studies to make the result robust. With the intensifying of the 25th solar circle, more geomagnetic storm events will be expected to occur, the analyzation and evaluation of the performance of the observed densities could become much more comprehensive.

The CSS is supposed to be on orbit for more than 10 years, this indicates that a large amount of observed density data will be available throughout the whole mission, and it will be undoubtedly helpful to the studies on upper atmosphere. For example, these in-situ observed densities could be used to analyze the accuracy of other data sources and make calibrations on the existing models such as NRLMSISE-00. What’s more, they will contribute to the establishment of a new empirical model.

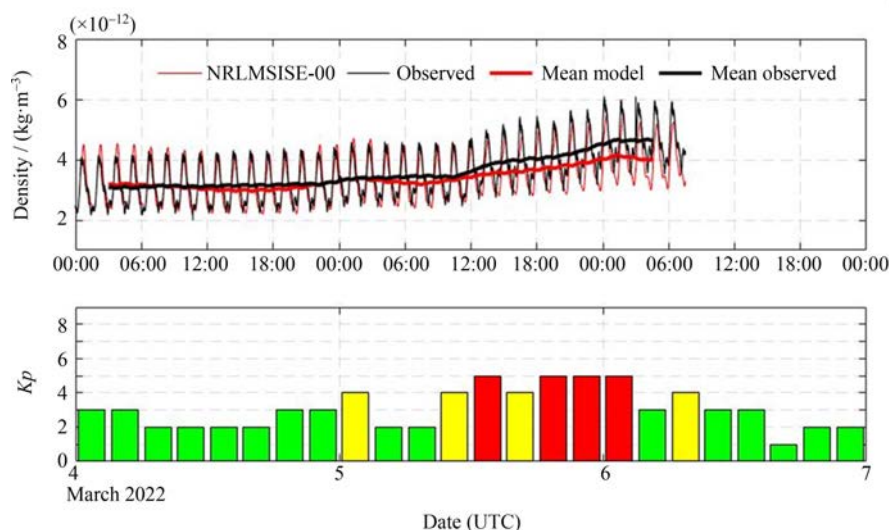


Fig. 8 Comparison between observed (black line) and NRLMSISE-00 model (red line) densities (top panel) on 4–6 March 2022

5 Conclusion and Outlook

The instruments onboard Tianhe provide real-time data of the orbital space environment, including solar flares, energetic particle variation and thermospheric atmospheric density enhancement, which contribute to the CSS space weather service for mission control and astronauts safety.

Comparing the Solar X-ray flux from PFSAD and GOES-16 satellite the peak flux were close. However, in the early and late stages of the flare, the X-ray flux monitored by Tianhe Core Module is slightly lower than that of GOES-16 satellite. Due to the CSS orbit, the solar X-ray flux observation was discontinuous.

The data of energetic particles from PFSAD can be used to alert the SAA crossings of low-latitude satellites with altitudes about 400 km, and to analyze the influence of radiation belts particles on spacecraft or astronauts. In the future, the data can also contribute to construct the radiation belts model to improve the prediction in the low altitude region.

From the geomagnetic storm cases, the observed densities of ADMDs may react more sensitive with the geomagnetic conditions than those from NRLMSISE-00 model. In the future, more storm cases should be analyzed to make the result robust. Meanwhile, as the atmospheric density data increase, it could be used to calibrate and improve the accuracy of the existing models, or establish a new empirical model.

The paper gives preliminary analysis of the space en-

vironment measurements from the PFSAD and the ADMDs. By further analysis, the 1024-channel fine spectra of the solar X-ray can be used to study the mechanism of solar flares and their impacts on the Earth's atmosphere. Data accumulation will be helpful for analyzing mid-term and long-term variation of the SAA and atmosphere density. Furthermore the data is useful to make calibrations to the empirical models and establish new models to study the space environment.

References

- [1] REITZ G. Characteristic of the radiation field in low earth orbit and in deep space[J]. *Zeitschrift für Medizinische Physik*, 2008, **18**(4): 233-243. DOI: 10.1016/j.zemedi.2008.06.015
- [2] National Research Council. HZE-Particle Effects in Manned Spaceflight[M]. Washington, DC: The National Academies Press, 1973
- [3] DURANTE M, CUCINOTTA F A. Physical basis of radiation protection in space travel[J]. *Reviews of Modern Physics*, 2011, **83**(4): 1245-1281. DOI: 10.1103/RevModPhys.83.1245
- [4] ESHAGH M, ALAMDARI M N. Perturbations in orbital elements of a low earth orbiting satellite[J]. *Journal of the Earth & Space Physics*, 2017, **33**(1): 1-12
- [5] SANTONI F, CORDELLI E, PIERGENTILI F. Determination of disposed-upper-stage attitude motion by ground-based optical observations[J]. *Journal of Spacecraft and Rockets*, 2013, **50**(3): 701-708. DOI: 10.2514/1.A32372
- [6] FENNELL J F, CLAUDEPIERRE S G, BLAKE J B, et al. Van Allen Probes show that the inner radiation zone contains no MeV electrons: ECT/MagEIS data[J]. *Geophysical Research Letters*, 2015, **42**(5): 1283-1289. DOI: 10.1002/2014GL062874
- [7] LI X, SELESNICK R S, BAKER D N, et al. Upper limit on the inner radiation belt MeV electron intensity[J]. *Journal of Geophysical Research: Space Physics*, 2015, **120**(2): 1215-1228. DOI: 10.1002/2014JA020777

Progress of Planetary Science in China*

HUI Hejiu^{1,2}, RONG Zhaojin², ZHANG Jinhai², HU Sen²,
LIN Honglei², WEI Yong², LIN Yangting²

1. State Key Laboratory for Mineral Deposits Research and Lunar and Planetary Science Institute, School of Earth Sciences and Engineering, Nanjing University, Nanjing 210023
2. Key Laboratory of Earth and Planetary Physics, Institute of Geology and Geophysics, Chinese Academy of Sciences, Beijing 100029

Abstract

The national and international progress in deep space exploration has greatly promoted the development of planetary science in China. Substantial progress in different areas of planetary science has been achieved in 2020–2022. In this report, we summarize the research achievements obtained in China in the last three years. The achievements include the research on geology, geochemistry, and space physics of the Moon, Mars, Mercury, Venus, giant planets, asteroids, and comets. The recent work on science objectives, mission payloads, and analytical capabilities that supports the lunar and deep space exploration program of China has also been introduced in this report. Finally, we report the progress on developments of discipline and research team of planetary science in China.

Key words

Planetary science, Progress, Exploration, Mission, Solar system

1 Research Progress of Planetary Science

1.1 Moon

The Chang'E-5 (CE-5) landing site is in the northern Oceanus Procellarum. CE-5 lander landed on the continuous ejecta of the Xu Guangqi crater within the eastern Eratosthenian-aged Em4 mare unit^[1–3]. The geological column of the CE-5 landing site was constructed through a synthesis of regional geology, the crater morphology technique to constrain regolith thickness, and the crater excavation technique to constrain mare flow thickness^[1,4]. CE-5 directly landed on and sampled the top of the 4–6 m-thick regolith^[1] at the landing site. The

lunar regolith formed on the Em4 mare flow with a thickness of about 50 m^[1]. There are no observable eruption fissures around the Em4 unit except for sinuous rilles. Detailed geomorphological investigations of the landing site yield four independent sinuous rilles in the northern Oceanus Procellarum, including Rima Sharp (1.9±0.3 Ga), Rima Mairan (1.4±0.2 Ga), Rima Louville, and Rima Harpalus^[4]. The majority of Em4 unit was produced by the eruption of Rima Sharp, whereas the deposits of Rima Mairan are limited to the southeast of the Em4 unit. Rima Sharp eruption started from a sheet flow followed by centration of lava flow in the late stage of eruption in which thermal erosion happened and the sinuous rille channel formed^[4]. Therefore, the returned CE-5 basaltic samples represent the lavas from

* Supported by National Natural Science Foundation of China (41941002, 41922031, 42125303) and China National Space Administration (D020205)

Received June 29, 2022

Rima Sharp. Qiao *et al.*^[5] performed an in-depth investigation into the geology of the specific CE-5 landing site and the nearby vicinity using high-resolution remote sensing datasets. Based on the geological characterizations around the landing site, a sequence of four geological events, including mare volcanism, tectonism, impact cratering and ejecta deposition, was identified. In particular, a northwest-southeast-direction and a northeast-southwest-direction secondary cratering features were identified across the CE-5 landing site, and their sources were traced back to Copernicus and Harpalus craters, respectively. The CE-5 mission may have collected materials ejected from these two Copernican-aged craters. Fu *et al.*^[6] also identified four major compositional groups (feldspathic highland materials, Imbrium basin ejecta, Aristarchus ejecta, and mare basalts) and several subgroups around the CE-5 landing site. Xie *et al.*^[7] quantitatively estimated the abundance of Distantly Sourced Particles (DSPs) in the regolith at the landing region using an updated ballistic sedimentation model. The results suggest that the total abundance of DSPs on the surface around the landing area varies from approximately 12% to 20%, and most of the DSPs on the surface are ejecta from the Pythagoras (about 5%) and/or Aristarchus (about 7%) craters.

The CE-5 lander carried four instruments including Landing Camera, Panoramic Camera (PCAM), Lunar Mineralogical Spectrometer (LMS), and Lunar Regolith Penetrating Radar to explore the landing region for supporting the sample collection and analysis. Bo *et al.*^[8] developed a catalogue of small craters (<100 m in diameter) using the centimeter-resolution images measured by the CE-5 Landing Camera, and found that the mean depth-to-diameter ratio of 231 craters in the CE-5 landing area is about 0.055. The diameters of these craters range from 7.0 to 371.2 m and the depths of these craters range from 0.21 to 45.9 m. The results indicate that the craters in the catalogue have a slightly low depth-to-diameter ratio compared with other larger craters and the small craters in the CE-4 landing area. Lin *et al.*^[9] analyzed the reflectance spectra acquired by the Lunar Mineralogical Spectrometer onboard the CE-5 lander on the lunar surface and estimated up to 120 parts per million (ppm) of water (OH+H₂O) in the lunar regolith, which is mostly attributed to solar wind implantation. A light-colored and surface-pitted rock was observed near the lander and its reflectance spectra suggest that it could be transported from an older basalt unit.

This rock exhibits a stronger absorption, near 2.85 μm , than the surrounding regolith, with an estimation of about 180 ppm of water if the model to determine water content of regolith is applicable to rock samples, which may suggest additional water from the lunar interior. The low water content of the regolith suggests the degassing of mantle reservoir beneath the CE-5 landing site. Su *et al.*^[10] constructed the hyperfine structures at the CE-5 landing site based on the Lunar Regolith Penetrating Radar data, suggesting that the top about 2.5 m of the landing site is dominated by fine grains with abundant rock fragments.

The lunar regolith samples returned by CE-5 mission have stimulated the research of lunar materials. Major contributions to lunar science have already resulted from the allocation of the first batch CE-5 regolith in the middle of 2021. The basic physical properties of bulk CE-5 regolith have been analyzed^[11,12]. The median grain size obtained via laser diffraction analysis is $55.24 \pm 0.96 \mu\text{m}$ ^[11], whereas that determined using optical microscope image analysis is $52.54 \mu\text{m}$ ^[12]. The bulk chemical compositions of CE-5 soil measured using instrumental neutron activation analysis are consistent with that of mare basalt^[12,13], which is also supported by the mineral compositions^[11,12]. This basalt has been argued to be low-Ti/low-Al/low-K type with rare-Earth-element contents lower than KREEP^[12]. The basalt clasts in CE-5 soils analyzed so far have a uniform young age, $2030 \pm 4 \text{ Ma}$ ^[14] and $1963 \pm 57 \text{ Ma}$ ^[15] from two independent groups. This is the youngest crystallization age reported for lunar basalts by radiometric dating, confirming that lunar volcanic activity lasted at least until 2 Ga. The μ value of the CE-5 basalt mantle source indicates that the CE-5 basalts were produced by melting of a KREEP-poor source^[14,15]. This is consistent with the petrogenesis of CE-5 basalts, which were produced by low-degree mantle partial melting and subsequent extensive fractional crystallization evidenced by major and trace elements, and strontium-neodymium isotopes^[16]. Therefore, the CE-5 basalts were not generated by high concentrations of heat-producing element in the deep mantle of CE-5 landing site, in contrast to its location in the Procellarum KREEP Terrane^[14-16]. Furthermore, the maximum water content of the parent magma of the CE-5 basalts was determined to be 283 ± 22 ppm and that of the mantle source was calculated to be 1–5 ppm, which is at the low end of the range estimated from mare basalts of about 4.0 Ga to 2.8 Ga^[17]. There-

fore, this low water content could not drive the young volcanism, whereas the mantle source of the CE-5 basalts could be dehydrated by previous melt extraction from the Procellarum KREEP Terrane mantle during prolonged volcanic activity^[17]. The apatites in CE-5 basaltic samples are F-dominated (0.91 wt%–3.93 wt%) with a Cl abundance range of 820 to 11989 ppm and a water abundance range of 134 to 6564 ppm^[18]. Apatite chlorine isotopic compositions vary from 4.5‰ to 18.9‰, positively correlated with the Cl abundances, suggesting that magmatic degassing of Cl-bearing species at or near the lunar surface during volcanic eruption could have resulted in a large Cl isotope fractionation^[18]. Olivine Ti contents of various basaltic clasts indicate that the CE-5 basalts originated from a low-Ti primary magma^[19], consistent with the low Ti content of bulk soil^[12]. On the other hand, a basaltic clast with extremely high ilmenite modal abundance has been suggested to be a high-Ti basalt with enriched REE contents^[20]. Different valence states of iron were discovered in the CE-5 soil, pure metallic iron, ferrous iron in olivine crystals, and ferric iron in the amorphous matrix^[21]. It has been demonstrated that the textures of the solar wind irradiation-damaged zone depend on the host mineral species, spherical nanophase Fe (npFe⁰) particles in the amorphized zone of pyroxene, elongated npFe⁰ in ilmenite, irregular npFe⁰ on the jagged surface of iron sulfide, no npFe⁰ found in Fe-poor merrillite, and vesicles found in the damaged zone of ilmenite and merrillite with different shapes^[22]. The comparison with Apollo samples shows no significant altitude-dependent effects on the space weathering, which is important for decoding the reflectance spectra of the Moon^[22]. On the other hand, a combined transmission electron microscopy and electron energy loss spectroscopy study reveals that the uppermost layer of soil grains exhibits the simultaneous coexistence of npFe⁰ with Si-rich material overlying an Mg-rich layer, as well as numerous irregular vesicles containing oxygen-rich (SiO and O₂) components embedded in the npFe⁰^[23]. These microscopic features are consistent with subsolidus olivine decomposition during impact-induced fragmentation or local heating processes, which may alter the reflectance spectra of the Moon^[23].

The diversified lunar meteorite studies in China have made important contributions to lunar science in the last couple of years. A new model has been proposed for the formation of lunar highlands anorthosites, which represent a feldspathic crust metasomatized by incompati-

ble-element-rich KREEP melts and mantle-derived partial melts rather than solely a derivative from the lunar magma ocean^[24]. This new proposed formation scenario is consistent with overlapping ranges of age and initial ϵ_{Nd} between lunar anorthosites and Mg-suite rocks, and with an overturn event of the cumulate mantle very early after primordial crust formation to produce the partial melts that metasomatized the crust^[24]. Calcium isotopic compositions of different lunar meteorites have been analyzed^[25], which are the first published lunar metal isotope data in China. The determined Ca isotopic compositions indicate a mean $\delta^{44/40}\text{Ca}$ value of $0.75 \pm 0.13\%$ for lunar crust, a $\delta^{44/40}\text{Ca}$ range of 0.96% – 1.11% for the lunar mantle, and the Ca isotopic composition of the bulk silicate Moon similar to the bulk silicate Earth^[25]. The oldest immiscible silica-rich melt observed in a zircon of NWA 10049 provides microscale evidence that evolved silica-rich melts were prevalent as early as about 4.38 Ga, implying a prolonged silicic magmatism on the Moon^[26]. This implication is consistent with the identification of a 4.32 Ga granitic fragment in the Th- and TiO₂-poor lunar breccia NWA 10447^[27]. This newly-discovered granitic fragment suggests that silicic magmatism may occur outside of the PKT of the Moon^[27]. Petrogeneses of two feldspathic meteorites NWA 1111^[28] and NWA 11460^[29], one mare basalt meteorite NWA 10597^[30], and one olivine gabbro meteorite NWA 6950^[31] have been carried out by different groups in the last couple of years. The Cr-Zr-Ca armalcolite in lunar rocks has been demonstrated to be loveringite using EBSD analyses^[32]. Several high-pressure phases have been discovered in the lunar regolith meteorites, including reidite in SaU 169^[33], tissantite and coesite in several feldspathic meteorites^[34]. The stabilities of these newly discovered phases were used to constrain the pressure and temperature ranges of meteoritic impacts on the Moon that facilitated the formation and lithification of lunar regolith^[33,34]. The Raman and FTIR spectra of plagioclase have also been used to investigate the shock history of lunar breccia meteorite NWA 4848, which is highly shocked with a pressure range of 20–48 GPa^[35]. This spectroscopic method has been applied to olivine and plagioclase of lunar meteorite NWA 13120, which has revealed a pressure higher than 20 GPa during shock metamorphism of this breccia^[36]. On the other hand, the mobility and deposition of sulfur- and phosphorous-poor fluid evidenced by the olivine veinlets observed in

lunar breccia NWA 11273 may have an endogenic origin on the Moon^[37].

The research on lunar space physics has shifted from macroscale to microscale in the last couple of years. Through detailed studies of satellite observations of plasma and electromagnetic fields near the Moon, the key evidence, manifestations and consequences of the interaction between the Moon and the solar wind were found and analyzed. Zhang *et al.*^[38] studied the interaction of small-scale lunar remnant magnetic fields with the solar wind, and found low-frequency whistling fluctuations propagating along the magnetic field lines. Their results demonstrated that ions are not the source of the low-frequency fluctuations, and the diversion of the electron fluid around the remnant magnetic field is the source for these low-frequency whistle-waves. Zhang *et al.*^[39] found that the magnetic field and plasma moments are periodically about every 2 lunar radii in lunar wake, and that the periodic increase in plasma temperature in the wake is direct evidence for the periodic intrusion of these reflected ions from remnant field. Using the magnetic field observations from the Lunar Prospector satellite, Zhang *et al.*^[40] carried out an in-depth study of the magnetic field disturbance near the Moon, and found that the lunar surface magnetic field disturbance exhibits a completely new spatial distribution characteristic, and that near the lunar terminator, there is asymmetric distribution about the direction of the solar wind electric field, and revealed that the pickup of solar wind-reflected particles is a new mechanism for the enhancement of the near-lunar surface magnetic field. Wei *et al.*^[41] proposed a hypothesis that the lunar soil on the farside could have recorded the evolution of Earth's dynamo process because the Earth's oxygen ions could be transported and implanted to the farside surface once the Earth's dynamo started. Wang *et al.*^[42] used data from the Chandrayaan-1 spacecraft to map water at the Moon's poles and found water levels remain about the same all month, and do not change during the period when Earth shields the Moon from the solar wind, which indicate Earth's "wind" might serve as a bridge to the Moon, providing an additional source of water. Wang *et al.*^[43] show that the Energetic Neutral Atom (ENA) cutoff energy and temperature are lower on the duskside than on the dawnside at the same solar wind energy using The Advanced Small Analyzer for Neutrals (ASAN) onboard the Yutu-2 rover. The observation difference of ENA

and solar wind between the dawnside and duskside is possibly caused by solar wind deflection and deceleration on the duskside, which can be attributed to the interaction between solar wind and the lunar magnetic anomalies located nearby in the northwestern direction of the CE-4 landing site. Shang *et al.*^[44] show that the magnetosphere can flap across the Moon much like a windsock, exposing it to hazardous solar wind particles. Previous simulations suggest that lunar satellites and astronauts on the surface could be considered safe during a full moon while they reside within the magnetosphere. However, the full moon may not be protected by Earth's magnetic field after all. They showed that the lunar exposure could occur even without a shockwave when the solar wind blows sideways, suggesting that the exposure could occur even more commonly than previously thought^[44].

1.2 Mars

China's first Mars rover, Zhurong, landed on the southern Utopia Planitia successfully on May 15, 2021. Many studies have been conducted to characterize the geologic features around the landing site. The landing region is within the Late Hesperian Lowland (LHL) unit and its estimated surface age is around 3.1–3.4 Ga^[45–47]. Vastitas Borealis Formation (VBF), likely oceanic deposits, covers most of LHL unit, including the landing site. Orbital imagery data show many geomorphic expressions such as pitted cones, mesa ridges, polygonal troughs, and various types of impact craters^[45–48]. The presence of layered ejecta from impact craters strongly suggests that water/ice/volatile in the subsurface of landing site has changed through time^[49]. The most prominent geomorphology is pitted cone that has various formations and pivotal implications, including volcanic origin (scoria cones, rootless cones, and tuff cones/rings), ice-related (pingos), and sedimentary origin (mud volcanos).

The regional evolutionary history of the landing area was synthesized and outlined by Wu *et al.*^[46], which provides an important framework to support in-situ investigation data analysis and interpretation on a broader scale. The Utopia basin formed during a huge impact event in the early Noachian. This basin has been modified and filled by sedimentary and volcanic materials. Subsequently, the northern lowlands were covered by Early Hesperian-aged volcanic plains which were then deformed by wrinkle ridges in the Middle Hesperian.

Late Hesperian-aged outflow channels were emplaced, producing sedimentary deposits that obscured and modified the ridged plains. Loss of flooding effluents in a geologically short time resulted in the formation of VBF, which is considered as a residual sedimentary deposit. The giant polygons formed due to tectonic rebound after the removal of the water/ice load or volumetric compaction. Finally, Amazonian-aged lava flows and lahars emanating from the Elysium Mons draped the southeastern portion of the basin.

Ye *et al.*^[47] mapped the distribution of geologic features around the landing site of the Zhurong rover closely. Strikingly, troughs and pitted cones are located in the northeast and southwest of the landing site respectively. This geomorphology transition boundary is not a straight line along the latitude but follows the topographic change of the basin. The troughs may have been formed by tectonic uplift and extension of the utopian basin resulting from sublimation of ice-rich basement or volume compaction. The spatial correlation between the troughs and pitted cones could partly be explained by the latitude-dependent water-ice abundance, thickness or possibility of melting. The topography has an important influence on the distribution of landforms, and sediment and ice may be the driving forces of landform development. By comparing the height/basal aspect ratios between the pitted cones around the landing site to terrestrial mud volcanoes, Ye *et al.*^[47] found similar relationships. Furthermore, these cones are also similar in scale to other putative mud volcanoes on Mars. Therefore, they thought pitted cones are likely mud volcanoes, which have important implications for climate and astrobiology of early Mars. A conceptual model was proposed: the magma chamber which fed these dike swarms could have been a heat source for maintaining the mobility of the mud reservoir and groundwater system. The rapid burial of aqueous sediments after water activities could have also fed an enormous mud reservoir around the Utopia basin and provided favorable conditions for sediment upwelling and methane releasing.

On a smaller scale, Zhao *et al.*^[48] outlined the key questions associated with the evolution of the northern lowlands through high resolution geologic mapping. They suggested that several questions could be addressed by the Zhurong rover, including (a) origin of pitted cones, (b) origin of graben-like troughs, (c) evi-

dence for ancient oceans, (d) evidence for mudflows, (e) origin of surface/near surface rocks, (f) nature of the Amazonian climate record, (g) impact crater stratigraphy, (h) nature/origin/age of aeolian features, and (i) stratigraphic sequence. A possible scenario of geological evolution was proposed for the landing region of the Zhurong rover. Basaltic lava was emplaced on the underlying Noachian cratered basement during the Early Hesperian, followed by the water/ice containing VBF materials. Amazonian lava flows or mudflows appear to have been emplaced on top of the VBF materials around about 757 Ma. Water ice and/or carbon dioxide ice are interpreted to have been deposited into the relatively loose materials due to changes in eccentricity and obliquity that altered the climatic conditions. Relatively light-toned aeolian bedforms developed and were subsequently covered by airfall dust.

The research progress on the Martian meteorites in the last three years focused on the petrogeneses^[50,51], hydrothermal activities^[52–57], dating^[50,55], and shock metamorphism^[58,59]. Mars could have a long duration (about 1.6 Ga to 150 Ma) of hydrothermal activities evidenced by the petrography, mineral chemistry, water abundance, hydrogen and chlorine isotopes, rare Earth elements, U-Pb and Sm-Nd dating of regolith breccia (NWA 7034 and its pair), olivine phyric shergottite NWA 6162, basaltic shergottite NWA 8656, and many other shergottites^[52–55,57]. Most Martian meteorites have experienced strong shock metamorphism which resulted in the formation of high-pressure phases of coesite, ringwoodite, and widespread of maskelynite^[58,59]. Asteroid impacts on Mars could have supplied adequate energy to melt the underground ice to create a temporary hydrothermal system, facilitating the water-rock interaction on Mars^[53]. The petrogenesis studies on the basaltic shergottite NWA 8653 and nakhlite NWA 5790 indicated that the Martian mantle is chemically heterogeneous^[50,51].

The climate of Mars has changed from a wet and hot environment to a dry and cold condition evidenced by the presence of phyllosilicates in old terrain (>3.0 Ga) and evaporate salts in young terrain (<3.0 Ga). The alteration products on Mars' surface have carried key records of how Mars has evolved into current state. Systematic laboratory simulations on the formation of salts and their derivatives (chloride, perchlorate, brines, akaganite, and manganese oxides) have been carried out to

study the formation conditions of these secondary phases and the environmental clues for understanding the climate evolution of Mars^[60-64]. Atmospheric escape played an essential role in Mars's water history and climate evolution. The Mars Atmosphere and Volatile Evolution (MAVEN) spacecraft carried out remote sensing measurements of the Mars upper atmosphere using an Imaging UltraViolet Spectrograph (IUVS) onboard. Using these remote sensing measurements, Qin^[65,66] reported comprehensive quantifications of the atmospheric state and escape rate associated with the O and H atoms in Mars' upper atmosphere. The solar cycle, seasonal, diurnal, and dust-storm-driven variations have been documented. A long-standing discrepancy between the Mars upper atmospheric temperatures derived from different methods has also been resolved^[66], showing that the daytime Martian exobase temperature varies typically in the range of about 150–280 K.

Mars has patches of localized intense remnant crustal fields, particularly in the southern hemisphere, in contrast to the induced magnetosphere of Venus and the intrinsic magnetosphere of Earth. These crustal fields contribute to solar wind interactions, complicating the Martian space environment. NASA's MAVEN spacecraft carried both magnetometer and plasma instruments enabling us to study the space environment of Mars. Using the scientific data measured by MAVEN, our Chinese team has made fruitful findings on Martian space environment. Using the plasma data and magnetic field data of MAVEN, Liu *et al.*^[67] statistically surveyed the distribution of solar wind parameters in the upstream of a bow shock, and revealed the radial profile of solar wind parameters between Earth-Mars and evaluated its variation with solar activity level. Liu *et al.*^[68] statistically surveyed the occurrence of Proton Cyclotron Wave (PCW), and found that the amplitude and occurrence frequency of PCW is higher when the orientation of IMF is closer to the Sun-Mars line. Wang *et al.*^[69] developed an automatic algorithm to identify the crossing of PEB by MAVEN based on the electron spectrum, which could be applied further to the dataset of MEX to study the long-term variation of Martian ionosphere. Zhang *et al.*^[70] studied an event of periodical plasma cloud at low altitude, and suggested that the cloud was triggered by reconnection driven by solar wind and crustal field, and that the cloud could carry planetary ions to escape significantly. Fan *et al.*^[71] statistically studied the interaction of solar wind with Martian crustal field,

and noticed that the solar wind flow can be deflected by the crustal field. Previous crustal field models were established based on the MGS data at the altitude of about 400 km, and the MAVEN's data collected down to the altitude of 120 km provides an opportunity to establish a more accurate model. Based on both datasets of MGS and MAVEN, Gao *et al.*^[72] developed a new Martian crustal field model which has the least fitting error than the previous models. To clarify the scientific objectives of the Lander of China's Mars mission, Li *et al.*^[73] developed a regional high-resolution crustal field model based on both datasets of MGS and MAVEN, and inferred the magnetic field distribution on the Mars surface. Zhang *et al.*^[74] statistically studied the 3-D magnetic field configuration around Mars, and found that the field structure in Martian magnetotail has an evident hemispheric asymmetry along the direction of solar wind electric field. Using the data from ASPERA-3 and MARSIS onboard Mars Express, Qin *et al.*^[75] found double-peaked Total Electron Content structures in the Martian crustal magnetic cusp regions and analyzed the possible links between this new phenomenon in the Martian nightside ionosphere with the patterns of precipitating electrons. The upper atmosphere and ionosphere of Mars is a region full of variations and frequently affected by the factors from above (solar radiation, solar wind, *etc.*) and below (dust storms, gravity waves, *etc.*). Qin *et al.*^[76] compared the observed neutral densities and MCD simulated neutral densities and found that in some cases MCD simulation results largely underestimated neutral densities. Recently, China's Mars mission team released the original plasma data sampled by Tianwen-1 spacecraft en route for Mars. Zhang *et al.*^[77] and Fan *et al.*^[78] processed the data and found that the plasma instrument works well in measuring the solar wind. More work will be carried out in the near future to investigate the data from plasma instrument of "Tianwen-1".

1.3 Mercury

Mercury, the closest planet to the Sun, is the only terrestrial planet other than Earth owning a global dipolar magnetic field in the solar system. Mercury's dipole moment, however, is only about 4/10000 of Earth's dipole moment. Furthermore, Mercury has no atmosphere but possesses a tenuous surface-bounded exosphere. As the closest planet to the Sun, Mercury encounters a much stronger impingement of solar wind, whose den-

sity and dynamic pressure are an order of magnitude higher than those at Earth, and thus, Mercury has a much smaller, weaker and more dynamic magnetosphere than Earth. Using the scientific data measured by MErcury Surface, Space ENvironment, GEochemistry, and Ranging (MESSENGER) orbiting Mercury from March 2011 to April 2015, our Chinese team has made fruitful findings about Mercury's magnetosphere, which enriches the knowledge and understanding of Mercury's space environment. Zhong *et al.*^[79] found that the direction of Interplanetary Magnetic Field (IMF) can modulate the scale of magnetopause that the magnetopause is inflated when IMF is quasi-parallel to solar wind, and shrunken when IMF is quasi-perpendicular to the solar wind. In addition to the large-scale magnetospheric field structures, many transient or dynamic processes were surveyed. Using the state-of-the-art technique, Zhang *et al.*^[80] studied the oscillation of magnetic field in magnetotail and argued that the oscillation with a period of about ten seconds can be propagated as kink-like waves from one tail flank to the opposite flank. Zhong *et al.*^[81,82] studied an event of crossing the diffusion region of reconnection in magnetotail and found evidence of giant flux rope/ plasmoid in tail plasma sheet, suggesting that the Mercury magnetotail is highly spatial-temporal dynamic under the "strong-driven" by solar wind. With the data-based magnetic field model, Jang *et al.*^[83] applied a series of test particle simulations to study the charged particle dynamics around the polar cusp and found that the polar cusp is capable of trapping energetic ions. Zhao *et al.*^[84] investigated the proton properties in Mercury's magnetotail plasma sheet, and the results reveal the non-adiabatic nature of proton in the central plasma sheet. It has been much debated whether Mercury's dipolar magnetic field could trap an ensemble of charged particles that, analogous to the Earth's ring current, drift as a westward current around the planet. Based on the analyses of plasma data and particle tests, Zhao *et al.*^[85] recently argued that Mercury has a westward ring current in the nightside inner tail, but becomes bifurcated when moving to the dayside high-latitude cusps. The existence of Mercury's ring current also indicates the magnetic storm at Mercury. Zong *et al.*^[86] derived the Disturbance storm time (*Dst*) index at Mercury based on a spacecraft-based *Dst* algorithm, and caught an Earth-like magnetic storm event just before the end of the MESSENGER mission. Nonetheless, the analysis of magnetic field by Shi *et al.*^[87] demonstrated

that there is no significant Earth-like ring current flowing westward around Mercury, but found, for the first time, an eastward current encircling the planet near the night side equator with an altitude of about 500–1000 km. The eastward current is closed with the dayside magnetopause current and could be driven by the gradient of plasma pressure as a diamagnetic current.

1.4 Venus

Venus, the closest planet to Earth, has neither a global dipole field nor an intrinsic remnant field. Venus only relies on its ionosphere as an obstacle to solar wind, and the interaction with solar wind results in an induced magnetosphere. The Venusian magnetosphere was previously surveyed by Pioneer Venus Orbiter (PVO, 1978–1992), but the covered region is restricted to the distant downstream tail (8–12 Venusian radii). The ESA's mission, Venus Express (2006–2014), with state-of-the-art instruments, can cover the near tail (0–3 Venusian radii). Using the scientific data measured by Venus Express, our Chinese team has made fruitful findings about Venusian space environment. The bow shock is the outermost boundary of Venusian space environment. Combining the dataset of PVO and Venus Express, Han *et al.*^[88] investigated the variation of the boundary, called ionopause, between ionosphere and the solar wind, and found that the altitude of ionopause increases with the solar EUV radiation. Based on the data analyses of Venus Express, Gao *et al.*^[89] reported the evidence of crossing the ion diffusion region of magnetic reconnection in Venusian plasma sheet, which demonstrated that the Venusian plasma sheet is highly dynamic and favors the triggering of magnetic reconnection.

1.5 Giant Planets

Literally, magnetic dipolarization describes the process when a magnetic field line change from a stretched configuration to a dipole shape. Magnetic dipolarization is expected as a consequence of substorm current wedge formation, during which the cross-tail currents are diverted into the ionosphere via field-aligned currents. The direction connection between dipolarization and auroral intensification was not yet made until the Juno era. Using coordinated observations from Juno and the Hubble Space Telescope, Yao *et al.*^[90] reveal that the auroral injection is associated with dipolarization injection, which is known to cause hot plasma injection in

the magnetosphere. Moreover, their results show that the auroral dawn storm is likely associated with magnetic reconnection, which continually produces plasma injections in the dawn-side magnetosphere, leading to multiple auroral injection structures when rotating to larger local times. Their proposed picture is consistent with that the poleward initiating auroral signature is likely a signature of magnetic reconnection. Using the joint measurements from Juno and the Hubble Space Telescope, Guo *et al.*^[91] showed the evolution of a double-auroral arc on the dawnside from observations by the Hubble Space Telescope, together with simultaneous in situ observations from the Juno spacecraft provide direct evidence of magnetic reconnection and magnetic dipolarization. Their results indicate that the evolution of the double-arc structure is likely a consequence of the non-steady progress of magnetic reconnection.

Besides the reconnection and dipolarization processes, plasma waves are known to play key roles in driving auroral emissions, while the observation evidence is mostly for the terrestrial environment. Using the large datasets from the Hubble Space Telescope and Juno since 2016, Pan *et al.*^[92] showed coherence between auroral emissions and Alfvénic plasma wave, which provide direct evidence for the wave driving aurora at Jupiter. Moreover, the low frequency compressional Alfvénic wave is found to modulate electromagnetic ion cyclotron waves that could efficiently scatter heavy ions to produce the energetic soft X-ray auroral emission^[93].

Research done with a newly developed global magnetohydrodynamic model of Jupiter's magnetosphere provides evidence in support of a previously controversial and criticized idea that Jupiter's polar cap is threaded in part with closed magnetic field lines rather than entirely with open magnetic field lines, as is the case with most other planets in our solar system^[94]. The results finally solved why Jupiter's polar cap emission is not as expected in the textbook used in past decades.

Besides Jupiter, good progress is made in the global picture of Saturn using the Cassini large dataset. The distributions of magnetic reconnection and the associated structures, such as plasmoids are established by several groups in China^[95-97]. The distribution of low-frequency waves and the associated connection to solar activities are systematically analyzed^[98]. In the past years, several Chinese groups have also made significant progress in Saturn and Jupiter on the radiation belt^[99-103] and radio

emissions^[104,105]. Guo *et al.*^[91] found that the formation of the double-arc structure on the main aurora was related to the magnetic reconnection process in the magnetosphere. By comparing observations on Saturn, Jupiter and Earth, Hao *et al.*^[99] found that the global convection electric field could accelerate radiation belt electrons on giant planets more efficiently than on Earth. This process is essential on giant planets due to their fast rotation and southward intrinsic magnetic field. The properties of the global convection electric field have also been systematically studied^[102]. Sun *et al.*^[101] revealed the impact of such convection on ions.

Deep dielectric charging/discharging is a serious space environmental effect on spacecraft in Jovian planets' orbits. Yu *et al.*^[106] used GEANT4, a Monte Carlo toolkit, and Radiation-induced Conductivity (RIC) to calculate deep dielectric charging effects for Jovian planets. The results were compared with the criteria for preventing deep dielectric charging effects in Earth orbit. The findings show that effective criteria used in Earth orbit are not always appropriate for preventing deep dielectric charging effects in Jovian orbits. Generally, Io, Europa, Saturn ($RS = 6$), Uranus ($L = 4.73$), and Ganymede missions should have a thicker shield or higher dielectric conductivity, whereas Neptune ($L = 7.4$) and Callisto missions can have a thinner shield thickness or a lower dielectric conductivity. Moreover, dielectrics grounded with double metal layers and thinner dielectrics can also decrease the likelihood of discharges.

1.6 Asteroids

A quantitative two-endmember mixing model of the noncarbonaceous (NC) bodies has been developed using the isotopic anomalies of different elements (Ca, Ti, Cr, Fe, Ni, Mo, and Ru) with different cosmochemical behaviors^[107]. Therefore, the isotopic anomalies of NC bodies for all the considered isotopes, including the isotopic anomalies that are difficult to measure or have been altered by spallation processes, can be calculated using this mixing model, as well as the mixing proportion between the two endmembers in each NC body and the feeding zones of the NC bodies^[107]. The estimated feeding zones of NC bodies indicate a large population of interlopers in the main asteroid belt and an indigenous origin of Vesta, and that the orbits of Jupiter and Saturn during the formation of terrestrial planets were likely to be more circular than their current ones^[107].

Detailed physical, petrographic, and isotopic system-

atic studies on Ca-Al-rich Inclusions (CAIs), the first condensation solids from solar nebula, and Al-rich chondrules, have been conducted on Kainsaz (CO₃), Ningqiang, Allende (CV₃), and NWA 3118 (CV₃) in the last three years^[108–114]. These studies indicate that the CAIs could have experienced post-formation alteration evidenced by triple oxygen isotope compositions probably on the parent bodies^[108,109,111,112]. The petrology, mineralogy, bulk compositions, rare Earth element abundances, and in situ oxygen isotopic compositions of Aluminum-Rich Chondrules (ARCs) from various carbonaceous chondrites revealed that the ARCs formed by melting of mixtures of diverse refractory components with Ferro Magnesian Chondrules (FMC) in the FMC-forming region^[113]. The potassium isotope measurements on chondritic components in meteorite Allende display that the nominally K-free refractory minerals are enriched in heavy K isotopes with $\delta^{41}K$ variation of -0.30% to -0.25% and the chondrules have lighter $\delta^{41}K$ values (-0.87% to -0.24%)^[110]. The correlation of K isotope with the components indicates that most of the Allende chondritic components experienced aqueous alteration and their K isotopic compositions are the ramification of Allende parent-body processing instead of primary nebular signatures^[110].

Many studies on the chondrites and achondrites have been carried out in the last three years. Olivine in diogenite NWA 8321 has been partly replaced by orthopyroxene, troilite, and minor metal, indicating a sulfur-involved metasomatism in the interior of Vesta^[115]. Sulfurization was also identified in monomict eucrite NWA 11591^[116]. A new occurrence of corundum was identified in eucrite NWA 8647, occurring as a mineral inclusion in a highly deformed pyroxene fragment^[117]. The disproportionation of iron in eucrite NWA 11592 reflects that the strong shock metamorphism took place on its parent body^[118]. Some metallic-Cu-bearing mineral assemblages have been identified in type-3 ordinary and CO type chondrites^[119]. The parent body of ungrouped achondrite NWA 7325 could have had sulfur-rich magmatism^[120]. Two unusual fragments dominated by Ca, Fe-rich olivine with various amounts of Al, Ti-rich augite, anorthite, oxide minerals, Ca-phosphate mineral, FeNi metal, enstatite, and less Al, Ti-rich augite, have been identified in CH3 carbonaceous chondrite SaU 290, revealing a new basaltic planetesimal^[121]. The U-Pb dating of phosphates in silicate inclusions of IIE iron meteorites^[122] could constrain the formation time of

their parent bodies and the following strong asteroid impact events. Noble gases of meteorites have been measured to constrain their exposure histories^[123,124]. The discovery of nanophase iron particles in shock-induced melt veins and pockets in ordinary chondrite supports the decomposition of host silicates under high temperature and pressure conditions^[125].

1.7 Comets

Sungrazing comet C/2011 W3 (Lovejoy) shows a distorted and unconventional tail shape near the perihelion ($1.2R_s$). Hou *et al.*^[126] simulated the dynamics of charged particles (ions and dust particles) released from the comet based on the modeling results of corona and inner heliosphere. They found that dust particles near the sun are affected by strong magnetic Lorentz forces, unlike dust particles farther away from the sun, which are mainly affected by the sun's gravity and radiation pressure. Based on their simulations, they proposed that the magnetic mirror effect, which bounces charged dust particles back from the sun, is considered one of the key causes of dust-free zones^[126]. They further found that the ions moved mainly along magnetic field lines, at an acute angle to the direction of the comet's movement. The direction of movement of the comet's ions is determined by the comet's speed and coronal magnetic field, which is responsible for the distinctive tail shape of C/2011 W 3 near the perihelion. In addition, ion particles undergo vertical drift motions, dominated mainly by electric field drift, which is similar to and can be used to approximate the lateral velocity of the solar wind in its source region.

The Parker Solar Probe (PSP) aims to explore new solar winds near the sun. The PSP is also expected to encounter small objects such as comets and asteroids. He *et al.*^[127] surveyed ephemeris for recent encounters and then modeled the interaction between the released dusty plasma and the solar wind plasma. On 2 September 2019, a comet-like object 322P just passed its perihelion, approaching the heliocentric distance of 0.12 AU, swept by the PSP at a relative distance of 0.025 AU. He *et al.*^[127] showed the dynamics of dust particles emitted from 322P, forming a curved dust tail. The plasma and magnetic field states were sampled and illustrated along the path of the PSP in the simulated inner heliosphere, and the simulated magnetic field sequences were directly compared with the in-situ measurements of PSP. By comparison, they concluded that

322P may be at a low activity level, emitting limited dust plasma during the evolution of becoming a "rock comet"^[127]. They also showed images of solar wind streamers recorded by the Wide Field Imager (WISPR), showing signs of dust bombardment superimposed on images with messy tracks. They found 322P's transition from dark to relatively bright streamer during perihelion passage from the Large Angle and Spectral Coronagraph (LASCO), and performed a simulation to confirm 322P's flight from relatively fast to slower solar currents, thus altering the state of local plasma flows^[127].

1.8 Meteoritic Impacts on Earth

A large number of meteorites have been recovered from Gobi desert in northern and western China in the last decade^[128,129]. At least 42 dense meteorite collection areas have been discovered, mainly in northern and western China. Most of the approved meteorites recovered in China are ordinary chondrites and iron meteorites with a few CO₃ chondrite, diogenite, ureilite, brachinite, and eucrite^[129,130]. The ongoing collection tour will supply more extraterrestrial materials to the planetary science community in the near future.

A new impact crater has been identified in Heilongjiang province and named as Yilan, which is supported by the presence of planar deformation features in quartz from the unmelted granite in drillcore samples^[131]. Detailed studies of high-pressure polymorphs of silica and feldspar have been carried out in samples from Xiuyan crater^[132,133]. The first natural redite was identified in terrestrial samples, which are from Chicxulub impact crater^[134]. A systematical search of Australasian microtektites in the Chinese Loess Plateau showed that no confirmed microtektites were discovered in the 19 loess sections, indicating that Australasian microtektites are not a widespread stratigraphic marker in the Chinese Loess Plateau^[135].

2 Mission Support to the Lunar and Deep Space Exploration

2.1 Science Goals and Mission Objectives

CE-4 mission has three main science objectives: (i) low-frequency radio astronomical observation, (ii) geomorphology, mineral compositions, shallow subsurface structure of and near the landing area, and (iii) lunar environment at farside of the Moon^[136,137]. To achieve

these objectives, different payloads were installed on the lander, rover or relay satellite to detect the solar low frequency radio radiation (0.1–40 MHz) and the low frequency radio radiation from other celestial bodies in solar system and galaxy (0.1–80 MHz), analyze the chemical composition (element content and distribution), mineral compositions (mineralogical content and distribution), regolith thickness and shallow subsurface structure in situ, and measure the electrically neutral component, neutrons, γ -rays, fast neutron flux, and thermal neutrons flux, neutral atom, and cation on the farside of the Moon^[136].

There are two scientific objectives for CE-5 mission: (i) to carry out in situ exploration in sample collection area, collect the samples with the scientific support from the in situ analyses and establish the connection between the data acquired on the Moon and those analyzed in the laboratory, and (ii) to systematically study about the lunar regolith samples in the laboratory, analyze the structure, physical properties, and mineralogical, chemical and isotopic compositions of lunar samples and investigate the origin and evolution history of the Moon^[137].

The scientific objectives of Tianwen-1 mission include: (i) map the morphology and geological structure, (ii) investigate the surface soil characteristics and water-ice distribution, (iii) analyze the surface material composition, (iv) measure the ionosphere and the characteristics of the Martian climate and environment at the surface, and (v) perceive the physical fields (electromagnetic, gravitational) and internal structure of Mars^[138–140]. To achieve these objectives, a scientific payload system, including those on the orbiter, the lander, and the rover, was developed to carry out these specific tasks: (i) to analyze the Martian ionosphere and survey the interplanetary environment, (ii) to detect Martian surface and subsurface water ice, (iii) to survey the characteristics of soil and structures of Mars, (iv) to survey the characteristics of topography and geomorphology of Mars, and (v) to analyze the composition of the Martian surface material for the orbiter, and (i) to study topography and geological structure of the roving area, (ii) to survey the soil structure (profile) of the roving area and to search for water ice, (iii) to survey elements, minerals and rock types of the roving area, and (iv) to survey the atmosphere physical characteristics and the

surface environment of roving area for the rover^[140].

2.2 Science Payloads in China's Missions

CE-4 mission has six scientific payloads^[136]: three on the lander, including the Landing CAMera (LCAM), the Terrain CAMera (TCAM), and the Low Frequency Spectrometer (LFS); and three on the rover, including the Panoramic CAMera (PCAM), the Lunar Penetrating Radar (LPR), and the Visible and Near-Infrared Imaging Spectrometer (VNIS). The LFS is newly developed for CE-4 and the others are inherited from CE-3. Besides, there are also three international joint collaboration payloads: the Lunar Lander Neutrons and Dosimetry (LND) on the lander with Germany, the Advanced Small Analyzer for Neutrals (ASAN) on the rover with Sweden, and the Netherlands-China Low-frequency Explorer (NCLE) on the relay satellite with the Netherlands.

Tianwen-1 mission has thirteen scientific payloads^[138,140]: seven onboard the orbiter, including two cameras, the Mars-Orbiting Subsurface Exploration Radar, Mars Mineralogy Spectrometer, Mars Magnetometer, Mars Ion and Neutral Particle Analyzer, and Mars Energetic Particle Analyzer; and six on the lander and rover, including Multispectral Camera, Terrain Camera, Mars-Rover Subsurface Exploration Radar, Mars Surface Composition Detector, Mars Magnetic Field Detector, and Mars Meteorology Monitor.

CE-7 plans to be equipped with two science payloads on the relay satellite, five on the orbiter, seven on the lander, four on the rover, and one on the mini-flying probe^[141]. The two science payloads on the relay satellite are a Grid-based Energetic Neural Atom Imager and a lunar orbit Very Long Baseline Interferometry system. The orbiter would carry High Resolution Stereo Mapping Camera, Miniature Synthetic Aperture Radar, Wide Band Infrared Spectrum Mineral Imaging Analyzer, Lunar Neutron Gamma Spectrometer, and Lunar Orbit Magnetometer. The lander would carry Landing Camera, Topography Camera, In-situ Measuring System of Volatiles and Isotopes on Lunar Surface, Lunar Soil Section Thermal Current Measuring, Lunar Surface Thermometer, Extreme Ultraviolet Camera, and Lunar Seismograph. The rover would carry Panoramic Camera, Rover Magnetometer, Lunar Penetrating Radar, and Lunar Raman Spectrometer. The Mini-Flying flight would carry Water Molecule and Hydrogen Isotope Analyzer.

2.3 Analytical Procedures and Methods for Planetary Materials

A series of in situ and high precisions analytical protocols and techniques have been established in the last several years, including water abundance measurements in olivine and pyroxene^[142], high spatial resolution measurements of volatile elements^[53], high-resolution U-Pb dating in zircon^[143], elemental mapping technique^[144], FIB-SEM technique for manipulating micrometer-sized particles^[145], and high precision measurements of Nd^[146] and Cr^[147] isotopic compositions. Different facilities for the curation of CE-5 lunar regolith have been constructed, which have supported a series of scientific research on these precious samples.

3 Developments of Discipline and Research Team of Planetary Science

About twenty years ago, China did not have its own spacecraft mission to study space physics exclusively, let alone the missions to the Moon and to Mars. Who could have imagined that China has successfully implemented the “Double Star” mission to explore Earth’s magnetosphere, the series of lunar missions of “CE-1, -2, -3, -4, -5”, and the first Mars mission of “Tianwen-1” over the past twenty years. These successful missions have undoubtedly driven the rapid development of China’s planetary science. This is because more and more planetary scientists are needed to become involved in analyzing the scientific data returned by spacecraft, and more scientific requirements are presented to regulate the mission as well as the scientific payloads onboard spacecraft.

In such circumstances, different branches of planetary science and their respective communities have developed gradually in China, such as planetary space physics, planetary atmosphere, planetary geology, planetary geochemistry, planetary interior dynamics, exoplanets, terrestrial small body, astrobiology, *etc.* Meanwhile, a few universities, represented by the University of Chinese Academy of Sciences (UCAS), have started to provide the related courses to educate students in planetary science. The academic consortiums and organizations of planetary science have also been established, like the China University Planetary Science Al-

liance, the Lunar Science and Comparative Planetology Committee of Chinese Space Science Society, the Planetary Committee of Chinese Astronomical Society, and the Planetary Physics committee of Chinese Geophysical Society. Moreover, to advertise the original studies of China's planetary science, the first international peer-reviewed journal of planetary science of China, named "Earth and Planetary Physics" (EPP), was issued in 2017. In summary, planetary science as a field of study has bloomed within China over the past 20 years.

In contrast to the booming development of China's planetary science, China, however, had not yet held its own national planetary conference. Due to this, many Chinese scientists have previously had to attend international conferences, such as the Lunar and Planetary Science Conference (LPSC) and the EuroPlanet Science Congress (EPSC) to seek academic communications. Given the rapid global development of planetary science and the current state of the COVID-19 overseas, Chinese scientists are more eager than ever to attend a nationally held conference. The time seemed ripe to hold a comprehensive planetary conference for the wide communities of planetary science in China.

The conference, the first Chinese Planetary Science Conference (CPSC), organized by the Planetary Physics committee of Chinese Geophysical Society, took place on 18–21 June 2021 in Suzhou, Jiangsu province of China, which will also serve as the base of the aerospace industry in China^[148]. CPSC received about 500 abstracts covering a wide range of disciplines within planetary science, including planetary space environment, planetary atmosphere, planetary geology, planetary interior dynamics, asteroids, comets, exoplanets, biology, future missions to space, and probing techniques, etc. It is also astounding to note that the conference attracted 1020 attendees together from 106 affiliates, including the attendees from the universities of Macau and Hong Kong. The size is comparable to that of the EPSC (regularly around 1000 attendees each year), and about half that of LPSC (regularly around 1800 attendees each year). It is regretful that CPSC was not open to the world yet due to COVID-19 restrictions on travel, but some non-Chinese scientists who have lived for a long time in China were able to attend this conference, and were also able to speak English in the sessions they attended. The sheer number of attendees demonstrates that planetary science within China has

developed rapidly in recent years and the number of planetary scientists has already grown to a massive scale.

Overall, some clear conclusions about the current status of China's planetary science can be drawn from this conference.

(1) Half of the attendees were students, and female scientists occupied nearly a quarter of the total attendees. Thus, the current community of China's planetary scientists is very youthful, and female scientists play an important role in this community.

(2) About half of the attendees were from the institutes of Chinese Academy and Sciences (CAS), which means that the main force to conduct planetary science in China is led by CAS.

(3) The abstracts received by the conference covered various aspects of planetary science, which implies that planetary science is being treated as a system science, and the interdisciplinary nature of planetary science in China is maturing.

(4) The abstracts of planetary space environment and planetary geology dominated the abstracts received by the conference, which suggests that the communities of planetary space and planetary geology are of particular importance to the current study of planetary science in China. The reasons are understandable, because, on one hand, conventional Earth space scientists can easily change to study planetary space science, and on the other hand, the series of China's Chang'E missions and the Mars mission of "Tianwen-1" brought about the rapid development of planetary geology.

(5) To encourage and facilitate comprehensive discussions, most presentations, including the presentations of graduate students, were delivered as oral presentations, which strengthens the training and education of young scientists, in particular. In contrast, both EPSC and LPSC assigned oral presentations only for a small number of attendees.

Several striking takeaways from the plenary lectures of this conference demonstrated that: (i) China will launch an optical telescope with 2 m-aperture, named China Space Station Telescope (CSST) around 2024, to detect celestial bodies within the solar system and cosmos; (ii) China is planning to launch a spacecraft around 2024, which is aiming to fly to 100 au and beyond till approximately 2049, allowing it to explore the boundary of the solar system or heliopause; (iii) the future of China's lunar missions will gradually shift to a

study of the Moon's interior, as China will look to establish research stations on the lunar surface with international collaborations; (iv) China is actively developing its discipline of modern planetary science, and the Chinese universities, represented by UCAS, have already made significant progress in facilitating the growth of the education system around planetary science.

All the attendees were eager to gather again for the next conference. As a response, the conference committee held an interim discussion with regards to the conference period and reached a consensus that being parallel to EPSC and LPSC, CPSC should be held consistently be held annually, and must open up to international planetary researchers. Moreover, we expect that more and more international planetary scientists will participate in this conference and become a part of the global collaboration with China to explore the mysteries of planets, for the common benefit of all humankind.

Reference

- [1] QIAN Y Q, XIAO L, HEAD J W, *et al.* Young lunar mare basalts in the Chang'E-5 sample return region, northern Oceanus Procellarum[J]. *Earth and Planetary Science Letters*, 2021, **555**: 116702
- [2] QIAN Y Q, XIAO L, HEAD J W, *et al.* Copernican-aged (<200 Ma) impact ejecta at the Chang'E-5 landing site: statistical evidence from crater morphology, morphometry, and degradation models[J]. *Geophysical Research Letters*, 2021, **48**(20): e2021GL095341
- [3] QIAN Y Q, XIAO L, WANG Q, *et al.* China's Chang'E-5 landing site: geology, stratigraphy, and provenance of materials[J]. *Earth and Planetary Science Letters*, 2021, **561**: 116855
- [4] QIAN Y Q, XIAO L, HEAD J W, *et al.* The long sinuous Rille system in northern Oceanus Procellarum and its relation to the Chang'E-5 returned samples[J]. *Geophysical Research Letters*, 2021, **48**(11): e2021GL092663
- [5] QIAO L, CHEN J, XU L Y, *et al.* Geology of the Chang'E-5 landing site: constraints on the sources of samples returned from a young nearside mare[J]. *Icarus*, 2021, **364**: 114480
- [6] FU X H, HOU X T, ZHANG J, *et al.* Possible non-mare lithologies in the regolith at the Chang'E-5 landing site: evidence from remote sensing data[J]. *Journal of Geophysical Research: Planets*, 2021, **126**(5): e2020JE006797
- [7] XIE M G, XIAO Z Y, ZHANG X Y, *et al.* The provenance of regolith at the Chang'E-5 candidate landing region[J]. *Journal of Geophysical Research: Planets*, 2020, **125**(5): e2019JE006112
- [8] BO Z, DI K C, LIU Z Q, *et al.* A catalogue of meter-scale impact craters in the Chang'E-5 landing area measured from centimeter-resolution descent imagery[J]. *Icarus*, 2022, **378**: 114943
- [9] LIN H L, LI S, XU R, *et al.* In situ detection of water on the moon by the Chang'E-5 lander[J]. *Science Advances*, 2022, **8**(1): eab19174
- [10] SU Y, WANG R G, DENG X J, *et al.* Hyperfine structure of regolith unveiled by Chang'E-5 lunar regolith penetrating radar[J]. *IEEE Transactions on Geoscience and Remote Sensing*, 2022, **60**: 5110414
- [11] ZHANG H, ZHANG X, ZHANG G, *et al.* Size, morphology, and composition of lunar samples returned by Chang'E-5 mission[J]. *Science China Physics, Mechanics & Astronomy*, 2022, **65**(2): 229511
- [12] LI C L, HU H, YANG M F, *et al.* Characteristics of the lunar samples returned by Chang'E-5 mission[J]. *National Science Review*, 2022, **9**(2): nwab188
- [13] YAO Y G, XIAO C J, WANG P S, *et al.* Instrumental neutron activation analysis of Chang'E-5 lunar regolith samples[J]. *Journal of the American Chemical Society*, 2022, **144**(12): 5478- 5484
- [14] LI Q L, ZHOU Q, LIU Y, *et al.* Two-billion-year-old volcanism on the moon from Chang'E-5 basalts[J]. *Nature*, 2021, **600**(7887): 54-58
- [15] CHE X C, NEMCHIN A, LIU D Y, *et al.* Age and composition of young basalts on the moon, measured from samples returned by Chang'E-5[J]. *Science*, 2021, **374**(6569): 887-890
- [16] TIAN H C, WANG H, CHEN Y, *et al.* Non-KREEP origin for Chang'E-5 basalts in the procellarum KREEP terrane[J]. *Nature*, 2021, **600**(7887): 59-63
- [17] HU S, HE H C, JI J L, *et al.* A dry lunar mantle reservoir for young mare basalts of Chang'E-5[J]. *Nature*, 2021, **600**(7887): 49-53
- [18] JI J L, HE H C, HU S, *et al.* Magmatic chlorine isotope fractionation recorded in apatite from Chang'E-5 basalts[J]. *Earth and Planetary Science Letters*, 2022, **591**: 117636
- [19] ZHANG D, SU B, CHEN Y, *et al.* Titanium in olivine reveals low-Ti origin of the Chang'E-5 lunar basalts[J]. *Lithos*, 2022, **414-415**: 106639
- [20] JIANG Y, LI Y, LIAO S Y, *et al.* Mineral chemistry and 3D tomography of a Chang'E-5 high-Ti basalt: implication for the lunar thermal evolution history[J]. *Science Bulletin*, 2022, **67**(7): 755-761
- [21] MO B, GUO Z, LI Y, *et al.* In situ investigation of the valence states of iron-bearing phases in Chang'E-5 lunar soil using FIB, AES, and TEM-EELS techniques[J]. *Atomic Spectroscopy*, 2022, **43**(1): 53-59
- [22] GU L X, CHEN Y J, XU Y C, *et al.* Space weathering of the Chang'E-5 lunar sample from a mid-high latitude region on the moon[J]. *Geophysical Research Letters*, 2022, **49**(7): e2022GL097875
- [23] GUO Z, LI C, LI Y, *et al.* Nanophase iron particles derived from fayalitic olivine decomposition in Chang'E-5 lunar soil: implications for thermal effects during impacts[J]. *Geophysical Research Letters*, 2022, **49**(5): e2021GL097323
- [24] XU X Q, HUI H J, CHEN W, *et al.* Formation of lunar highlands anorthosites[J]. *Earth and Planetary Science Letters*, 2020, **536**: 116138
- [25] WU W, XU Y G, ZHANG Z F, *et al.* Calcium isotopic composition of the lunar crust, mantle, and bulk silicate moon: a preliminary study[J]. *Geochimica et Cosmochimica Acta*, 2020, **270**: 313-324
- [26] ZENG X J, JOY K H, LI S J, *et al.* Oldest immiscible silica-rich melt on the moon recorded in a ~4.38 Ga zircon[J]. *Geophysical Research Letters*, 2020, **47**(4): e2019GL085997
- [27] ZENG X J, LI X Y, XIA X P, *et al.* New evidence for 4.32 Ga ancient silicic volcanism on the moon[J]. *Geophysical Research Letters*, 2021, **48**(13): e2021GL092639
- [28] FU X H, CAO H J, CHEN J, *et al.* Petrology and geochemistry of lunar feldspathic meteorite Northwest Africa 11111: insights into

- the lithology of the lunar farside highlands[J]. *Meteoritics & Planetary Science*, 2021, **56**(10): 1829-1856
- [29] CAO H J, LING Z C, CHEN J, et al. Petrography, mineralogy, and geochemistry of a new lunar magnesian feldspathic meteorite Northwest Africa 11460[J]. *Meteoritics & Planetary Science*, 2021, **56**(10): 1857-1889
- [30] WU Y H, HSU W. Mineral chemistry and in situ U–Pb geochronology of the mare basalt Northwest Africa 10597: implications for low-Ti mare volcanism around 3.0 Ga[J]. *Icarus*, 2020, **338**: 113531
- [31] BAO Z M, SHI Y R, ANDERSON J L, et al. Petrography and chronology of lunar meteorite Northwest Africa 6950[J]. *Science China Information Sciences*, 2020, **63**(4): 140902
- [32] ZHANG A C, PANG R L, SAKAMOTO N, et al. The Cr–Zr–Ca armalcolite in lunar rocks is loveringite: constraints from electron backscatter diffraction measurements[J]. *American Mineralogist*, 2020, **105**(7): 1021-1029
- [33] XING W F, LIN Y T, ZHANG C, et al. Discovery of reidite in the lunar meteorite Sayh al Uhaymir 169[J]. *Geophysical Research Letters*, 2020, **47**(21): e2020GL089583
- [34] ZHANG A C, JIANG Q T, TOMIOKA N, et al. Widespread tissintite in strongly shock-lithified lunar regolith breccias[J]. *Geophysical Research Letters*, 2021, **48**(5): e2020GL091554
- [35] CAO H J, CHEN J, FU X H, et al. Raman and infrared spectroscopic perspectives of lunar meteorite Northwest Africa 4884[J]. *Journal of Raman Spectroscopy*, 2020, **51**(9): 1652-1666
- [36] XIA Z P, MIAO B K, ZHANG C T, et al. Petrography and shock metamorphism of the lunar breccia meteorite NWA 13120[J]. *Minerals*, 2021, **11**(8): 899
- [37] ZENG X J, LI S J, JOY K H, et al. Occurrence and implications of secondary olivine veinlets in lunar highland breccia Northwest Africa 11273[J]. *Meteoritics & Planetary Science*, 2020, **55**(1): 36-55
- [38] ZHANG H, WEI Y, ZHONG J, et al. Whistler wings and reflected particles during solar wind interaction of lunar magnetic anomalies[J]. *Geophysical Research Letters*, 2021, **48**(8): e2021GL092425
- [39] ZHANG H, ZHONG J, ZHANG T X, et al. A meandering lunar wake produced by the pickup of reflected solar wind ions[J]. *Geophysical Research Letters*, 2021, **48**(24): e2021GL096039
- [40] ZHANG T X, ZHANG H, LAI H R, et al. Asymmetric lunar magnetic perturbations produced by reflected solar wind particles[J]. *The Astrophysical Journal Letters*, 2020, **893**(2): L36
- [41] WEI Y, ZHONG J, HUI H, et al. Implantation of Earth's atmospheric ions into the nearside and farside lunar soil: implications to geodynamo evolution[J]. *Geophysical Research Letters*, 2020, **47**(3): e2019GL086208
- [42] WANG H Z, ZHANG J, SHI Q Q, et al. Earth wind as a possible exogenous source of lunar surface hydration[J]. *The Astrophysical Journal Letters*, 2021, **907**(2): L32
- [43] WANG H, Z XIAO C, SHI Q Q, et al. Energetic neutral atom distribution on the lunar surface and its relationship with solar wind conditions[J]. *The Astrophysical Journal Letters*, 2021, **922**(2): L41
- [44] SHANG W S, TANG B B, SHI Q Q, et al. Unusual location of the Geotail magnetopause near lunar orbit: a case study[J]. *Journal of Geophysical Research: Space Physics*, 2020, **125**(4): e2019JA027401
- [45] WU B, DONG J, WANG Y R, et al. Characterization of the candidate landing region for Tianwen-1—China's first mission to Mars[J]. *Earth and Planetary Physics*, 2021, **8**(6): e2021EA001670
- [46] WU X, LIU Y, ZHANG C L, et al. Geological characteristics of China's Tianwen-1 landing site at Utopia Planitia, Mars[J]. *Icarus*, 2021, **370**: 114657
- [47] YE B L, QIAN Y Q, XIAO L, et al. Geomorphologic exploration targets at the Zhurong landing site in the southern Utopia Planitia of Mars[J]. *Earth and Planetary Science Letters*, 2021, **576**: 117199
- [48] ZHAO J N, XIAO Z J, HUANG J, et al. Geological characteristics and targets of high scientific interest in the Zhurong landing region on Mars[J]. *Geophysical Research Letters*, 2021, **48**(20): e2021GL094903
- [49] NIU S L, ZHANG F, DI K C, et al. Layered ejecta craters in the candidate landing areas of China's first Mars mission (Tianwen-1): implications for subsurface volatile concentrations[J]. *Journal of Geophysical Research: Planets*, 2022, **127**(3): e2021JE007089
- [50] WU Y H, HSU W B, LI Q L, et al. Heterogeneous Martian mantle: evidence from petrology, mineral chemistry, and in situ U–Pb chronology of the basaltic Shergottite Northwest Africa 8653[J]. *Geochimica et Cosmochimica Acta*, 2021, **309**: 352-365
- [51] WANG Z L, TIAN W, DI Y K. New temperature and oxygen fugacity data of Martian nakhlite from Northwest Africa (NWA) 5790 and implications for shallow sulphur degassing[J]. *Earth, Planets and Space*, 2021, **73**(1): 164
- [52] HU S, LIN Y, ANAND M, et al. Deuterium and ³⁷chlorine rich fluids on the surface of Mars: evidence from the enriched basaltic Shergottite Northwest Africa 8657[J]. *Journal of Geophysical Research: Planets*, 2020, **125**(9): e2020JE006537
- [53] HU S, LIN Y T, ZHANG J C, et al. Volatiles in the Martian crust and mantle: clues from the NWA 6162 Shergottite[J]. *Earth and Planetary Science Letters*, 2020, **530**: 115902
- [54] WANG S, HU S. Hydrogen isotopic variations in the Shergottites[J]. *Geosciences*, 2020, **10**(4): 148
- [55] SHANG S, HUI H J, YANG Y H, et al. Martian hydrothermal fluids recorded in the Sm–Nd isotopic systematics of apatite in regolith breccia meteorites[J]. *Earth and Planetary Science Letters*, 2022, **581**: 117413
- [56] CAO H J, CHEN J, FU X H, et al. Raman spectroscopic and geochemical studies of primary and secondary minerals in Martian meteorite Northwest Africa 10720[J]. *Journal of Raman Spectroscopy*, 2022, **53**(3): 420-434
- [57] ZENG X J, WU Y X, ZHAO Y S, et al. Revealing high-manganese material on Mars at microscale[J]. *Geophysical Research Letters*, 2021, **48**(17): e2021GL093410
- [58] HU S, LI Y, GU L X, et al. Discovery of coesite from the Martian Shergottite Northwest Africa 8657[J]. *Geochimica et Cosmochimica Acta*, 2020, **286**: 404-417
- [59] ZHANG T, HU S, WANG N, et al. Formation mechanisms of ringwoodite: clues from the Martian meteorite Northwest Africa 8705[J]. *Earth, Planets and Space*, 2021, **73**: 165
- [60] FU X H, JIA L C, WANG A L, et al. Thermal stability of akaganeite and its desiccation process under conditions relevant to Mars[J]. *Icarus*, 2020, **336**: 113435
- [61] MAO W S, FU X H, WU Z C, et al. The color centers in halite induced by Martian dust activities[J]. *Earth and Planetary Science Letters*, 2022, **578**: 117302
- [62] QU S Y, ZHAO Y Y S, CUI H, et al. Preferential formation of chlorate over perchlorate on Mars controlled by iron mineral-

- ogy[J]. *Nature Astronomy*, 2022, **6**(4): 436-441
- [63] WANG X Y, ZHAO Y Y S, HOOD D R, *et al.* Multiphase volatilization of halogens at the soil-atmosphere interface on Mars[J]. *Journal of Geophysical Research: Planets*, 2021, **126**(12): e2021JE006929
- [64] LI D D, ZHAO Y Y S, MESLIN P Y, *et al.* Cryogenic origin of fractionation between perchlorate and chloride under modern Martian climate[J]. *Communications Earth & Environment*, 2022, **3**(1): 15
- [65] QIN J Q. Mars upper atmospheric temperature and atomic oxygen density derived from the O_I 130.4 nm emission observed by NASA's MAVEN mission[J]. *The Astronomical Journal*, 2020, **159**(5): 206
- [66] QIN J Q. Solar cycle, seasonal, and dust-storm-driven variations of the Mars upper atmospheric state and H escape rate derived from the Ly α emission observed by NASA's MAVEN mission[J]. *The Astrophysical Journal*, 2021, **912**(1): 77
- [67] LIU D, YAO Z H, WEI Y, *et al.* Upstream proton cyclotron waves: occurrence and amplitude dependence on IMF cone angle at Mars — from MAVEN observations[J]. *Earth and Planetary Physics*, 2020, **4**(1): 51-61
- [68] LIU D, RONG Z J, GAO J W, *et al.* Statistical properties of solar wind upstream of Mars: MAVEN observations[J]. *The Astrophysical Journal*, 2021, **911**(2): 113
- [69] WANG Y Q, CAO Y T, CUI J, *et al.* An automatic identification method for the photoelectron boundary at Mars[J]. *The Astronomical Journal*, 2022, **163**(4): 186
- [70] ZHANG C, RONG Z J, NILSSON H, *et al.* MAVEN observations of periodic low-altitude plasma clouds at Mars[J]. *The Astrophysical Journal Letters*, 2021, **922**(2): L33
- [71] FAN K, FRAENZ M, WEI Y, *et al.* Deflection of global ion flow by the Martian crustal magnetic fields[J]. *The Astrophysical Journal Letters*, 2020, **898**(2): L54
- [72] GAO J W, RONG Z J, KLINGER L, *et al.* A spherical harmonic Martian crustal magnetic field model combining data sets of MAVEN and MGS[J]. *Earth and Planetary Physics*, 2021, **8**(10): e2021EA001860
- [73] LI X Z, RONG Z J, GAO J W, *et al.* A local Martian crustal field model: targeting the candidate landing site of the 2020 Chinese Mars Rover[J]. *Earth and Planetary Physics*, 2020, **4**(4): 420-428
- [74] ZHANG C, RONG Z J, KLINGER L, *et al.* Three-dimensional configuration of induced magnetic fields around Mars[J/OL]. *Earth and Space Science Open Archive*, 2022. <https://doi.org/10.1002/essoar.10511148.1>
- [75] QIN J F, ZOU H, FUTAANA Y, *et al.* Double-peak structures of Martian nightside total electron content in strong crustal magnetic cusp regions[J]. *Geophysical Research Letters*, 2021, **48**(7): e2021GL092662
- [76] QIN J F, ZOU H, YE Y G, *et al.* A method of estimating the Martian neutral atmospheric density at 130 km, and comparison of its results with Mars global surveyor and Mars odyssey aerobraking observations based on the Mars climate database outputs[J]. *Earth and Planetary Physics*, 2020, **4**(4): 408-419
- [77] ZHANG A B, KONG L G, LI W Y, *et al.* Tianwen-1 MINPA observations in the solar wind[J]. *Earth and Planetary Physics*, 2022, **6**(1): 1-9
- [78] FAN K, YAN L M, WEI Y, *et al.* The solar wind plasma upstream of Mars observed by Tianwen-1: comparison with Mars express and MAVEN[J]. *Science China Earth Sciences* 2022, **65**(4): 759-768
- [79] ZHONG J, SHUE J H, WEI Y, *et al.* Effects of orbital eccentricity and IMF cone angle on the dimensions of Mercury's magnetosphere[J]. *The Astrophysical Journal*, 2020, **892**(1): 2
- [80] ZHANG C, RONG Z J, GAO J W, *et al.* The flapping motion of Mercury's magnetotail current sheet: MESSENGER observations[J]. *Geophysical Research Letters*, 2020, **47**(4): e2019GL086011
- [81] ZHONG J, LEE L C, WANG X G, *et al.* Multiple X-line reconnection observed in Mercury's magnetotail driven by an interplanetary coronal mass ejection[J]. *The Astrophysical Journal Letters*, 2020, **893**(1): L11
- [82] ZHONG J, WEI Y, LEE L C, *et al.* Formation of macroscale flux transfer events at Mercury[J]. *The Astrophysical Journal Letters*, 2020, **893**(1): L18
- [83] JANG E, ZHAO J T, YUE C, *et al.* Energetic ion dynamics near the cusp region of Mercury[J]. *The Astrophysical Journal Letters*, 2020, **892**(1): 10
- [84] ZHAO J T, ZONG Q G, SLAVIN J A, *et al.* Proton properties in Mercury's magnetotail: a statistical study[J]. *Geophysical Research Letters*, 2020, **47**(19): e2020GL088075
- [85] ZHAO J T, ZONG Q G, YUE C, *et al.* Observational evidence of ring current in the magnetosphere of Mercury[J]. *Nature Communications*, 2022, **13**(1): 924
- [86] ZONG Q G, ZHAO J T, LIU J J, *et al.* Magnetic storms in Mercury's magnetosphere[J]. *Science China Technological Sciences*, 2022, **65**(6): 1427-1432
- [87] SHI Z, RONG Z J, FATEMI S, *et al.* An eastward current encircling Mercury[J]. *Geophysical Research Letters*, 2022, **49**(10): e2022GL098415
- [88] HAN Q Q, FRAENZ M, WEI Y, *et al.* EUV-dependence of Venusian dayside ionopause altitude: VEX and PVO observations[J]. *Earth and Planetary Physics*, 2020, **4**(1): 73-81
- [89] GAO J W, RONG Z J, PERSSON M, *et al.* In situ observations of the ion diffusion region in the Venusian magnetotail[J]. *Journal of Geophysical Research: Space Physics*, 2021, **126**(1): e2020JA028547
- [90] YAO Z H, BONFOND B, CLARK G, *et al.* Reconnection- and dipolarization-driven auroral dawn storms and injections[J]. *Journal of Geophysical Research: Space Physics*, 2020, **125**(8): e2019JA027663
- [91] GUO R L, YAO Z H, GRODENT D, *et al.* Jupiter's double-arc aurora as a signature of magnetic reconnection: simultaneous observations from HST and Juno[J]. *Geophysical Research Letters*, 2021, **48**(14): e2021GL093964
- [92] PAN D X, YAO Z H, MANNERS H, *et al.* Ultralow-frequency waves in driving Jovian aurorae revealed by observations from HST and Juno[J]. *Geophysical Research Letters*, 2021, **48**(5): e2020GL091579
- [93] YAO Z H, DUNN W R, WOODFIELD E E, *et al.* Revealing the source of Jupiter's x-ray auroral flares[J]. *Science Advances*, 2021, **7**(28): eabf0851
- [94] ZHANG B Z, DELAMERE P A, YAO Z H, *et al.* How Jupiter's unusual magnetospheric topology structures its aurora[J]. *Science Advances*, 2021, **7**(15): eabd1204
- [95] XU S B, HUANG S Y, YUAN Z G, *et al.* Global spatial distribution of dipolarization fronts in the Saturn's magnetosphere: Cassini observations[J]. *Geophysical Research Letters*, 2021, **48**(17): e2021GL092701
- [96] XU S B, HUANG S Y, YUAN Z G, *et al.* Successive dipolarization fronts with a stepwise electron acceleration during a substorm in

- Saturn's magnetotail[J]. *Geophysical Research Letters*, 2022, **49**(5): e2021GL097227
- [97] XU Y, GUO R L, YAO Z H, et al. Properties of plasmoids observed in Saturn's dayside and nightside magnetodisc[J]. *Geophysical Research Letters*, 2021, **48**(24): e2021GL096765
- [98] PAN D X, YAO Z H, GUO R L, et al. A statistical survey of low-frequency magnetic fluctuations at Saturn[J]. *Journal of Geophysical Research: Space Physics*, 2021, **126**(2): e2020JA028387
- [99] HAO Y X, SUN Y X, ROUSSOS E, et al. The formation of Saturn's and Jupiter's electron radiation belts by magnetospheric electric fields[J]. *The Astrophysical Journal Letters*, 2020, **905**(1): L10
- [100] LONG M Y, NI B B, CAO X, et al. Losses of radiation belt energetic particles by encounters with four of the inner moons of Jupiter[J]. *Journal of Geophysical Research: Planets*, 2022, **127**(2): e2021JE007050
- [101] SUN Y X, HAO Y X, ROUSSOS E, et al. Zebra stripe patterns in energetic ion spectra at Saturn[J]. *Geophysical Research Letters*, 2022, **49**(4): e2021GL097691
- [102] [102] SUN Y X, ROUSSOS E, HAO Y X, et al. Saturn's inner magnetospheric convection in the view of zebra stripe patterns in energetic electron spectra[J]. *Journal of Geophysical Research: Space Physics*, 2021, **126**(10): e2021JA029600
- [103] YUAN C J, ROUSSOS E, WEI Y, et al. Cassini observation of relativistic electron butterfly distributions in Saturn's inner radiation belts: evidence for acceleration by local processes[J]. *Geophysical Research Letters*, 2021, **48**(14): e2021GL092690
- [104] WU S Y, YE S Y, FISCHER G, et al. Statistical study on spatial distribution and polarization of Saturn narrowband emissions[J]. *The Astrophysical Journal*, 2021, **918**(2): 64
- [105] YE S Y, AVERKAMP T F, KURTH W S, et al. Juno waves detection of dust impacts near Jupiter[J]. *Journal of Geophysical Research: Planets*, 2020, **125**(6): e2019JE006367
- [106] YU X Q, SONG S Y, CHEN H F, et al. Mitigating deep dielectric charging effects at the orbits of Jovian planets[J]. *Transactions of Nanjing University of Aeronautics & Astronautics*, 2020, **37**(5): 804-815
- [107] SHUAI K, HUI H J, ZHOU L Y, et al. Accretion regions of meteorite parent bodies inferred from a two-endmember isotopic mixing model[J]. *Monthly Notices of the Royal Astronomical Society*, 2022, **513**(1): 363-373
- [108] DAI D Q, BAO H M, LIU S, et al. The origins and oxygen isotopes in two Al-rich chondrules from Kainsaz CO₃ carbonaceous chondrites[J]. *Acta Petrologica Sinica*, 2020, **36**(6): 1850-1856
- [109] DAI D Q, BAO H M, LIU S, et al. Oxygen isotopic compositions in a plagioclase-olivine inclusion from Ningqiang similar to those in Al-rich chondrules[J]. *Acta Geologica Sinica (English Edition)*, 2021, **95**(5): 1583-1590
- [110] JIANG Y, KOEFOED P, PRAVDIVITSEVA O, et al. Early solar system aqueous activity: K isotope evidence from Allende[J]. *Meteoritics & Planetary Science*, 2021, **56**(1): 61-76
- [111] XIONG Y, ZHANG A C, KAWASAKI N, et al. Mineralogical and oxygen isotopic study of a new ultrarefractory inclusion in the Northwest Africa 3118 CV3 chondrite[J]. *Meteoritics & Planetary Science*, 2020, **55**(10): 2184-2205
- [112] ZHANG M M, BONATO E, KING A J, et al. Petrology and oxygen isotopic compositions of calcium-aluminum-rich inclusions in primitive CO3.0-3.1 chondrites[J]. *Meteoritics & Planetary Science*, 2020, **55**(4): 911-935
- [113] ZHANG M M, LIN Y T, TANG G Q, et al. Origin of Al-rich chondrules in CV chondrites: incorporation of diverse refractory components into the ferromagnesian chondrule-forming region[J]. *Geochimica et Cosmochimica Acta*, 2020, **272**: 198-217
- [114] ZHANG M M, CLARK B, KING A J, et al. Shape and porosity of refractory inclusions in CV3 chondrites: a micro-computed tomography (μ CT) study[J]. *Meteoritics & Planetary Science*, 2021, **56**(3): 500-514
- [115] ZHANG A C, KAWASAKI N, BAO H M, et al. Evidence of metasomatism in the interior of Vesta[J]. *Nature Communications*, 2020, **11**(1): 1289
- [116] HUANG L L, MIAO B K, CHEN G Z, et al. The sulfurization recorded in tridymite in the monomict eucrite Northwest Africa 11591[J]. *Meteoritics & Planetary Science*, 2020, **55**(7): 1441-1457
- [117] LI J Y, ZHANG A C, SAKAMOTO N, et al. A new occurrence of corundum in eucrite and its significance[J]. *American Mineralogist*, 2020, **105**(11): 1656-1661
- [118] GUO Z, LI Y, CHEN H Y, et al. Evidence for the disproportionation of iron in a eucrite meteorite: implications for impact processes on Vesta[J]. *Journal of Geophysical Research: Planets*, 2021, **126**(8): e2020JE006816
- [119] LI Y, RUBIN A E, HSU W. et al. Formation of metallic-Cu-bearing mineral assemblages in type-3 ordinary and CO chondrites[J]. *American Mineralogist*, 2021, **106**(11): 1751-1767
- [120] YANG J, LIN Y T, CHANGELA H, et al. Early sulfur-rich magmatism on the ungrouped achondrite Northwest Africa 7325 differentiated parent body[J]. *Meteoritics & Planetary Science*, 2020, **55**(9): 1951-1978
- [121] ZHANG A C, KAWASAKI N, KURODA M, et al. Unique angrite-like fragments in a CH3 chondrite reveal a new basaltic planetesimal[J]. *Geochimica et Cosmochimica Acta*, 2020, **275**: 48-63
- [122] LI S L, HSU W B, NEMCHIN A, et al. Multiple thermal events recorded in IIE silicate inclusions: evidence from *in situ* U-Pb dating of phosphates in Weekeroo Station[J]. *Geochimica et Cosmochimica Acta*, 2021, **309**: 79-95
- [123] SMITH T, HE H Y, LI S J, et al. Light noble gas records and cosmic ray exposure histories of recent ordinary chondrite falls[J]. *Meteoritics & Planetary Science*, 2021, **56**(11): 2002-2016
- [124] WANG Y, HE H Y, LEYA I, et al. The noble gases in five ordinary chondrites from Grove Mountains in Antarctica[J]. *Planetary and Space Science*, 2020, **192**: 105045
- [125] GUO Z, LI Y, LIU S, et al. Discovery of nanophase iron particles and high pressure clinoenstatite in a heavily shocked ordinary chondrite: implications for the decomposition of pyroxene[J]. *Geochimica et Cosmochimica Acta*, 2020, **272**: 276-286
- [126] HOU C P, HE J S, ZHANG L, et al. Dynamics of the charged particles released from a sun-grazing comet in the solar corona[J]. *Earth and Planetary Physics*, 2021, **5**(3): 232-238
- [127] HE J S, CUI B, YANG L P, et al. The encounter of the parker solar probe and a comet-like object near the sun: model predictions and measurements[J]. *The Astrophysical Journal*, 2021, **910**(1): 7
- [128] DU K, LI S J, LEYA I, et al. The Kumtag meteorite strewn field[J]. *Advances in Space Research*, 2021, **67**(12): 4089-4098
- [129] FAN Y, LI S J, LIU S, et al. The distribution of the desert meteorites in China and their classification[J]. *Meteoritics & Planetary Science*, 2022, **57**(3): 683-701

- [130] WANG N, WANG G Q, ZHANG T, *et al.* Metallographic cooling rate and petrogenesis of the recently found Huoyanshan iron meteorite shower[J]. *Journal of Geophysical Research: Planets*, 2021, **126**(9): e2021JE006847
- [131] CHEN M, KOEBERL C, TAN D Y, *et al.* Yilan crater, China: evidence for an origin by meteorite impact[J]. *Meteoritics & Planetary Science*, 2021, **56**(7): 1274-1292
- [132] YIN F, DAI D Q. A study of shock-metamorphic features of feldspars from the Xiuyan impact crater[J]. *Minerals*, 2020, **10**(3): 231
- [133] YIN F, SHARP T G, CHEN M. Nanotextures and formation process of coesite in silica glass from the Xiuyan impact crater[J]. *Meteoritics & Planetary Science*, 2021, **56**(6): 1212-1223
- [134] ZHAO J W, XIAO L, XIAO Z Y, *et al.* Shock-deformed zircon from the Chicxulub impact crater and implications for cratering process[J]. *Geology*, 2021, **49**(7): 755-760
- [135] YAN P, XIAO Z Y, XIAO G Q, *et al.* Undetection of Australasian microtektites in the Chinese Loess Plateau[J]. *Palaeogeography, Palaeoclimatology, Palaeoecology*, 2022, **585**: 110721
- [136] LI C L, ZUO W, WEN W B, *et al.* Overview of the Chang'E-4 mission: opening the frontier of scientific exploration of the lunar far side[J]. *Space Science Reviews*, 2021, **217**(2): 35
- [137] ZHOU C Y, JIA Y Z, LIU J Z, *et al.* Scientific objectives and payloads of the lunar sample return mission—Chang'E-5[J]. *Advances in Space Research*, 2022, **69**(1): 823-836
- [138] WAN W X, WANG C, LI C L, *et al.* China's first mission to Mars[J]. *Nature Astronomy*, 2020, **4**(7): 721
- [139] LI C L, ZHANG R Q, YU D Y, *et al.* China's Mars exploration mission and science investigation[J]. *Space Science Reviews*, 2021, **217**(4): 57
- [140] ZOU Y L, ZHU Y, BAI Y F, *et al.* Scientific objectives and payloads of Tianwen-1, China's first Mars exploration mission[J]. *Advances in Space Research*, 2021, **67**(2): 812-823
- [141] ZOU Y L, LIU Y, JIA Y Z. Overview of China's upcoming Chang'E series and the scientific objectives and payloads for Chang'E 7 mission[C]//Proceedings of the 51st Lunar and Planetary Science Conference. The Woodlands: LPI, 2020: 1755
- [142] LI R Y, HAO J L, HU S, *et al.* High-spatial-resolution measurement of water content in olivine using NanoSIMS 50L[J]. *Atomic Spectroscopy*, 2022, **43**(1): 77-83
- [143] HAO J L, YANG W, HU S, *et al.* Submicron spatial resolution Pb-Pb and U-Pb dating by using a NanoSIMS equipped with the new radio-frequency ion source[J]. *Journal of Analytical Atomic Spectrometry*, 2021, **36**(8): 1625-1633
- [144] LIN Y, HAO J L, MIAO Z Z, *et al.* NanoSIMS image enhancement by reducing random noise using low-rank method[J]. *Surface and Interface Analysis*, 2020, **52**(5): 240-248
- [145] GU L X, WANG N, TANG X, *et al.* Application of FIB-SEM techniques for the advanced characterization of Earth and planetary materials[J]. *Scanning*, 2020, **2020**: 8406917
- [146] BAI J H, LIU F, ZHANG Z F, *et al.* Simultaneous measurement stable and radiogenic Nd isotopic compositions by MC-ICP-MS with a single-step chromatographic extraction technique[J]. *Journal of Analytical Atomic Spectrometry*, 2021, **36**(12): 2695-2703
- [147] SHUAI K, LI W Q, HUI H J. Isobaric spike method for absolute isotopic ratio determination by MC-ICP-MS[J]. *Analytical Chemistry*, 2020, **92**(7): 4820-4828
- [148] RONG Z, CUI J, WEI Y. Inaugural Chinese Planetary Science Conference. *Nature Astronomy*, 2021, **5**: 991-992

ZHAO Jianfu, DU Wangfang, KANG Qi, LAN Ding, LI Kai, LI Weibin, LIU Youcheng, LUO Xinghong, MIAO Jianyin, WANG Qinggong, WANG Shuangfeng, ZHANG Tao, ZHANG Xingwang, ZHANG Yonghai, ZHENG Huiqiong. Recent Progress of Microgravity Science Research in China. *Chinese Journal of Space Science*, 2022, 42(4). DOI:10.11728/cjss2022.04.yg23

Recent Progress of Microgravity Science Research in China

ZHAO Jianfu^{1,2}, DU Wangfang^{1,2}, KANG Qi^{1,2}, LAN Ding¹,
LI Kai^{1,2}, LI Weibin¹, LIU Youcheng³, LUO Xinghong⁴,
MIAO Jianyin⁵, WANG Qinggong⁶, WANG Shuangfeng^{1,2},
ZHANG Tao⁷, ZHANG Xingwang⁸, ZHANG Yonghai⁹,
ZHENG Huiqiong¹⁰

1. CAS Key Laboratory of Microgravity, Institute of Mechanics, Chinese Academy of Sciences, Beijing 100190
2. School of Engineering Science, University of Chinese Academy of Sciences, Beijing 100049
3. Tsinghua University, Beijing 100084
4. Institute of Metal Research, Chinese Academy of Sciences, Shenyang 110016
5. Institute of Spacecraft System Engineering, China Academy of Space Technology, Beijing 100094
6. Qian Xuesen Laboratory of Space Technology, China Academy of Space Technology, Beijing 100094
7. Shanghai Institute of Technical Physics, Chinese Academy of Sciences, Shanghai 200083
8. Institute of Semiconductors, Chinese Academy of Sciences, Beijing 100083
9. Xi'an Jiaotong University, Xi'an 710049
10. Center for Excellence in Molecular Plant Sciences, Chinese Academy of Sciences, Shanghai 200032

Abstract

Microgravity science is an important branch of space science. Its major objective is to study the laws of materials movement in microgravity, as well as to reveal the influence of gravity on the movement of materials in different gravity environments. Application researches relevant to these basic studies are also important contents of microgravity science. The advanced subjects, to some extent, reflect the ability of human beings to understand nature and the R&D level in this field in various countries. In this paper, the recent progress and the latest achievements of microgravity science and application researches in China aboard space platforms such as the Core Capsule Tianhe of the China Space Station (CSS) and satellites, as well as utilizing ground-based short-term microgravity facilities such as the Drop Tower Beijing and TUFF, are summarized, which cover the following sub-disciplines: microgravity fluid physics, microgravity combustion science, space materials science, space fundamental physics, space bio-technology, and relevant space technology applications.

Key words

Microgravity science, China Space Station (CSS), Ground-based short-term microgravity platforms, Microgravity fluid physics, Microgravity combustion science, Space materials science, Space fundamental physics, Space bio- technology

1 Introduction

Microgravity is one of the extreme conditions of space environment, as well as its most valuable resource. In this environment, there are potential possibilities to discover new phenomena and new laws in physical and chemical processes as well as material fabrication and biological processes, and to test and verify some fundamental laws of physics with higher precision. Studies on microgravity science and technology not only have scientific significance for people to understand nature, but also have great application values both in activities of space exploration and in development of new ground-based technologies.

Microgravity science and application research in China can be traced back to the 1960s, but it really rose in the late 1980s^[1,2]. The rapid progress of China's aerospace industry, especially that relevant to manned spaceflight and deep space exploration, not only puts forward an urgent demand for microgravity science, but also provides a great opportunity for microgravity science experiments. Furthermore, the construction and operation of the China Space Station (CSS) will provide a great opportunity for the development of microgravity science, which arouses more enthusiasm of scientific research on microgravity science in China. In the present paper, the most recent progress of microgravity science in China is summarized. The vision of China's microgravity science, looking into the coming era of the CSS, is to promote the rapid and sustainable development of microgravity science and application researches in China, for better serving the country and benefiting mankind.

2 Interfacial Phenomena-Capillary Flow, Marangoni Convection and the Instability

Interfacial phenomena, in which flow is driven by the difference of interfacial tension along the interface, are of great importance in microgravity science and technology. There are two categories of interfacial phenomena. The first category, in which the difference of interfacial tension is caused by the gradient of applied fields such as temperature, solution concentration, electric, or other fields, is usually called as Marangoni phenomenon. In the second category, the difference of in-

terfacial tension is caused by the difference of the curvature itself along the interface, and is usually called as capillary phenomenon. Chinese scholars paid some special attentions on these themes, including in-orbit long-term microgravity experiments, ground-based short-term microgravity experiments, numerical simulations, and theoretical analyses.

In the first category, a large amount of efforts have been made on Marangoni convection and the instability, focusing mainly on enriching human's understanding of nonlinear dynamics of fluid flows in extreme conditions.

Focusing on the thermocapillary convection of liquid bridge with large Prandtl number, Kang *et al.*^[3] performed a series of experiments aboard China's Tian-gong-2 (TG-2) space lab. They established large-scale liquid bridges with different geometric shapes (maximum height 22 mm) and studied their bifurcation mechanism of oscillatory thermal capillary convection. More than 740 groups of experiments have been completed during 32 months.

The space experiment gives the critical Marangoni number and the critical spectrum of liquid bridge thermocapillary convective oscillation tanking geometric parameter effect into account (covering volume ratio and height diameter ratio). An abrupt jump of the oscillation mode is found as the geometry changes. Two regions corresponding to two basic modes are defined in the parameter space of geometry. Multiple transitions are found in the marginal region between these regions and a neutral stability with the novel configuration of the two branches is concluded from the experimental data. The diagram of the transitions between the traveling waves and standing wave under different geometric parameters is drawn (Fig. 1). Moreover, abundant and complex coupling bifurcation routes under microgravity are discussed^[4,5].

Apart from space experimental studies, a large number of ground experiments, theoretical analyses and numerical simulations have also been carried out on the instabilities of thermocapillary flow both in liquid bridge and in annular liquid pool with low Prandtl number fluids, including the effects of aspect ratio, volume ratio, rotation, heating strategy, magnetic field, and so on^[6]. Thermocapillary convection of nano-fluids was also investigated numerically^[7,8]. A POD reduced-order model and numerical bifurcation analysis are applied to explore the bifurcation behavior of thermocapillary convection in two-dimensional cavity^[9].

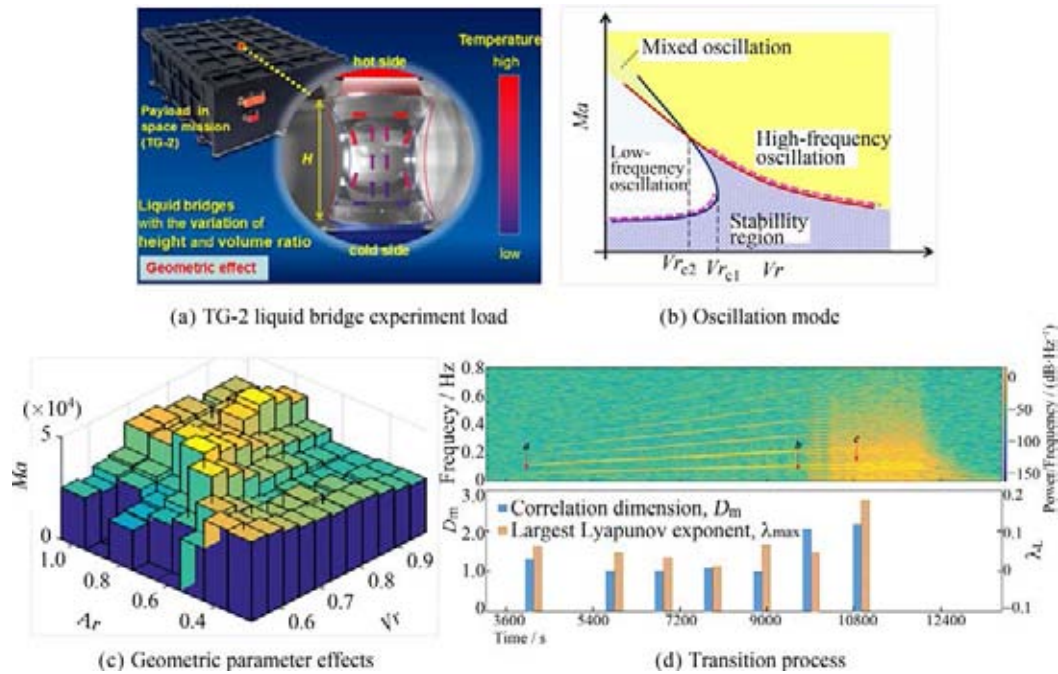


Fig. 1 Experiments on the microcapillary convection of liquid bridge aboard the China Space Lab TG-2

Wang *et al.*^[10–12] studied the phenomenon of electrocapillary of an oil-water system concerning the interface control under both DC and AC electric fields, which uses the principle of electrowetting to enhance fluid wicking in a weightless environment.

In the second category, the dynamics of liquid flow in capillaries, metallic wire meshes, and vane tanks are studied intensively in China, focusing on the potential applications for advanced propellant management in space.

The dynamics of capillary flow in tubes with different cross-sections are studied by using theoretical analysis and drop tower experiments^[13–16]. The wicking performance of cryogenic propellants within metallic screens including vapor evaporation effect is also studied by Ma *et al.*^[17]. The results showed that the wicking velocity and maximal wicking height both have a negative correlation with the gravity and superheated degree.

To investigate the liquid transport in a vane type tank, several series of experiments in the Drop Tower Beijing, as well as numerical simulations, were performed^[18–24]. It was found that the direction of microgravity had great effects on the expulsion efficiency of a vane-type tank. The influence of liquid flow in vane tank under different filling volumes, number of vanes, clearances and guiding vanes' thickness on the climbing height of the fluid were discussed in detail. Li *et al.*^[25] considered the problem of temperature stratification for a hydrogen

propellant tank, and introduced the cryogenic jet mixing effect to suppress temperature stratification. The results showed that a higher incident mass flow rate effectively destroyed the temperature stratification inside the tank and promoted an inside fluid flow for a given liquid filling ratio, while a smaller filling ratio resulted in a faster growth in both average temperature and average pressure and a larger amount of mass transfer inside the tank.

In the near future, the Fluid Physics Rack (FPR) aboard the Experimental Capsule II Mengtian of the CSS, which is a specific experimental device for microgravity fluid science including capillary flow, Marangoni convection and the instability, soft matter or complex fluids, *etc.*, is planned to be launched. More opportunities will be provided to carry out space experiments and then provide more insights on interfacial phenomena.

3 Two-phase Flow and Heat Transfer with Phase Change

Two-phase systems have great potential advantages for space applications. The huge density difference between liquid and gas phases in two-phase systems leads to significant gravity effects, which makes the flow structure and relevant characteristics of dynamics and heat trans-

fer in microgravity environment in space very different from those in normal gravity environment on the ground. Furthermore, spacecraft often experience different levels of gravity or acceleration during the whole mission cycle. Thus, the influence of gravity on two-phase flow and heat transfer with or without phase change plays an important role in this topic.

Du *et al.*^[26] reviewed comprehensively the gravity-independent criteria in the literature. They found that the dominant force criteria proposed by Zhao *et al.*^[27] can better predict the boundaries of gravity independence regions of a two-phase system. It defines two dimensionless parameters and introduces the corresponding critical values as follows,

$$Bo = \frac{(\rho_L - \rho_G)gd^2}{\sigma} \leq Bo_{cr}, Fr_{SG} = \frac{U_{SG}}{\sqrt{(\rho_L - \rho_G)gd / \rho_G}} \geq Fr_{SG,cr} \quad (1)$$

where the critical values were suggested as $Bo_{cr} = 1.5\text{--}6$, and $Fr_{SG,cr} = 0.54\text{--}2.2$, respectively. Fig. 2 shows three regions, namely the gravity dominant region (GDR), surface tension dominant region (SDR), and gas-phase inertial force dominant region (IDR). Two-phase flow in the latter two regions is gravity independent. The boundary corresponding to a constant of the gas phase superficial Weber number $We_{SG} = \rho_G U_{SG}^2 d / \sigma = Fr_{SG}^2 / Bo$ was also suggested between these two regions. The critical value of the gas phase superficial Weber number can be obtained by solving the intersection of Eq. (1) for the first two boundaries. The dominant force criteria were

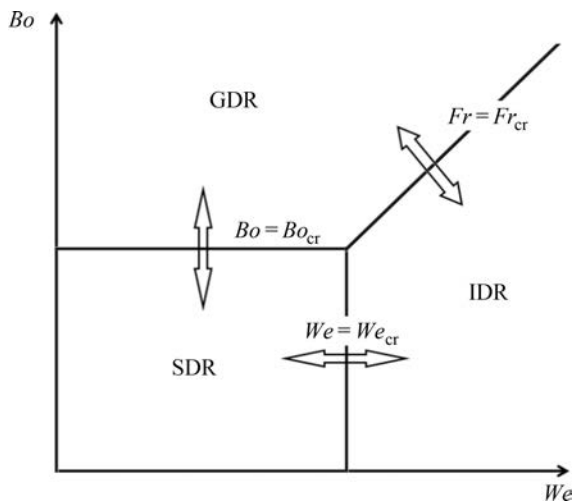


Fig. 2 Dominant force regions in the *Bo-We* parameter space

used successfully in the design of the cryogenic loop heat pipe^[28] for space test on cryogenic two-phase thermal transport aboard China’s new technology test satellite SJ-20, which was launched at the end of 2019. It was also recommended by Brendel *et al.*^[29] for potential space applications.

Du and Zhao^[30] reviewed the up-to-date progress on gravity scaling law of nucleate pool boiling heat transfer. They pointed out that there are some deficiencies and/or unsolved problems in the RKM (Raj-Kim-McQuillen) gravity scaling law^[31], which implicitly assumed that the characteristic temperature of the boiling incipency and that of the CHF (critical heat flux) are constants in different gravity conditions. These assumptions, however, have no theoretical or empirical basis in fact. Moreover, recent numerical studies utilizing the lattice Boltzmann method^[32], as well as some experimental evidences including recent results obtained from the project SOBER-SJ10^[33], showed that the temperature of CHF increases with the gravity level. Furthermore, the hypotheses on the asymptotic behaviors near the boiling incipency and the critical heat flux confused the meaning of different gravity scaling parameters, which are defined clearly by Du and Zhao^[30]. An important reason for the deficiencies of the RKM gravity scaling law is the lack of empirical data, especially experimental results in long-term, steady state pool boiling in different levels of reduced gravity. Thus, a variable gravity pool boiling experiment project utilizing CSS (the Chinese Manned Space Station) under construction, as well as systematic numerical simulations, are suggested in order to promote the research in this field.

Liu *et al.*^[34] studied the effects of electric field on pool boiling heat transfer over microstructured surfaces in normal and microgravity. The results showed that the CHF enhancement of the smooth surface by the electric field ranges from 15% to 23% and increases with liquid subcooling. The effects of electric field on CHF of micro-pin-finned surfaces depend on the liquid subcooling and size of micro-pin-fins. The enhancement of CHF due to the electric field is closely related to the field-trap effect, which can be strengthened by liquid subcooling.

In order to obtain the influence law and microscale mechanism of droplet wetting state in microgravity, the model of nano-droplet on micro-structured surface with different wettability and gravity was built and simulated by molecular dynamics^[35,36]. As shown in Fig. 3, the

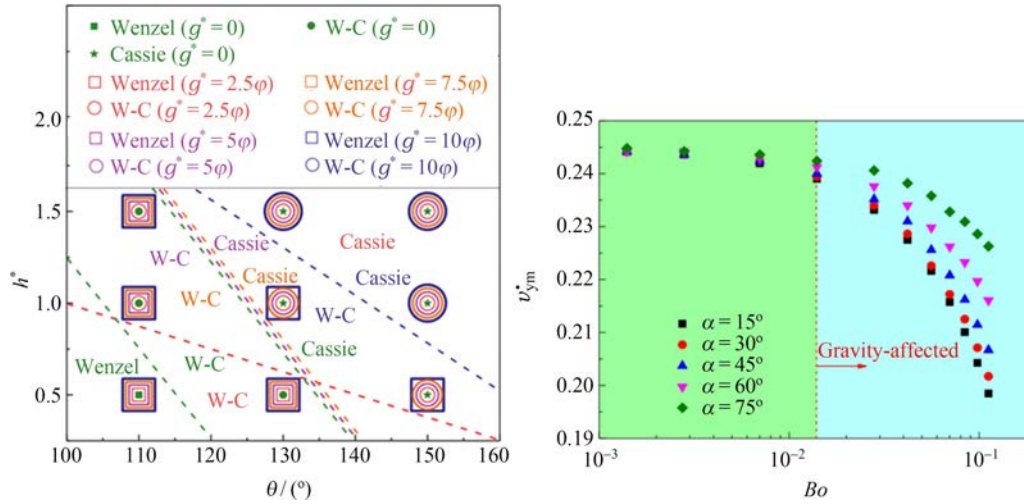


Fig. 3 Change of droplet wetting state under different gravity (a) and the effect of the Bond number on maximum vertical jumping velocity (b)

simulation results showed that keeping droplets in the environment of no gravity or microgravity as far as possible is more beneficial to the rolling and shedding of droplets, and gravity is more important to change the overall trend of droplet contact angle. Moreover, a reliable method was put forward to judge the droplets wetting state under different gravity. The effect of gravity on the motion of droplets on the surface is studied by lattice Boltzmann method^[37]. And the results show that the existence of gravity reduces the bouncing frequency and energy conversion rate of droplets on the surface. The ground experiments of steam condensation based on various microstructured surfaces have been carried out, which provides guidance for the selection of space condensation heat transfer surface. Meanwhile, a microgravity condensation experimental platform that can be used in the platform of The Chinese Space Station has been built and is currently undergoing ground basic experiment debugging.

A kind of shape-stable water/PVA sponge composite PCM for space microgravity application, including the development of the Two-Phase System Rack (TPSR) aboard the Experimental Capsule II Mengtian of the CSS, was proposed to overcome the expansion issue of water-based PCM^[38]. The effective cold storage density of the prepared PCMs is about $254.8 \text{ kJ}\cdot\text{kg}^{-1}$. The phase change temperature range was $-1 \text{ }^{\circ}\text{C}$ to $1 \text{ }^{\circ}\text{C}$, the undercooling temperature was no more than $0.8 \text{ }^{\circ}\text{C}$, and the effective cold storage was about $254.8 \text{ kJ}\cdot\text{kg}^{-1}$. The melting characteristics of the proposed PCM and the movement of the solid-liquid interface were explored

through two-dimensional numerical simulation. The cold storage and release capacity were verified by heat absorption and release experiments.

4 Soft Matter or Complex Fluids

Soft matter or complex fluids is another important topic in Chinese activities of microgravity fluid physics.

Experimental investigations of granular mechanical properties under microgravity were carried out in SJ-10 satellite and in the drop tower Beijing, as well as *via* on-ground experiment and simulation^[39–42]. In SJ-10, experimental observation provides us data for the granular clustering phase diagram. The segregation mechanism was further studied by CT analyses. A constitutive model for shear flow transitions in moderate dense granular systems was proposed which provided a theoretical basis to understand the high friction angle of granular materials observed in microgravity. The model is verified by simulation for predicting the bearing capacity of the foundation in low-gravity condition^[43]. The colloidal suspension as a model system of functional solutions to investigate two key processes of printing under a microgravity environment: manipulation of the droplet and formation of the drying patterns. It was showed that the dynamics of the droplet, which would determine the size of the features, could be controlled by tuning the wettability of the needles and the solid surface. Compared to the ground, the “coffee ring” effect was weakened for the drying patterns because of the strong interfacial effect

under weightless conditions. They further developed an ultrafast, robust, and scalable approach of Imbibition-Induced Assembly (IIA). The solvent imbibition of the nanoporous media will induce the strong capillary flow that can make the rapid transport of the colloidal particles towards the triple contact line, and the nanoporous surface will further direct the self-assembly of particles into colloidal crystals. Additionally, the IIA is spatially and temporally combined with the meniscus-guided printing method to fabricate multiscale and patterned colloidal photonic crystals. The printing speed (about $10 \text{ mm}\cdot\text{s}^{-1}$) is improved by 1–3 orders of magnitude than the traditional evaporation methods (Fig. 4). An effective and ultrafast approach was demonstrated by the authors for assembling microscale particles into colloidal photonic crystals with controllable sizes and shapes on the macroscale.

5 Microgravity Combustion

Microgravity combustion phenomena, including ignition and combustion characteristics of overloaded wire insulations, flame spread over flat and cylindrical Polymethyl Methacrylate (PMMA) in low-speed forced flows, burning behaviors and models for single coal particles, dripping droplet combustion of Polyethylene (PE), and flame extinction of spherical PMMA, were recently reported based on experimental results from the recoverable satellite SJ-10 and the Drop Tower Beijing. Primary institutes include Tsinghua University, Huazhong University of Science and Technology, Institutes of Engineering Thermophysics and Institutes of Mechanics of

Chinese Academy of Sciences, Hong Kong Polytechnic University, *etc.* In particular, a 1-D transient model considering intra-particle thermal combustion^[44] and devolatilization models^[45] was shown to improve predictability of ignition of isolated coal particles. Burning rate models with gasification efficiency developed with validations from microgravity dripping droplet experiments showed fundamental insights regarding comet flame due to fuel ejection for the burning of thermoplastic materials^[46]. For microgravity flame of spherical fuels, critical mass flux and the mass-transfer number were adopted to reveal underlying mechanisms of extinction limit^[47,48], providing the foundation for developing “fire-safe” shape materials for spacecraft usage. The SJ-10 experiments of smoke emission of the overloaded wire insulations were investigated in long-term microgravity for the first time^[49]. Two smoke emission modes, namely the end smoke jet and the bubbling smoke jet, were identified with PE insulations^[50]. The SJ-10 experiments of opposed flame spread over cylindrical PMMA revealed that the acceleration of flame spread in microgravity due to increased oxygen levels and corresponding fire risk can be overestimated by ground-based test methods^[51].

In contrast with the Narrow Channel Apparatus (NCA) that has been employed to suppress buoyancy flow to emulate microgravity flame spread over solid materials, a Horizontal Channel Apparatus (HCA) was proposed^[52, 53] based on scaling analysis to extend the buoyancy effect and study opposed flame spread in partial gravity conditions. Thin solid materials investigated include napkin and dictionary paper, with comparison

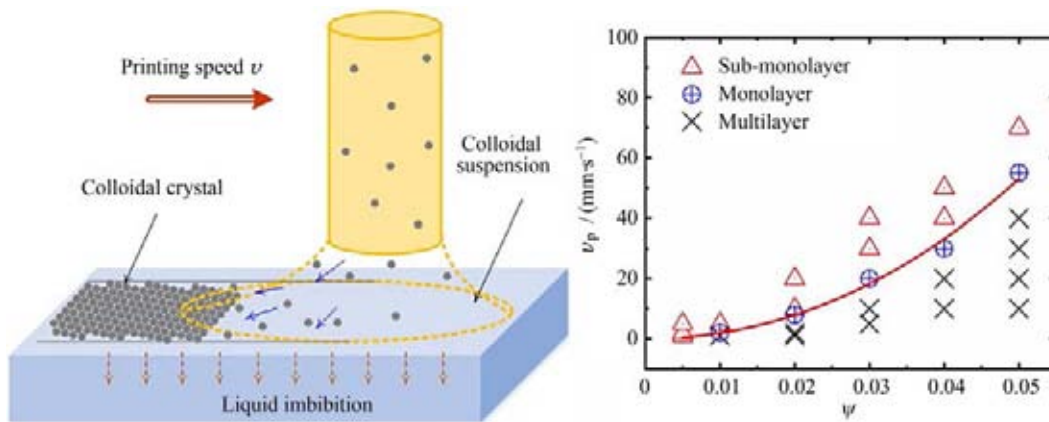


Fig. 4 Schematic diagram of convective flux induced by solvent imbibition during meniscus-guided printing (Left). A phase diagram where sub-monolayer, monolayer, and multilayer phases are plotted as a function of the particle volume fraction ϕ and the printing speed v_p (Right)

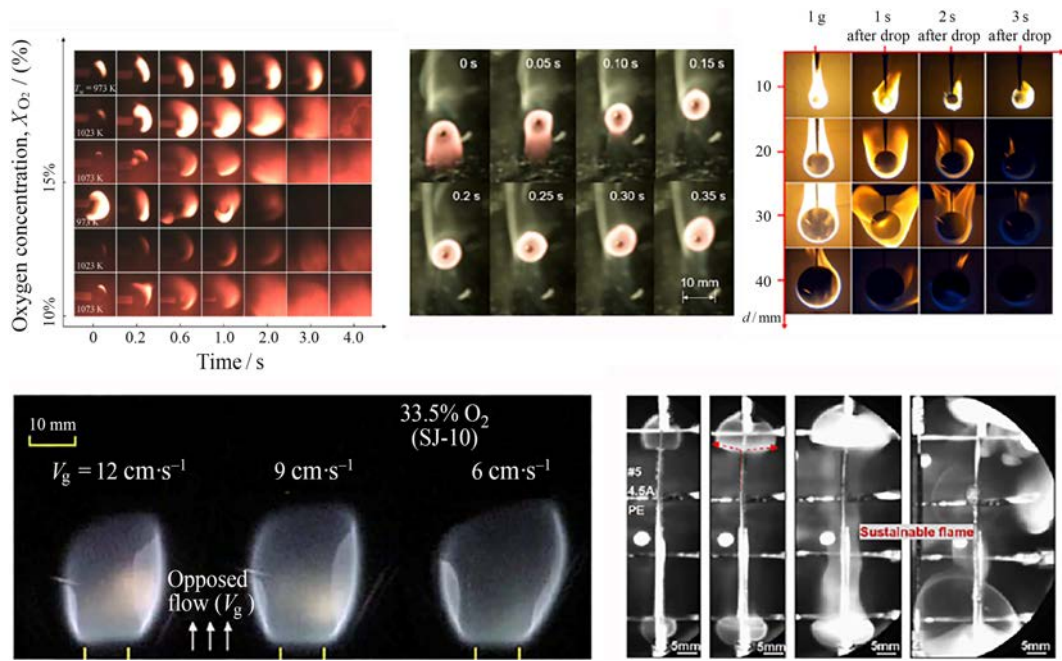


Fig. 5 Recent microgravity combustion investigations on coal particles, dripping PE droplets, spherical and cylindrical PMMA, and PE isolated wires

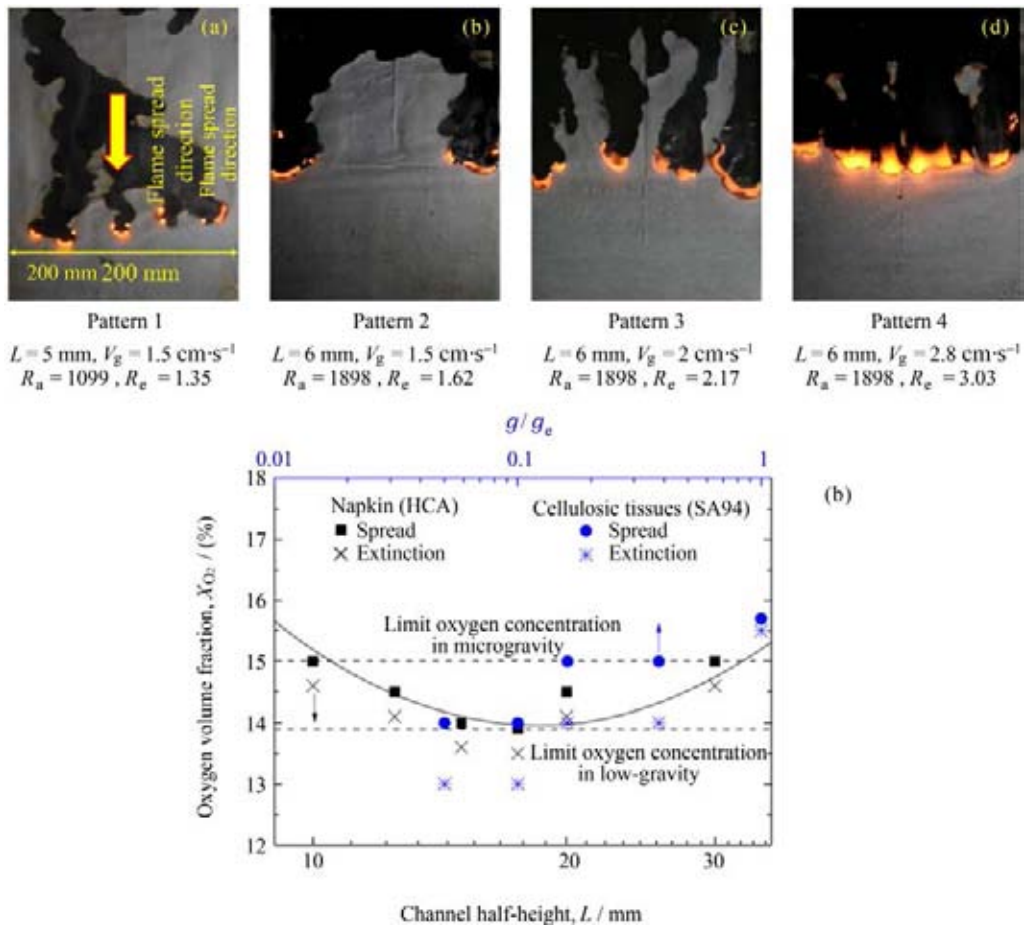


Fig. 6 Recent development of partial gravity flame spread and extinction of thin materials using the HCA

with data of cellulose tissues (parabolic flight experiments) in literature. Collectively with the experimental results (also from the ISS) and modeling efforts, a review for effects of buoyant flow, fingering spread, smoldering spread, and various transition behaviors for near-limit opposed fire spread was provided to suggest valuable issues for future research^[54].

Microgravity group combustion behaviors for coal particles and droplets were numerically investigated. Particle and droplet burning models with 1-D configuration and Neumann boundary conditions were used to examine effects of particle distance on diffusion, vaporization, and chemistry-controlled phenomena^[55, 56]. An ignition group number (Gig) was proposed to differentiate various ignition mode regimes of two-stage external group combustion^[57]. Further experimental validation of the proposed model is expected to be conducted using Tsinghua University Freefall Facility (TUFF)^[58].

The Combustion Science Rack (CSR), which is planned to be aboard the Experimental Module II Mengtian of the CSS, will facilitate investigations in gaseous flame dynamics, combustion of solid and energetic materials, and liquid combustion in various configurations in long-duration microgravity environment through utilization of different Combustion Experimental Inserts (CEIs). Corresponding strategic goals of the space-based combustion program include: to extend combustion limits and associated theories for multiphase reacting flows and flame instabilities, to improve predictability of space fire incident and lay foundation for material selection for space utilization, and to promote original research approach and technology transfer for low pollution combustion and future space exploration. The first batch of domestic and international collaborative projects for combustion sciences onboard the CSS will make full usage of the gaseous CEI for ex-

ploring near-limit flame stagnation, liftoff and blowoff mechanisms, weakly turbulent flame dynamics, sooting flame structure and sooting limits, flame synthesis of functional particle materials, as well as flame instabilities under vortices and acoustic waves.

6 Space Material Science

Big progress in space material field has been made in the past two years in terms of platform construction. One of the two material experiment racks on the CSS, Containerless Material Experiment Rack (CMER), had been completed and was launched with the core module Tianhe of China Space Station (CSS) on 29 April 2021. Meanwhile, after selection and ground tests a batch of experimental samples were also sent into space with the rack. An electrostatic levitation facility installed in the rack would be applied to study the containerless solidification mechanism and thermophysical properties of the material samples in microgravity environment. Till now, the on-orbit functional verification of the rack and electrostatic levitation facility have been successfully completed. Spherical samples of Zr were melted and some thermophysical properties were measured under microgravity condition, as shown in Fig. 7. Next, containerless experiments on various material samples, such as superalloys, metallic glasses, and oxide ceramics, *etc.*, will be conducted gradually.

The main performances of the containerless experimental device included as follows: (i) a coupling laser heating system composed of semiconductor laser with output power of 300 W and carbon dioxide laser can heat the samples heated up to 3000 °C; (ii) a molecular pump vacuum system and argon pressurization unit are installed in the rack to supply pressure environments

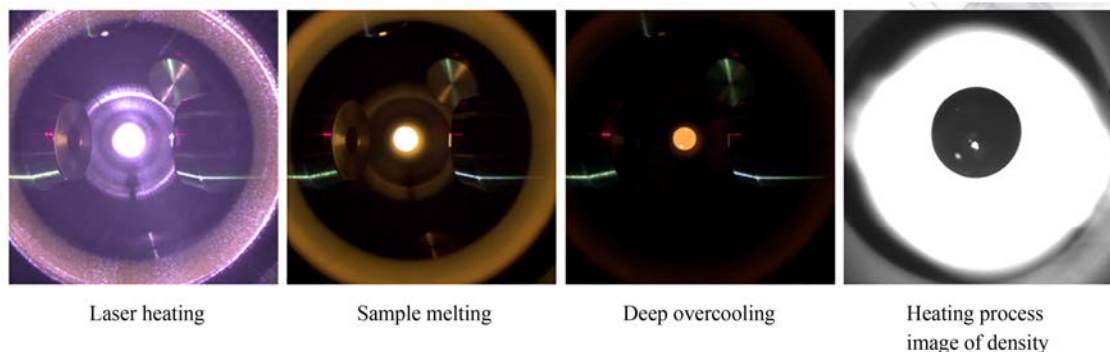


Fig. 7 Containerless experiment of a Zr sample on CSS

from 10^{-4} Pa to 3 atm; (iii) a series of optical devices are mounted on a polyhedron chamber with 38 faces for the positioning of samples with an accuracy of ± 0.1 mm, measuring of thermophysical property such as density, viscosity, surface tension, specific heat and spectral emissivity, and providing a triggering nucleation function to realize different supercooling degrees.

The other CSS material experiment rack, High Temperature Material Rack (HTMR), has been almost completed and the test of it is underway. It is scheduled to be launched with the Mengtian module in October 2022, followed by a series of material science experiments. The rack allows for study of a variety of materials, including high-temperature metals & alloys, semiconductors, crystals, ceramics, glasses, *etc.*, onboard the CSS.

Some ground-based microgravity material researches were still ongoing. Using the 50-meter-high drop tube at IMR, CAS, Luo *et al.* [59] investigated the effect of microgravity on the solute segregation and dendrite growth of Al-2.8 wt.% Cu alloy, grain and bubble morphology evolution of Al-9.5 wt.% Zn alloy, and primary phase formation and peritectic reactions of Sn-20 wt.% Ni, Ni-25 wt.% Zr, and Cu-15 wt.% Ge alloys. Some phenomena, such as, microgravity weakened central enrichment of Cu solute and led to smaller dendrite spacing and more mild microsegregation in Al-2.8 wt.% Cu alloy, did not cause grain and bubble movement and produced larger grain size in Al-9.5 wt.% Zn alloy, and was favorable to the formation and growth of the primary phase but not peritectic reaction in Sn-20 wt.% Ni alloy, were observed. Other alloys such as the ternary alloy Cr-Ni-Fe, Ni-Fe-Ti, Al-Ag-Ge, and Ga-In-Sb, are also studied respectively in the Northwestern Polytechnical University and the Tianjin Polytechnic University, focusing on the heat transfer dynamics, eutectic growth mechanism, structural evolution, micromechanical properties, and so on.

Wang *et al.* [60] investigated the Marangoni effect by using a new method to directly measure the acetic acid (solute) concentration with a Planar Laser-Induced Fluorescence (PLIF) system. Based on the concentration contours of solute, they could probe into the bulk flow and occurrence of the Marangoni effect. It was found that the density effect of solute, coupled with Marangoni effect, further affected the distribution of solute and then influenced the location and evolution of Marangoni effect. In the same group, the effect of gravity

(including 0, 0.16, 0.38, 1 and 1.8 g) on the polymorphs was studied with the anti-solvent crystallization of L-histidine from an ethanol water mixture by adding ethanol, operated in both continuous and batch modes [61]. The experiments were conducted in a self-designed micro-channel crystallizer on a zero-G flight. The stable form of L-histidine was obtained under microgravity, while only the metastable form can be observed in the ground experiments with the same inlet conditions. The possible reason is the extremely ordered flow field of the system in microgravity environment. A large amount of small particles aggregated at 1.8 g due to the enhanced micro-mixing, which favors nucleation. Bigger particles crystallized at Moon gravity (0.16 g) without the excessive consumption of the supersaturation by explosive nucleation and with moderate convection of the system. It is concluded that both nucleation and crystal growth were influenced by the micro-mixing status in the system due to the altered gravity extent.

7 Space Fundamental Physics

The projects Taiji and Tianqin, which are all scheduled to be launched in the early 2030s, are two missions for gravitational wave detection in space [62]. The pilot satellite missions for these two projects, namely Taiji-1 and Tianqin-1, were launched successfully in the middle and end of 2019, respectively. Fig. 8 shows the distribution of the payloads in Taiji-1. The successful flights of Taiji-1 and Tianqin-1 have verified the feasibility of the corresponding projects. Meanwhile, with the support of the Strategic Priority Research Program of the Chinese Academy of Sciences, the key technology research of Taiji-2 was completed, laying a foundation for the implementation of Taiji-2 project.

Cold atomic physics is another topic in China's space fundamental physics researches. The successful operation of the space cold atomic clock aboard the China Space Lab Tiangong-2 is the first time in the world [63]. It was found that the performance remained stable after three-year in-orbit test, paving the way for the space application of cold atom technology. Recently, the same team developed a simple, reliable and universal method for generating one-dimensional cold gases of ^{87}Rb atoms by diffuse laser cooling [64]. A horizontal slender vacuum glass tube with a length of 105 cm and diameter of 2 cm was used in the experiment. The diffuse laser light inside the tube, which was generated by multiple

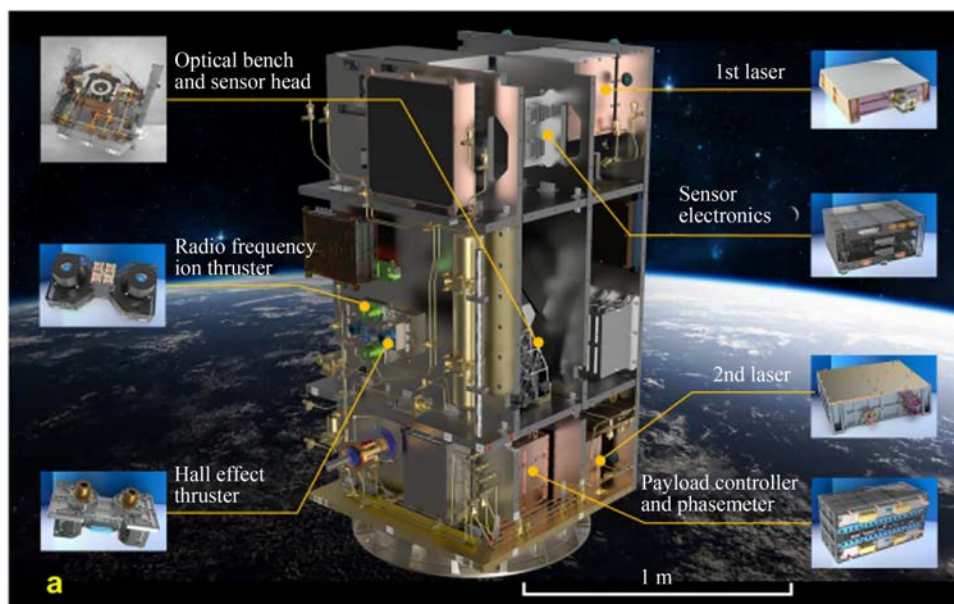


Fig. 8 Anatomy of Taiji-1 and its payloads

flection of injected lasers, cooled the background vapour atoms. With 250 mW of cooling light and 50 mW of repumping light, an evenly distributed 1-m-long profile of cold atom cloud is obtained. A factor 4 improvement in the atomic optical density was observed for a typical cooling duration of 170 ms and a sub-Doppler atomic temperature of 25 μ K. The central number of detected cold atoms remained constant for a free-fall duration of 30 ms.

8 Space Life Science and Bio-Technology

Spaceflight conditions, including microgravity or low gravity, radiation, temperature, air and soil composition constraints, etc., greatly affect life survival and adaptation. Moreover, the volume and energy supply in the isolation chambers in space used to live are very limited. Thus, a systematic analysis of regulatory mechanism of higher plants and other organisms in response to space environments and construction of higher resource-use efficiency life support system are needed.

The Chinese space life research activities on board the Chinese recoverable satellite SJ-10 in 2016 spanned three life science fields, including micro-gravitational biological effects, space radiation biological effects and space cell culture biotechnology. In the same year, a seed-to-seed experiment on board the Chinese space lab TG-2 was carried out. One of the most prolific series of investigations is the Higher Plant Flowering Experiment (HPFE) in space on board SJ-10 and TG-2. In these two

years, samples of HPFE recovered from the SJ-10 and TG-2 were used to test molecular basis to integrate microgravity signals into the photoperiodic flowering pathway^[65]. Potential evidence for transgenerational epigenetic memory in *Arabidopsis* and metabolomics of rice seeds after spaceflight were also investigated^[66-69]. The data indicated that the roles of the circadian oscillator could act as integrators of spaceflight response and photoperiodic signals in plants grown in space and changes in epigenetic modifications caused by spaceflight affected the growth of two future seed generations. In addition, effects of microgravity on early mouse embryonic development and embryonic stem cell differentiation on board SJ-10 were analyzed^[70, 71].

Data from SJ-10 and TG-2 operation have been used in the design of additional space experiments, which will be performed on board the CSS. The first 17 projects on life science and biotechnology in space have been considered for the CSS missions in the near future.

9 New Ground-based Facilities Developed in China

As effective complements to the CSS, several ground-based facilities have also been developed recently in China.

In addition to the Drop Tower Beijing operated by the National Microgravity Laboratory/CAS, a new drop tower, namely Tsinghua University Freefall Facility (TUFF), has been built and open for national users to

conduct short-term microgravity experiments mainly in the field of combustion. TUFF allows for 2.2 s freefall with $10^{-3} g$ followed by a 10 m deceleration using magnetic breaks^[58]. Another new microgravity experiment facility with electromagnetic launch is also under construction in the Technology and Engineering Center for Space Utilization of CAS^[72] in order to meet the rapid increasing requirements of extensive preliminary ground experiments for projects aboard CSS, as well as those of scientific experiments utilizing ground-based short-term microgravity facilities. It is mainly composed of double layered tower, linear induction motors, experimental capsule, energy storing device, high-power converters, electrical control system and electromagnetic release device. The microgravity level of $10^{-5} g$ can be achieved for 4 s and optional gravity level from $10^{-5} g$ to $1 g$ can be created.

The quick progress of commercial spaceflight in China also provides some short-term microgravity experiment opportunities. For example, DEAR (Discovery, Exploration, Advance, Recovery) family spacecraft, developed by AZSPACE, which was founded in 2019 as a Chinese spacecraft manufacturer, a provider of orbital experiment and recovery services, are developed for implementing scientific experiments, and then bring experimental items back to the Earth by recovery part. Inner or out of spacecraft, the experiments can be customized in the space natural environment, mixing the features of microgravity, weak geomagnetic, strong radiation, high vacuum, and ultra-low temperature. In orbital spaceflights, DEAR spacecraft is launched into space and flies in Low Earth orbit at 350 km altitude. Microgravity in orbital laboratory can be 10^{-5} to $10^{-6} g$. The recovery part will fly in space for nearly four weeks and then return to the Earth. The orbital part will stay in space for over one year and then burn down through the atmosphere. Different options on time periods will match different experiments as needed. Suborbital flights and experiment services can also be provided. In suborbital flights, DEAR spacecraft is launched to the space at 150 km altitude and land on the Earth. Microgravity (10^{-3} to $10^{-4} g$) environment will last 3–5 min.

10 Conclusions

Microgravity science has great importance in fundamental studies, affects directly mans' understanding of

physical laws of nature, and has great application values in the development of space exploration and new ground-based technologies. The most recent progress of microgravity science in China is summarized briefly in the present paper, including microgravity fluid physics, microgravity combustion science, space material science, space bio-technology, and space fundamental physics. Several ground-based facilities for short-term microgravity experimental research are also developed in China, which will be effective complements to the CSS.

The Core Module Tianhe of the CSS was successfully launched into orbit last year. There have been six astronauts from two teams visiting successfully the Core Module Tianhe. On 10 May 2022, the cargo spacecraft TZ-4 was launched successfully, which opened the on orbit construction stage of the CSS. The two experiment modules, namely the Experiment Module I Wentian and the Experiment Module II Mengtian, will be launched into orbit this year to complete the construction of the CSS. The new era of the CSS is coming. The CSS will provide essential conditions for carrying out multi-disciplinary space scientific experiments, especially long-term microgravity space experiments on microgravity science and application. It is bound to contribute to the further prosperity of China's microgravity research and to benefit microgravity research all over the world.

Acknowledgement

The authors appreciate supports from all members of the National Society of Microgravity Science and Application (NSMSA), Chinese Society of Space Research (CSSR).

References

- [1] ZHAO J F, WANG S F, LIU Q, *et al.* Retrospect and perspective on microgravity science in China (in Chinese)[J]. *Chin. J. Space Sci.*, 2021, **41**(1): 34-45
- [2] LI K, ZHAO J F, KANG Q, *et al.* Academician Wen-Rui Hu – eminent pioneer and prominent leader of microgravity science in China[J]. *Microgravity Sci. Tech.*, 2022, **34**(2): 19
- [3] KANG Q, WU D, DUAN L, *et al.* Space experimental study on wave modes under instability of thermocapillary convection in liquid bridges on Tiangong-2[J]. *Phys. Fluids*, 2020, **32**(3): 16
- [4] KANG Q, WU D, DUAN L, *et al.* The effects of geometry and heating rate on thermocapillary convection in the liquid bridge[J]. *J. Fluid Mech.*, 2019, **881**: 951-982
- [5] KANG Q, WANG J, DUAN L, *et al.* The volume ratio effect on flow patterns and transition processes of thermocapillary convec-

- tion[J]. *J. Fluid Mech.*, 2019, **868**: 560-583
- [6] GUO Z Y, LI K, KANG Q, *et al.* Study on bifurcation to chaos of surface tension gradient driven flow (in Chinese) [J]. *Adv. Mech.*, 2021, **51**: 1-28
- [7] CHEN C, FENG S, PENG H, *et al.* Thermocapillary convection flow and heat transfer characteristics of graphene nanoplatelet based nanofluid under microgravity[J]. *Microgravity Science and Technology*, 2021, **33**(3): 1-12.
- [8] ZHOU X, CHI F, JIANG Y, *et al.* Effect of moderate Prandtl number nanofluid thermocapillary convection instability in rectangular cavity[J]. *Microgravity Sci. Tech.*, 2022, **34**: 24
- [9] GUO Z Y, ZHAO J F, LI K, *et al.* Bifurcation analysis of thermocapillary convection based on POD-Galerkin reduced order method (in Chinese) [J]. *Chin. J. Theo. Appl. Mech.*, 2022, **54**: 1186-1198
- [10] WANG Q, XU M, WANG C, *et al.* Actuation of a nonconductive droplet in an aqueous fluid by reversed electrowetting effect[J]. *Langmuir*, 2020, **36**: 8152-8164
- [11] WENG N, WANG Q, GU J, *et al.* The dynamics of droplet detachment in Reversed Electrowetting (REW) [J]. *Colloids and Surfaces A*, 2021, **616**: 126303
- [12] WANG Q, LI L, GU J, *et al.* Manipulation of a nonconductive droplet in an aqueous fluid with AC electric fields: droplet dewetting, oscillation, and detachment[J]. *Langmuir*, 2021, **37**: 12098-12111
- [13] CHEN S, YE Z, DUAN L, *et al.* Capillary driven flow in oval tubes under microgravity[J]. *Physics of Fluids*, 2021, **33**(3): 032111
- [14] LEI J, XU Z, XIN F, *et al.* Dynamics of capillary flow in an undulated tube[J]. *Phys. Fluids*, 2021, **33**(5): 052109
- [15] ZHU C, ZHOU X, ZHANG G. Capillary plugs in horizontal rectangular tubes with non-uniform contact angles[J]. *J. Fluid Mech.*, 2020, **901**
- [16] WENG N, WANG Q, LI J, *et al.* Liquid penetration in metal wire mesh between parallel plates under normal gravity and microgravity conditions[J]. *Appl. Thermal Eng.*, 2020, **167**: 114722
- [17] MA Y, LI Y, XIE F, *et al.* Investigation on wicking performance of cryogenic propellants within woven screens under different thermal and gravity conditions[J]. *J. Low Temp. Phys.*, 2020, **199**(5): 1344-1362
- [18] LIU J, LI Y, LI W, *et al.* Experimental investigation of liquid transport in a vane type tank of satellite with microgravity[J]. *Aerospace Sci. Tech.*, 2020, **105**: 106007
- [19] ZHUANG B, LI Y, LIU J, *et al.* Numerical simulation of fluid transport along parallel vanes for vane type propellant tanks[J]. *Microgravity Sci. Tech.*, 2020, **32**: 129-138
- [20] LI Y Q, DONG J Y, RUI W. Numerical simulation for capillary driven flow in capsule-type vane tank with clearances under microgravity[J]. *Microgravity Sci. Tech.*, 2020, **32**: 321-329
- [21] LI J C, LIN H, LI K, *et al.* Liquid sloshing in partially filled capsule storage tank undergoing gravity reduction to low/micro-gravity Condition[J]. *Microgravity Sci. Tech.*, 2020, **32**: 587-596
- [22] ZHANG D, MENG L, LI Y Q. Numerical simulation analysis of liquid transportation in capsule-type vane tank under microgravity[J]. *Microgravity Sci. Tech.*, 2020, **32**: 817-824
- [23] LI J C, LIN H, LI K, *et al.* Dynamic behavior in a storage tank in reduced gravity using dynamic contact angle method[J]. *Microgravity Sci. Tech.*, 2020, **32**: 1039-1048
- [24] CHEN S, DUAN L, KANG Q. Study on propellant management device in plate surface tension tanks[J]. *Acta Mech. Sin.*, 2021, **37**: 1498-1508
- [25] LI J C, GUO B, ZHAO J F, *et al.* On the space thermal de-stratification in a partially filled hydrogen propellant tank by jet injection[J]. *Microgravity Sci. Tech.*, 2022, **34**: 6
- [26] DU W F, YUE S W, ZHAO J F, *et al.* Criteria of gravity independence in multiphase thermal fluid systems (in Chinese) [J]. *J. Hebei Univ. Water Res. Elec. Eng.*, 2019, (1): 1-8
- [27] ZHAO J F, XIE J C, LIN H, *et al.* Experimental study of two-phase flow in microgravity[R]//51st Int. Astronautical Cong., Rio de Janeiro, Brazil, October 2-6, 2000
- [28] HE F L, DU W F, ZHAO J F, *et al.* Numerical simulation on the effects of component layout orientation on the performance of a neon-charged cryogenic loop heat pipe[J]. *Microgravity Sci. Tech.*, 2020, **32**: 179-188
- [29] BRENDDEL L P M, BRAUN J E, GROLL E A. Comparison of gravity independence criteria for two-phase flow[J]. *J. Thermophys. Heat Transfer*, 2021, **35**: 830-842
- [30] DU W F, ZHAO J F. Gravity scaling law of heat transfer in nucleate pool boiling (in Chinese) [J]. *Chin. Sci. Bull.*, 2020, **65**: 1629-1637
- [31] RAJ R, KIM J, McQUILLEN J. Pool boiling heat transfer on the International Space Station: Experimental results and model verification[J]. *J. Heat Transfer*, 2012, **134**: 101504.
- [32] FENG Y, LI H, ZHAO J, *et al.* Lattice Boltzmann study on influence of gravitational acceleration on pool nucleate boiling heat transfer[J]. *Microgravity Sci. Tech.*, 2021, **33**: 21
- [33] LIU P, DU W F, WU K, *et al.* Study on performance of pool boiling heat transfer in SOBER-SJ10 based on genetic algorithm (in Chinese) [J]. *J. Eng. Thermophys.*, 2021, **42**: 1784-1790
- [34] LIU B, GARIVALIS A I, CAO Z, *et al.* Effects of electric field on pool boiling heat transfer over microstructured surfaces under different liquid subcoolings[J]. *Int. J. Heat Mass Transfer*, 2022, **183**: 122154
- [35] XU B, ZHANG C, CHEN Z, *et al.* Investigation of nano-droplet wetting states on array micro-structured surfaces with different gravity[J]. *Computers & Fluids*, 2021, **222**
- [36] WANG X, XU B, WANG Y, *et al.* Directional migration of single droplet on multi-wetting gradient surface by 3D lattice Boltzmann method[J]. *Computers & Fluids*, 2020, **198**
- [37] WANG X, XU B, CHEN Z, *et al.* Effects of gravitational force and surface orientation on the jumping velocity and energy conversion efficiency of coalesced droplets[J]. *Microgravity Sci. Tech.*, 2020, **32**: 1185-1197
- [38] MO S Y, CHEN Y S, HUANG L P, *et al.* Preparation and the cold storage performance of water/PVA sponge PCMs for aerospace applications[J]. *Microgravity Sci. Tech.*, 2022, **34**, in press
- [39] LI Z, ZENG Z, XING Y, *et al.* Microscopic structure and dynamics study of granular segregation mechanism by cyclic shear[J]. *Sci. Adv.*, 2021, **7**: eabe8737
- [40] WU Q, HOU M, YANG L, *et al.* Parametric study of the clustering transition in vibration driven granular gas system[J]. *Chin. Phys. B*, 2020, **29**: 054502
- [41] XIAO S, CHENG X, HOU M. Bearing capacity of shallow foundation and mechanical properties of sand under low gravity[J]. *Microgravity Sci. Tech.*, 2022, **34**: 16
- [42] CHENG X, XIAO S, CAO A S, *et al.* A unified constitutive model for pressure sensitive shear flow transitions in moderate dense granular materials[J]. *Sci. Rep.*, 2021, **11**: 19669

- [43] LI W, LAN D, WANG Y. Exploration of direct-ink-write 3D printing in space: droplet dynamics and patterns formation in microgravity[J]. *Microgravity Sci. Tech.*, 2020, **32**: 935-940
- [44] YANG W, ZHANG Y, HU L, et al. An Experimental study on ignition of single coal particles at low oxygen concentrations[J]. *Frontiers Energy*, 2021, **15**: 38-45
- [45] YANG W, LIU B, ZHANG H, et al. Prediction improvements of ignition characteristics of isolated coal particles with a one-dimensional transient model[J]. *Proc. Combustion Inst.*, 2021, **38**: 4083-4089
- [46] YANG W, ZHANG Y, LIU B, et al. Ignition predictions of isolated coal particles by different ignition criteria and devolatilization models[J]. *Fuel*, 2022, **314**: 122772
- [47] SUN P, WU C, ZHU F, et al. Microgravity combustion of polyethylene droplet in drop tower[J]. *Combustion Flame*, 2020, **222**: 18-26
- [48] WU C, SUN P, WANG W, et al. Flame extinction of spherical PMMA in microgravity: Effect of fuel diameter and conduction[J]. *Microgravity Sci. Tech.*, 2020, **32**: 1065-1075.
- [49] KONG W, WANG K, XIA W, et al. Ignition and combustion characteristics of overloaded wire insulations under weakly buoyancy or microgravity environments//W. Hu, Q. Kang (eds) *Physical Science Under Microgravity: Experiments on Board the SJ-10 Recoverable Satellite*[M]. Research for Development. Springer, Singapore, 2019
- [50] XUE S, KONG W. Smoke emission and temperature characteristics of the long-term overloaded wire in space[J]. *J. Fire Sci.*, 2019, **37**: 99-116
- [51] WU C, WANG S, ZHU F, et al. Opposed flame spread over cylindrical PMMA under oxygen-enriched microgravity environment[J]. *Fire Tech.*, 2020, **56**: 71-89
- [52] WU C, XIAO Y, WANG S, et al. Horizontal flame spread over thin solids in reduced buoyancy environments[J]. *Combustion Flame*, 2022, **240**: 112008
- [53] ZHU F, HUANG X, WANG S. Flame spread over polyethylene film: effects of gravity and fuel inclination[J]. *Microgravity Sci. Tech.*, 2022, **34**: 26
- [54] HUANG X, GAO J. A review of near-limit opposed fire spread[J]. *Fire Safety J.*, 2021, **120**: 103141
- [55] FENG L, WU Y, XU K, et al. Effect of particle distance on combustion behaviors through 1-D model with Neumann boundary condition[J]. *Fuel*, 2020, **276**: 117974
- [56] ZHOU H, ZHANG W, Liu YC. A cell model analysis for droplets inside non-dilute n-heptane droplet clouds near autoignition limit[J]. *Int. J. Heat Mass Transfer*, 2021, **175**: 121189
- [57] ZHOU H, LIU Y C. External group combustion of droplet clouds under two-stage autoignition conditions[J]. *Combustion Flame*, 2021, **234**: 111689.
- [58] Luo L, Zhou H, Sun Y, et al. Tsinghua university freefall facility (TUFF): A 2.2 second drop tunnel for microgravity research[J]. *Microgravity Sci. Tech.*, 2021, **33**: 26
- [59] KONG Y, LUO X, LI Y, et al. Gravity-induced solidification segregation and its effect on dendrite growth in Al-2.8wt.% Cu alloy[J]. *Microgravity Sci. Tech.*, 2021, **33**: 72
- [60] WANG Z, CHEN J, FENG X, et al. Visual dynamical measurement of the solute-induced Marangoni effect of a growing drop with a PLIF method[J]. *Chem. Eng. Sci.*, 2021, **233**: 116401
- [61] ZHANG Y, CHENG J, GLICK Y, et al. Antisolvent crystallization of l-histidine in micro-channel reactor under microgravity[J]. *Microgravity Sci. Tech.*, 2020, **32**: 27-33
- [62] WU Y L, LUO Z R, WANG J Y, et al. China's first step towards probing the expanding universe and the nature of gravity using a space borne gravitational wave antenna[J]. *Comm. Phys.*, 2021, **4**(1): 34
- [63] LIU L, LÜ D, CHEN W. In-orbit operation of an atomic clock based on laser-cooled ⁸⁷Rb atoms[J]. *Nat. Commun.*, 2018, **9**: 2760
- [64] WAN J Y, WANG X, ZHANG X, et al. Quasi-one-dimensional diffuse laser cooling of atoms[J]. *Phys. Rev. A*, 2022, **105**: 033110
- [65] WANG L, XIE J, MOU C, et al. Transcriptomic analysis of the interaction between FLOWERING LOCUS T induction and photoperiodic signaling in response to spaceflight[J]. *Front Cell Dev Biol.*, 2021, **9**: 813246
- [66] WU Y, XIE J, WANG L, et al. Circumnutations and growth of inflorescence stems of *Arabidopsis thaliana* in response to microgravity under different photoperiod conditions[J]. *Life*, 2020, **10**: 26
- [67] XIE J, WANG L, ZHENG H. Molecular Basis to integrate microgravity signals into the photoperiodic flowering pathway in *Arabidopsis thaliana* under spaceflight condition[J]. *Int. J. Mol. Sci.*, 2022, **23**: 63
- [68] XU P, CHEN H, HU J, et al. Potential evidence for transgenerational epigenetic memory in *Arabidopsis thaliana* following spaceflight[J]. *Comm Biol.*, 2021, **4**: 835
- [69] ZENG D, CUI J, YIN Y, et al. Metabolomics analysis in different development stages on SP0 generation of rice seeds after spaceflight[J]. *Front. Plant Sci.*, 2021, **12**:700267
- [70] LEI X, CAO Y, MA B, et al. Development of mouse preimplantation embryos in space[J]. *Natl. Sci. Rev.*, 2020, **7**: 1437-1446
- [71] LI F, YE Y, LEI X, et al. Effects of microgravity on early embryonic development and embryonic stem cell differentiation: phenotypic characterization and potential mechanisms[J]. *Front Cell Dev Biol.*, 2021, **9**: 79716
- [72] ZHANG J, DONG W, WANG Z, et al. Development of a new microgravity experiment facility with electromagnetic launch[J]. *Microgravity Sci. Tech.*, 2021, **33**: 68.

Space Life Science in China

MA Hong¹, ZHANG Chen², LI Yujuan¹, LÜ Xuefei¹,
LI Xiaoqiong¹, ZHANG Ying¹, YANG Chunhua¹,
LIU Huayan¹, FAN Yunlong¹, DENG Yulin¹

1. School of Life Science, Beijing Institute of Technology, Beijing 100081
2. School of Medical Technology, Beijing Institute of Technology, Beijing 100081

Abstract

With the further advancement of China's major manned spaceflight project, the national space laboratory was successfully built. China has also made considerable progress and breakthroughs in the field of space life sciences. This paper reviews the related biological effects under space flight conditions, mainly including epigenetic effects, skeleton remodeling and peripheral body fluid circulation effects, as well as the research and application of space life science related biotechnology in the field of microbial culture and biological regeneration life support system.

Key words

Space life sciences, Space biology technology, Microgravity, Ionizing radiation

1 Introduction

With the entry of human beings and other life forms into outer space and the exploration of life outside the Earth, the new interdisciplinary subject of space life science was born. The basic problems of space life science include: how do Earth life bodies (including astronauts) perceive, respond to and adapt to the space environment, and what are their basic laws? How to further support human space exploration for a longer time in space? How does life originate and evolve? Is there any other life in the universe? How to use the special space environment to understand the essence of life on the Earth and play a role in improving human life on the Earth? In the past two years, China's space life science has made remarkable breakthroughs in many aspects.

2 Spaceflight-associated Biology Effects

2.1 Cell Adhesion Effects

Microgravity induces a number of significant physiological changes in the cardiovascular, nervous, immune systems, as well as the bone tissue of astronauts. Changes in cell adhesion properties are one aspect affected during long-term spaceflights in mammalian cells. Cellular adhesion behaviors can be divided into cell-cell and cell-matrix adhesion. These behaviors trigger cell-cell recognition, conjugation, migration, cytoskeletal rearrangement, and signal transduction. Cellular Adhesion Molecule (CAM) is a general term for macromolecules that mediate the contact and binding between cells or between cells and the Extracellular Matrix (ECM).

The four major classes of adhesion molecules that regulate cell adhesion, including integrins, Immunoglobulin Superfamily (Ig-SF), cadherins, and selectin, which induced the effects of spaceflight and simulated microgravity on the adhesion of endothelial cells, immune cells, tumor cells, stem cells, osteoblasts, muscle cells, and other types of cells. Moreover, these adhesion molecules can activate the following signal pathway and biological effects. Spaceflight-associated immune system weakening ultimately limits the ability of humans to expand their presence beyond the Earth's orbit. A mechanistic study of microgravity-regulated immune cell function is necessary to overcome this challenge. Qian *et al.* demonstrate that both spaceflight and simulated microgravity significantly reduce macrophage differentiation, decrease macrophage quantity and functional polarization, and lead to metabolic reprogramming, as demonstrated by changes in gene expression profiles. Moreover, they identified RAS/ERK/NFκB as a major microgravity-regulated pathway. Exogenous ERK and NFκB activators significantly counteracted the effect of microgravity on macrophage differentiation. In addition, microgravity also affects the p53 pathway, which might reveal a new mechanism for the effects of microgravity on macrophage development and provide potential molecular targets for the prevention or treatment of macrophage differentiation deficiency in spaceflight^[1-3]. Further studies on the effects of microgravity on cell adhesion and the corresponding physiological behaviors may help increase the safety and improve the health of astronauts in space.

2.2 Peripheral System Effect

2.2.1 Intestinal Injury and Protection

The space environment mainly includes microgravity, strong radiation, and high noise. Recent studies show that Microgravity (MG) could cause injury of the digestive system. It has been reported that spaceflight significantly decreased mucin production of Intestinal Epithelial Cells (IECs) in rats. SMG damaged intestinal homeostasis *via* increasing intestinal permeability, impairing barrier function, and increasing the susceptibility to colitis and the risk of intestinal infection. The above evidence suggests that MG or SMG damages Intestinal Epithelial Barrier (IEB) function.

The small intestine is an important organ in the human body. The intestine mucosal structure forms an

essential barrier between the external environment and internal milieu, restricting the passage of harmful substances, infectious agents, and microorganisms into circulation in human body. IEB dysfunction could lead to malnutrition, diarrhea, and Inflammatory Bowel Diseases (IBDs), which may increase the intestinal infection risk of astronauts during long-term space travel. Thus, it is critical to investigate the underlying mechanism of IEB damage under SMG and seek for protection strategy against IEB dysfunction.

Based on histomorphology, TEM, permeability of intestine, inflammatory factors in rat plasma and intestine, expression of tight and adherens junction proteins, and the proteomic approach with the tail-suspended rat model to simulate microgravity for 21 days, it has been found that IEB has been damaged with histomorphology injury, increased intestinal permeability, down-regulated adhesion molecules. 416 Differentially Expressed Proteins (DEPs) were identified and clustered into pathways for metabolism, focal adhesion, regulation of actin cytoskeleton, drug metabolism enzymes and so on. It has been found that MLCK dependent up-regulation MLC phosphorylation mediates intestinal barrier dysfunction during simulated microgravity injury. This may indicate that the regulation of epithelial MLCK is a potential target for the therapeutic treatment of microgravity injury. SMG could damage IEB also through the formation of focal adhesions mediated by the Rac1-WAVE2-Arp2/3 pathway, which benefits intestinal epithelial cell migration and barrier repair.

The study has been carried out on the alteration of Intestinal Drug Metabolizing Enzymes (IDMEs) following 14-day simulated microgravity in rat intestinal mucosa. Totally 335 DEPs were identified, 190 DEPs were up-regulated and 145 DEPs were down-regulated. Most of DEPs exhibited hydrolase, oxidoreductase, transferase, ligase or lyase catalytic activity. DEPs were mainly enriched in metabolic pathways, including the metabolism of amino acid, glucose, and carbon. 11 of DEPs were involved in exogenous drug and xenobiotics metabolism. Because the IDMEs are important for the efficacy and safety of oral drugs the expression of cytochrome P1A2 (CYP1A2), CYP2D1, CYP3A2, CYP2E1, Alcohol Dehydrogenase 1 (ADH1) and glutathione S-transferase mu 5 (GSTM5) in rat intestine mucosa was determined by Western-blot. The activity of ADH, Aldehyde Dehydrogenase (ALDH) and GST

was evaluated. SMG led to dramatically decreased expression of CYP1A2, CYP2D1, CYP3A2 and ADH1, while the GSTM5 was significantly up-regulated. ADH activity was reduced, and ALDH and GST activities did not alter remarkably. It could be concluded that SMG dramatically affected the expression and activity of some IDMEs, which might alter the efficacy or safety of their substrate drugs under microgravity^[4].

A traditional Chinese medicinal herb, Dragon's Blood (DB), was used to prevent IEB damage induced by SMG. It has been found that DB could protect histomorphology, reduce permeability and increase the expression of junction proteins in SMG-rat ileum. Proteomic analysis showed that DB regulated 1080 DEPs in rat ileum mucosa, including proteins for cell-cell adhesion, focal adhesion and cytoskeleton regulation. DB increased the expression of Rac1-WAVE2-Arp2/3 pathway proteins and F-actin to G-actin ratio, which promoted the formation of focal adhesions and finally benefits intestinal epithelial cell migration and barrier repair. The present study firstly provided some preliminary information on IDMEs under microgravity. It may be helpful to understand the intestinal health of astronauts, and supply a scientific basis for medication use during space travel^[5].

2.2.2 Peripheral Metabolic Effect

In order to screen the biomarkers of neurochemicals in peripheral blood of rats after nerve injury induced by whole brain irradiation, Meng *et al.* established a method of chemical derivation of neurochemicals in serum-ultra high performance liquid chromatography tandem mass spectrometry was used to analyze different whole brain irradiation doses (0, 10, 30 Gy) and fractional cumulative irradiation (10 Gy \times 3). The concentrations of 42 neurochemicals in rat serum were measured and statistically analyzed based on the targeted metabolomics strategy. The change degree of neurochemical content in irradiation groups was lower than the control group, indicating that acetylcholine, glutamate, tyramine and melatonin can be used as potential biomarkers of nerve injury induced by whole brain irradiation. Deng *et al.* used the similar established rat model of nerve radiation injury to evaluate the characteristic changes of neurochemicals in rat serum, including neurotransmitters, amino acids and biogenic amines. The researchers combined reversed-phase liquid chromatography tandem mass spectrometry with chemical derivatization to establish an efficient and sensitive

method for the detection of 42 polar neurochemicals. The optimized benzoyl chloride derivatization reaction can be easily carried out in one-pot reaction, and stable neurochemical derivatives (except acetylcholine and melatonin) can be obtained under mild conditions within 5 min. Derivatization can also realize rapid chromatographic separation on the HSS T3 column by gradient elution by re-labeling the analyte with labeled derivatization reagent. The multiple reaction monitoring acquisition mode can quantify the neurochemicals in rat serum, with the detection limit of 0.05 nm to 11.63 nm and the lower limit of quantification of 0.09 nm to 46.50 nm. The method has been well verified in terms of linearity and extraction recovery. This method is also effective for the extensive targeted analysis of 42 neurochemicals in serum^[6].

2.3 Epigenetic Effects

Plants grown in spaceflight exhibited differential methylation responses and this is important because plants are sessile, they are constantly exposed to a variety of environmental pressures and respond to them in many ways. Xu *et al.* previously showed that the Arabidopsis genome exhibited a lower methylation level after spaceflight for 60 h in orbit. Here, using the offspring of the seedlings grown in microgravity environment in the SJ-10 satellite for 11 days and returned to Earth, they systematically studied the potential effects of spaceflight on DNA methylation, transcriptome, and phenotype in the offspring. Whole-genome methylation analysis in the first generation of offspring (F1) showed that, although there was no significant difference in methylation level as had previously been observed in the parent plants, some residual imprints of DNA methylation differences were detected. Combined DNA methylation and RNA-sequencing analysis indicated that the expression of many pathways, such as the abscisic acid-activated pathway, protein phosphorylation, and nitrate signaling pathway, *etc.* were enriched in the F1 population. As some phenotypic differences still existed in the F2 generation, it was suggested that these epigenetic DNA methylation modifications were partially retained, resulting in phenotypic differences in the offspring. Furthermore, some of the spaceflight-induced heritable Differentially Methylated Regions (DMRs) were retained. Changes in epigenetic modifications caused by spaceflight affected the growth of two future seed generations. Altogether, their research is helpful in

better understanding the adaptation mechanism of plants to the spaceflight environment^[7].

Moreover, the epigenetic effects of mammalian cells also involve some important physiological systems. The Central Nervous System (CNS) is one of the most important systems in the human brain. During spaceflight, radiation and microgravity have different biological effects on the human brain. The inflammatory activation of glial cells is the main sign of impaired neural function. By establishing an *in vitro* model of radiation, simulated microgravity and a combination of the two conditions, Ma *et al.* explored the biological changes in human glial cells, including the release of inflammatory factors, the changes of autophagy and the transcriptional expression of the key regulator of histone methyltransferase enzyme Enhancer of Zeste Homolog 2 (EZH2), a potential dual regulator of inflammation and autophagy. Their results showed that the simulated space environment significantly affected the growth and morphological changes of nerve cells, neurons released cytokines, recruited monocytes, triggered inflammatory response, and both radiation and microgravity could activate autophagy. In a simulated space environment, the transcriptional level of EZH2 decreased, and the down-regulation of EZH2 induced autophagy by activating the mTOR pathway. The change of autophagy level can activate NF- κ B and induce the release of inflammatory factor IL-6. At the same time, the interaction between NF- κ B and EZH2 may in turn affect the expression of EZH2, suggesting that EZH2 may be a dual regulator regulating inflammatory activation and autophagy in the space environment, which helps to explain the biological damage of the central nervous system caused by neuroinflammation observed in the space environment and provide a molecular target for the health protection of astronauts in long-term space flight^[8].

2.4 Cytoskeleton Reorganization Effects

Decades of spaceflight studies have provided abundant evidence that individual cells *in vitro* are capable of sensing space microgravity and responding to cellular changes both structurally and functionally. However, how microgravity is perceived, transmitted, and converted to biochemical signals by single cells remains unrevealed. Studies on cells of the musculoskeletal system, cardiovascular system, and immune system were covered. Among all the reported cellular changes in response to space microgravity, Cytoskeleton (CSK) re-

organization emerges as a key indicator. The CSK network is a complex and elaborate system. With the MFs, IFs, and MTs constituting the backbone of the CSK, other structures, like the spectrin network, primary cilium, septin, and Lamin A/C nucleoskeleton have also been demonstrated to be involved in cell mechanotransduction. Based on the evidence of CSK reorganization from space flight research, a possible mechanism from the standpoint of “cellular mechanical equilibrium” is proposed for the explanation of cellular response to space microgravity. Cytoskeletal equilibrium is broken by the gravitational change from ground to space and is followed by cellular morphological changes, cell mechanical properties changes, extracellular matrix reorganization, as well as signaling pathway activation/inactivation, all of which ultimately lead to the cell functional changes in space microgravity. The polymerization/depolymerization of CSK filaments is dynamic. Cytoskeletal reorganization might be different at the beginning of entering space with accommodation after long-term spaceflight, their role in gravitational sensation still needs further investigation^[9-11].

3 Space Biology Technology

3.1 Microfluidic Chip-based Long-term Preservation and Culture of Engineering Bacteria for DNA Damage Evaluation

Understanding the effects of long-term exposure to space environment is paramount to maintaining the safety and health of astronauts. The physical dosimeters currently used on the space station cannot be used to assess the physiological effects of radiation. Moreover, some developed biological methods are time-consuming and passive, and cannot be used for active and real-time detection of the physiological effects of radiation in space environment. Here, the SOS promoter: *recA*-eGFP genetic engineering bacteria was constructed and characterized, and DNA damage effects of some chemical reagents and radiation were evaluated. The results indicated the constructed engineering bacteria can distinguish DNA damage reagents from non-damage reagents, and have a good dose-fluorescence effect against Co-60 radiation with the detection limit of 0.64 Gy (Fig. 1 and Fig. 2). To overcome the restriction of long-term preservation of bacteria in space environment, the bacteria were freeze-dried, and the protectants were optimized, the

storage time of bacteria under dry conditions was explored by accelerated storage experiments. Finally, a microfluidic chip was designed and fabricated for freeze-drying genetic engineering bacteria recovery, culture,

and analysis in space environment (Fig. 3). This study can provide support for the establishment of on-orbit radiation damage risk monitoring and early warning, and can provide basic data for maintaining the

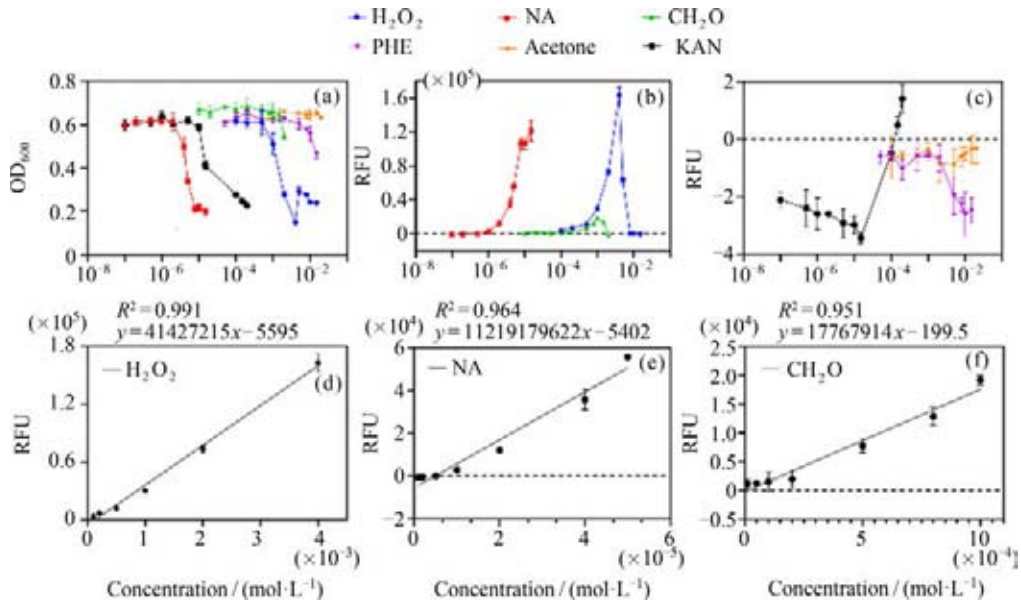


Fig. 1 Damage and fluorescence effect of engineering bacteria induced by chemical reagents

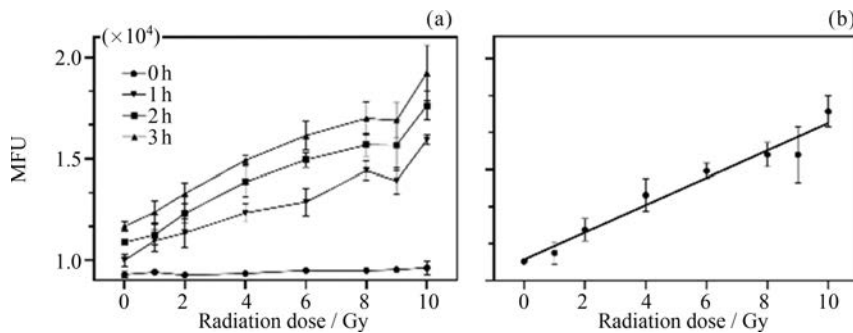


Fig. 2 Response of genetic engineering bacterial strain to different doses of Co-60 radiation

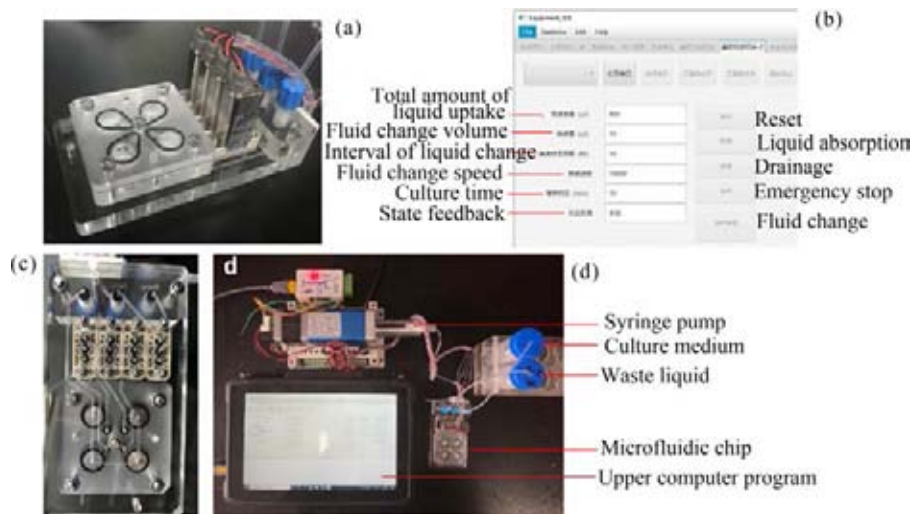


Fig. 3 Microfluidic chip structure and culture system

health and performance of astronauts on long-term space flight missions. Moreover, the technique developed herein has a great potential to be used as a powerful tool for efficiently screening of various radioactive substances, toxic chemicals, drugs, *etc.*

3.2 Microorganism Culture and Detection Payload in the China Space Station

The research project on the prevention and control technology of microorganisms in extraterrestrial habitats undertaken by Deng *et al.* of Beijing Institute of Technology has completed most of the work since the project started in 2020. The project aims to carry out on-orbit cultivation and analysis of specific microorganisms for the needs of microorganism prevention and control in the China space station, as well as in the extraterrestrial habitation facilities for future lunar exploration projects and deep space exploration. The project uses microorganisms that have the ability to degrade certain aviation materials collected in the final assembly workshop of the space station as the research object, and develops a special culture chip to study the corrosion process of microorganisms on aviation materials in the space environment.

Based on the results of ground-based experiments, the project developed a microorganism culture and detection payload, and two chip cartridges that support quick installation. Among the two chip cartridges, the culture chip cartridge is used to provide solution environment and temperature control for microorganism culture, and the microbes are photographed by the payload. The detection chip cartridge is used for quantitative detection of specific microorganisms. The detection principle is based on Q-LAMP technology. A microfluidic chip is used to lyse microorganisms and amplify nucleic acids, and the payload is responsible for fluorescence collection and quantitative analysis. The entire detection process takes about 60 min. In the future, this payload will be upgraded to support on-orbit sampling and detection of microorganisms. These two chip cartridges contain all the reagents, chips and liquid drive systems, and have high air tightness, which is convenient for astronauts to operate in orbit and has high biological safety. The payload has a power supply interface and a communication port that are compatible with the relevant cabinet platform of the Mengtian experimental module of the China Space Station, and supports the

downloading of on-orbit experimental data to the ground. The payload will be launched with the Mengtian experimental module to dock with the China Space Station in 2022, and follow-up on-orbit tests will be carried out as planned. (See Fig. 4)

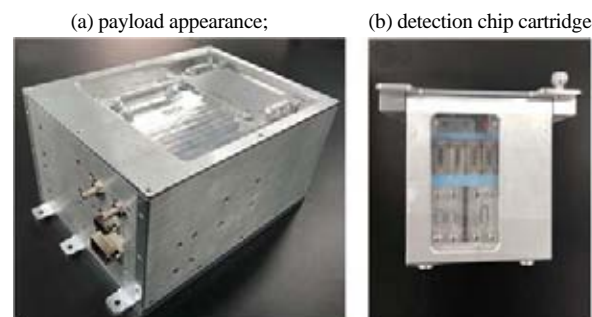


Fig. 4 Microorganism culture and detection payload.

During a spaceflight, astronauts need to live in a spacecraft on-orbit for a long time, and the relationship between humans and microorganisms in the closed environment of space is not as same as on the ground. The dynamic study of microorganisms in confined space shows that with the extension of the isolation time, harmful bacteria gradually accumulate. Monitoring and controlling microbial pollution in a confined environment system are very important for crew health and the sustainable operation of a space life support system. Culture-based assays have been used traditionally to assess the microbial loads in a spacecraft, and uncultured-based techniques are already underway according to the NASA global exploration roadmap. High-throughput sequencing technology has been used generally to study the communities of the environment and humans on the ground, and shows its broad prospects applied onboard. Chen *et al.* reviewed the recent application of high-throughput sequencing on space microbiology and analyze its feasibility and potential as an on-orbit detection technology^[12].

3.3 Bioregenerative Life Support Systems Which Can Support Humans Living in Space

In order to travel outside the Earth and achieve long-term survival in the deep space, humans need to build a Biological system-regenerative Life Support System (BLSS), which reduces the demand for Earth supply by regenerating the oxygen, water and food required by astronauts, and prevents astronauts from polluting outer stars by recycling waste. In 2016, Yuegong

No. 1 completed the technical upgrade, and the “Yuegong 365” experiment began on 10 May 2017 and was completed on 15 May 2018, lasting 370 days. The influence of unit shift change and electromechanical failure on the stability of BLSS under long-term operation conditions is studied, the regulation technology of long-term operation is established, two groups of units with different metabolic levels are established, and three shift change stages are formed. The results show that Yuegong BLSS has good stability in the long-term operation process, eliminates the influence of gas interference caused by shift and electromechanical fault through self-feedback adjustment, and has strong robustness. The crew planted 35 kinds of plants, including grains, vegetables and berries. The production of the factory fully meets the crew’s demand for plant food. The purification effect of domestic sewage has reached the standard of plant irrigation, and urine and solid waste have also been recycled. Under the load of four crew members, the experiment achieved 100% oxygen and water regeneration, 83% food regeneration and 98.2% overall material closure. However, the overall impact of space environment on BLSS is not clear, and research work is still needed. Lunar exploration projects such as lunar village and lunar research station are being carried out one after another. Therefore, the future BLSS research will focus on the payload carrying experiment of lunar probe, so as to study the mechanism of space closed ecosystem without covering the moon, clarify the impact of space environmental conditions on the ecosystem, and correct the design and operation parameters of ground-based BLSS. These studies will provide technical support for the application of BLSS in manned deep space exploration^[13-14].

4 Conclusion

Since 1992, with the continuous development and deepening of China’s manned spaceflight and space exploration activities, especially the start-up and construction of China’s manned space station project, the next 20 years will be a golden period in the development history of China’s space life science. Chinese scientists will continue to develop and obtain innovative achievements belonging to China on the basis of the

achievements inherited from their predecessors, so as to serve human space exploration and benefit human life on the ground.

References

- [1] LIN X, ZHANG K W, WEI D X, *et al.* The impact of spaceflight and simulated microgravity on cell adhesion[J]. *International Journal of Molecular Sciences*, 2020, **21**(9): 3031
- [2] SHI L, TIAN H L, WANG P, *et al.* Spaceflight and simulated microgravity suppresses macrophage development via altered RAS/ERK/NFκB and metabolic pathways[J]. *Cellular & Molecular Immunology*, 2021, **18**(6): 1489-1502
- [3] SHI S L, LI Q, CAO Q Y, *et al.* EMT transcription factors are involved in the altered cell adhesion under simulated microgravity effect or overloading by regulation of E-cadherin[J]. *International Journal of Molecular Sciences*, 2020, **21**(4): 1349
- [4] LIU H Y, GUO J J, LI Y J, *et al.* Investigation on intestinal proteins and drug metabolizing enzymes in simulated microgravity rats by a proteomics method[J]. *Molecules*, 2020, **25**(19): 4391
- [5] LI Y J, LIU S, LIU H Y, *et al.* Dragon’s blood regulates rac1-WAVE2-Arp2/3 signaling pathway to protect rat intestinal epithelial barrier dysfunction induced by simulated microgravity[J]. *International Journal of Molecular Sciences*, 2021, **22**(5): 2722
- [6] MENG X S, BAI H, MA Q, *et al.* Broad targeted analysis of neurochemicals in rat serum using liquid chromatography tandem mass spectrometry with chemical derivatization[J]. *Journal of Separation Science*, 2020, **43**(21): 4006-4017
- [7] XU P P, CHEN H Y, HU J B, *et al.* Potential evidence for trans-generational epigenetic memory in *Arabidopsis thaliana* following spaceflight[J]. *Communications Biology*, 2021, **4**(1): 835
- [8] ZHAO S C, PEI S Z, WANG A L, *et al.* Possible role of a dual regulator of neuroinflammation and autophagy in a simulated space environment[J]. *Acta Astronautica*, 2021, **187**: 181-189
- [9] SHI W G, ZHANG Y N, CHEN K M, *et al.* Primary cilia act as microgravity sensors by depolymerizing microtubules to inhibit osteoblastic differentiation and mineralization[J]. *Bone*, 2020, **136**: 115346
- [10] DING D, YANG X, LUAN H Q, *et al.* The microgravity induces the ciliary shortening and an increased ratio of anterograde/ retrograde intraflagellar transport of osteocytes[J]. *Biochemical and Biophysical Research Communications*, 2020, **530**(1): 167-172
- [11] WU X T, YANG X, TIAN R, *et al.* Cells respond to space microgravity through cytoskeleton reorganization[J]. *FASEB Journal*, 2022, **36**(2): e22114
- [12] CHEN Y W, WU B, ZHANG C, *et al.* Current progression: application of high-throughput sequencing technique in space microbiology[J]. *BioMed Research International*, 2020, 2020: 4094191
- [13] Fu Y, Yi Z, Du Y, *et al.* Establishment of a closed artificial ecosystem to ensure human long-term survival on the moon[J]. *bioRxiv*, 2021: 2021.01.12.426282.
- [14] LIU H, YAO Z K, FU Y M, *et al.* Review of research into bioregenerative life support system(s) which can support humans living in space[J]. *Life Sciences in Space Research*, 2021, **31**: 113-120

Progress on Space Materials Science in China: I Debris Shielding Fibrous Materials and High Specific Energy Lithium Sulfur Batteries*

WU Nan, LIU Shuangke, ZHANG Xiaoshan, SUN Weiwei, ZHENG Chunman, WANG Yingde

College of Aerospace Science and Engineering, National University of Defense Technology, Changsha 410073

Abstract

The development of China's space industry puts forward urgent requirements for high-performance debris shielding materials and high energy density rechargeable battery. In this review, the recent progress on debris shielding fibrous materials and high energy density Li-S battery are particularly summarized. According to the experimental results, basalt fibers and silicon carbide fibers were chosen as the effective filling shielding materials. The geometric structure of fabrics was also investigated. For the novel shielding materials, high-strength and flexible silicon carbide micro-nano fibrous membranes were designed and fabricated. The obtained membranes with excellent mechanical properties portend the potential applications in debris protection structure. Furthermore, the high specific energy lithium sulfur batteries have made remarkable progress in basic research and application research in recent years. In order to solve the key problems of polysulfides shuttle and slow redox kinetics in lithium sulfur battery, a series of transition metal compound@hollow structure carbon-based material as sulfur host with dual functions of catalysis and adsorption towards polysulfides were designed and constructed. The obtained Li-S pouch cells with high areal sulfur loading of $6.9 \text{ mg}\cdot\text{cm}^{-2}$ yield exceptional high practical energy density of $382 \text{ W}\cdot\text{h}\cdot\text{kg}^{-1}$ under lean electrolyte of $3.5 \mu\text{L}\cdot\text{mg}^{-1}$, demonstrating the great potential of realistic high-energy Li-S batteries.

Key words

Space materials, Silicon carbide fibers, Debris shielding, Li-S battery

1 Research Progress of Space Debris Shielding Fibrous Materials

According to the design requirements of spacecraft

reliability and the results of space debris risk assessment, space debris shielding design is required for Tiangong-1 and Tiangong-2 of China's manned spaceflight project II and the Tiangong Space Station of the manned spaceflight project III. It is well known that the Tianhe

* Supported by the National Natural Science Foundation of China (52002400), Young Elite Scientists Sponsorship Program by CAST (YESS20200093)

Received June 29, 2022

core module, which was successfully launched on 29 April 2021, is used to unify the control and management of the space station assembly. It provides living and working space for astronauts and supports scientific research in some disciplines, while the Mengtian and Wentian experimental modules to be launched subsequently are mainly used to support space science and application research. The core module of the Tiangong Space Station is 18.1 m long, with a maximum diameter of 4.2 m, and has an orbital lifetime of 15 years, making it much more vulnerable to space debris. The results of the space debris risk assessment indicated that the Whipple shielding structure could not be used to protect the space station to meet the overall specifications. In response, the General Design Department of Beijing Space Vehicle adopted ceramic fibers into the debris shielding structure. A large number of numerical simulations and hypervelocity impact tests were carried out to complete the screening of the stuffed layer of ceramic fibers after thermal cycle tests and thermal vacuum tests^[1].

1.1 Experimental Results of Silicon Carbide Fibers

To date, the General Design Department of Beijing Space Vehicle has tried more than a dozen materials such as carbon fiber fabrics, glass fiber fabrics, Kevlar fiber fabrics, silica fiber fabrics, basalt fiber fabrics, SiC fiber fabrics, SiC blankets, and PBO fiber fabrics. After engineering screening of these fabrics, two engineering schemes of SiC and basalt stuffed shields are finally determined. The comparative schematic diagrams of ballistic characteristics of the SiC stuffed shield, basalt stuffed shield, Nextel stuffed shield and three-layer aluminum plate shield are given in Fig. 1 (the data above $7 \text{ km}\cdot\text{s}^{-1}$ is the fitting result). The ballistic limits

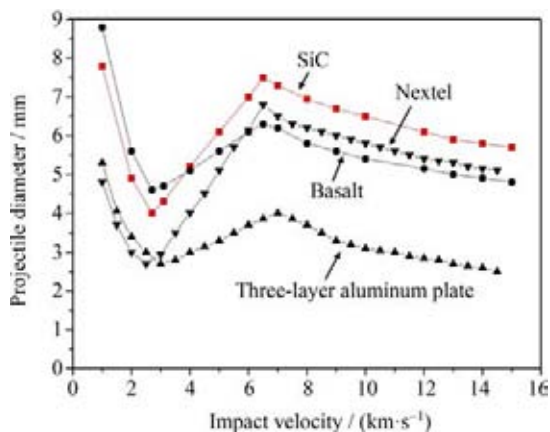


Fig. 1 Comparison of ballistic limit curves of filled protective structures

of the basalt stuffed shield at low velocities are slightly higher, and the ballistic limits of the SiC stuffed shield at high velocities are slightly higher. The overall protection property of the two stuffed shields is comparable to that of the Nextel stuffed shield used on the ISS, and much better than that of the three-layer aluminum plate shield of equal surface densities.

For the excellent protection effect of SiC fibers, the shielding property of its structure under high-speed impacts in large diameter debris (diameter greater than 1 cm) was studied experimentally and compared with that of the three-layer aluminum shield, in which the surface density remains the same as the other two stuffed layers. Fig. 2(a) shows the test results of a projectile with a diameter of 4.22 cm and a velocity of $3.16 \text{ km}\cdot\text{s}^{-1}$ striking a SiC stuffed shield. Fig. 2(b) shows the test results of a projectile with a diameter of 4.22 cm and a velocity of $3.23 \text{ km}\cdot\text{s}^{-1}$ striking a three-layer aluminum plate shield. Under the given operating conditions, both the SiC stuffed shield and the three-layer aluminum plate shield are found slightly damaged, but the damaged condition of the former rear plate is smaller than that of the latter, but the difference is relatively insignificant. In addition, the protection property under hypervelocity impacts was also evaluated in tests. Fig. 2(c) shows the test results of a projectile with a diameter of 6.50 cm and a velocity of $6.57 \text{ km}\cdot\text{s}^{-1}$ striking a SiC stuffed shield, and Fig. 2(d) shows the test results of a projectile with a diameter of 6.50 cm and a velocity of $6.43 \text{ km}\cdot\text{s}^{-1}$ striking a three-layer aluminum plate shield. Under the given operating conditions, a minor damage is found to occur in the SiC stuffed shield, while a severe burst damage is found to occur in the three-layer aluminum plate shield, which is a significant difference.

The comprehensive experimental study and simulation results demonstrate that the application of SiC fibers in the space station debris shield is feasible and can meet the safety threshold requirements of the space station. Later, research will carry on the improvement research on the weaving properties, scale preparation and cost reduction of SiC fibers.

1.2 Optimization of Silicon Carbide Fabric Structure

Based on the characterization analysis of SiC fiber properties, the optimized design of the fabric structure can further enhance the protection effect under the premise

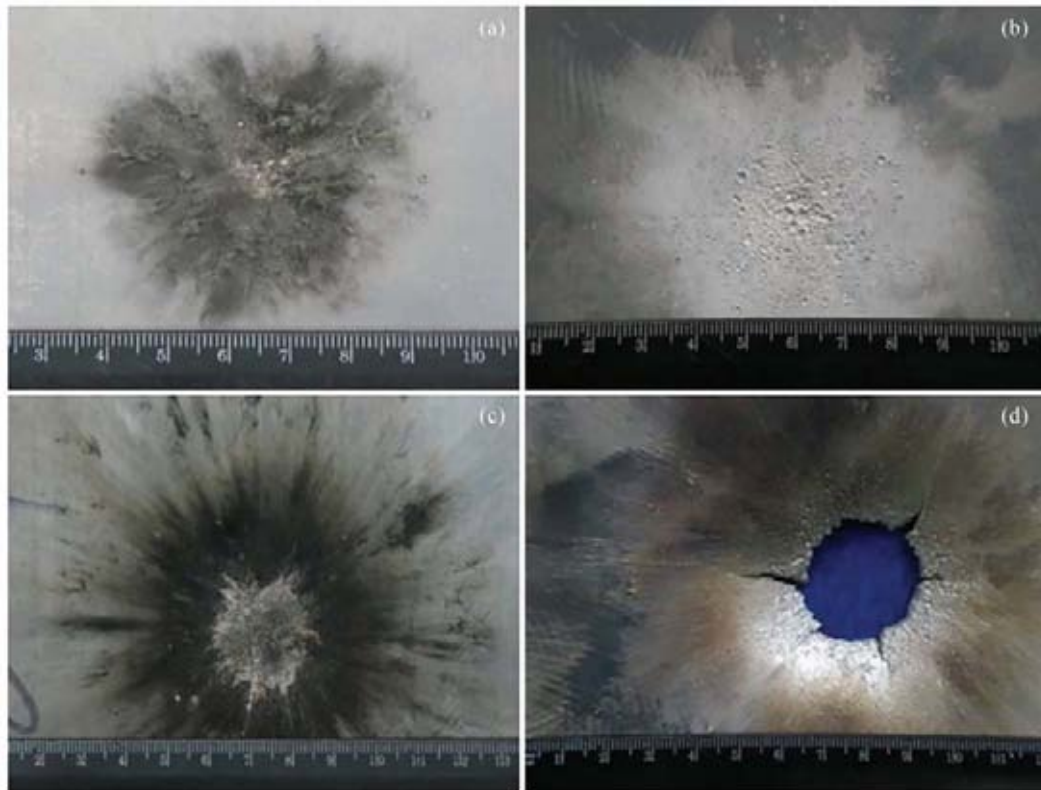


Fig. 2 Structural damage of three-layer aluminum and SiC fibers after different impacting velocity and different projectile diameter

of meeting the requirements of the overall shield on the thickness of the fabric stuffed layer and the surface density index. The design of the fabric structure needs to take into account several aspects. (i) The bending of the fibers in the fabric will cause some damage to itself, further reducing the mechanical strength of the fibers, which seriously affects the structural integrity of the fabric and the mechanical properties it exerts. (ii) The increase in the number of fiber yarns per unit area of the fabric can increase the number of SiC fibers that collide with the incident debris, which is conducive to a more adequate fragmentation of the projectile. (iii) The fiber convexity of the fabric surface is the initial contact point between the whole structure and the incident debris, and the design to increase the density of the convexity is conducive to increasing the impact point between the fabric and the debris within the unit surface density. (iv) The yarn orientation, winding method and entanglement point density in the fabric determine whether the response behavior of the stuffed layer tends to be rigid or flexible under the hypervelocity impact of the debris cloud, which is also of vital significance to whether the stuffed layer can effectively intercept the debris cloud.

1.2.1 Choice of Fabric Type

According to the above analysis, the fabric type was firstly studied. The original tissue of the two-dimensional fabrics includes plain, twill and satin weaves. In the shield, the fabric as the stuffed layer must have a certain degree of stiffness to resist the deformation brought about by the impact of the debris cloud, so as to achieve a better incision effect and interception effect on the debris. Therefore, it is required to use the type with high entanglement and stronger fabric structure for fabric in the stuffed layer, and finally the plain weave fabric type is preferred.

1.2.2 Optimization of Buckling Wave Height of Warp and Weft Yarns in Fabrics

The geometric structure of the fabric refers to the different coordination conditions of buckling wave heights in the interweaving of warp and weft yarns. The larger the buckling wave height of SiC fiber bundles in the interwoven state, the more severe the bending deformation. The fibers break when the radius of curvature formed by the buckling wave height is smaller than the minimum radius of curvature allowed to resist fracture. Judging from the mechanism of the fiber bundle fracture

and disintegration, the fracture is caused not only by slip among fibers but also by fiber itself. The fiber fracture will seriously damage the strength of the fabric, so it is an effective way to prevent the loss of strength of the fabric to control the buckling wave height of the fiber bundle and choose the fabric structure rationally.

The supporting surface of the fabric refers to the ratio of the area of the fabric in contact with a certain plane under a certain pressure. In the 5th phase geometry, the warp and weft yarns have the same buckling wave height, and both warp and weft yarns are displayed on the fabric surface, so there are more surface supporting points. The supporting point is reflected in the hypervelocity impact protection as its impact point with the secondary debris cloud, which directly affects the ability of the stuffed fabric layer to break and intercept the secondary debris. Taking the above two aspects into consideration, the 5th phase of the fabric structure on the one hand can unify the buckling wave height of the fiber bundle in $L_0/2$, which avoids the fiber damage caused by excessive bending of some yarns in the fabric (such as warp or weft), and ensures the integrity of the fabric structure. On the other hand, it also increases the impact point between the fabric surface and the debris cloud, which can effectively improve the capacity of the fabric to break and intercept the debris.

1.2.3 Determination of Geometric Structure

Parameters of Fabrics

In order to reduce the fracture of SiC fibers during the weaving process, we focus on the following points from the perspective of fabric structure design: To avoid excessive bending of fibers and fiber bundles during interweaving of SiC fabrics, reasonable fabric weaves and interweaving structures are selected according to different fiber bundles and fabric densities. The warp and weft density and fabric tightness of SiC fabrics are reasonably determined to avoid excessive bending and fracture of SiC fabrics and fiber bundles during interweaving as far as possible. Although the elongation of the fiber is smaller than the calculated value due to the incline and the change of the inside and outside position of the fiber in the twisting process, the minimum allowable radius of curvature for the fiber not to be broken is reduced, and the actual woven density of the fiber fabric is increased. Therefore, the actual weavable density and tightness of the non-compact structure fiber fabric can be greater than the calculated value in actual production. However, considering that SiC fibers are

ceramic brittle fibers with low twist resistance, and twisting may make the fibers break easily, the SiC fabrics are generally not twisted during the weaving process.

In summary, the structural parameters of the SiC fiber fabric are preferably selected as follows. (i) Determination of fabric type and thickness: Plain weave fabric type is adopted as required by protection properties for fabric fastness, with a preferred fabric thickness of 0.4mm. (ii) Determination of geometric structure phase: On the one hand, it aims to make the buckling wave height of the warp yarn and the weft yarn the same and reduce the deformation damage of the fiber; in addition, the warp and weft yarns are subjected to external forces simultaneously in the protection process, so it is necessary to use the same supporting surface to increase the impact point between the fabric and the debris, so the 5th structural phase is preferred. (iii) Warp and weft yarn tightness: Considering the consistent tightness of warp and weft, the warp tightness is 48% and the weft tightness is 50%. (iv) Warp and weft yarn density: According to the warp and weft yarn tightness, the warp yarn density should be 48 threads/10 cm and the weft yarn density should be 50 threads/10 cm.

1.3 Micro-nano Ceramic Fibers for Space Debris Shielding

As is well known that the main yarn is the main body of energy absorption in the fabrics. Due to the failure model is tension fracture, the selected fibers with high-strength, high-fracture elongation is one of the effective ways to improve the energy absorption of three-dimensional fabrics. In addition, under the penetration of high-speed ballistics, the friction among multiple layers of fabric layers is negligible. The total absorbed energy by the whole fabric during ballistic penetration is equal to the product of the energy absorbed by the single-layer fabric and the number of layers. Therefore, the more layers there are, the more energy the fabric absorbs. In summary, SiC fibers with the decreased diameter, high strength and high modulus are beneficial to improve the shielding effect^[2].

According to the above analysis, robust micro to nano SiC fibrous membranes were developed recently in China^[3]. The membranes composed of randomly oriented nanofibers with an average diameter of 550 nm were fabricated by a combination of electrospinning and post-heat-treatment process. The mechanical properties of the as-prepared membranes were enhanced significantly through in-situ embedded nanoparticles into the

SiC fibers. The optimized SiC fibrous membrane demonstrated a low flexural modulus of 7.79 kPa, a high tensile strength of 33.2 MPa and the elastic modulus of 618 MPa, respectively. The smaller flaw size, initiation of nanocracks and pinning effect by the in-situ formed nanoparticles are believed to contribute mostly to the enhanced mechanical properties. The obtained SiC fibrous membranes with good thermal stability and excellent mechanical properties display potential applications on debris shielding structures.

The space station operating in the earth orbits needs insulating treatment. The filled fabrics in the debris shielding structure with thermal insulation property are favorable for the weight reduction. It has been found that constructing porous structure is an effective way to reduce thermal conductivity of fibers. On the one hand, this structure can lengthen the heat transfer path, leading to solid heat transfer reduced. On the other hand, this structure contributes to enhance multiple reflection-absorption of IR radiation, which can decrease radiation heat transfer. Therefore, ceramic fibers with proper porous

structure may effectively enhance their thermal insulation performance.

Based on the above demand, the SiZrOC NFs with integrated properties of high flexibility, excellent fire resistance, oxidation resistant (850°C in Air), high-temperature stability (1200°C in Ar) and low thermal conductivity ($\sim 0.0511 \text{ W}\cdot\text{m}^{-1}\cdot\text{K}^{-1}$ at 25°C in Air) were fabricated (Fig. 3).^[4,5] Furthermore, the obtained SiZrOC NF membranes pyrolyzed at 1200°C showed a maximum tensile strength of 0.812 ± 0.086 MPa, which was similar to the most reported high-strength ceramic NF membranes. A piece of SiZrOC NF membrane (with a width of about 15 mm) pyrolyzed at 1200°C exhibited robust mechanical strength that could hang a 100 g weight without fracture. The tensile strength (0.792 ± 0.101 MPa) of the SiZrOC NF membranes was well maintained after the bending test. The ultralow thermal conductivity benefits from the reasonably designed multi-phase microstructure, which enhanced the phonon transfer barrier and effectively decreased the infrared

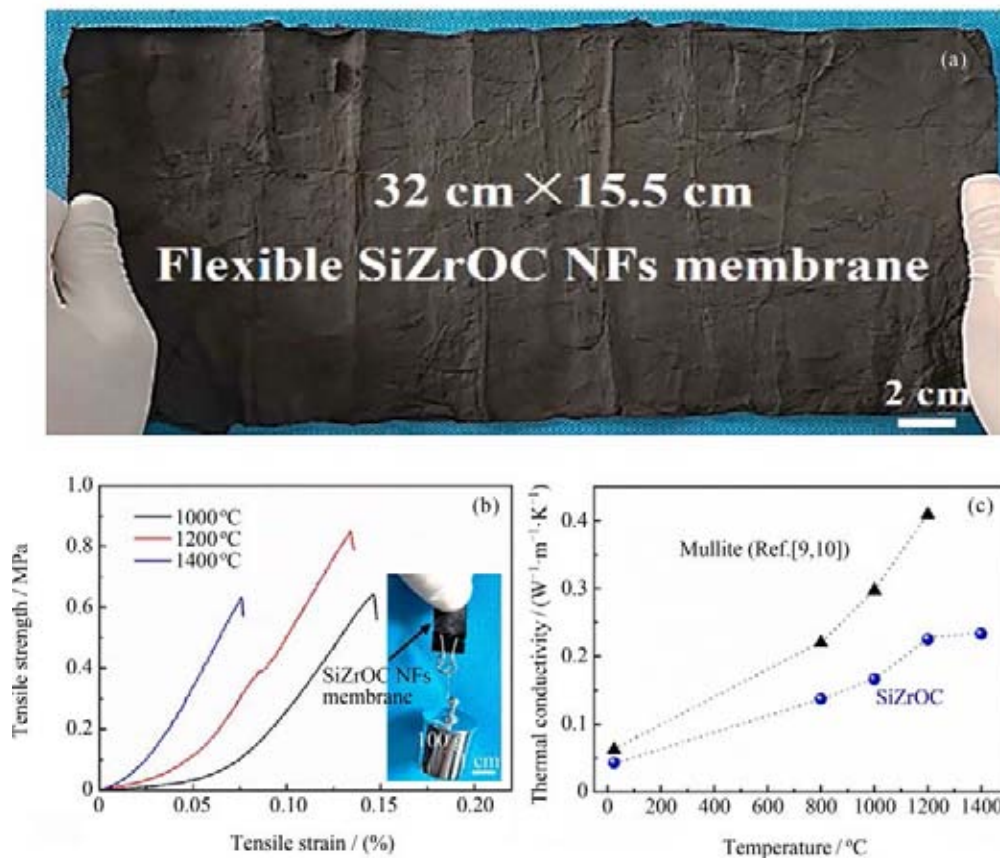


Fig. 3 (a) Digital image of the large-scale SiZrOC NF membrane; (b) Stress-strain curves of the SiZrOC NF membranes; (c) Thermal conductivity of the SiZrOC NFs and reported mullite fibers membranes

radiation heat transfer. The excellent thermal stability is likely attributed to the formation of thermal stable Si-O-Zr structure. These outstanding properties of high strength and excellent thermal insulation make our SiZrOC NFs promising debris shielding materials in extreme conditions.

2 Recent Progress of High Energy Density Li-S Battery

Due to the outstanding theoretical energy density of $2600 \text{ W}\cdot\text{h}\cdot\text{kg}^{-1}$, natural abundance, low cost, environment-friendly and good safety, lithium sulfur battery with sulfur as the cathode and lithium metal as the anode is regarded as one of the most promising new high energy density rechargeable battery technologies.

For the urgent demand for HALE UAVs, Near Space Airships, Electric Aircraft, and Submarines for high energy density rechargeable battery, many countries attach great importance to the research and development of high energy density lithium sulfur batteries. NASA has positioned it as one of the five key technologies “supporting the future space platform” and “new technology of earth observation technology and long-life secondary battery”. In the “Horizon 2020” R&D plan, the EU launched the ALISE plan, focusing on the research and development of new materials and electrochemical technology involving lithium sulfur battery, aiming to reach a $500 \text{ W}\cdot\text{h}\cdot\text{kg}^{-1}$ lithium sulfur battery that works stable. The Italian Space Agency launched the CORDIS program and jointly developed lithium sulfur batteries without metal lithium with research institutions in Germany, Britain, Sweden and other countries.

In view of the power supply demand for long-term air residence of stratospheric airships and solar aircraft, lithium sulfur batteries with high energy density and good performance under low-temperature are ideal working batteries. China has continuously funded the research and development of lithium sulfur batteries in major projects of high-resolution earth observation system. Supported by the National Natural Science Foundation of China and the Major Projects of High-Resolution Earth Observation System, our group has carried out systematic and in-depth research on high specific energy lithium sulfur batteries, and has made remarkable progress in basic research and application research in recent years.

Despite the outstanding advantages, the practical application of Li-S batteries is hindered by three major challenges: (i) the intrinsic insulating nature of S_8 molecules; (ii) the huge volumetric changes during discharge/charge processes; and (iii) the shuttle effects along with the intermediate lithium polysulfide (LiPSs) dissolution into ether-based electrolyte. All these problems will result in low utilization of sulfur, poor rate capability and cycling stability.

3 Transition Metal Compound@hollow Structure Carbon-based Material

In order to solve the key problems of polysulfides shuttle and slow redox kinetics in lithium sulfur battery, we designed and constructed a series of transition metal compound@hollow structure carbon-based material as sulfur host with dual functions of catalysis and adsorption towards polysulfides.

Sun *et al.*^[6] designed a multifunctional sulfur host based on yolk-shelled $\text{Fe}_2\text{N}@C$ nanoboxes ($\text{Fe}_2\text{N}@C$ NBs) as shown in Fig. 4 through a strategy of etching combined with nitridation for high-rate and ultralong Li-S batteries. The highly conductive carbon shell physically confines the active material and provides efficient pathways for fast electron/ion transport. Meanwhile, the polar Fe_2N core provides strong chemical bonding and effective catalytic activity for polysulfides, which is proved by density functional theory calculations and electrochemical analysis techniques. Benefiting from these merits, the $\text{S}/\text{Fe}_2\text{N}@C$ NBs electrode with a high sulfur content manifests a high specific capacity, superior rate capability, and long-term cycling stability. Specifically, even after 600 cycles at 1 C, a capacity of $881 \text{ mA}\cdot\text{h}\cdot\text{g}^{-1}$ with an average fading rate of only 0.036% can be retained, which is among the best cycling performances reported. Then they further designed and prepared catalytic FeSe_2 nanoparticles encapsulated with carbon nanoboxes ($\text{FeSe}_2@C$ NBs) with similar structures as a multifunctional sulfur host to restrain the polysulfide shuttle effect and accelerate the polysulfide redox conversion^[7]. The experimental results display that the $\text{S}/\text{FeSe}_2@C$ cathode exhibits better sulfur utilization, higher rate performance, and longer cycle life compared to $\text{S}/\text{Fe}_3\text{O}_4@C$ cathode. Even after 700 cycles

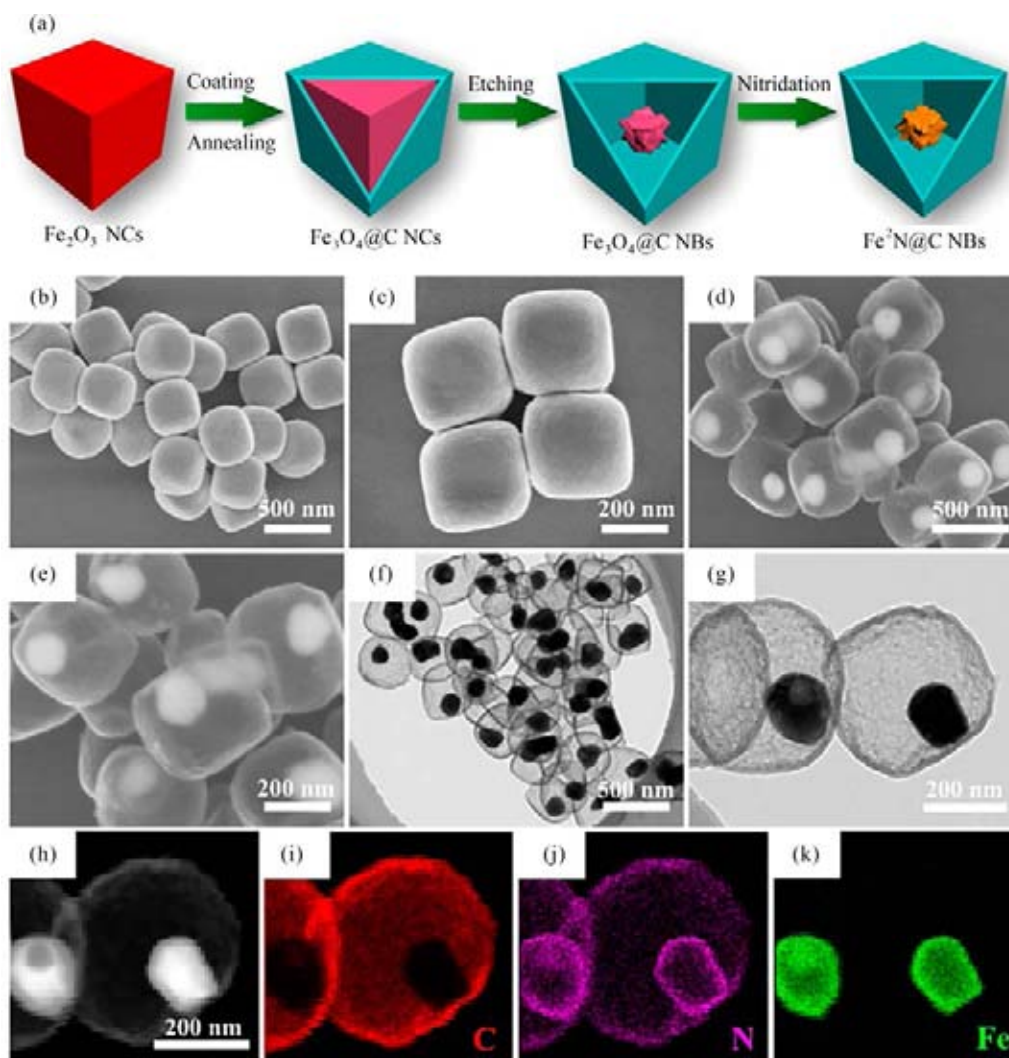


Fig. 4 (a) Schematic illustration of the fabrication process of yolk-shelled Fe₂N@C NBs. SEM of Fe₂O₃ nanocubes (b) (c) and Fe₂N@C NBs (d)(e). TEM images (f) (g) and elemental mapping images of Fe₂N@C NBs (h)–(k)

at 1C, an ultralow capacity decay of 0.04% per cycle of S/FeSe₂@C cathode can still be maintained. The Density Functional Theory (DFT) calculations reveal that FeSe₂@C NBs possess stronger chemical affinity to polysulfides and lower energy gap between bonding and antibonding orbitals, which could promote the interfacial charge transfer kinetics, thus enabling better Li-S battery performance. The strategy provides an approach to the design and construction of yolk-shelled iron-based compounds@carbon nanoarchitectures as inexpensive and efficient sulfur hosts for realizing practically usable Li-S batteries.

In addition, Sun *et al.*^[8] also reported similar yolk-shell nanostructured polar Co₉S₈ inlaid carbon nanoboxes (Co₉S₈@C NBs) as cathode host for high-

performance Li-S batteries. In this integrated structure, Co₉S₈ nanocrystals not only provide strong chemisorptive capability for polar LiPSs, but also act as a catalyst to accelerate polysulfide redox reactions, while carbon nanobox with large inner space can offer enough space to relieve the volume expansion and physically confine LiPSs' dissolution. As a result, the S/Co₉S₈@C NBs cathode exhibits high specific capacity at 1C and the capacity retention was about 83% after 400 cycles, corresponding to an average decay rate of only 0.043% per cycle. Liu *et al.*^[9] reported a rational design and fabrication of multi yolk-shell Co-NC@nitrogen doped hollow carbon spheres (Co-NC@N-HCSs) as sulfur host for high performance Li-S batteries *via* a nano-confined synthesis strategy. The growth mechanism of multi-

yolk-shell ZIF-67s@N-HCSs nanostructure was studied and the ZIF-67 yolks were tunable by changing the reactant concentration. Regarding to multi-yolk-shell Co-NC@N-HCSs hybrid, the nitrogen doped carbon shell provides effective physical confinement, abundant sulfur loading space and volume expansion alleviation, while the multi polar Co-NC yolks can enhance the internal electron conductivity inside the cavity and offer stronger chemisorption capability for LiPSs as well as catalytic effects on the redox reaction of LiPSs. Benefiting from the unique multi yolk-shell design, the S/Co-NC@N-HCSs electrode with sulfur content of 80.82 wt%, exhibits high discharge capacity of 1173 mA·h·g⁻¹ at 0.1 C and 995.8 mA·h·g⁻¹ at 1 C. It also shows long cycle life up to 450 cycles with a slow capacity decay rate of 0.13% per cycle.

Despite the great progress of Li-S battery performance at coin-level, both key parameters and challenges at pouch cell scale to achieve practical high energy density require high-sulfur-loading cathodes and lean electrolytes. In order to improve the sulfur content and sulfur areal density while remain good electrochemical activity to obtain high energy density of Li-S battery at

pouch cell level, constructing multifunctional carbon materials with high conductivity and high pore volume is very important. Wang and Liu *et al.*^[10] reported a carbon-bubble-constructed 3D interconnected hierarchically porous carbon with tunable wall thickness and ultrahigh pore volume through catalytic conversion of ethanol on ZnO foam template and subsequent template removal. The carbon foam integrated by hollow carbon bubble nanoreactors with ultrahigh pore volume up to 6.9 cm³·g⁻¹ is able to host 96 wt.% sulfur in the composite. Tailoring polysulfide trapping and ion/electron transport kinetics during the charge-discharge process can be achieved by adjusting the wall thickness of hollow carbon bubbles. And a further in-depth understanding of electrochemical reaction mechanism for the cathode is impelled by the in-situ Raman spectroscopy. As a result, the as-prepared cathode delivers high specific capacitances of 1269 and 695 mA·h·g⁻¹ at 0.1 and 5 C, respectively. As shown in Fig. 5, Li-S pouch cells with high areal sulfur loading of 6.9 mg·cm⁻² yield exceptional high practical energy density of 382 W·h·kg⁻¹ under lean electrolyte of 3.5 μL·mg⁻¹, demonstrating the great potential for realistic high-energy Li-S batteries.

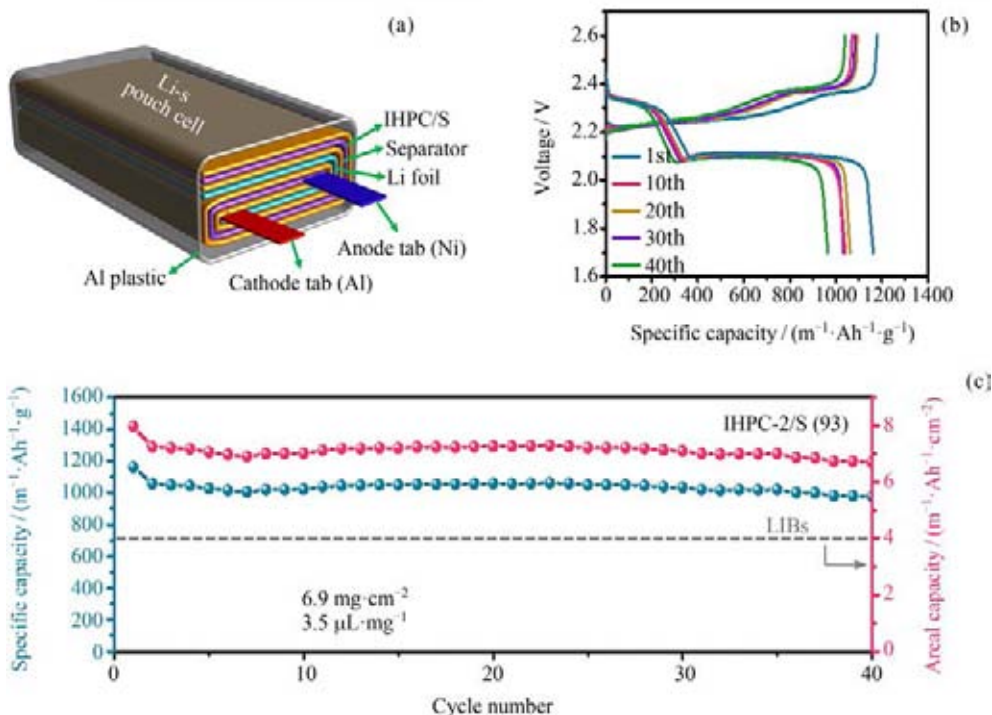


Fig. 5 Assessment of electrochemical capability for the industrial grade Li-S pouch cells based on the IHPC-2/S (93) nanocomposite. (a) Schematic diagram of as-assembled Li-S pouch cells. (b) GCD curves and (c) cycling performance of the Li-S pouch cell at 0.1 C. (d) Comparison of energy density at the device level between the Li-S pouch cell in this work and other reported Li-S cells

References

- [1] YAN Jun, ZHENG Shigui. Space debris protection design for the space station[J]. *Space Debris Research*, 2017, **17**(1): 25-29
- [2] GU Bohong, SUN Baozhong. Impact Dynamics of Textile Structural Composites[M]. Beijing: Science Press, 2012
- [3] WU N, WANG B, WANG Y D. Enhanced mechanical properties of amorphous SiOC nanofibrous membrane through in situ embedding nanoparticles[J]. *Journal of the American Ceramic Society*, 2018, **101**(10): 4763-4772
- [4] ZHANG X S, WANG B, WU N, *et al.* Multi-phase SiZrOC nanofibers with outstanding flexibility and stability for thermal insulation up to 1400 °C[J]. *Chemical Engineering Journal*, 2021, **410**: 128304
- [5] ZHANG X S, TIAN Q, WANG B, *et al.* Flexible porous SiZrOC ultrafine fibers for high-temperature thermal insulation[J]. *Materials Letters*, 2021, **299**: 130131
- [6] SUN W W, LIU C, LI Y J, *et al.* Rational construction of Fe₂N@C yolk-shell nanoboxes as multifunctional hosts for ultralong lithium-sulfur batteries[J]. *ACS Nano*, 2019, **13**(10): 12137-12147
- [7] SUN W W, LI Y J, LIU S K, *et al.* Mechanism investigation of iron selenide as polysulfide mediator for long-life lithium-sulfur batteries[J]. *Chemical Engineering Journal*, 2021, **416**: 129166
- [8] SUN W W, LI Y J, LIU S K, *et al.* Catalytic Co₉S₈ decorated carbon nanoboxes as efficient cathode host for long-life lithium-sulfur batteries[J]. *Nano Research*, 2020, **13**(8): 2143-2148
- [9] SUN X X, LIU S K, SUN W W, *et al.* Nano-confined synthesis of multi yolk-shell Co-NC@N-HCSs hybrid as sulfur host for high performance lithium-sulfur batteries[J]. *Electrochimica Acta*, 2021, **398**: 139302
- [10] WANG L, LIU S K, HU J, *et al.* Tailoring polysulfide trapping and kinetics by engineering hollow carbon bubble nanoreactors for high-energy Li-S pouch cells[J]. *Nano Research*, 2021, **14**(5): 1355-1363

Progress of Materials Science in Space Technology in China (2020–2022)*

WEI Qiang¹, DONG Shaoming^{2,3}

1. School of Materials Mechanical Engineering, Hebei University of Technology, Tianjin, 300401
2. State Key Laboratory of High Performance Ceramics and Superfine Microstructure, Shanghai Institute of Ceramics, Chinese Academy of Sciences, Shanghai 200050
3. Structural Ceramics and Composites Engineering Research Center, Shanghai Institute of Ceramics, Chinese Academy of Sciences, Shanghai 200050

Abstract

In this paper, the main research work and related reports of materials science research in China's space technology field during 2020–2022 are summarized. This paper covers Materials Sciences in Space Environment, Materials Sciences for Space Environment, Materials Behavior in Space Environment and Space experimental hardware for material investigation. With the rapid development of China's space industry, more scientists will be involved in materials science, space technology and earth science researches. In the future, a series of disciplines such as space science, machinery, artificial intelligence, digital twin and big data will be further integrated with materials science, and space materials will also usher in new development opportunities.

Key words

Materials sciences in space environment, Materials sciences for space environment, Materials behavior in space environment, Space experimental hardware for material investigation

1 Introduction

The integration of space technology and material science has formed a series of new disciplines with space environment as the intersection point. As a new interdisciplinary field, space materials science describes the relation between space environment and materials. On the one hand, space environment effects on materials are harsh to spacecraft and its materials, such as charged particle radiation and atomic oxygen^[1–3]. Under the space environment the research and protection of damage mechanism and performance evolution of materials is necessary. On the other hand, space environment is special environment, such as weightlessness, and novel

materials can be prepared in the special environment^[4–6].

Generally speaking, space material science is the science of studying the structure and properties of materials and the laws of the preparation process, as well as the physical and chemical properties of materials and their working behavior under the space environment conditions such as microgravity, space radiation and high vacuum^[7–8]. Aerospace materials science is the study of the design, preparation, properties and adaptability of materials used in spacecraft. In recent years, the on-orbit manufacturing of spacecraft materials in the space station has been realized^[9–10]. At the same time, ground simulators are becoming more and more perfect. Space environment, as an extreme environment, can be

* Supported by the National Natural Science Fund of China (51873146)

Received June 29, 2022

more effectively reproduced. Material structure, properties, preparation and service behavior can be further studied on the ground. With space environment as the link, space materials and aerospace materials are further integrated to form three research directions, as shown in Fig. 1. These research directions are as follows.

(1) Materials Sciences in Space Environment: study on physical and chemical properties, phase transformation process, synthesis and forming principle of new materials under space environment.

(2) Materials Sciences for Space Environment: research on design, manufacture, processing and production technology and principle of space materials for service and development in space environment.

(3) Materials Behavior in Space Environment: Study on the behavior and adaptability of various materials in service under space environment.

Based on literature retrieval and online public information, this paper focuses on the reports in China's space and space materials field from 2020 to 2022, and summarizes relevant Chinese scholars' literature and reports to reflect the progress of materials science in China's space technology field in recent years.

2 Materials Sciences in Space Environment

2.1 Development Strategy Album on Space Materials^[7]

Space materials science has gone through half a century since its birth in 1969 and its subsequent development until 2019. In 2019, The National Natural Science Foundation of China and the Chinese Academy of Sci-

ences jointly released the “China Discipline Development Strategy-Space Science”, and space material science has become one of the space science fields supported by the development of China's manned space station and Space Science Pilot project. The development strategy outlines the development of China's space materials science in the next 10 years and up to 2050. Under the guidance of the development strategy of space science, it was reported that some research results of materials and components manufacturing experiments and applications carried out by Chinese scientists on the Shijian-10 microgravity science satellite, Tian-gong-2 space flight platform in recent years. At the same time, some basic and applied research results and future research trends of materials science in space microgravity, which cannot be simulated on the ground, are introduced.

2.2 Recent Achievements in Space Materials Research

Prof. Bingbo Wei and his team from Northwestern Polytechnical University have been conducting research on space materials for many years and have achieved fruitful results. In 2020, the team summarized the main progress in the study of four aspects from home and abroad in the recent 20 years, including space environment physical and chemical characteristics, space liquid nature of the material under the condition of forming process of kinematics and kinetics of phase transformation, space materials preparation, as well as microstructure and properties of material in space environment regulation, and the future development trend of this field is further analyzed and forecasted^[8].

In 2020–2022, the team also achieved new results in

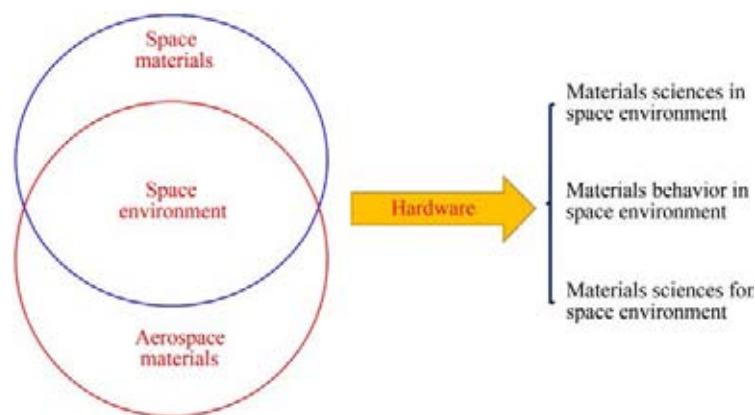


Fig. 1 Cross fusion of Materials Science in Space Technology

ground simulation of microgravity and containerless preparation and characterization of Mo-Ni and Ni-Ge alloys.

2.2.1 Mo-Ni alloy under Containerless Microgravity Condition^[11]

The microgravity rapid solidification and microstructure control of Mo-48%Ni alloy with droplet diameter from 144 μm to 1530 μm was achieved by using free-fall technique to simulate space environment conditions. The results show that the rapid solidification microstructure was composed of primary NiMo dendrites and (Ni+NiMo) eutectic, and the rapid cooling condition inhibited the subsequent solid phase transition. With the increase of droplet cooling rate and subcooling degree, the coarse NiMo dendrites were gradually refined, and the solute Ni content first decreased and then increased. The eutectic morphology changes from regular lamellar to irregular structure, in which the content of solute Mo increased first and then decreased. The elastic modulus of primary phase and eutectic structure decreased monotonically. The microhardness of primary phase increased slowly at first and then decreased, and the microhardness of eutectic microstructure decreased as a whole. At the same time, the magnetization of the alloy decreased, but the coercivity and the temperature resistance were improved.

2.2.2 Ni-Ge Alloys under Simulated Microgravity Condition^[12]

The rapid solidification of Ni95Ge5 single-phase alloy and Ni33Ge67 eutectic alloy was achieved by means of drop-tube containerless processing and copper-mold injection casting. The microstructure evolution, hardening mechanism and multi-scale mechanical properties of Ni95Ge5 and Ni33Ge67 eutectic alloy were systematically studied. It is found that with the increase of melt cooling rate, the microstructure of Ni95Ge5 single-phase alloy changes from coarse dendritic structure to equiaxed grains structure, while Ni33Ge67 eutectic alloy gradually changes from regular eutectic to hypereutectic with a few primary Ge phases. The hardening behavior of the single-phase alloy is grain boundary dominated, while that of the eutectic alloy is multi-phase co-hardening. Nanomechanics analysis shows that the eutectic alloy has higher surface stress and higher elastic recovery during unloading. While, single-phase alloy is more prone to plastic deformation. The special morphology evolution and lower strain hardening exponent of Ni95Ge5 alloy remarkably improved the hardening

proved the hardening ability. Its hardness increased up to 56.6%, which was much higher than the eutectic alloy. The average ratio of microhardness to yield strength of single-phase alloy is 2.75, while that of eutectic alloy is 9.09. Therefore, the microstructure evolution caused by high cooling rate can also improve the yield strength of alloy materials. Due to the higher cooling rate of the droplet in the falling tube, the hardness and strength of the alloy after rapid solidification are significantly better than those of the spray casting alloy.

2.3 Research on Space Additive Manufacturing Process

In February 2016, the Center for Space Application Engineering and Technology of the Chinese Academy of Sciences carried out experiments on space additive manufacturing technology, carrying out 93 parabolic flight tests in three sorties in Bordeaux, France. In this experiment, five kinds of materials and two kinds of manufacturing processes were verified in microgravity test, and the data of different materials and processes in microgravity environment were obtained. In the experiment, the equipment and process independently developed by China were used to not only print the target sample, but also observe the influence of microgravity environment on the manufacturing process and materials, and collect a lot of important data^[13].

In addition to flight tests, some Chinese scholars have also carried out experimental research on the ground forming process of different materials in order to solve the space application problems of FDM technology. Three pure resin materials including Polylactic Acid (PLA), Polycarbonate (PC) and Polyether Ether Ketone (PEEK) as well as carbon fiber reinforced PLA materials were selected as the research objects. The standard sample was successfully printed using the self-developed space microgravity principle prototype. The mechanical properties, flame retardant properties, gas concentration after combustion, mass loss, volatilization and other data were tested. The performance differences of PLA, PC, PEEK material FDM forming parts and traditional injection parts were compared and analyzed, as well as the tensile properties of carbon fiber PLA composite samples with different fiber directions^[14]. Results showed that binding strength between different materials is the main factor affecting the performance of FDM molding parts. The stronger the binding ability, the

higher the quality of FDM forming materials. The forming quality of crystal materials is also affected by crystallinity, the higher the crystallinity, the better the performance of parts.

On 7 May 2020, China successfully launched its new generation of manned spacecraft aboard a Long March-5B carrier rocket. A “3D printer” on board the test spacecraft carried out China’s first additive manufacturing experiment in space. There are two objects printed in this experiment. One of them is the honeycomb structure (representing the lightweight structure of the spacecraft), and the other is the CASC logo (China Aerospace Science and Technology Corporation Limited). Continuous fiber-reinforced composites are the main materials for spacecraft structures at home and abroad because of their low density and high strength. Research on 3D printing technology of composite materials in space is of great significance for long-term in-orbit operation of future space stations and in-orbit manufacturing of super-large space structures^[15]. For example, the technology could enable on-orbit manufacturing on demand to support long-term manned operations and maintenance of space stations in orbit. It will also make it possible for China to expand its space station in orbit.

3 Materials Sciences for Space Environment

Aerospace material engineering involves many aspects of space environment and material science including space environment and effect analysis of aerospace materials, adaptability evaluation of space environment for aerospace materials, flight test technology of aerospace materials, space material science experiment with space material as research object, aerospace material guarantee related to the selection of aerospace materials and the development of new aerospace materials, and so on. With the longer and longer in-orbit operation time of spacecraft, the achievements of space materials science have gradually become the way to develop new materials for spacecraft, so there are more and more studies on the cross fusion of space materials and space materials.

3.1 Metal Materials

In recent years, the research group of Professor Riping Liu from Yanshan University has cooperated with The General Design Department of Beijing Space Aircraft,

Baoji Titanium Industry Co., Ltd., and Western Metal Materials Co., Ltd., in the research and development, application and promotion of new TiZr-based alloys (Ti-Zr, Ti-Zr-Al, Ti-Zr-Al-V, Ti-Zr-Al-V-O, *etc.*)^[16–19]. Smelting and forging processes were established, and a series of new types of high strength and toughness TiZr-based alloys were prepared. The new TiZr-based alloys were successfully applied to space-critical components.

Based on metal matrix composites, the team of Professor Lin Geng of Harbin Institute of Technology has carried out the design and verification of two-dimensional layered structure of metal matrix composites and three-dimensional network structure of titanium matrix composites^[20–22]. By adjusting the content, size and distribution of component phase, the optimal configuration of mechanical properties of metal matrix composites can be achieved. The inversion relationship between strength and plasticity (toughness) of metal matrix composites was solved by the design of component phase structure. Huang *et al.* from Harbin Institute of Technology significantly improved the plasticity and strength of Titanium Matrix Composites (TMC) manufactured by Powder Metallurgy (PM) by designing the reinforcement distribution of a novel network structure. The design concept of Ti5Si3 +TiBw/Ti6Al4V composite was proposed based on Hashin-Shtrikma grain boundary theory^[23]. Zhang *et al.* from Southeast University prepared Ti6Al4V (TC4) based nanocomposites with 3D network structure by SPS, which had excellent mechanical properties and ductility, and realized the network Distribution of Nanodiamond (ND) reinforced materials in TMC, effectively resolving the conflict between strength and ductility of TMC^[24].

A high-performance silicon carbide particle reinforced aluminum matrix composite (SiC/Al) developed by the team of Ma from Shi Changxu Advanced Materials Innovation Center of Shenyang Institute of Metal Materials, Chinese Academy of Sciences, has been applied to the key components of solar wing extension mechanism and the core module of Tianhe in China space Station^[25–26]. The team broke through the batch preparation technology of powder metallurgy and the plastic forming technology of isotropic medium thick plate. The production efficiency of billet was increased by more than 5 times, the finished product rate of plate was increased by 20%, and the performance difference between product batches was less than 5%. The magnesium alloy surface treatment technology developed by

the team of Han and Song from the Material Corrosion and Protection Center of the Institute of Metals has been applied to the medical sample analysis of the core cabin and the high microgravity scientific experiment cabinet (short for high microgravity cabinet), the main structural subsystem of containerless scientific materials laboratory cabinet, and magnesium components used in automatic locking release mechanism of high micro cabinet suspension test system. It meets the multifunctional requirements of weight reduction, corrosion resistance and electric conductivity^[26].

3.2 Inorganic Nonmetallic Materials

Shaoming Dong, Director of Shanghai Institute of Ceramics, Chinese Academy of Sciences, invented ceramic matrix composites with high structural stability. In the case of temperature change and stress in space environment, the deformation is close to zero, which creates a new system of supporting structure materials for space camera in China. The innovation called a “stationary bracket” for a camera, has helped China’s satellite reach the Yami level (Gaofen-2) for the first time. The team established the preparation technology of ceramic matrix composites based on in-situ reaction, realizing the low-cost preparation and engineering of high-performance (ultra) high-temperature ceramic matrix composites that can withstand high temperatures up to 2000°C for new high-speed aircraft^[27–28]. The integral structural design concept of components is developed, and the technical route of large complex structure ceramic matrix composite integral components is opened, which greatly improves the application reliability of components^[29].

Jixin Chen, associate researcher of Shenyang National Research Center for Materials Science, Institute of Metal Research, led the team to solve the problems of boron nitride ceramic materials, such as low strength, easy moisture absorption, unstable cavity discharge state, poor ion sputtering resistance^[26]. The boron nitride composite has the advantages of low density, high strength, thermal shock resistance, sputtering resistance, easy machining and good insulation performance, and is applied to hall thruster cavity in the core cabin electric propulsion system.

In view of the problem of maintaining the thermal balance in sealed capsule spacecraft under the extreme conditions of manned lunar landing, round-trip and

round-trip flight around the moon, Ping *et al.* proposed a thermal control coating material system with low absorption and low emissivity, which is suitable for space and ground environment^[30]. The material system used aluminum powder and silicone resin as the main raw materials. The Bruggeman model effective medium theory and Fresnel formula were used to calculate the variation between the volume fraction and the reflectance of the coating. Thermal controlled coatings with different ratios were prepared and their thermal radiation properties were tested. The results show that solar absorption ratio α_S and hemispheric emissivity ε_H of low absorption-low emissivity thermal control coating are 0.15 and 0.15, respectively. The higher the proportion of aluminum powder filler is, the lower the thermal radiation performance of the coating is, which accords with the simulation conclusion between the volume fraction and the reflectance of the coating.

Spacecraft materials produce organic small molecule coagulable volatiles in space environment. These organic molecules condense on sensitive surfaces such as optical lenses and solar cells, which will greatly affect the safety and reliability of spacecraft. The active control of pollutants by adsorbent materials is one of the effective methods to solve space molecular pollution. Zeolite material with uniform pore size distribution and excellent adsorption performance is one of the ideal materials for the adsorption of spatial molecular pollutants. Pan *et al.* from Tianjin University prepared a monolithic adsorption material with 13X-sic adsorption coating by microwave sintering technology using cordierite as the substrate^[31]. Zhang *et al.* prepared zeolite @ TiO₂ composite material with high adsorption performance by designing modified zeolite material. Gong *et al.* prepared Al₂O₃@5A zeolite molecular sieve composites by atomic layer deposition (ALD)^[32]. These results provide theoretical and technical basis for material selection and application of adsorption materials for space molecular pollutants^[33].

4 Materials Behavior in Space Environment

The interaction between space environment and matter is a key research field of space materials. The science of interaction between space environment and matter not only reveals the basic laws of the evolution of matter

structure under the action of space environment supporting for reliable, stable and long-life operation of spacecraft and safe activities of human beings, but also makes new breakthroughs in the fields of physics, chemistry, material science and life science under the special environment of space enriching its scientific connotation and promoting the development of related basic science.

4.1 Numerical simulation for Materials Behavior

Ma *et al.* from Beijing Jiaotong University used molecular dynamics method to simulate the irradiation damage of GaAs material and the effect of pre-strain on the irradiation damage process^[34]. By analyzing the relationship between the number and recombination rate of crystal defects caused by irradiation damage and temperature, irradiation energy and pre-strain, the irradiation damage rule of GaAs material under Ga primary dissociated atom and As primary dissociated atom was obtained. The results can provide a theoretical basis for the protection of these materials in space application.

During the process of deorbiting, the sail must be exposed to the harsh space environment in low earth orbit for a long time. The erosion effect of atomic oxygen on the sail film material will cause serious damage to the sail structure. In order to reasonably evaluate the life of sail surface materials for off-orbit thin film sails, Fu *et al.* established a numerical simulation model based on the experimental characterization results of sail surface pores, cracks, crease and other defects by using Monte Carlo numerical simulation method to analyze the erosion of sail surface materials by atomic oxygen at different scales of defects. The effect of atomic oxygen cutting defect density on sail film was studied^[35]. The deorbit process of a sail from 750 km orbit for 38 months is studied as an example. The calculation results show that when the sail width defect is 500 nm and 1 μm , the cut depth is 1.2 μm and 1.4 μm , and the cut width is 600 nm and 1.1 μm , respectively. The simulation results were compared with NASA's long-term exposure test results to verify the effectiveness of the model. This model can provide a preliminary theoretical basis for the life evaluation of an off-orbit sail.

4.2 Materials Behavior in Ground Space Environment Simulator

During the operation of spacecraft in low Earth orbit,

both atomic oxygen and ultraviolet radiation in space environment will affect the mechanical properties of non-metallic materials. Sui *et al.* studied the mechanical strength properties of nylon under the synergistic effect of atomic oxygen and ultraviolet irradiation^[36]. The results show that the material fades obviously under UV irradiation. Both UV irradiation and atomic oxygen can reduce the breaking strength of nylon materials. The synergistic action of atomic oxygen and ultraviolet irradiation can enhance the mechanical properties of monolayer nylon. The penetration of UV irradiation on multilayer nylon is weak. The mechanical properties of the warp-stitched test parts are better.

Lu *et al.* studied the effect of simulated space environment on the mechanical properties of polyurethane coated fabrics^[37]. The results showed that the mechanical properties of single-side polyurethane aramid composites decrease at high and low temperatures. However, the effects of humidity and heat, alternating high and low temperatures and combined environment on mechanical properties were not obvious. The mechanical properties of double-sided coated polyurethane nylon fibers were significantly enhanced at low temperature, but decreased at high temperature and humid heat. Similarly, the effects of alternating high and low temperatures and compound environment on mechanical properties were not obvious.

Polyimide film is an important polymer material used for the construction of spacecraft. The performance of Kapton can be degraded for atomic oxygen erosion in space. Commonly used atomic oxygen protective layers have issues such as poor toughness and poor adhesion with the film. Donghua Jiang from Tianjin University carried out relevant research titled "Atomic Oxygen Adaptability of Flexible Kapton/ Al_2O_3 Composite Thin Films Prepared by Ion Exchange Method"^[38]. Kapton/ Al_2O_3 nanocomposite films were prepared *via* an ion exchange method, and the optical properties, mechanical properties, and mechanisms for the change in the mass and microstructure, before and after atomic oxygen exposure, were analyzed. The behavior of the Kapton/ Al_2O_3 composite film under the atomic oxygen environment of space is investigated, which provides the basis for studying the effects of atomic oxygen on the flexible protective Kapton film.

Tong *et al.*, from Hebei University of Technology, focused on the damage effect and mechanism of Kapton thin film under the synergistic environmental factors of

atomic oxygen and micro debris^[39]. The performance evolution of Kapton films under the conditions of MD (micro debris), AO (atomic oxygen) single factor load spectrum and MD + AO, AO + MD asynchronous synergistic load spectrum were studied by laser driven flyer and microwave atomic oxygen technology. The macro morphology, optical properties and quality changes of Kapton films before and after each load spectrum were compared, and the mechanism of micro-morphology and structure changes was explored.

The damage behavior of Polyimide (PI) fibers under electron irradiation, proton irradiation and stress-coupled proton irradiation was investigated. Ju, from Changchun Institute of Applied Chemistry, Chinese Academy of Sciences, studied the mechanical damage behavior of polyimide fibers irradiated by space-charged particles under the condition of space environment simulation equipment irradiation^[40]. The tensile tests of the samples before and after irradiation were carried out by XQ-1 fiber strength tester. Under low energy and high energy electron irradiation conditions, the mechanical properties of polyimide fibers are weakly affected. Proton irradiation will greatly reduce the mechanical properties of the materials. When the stress coupling effect is increased, the effect of proton irradiation on mechanical properties is weakened.

Wu *et al.* designed and developed a modified phosphate-bonded solid lubrication protective coating to solve the problems of surface degradation, densification and lubrication failure of organic solid lubrication protective coating exposed to space environment for a long time^[41]. The structural changes and vacuum tribological properties of modified phosphate bonded solid lubricating protective coating were analyzed by ground simulated space integrated environment equipment system after irradiation with ultraviolet, atomic oxygen, high-energy proton and electron for a long time. The results show that UV and high-energy particle irradiation have no effect on the mechanical and vacuum tribological properties of modified phosphate bonded solid lubricating coatings. Atomic oxygen has a certain oxidation effect on the surface of the coating, but it does not affect the friction and wear properties of the coating, and the coating still shows good lubrication after various irradiation.

Zhang *et al.* prepared high stability inorganic thermal control coating by using new inorganic white filler and

inorganic binder. The thickness, surface density, thermal radiation performance, vacuum volatility, thermal cycling performance, space environment stability (vacuum-ultraviolet, vacuum proton, vacuum-electron, atomic oxygen) and adaptability of various substrates of thermal control coating were tested and verified^[42]. The results show that the solar absorption ratio of the new inorganic thermal control coating is less than 0.07, the hemispheric emissivity is more than 0.90, and the surface density is 200–360 g·m⁻². After ground simulated space environment test, the solar absorption ratio degradation of the coating is small, with excellent space environment stability, suitable for a variety of substrate surface.

Carbon nanotube is a kind of one-dimensional quantum material with special structure, which has excellent mechanical, electrical and chemical properties. It is an ideal candidate material for future electronic components and has a broad application prospect. When carbon nanotubes are used in spacecraft, the influence of space-charged particle radiation environment on their performance should be fully considered. Tian *et al.* studied the effects of electrons and protons on the microstructure and conductivity of carbon nanotube paper based on the radiation environment of charged particles in geosynchronous orbit for the space application of carbon nanotubes^[43]. The results show that the degradation of the electrical properties of carbon nanotube paper is due to the change of the surface structure of the material and the increase of the number of defects in the material under the irradiation, which affects the migration path of carriers in the material and leads to the decrease of its electrical conductivity.

The preparation of suitable coating materials is crucial for enhancing the atomic oxygen erosion of zirconium alloys. Zr-Al-C ceramics composed of MAX phase have excellent inherited properties of metal and ceramic, making them useful as spacecraft materials for atomic oxygen protection. Guo *et al.* from Tianjin University explored the possibility of applying MAX phase, a new material, in the field of space atomic oxygen protection^[44]. Zr-Al-C coatings were successfully prepared by the magnetron sputtering method. The macroscopy morphology, microstructure, adhesion and the effect of atomic oxygen of Zr-Al-C coatings were all investigated. Zr-Al-C coating could protect Zr alloy under certain exposure dosage of atomic oxygen. Meanwhile, further

increase in exposure time of atomic oxygen led to the formation of ZrO, ZrO₂, Al₂O₃ on Zr-Al-C coating. Also, more pores appeared on Zr-Al-C coating surface due to the oxidation of carbon elements in the coatings to form volatile oxides, such as CO and CO₂. As atomic oxygen erosion continued, the existing holes became connected to form complex channel-like labyrinthine two-dimensional network structures. The latter penetrated further the atomic oxygen into the interior of Zr-Al-C coating to continue the corrosion effect of atomic oxygen. By considering the protection effect of Zr-Al-C coating on Zr alloy under a certain exposure dosage of atomic oxygen, the protection time can be calculated and experiments can be designed according to the linear law obtained as a function of the thickness of Zr-Al-C coating.

4.3 Materials Behavior in Orbit Exposure

On 22 December 2020, the “Yuanguang” scientific experimental satellite of Hebei University of Technology successfully took off in Wenchang, Hainan province. “Yuanguang” satellite is a 20 kg space science experiment satellite. Its main load is the space tribology experiment load developed by Hebei University of Technology. Its main task is to carry out space mechanism and tribology experiment with Cubic star, so as to explore the variation rule of mechanical properties from material level, component level to system level with service time. A cross-scale mechanical model of interface micro-mechanical behavior and mechanism macro-motion will be established. The designed scientific load scheme can realize dynamic observation on two-dimensional scale, which provides a reference for subsequent space observation^[45].

5 Space Experimental Hardware for Material Investigation

Experimental equipment is the foundation and guarantee of space material research. In recent years, China has established an in-orbit space station, ground simulation equipment for space environment, and a small ground simulation platform for space environment adapted to low-cost commercialization.

5.1 Material Experiment Cabinet in China Space Station^[46]

Due to the pace of China’s space technology development and the constraints of space resources, China’s

space material science will mainly focus on exploratory experimental research and space experimental ability cultivation before the construction of China’s own space station in 2020. In May 2021, the station and core module completed in-orbit tests and verification. On 17 June 2021, the Chinese enter their own space station for the first time. The Construction of the China Manned Space Station will be completed around 2022. It will support large-scale and multidisciplinary space scientific research, technology verification and space application, and will have unique advantages such as astronauts participating in experimental operations, maintenance and upgrading of experimental equipment, return of experimental samples, and transmission of space-earth information. China’s space station, which will operate in orbit for more than 10 years, has ample experimental resources, providing historic opportunities for multidisciplinary, serialized and long-term space research.

The China Space Station will conduct research in the direction of space material science, closely combining application requirements, aiming to reveal the laws of material physical and chemical processes in microgravity environment, improve and develop materials science theories, and guide and promote the improvement of materials processing technology on the ground. High performance materials of scientific importance are studied and prepared and validated by space tests. These results provide scientific basis for the design and research of space component materials in the future, and make positive contributions to the formation of new material science.

The space materials science direction of the space Station mainly supports the following research contents: growth (solidification) interface stability and defect control, undercooling, nucleation and crystal growth, Phase separation and aggregation behavior, research on space preparation and technology of high performance materials, Measurement and research of melt physical properties, materials behavior in space environment, and other space material science experiments suitable for the space station. The high-temperature material science experiment cabinet and container-free material experiment cabinet are arranged in the space station cabin to realize the above space material science research.

The high temperature material science laboratory cabinet supports the research of material preparation process mechanism under microgravity, material preparation and research of important application background,

and other relevant material experimental research. Scientific experiments on melt growth and solidification of metal alloys, semiconductor optoelectronic materials, nano and mesoporous materials, inorganic functional materials and other materials have been carried out in the form of ampoule structure encapsulation.

In the containerless material laboratory cabinet, the research on the mechanism of the material preparation process under microgravity, the material preparation and research of important application background, and other relevant material experiments were completed. The containerless processing is realized through electrostatic suspension technology, and the research on containerless processing of metal and non-metal materials under microgravity, deep undercooling of materials, and thermal property measurement of material melts are mainly carried out.

In addition, some space material exposure tests need to be performed on the extravehicular exposure test unit of the space station. These space material experiments mainly include space damage and service performance experiments of space application materials (lubrication, thermal control, film coating, shape memory, functional coating, polymer, composite materials, *etc.*), tribology and other cross studies.

5.2 Ground Simulator for Space Environment

The first Space materials and environment Engineering laboratory of China was established in Harbin Institute of Technology on 27 February 2000^[47]. On 28 January 2005, the National Defense Key Laboratory of Materials Behavior and Evaluation Technology for Space Environment was established, mainly carrying out basic research on interaction between space environment and materials^[48]. In China's 12th Five-Year Plan, Chinese scientists further put forward the idea of building a ground simulation device for space environment. On 29 August 2017, the project officially started construction. On 10 July 2021, the thermal vacuum test of the integrated radiation simulation test module and the lunar dust environment simulation test module of the integrated environmental simulation system of "Space Environment Ground Simulation Device" was successfully completed. At the same time, two typical environmental factors of solar system vacuum and low temperature can be simulated on the ground^[49].

Ground Simulation Device of Space Environment of

Harbin Institute of Technology is the main installation of national science project based on comprehensive simulation of many space environment factors^[49,50]. The device can realize in situ/semi-in-situ characterization of the interaction process between space integrated environment and matter, and study the coupling effect mechanism of multiple space integrated environment on the same platform. By exploring the spatiotemporal evolution theory of performance/function degradation of materials, devices and systems in space integrated environment, the evaluation theory and method of on-orbit reliability and life of space materials, devices and systems will be established. As a whole, the facility will build a world-class simulation platform for space integrated environment (vacuum, high and low temperature and alternating, plasma, weak magnetic/zero magnetic, particle irradiation, electromagnetic radiation, atomic oxygen, molecular pollution, *etc.*). At the same time, the facility is equipped with many advanced in situ and semi-in-situ analysis and testing devices, forming the most complete conditions and capabilities in the world for the study of space environment and mechanism of interaction with matter. The "Ground Simulator for Space Environment" national Science project of Harbin Institute of Technology is composed of space integrated environment simulation and research system (including integrated environment simulation subsystem, space life science subsystem, micro mechanism analysis subsystem, ion accelerator subsystem and device ion irradiation subsystem), space magnetic environment simulation and research system, space plasma environment simulation and research system, numerical simulation and ZY monitoring system and supporting system, *etc.*

5.3 Low Cost Small Space Environment Simulation Platform

At present, large space environment ground simulation equipment in the world is based on the principle of ground reproduction of space environment. By reproducing the real space environment as much as possible, the action mechanism of materials in the simulated environment is the same as that in orbit^[4]. The sameness or similarity between simulated environment and real space environment is emphasized. This research method has high engineering reliability, which helps to reveal the basic law of material structure evolution under the action of space environment, and provides important

scientific support for the reliable, stable and long-life operation of spacecraft and human safety activities.

However, the operation cost of large-scale ground simulation equipment for space environment is generally high, which requires strong support from the state to carry out relevant research. For a few individuals or groups, it is difficult to carry out space science and technology research because of lack of funds. Especially in recent years, with the rapid development of commercial spaceflight, the miniaturization of spacecraft will be a development trend. Micro-satellite is a new generation of spacecraft with clear purpose in space science and technology, which has shown great application value. Many scholars have proposed and are carrying out research on small-scale ground simulation devices for space environment^[52-54]. At present, many small sample service behavior and commercial space materials service evaluation test requirements appear in the research and development of new spacecraft materials. The ground simulation method of space environment has gradually changed from the principle of reproducing space environment factors on the ground (oriented to environmental factors) to the principle of studying the consistency between ground and in-orbit (oriented to material factors) of the main properties and mechanism of materials.

The single-particle effect on spacecraft is mainly caused by heavy ions and protons, and protons also produce heavy ions through nuclear interaction with semiconductor materials and then induce single-particle effects by heavy ions. In the process of simulating single-particle effects with pulsed laser, although the laser is used as an environmental factor, which is quite different from the heavy-ion environment, the physical mechanism generated in semiconductor materials is similar to that of heavy ions^[55]. At the same time, atomic oxygen does not exist in the form of neutral atomic oxygen in the ground atomic oxygen simulation methods of ion beam type and plasma type, but its response mechanism is similar to that of space flight tests and experimental phenomena and reaction laws can be obtained. The space atomic oxygen equipment developed by Beihang University belongs to plasma type^[56]. Yang *et al.*, Tianjin University, took ozone as the corrosive medium and realized the relative scouring of samples by high-speed relative movement. Similar phenomena and laws were also obtained^[57].

6 Summary

From 2020 to 2022, the rapid development of China's space industry has promoted the further and more integrated development of materials science research in space field. With space environment as the link, Space materials and Aerospace materials are further integrated to form three research directions including Materials Sciences in Space Environment, Materials Sciences for Space Environment, Materials Behavior in Space Environment. Multi-level space material infrastructure and experimental equipment will be built, including China's space station, ground simulation equipment for space environment and small low-cost ground simulation platform. It will enable more scientists to participate in materials science, space technology and earth science research, and promote the integration and development of machinery, artificial intelligence, big data and other disciplines.

References

- [1] HE Shiyu, YANG Dezhuang, JIAO Zhengkuan. Handbook of Space Materials (Vol. 1) - Physical State of Space Environment[M]. Beijing: China Astronautic Publishing House, 2012
- [2] DANIEL H, HENRY G. Spacecraft-Environment Interactions[M]. YANG Xiaoning, HUANG Jianguo, trans. Beijing: China Astronautic Publishing House, 2020
- [3] YANG Xiaoning, YANG Yong. Space Environment Engineering for Spacecraft[M]. Beijing: Beijing Institute of Technology Press, 2018
- [4] HE Shiyu, YANG Dezhuang. Handbook of Space Materials (Vol. 2)-Space Environment and Effect Calculation and Ground Simulation Test[M]. Beijing: China Astronautic Publishing House, 2021
- [5] FEUERBACHER B, HAMACHER H, NAUMANN R J. Materials Sciences in Space: A Contribution to the Scientific Basis of Space Processing[M]. Berlin: Springer, 1986. DOI: 10.1007/978-3-642-82761-7
- [6] ZIMMERMANN G. Materials Science in Space[M]. 2003.
- [7] PAN Mingxiang, WANG Weihua. Special topic: materials science in space[J]. *Scientia Sinica (Physica, Mechanica & Astronomica)*, 2020, 50(4): 1
- [8] RUAN Ying, HU Liang, YAN Na, *et al.* Recent advances and future perspectives of space materials science[J]. *Scientia Sinica Technologica*, 2020, 50(6): 603-649
- [9] XING Yan, WANG Xiangke. Spacecraft Materials[M]. Beijing: Beijing Institute of Technology Press, 2018: 5
- [10] SHEN Zicai, GAO Hong, OUYANG Xiaoping. Connotation and system construction of aerospace material engineering[J]. *Aerospace Materials & Technology*, 2018, 48(2): 1-6. DOI: 10.12044/j.issn.1007-2330.2018.02.001
- [11] ZHAO Xiaolei, WANG Weili, SHA Sha, *et al.* Rapid solidification and physical properties of a refractory Mo-Ni alloy under contain-

- erless microgravity condition[J]. *Scientia Sinica Technologica*, 2021, **51**(9): 1127-1134. DOI: 10.1360/SST-2021-0161
- [12] YAN Pengxu, WANG Weili, YAN Na, *et al.* Microstructural evolution and mechanical properties of rapidly solidified Ni-Ge alloys[J]. *Scientia Sinica Technologica*, 2020, **50**(8): 1042-1054. DOI: 10.1360/SST-2020-0022
- [13] WANG Gong, LIU Yifei, CHENG Tianjin, *et al.* Application of additive manufacturing technology for space[J]. *Chinese Journal of Space Science*, 2016, **36**(4): 571-576. DOI: 10.11728/cjss2016.04.571
- [14] WANG Zhen, LI Jingyang, ZHANG Jianchao, *et al.* Research on the space application of fused deposition modeling[J]. *Aerospace Materials & Technology*, 2020, **50**(2): 90-93. DOI: 10.12044/j.issn.1007-2330.2020.02.017
- [15] ZHAI Yuanyuan, FANG Lei. China completes the first space 3D printing of continuous fiber reinforced composite materials[J]. *Journal of Henan Science and Technology*, 2020(13): 1. DOI: 10.3969/j.issn.1003-5168.2020.13.002
- [16] LI B, JI P F, CHEN B H, *et al.* The effect of Zr addition on the microstructure evolution and mechanical properties of hot-rolled TiAlNbZr alloy[J]. *Materials Science and Engineering: A*, 2021, **828**: 142114
- [17] WANG F, WANG S T, CHEN B H, *et al.* Effect of Ti addition on the mechanical properties and microstructure of novel Al-rich low-density multi-principal-element alloys[J]. *Journal of Alloys and Compounds*, 2022, **891**: 162028
- [18] MA W, WANG F, CHEN B H, *et al.* Thermal compression behavior and microstructural evolution of Ti-30-5-3 alloys in lower $\alpha + \beta$ region[J]. *Materials Letters*, 2021, **297**: 129876
- [19] JI P F, LIU S G, SHI C B, *et al.* Synergistic effect of Zr addition and grain refinement on corrosion resistance and pitting corrosion behavior of single α -phase Ti-Zr-based alloys[J]. *Journal of Alloys and Compounds*, 2022, **896**: 163013
- [20] CHEN R, AN Q, WANG S, *et al.* Overcoming the strength-ductility trade-off dilemma in TiBw/TC18 composites via network architecture with trace reinforcement[J]. *Materials Science and Engineering: A*, 2022, **842**: 143092
- [21] ZHU X J, ZHANG X X, QIAN M F, *et al.* Enhanced elastocaloric stability in NiTi alloys under shear stress[J]. *Materials Science and Engineering: A*, 2022, **838**: 142787
- [22] DING H, CUI X P, WANG Z Q, *et al.* A new strategy for fabrication of unique heterostructured titanium laminates and visually tracking their synchronous evolution of strain partitions versus microstructure[J]. *Journal of Materials Science & Technology*, 2022, **107**: 70-81
- [23] WANG S, AN Q, ZHANG R, *et al.* Microstructure characteristics and enhanced properties of network-structured TiB/(TA15-Si) composites via rolling deformation at different temperatures[J]. *Materials Science and Engineering: A*, 2022, **829**: 142176
- [24] ZHANG B, ZHANG F M, SABA F, *et al.* Graphene-TiC hybrid reinforced titanium matrix composites with 3D network architecture: Fabrication, microstructure and mechanical properties[J]. *Journal of Alloys and Compounds*, 2021, **859**: 157777
- [25] HUANG Z Y, ZHANG X X, XIAO B, *et al.* Hot deformation mechanisms and microstructure evolution of SiCp/2014Al composite[J]. *Journal of Alloys and Compounds*, 2017, **722**: 145-157
- [26] Institute of Metals, Chinese Academy of Sciences. A number of materials and technologies of the institute of metal materials have been used in the Tianhe core module of the space station[J]. *Surface Engineering & Remanufacturing*, 2021, (S1): 43
- [27] ZHANG D Y, YU H Y, WANG A Z, *et al.* Ablation behavior and mechanisms of 3D Cf/ZrB₂-SiC composite applied in long-term temperature up to 2400 °C[J]. *Corrosion Science*, 2021, **190**: 109706
- [28] DING Q, NI D W, NI N, *et al.* Thermal damage and microstructure evolution mechanisms of C_f/SiBCN composites during plasma ablation[J]. *Corrosion Science*, 2020, **169**: 108621
- [29] RUAN J, YANG J S, DONG S M, *et al.* Interfacial optimization of SiC nanocomposites reinforced by SiC nanowires with high volume fraction[J]. *Journal of the American Ceramic Society*, 2019, **102**(9): 5033-5037
- [30] PING T, ZHENG Y, LI Z Y, *et al.* Design and preparation of thermal control coatings with low absorption and emissivity for spacecraft[J]. *Manned Space Flight*, 2020, **26**(2): 214-221
- [31] PAN Yating, WEI Qiang, ZHANG Lixian, *et al.* Rapid preparation and evaluation of 13X-SiC adsorption coating on cordierite surface by microwave method[J]. *Surface Technology*, 2021, **50**(11): 129-136
- [32] ZHANG Zhen. Study on 5A Zeolite Material Modified by TiO₂ and Its Adsorption Properties for Space Molecular Pollutants[D]. Harbin: Harbin Institute of Technology, 2020
- [33] GONG Xianghua, ZU Lijie, WU Jinzhu, *et al.* Preparation and adsorption properties of Al₂O₃@5A zeolite composites for space molecular contamination[J]. *Surface Technology*, 2020, **49**(12): 14-22
- [34] MA Xuelin. Molecular Dynamics Study on the Irradiation-induced Damage in GaAs[D]. Beijing: Beijing Jiaotong University, 2020
- [35] FU Yulei, YUN Weidong, CAO Zhengli, *et al.* Numerical simulation on atomic oxygen undercutting of deorbit sail using Monte Carlo method[J]. *Space Debris Research*, 2020, **20**(2): 14-21
- [36] SUI Rong, ZHANG Wenbo, JIANG Wei. Experimental study on synergistic effect of atomic oxygen and ultraviolet irradiation on mechanical properties of nylon materials[J]. *Spacecraft Environment Engineering*, 2021, **38**(2): 171-175
- [37] LU Ping, GAO Hong, LI Yan, *et al.* Experimental study of space environmental effects on the degradation of mechanical properties of polyurethane coated fabric[J]. *Spacecraft Environment Engineering*, 2021, **38**(2): 183-187
- [38] JIANG D H, WANG D, LIU G, *et al.* Atomic oxygen adaptability of flexible kapton/Al₂O₃ composite thin films prepared by ion exchange method[J]. *Coatings*, 2019, **9**(10): 624
- [39] TONG P Y, WEI Q, HU N, *et al.* Asynchronous synergistic damage effect of atomic oxygen and space micro debris on Kapton film[J]. *Coatings*, 2022, **12**(2): 179
- [40] JU Dandan, WANG Xinmin, SUN Chengyue, *et al.* Mechanical properties of polyimide fibers under the irradiation of space charged particles[J]. *Equipment Environmental Engineering*, 2020, **17**(3): 1-7
- [41] WU Yanping, XU Haiyan, JUN Pengfei, *et al.* Tribological behavior of phosphate coatings in ground-based simulation environment[J]. *Aerospace Shanghai*, 2020, **37**(3): 45-50, 60
- [42] ZHANG Hang, ZHANG Jiaqiang, CUI Qingxin, *et al.* [J]. *Journal of Aerospace Materials and Technology*, 201, **51**(5): 103-107
- [43] TIAN Hai, FENG Zhanzu, WANG Yi, *et al.* Effect of charged particle radiation on electrical properties of carbon nanotube paper[J]. *Vacuum*, 2022, **3**: 1-8

- [44] WEI Q, GUO Z, XU J, *et al.* Atomic oxygen effect of Zr-Al-C coatings on ZrNb alloys used in space environment[J]. *Applied Surface Science*, 2021, **564**: 150420
- [45] WEI Qiang, BI Xiaoyang, HU Ning. “YuanGuang” science experiment satellite positioning interdisciplinary integration[J]. *Science Popularization in University*, 2021(1): 13-17
- [46] China Manned Space Engineering Office. Chinese Space Station Experiment Manual, 2019: 1-65
- [47] China establishes first space materials and environment engineering laboratory[J]. *Journal of North China University of Technology*, 2000(1): 81
- [48] ZHOU Weijuan, ZHOU Haisu. Professor He Shiyu and his team, state key laboratory of materials behavior and evaluation technology for space environment, harbin institute of technology[J]. *China Awards for Science and Technology*, 2014(175): 77-80
- [49] FANG Xing. Radiation protection design of SESRI in low energy range[D]. Lanzhou: Lanzhou University, 2017
- [50] ZHAO Yinuo, DING Yan. Harbin institute of technology builds “ground space station”[N]. Heilongjiang Daily, 2021-08-02(001)
- [51] XIAO Fugen. A future trend of the development of miniature space environment simulator[J]. *Spacecraft Environment Engineering*, 1999(3): 38-43
- [52] JOHNSON R H, MONTIERTH L D, DENNISON J R, *et al.* Small-scale simulation chamber for space environment survivability testing[J]. *IEEE Transactions on Plasma Science*, 2013, **41**(12): 3453-3458
- [53] SONG Lihong, WEI Qiang, BAI Yu, *et al.* Review on the laser technology application in space environment ground simulation[J]. *Optoelectronic Technology*, 2013, **33**(2): 96-102
- [54] HUANG Jianguo, HAN Jianwei. Mechanism of pulsed laser induced single particle effect[J]. *Science in China Series G Physics, Mechanics Astronomy*, 2004, **34**(2): 121-130
- [55] SHEN Zhigang, ZHAO Xiaohu, WANG Xin. Atomic Oxygen Effects and the Ground-Based Simulation Experiments[M]. Beijing: National Defense Industry Press, 2006
- [56] WEI Q, YANG G M, LIU G, *et al.* Effects and mechanism on Kapton film under ozone exposure in a ground near space simulator[J]. *Applied Surface Science*, 2018, **440**: 1083-1090

Progress of China's Space Debris Research

LIU Jing^{1,2}, YANG Xu¹, CHENG Haowen¹, JIANG Hai¹,
ZHANG Yao¹, WANG Yueer¹

1. National Astronomical Observatories, Chinese Academy of Sciences, Beijing 100101

2. School of Astronomy and Space Science, University of Chinese Academy of Sciences, Beijing 100190

Abstract

China has continually worked on space debris research, complying with the White Paper "China's Space Program: A 2021 Perspective". This article aims to clarify China's research and application progress from 2020 to 2021 in space debris observation, prediction, protection, and mitigation. In this context, it also summarizes the space debris mitigation efforts made by the Chinese government and provides the expectation of future direction for the work.

Key words

Space debris, Observation, Prediction, Protection, Mitigation

1 Introduction

Space debris has become a serious threat to space safety, and the rising population of space debris poses a great challenge to long-term sustainability of outer space activities. With the vigorous implementation of large constellation projects, the possibility of collision between space objects has increased dramatically, and the occurrence of catastrophic events such as collisions and break-ups has become an actual existence. Space debris issue has become the hot topic of international scientific research and the focus of long-term sustainability of outer space activities.

It is of great significance to ensure space safety, maintain the long-term sustainability of outer space activities, and maintain the development of human space by maintaining the dynamic catalog of space debris through long-term continuous monitoring of large space domain; and improving the prediction accuracy of space

debris for accurately grasping for giving timely and precise warning of its threats to space activities and ground personnel and assets; and studying the means and methods of active debris removal or the environment remediation to curb increasing trend of space debris population.

The year 2020 to 2021 is the final year of China's 13th Five-Year Plan and the planning year of its 14th Five-Year Plan. The White Paper "China's Space Program: A 2021 Perspective"^[1], issued by China National Space Administration (CNSA) in January 2022, concisely generalized and summarized China's progress in space debris research in chapter 7 "Space Environment Governance" of the second part: With a growing database, China's space debris monitoring system is becoming more capable of collision warning and space event perception and response, effectively ensuring the safety of on-orbit spacecraft. In compliance with the Space Debris Mitigation Guidelines and the Guidelines

for the Long-term Sustainability of Outer Space Activities, China has applied upper stage passivation to all its carrier rockets and completed end of life active deorbit of the Tiangong-2 and other spacecraft, making a positive contribution to mitigating space debris.

This article briefly introduced the progress of China's space debris research in the past two years from the aspects of observation and prediction, protection and mitigation, national mitigation effort, and standardization.

2 Promotion of the Observation and Prediction Capability

Comprehensive awareness of space debris, accurate prediction of situation and status, and effective disposal capability are the basis for dealing with the problem of space debris. Space debris orbit is affected by various perturbations forces with great uncertainty. Strengthening capability of surveillance facilities and increasing the observation frequency are effective means to improve the orbit data accuracy of space debris. In recent years, China has strengthened its observation capacity building of space debris. A set of telescopes are deployed, and the distribution of the space debris observation network is continuously optimized. The 1.2 m aperture large field of view telescope has been preliminarily completed with its first image, is carrying out optimization and debugging of space debris and near-Earth asteroid observation^[2]. The Xinglong 60 cm aperture telescope (see Fig.1) for both space debris and asteroid observation, has been put into operation and participated in the international joint observation campaign of near-Earth asteroids organized by the International Asteroid Warning Network (IAWN). The 36 cm test telescope array (see Fig.2) has been put into operation with wide-field

survey and synthetic tracking^[3]; the construction of Multi-Application Sky Survey Telescope Array (MASTA) project can improve the ability of faint and small space debris^[4]. The network of the Asia Pacific Space Science Observatory (APSSO) is under joint construction, and will enhance observation and research capabilities for space debris and near-Earth asteroid, and serve for research on space science and time domain astronomy for Member States of Asia-Pacific Space Cooperation Organization (APSCO)^[5-6].

To effectively avoid the collision of space debris and timely respond to space debris related events, the accuracy of the collision avoidance assessment model and the algorithm has been improved^[7], and a new generation of highly automated and efficient data processing and collision risk assessment system supported by a unified database has been built^[8,9]. The space events analysis model was improved and the analysis and research for space events, including the upper stage reentry analysis, satellite anomaly analysis, launch vehicle and satellite breakup analysis, were carried out.

China continuously improves the level of re-entry joint observation and prediction, actively participates in the joint re-entry prediction campaign organized by Space Debris Coordination Committee (IADC), and shares relevant data and information^[10-12].

To serve the research on the long-term sustainability of outer space activities, the space debris long-term evolution model SOLEM was continuously improved by increasing calculation efficiency, expanding application scope, and doing the research on long-term environmental evolution model comparison under the influence of various natural and human space activities^[13] with IADC member agencies. The simulation study has been done on the impact of LEO large constellation on



Fig. 1 YaoLight telescope and the Xinglong 60 cm diameter telescope

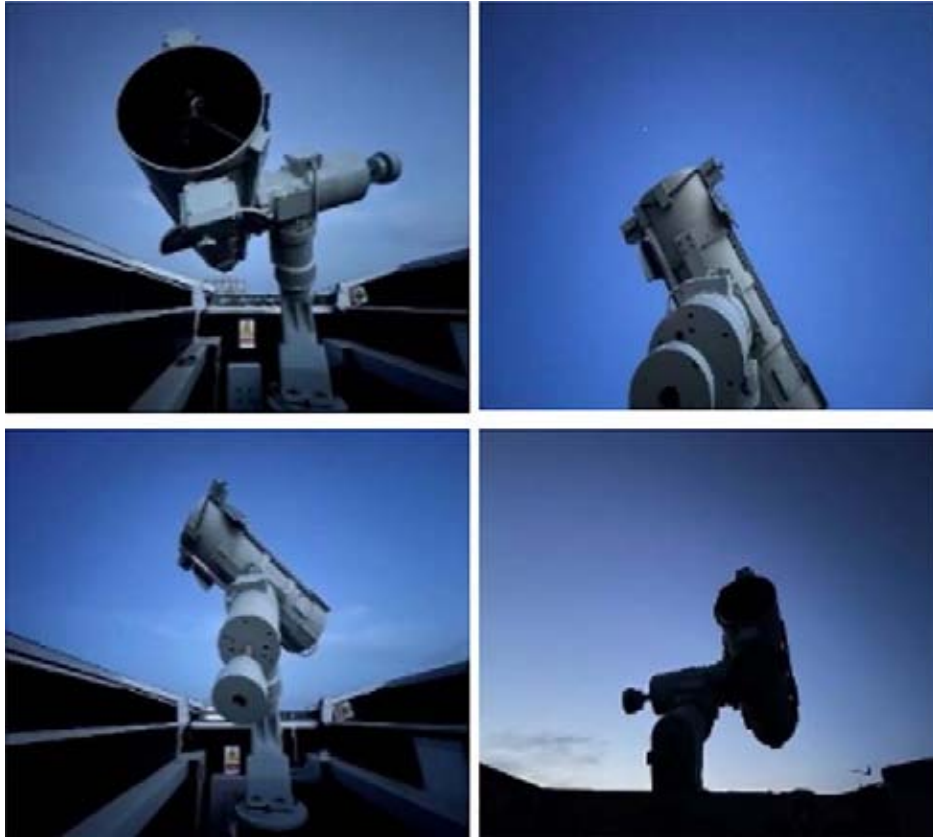


Fig. 2 36 cm test telescope array

space environment, and the results can support Chinese government in formulating LEO satellite management measures. Also, the model was used to analyze the ranking of potentially dangerous space debris^[14], which provided a technical basis for the planning and design of ADR in the future.

The new space debris environment engineering model SDEEM 2019^[15] has been developed, and the work on revising standards for space debris models^[16] has been completed cooperated with international scholars under the framework of the International Organization for Standardization (ISO).

3 Development and Application of Protection and Mitigation

It is an effective way that design space debris protection to deal with the impact threat of the long-duration operating spacecraft among the environment of small space debris and micro-meteoroid. The optimized design model for typical protective structures and the space debris protection design system, which are developed with the support of the China National Space Admini-

stration, have been applied to the manned space stations after continuous improvement and accumulation of experiments^[17].

The basic work of protection design has been supported. At present, the ground hypervelocity impact test facility has achieved the stable launch velocity of $8 \text{ km}\cdot\text{s}^{-1}$ ^[18], and obtained the hypervelocity impact characteristic data of various materials at the speed of $8\text{--}10 \text{ km}\cdot\text{s}^{-1}$ ^[19]. The data have been continuously accumulated and provided basic technical data for spacecraft protection design and impact effect evaluation of components and structural materials.

It has continuously supported and carried out the study on impact vulnerability assessment to promote the refined protection design of spacecraft. The spacecraft survivability assessment calculation has been preliminarily realized by studying the spacecraft impact sensitivity assessment technology^[20], vulnerability assessment technology of key components^[21], and survivability assessment technology of spacecraft systems^[22].

An engineering-oriented design and evaluation system for space debris mitigation was developed to support space debris mitigation. Some ground verification

and on-orbit technology validation of drag-enhancing de-orbit technologies^[23] have been carried out to routinely implement the work of LEO de-orbit in the future. Debris removal is an effective way to curb the growth of space debris, and various means of space debris removal have been explored and verified, laying a foundation for expanded application in the future.

4 National Effort on Space Debris Mitigation

It promotes the long-term sustainability of outer space activities that China has actively participated in reaching a consensus on the long-term sustainability of outer space activities under the UN framework (e.g., joining the Space Debris Expert Group, EGB), and also contributed to the unanimous adoption of the first set of 21 UN LTS guidelines for the long-term sustainability of outer space activities,

Meanwhile, cooperation mechanisms, such as the Space Debris Working Group of the China-Russian space cooperation subcommittee and the China-US expert seminar on space debris and space flight safety, will strengthen communication in the fields of space debris and the long-term sustainability of outer space activities. China has actively participated in joint research, test, comparison, and other technical work to support the activities of international organizations, such as the Inter-agency Space Debris Coordination Committee (IADC) and the Consultative Committee for Space Data Systems (CCSDS).

It promotes the implementation of the space debris mitigation guidelines and effectively supervises space activities that China has published the guidelines "Notice on Promoting the Orderly Development of Microsatellites and Strengthening Safety Management"^[24], which defined the further requirements for collision avoidance and mitigation of space debris of microsatellites. For example, Necessary measures should be taken for the design and manufacture of microsatellites so that their bodies can be detected on the ground during their orbit; Microsatellites shall have certain collision avoidance and orbit control capability. When deployed in network or constellation, technical measures shall be taken to avoid a collision; Microsatellites should have the necessary capabilities to facilitate the implementation of de-orbit action, avoid long-term occupation of common orbit, and the adopted de-orbit technology

should be mature and reliable; After the end, termination or expiration of the mission, the orbit dwell time of microsatellites with an operating orbit height of no more than 2000 km shall be less than 25 years, and microsatellites with an operating orbit height of more than 2000 km shall actively enter the grave orbit or uncommon orbit; Necessary technical measures shall be taken for microsatellites to avoid the generation of separable debris in orbit, including falling off, discarding, and throwing; Avoid explosion and other breakup events of energy storage components such as fuel storage tank and battery^[24].

CNSA has incorporated the review of space debris elements into the space launch project license review procedure. It is necessary to review space debris mitigation measures for spacecraft and launch vehicles before launch, including taking measures to avoid launch vehicle and satellite breakups, avoiding generating new debris, avoiding collision during the on-orbit operation phase, carrying out passivation and de-orbit measures at the end of the mission, and meeting the 25 years requirements of the LEO orbital life.

5 Promotion and Development of Standardization

Chinese government's regulatory requirements for space debris mitigation are top-level documents, which need to be supported by relevant implementation rules, management standards, and technical standards to facilitate enforcement. Subcommittee 5 on Space debris of National Technical Committee 425 on Space Technology and Operation of Standardization Administration of China (SAC/TC425/SC5) was approved to be established in August 2020.

Subcommittee proposed a space debris standard system, which consists of four branches: foundation and management, observation and awareness, mitigation and protection, and space traffic management (see Fig.3). The preliminary demonstration includes a total of 68 standards. At present, 10 standards have been issued or approved for preparation under the framework system^[25].

The published standards include Requirements for post-mission disposal of GEO satellites, Design requirements for residual propellant venting of a launch vehicle, Space debris mitigation requirements, Estimating methods for the mass of remaining propellant of spacecraft, Design requirements for mitigation of operational

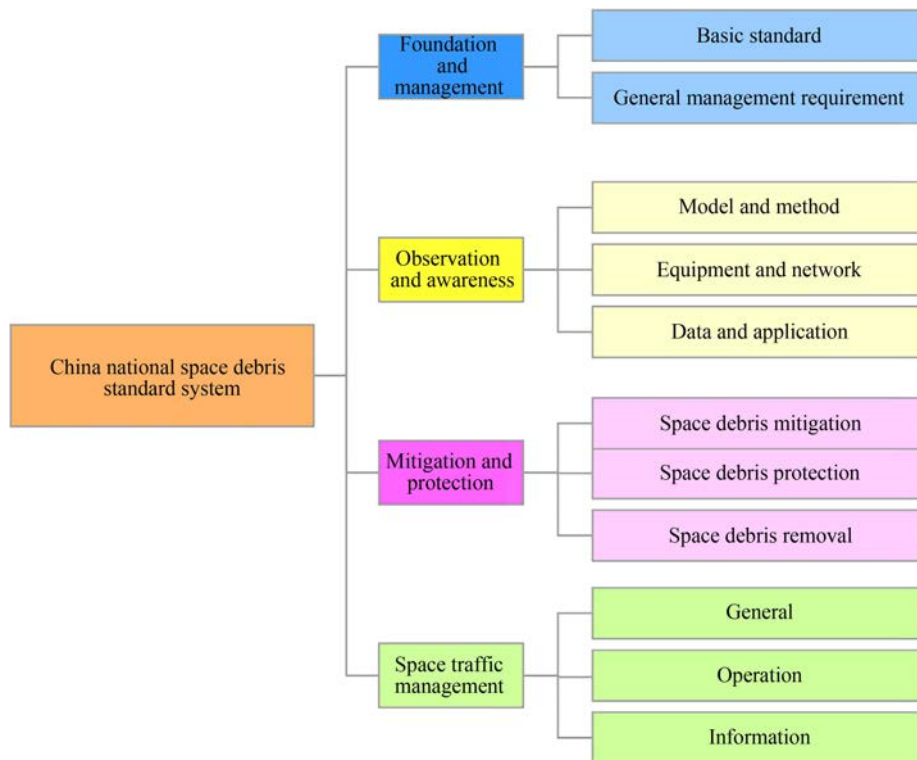


Fig. 3 Space debris standard system

debris of launch vehicle, Design requirements for residual propellant venting of Spacecraft. The standards under preparation include Space Object Registration Requirements, Space Objects Observation Data Standard, Space object orbital data standards, and Detailed disposal requirements for launch vehicle orbital stages. A new round of standard collection in 2022 is underway. In the future, China's space debris management and space debris environmental governance will be steadily promoted with the support of these gradually completed standards.

6 Vision of the Future

In view of the current situation of numerous and rapidly growing space debris and the frequent occurrence of space emergencies, China's vast space debris research institutes and application departments will focus on searching and tracking centimeter-sized small debris, multi-band, and multi-dimensional detection of space debris, and conduct in-depth research in predicting accurate prediction of high uncertainty debris, responding to high-precision sensing and time-sensitive space events, life-span protection of spacecraft and space debris mitigation measures, and new efficient and low-cost

removal methods and applications.

At the same time, China will expand bilateral and multilateral cooperation mechanisms with a more active and open attitude, conduct extensive international space exchanges and cooperation under the UN framework, take an active part in the formulation of international outer space rules, and jointly address the challenges facing the long-term sustainable development of outer space activities. China will also actively participate in international discussions and mechanism building in the field of space environment governance. We will actively carry out cooperation in space environment governance, and improve the effectiveness of space crisis management and comprehensive management^[1].

References

- [1] The State Council the People's Republic of China, 2021 China's Aerospace[OL]. [2022-01-28]. http://www.gov.cn/zhengce/2022-01/28/content_5670920.htm
- [2] LIU Jing. Progress and prospect of ali 1.2 m large field of view sky survey telescope[R]//The 11th National Space Debris Academic Conference, Hainan, 2022-01
- [3] SUN Jian, CHENG H W, JIANG Hai, *et al.* A 36 cm robotic optical telescope: equipment and software[J]. *Frontiers in Astronomy and Space Sciences*. doi: 10.3389/fspas.2022.897065

- [4] Xinhuanet. Embrace the Stars in the Cold Lake[OL]. [2022-01-17]. http://www.xinhuanet.com/globe/2022-01/17/c_1310417055.htm
- [5] APSCO. APSSO Project Successfully Passed the PDR[OL]. [2021-03-18]. <http://www.apsco.int/html/comp1/content/NewsHighlights/2021-03-18/54-429-1.shtml>, 2021-03
- [6] APSCO. APSCO Organized an Intermediate Progress Review Meeting on the APSSO Project[OL]. [2022-05-01]. <http://www.apsco.int/html/comp1/content/NewsHighlights/2022-05-12/54-516-1.shtml>
- [7] Dan Shen, Xu Yang, Xiangbin Wu, et al. Application of Chebyshev inequality in confidence degree of space debris collision probability[J]. *Chinese Journal of Space Science*, 2017, **37**(4): 448-454
- [8] GAN Qingbo, ZHAO Kexin, LIU Jing. Initial Value Selection for Initial Orbit Determination ff Short Arc Optical Data[R]//The 11th National Space Debris Academic Conference, Hainan, 2022-01
- [9] ZHANG Yao. Research on Key Issues of Space Debris Cataloging Management[D]. Beijing: University of the Chinese Academy of Sciences, 2022
- [10] IADC. IADC Re-Entry Test Campaign 2020-01[R]. Jun. 30, 2020
- [11] IADC. IADC Re-Entry Test Campaign 2021-01[R]. Apr. 12, 2021
- [12] IADC. IADC Re-Entry Test Campaign 2021-02[R]. Jun. 30, 2021
- [13] SHENDan. Study on the Confidence Level of Early Warning of Space Debris Collision and the Influencing Factors of Long-term Evolution Modeling[D]. Beijing: University of the Chinese Academy of Sciences, 2020
- [14] Darren McKnight, Rachel Witner, Francesca Letizia et al. Identifying the 50 statistically-most-concerning derelict objects in LEO[J]. *Acta Astronautica*, 2021, **181**: 282-291
- [15] PANG Baojun. Space Debris Environment Engineering Model SDEEM 2019[OL]. [2020-08-03]. <https://www.eventi.polimi.it/events/space-debris-environment-engineering-model-sdeem-2019/>
- [16] ISO (14200:2021). Space environment (natural and artificial) — Process-based implementation of meteoroid and debris environment models (orbital altitudes below GEO + 2 000 km) [OL]. [2021]
- [17] YAN Jun, ZHENG Shigui, YU Wei, et al. Design and practice of debris protection for space station [J]. *Space Debris Research*, 2021, **21**(02): 1-9. DOI: 10.19963/j.cnki.2096-4099.2021.02.001
- [18] ZHANG Pinliang, GONG Zizheng, TIAN Dongbo, et al. Damage characteristics of debris cloud and whipple structure under 8 km/s hypervelocity impact[J]. *Space Debris Research*, 2020, **20**(03): 37-42
- [19] WANG Mafa, ZHOU Zhixuan, HUANG Jie, et al. Experiment on cratering characteristics of magnesium alloy projectile impacting aluminum target at 10 km·s⁻¹[J]. *Explosion and Shock Waves*, 2021, **41**(05): 67-75
- [20] HU D Q, CHI R Q, LIU Y Y, et al. Sensitivity analysis of spacecraft in micrometeoroids and orbital debris environment based on panel method[OL]. [2021-11] <https://doi.org/10.1016/j.dt.2021.11.001>
- [21] ZHENG Shigui, YAN Jun, GONG Weiwei. Hypervelocity impact failure modes of typical spacecraft components[J]. *Space International*, 2022, (04): 29-32
- [22] HU D Q, PANG B J, CHI R Q, et al. Survivability assessment of spacecraft impacted by orbit debris[J]. *Defense Technology*, 2020. <https://doi.org/10.1016/j.dt.2020.06.003>
- [23] LIU Jing, JIANG Hai, YANG Xu, et al. Space debris research progress of China. *Chinese Journal of Space Science.*, 2020, **40**(5): 956-961
- [24] State Administration of Science. Technology and Industry for National Defense, Notice on Promoting the Orderly Development of Microsatellites and Strengthening Safety Management[OL]. [2021-05-19]. <http://www.sastind.gov.cn/n157/c6812015/content.html>
- [25] National Public Service Platform for Standards Information[OL]. [2022]. <http://std.samr.gov.cn/gb>

Progress of Planetary Defense Research in China*

LI Mingtao

National Space Science Center, Chinese Academy of Sciences, Beijing 100190
University of Chinese Academy of Sciences, Beijing 100049

Abstract

Near-Earth Asteroids (NEA) impose potential major disaster to humanity. Planetary defense is an inevitable requirement for the survival of human civilization. In recent years, China has made rapid progress in planetary defense research, which has won the attention of the government and attracted more and more scholars and organizations. This paper summarizes the research progress in planetary defense in China in recent years, including the past five fireball events in China, academic activities and policy planning, monitoring and warning technology, on-orbit defense technology, impact hazard assessment, international cooperation and science popularization.

Key words

Near-Earth asteroids, Planetary defense, Kinetic impact, Space-based observation, Hazard assessment

1 Introduction

Near-Earth Asteroid (NEA) impact is a major potential threat to human society. NEAs have impacted our planet Earth numerous times in history, profoundly shaping the evolution of the Earth's climate and ecological environment, and triggering the extinction and evolution of species. 66 million years ago, an NEA with a diameter of about 10 kilometers impacted the Gulf of Mexico in North America, resulting in the extinction of more than 70% of the global species, including dinosaurs^[1]. It is also because of this impact that human beings have the opportunity to dominate the Earth and develop today's highly developed human civilization. If we do not want to repeat the fates of dinosaurs, we must pay attention to the threat of NEA impacts.

Even if a small-scale NEA impact will bring signifi-

cant disaster. On 15 February 2013, an NEA with a diameter of about 18 m exploded above the Chelyabinsk region of Russia, causing damage to nearly 1500 people and 3000 houses^[2]. If it happened in densely populated regions, the consequences will be even more serious.

It has become a consensus all over the world to strengthen the response to NEA impact risk. After the Chelyabinsk impact in 2013, two organizations, IAWN (International Asteroid Warning Network) and SMPAG (Space Mission Planning Advisory Group), were established under the promotion of the United Nations Office for Outer Space Affairs (UNOOSA). IAWN aims to coordinate global organizations to discover and warn potential threat NEAs that may impact the Earth; SMPAG aims to research and develop defense means against NEAs impact. At present, the United States and Europe are leaders in global planetary defense. The United

* Supported by the Beijing Municipal Science and Technology Commission (Z181100002918004), the Strategic Priority Program on Space Science (XDA15014900), the Civil Aerospace Preliminary Research Project (sociation, CAS)

Received June 29, 2022

States has discovered 98% of the total discovered NEAs, and has launched the DART (Double Asteroid Redirection Test) mission on 24 November 2021. It is expected that it will impact the moonlet of the Didymos double asteroid system by the end of September 2022. This is also the world's first dedicated planetary defense mission. As part of the AIDA (Asteroid Impact Deflection Assessment) program of the US Europe cooperation, Europe will launch the Hera mission in 2024 to conduct a detailed rendezvous survey of the Didymos double asteroid system to better evaluate the impact effect.

In recent years, China has made rapid progress in planetary defense. The Chinese government joined IAWN and SMPAG^[3] in 2018. On the China Space Day in 2021, ZHANG Kejian, director of the China National Space Administration(CNSA), pointed out in his speech that China will build a NEA defense system. In 2022, the Information Office of the State Council issued the white paper “China’s space in 2021”, pointing out that the NEA defense system will be established in the future. On China Space Day in 2022, WU Yanhua, deputy director of CNSA, pointed out that a NEA impact mission would be implemented in 2025 or 2026. Chinese scholars have also made significant progress in NEA monitoring and warning, on-orbit defense means, risk assessment, etc. This report will provide an overview of the above progress, focusing on the achievements since 2020.

2 Recent Fireball Events

From 2017 to 2021, there was at least one eye-catching fireball event every year, including the Shangri-La event in 2017, the Xishuangbanna event in 2018, the Songyuan event in Jilin in 2019, the Yushu event in Qinghai in 2020, and the Henan event in 2021 (see Fig.1).



Fig. 1 Yushu Fireball event in 2020

These fireball events did not cause any threat or property damage, but they attracted public attention and were widely spread on the internet. At the same time, these fireball events also attracted the attention of scientific research experts and governments. Scientists studied and interpreted the fireball event. The government has gradually paid attention to the threat of NEA impacts as a serious scientific issue and potential disasters that may occur in the future.

3 Academic Activities and Policy Planning

In the past few years, Chinese academia has paid more and more attention to the issue of NEA defense.

In 2018, the China Aerodynamics Research and Development Center (CARDIC) organized a seminar on “Hypervelocity Problem of Asteroid Impacting the Earth”. The seminar later evolved into a National Symposium on Planetary Defense (NSPD). The second NSPD was held in Beijing in 2019, also organized by CARDIC; and the third NSPD was held in Nanjing in 2020 by Purple Mountain Observatory, Chinese Academy of Sciences (PMO, CAS). In 2021, the fourth NSPD and the 1st China Planetary Defense Conference (CPDC) were held in Guilin, Guangxi (see Fig.2). Academician WU Weiren of the Chinese Academy of Engineering served as the chairman of the conference, with more than 300 participants.

In 2018, the 634th Xiangshan Science Conference was held, with the theme of frontier scientific issues and key technologies in asteroid monitoring and warning, defense and resource utilization^[4]. More than 40 experts and scholars from nearly 30 organizations attended the meeting. China National Space Administration (CNSA) also had representatives in the meeting.

In terms of government activities and policy planning, there is also much progress.

In 2018, CNSA officially joined IAWN and SMPAG, marking that the government officially paid attentions to NEA impacts. In 2019, “Investigation, Defense and Utilization of Small Bodies” were selected as one of the 20 major scientific issues and key technical problems issued by the China Association for Science and Technology (CAST)^[5].

On China space day in 2021, ZHANG Kejian, director of the CNSA, pointed out in his speech that China will build an NEA defense system. This was the first

time that NEA defense system was announced by Chinese government.

On China Space Day in 2022, WU Yanhua, deputy director of CNSA, pointed out that a NEA impact mission would be implemented in 2025 or 2026. This was the first time that a NEA impact mission was announced by Chinese government.

In 2022, the Information Office of the State Council issued the white paper “China’s space activities in 2021”, pointing out that the NEA defense system will be constructed in future.

In 2022, the Deep Space Exploration Laboratory (DSEL) was kicked off in Hefei, Anhui province. It was mentioned in the press release that DSEL would be responsible for leading the feasibility study and implementation of major projects such as the NEA defense system.

In 2022, academician WU Weiren published an article in China’s Engineering Science journal^[6], presenting the strategic thoughts on NEA impact risk mitigation, including monitoring and warning, on-orbit defense and hazard assessment, and making a prospect for future development.

4 Monitoring and Warning Technology

In 2018, the 2.5 m large field of view sky survey telescope jointly operated by the University of Science and Technology of China (USTC) and PMO was kicked off in Lenghu and was expected to be completed in 2022. In 2021, the National Astronomical Observatory, Chinese Academy of Sciences (NAO, CAS) and other organizations discovered that Lenghu is a world-class optical observatory site, laying the foundation for the construction of optical sky survey telescopes in China.

China is developing the Chinese Space Station Telescope (CSST), which is expected to have powerful ca-

pability to make follow-up observations of NEA. The CSST also has the potential to discover NEA if the survey strategy is dedicatedly designed. The commercial space enterprise “Origin Space” launched the “Yangwang 1st” space-based telescope in 2021, which claimed to have performed the survey and observation of NEAs. Optical satellites of other commercial space enterprises are also said to have the capability to observe brighter NEAs.

In terms of NEAs discovery, China now has only one dedicated ground telescope, the Chinese Near-Earth Objects Survey Telescope (CNEOST) of PMO. CNEOST is a 1.2 m aperture telescope in Xuyi, Jiangsu Province. Using CNEOST, PMO has discovered 5, 5 and 1 NEAs in 2020, 2021 and 2022 respectively. PMO, Yunnan Observatory, and NAO also studied the NEA characteristics observation, including spectral observation and light curve observation

Qianxuesen Space Technology Laboratory (QianLab)^[4], National Space Science Center, Chinese Academy of Sciences (NNSC, CAS)^[7], PMO^[7], NAO^[8] and other organizations studied space-based monitoring mission concepts. QianLab proposed Constellation of Heterogeneous Wide-field Near-Earth Object Surveyors (CROWN) mission concepts^[4], a hybrid constellation including a main satellite telescope and several micro satellite telescopes in the Venus-like orbits.

The NNSC and PMO have cooperated to propose the Earth-leading orbit telescope mission concept^[7]. The telescope is proposed to be deployed about ten or twenty million kilometers in front of the Earth. Simulation shows that it has a good warning efficiency on NEAs approaching the Earth from the direction of the Sun. It is of great significance to compensate for the blind sky region of ground-based optical observatories and improve the completeness and integrity of the NEA monitoring and warning system. Fig. 3 showed Earth



Fig. 2 1st China planetary defense conference

leading orbit telescope mission concept.

5 On-orbit Defense Technology

NSSC^[9,10], Beijing Institute of Spacecraft Environmental Engineering (BISEE)^[11], CARDC^[12,13] and other organizations researched on on-orbit defense technology of NEAs. Progress has been made on the evaluation of applicable scenarios of typical planetary defense means, and new concepts on-orbit defense mission concepts.

In view of the disadvantages of the traditional kinetic energy impact means that is difficult to deal with large-scale NEA under short-term warning time, NSSC

proposed two new mission concepts, namely the “Enhanced Kinetic Impactor (EKI)^[8]” and “Assembled Kinetic Impactor (AKI)^[9]”, the orbital deflection distance of NEA can be increased to 3–10 times, providing innovative solutions for dealing with large-scale NEA under short-term warning time.

The EKI mission captures a stone with the mass of about 200 tons to form an enhanced kinetic impactor, the orbit deflection distance can be increased to 10 times compared with the traditional kinetic impactor (see Fig.4). While the AKI mission will impact the asteroid with a satellite in combined with the final stage of the launch vehicles. The orbital deflection distance of

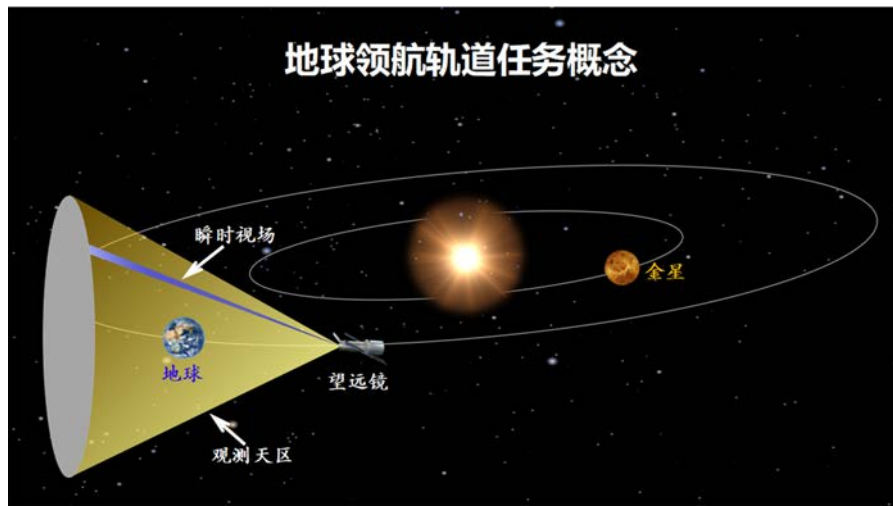


Fig. 3 Earth leading orbit telescope mission concept



Fig. 4 EKI mission concept

the AKI launched by a single Long March 5 launcher to the asteroid is equivalent to that of three traditional impactors launched by three Long March 5 launchers.

6 Impact Hazard Assessment

National Institute of Natural Hazard of the Ministry of Emergency Management (NINH, MEM), NSSC^[14], PMO^[15], CARDC^[16,17], Beijing Institute of Technology (BIT) and BISEE^[18,19] and other organizations have researched on NEA hazard assessment. Significant Progress has been made in NEA atmospheric entry process.

In 2021, NSSC revealed 5 atmospheric entry modes of NEA impacts^[10], including the asteroids entering the atmosphere layer at a small angle, which may be temporarily captured by the gravity of the Earth and finally impact the Earth, resulting in a particularly long flight range of asteroids, which poses a challenge to the prediction of asteroid impact and impact sites.

In 2022, PMO analyzed the Aletai meteorite super long strewn field in Xinjiang, and confirmed that asteroids can impact the Earth by skipping^[11]. Numerical modeling suggests that the stone skipping-like trajectory (see Fig.5) associated with a shallow entry angle is responsible for Aletai's exceptionally long strewn field if a single-body entry scenario is considered. The stone skipping-like trajectory would not result in the deposition of large impact energy on the ground but may lead to the dissipation of energy during its extremely long-distance flight.

7 International Cooperation and Science Popularization

In 2018, CNSA officially joined IAWN and SMPAG. The PMO and NAO have been participating in the international joint NEA observation activities organized by IWAN.

In 2021, CARDC, as a co-organizer, participated in the organization of the 7th International Planetary Defense Conference (IPDC), which was also the first time that China participated in the organization of the IPDC.

In 2022, A group of graduate students of NSSC won the graduate student grant of the 8th IPDC through serious professional review, and was invited to present the study on the conference.

In terms of science popularization, NSSC^[20], PMO and other organizations have created a large number of science popularization works. A special WeChat platform "Planetary Defense and Utilization" has been established to spread science popularization works and news related to planetary defense.

8 Conclusion

In the past few years, China's planetary defense has made rapid progress. Chinese scholars have successfully held the first China Conference on Planetary Defense, attracting more and more researchers to engage in planetary defense research. The Chinese government announced to build an NEA defense system and planned

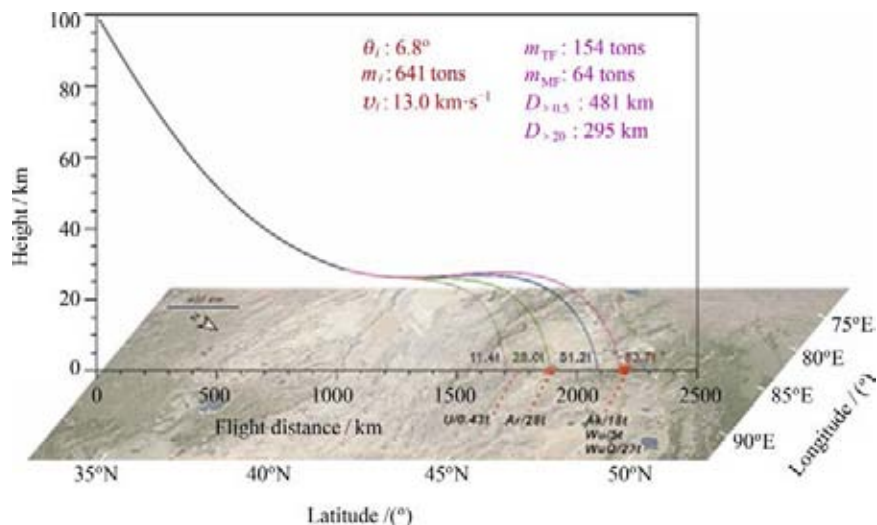


Fig. 5 Skipping-like trajectory of Aletai's meteorite (Source: Science Advances)

the implementation of the on-orbit demonstration mission of NEA defense. In terms of monitoring and warning, world-class optical observation site has been found, new observatories will soon be put into operation, and innovative space-based monitoring and warning missions have been proposed; In the aspect of on-orbit defense technology, the applicable scenarios of typical on-orbit defense technologies are analyzed, and new concepts on-orbit defense means are proposed; In the aspect of hazard assessment, the impact hazard evolution chain is analyzed, and a new mechanism of NEA entry into the atmosphere is analyzed and verified. China has more extensively participated in international planetary defense cooperation and has made remarkable progress in science popularization.

It is expected that in the next five years, China's planetary defense will make greater breakthroughs and make greater contributions to safeguarding the security of the Earth life and building a community with a shared future for mankind

References

- [1] BOTTKE W, VOKROUHLICKÝ D, NESVORNÝ D. An asteroid breakup 160 Myr ago as the probable source of the K/T impactor[J]. *Nature*, 2007, **449**: 48-53
- [2] BROWN P, ASSINK J, ASTIZ L, *et al.* A 500-kiloton airburst over Chelyabinsk and an enhanced hazard from small impactors[J]. *Nature*, 2013, **503**(7475): 238-241
- [3] ROMANA Kofler, GERHARD Drolshagen, *et al.* International coordination on planetary defence: the work of the IAWN and the SMPAG[J]. *Acta Astronautica*, 2019, **156**: 409-415
- [4] GONG Zizheng, LI Ming, *et al.* The frontier science and key technologies of asteroid monitoring and early warning, security defense and resource utilization[J]. *Chinese Science Bulletin*, 2020, **65**(05): 346-372 (龚自正, 李明, 陈川, 赵长印. 小行星监测预警、安全防护和资源利用的前沿科学问题及关键技术[J]. *科学通报*, 2020, **65**(05): 346-372)
- [5] LIU Huigen, ZHAO Haibin, ZHOU Jilin. Survey, defence and resource development of NEO[J]. *Chinese Science Bulletin*, 2020, **65**(09): 757-763 (刘慧根, 赵海斌, 周济林. 近地小天体调查、防御与开发[J]. *科学通报*, 2020, **65**(09): 757-763)
- [6] WU Weiren, GONG Zizheng, *et al.* Response to risk of Near-Earth asteroid impact[J]. *Strategic Study of CAE*, 2022, **24**(02): 140-151 (吴伟仁, 龚自正, 唐玉华, 张品亮. 近地小行星撞击风险应对战略研究[J]. *中国工程科学*, 2022, **24**(02): 140-151)
- [7] WANG Xintao, ZHENG Jianhua, LI Mingtao, *et al.* Warning of asteroids approaching Earth from the sunward direction using two Earth-leading heliocentric orbiting telescopes[J]. *Icarus*, 2022, **377**: 114906
- [8] YANG Xu, ZHAO Kexin, GAN Qingbo, *et al.* Analysis of ground-based and space-based optical observation system warning capability of Near-Earth asteroids[J]. *Transactions of Beijing Institute of Technology*, 2021, **41**(12): 1307-1313 (杨旭, 赵柯昕, 甘庆波, 等. 近地小行星天地基光学监测系统预警能力分析[J]. *北京理工大学学报*, 2021, **41**(12): 1307-1313)
- [9] LI Mingtao, WANG Yirui, *et al.* Enhanced Kinetic impactor for deflecting large potentially hazardous asteroids via maneuvering space rocks[J]. *Scientific Reports*, 2020, **10**: 8506
- [10] WANG Yirui, LI Mingtao, *et al.* Assembled kinetic impactor for deflecting asteroids by combining the spacecraft with the launch vehicle upper stage[J]. *Icarus*, 2021, **368**: 114596
- [11] SONG Guangming, WU Qiang, *et al.* Advances on Mission Analysis and Design Software for Active Planetary Defense Against Near Earth Asteroids[J]. *Space Debris Research*, 2021, **21**(02): 27-34 (宋光明, 武强, 陈川, 等. 国外近地小行星在轨处置任务分析与设计软件研究进展[J]. *空间碎片研究*, 2021, **21**(02): 27-34)
- [12] LI Yi, CHEN Hong, *et al.* A method to improve interception efficiency in the defense against near-Earth asteroids[J]. *Spacecraft Environment Engineering*, 2017, **34**(06): 585-592 (李毅, 陈鸿, 兰胜威, 任磊生, 柳森. 一种提升近地小行星防御中拦截效率的方法[J]. *航天器环境工程*, 2017, **34**(06): 585-592)
- [13] LI Tao, QIN Jingui, *et al.* Optimal interception orbit analysis in the kinetic impact of near Earth asteroids[J]. *Space Debris Research*, 2021, **21**(04): 49-54 (李涛, 覃金贵, 任磊生, 李毅. 近地小行星动能撞击的最优撞击方案分析[J]. *空间碎片研究*, 2021, **21**(04): 49-54)
- [14] GENG Shujuan, ZHOU Binghong, Li Mingtao. On the capture of small stony asteroids into the Earth's orbit by atmospheric grazing[J]. *Monthly Notices of the Royal Astronomical Society*, 2021, **507**: 4661-4668
- [15] LI Ye, LI Bin, *et al.* A unique stone skipping-like trajectory of asteroid Aletai[J]. *Science Advances*, 2022, **8**: 25
- [16] DANG Leining, LIU Sen, BAI Zhiyong, SHI Yilei. Sensitivity research on models of Earth entry and impact effects by asteroids[J]. *Chinese Journal of Theoretical and Applied Mechanics*, 2021, **53**(01): 278-292 (党雷宁, 柳森, 白智勇, 石义雷. 小行星进入与撞击效应评估模型敏感性研究[J]. *力学学报*, 2021, **53**(01): 278-292)
- [17] DANG Leining, LIANG Shi-chang, *et al.* analysis on earth entry process and influence on ground of songyuan meteor[J]. *Space Debris Research*, 2021, **21**(04): 62-71 (党雷宁, 梁世昌, 黄洁, 柳森. 吉林松原流星进入大气层过程及对地面的影响分析[J]. *空间碎片研究*, 2021, **21**(04): 62-71)
- [18] REN Jiankang, ZHANG Qingming, *et al.* Numerical simulation of Yilan crater formation process[J/OL]. *Explosion and Shock Waves*: 1-12 (任健康, 张庆明, 刘文近, 等. 依兰陨石坑形成过程数值模拟研究[J/OL]. *爆炸与冲击*: 1-12)
- [19] LIU Wenjin, ZHANG Qingming, *et al.* A review of the models of near-Earth object impact cratering on Earth[J]. *Explosion and Shock Waves*, 2021, **41**(12): 119-134. 刘文近, 张庆明, 马晓荷, 等. 近地小天体对地撞击成坑模型研究进展[J]. *爆炸与冲击*, 2021, **41**(12): 119-134
- [20] LI Mingtao. 2016 HO₃ asteroid may be the "little moon" of the Earth[N]. *Science and Technology Daily*, 2021-11-23(008) (李明涛. 2016 HO₃ 小行星或是地球的“小月亮”[N]. *科技日报*, 2021-11-23(008))

Progress of Radiation Belt Exploration by a Constellation of Small Satellites TGCSS/SGRB, COSPAR

WU Ji, YANG Xiaochao, DAI Lei

National Space Science Center, Chinese Academy of Sciences, Beijing 100190

Abstract

A Constellation of Radiation Belt Survey (CORBES) program is proposed by the Sub-Group on Radiation Belt (SGRB) of TGCSS, COSPAR. The CORBES mission is expected to have a constellation of 10-plus small/ Cube-Sats to take an ultra-fast survey of the Earth's radiation belt. The general science goal for CORBES is to investigate two groups of physical processes related to the radiation belts: wave-particle interactions and radial transport. This mission is an international multilateral cooperation mission, an open and sharing data policy will be implemented. The data set of observations will be shared within the contributors of the constellation and the broad research community at large, then would be of great use for comprehensively understanding the dynamics of magnetospheric energetic populations and developing more standard models of the Earth's radiation belts. Furthermore, from the application perspective, the ultra-fast survey of the radiation belt could serve as an important facility for monitoring space weather of the Earth as well.

Key words

Radiation belts, Ultra-fast survey, Constellation

1 Introduction

In 2017, Committee On SPACe Research (COSPAR), which devote to bringing the nations of the world together to undertake creative space endeavors for a long time, assembled a group of researchers, managers, and policy makers to examine the question of how small satellites might be used to advance technology, science research, and space applications. The two-year COSPAR study^[1] laid out a compelling scientific roadmap to give specific guidance concerning small spacecraft utilization.

To develop a performable plan for implementing the recommendations of the COSPAR Strategic Action Plan and the COSPAR Scientific Roadmap on Small Satel-

lites for Space Science, the Task Group on establishing a Constellation of Small Satellites (TGCSS) was established by COSPAR in late 2019 and chaired by Daniel Baker. In pursuit of these objectives, the COSPAR leadership team also drew guidance from the organization's Scientific Roadmap:

“COSPAR should facilitate a process whereby international teams can come together to define science goals and rules for a modular, international small satellite constellation. The role of COSPAR is one of an honest broker, coordinating not funding. The results of an international effort to build small satellite constellations would be valuable for all participants and would be more valuable than the individual parts. COSPAR is in a

position to help foster this international collaboration, creating a precedent for setting up community science in a very open way.”

The TGCSS aims to encourage international cooperation and make a meaningful contribution to solutions of the problems that are important to humanity. The subsequent work of TGCSS has emphasized the need to address several program elements, *e.g.* ionosphere/thermosphere, radiation belt, solar energetic particle events, atmospheric remote sensing and also various other operational aspects such as ground station design, radio licensing, access to space, and data management and distribution.

For this purpose, a sub-group of TGCSS, Sub-Group on Radiation Belt (SGRB) was established to deal with radiation belt measurements. SGRB is chaired by Ji Wu, a member of TGCSS. SGRB members include Ji Wu from National Space Science Center (NSSC) of China, Lei Dai from NSSC of China, Maurizio Falanga from ISSI in Switzerland, Vladimir Kalegaev from Moscow State University of Russia, Wen Li from Boston University of USA, Yoshizumi Miyoshi from Nagoya University of Japan, Rumi Nakamura from Space Research Institute (IWF/OEAW) in Austria, Minna Palmroth from the University of Helsinki in Finland, Anatoli Petrukovich from Space Research Institute (IKI) of Russia, and Mohammad Ebrahimi Seyedabadi from APSCO. Besides, all TGCSS members are invited to join SGRB and participate in its meetings.

SGRB will focus on the implementation of a Small/CubeSats constellation mission for radiation belt exploration. In pursuit of this goal, a proposal of a program called CONstellation of Radiation BELt Survey (CORBES) from China has been presented at TGCSS in July 2021.

2 CORBES Mission

The idea for the CORBES mission is to carry out an ultra-fast survey of the Earth’s radiation belt by a constellation of 10-plus Small/CubeSats. Making use of the multi-satellite constellation, this mission is expected to significantly enhance both time and spatial resolutions to significantly improve the understanding of the Earth’s radiation belt dynamics.

The orbit of CORBES is designed to be near the equatorial plane and with an apogee altitude of about 7 Earth radius or similar to GTO (see Fig. 1). The lifetime

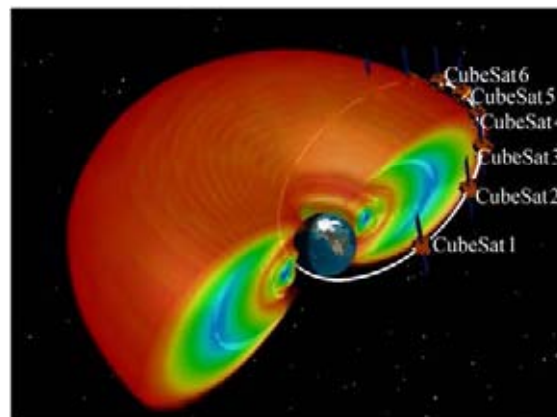


Fig. 1 A constellation of 10 (or more) CubeSats to probe energetic particles of the radiation belt

of each Small/CubeSat is expected to be at least one year to limit the cost of them.

CORBES is an international multilateral cooperation mission, multiple institute/university/industry from Asia, Europe and America are potential participants in this mission. It is proposed that, each participating institute/university/industry should contribute one or several satellites to form the constellation. Each Small/CubeSat is equipped with baseline instruments to meet the primary science goal of CORBES, but not limited to these instruments. An open and sharing data policy will be implemented in CORBES mission, and the data set of observations will be shared within the contributors of the constellation and the broad research community at large.

3 CORBES Science Objectives and Instrument Requirements

The science goal of CORBES is to carry out a survey over outer radiation belt in both high temporal and spatial resolutions. It will provide high-time resolution measurements of energetic electron fluxes, the geomagnetic field and plasma waves, then investigate the physical processes responsible for the fast dynamics of the Earth’s outer radiation belt. Principal (and incomplete) targeted physical processes for investigation by CORBES are listed briefly as follows (schematically shown in Fig. 2)^[2]. (1) Local resonant interactions between electron and Very Low Frequency (VLF) waves such as the whistler-mode waves that are produced by unstable plasma distributions arising during storms (see Fig. 3)^[3,4].

(2) Acceleration and transport of radiation belt electrons by radial diffusion that is driven by Ultralow-Frequency (ULF) magnetospheric disturbances^[3,5].

(3) Sudden, intense electron radial transport events such as shock-induced injection, substorm injection, storm convection caused by solar eruptions that hit the magnetosphere and subsequent large-scale reconfiguration of the electric and magnetic fields (see Fig. 4)^[6].

(4) Losses of electrons by precipitation into the atmosphere attributed to the scattering by a variety of waves such as whistler hiss and Electromagnetic Ion Cyclotron (EMIC) waves, as well as the magnetopause

shadowing that causes electrons to escape from the magnetosphere into the solar wind due to movement of the magnetopause.

Preliminary requirements on baseline instruments of CORBES can be deduced from the general science goal. Two types of instruments are considered primary for the program: the magnetometers including Magnetometer (MAG) and Search Coil Wave Detector (SCWD), which are required to measure the magnetic field, shock-induced pulse, substorm dipolarization, and magnetospheric plasma waves such as ULF waves, EMIC waves, whistler-mode chorus waves, plasmaspheric hiss, magnetosonic waves, as well as the High Energy Electron Detector (HEED), which is required to detect energetic electrons trapped by the geomagnetic field.

Proposed performance parameters for baseline instruments of CORBES have been presented by NSSC and agreed at the SGRB meeting. MAG: the measurement range is ± 40000 nT; the dynamic range is > 80000 nT; the frequency response is Dc-10Hz; the resolution is better than 0.1 nT; the accuracy is 1–2 nT at Apogee. SCWD: the noise is $30 \text{ fT/Hz}^{1/2}$ @1kHz; the frequency response is 10–10 kHz. HEED: FOV is about 30° ; the energy range is 0.1–4 MeV, which is logarithmically divided into 20 equal channels.

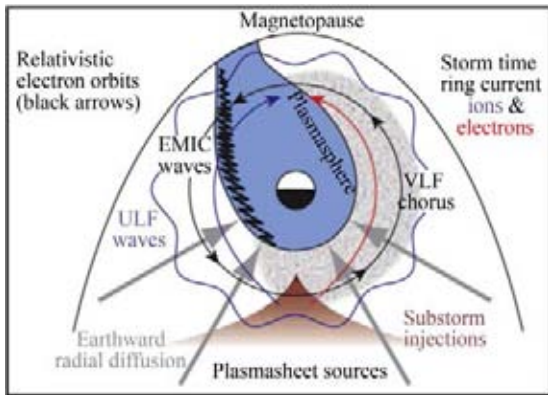


Fig. 2 Schematic for low-frequency plasma waves and wave-particle interactions in the magnetosphere^[2]

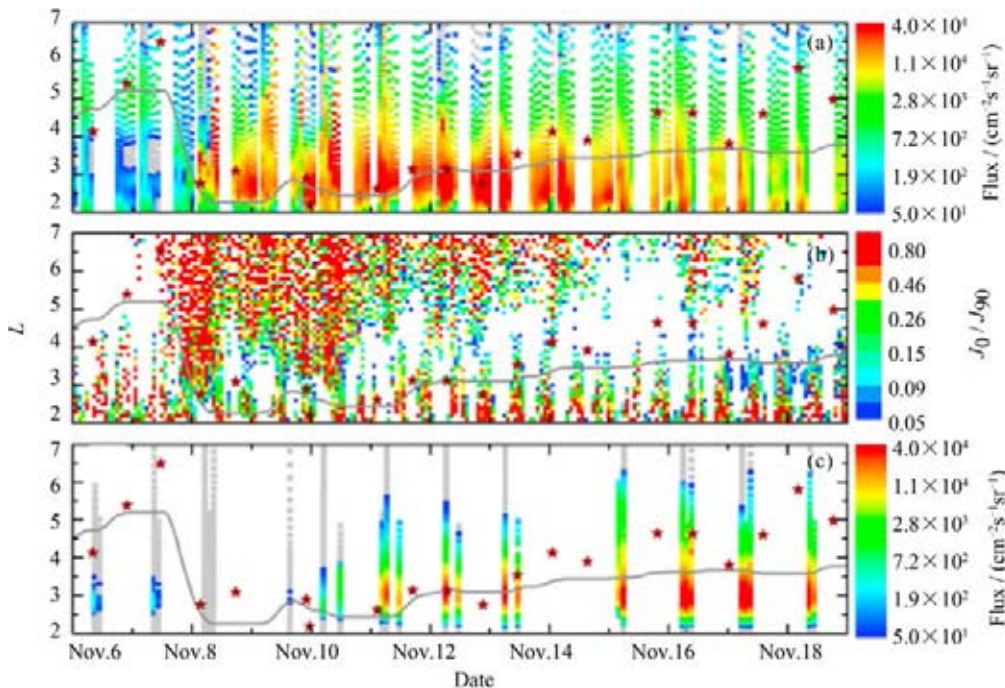


Fig. 3 Local resonant interactions between electron and VLF waves^[4] (L is the geocentric distance in Earth radii of the location where the corresponding magnetic field line crosses the geomagnetic equator)

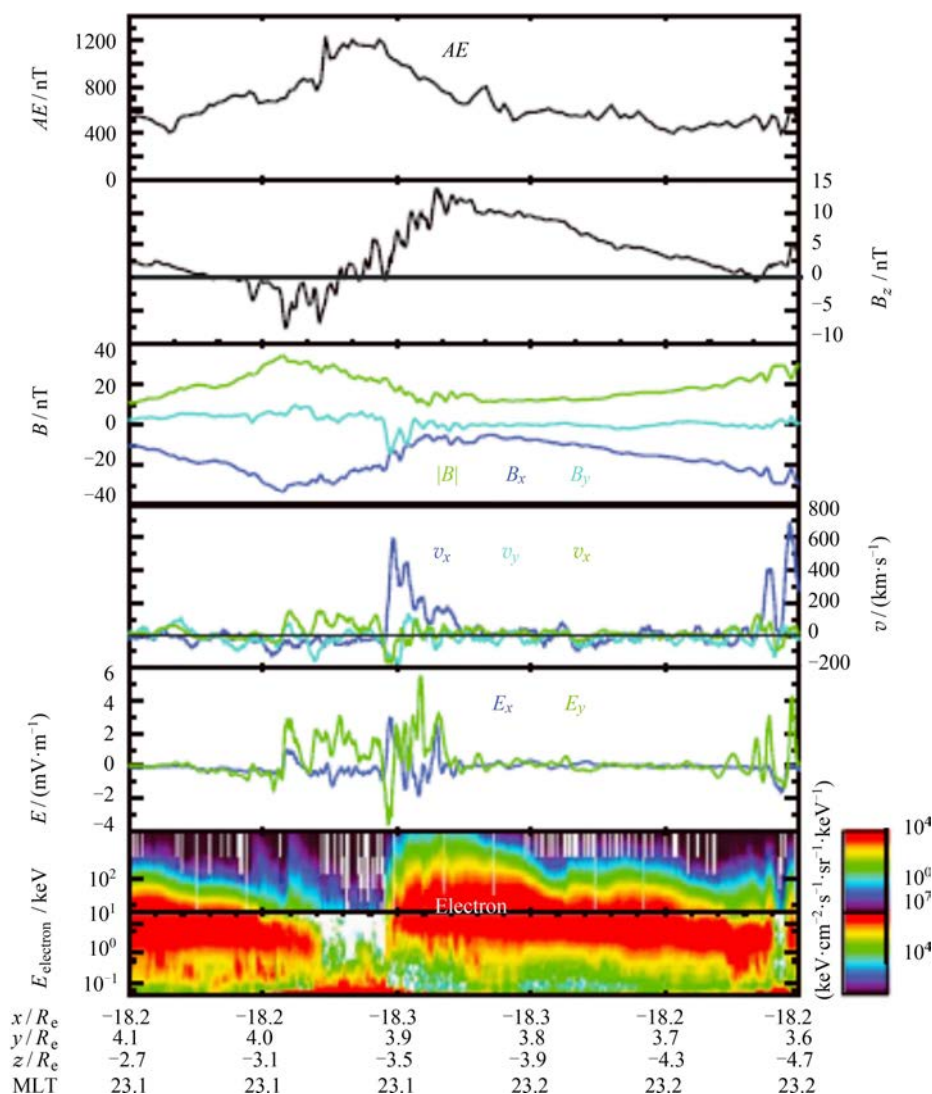


Fig. 4 Radial transport processes of energetic electrons in the magnetosphere^[6]

4 SGRB Science Activities on CORBES

Since the establishment of SGRB, there have been intensive discussions on the implementation of CORBES. More than twenty reports from potential participants have been invited to be presented in SGRB meetings. The profile, science objectives and instrument requirements of CORBES mission have been discussed in detail and preliminarily defined, and intensive discussions on science payloads, the CubeSat constellation, the ground support system, the launcher and CubeSat deployer for the CORBES project have been carried out. A possible AIT and launch approach to avoid the ITAR restrictions has been proposed as well.

A commercial company of launcher called CAS Space has shown their willingness to provide a free launch opportunity and CubeSat separations mechanism for CORBES. NSSC and Peking University (PKU) also showed their willingness to provide support for science operations. Several research institutes where the SGRB members come from, PKU, Beihang University (BU), Institute of Space and Astronautical Science (ISAS) Japan Aerospace Exploration Agency, Kanazawa University (KU) and Paul Scherrer Institute (PSI) have also presented their capabilities of one or all of baseline instruments (MAG, SCWD and HEED). Innovation Academy of Microsatellites of CAS (IAMC), Shanghai Jiao Tong University (SJTU), Harbin Institute of Technology (HIT), Kyushu Institute of Technology (KIT), and two commercial companies ZeroG and Cosats, are willing to participate in CORBES program

willing to participate in CORBES program and provide one or two CubeSats. National Institute for Space Research (INPE), Brazil expressed the willingness to participate in CORBES program and would provide CubeSats, ground support services for the mission.

CAS Space, the commercial company that will provide the free ride, has the ability to launch their rocket from a sea launch pad. In that case, the final integration of all CORBES satellites could be considered to carry out outside of China, for example in Singapore. While the sea launch pad sails to the launch location in the Pacific, it could stop at a harbor near the final integration site. In this way, the participants who had the ITAR or similar problems could ship their satellites to this location instead of China.

5 Summary

The Task Group on establishing a Constellation of Small Satellites (TGCSS) was established by COSPAR to develop an actionable plan for implementing the recommendations of the COSPAR Strategic Action Plan and the COSPAR Scientific Road map on Small Satellites for Space Science. To address the Earth's radiation belt program, one of several programs addressed by the TGCSS, CORBES program from China was proposed in 2021 by the Sub-Group on Radiation Belt (SGRB) of TGCSS.

The CORBES mission is expected to have a constellation of 10-plus small/CubeSats to take an ultra-fast survey of the Earth's radiation belt. The general science goal for CORBES is to investigate two groups of physical processes related to the radiation belts: wave-particle interactions and radial transport. It is proposed that each participating institute/university/industry can contribute one or several payloads/spacecraft to form

the constellation. The data set from CORBES, which shall be shared by the contributors of the constellation and within the broad research community at large, would be of great use for comprehensively understanding the dynamics of magnetospheric energetic populations and developing a more standard model of the Earth's radiation belts. Furthermore, from the application perspective, the ultra-fast survey of the radiation belt could be an important facility for monitoring the space weather of Earth as well.

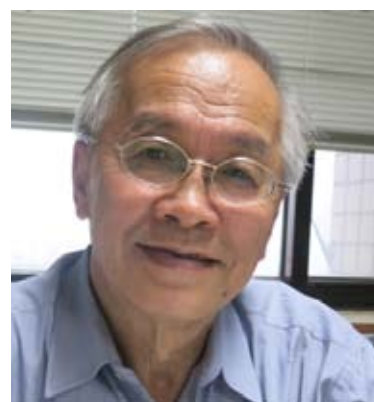
The principle of this initiative is based on a no-money exchange policy. However, COSPAR will act as the main role to coordinate the whole process whenever needed. COSPAR will act as a mutual negotiator between participating governments, universities and research institutions.

References

- [1] MILLAN R M, VON STEIGER R, ARIEL M, *et al.* Small satellites for space science: a COSPAR scientific roadmap[J]. *Advances in Space Research*, 2019, **64**(8): 1466-1517
- [2] REEVES G D. Radiation belt storm probes: a new mission for space weather forecasting[J]. *Space Weather*, 2007, **5**(11): S11002.
- [3] REEVES G D, SPENCE H E, HENDERSON M G, *et al.* Electron acceleration in the heart of the Van Allen radiation belts[J]. *Science*, 2013, **341**(6149): 991-994
- [4] YANG X C, NI B B, YU J, *et al.* Unusual refilling of the slot region between the van Allen radiation belts from November 2004 to January 2005[J]. *Journal of Geophysical Research: Space Physics*, 2017, **122**(6): 6255-6270
- [5] YANG X C, ZHU G W, ZHANG X X, *et al.* An unusual long-lived relativistic electron enhancement event excited by sequential CMEs[J]. *Journal of Geophysical Research: Space Physics*, 2014, **119**(11): 9038-9050
- [6] DAI L, WYGANT J R, CATTELL C A, *et al.* Evidence for injection of relativistic electrons into the Earth's outer radiation belt via intense substorm electric fields[J]. *Geophysical Research Letters*, 2014, **41**(4): 1133-1141

Prof. Wing-Huen Ip received the CAS/COSPAR Jeoujang JAW Award in 2020

Professor Wing-Huen Ip, a renowned space scientist, was bestowed the CAS/COSPAR Jeoujang JAW Award in 2020. He was selected as one of the candidates by the COSPAR Award Committee and then passed the review organized by the Chinese Academy of Sciences. Due to his significant achievements in planetary science and related missions, Professor Ip is the most worthy awardee.



Professor Wing-Huen Ip has made significant contributions to deep-space exploration, including comets and outer Planets. In particular, his contribution to the CASSINI-Huygens mission was recognized as pioneering and non-replaceable. He is also a pioneer in the study of the interrelation of planetesimals with Uranus and Neptune in the early solar system and in satellite-ring-magnetosphere interaction.

The Jeoujang Jaw Award, bestowed jointly by the Chinese Academy of Sciences and COSPAR, recognizes scientists who have made distinguished pioneering contributions to promoting space research, establishing new space science research branches and founding new exploration programs.



Secretariat Contact:

LI Xiaoyu, XU Yongjian

**CN-COSPAR Secretariat c/o NSSC, No.1 Nanertiao,
Zhongguancun, 100190, Beijing, China**

Tel: 86-10-6258 6404

Fax: 86-10-6263 2257

E-mail: xuyongjian@nssc.ac.cn